RL-79-036

Rutherford Laboratory
CHILTON, DIDCOT, OXON, OX11 0QX

RL-79-036

Science Research Council
Central Laser Facility

Annual Report to the
Laser Facility Committee 1979

Laser Division
Rutherford Laboratory

RL-79-036

GENERAL INDEX

SCIENCE RESEARCH COUNCIL

CENTRAL LASER FACILITY

ANNUAL REPORT TO THE LASER FACILITY COMMITTEE, 1979

Preface

The report covers the work done at the Central Laser Facility, Rutherford Laboratory during the year preceding 31 March 1979. It is arranged in eight chapters based on the scientific group structure adopted a year ago and described in the previous report. Publications based on work done at, or in conjunction with, the Facility are listed in an appendix.

The titles of the scientific groups, the names of their Chairmen and secretaries, and the time allocated to each group are listed in the table below. The success of the programme owes a very great deal to the hard work of the individuals listed together with the scientific programme coordinator, Dr M H Key. There has been a steady increase in demand for glass laser time during the year so that the ratio of requested to allocated time has fallen. Averaged over the year as a whole the ratio of time requested by the experimental user groups to time allocated was 0.34. It is likely that this ratio will fall further during the coming year when the major part of the current upgrade of the glass laser and target areas will be undertaken. Preliminary work on this upgrade, eg the relocation of the two beam target chamber and tests on phosphate glass, is described in Chapter 1.

Apart from the completion of a building extension to allow the upgrading of the glass laser referred to in the previous paragraph the most important development in the Laboratory's facilities has been the completion of the electron beam generator described in

Chapter 2. During the coming year this will be made available to University users for research on high power gas laser systems on a similar basis to that adopted for the glass laser and an "E-beam Programme Committee" is being formed.

Chapters 3 to 7 inclusive describe the work of the experimental groups using the glass laser facility and chapter 8 the work of the theory group. Group membership has grown slightly during the year and the number of individuals, experimentalists and theorists, associated with the Facility now exceeds one hundred. Significant progress has been made by all groups: in Xray spectroscopy and the development of Xray diagnostic techniques, in the study of harmonic emission from laser heated plasmas, magnetic field generation, transport by hot electrons and in a number of other fields. Perhaps most striking has been the growth in work on ablative compression (chapter 5) using the Xray backlighting technique first described in last year's report. There has also been a significant increase in the amount of theoretical work in the Universities associated with the Facility and within the Laboratory ranging from energy deposition by relativistic electrons in gases to the development of a sophisticated particle-in-cell code to describe laser-plasma interactions.

A F Gibson
31 March 1979

GLASS LASER SCIENTIFIC PROGRAMME AND SCHEDULING COMMITTEE

SCIENTIFIC GROUPS

Group Title (Membership)	Chairman	Secretary	Time Allocated during year (wks)
Laser-Plasma Interactions (43)	Mr T P Hughes Essex University	Dr D J Nicholas	10
Transport & Particle Emission (42)	Dr J Kilkenny Imperial College	Mr W Toner	10
Atomic & Radiation Physics (25)	Dr B C Fawcett ARD	Dr R G Evans	5
XUV Lasers (25)	Dr N J Peacock AEA, Culham	Dr I N Ross	2
Ablative Compression (40)	Dr T A Hall Essex University Professor M G Haines Imperial College	Dr P T Rumsby	8
Facility Development (17)	Dr P R Williams Rutherford Laboratory	Mr J E Boon	Development 9 Maintenance 8
Theory & Computational Modelling (32)	Prof M G Haines Imperial College Prof T J M Boyd Univ Coll of N Wales	Dr C Webb	-

CHAPTER 1 GLASS LASER FACILITY DEVELOPMENT

INDEX

CHAPTER EDITOR J E Boon

CONTRIBUTORS J E Boon, A J Cole, L Cooke, P Gottfeldt, J D Kilkenny, C L S Lewis, J G Lunney, D J Nicholas, G M Parker, A Raven, I N Ross, P T Rumsby, W T Toner, J M Ward, M S White, P R Williams

CHAPTER 1 GLASS LASER FACILITY DEVELOPMENT

1.1 Introduction

During 1978/79 routine operation of the glass laser has been interleaved with periods set aside for the development and modification of the facility.

The principal developments have been to increase the range of operating parameters available to the plasma physicists using the laser and to make preparations for the change of active media to phosphate glass during 1979/80. An alternative oscillator and pulse generator has been assembled to allow pulses of 1ns to 2ns to be provided to complement the ~100 ps pulses previously available.

An operations shutdown of five weeks was scheduled over the Christmas period 1978 during which the old target area was completely dismantled and equipment was transferred to the new single/double beam target area in the laser laboratory extension. Some reconfiguration of the output end of the laser was necessary to allow the beam to be transported through ~30 m of beam pipe to new area. Measurements of the stability of the new beam transfer system indicated that the rigidity of the towers feeding the high level transfer pipe presented no problems.

The routine operation of the laser followed the pattern established in the previous year; periods of single and double beam operation were mixed to meet the requirements of the experimental programme. It was usual to allocate one day in each operating week for maintenance of the laser although occasionally this day was given over to experiments to enable a particular series of observations to be completed. More extensive maintenance and change over from one beam to two beams or long pulse to short pulse occupied periods of one week in four.

Some time was devoted during the year to measurements aimed at fuller characterisation of the laser. Measurements were complimented by computational studies using the suite of laser propagation codes which allow geometrical and diffraction effects to be studied. The laser was used for full scale tests of phosphate glass rods and discs prior to the purchasing exercise which took place at the end of the review year.

Considerable effort was devoted during the year to the design and development of the target areas and associated equipment. The relocation of the single/double beam target area referred to above constituted a major disturbance; in the course of the move the opportunity was taken to make improvements to the beam alignment and focussing systems. New, motorised, lens mounts and target positioners were designed and installed and a much improved TV microscope alignment system was introduced.

Design and procurement of components for the six beam area was well advanced by the end of the period under review. The target chamber was installed and preparation of the beam steering and diagnostic equipment was under way.

The existence of two target areas together with the requirements for probe and backlighting beams has led to a redesign of the supplementary beam generation systems. It is planned to provide a flexible system of supplementary beams to both target areas allowing for the possibility of generating, for instance, short probe pulses synchronised to long (~1ns) target illumination pulses. The design of this system has been started and should be implemented in 1979/80.

Detailed descriptions of the work outlined above follow in the remaining sections of this chapter.

1.2 Glass Laser Physics and Development

1.2.1 Pulse Generator Development

The year's work on pulse generator development has been directed at three main areas:

To provide reliable "long" pulses (duration 1-2 ns) for use with the existing silicate glass laser system.

To be able to provide reliable "short" (∿100 ps) and "long" (1-2 ns) pulses at a wavelength suitable for the phosphate glass amplifier chain, after the conversion and upgrade of May 1979.

To study other methods of pulse generation and selection for future use in the system.

1.2.1(a) Single Longitudinal Mode Q Switched YAG oscillators at 1.064 μm and 1.052 μm

Because of the increasing emphasis in the programme on longer pulse experiments it became necessary to install a pulse generator of nanosecond duration on the laser, a similar generator will be required for the phosphate glass system. After considering several options it was decided to use a single longitudinal single transverse mode Q switched oscillator generating a smooth pulse of duration ∿ 20ns, and then slice out a portion of controlled length using an electro-optic gate.

In the course of developing the pulse generator, passively (dye), actively (Pockels cell) and mixed active/passive Q switched oscillators were investigated together with different etalon configurations to constrain the laser to single longitudinal mode operation. The most reliable generation of smooth unmodulated pulses was attained using a dye (Kodak BON) passive Q switch and a resonant reflector output coupler consisting of a long (150 mm) and a short (5 mm) etalon separated by an intermediate(10 cm) air gap. Neither active nor active/passive Q switching produced smooth pulses reliably, although a feedback controlled active Q switch (1.01) was not tried. (The enhanced mode selectivity inherent in passive Q switching is well known, eg (1.02).

Passive Q switching and the resonant etalon output coupler were incorporated as an option on the Quantel oscillator of the main laser system in August 1978, as described in the next subsection.

For operation after the conversion to phosphate glass, the same passive Q switching and etalon longitudinal mode control was tested at 1.052 μm in the J K Lasers prism tuned YAG oscillator. When setting up the internal 150 mm etalon in resonance with the 5mm output etalon, great care was required to avoid tuning onto the stronger 1.064 μm line. However when the resonant reflector was correctly aligned, smooth single mode Q switched pulses were obtained. The available output energy was similar to the 1.064 μm case - 5 to 7 mJ depending on the exact conditions. The pulse duration at 1.052 μm was longer, because a lower concentration dye was required for Q switching the lower gain 1.052 μm line. Typical pulse durations were 40-50ns (fwhm) in the normal operating range, compared with 10-30 ns for the 1.064 μm pulses.

1.2.1(b) 1.064 μm Long Pulse Generator for the Main Laser

After three successful long pulse runs during the year, most of the initial problems were overcome, and pulses of 1.7 ns (fwhm) duration were routinely available for target experiments. The oscillator bench arrangement used is shown in Fig.1.01. The one Quantel 6 mm YAG oscillator was operated either Q switched or mode locked as selected by the positions of the stacked plate polarizer, long etalon, and dye cell. Changing from one cavity to another could be accomplished without realignment. The 20 ns (FWHM) 6 mJ Q switched pulse was first preamplified to about 50 mJ then passed through the Electro Optic Developments Ltd pulse slicer which chopped out a 1.7 ns duration spike from the pulse peak. After further preamplification the pulse rejoined the common path through the dye cell and double passed 16 mm glass rod amplifier. Up to 230 mJ were routinely delivered through the spatial filter pinhole to the main amplifier chain. The prepulse, caused by the leakage of the remainder of the Q switched pulse, was very low being 10^{-4} in power after pulse slicer, 10^{-6} after the oscillator bench dye cell, and 10^{-7} after the amplifier chain dye cell.

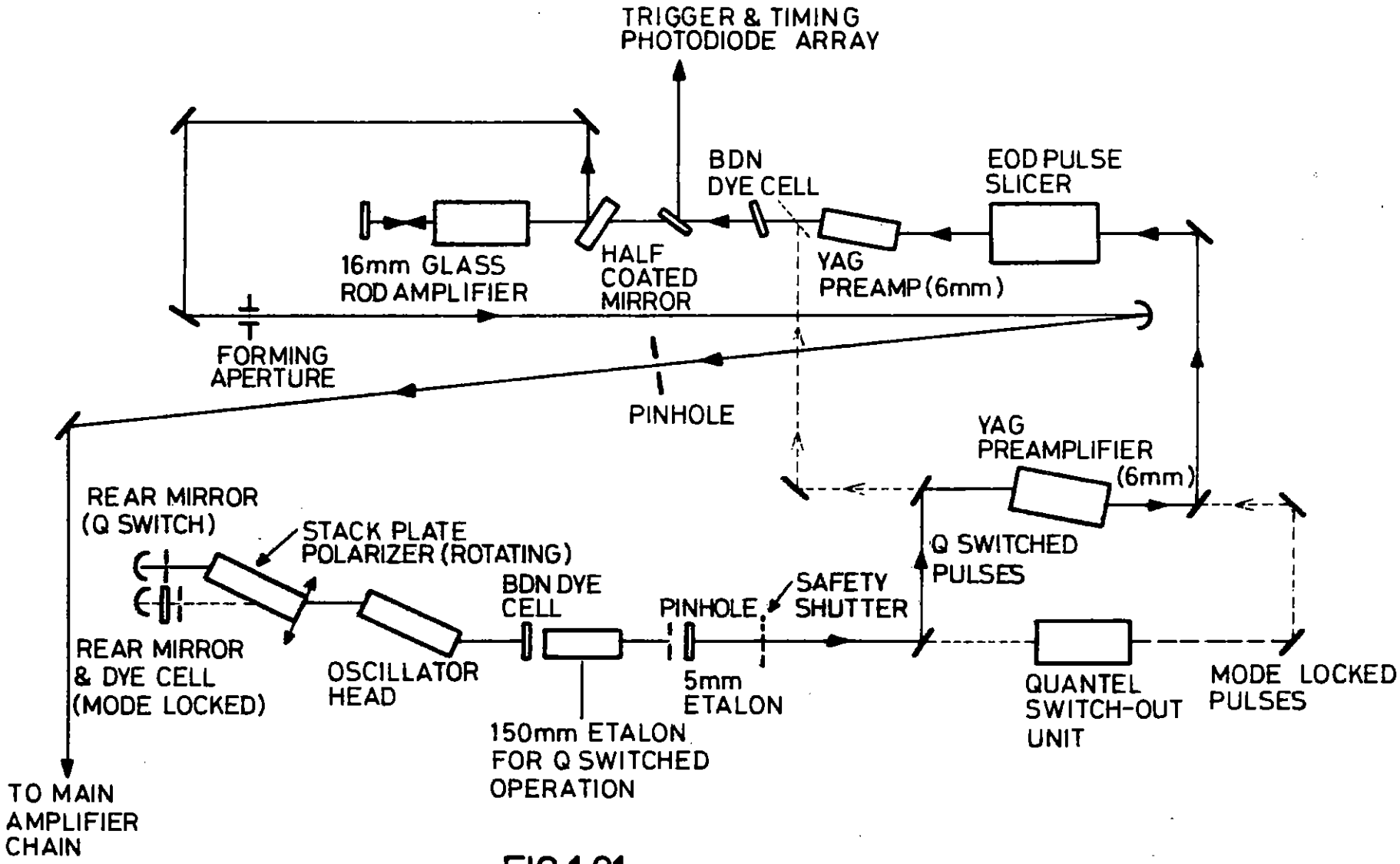
TRIGGER & TIMING
PHOTODIODE ARRAY
BDN
DYE CELL
EOD PULSE
SLICER
16mm GLASS
ROD AMPLIFIER
HALF
COATED
MIRROR
YAG
PREAMP (6mm)
FORMING
APERTURE
PINHOLE
YAG
PREAMPLIFIER
(6mm)
REAR MIRROR
(Q SWITCH)
STACK PLATE
POLARIZER (ROTATING)
Q SWITCHED
PULSES
BDN DYE
CELL
PINHOLE
SAFETY
SHUTTER
REAR MIRROR
& DYE CELL
(MODE LOCKED)
OSCILLATOR
HEAD
5mm
ETALON
QUANTEL
SWITCH-OUT
UNIT
MODE LOCKED
PULSES
150mm ETALON
FOR Q SWITCHED
OPERATION
TO MAIN
AMPLIFIER
CHAIN

FIG 1·01

The oscillator was passively Q switched and constrained to single longitudinal mode 1.064 μm output by a resonant output reflector, as described in section (1.2.1(a)). A spatially and temporally smooth pulse was produced, with less than a 1% failure rate of modulated pulses. Once set up the oscillator worked without attention for several weeks at a time.

The pulse selector was constructed from a pair of Pockels cells, driven by a laser-triggered spark gap, between Glan Taylor prisms. For the runs in 1978/79, the system was usually operated in a modified form, using only one Pockels cell with pulse duration controlled by a short circuited stub 1.7 ns.

1.2.1(c) Short Pulse Q Switched Oscillator

An alternative generator of pulses in the several nanosecond range would be a Q switched oscillator with a very short cavity. Although less flexible than a longer pulse oscillator followed by an electro-optic shutter, the short cavity oscillator should be rugged and reliable by virtue of its simplicity, as long as smooth unmodulated single longitudinal mode pulses can be obtained.

A 1.064 μm passively Q switched oscillator was assembled using J K Lasers System 2000 components. Longitudinal mode control was effected by a compact resonant output coupler made up from a $\frac{1}{4}$" thick etalon parallel with the 30% reflectivity output mirror, and separated by a 5 cm air gap. Transverse mode selection was via a 2 mm aperture in the cavity. Two 1 mm thick dye cells containing Kodak BON controlled the Q switching. The cavity round trip time for this particular test was limited to 4.5 ns by mechanical constraints.

This oscillator showed that smooth single mode Q switched pulses were reliably obtainable at energies up to 18 mJ. As the dye concentration was increased the pulse duration decreased to 4.8 ns (fwhm), athough minor low frequency modulation (depth about 10%) was apparent on pulses shorter than 6 ns. No damage problems were encountered in spite of the high circulating power.

It is planned that the work will be continued using a more compact laser head and specially designed components to reduce the cavity round trip time to 2-3 ns.

1.2.1(d) Pulse Duration Control of the 1.052 μm Passively Mode Locked YAG Oscillator

The pulse duration of a 1.064 μm passively mode locked YAG oscillator is easily controlled by using a variable thickness uncoated etalon as the output coupler. However this simple technique is not applicable at 1.052 μm because a higher coupler reflectivity is required for oscillation on the lower gain line.

The problem was investigated using the J K Lasers tunable YAG oscillator set up for passive 1.052 μm mode locking. The output pulse duration was observed directly using an S1 streak camera. It was found that without any bandwidth control etalons, in a simple 100% + 30% mirror cavity, the laser gave clean 100 ps mode locked pulses. The pulse duration could be stretched very significantly by the simple expedient of inserting a single tilted ultra-cavity etalon. Clean reliable mode locking has been obtained up to 220 ps (fwhm, +20%) with a 6 mm etalon. The use of even thicker etalons will be investigated to establish the full range of pulse durations attainable using the simple passively mode locked 1.052 μm oscillator.

1.2.1(e) Future Work

Pulse generator development in the immediate future will concentrate on actively mode locked oscillators and regenerative amplifiers. Initially an actively mode locked passively Q switched oscillator (1.03), possibly followed by an actively mode locked actively Q switched oscillator (1.04), will be investigated with a view to improving the stability in energy and pulse duration of the single pulse injected into the amplifier chain. The new oscillators will operate at a phosphate-glass compatible wavelength, and the relative merits of YLF, glass and YAG will be studied during the development phase. The achievable performance of regenerative amplifiers will be studied in stretching or compressing the oscillator pulse, and compared with the requirements for the main beam and probe beam pulse durations.

1.2.2 Beam Propagation Studies

Following previous investigations to characterize the laser and hence determine its limits of operation, it has been felt necessary to characterize the propagation of the laser beam so as to (i) provide quantitative information on target irradiation and alignment stability on target (ii) enable improved target irradiation and alignment stability on target (iii) determine the limits of laser operation with respect to damage to target chamber optics.

Three separate studies have provided information on these questions:

(a) Investigation of methods of improving the focussable intensity and alignment stability of the output laser beam.

(b) Direct measurement to relate the standard 'near field' distributions measured at various power levels with the distribution incident on the main beam focussing lenses.

(c) Measurement of the changes in distribution on propagation of the output beam over distances up to 30 metres, the approximate distance from laser output to target chamber in area TA2.

1.2.2(a) A continuous 1.06 μm Nd:YAG laser propagating through the laser system and far field recording arrangement and incident in the best focal plane on an infra-red TV camera has been used to monitor the effect of attempts to improve the beam directionality and focus spot distribution. Three observations were made. Beamtube covering about three quarters of the laser system offered no great improvement. Removal of the air conditioning air flow in the laser room stabilised the distribution. Removal of the disc module nitrogen flow further improved the focus distribution and suggested that the heat exchangers on the nitrogen input are not quite effective enough. Fig.1.02 shows the best focal spot distribution and Fig.1.03 gives a graph of the fraction of the total power transmitted by apertures of different sizes in the best focal plane.

Measures are being taken to overcome the harmful effects of the air conditioning and the disc nitrogen.

1.2.2(b) Currently the 'near-field' recordings shot by shot measure the intensity distribution in a plane equivalent to the entrance to the target chamber. They do not however account for imperfections and nonlinear distortion introduced onto the beam by target area optics.

To ascertain these effects, simultaneous recordings on 12 materials were made in the near field monitor and in a plane immediately following the target window. Good correspondence of the intensity distribution was obtained except that at high power hot spots had a higher peak to average intensity at the target chamber due to self focussing in both the beamsplitter plate and target chamber window. Fig.1.04 shows microdensitometer traces from corresponding high power distributions in laser room and target room. Peak to average was 3.0 and 21.0 respectively showing an increase of a factor 7 due to self focussing in these components. Peak power rose from 11.5 GW/cm^2 to 80 GW/cm^2 through these components resulting in an energy density of 8J/cm^2, above the damage level of current anti reflection coatings. The B-integral of the beamsplitter and target window at 11.5 GW/cm^2 is 0.87 giving an expected increase in peak to average of a factor 2:4. This is well below the factor 7 observed because we are well outside the region of small modulation depth for which the theory applies. A more relevant calculation would be to allow the peak intensity to rise with the growth of B-integrals. Thus for a small element (dl) of the glass plate:-

$$\frac{I + dI}{I} = \exp.dB = \exp KIdl \simeq 1 + KIdl$$

where I = peak power density : K = constant

$$\therefore \frac{dI}{I^2} = Kdl$$

therefore by integration $$\frac{1}{I_{in}} - \frac{1}{I_{out}} = Kl$$

or $$\frac{I_{out}}{I_{in}} = \frac{1}{1-B} \quad \text{where} \quad B = KI_{in}l$$

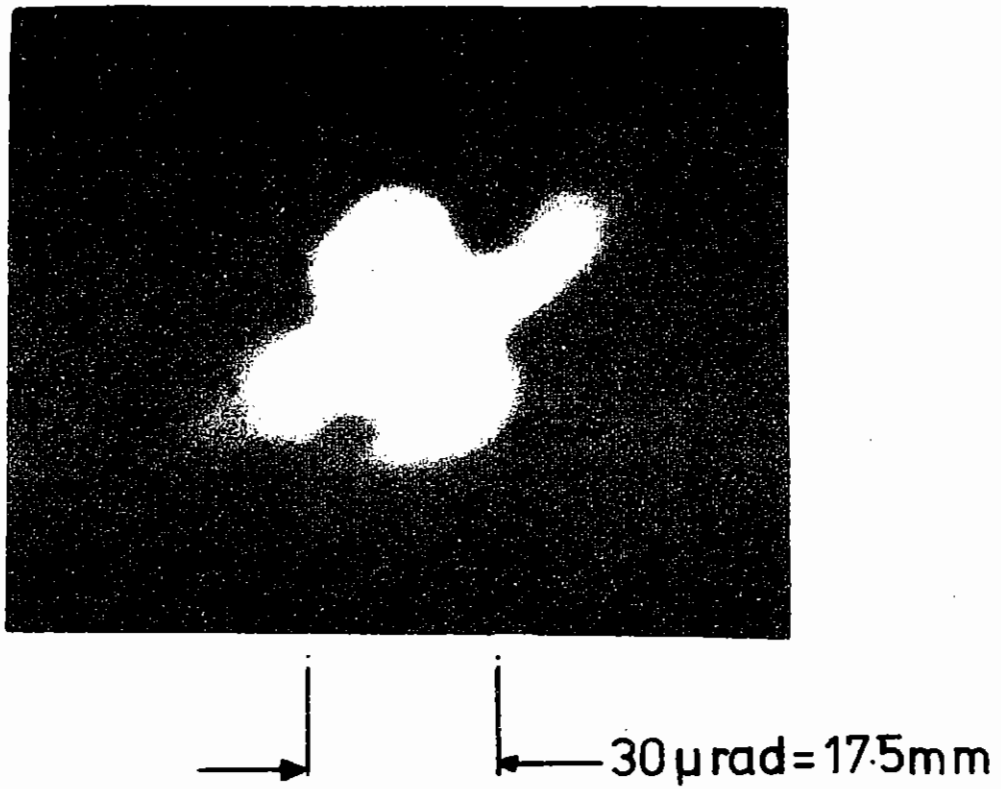

FIGURE 1·02. BEST FOCAL SPOT DISTRIBUTION IN CW ILLUMINATION.

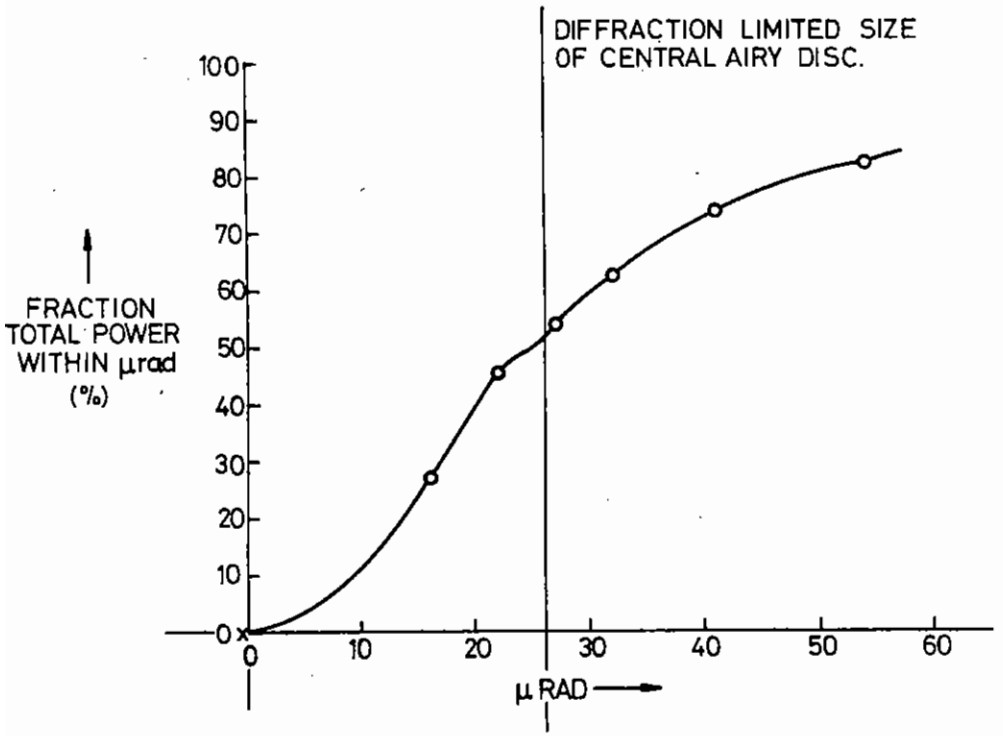

FIG 1·03 DISTRIBUTION OF POWER IN FOCAL PLANE - CW YAG THROUGH QUANTEL. DISCS

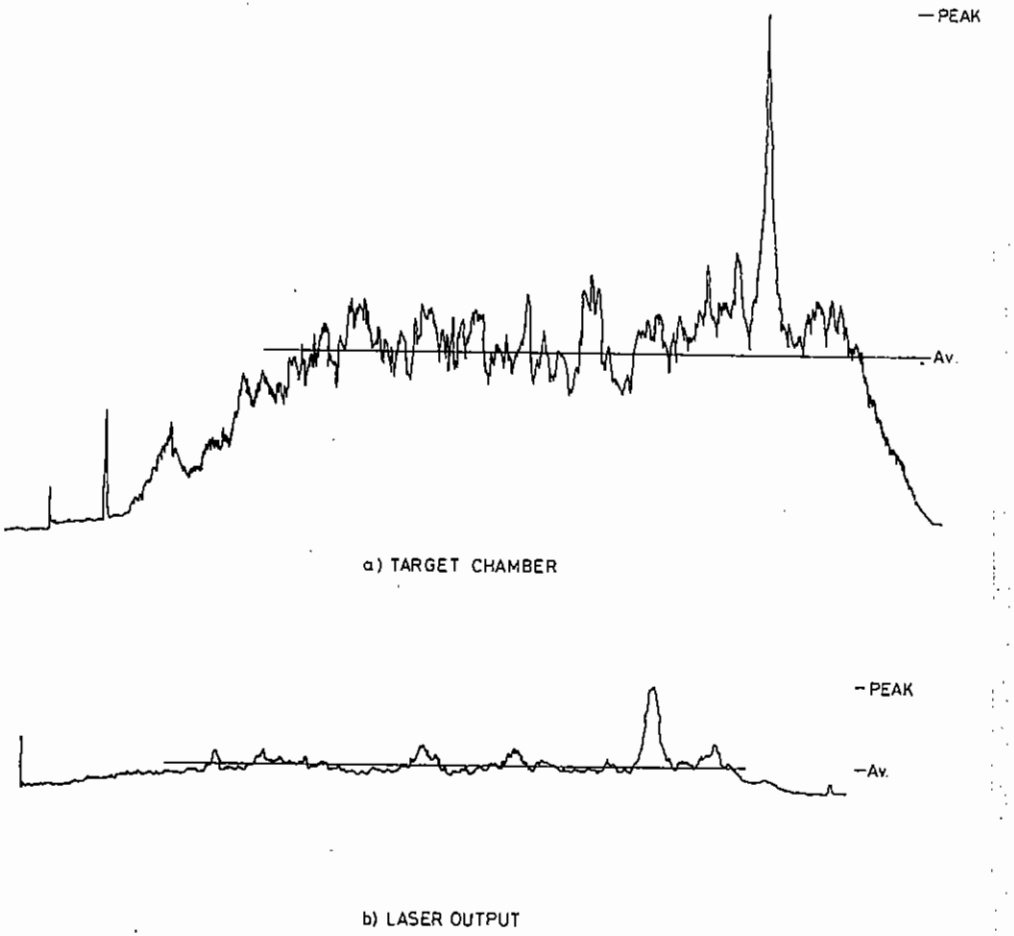

FIGURE 1·04. INTENSITY DISTRIBUTION IN MAIN LASER BEAM

in this case B = 0.87 giving a peak intensity increase by a factor 7.7.

This compares with the experimentally observed factor of 7.

1.2.2(c) Measurements have been made to determine whether or not the output beam is seriously degraded during propagation in air over distances comparable with that between the laser and the new target areas. This distance may be as high as 30m. and it is important to know if the optics in the target areas are more vulnerable now that they are further away. For parallel beams the peak to average intensity was used as the appropriate parameter.

The output pulse was reflected up and down the laser room and IZ recordings made simultaneously at 0m, 15m, and 30m. Fig.1.05 shows beam distributions at low and high power. Two effects are immediately apparent - there is beam deterioration even at low power and this is largely due to air fluctuations -and at high power the size of the intense filaments increases as one would expect. Microdensitometer traces showed that the peak to average intensity increased by a factor 1.7 for a propagation distance of 30m and at 30m the peak to average intensity increased by a factor 1.6 when comparing low and high power.

This preliminary investigation, shows that for the Rutherford system there should be some extra restriction to the operating limits to provide the currently accepted safety margins to target area optics. In particular these restrictions are most severe for low power or 'long pulse' operation due to the effects of air movements. Further tests under improved air conditions should relax this restriction.

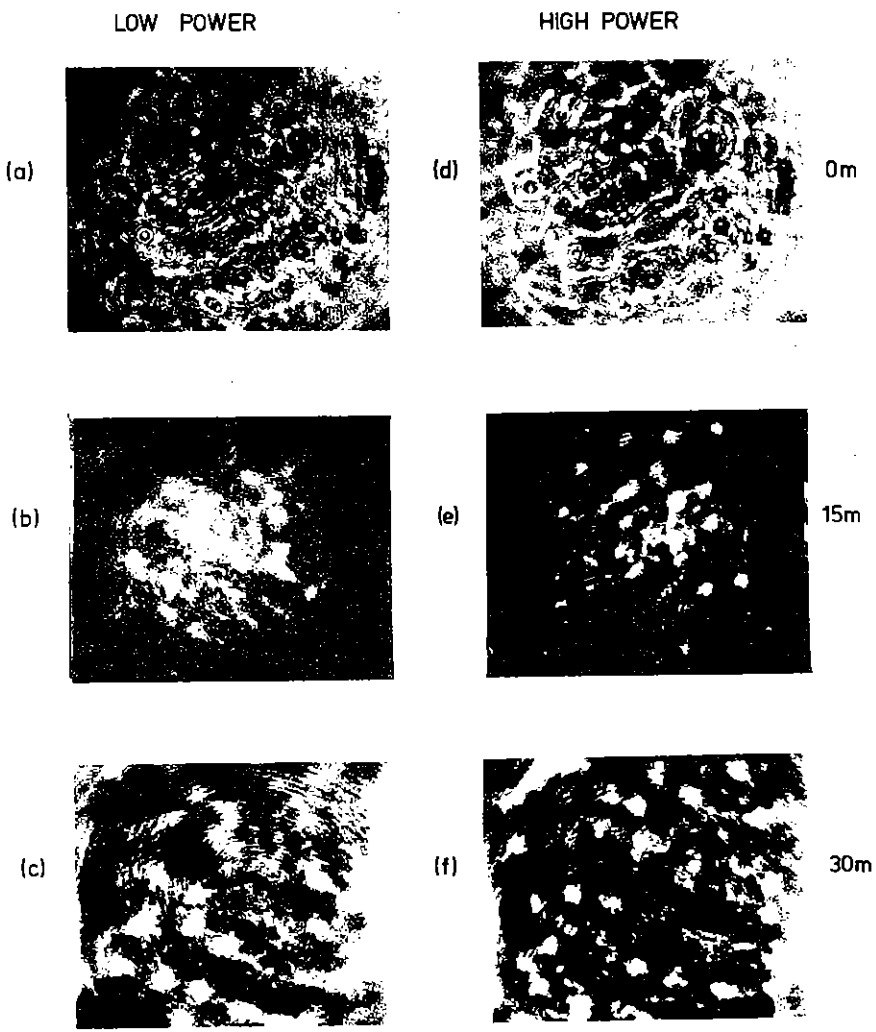

FIG 1.05 BEAM PROPAGATION AT LOW & HIGH POWER.

1.2.3 Harmonic Generation

Due to the need for shorter wavelengths in the experimental programme a second harmonic crystal was purchased and tested for efficient generation of radiation at 0.53 μm. The purpose of the evaluation tests were to measure the efficiency of conversion, the limits set by damage to crystal and cell windows, the angular (and hence temperature) tolerances, and the effects of harmonic conversion on the intensity distribution across the beam.

Fig.1.06 is a diagram of the experimental arrangement. Energy and beam profiles were recorded at both the fundamental and second harmonic. Two in series narrow band reflectors at 1.06 μm proved to be a very effective means of separating the two wavelengths. Fig.1.07 shows graphically the way the conversion efficiency varies with input intensity for the rod driven system and for the rod driver plus double pass discs. Conversion of both short (100 ps) and long (1.7 ns) pulses is shown. We see that efficiencies of 50% were achieved and that the efficiency was greater than 35% over a 3:1 range of intensity and from 6 joules Quantel driver only up to 75 joules for the complete system long pulse. There is a definite correlation between high efficiency and low level of filamentation which explains some of the spread in values. Saturation of the nonlinear process must also contribute to the low increase of efficiency with increasing input intensity. Fig.1.08 shows photographic records of corresponding beam profiles at 1.06 μm and 0.53 μm respectively. The notable aspect is the reduction in depth of modulation on the second harmonic profiles. This demonstrates two effects, the considerable saturation of the nonlinear conversion process and perhaps more important, the effects of double refraction which shears the second harmonic beam with respect to the fundamental and hence requires an essentially constant amplitude and phase over the shear length to retain good conversion efficiency. The beams are sheared by 0.4 mm in the crystal and the scale of the self focus filaments is submillimeter so a reduction in second harmonic efficiency in the region of the filaments would be expected.

Some slight damage to the anti-reflection coatings was sustained for short pulses (100 ps) at fundamental and second harmonics at intensities of more than 30GW/cm^2 and 3GW/cm^2 respectively. Angular setting tolerances of the crystal were large, as expected. The 90% points were at $\pm$1 min arc confirming that temperature stability to only $\pm 2^{o}$C is required.

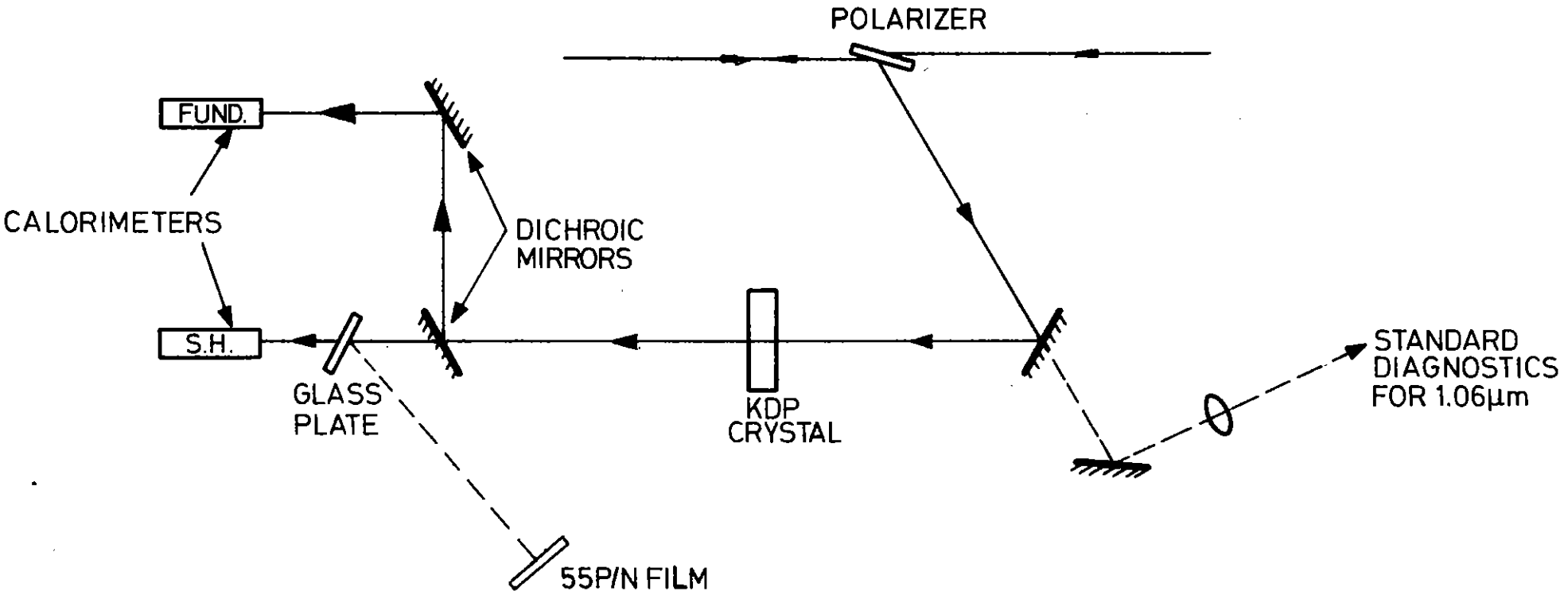

FIGURE 1·06. ARRANGEMENT FOR GENERATION AND MEARSUREMENT OE SECOND HARMONIC.

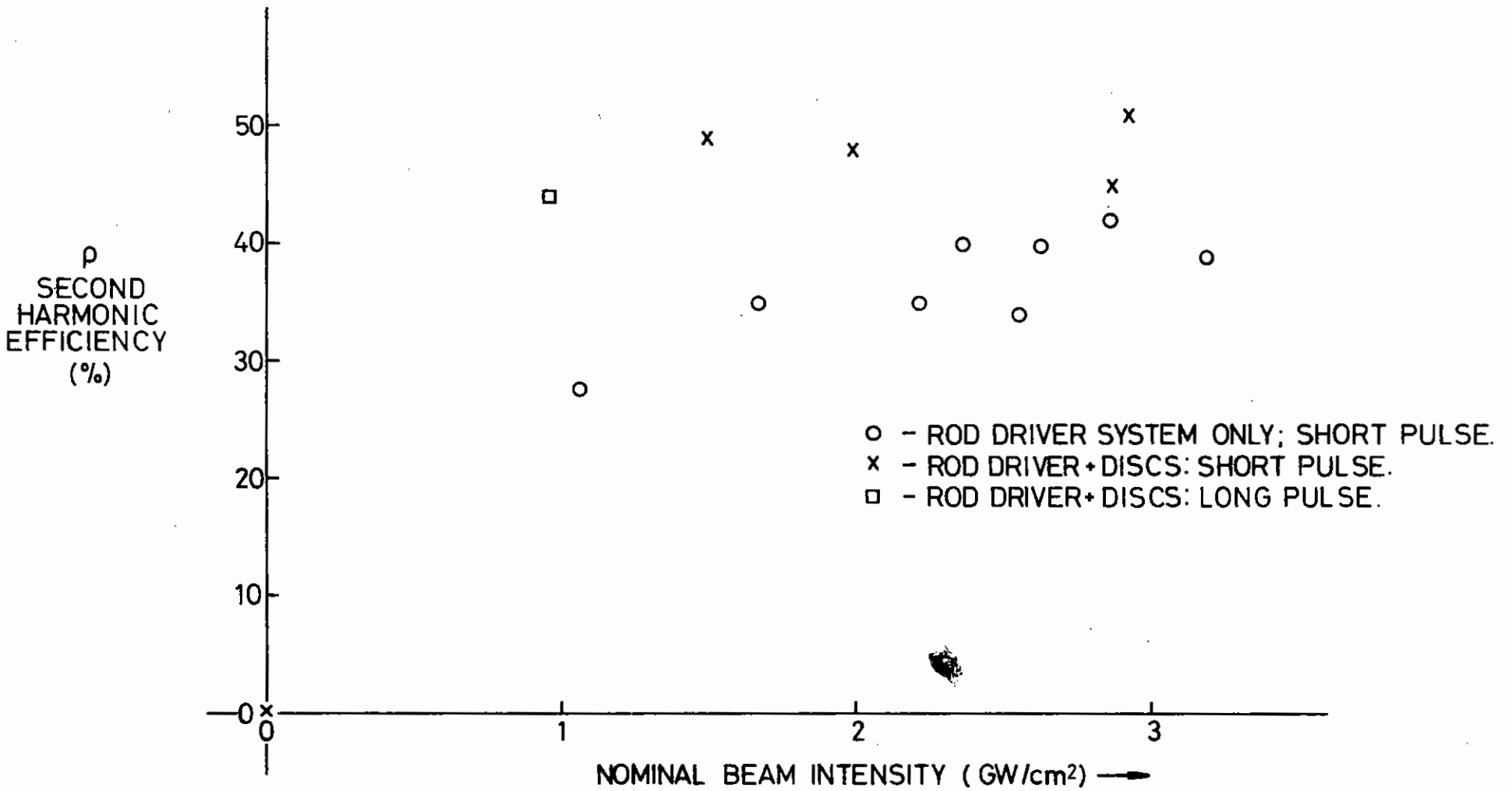

Fig1·07

SECOND HARMONIC GENERATION EFFICIENCY OF INRAD. KDP CRYSTAL.

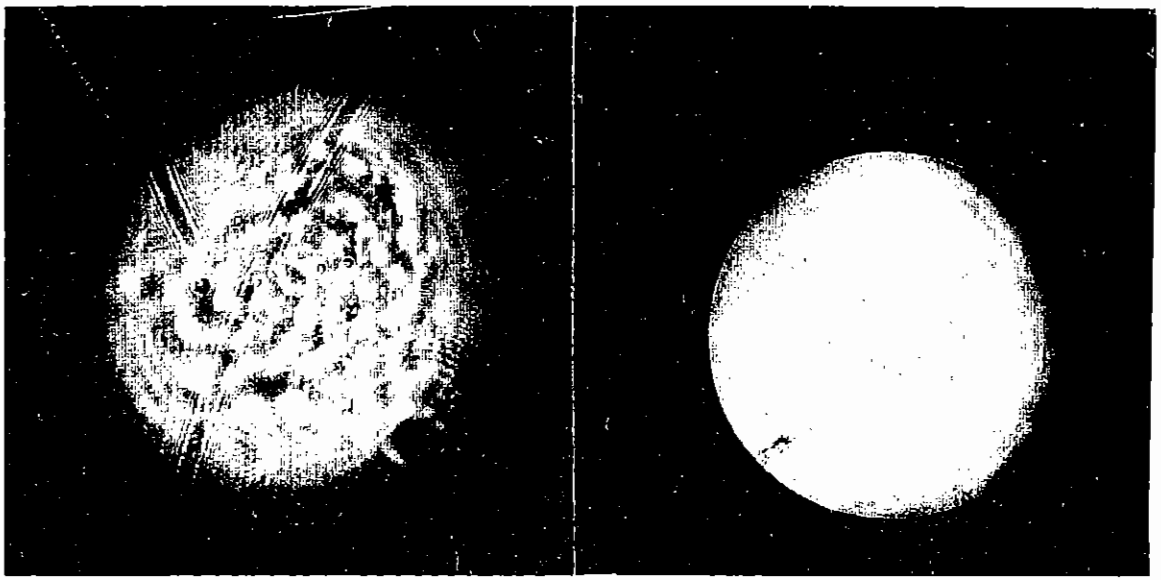

(a) (b)

FIGURE 1.08. BEAM DISTRIBUTIONS AT a) 1.06 μm AND b) 0.53 μm

1.2.4 Phosphate Glass Studies

A cross comparison study of the commerically available phosphate laser glasses was carried out to meet the ordering deadline for the planned facility upgrade scheduled in April/May 1979. The candidate glasses for the disc modules were Hoya LHG8, Owens Illinois EV2 and EV4, and Kigre Q88. Those considered for the rods were LHG8, EV2 and Q88. The main selection criteria were high gain, good passive optical quality, and good dynamic pumped optical quality. From this latter point of view, LHG8 and EV4 have the advantage of being athermal glasses - where the coefficient of optical path length change with temperature is very small. The use of an athermal glass would not only help reduce dynamic beam distortion, but also eliminate problems of thermal lensing (thermally induced focal shift) in the rod amplifier stages. Though it is possible to make a predicted correction to allow for thermal lensing, its elimination would be advantageous.

As a result of the detailed comparisons described below, EV4 was selected for the disc amplifiers and LHG8 for the rod stages. High gain in the case of EV4 and extremely good optical quality in the case of LHG8, both being athermal glasses, were the main criteria to the final choice.

1.2.4(a) Disc Gain Measurements

Two samples of each type of disc were tested. For the gain measurements the two discs were mounted in turn at the centre of the same 108 mm diameter disc amplifier and the mode locked train from the tunable YAG oscillator was double passed through them using a beamsplitter arrangement. A miniature spectrometer mounted on the oscillator chassis provided output wavelength monitoring for the tunable oscillator. The probe beam diameter was 4mm through the discs. Most measurements were made on the amplifier axis, although a scan of spatial gain variation performed on the Q88 discs showed variations of about 8% across the disc area. For each glass the relative timing of the oscillator and amplifier was varied until maximum gain was observed. The disc module and the parameters used were those routinely used for silicate glass - at this stage no attempt was made at further optimization for the phosphate glass by reducing the duration of the flashlamp current pulse or using flashlamps containing no UV absorber.

The results from the disc amplifier gain measurements are summarized in Table 1.01. The recorded small signal gain coefficients across the first two lines are for the two-disc case at bank energies of 200KJ. Measurements using the ED2 silicate glass indicated that the two-disc measurements exaggerated the normally achievable gain coefficient (when the amplifier is filled with 6 discs) by 5.5%, since with only two discs some multiple reflected pump light arrived at the test discs when it would normally have been intercepted by other discs in the module. From the design calculations, the target figure for the double pass small signal gain of the 108 mm disc amplifier was 100. After correction for the six disc case, the achieved figure for the three types of 2.2% Nd doped discs would be 60 (Q88), 97 (EV2) and 73(LHG8). The EV4 discs were tested at the higher concentration of 2.5% Nd in order to compensate for the lower stimulated emission cross section of this glass. The achieved gain in this case gave a projection of 119 for the double passed disc amplifier.

The relative variation of the gain coefficients is in broad agreement with published data on the glasses. For instance the Q88 was found to have a small signal gain coefficient about 11% lower than the EV2. This difference can be accounted for by summing the effects of the lower stimulated emission cross section for the Q88 and the better matching of the EV2 gain profile to the 1.052 μm YAG line. The two glasses appear to have similar pump absorption efficiencies in these (non optimized) tests. However for the double passed disc amplifier, it is clear that small differences between glasses in their small signal gain coefficients result in large differences in the achievable gain.

The third line of Table 1.01 gives the measured ratio of the gain coefficients at 1.052 μm and 1.064 μm, and compares them with the values derived from the published fluorescence intensity curves for each glass.

The fourth line shows the time of peak gain, relative to that of the ED2 silicate glass discs. From these results it is clear that Q88 had the shortest decay lifetime of the glasses tested, while LHG8 and EV4 had the longest.

TABLE 1.01 COMPARATIVE TESTS ON PHOSPHATE LASER DISCS - RUTHERFORD LABORATORY

		ED2 2.2%	Q88 2.2%	EV2 2.2%	LHG8 2.2%	EV4 2.5%
conc						
Gain coefficeint @ 1.052 μm % cm		-	10.1	11.3	10.6	11.8
Gain coefficient @ 1.064 μm % cm		7.4	7.1	7.2	6.8	
Ratio $\frac{\text{gain @ 1.052}}{\text{gain @ 1.064}}$	measured	-	1.35-1.40	1.54	1.56	
	fluorescence curve	-	1.35	1.67	1.61	
Relative time of peak gain* (indication of r)		0	-125μs	-100μs	-75μs	-75μs*
Optical density/cm @ 2.2 μm	Disc 1	-	0.071		0.085	
	Disc 2	-	0.059		0.027	
	Sample	-	0.033	0.07	0.020	
Optical density/cm @ 0.37 μm	Sample	-	0.034	0.021	0.019	
Transmitted wavefront quality	Disc 1	<λ/10	λ/8	λ/4	λ/4	†
	Disc 2	<λ/10	λ/8	λ/4	λ/8	†
Dynamic thermal distortion - compared with ED2		-	Similar	Similar	Similar	
Other comments			excellent cladding $\Delta\mu = 0$	cladding $\mu c/\mu g = 1.014$		

* ie LHG8 and EV4 have longest τ, Q88 shortest

† inspection polish only on samples

The fifth and sixth lines give some of the spectrophotometry results on the discs and their melt samples. Of particular interest are the figures for the absorption at three wavelengths ~2.2 μm, 0.37 μm, and ∿ 0.52 μm. The absorption at 2.2 μm is a good indicator of the extent of water contamination in the glass. That at 0.37 μm shows up any platinum contamination and the absorption around 0.52 μm, in conjunction with calibrations performed at the University of Rochester (1.05) provides a check on the Nd doping level of the glass. Broadly speaking 2.2 μm and 0.37 μm absorption figures not too far in excess of 0.05 optical density units per cm would indicate an acceptably low contamination level. Checks on the doping levels of the glasses via the 0.52 μm absorption confirmed the manufacturer's figures.

The results of transmitted wavefront measurements are shown across the next line of the table. The dynamic thermal distortion is discussed in detail in section 1.2.4(c).

1.2.4(b) Rod Gain Measurements

The three glasses available in rod form were directly compared for gain in the J K Lasers 16 mm rod amplifier. The complete mode locked train of the wavelength tunable oscillator was used as the probe beam to explore the rod gain versus bank voltage and delay, at wavelengths of 1.052 μm and 1.064 μm. The gain was measured both for a fully filled aperture - after expanding the probe beam through a Galilean telescope - and as a function of radial position across the rod - by scanning a narrow probe beam across the aperture. The radial gain profile is of particular interest for phosphate glass amplifier rods. They have stronger, narrower absorption lines for the pump radiation than silicate glasses, resulting in a gain profile which tends to be more strongly edge-peaked than for a silicate glass of the same concentration. The neodymium concentration in a phosphate glass amplifier would have to be lower than in the comparable silicate rod to produce a similar flat radial gain profile.

For the first set of measurements the amplifier flashlamp current pulse duration was held constant for each glass. UV absorbing sodium nitrite solution was circulated between the flashlamps and the rod. The rod length was 236 mm of which 200 mm was pumped.

TABLE 1.02 PHOSPHATE GLASS - THERMAL EFFECTS

GLASS TYPE	ED2	EV2	EV4	LHG8	Q88
NON LINEAR INDEX M_2 (10^{-13} esu)	1.5	0.9	1.0	1.0	1.2
TEMPERATURE COEFFICIENT OF OPTICAL PATH $\frac{1}{(\mu-1)l} d(\mu-1)l$ (10^{-7}/°C)	145	-61	∿0	10	92
COEFFICIENT OF THERMAL BIREFRINGENCE $n_o^3 \sigma Y \alpha$ (RELATIVE TO ED2)	1	0.46	-	0.60	0.82

Some examples of the results are shown in Figs. 1.09 and 1.10. Fig.1.09 compares the on-axis gain achieved for the three glasses (probe beam diameter about 2 mm) as a function of bank voltage, using the optimum delay for each glass. The results for Q88 are shown only over a limited range because the particular sample rod used had uncoated plane parallel ends, and was parasitic limited to gains less than about 20 (at 1.052 μm). The neodymium concentrations were not the same, which precludes a simple comparison, the EV2 glass showed the highest axial gain even at the lowest concentration.

Fig.1.10 shows an example of a radial gain profile - that recorded for the LHG8 rod at maximum pumping. The ratio of small signal gain coefficients between edge and centre is 1.23, corresponding to an undesirably high ratio of 2.3 in the gross gain. The ratio of gain coefficients between full aperture fill and centre-only was 1.15 and the ratio of gross gains 1.7. In contrast the EV2 glass used at lower concentration gave a much flatter profile, with the ratio of gross gains between full aperture fill and centre-only being down to 1.35.

Extremely high gains have been achieved from this rod amplifier, without any problems of parasitic mode limitation. With full aperture fill of the EV2 rod, gross gains of over 80 have been measured, corresponding to the small signal gain coefficients of over 20%/cm.

1.2.4(c) Phosphate glass tests - dynamic thermal effects

One of the hoped-for advantages of using phosphate glass results from its lower temperature index of optical path. This property should reduce the dynamic thermal effects and in particular should lead to a very small dynamic thermal focussing in the laser rods. Table 1.02 gives published optical path coefficients of the glasses in question.

Also shown in Table 1.02 is a parameter indicating the stress birefringence resulting from temperature gradients in the glass. This parameter shows no advantage for phosphates and because there is an optical path change as well as birefringence associated with stress, it is only in the absence of stress that phosphate is optically superior

when pumped.

Comparative tests were carried out to assess the phosphate glasses both in rod and disc form. The tests involved continuous viewing before and after firing the amplifiers of the far field distribution in the usual multiple image arrangement using a continuous Nd:YAG laser and infra red sensitive TV system. The rod tests were carried out using a ϕ 76mm and ϕ 45mm amplifier fitted with the appropriate glass. The dominant effect when firing these amplifiers is the thermal focussing. Other dynamic distortions are very small compared to those of the disc amplifiers and were not assessed during these tests. The figure used for assessing the thermal focussing was the sudden focal shift occurring over the duration of the pumping. This was measured for silicate glass and LHG8 the phosphate glass with the best thermal properties. Maximum focal shifts equivalent to 14 μm at the target were measured for silicate glass while LHG8 gave less than 2 μm. This reflects the factor of 14 expected difference in optical path coefficient.

Similar tests were made on the distortion of two discs of each glass type operating in double pass in one of the disc modules. Any focus shift is obscured by a large astigmatic distortion of the focal spot which grows rapidly after the end of the flash and continues to change over the following 30 min and more. The different glasses showed some qualitative differences in the form of the distortion but no significant differences in the magnitude of the distortion. It is believed that the distortion does not arise only from the optical path coefficient but from a combination of two other effects: in thermally induced stress, arising from the edge coating which heavily absorbs flash light incident on it, and distortion of the wavefront by non uniform heating of the nitrogen gas flowing through the disc module. Some evidence that the latter effect is important is presented in paragraph 1.2.2(a).

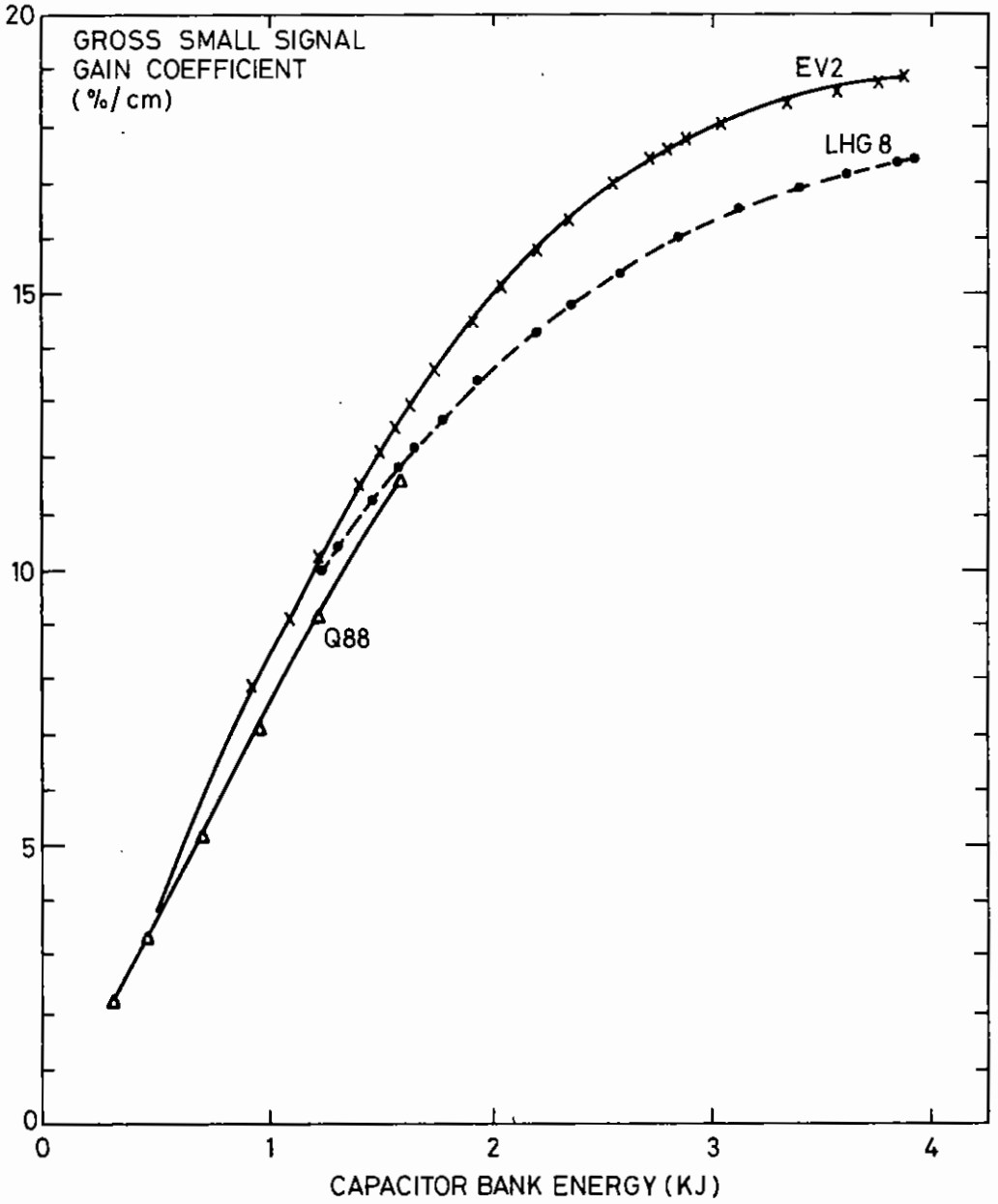

Fig 1·09

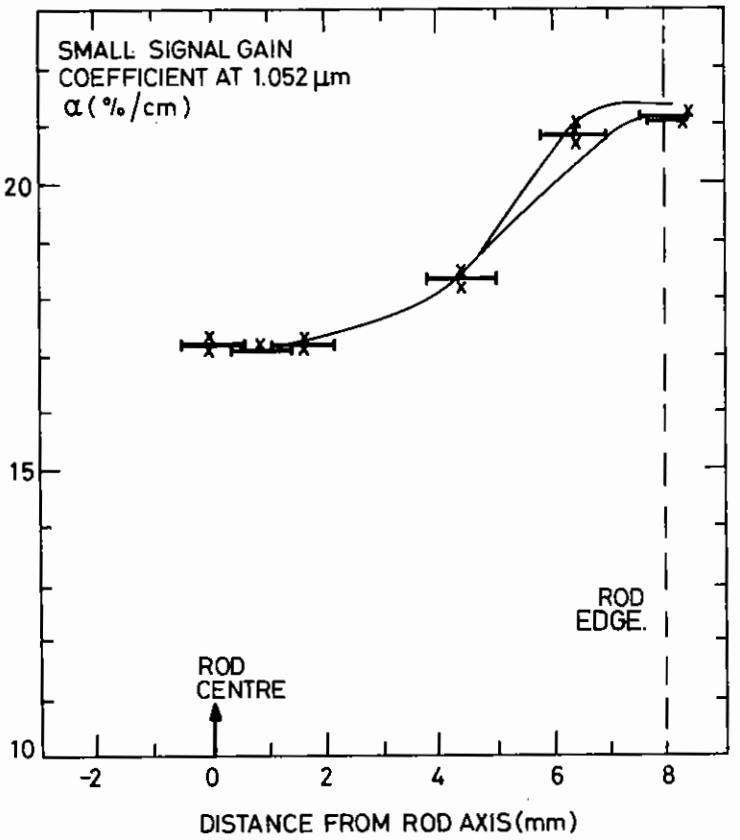

Fig 1·10

1.2.5 6-Beam Enhancement

Fig.1.11 is a diagram of the staging of the 6-beam system. The rationale for this staging arises from considerations such as:-

(i) Maximum power is required for 100 ps pulses. This demands that the B-integral be restricted to prevent overmodulation at the target chamber and hence damage to target chamber optics. A second requirement asks for a restriction in average energy density at target chamber so that, given a maximum allowable peak to average intensity of say 8:1, the damage level of optics is not exceeded. Hence one arrives at a figure of 1 TW per beam, since the power density is then 12.5GW/cm^2 leading to a B-integral for target optics of 1.5 and the energy density is 1.25J/cm^2, a factor of at least 8 below damage levels (except for anti-reflection coatings and these should not be used). B-integral for the laser is 5 at 1TW output and hence acceptable (with a vacuum spatial filter).

(ii) Maximum energy is required for 1ns pulses. The maximum allowable mean energy density at the target chamber can be increased in the absence of appreciable small scale self focussing. Assuming a maximum allowable peak to average intensity of 3:1 and assuming a damage threshold at 15J/cm^2 for 1ns pulses, the maximum energy density per beam is 5J/cm^2 and maximum energy 400J per beam. The laser must of course have sufficient gain under long pulse operation.

(iii) The design uses only existing components.

(iv) A vacuum spatial filter is used to divide the system into two parts with equal B-integrals.

(v) As few components as possible are used to minimise spatial noise and hence minimise the peak to average intensity at the output.

(vi) The intensity profile (apart from small scale effects) should be essentially flat at the output. From the viewpoint of maximum efficiency and maximum gain it is desirable to maximise the neodymium concentration in the rods. However increasing the concentration increases the edge to centre gain of the rods and hence leads to an output beam with higher intensity at edge than centre. The system is optimum when this edge to centre intensity is set at a maximum allowable value, say 1.1.

Fig.1.11 shows the calculated (using TOODLES - a non diffraction code) performance of the proposed system for long and short pulses.
The system produced for short pulses 1TW with a B-integral of 2.5 on either side of the vacuum spatial filter, and for long pulses, with no extra amplifiers, it produces 340J. There is adequate protection for back reflection up to 100%.
It will be noted that the system has two less amplifiers in the chain than at present.

1.2.6 Long Pulse Operation of the Main Laser

The main laser has now been successfully run three times with long pulses of $\sim$ 1.7ns (Fwhm) duration. Details of the oscillator bench, where the nanosecond pulse is sliced from a long Q switched pulse by an electrooptic gate, are given in section 1.2.1b.

In the most successful third run of February 1979, up to 230 mJ were delivered through the oscillator bench spatial filter and output energies of 200J were obtained from a single beam configuration. Earlier runs gave two-beam energies of 80 to 100 joules per beam. The prepulse power on target - from the unrejected Gaussian Q switched pulse - was better than 10^{-7} of the pulse power. The comparatively modest power loading meant that the vacuum spatial filter pinhole could safely be removed, and non linear effects were only just starting to cause perturbation of the near field beam profile at the highest recorded outputs. No significant damage problems were encountered.

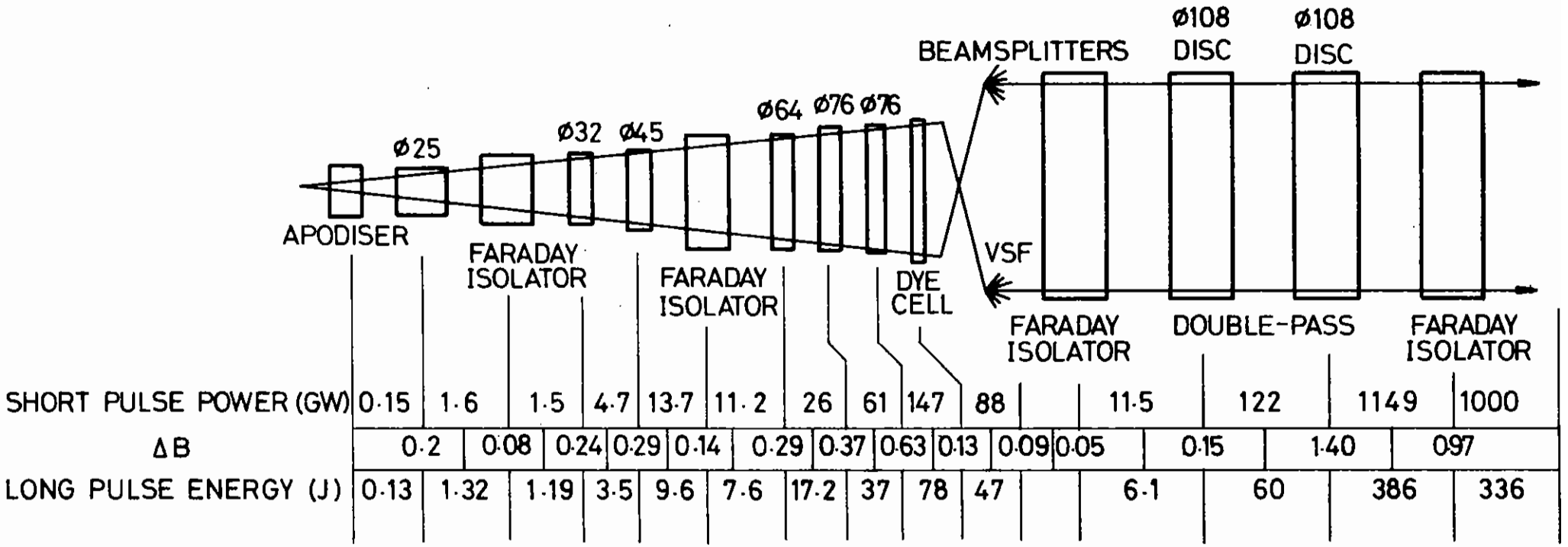

FIGURE 1·11. STAGING OF 6-BEAM PHOSPHATE LASER SYSTEM.

1.3 Operating Performance of the Laser

1.3.1 Performance Statistics

The plasma physics programme, during the year, has led to a requirement to operate the laser in several different configurations and with short ∿ 100ps and long ∿ 1.7ns pulses. In the short pulse regions both double and single beam configuration of the whole laser have been used. A significant feature of the operation has been the use of a large number of pulses from the single beam rod amplifiers only, particularly in the interaction physics experiments. This year was the first in which the laser was capable of operation in the long pulse mode. Although the total output energy was relatively low over 100 pulses in single and double beam configuration were made available to the users.

The performance statistics presented below are based on the laser shots recorded in the computer system and include all the laser operation in scheduled time. Laser operation during alignment checks each morning and during scheduled maintenance are not recorded but laser shots in scheduled laser development time are included in the data.

During the year the schedule was arranged as follows

	Weeks
Single beam 100ps operation	19½
Single beam 1.7ns operation	3
Double beam 100ps operation	11
Double beam 1.7ns operation	2
Laser development	2½
Laser maintenance	9
Shut down to instal new target area	5
	52

1.3.2 Reliability

The total number of recorded shots was 989 of which 756 shots were provided to the plasma physics experiments and 173 shots were used for laser development and for energy calibration purposes. Of the 756 plasma physics shots 60 were abortive mainly as a result of pulse generator misoperation. In summary of the total recorded shots 76.6% were used for plasma physics, 17.4% were used for calibration and laser development and 6% were misfires. The detailed laser performance for 652 of the used target shots is presented in Fig.1.13. A miscellany of 44 shots which do not readily fall into one of the analysed categories is excluded from this presentation.

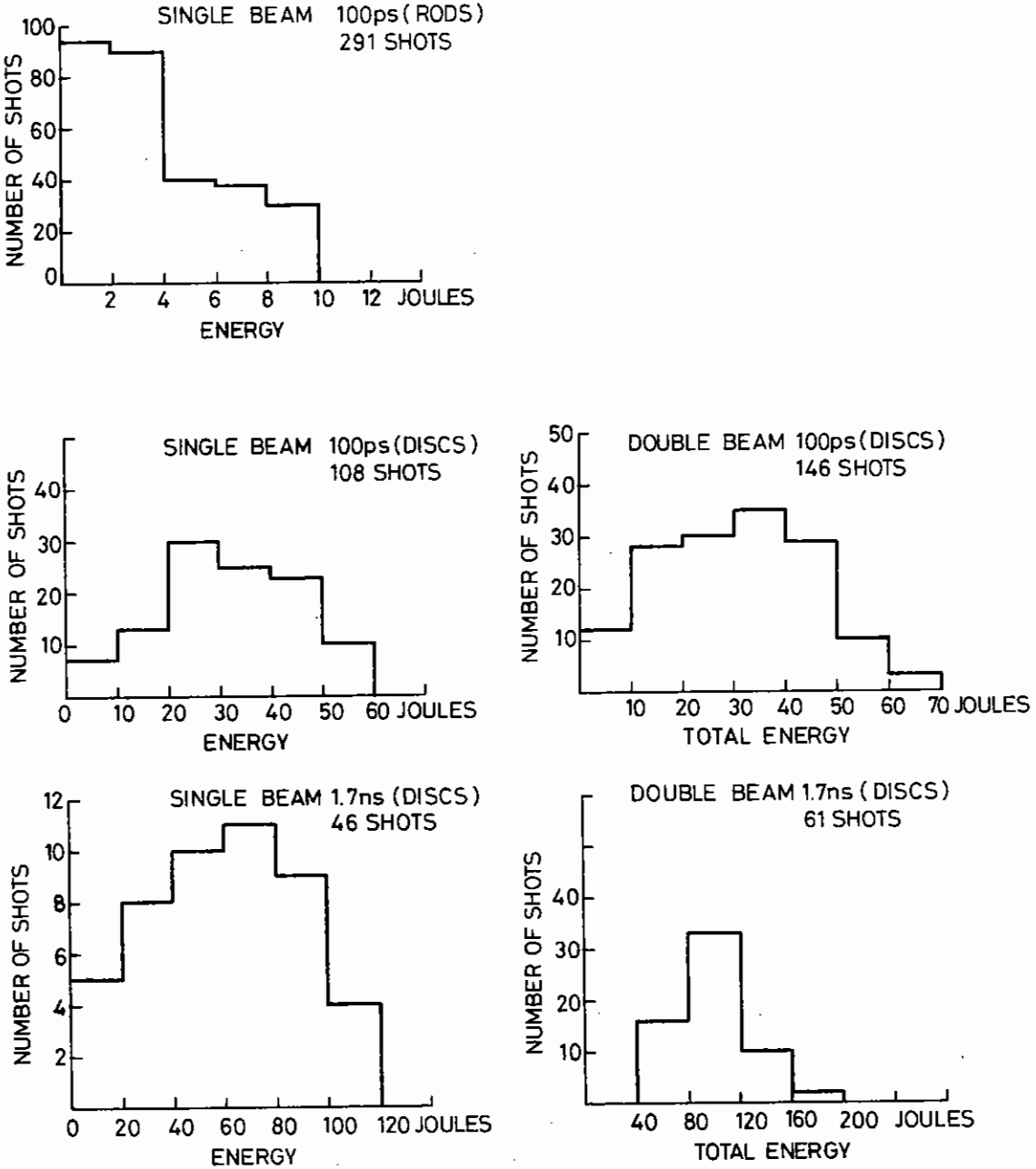

FIGURE 1.13 SHOT ENERGY DISTRIBUTIONS FOR THE VARIOUS COMBINATIONS OF PULSE LENGTH AND LASER CONFIGURATION USED DURING 1978/79

1.4 Real Time Computer System

The computer hardware has been previously described and remains, apart from the following, essentially unchanged. A VDU has been added for the sole use of the laser operator. A further VDU has been provided principally for file management in connection with data transfer between the Laser computer and the RL IBM 360/195 mainframe. It also serves for general access to the IBM 360/195 via the user system ELECTRIC. The CAMAC interface has been upgraded by the addition of an autonomous memory channel in readiness for on-line data transfer from a 2D-OMA to the computer without intermediate data storage. The number of Lecroy charge detecting ADC's has been increased to 3, 12 channel units. The CCD based waveform digitizer, briefly described in the previous report, is now in use for observing charged particle fluxes from the Faraday cup collectors.

Detailed improvements have been made to the operating system for laser control although the general principles remain unchanged. A log sheet as shown in Fig.1.14 is now available with each significant laser shot and the data is archived. The waveforms showing the oscillator pulse train and pre-pulse energy are produced from Tektronix R7912 waveform digitizers. The output is a photocopy from a Tektronix 4006 graphics terminal. The number of parameters checked by the computer before a laser shot has been increased and the pre-ionisation lamp check (PILC) is now an integral part of the computer controlled charging sequence. Routine archiving of data from computer controlled user equipment is now available.

Use of the computer for off-line data analysis via the graphics tablet has been an important development during the year and other such uses are envisaged. Programs have been written for processing oscilloscope traces, interferograms and densitometer output.

1.5 Target Areas

1.5.1 New Single Beam Target Area (TAII)

Target area II is designed to accommodate single beam interaction experiments and two beam compression experiments. It is fed with a single full-aperture beam from a double-passed disc amplifier in the laser room. The move to the new area gave an opportunity to make several improvements to the target chamber, the alignment and focussing system, to speed up turn-round, and decouple the target area from laser area activities. A general view of the area is shown in Fig.1.15.

The layout of high power beams is shown in Fig.1.16. The beam travels for some 30 meters in a metal pipe from the laser area, through target area 1 at high level, to a point just inside target area 2 where local and distant alignment beams can be compared and made colinear. The beam may then be split or a fraction used to make a third (backlighting) beam, before it is transported to the target chamber. Beam splitters just before the target chamber direct a small fraction (4%) to incident beam monitors and to the alignment and focussing telemicroscope system mounted above the target chamber.

The arrangement used to generate local expanded beams for target alignment and focussing, and to compare them with the laser area CW YAG alignment beam is shown in Fig.1.17. A single fixed pinhole is used for all beams. The main collimating lens is an f/5 air-spaced doublet designed in the Division. Local and distant beams are combined on the 90%R splitter (removed during laser shots) and compared on a telemicroscope TU3 with an angular definition of a few micro-radians. The overall stability of the mirror-tower system which brings the beam to Target Area 2 is good. An angular jitter of more than a milliradian on a time-scale of about a second was seen initially. This was traced to air-currents in the beam pipe caused by the small overpressure maintained by the airconditioning system in the laser room and was cured by placing a plastic film window over the entrance to the beam pipe. A Brewster angle window will be installed later.

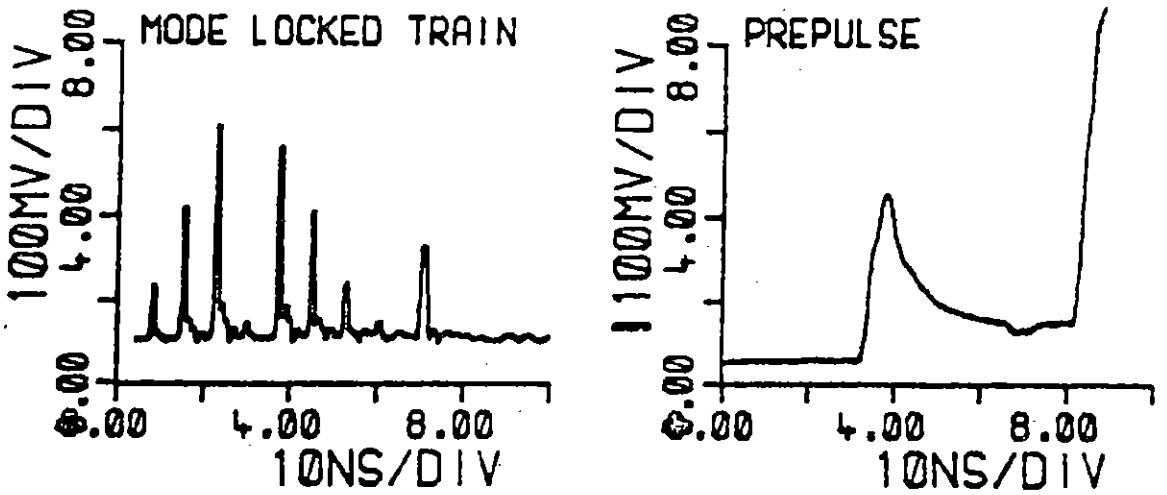


```
SHOT NO=  21        THU 10 AUG 1978 11:51:56        MODE=4
ENERGY BENCH=17.5 MJ          QL E=0.00 J          QL W=0.00 J
       E BEAM=19.9 J          W BEAM=20.6 J
APODISER TEMP=32.4 C   DYE CELL IN
CAPACITOR BANK VOLTAGES IN KV
OSC=1.38        PREAMP=1.38     16MM=2.37     25MM=2.36     25MM=2.34
32MM=2.20       45MM=2.39       45MM=2.39     64MM=2.42     76MM=2.34
FR32=1.80       FR80=2.14       76MME=1.93    76MMW=2.36
ILC FARA=6.30  ILC AMP=20.1
PROFILE MEASUREMENT
NO COMMENT
```

FIG 1.14 COMPUTOR PRINT-OUT OF TYPICAL LASER LOG SHEET.

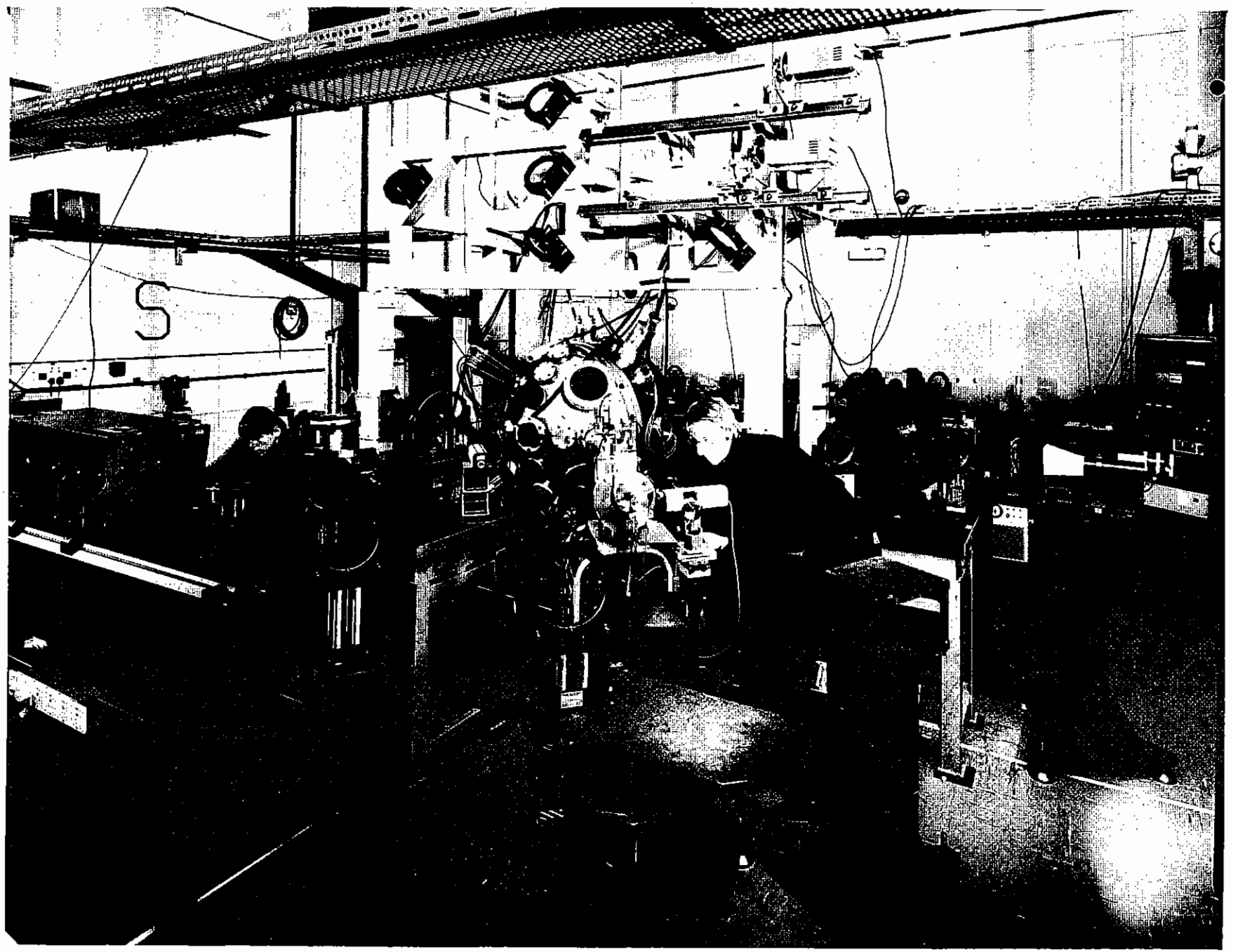

FIG 1.15 NEW TARGET AREA II

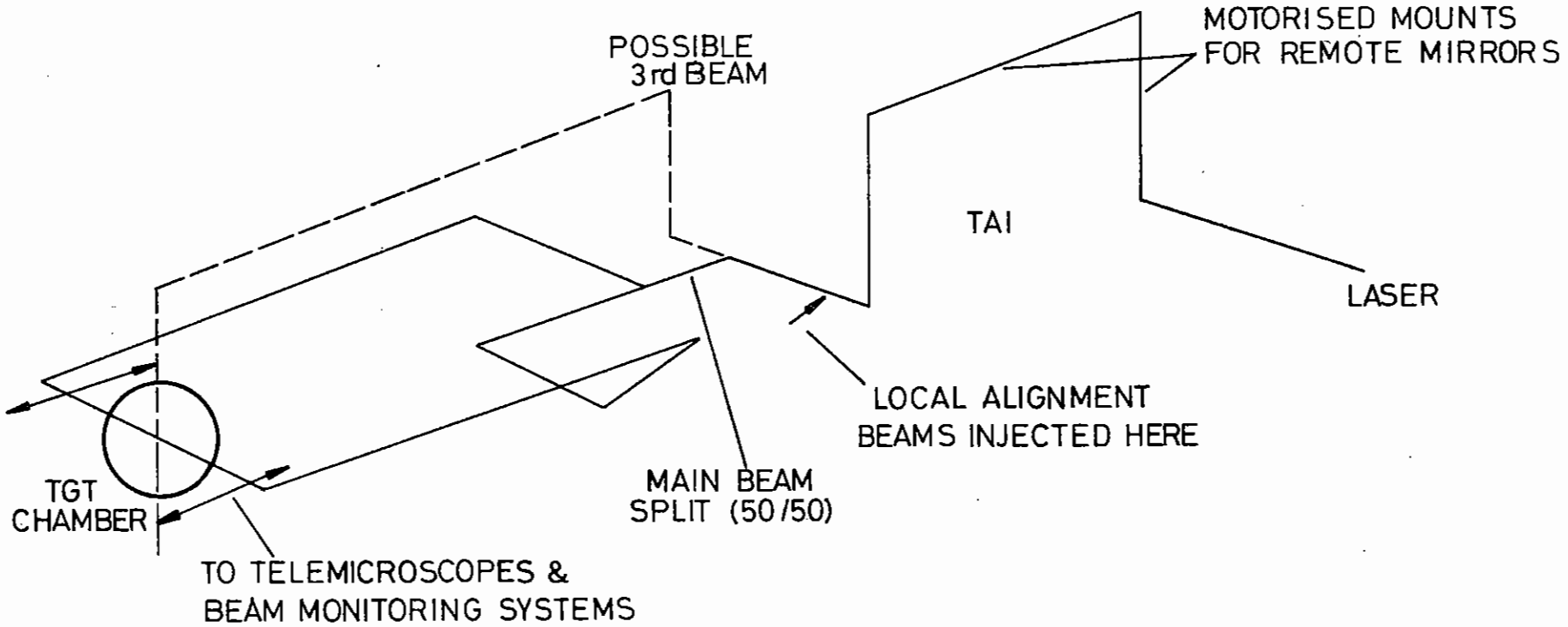

LAYOUT OF HIGH POWER BEAMS IN TA II

FIG 1.16

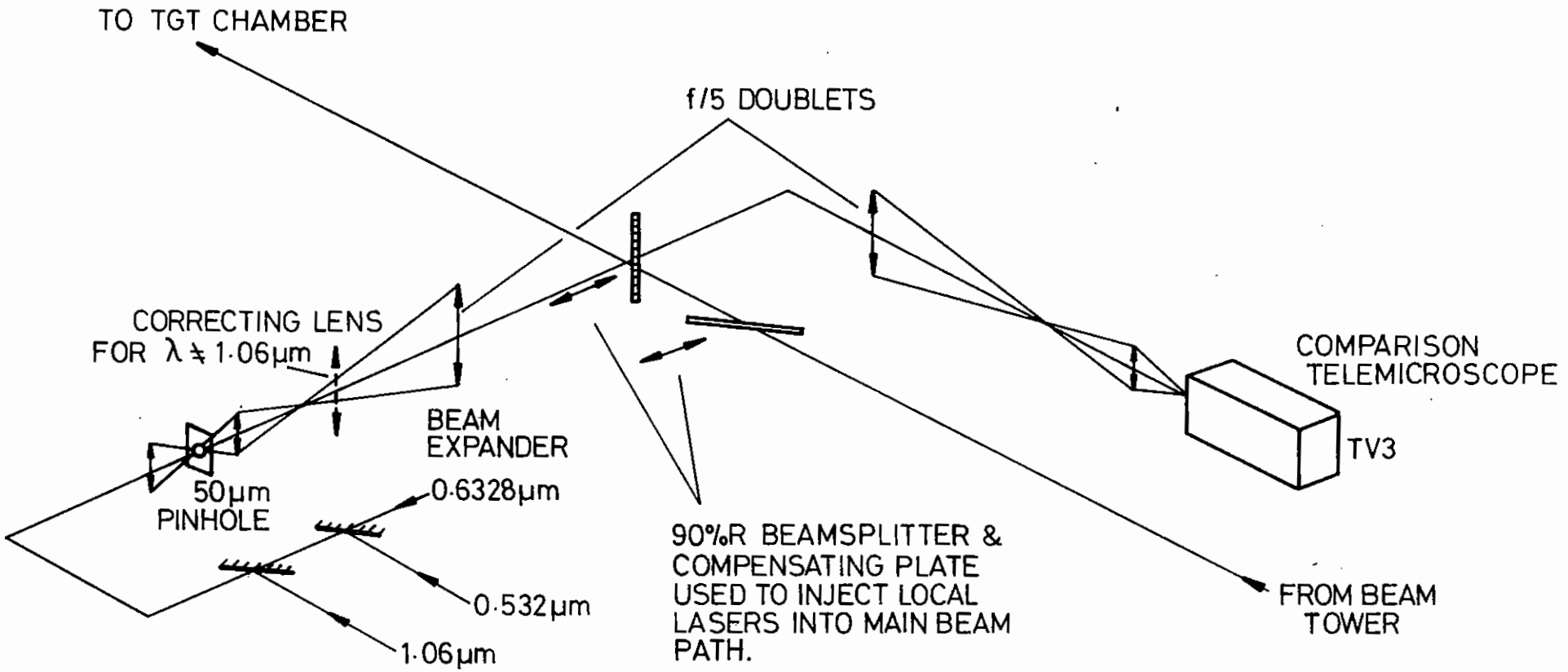

LOCAL LASERS IN TA II

FIG 1.17

The use of locally produced beams for most alignment and focussing operations allows work to proceed in Target Area II while the main laser is being tuned. The laser area beam is checked against the local beam before each shot and brought into colinearity by adjusting a pair of mirrors. If no realignment has been made elsewhere in the laser it is usually not necessary to make any corrections.

The target focussing and alignment telemicroscopes are mounted on a gantry above the target chamber as shown in Fig.1.18 in order to leave as much floor space as possible available for experiments. The telemicroscope system operates in three modes:

(a) TV1: Fine monitoring of the target plane at a magnification of 400x.

(b) TV2: Coarse monitoring of the target plane at x10 magnification.

(c) TV2: Lens plane view at x1/10 magnification.

The beams to the telemicroscopes are taken upwards by 50% splitters so that backscattered (or transmitted) light is available at normal beam height for spectroscopy etc. During shots, calorimeters are mounted on the gantry in front of the telemicroscopes.

The lenses and the target platform are driven by the stepping motor system described in section 1.5.4 which is controlled from a rack placed beside the alignment laser system. This rack also houses the readouts, television monitors, laser controls, remote filter drives etc. A readout of step-count and of absolute position (from linear potentiometers mounted on the drives) is provided. A small hand-held controller can be used at any point in the room to make remote lens or target adjustments in order to facilitate setting up diagnostic equipment. Ease and sensitivity of control, reproducibility of position and backlash are now very good.

The improved vacuum system also described in section 1.5.4 enables the tank to be pumped down to diffusion pump pressure in less than three minutes. Let-up to dry nitrogen at atmospheric pressure is as fast. The pump-down and let-up sequences are under automatic control.

The area was commissioned in January 1979 and used for experiments in rapid succession on Xray spectroscopy, Brillouin backscatter and $2\omega_o$ emission, thermal transport with $2\omega_o$ irradiation, and time-resolved Xray diagnosis of exploding pushers.

1.5.2 Six Beam Target Area Design (TA1)

The production of high density plasmas by means of ablative laser driven implosions requires a much greater uniformity of target illumination than is possible with the system of two opposing beams used for all compression experiments so far.

Two schemes for obtaining improved illumination uniformity have been considered and studied: multiple laser beams in combination with lenses, and clam-shell type mirrors fed by only two beams. The former system has been chosen because of its greater experimental flexibility, ease of diagnostic access and compatibility with laser development plans. These are based on installation of high gain phosphate glass leading to a laser system with a multiplicity of small beams rather than two large ones. Consequently we have designed and constructed a new vacuum chamber in which targets will be irradiated with 6 laser beams via f/1 doublet lenses.

A symmetric system involving 6 beams requires that the lenses be situated on the 6 faces of a cube leading to maximum diagnostic access in the 8 directions corresponding to the cube corners. For ease of experimental operation the target chamber has been arranged such that 4 of these 8 major access directions lie in the horizontal plane. Fig.1.19 shows a photograph of the target chamber situated in its new experimental area (target area 1).

Compression experiments will be the major type of experiment carried out in this area and consequently suitable diagnostic systems have been planned. For example Xray backlighting techniques will be used extensively to diagnose the high density plasmas produced by ablative implosions. In order to make this type of diagnostic system more versatile two target mounting and positioning assemblies have been designed: one to position the microsphere target, the other to position an auxilliary target (lollipop or wire) to act as the Xray backlighting source. An f/2.5 doublet lens has been designed to focus a

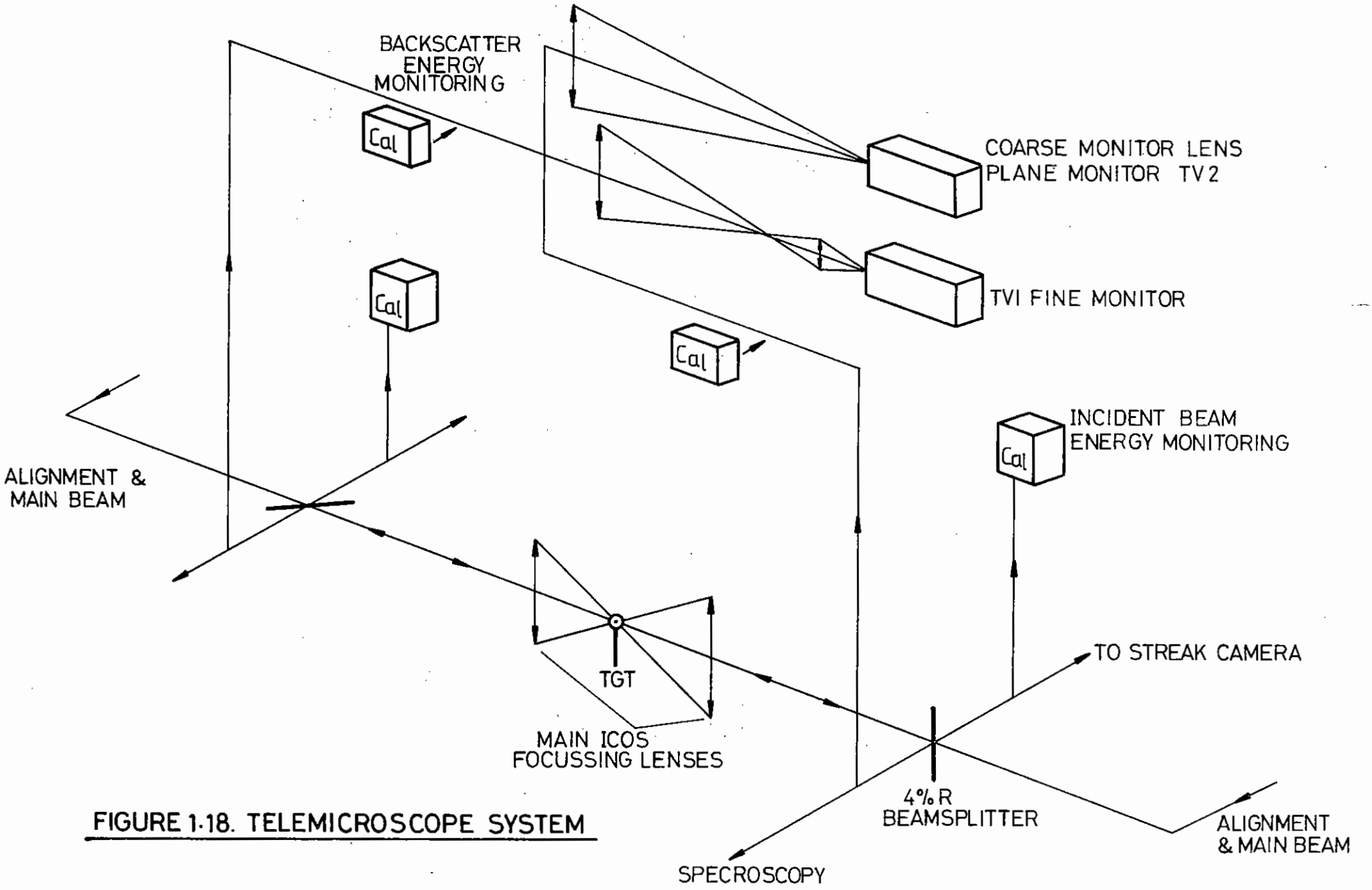

FIGURE 1.18. TELEMICROSCOPE SYSTEM

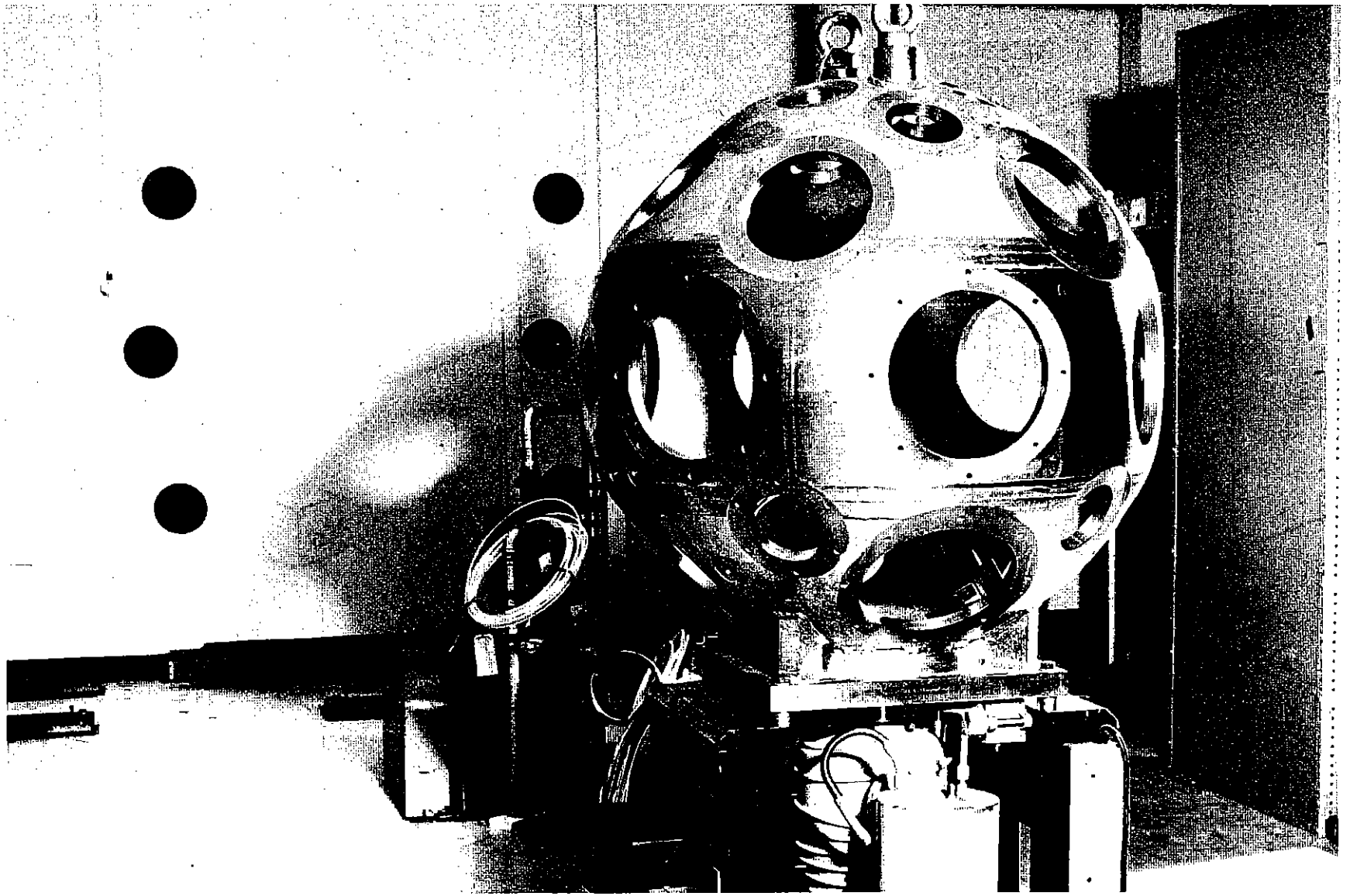

FIG1.19 INSTALLATION OF 6-BEAM TARGET CHAMBER.

7th beam from the laser onto this target. To observe implosion events an Xray microscope and streak camera system has been designed to couple to the chamber via one of the major access ports in the horizontal plane. In addition a miniature X-ray streak tube which can fit inside the chamber is being developed. Fig.1.20 shows the layout of the experimental area and indicates the position of other diagnostic systems such as probe beams, particle detectors and spectrometers.

The 6 main beams from the laser area do not pass directly to the target chamber but are intercepted via mirrors on a three level alignment and reference platform. This platform contains He-Ne and CW-YAG alignment lasers which can be injected into each of the 6 beams so that experiments can be prepared and targets aligned in the vacuum chamber while the main laser system is feeding shots to the other experimental area (TA2) or maintenance is being carried out. Before experiments commence the beams from the laser area must be adjusted to be coincident with those in the experimental area by means of near and far field reference and alignment monitors. Operational experience with the previous target area has shown that when new experiments were being prepared considerable time was required for local alignment using the CW-YAG laser beam derived from the laser area. This problem will now be avoided and consequently laser time will be utilized more efficiently.

Compression experiments in the 6 beam target chamber are due to commence in May 1979 after the laser system has been reconfigured and phosphate glass installed. The commissioning experiments will be a series of exploding pusher shots designed to study the effect of illumination uniformly on core density and temperature at powers on target of greater than 1TW.

1.5.3. Multi Lens Illumination System

In the following discussion the uniformity of target illumination (1.06, 1.07) by a multi beam irradiation system is considered. The contribution of each laser beam to the overall intensity on the target surface is derived either from the idealised lens formula (1.08).

$$I(\theta) = I(r)\frac{f}{R_T}\frac{(1 + \delta\cos\theta)}{(\cos\theta + \delta)}$$

or, in our case (1.09), from the numerical equivalent of the equation obtained directly from a geometric optics ray trace programme.

θ in this equation is the angle subtended from the target centre and δ the relative focal shift (Fig.1.21).

The contribution to the total irradiance at the target surface made by a number of beams is summed in a scalar fashion. For a given beam configuration and lens F number, the uniformity of the illumination over the target surface $n = 1-\left(\frac{1-\kappa}{1-\kappa}\right)$ where $\kappa = \frac{Imin}{Imax}$ is calculated as a function of ϕ the central target angle defined as follows: when the target is not fully illuminated then n is = 0, since $I_{min} = 0$ at some point, ϕ will therefore have some minimum value ϕ_{min} at which complete coverage of the target is first established and will vary between this and ϕ_{max} given by

$$\phi_{max} = \pm(\pi/_2 + \tan^{-1}\frac{1}{2F})$$

1.5.3(a) Numerical Results

Calculations have been made of the uniformity of irradiation by a large number of laser beams ≥ 8 for comparison with previous published work (1.07). Fig.1.22 compares the available data with our own calculations. The solid lines are the data taken from this latter work for the 20, 12 and 8 laser beam systems. The dashed lines are our calculations for similar configurations. Also displayed are calculations for six and two beam systems which are of particular interest.

Repeating these calculations for a super-gaussian beam profile $I(r) \propto e^{-(r/a)P}$ with p set at 3 and a = 0.7, provides a set of conditions very similar to those chosen by LLL (1.06) who used a filleted quadratic closely approximating to this profile. Fig.1.23 compares the results obtained from both these sources with our calculations. These comparisons established the base for our computations. The results show that the uniformity of irradiance for a six or eight beam system is significantly worse than a large number of beams. Although the two beam system with F/1.5 lenses appears to be almost as uniform as six beams, allowance has to be made for the large increase in marginal ray angle. In practice our laser beams have a much more "super-gaussian" profile than those considered above. In Fig.1.24 the dotted curve represents a super gaussian fit onto our beam profile. The ordinate scale is logarithmic showing the beam with $\sim$3db of 'spiking' on it.

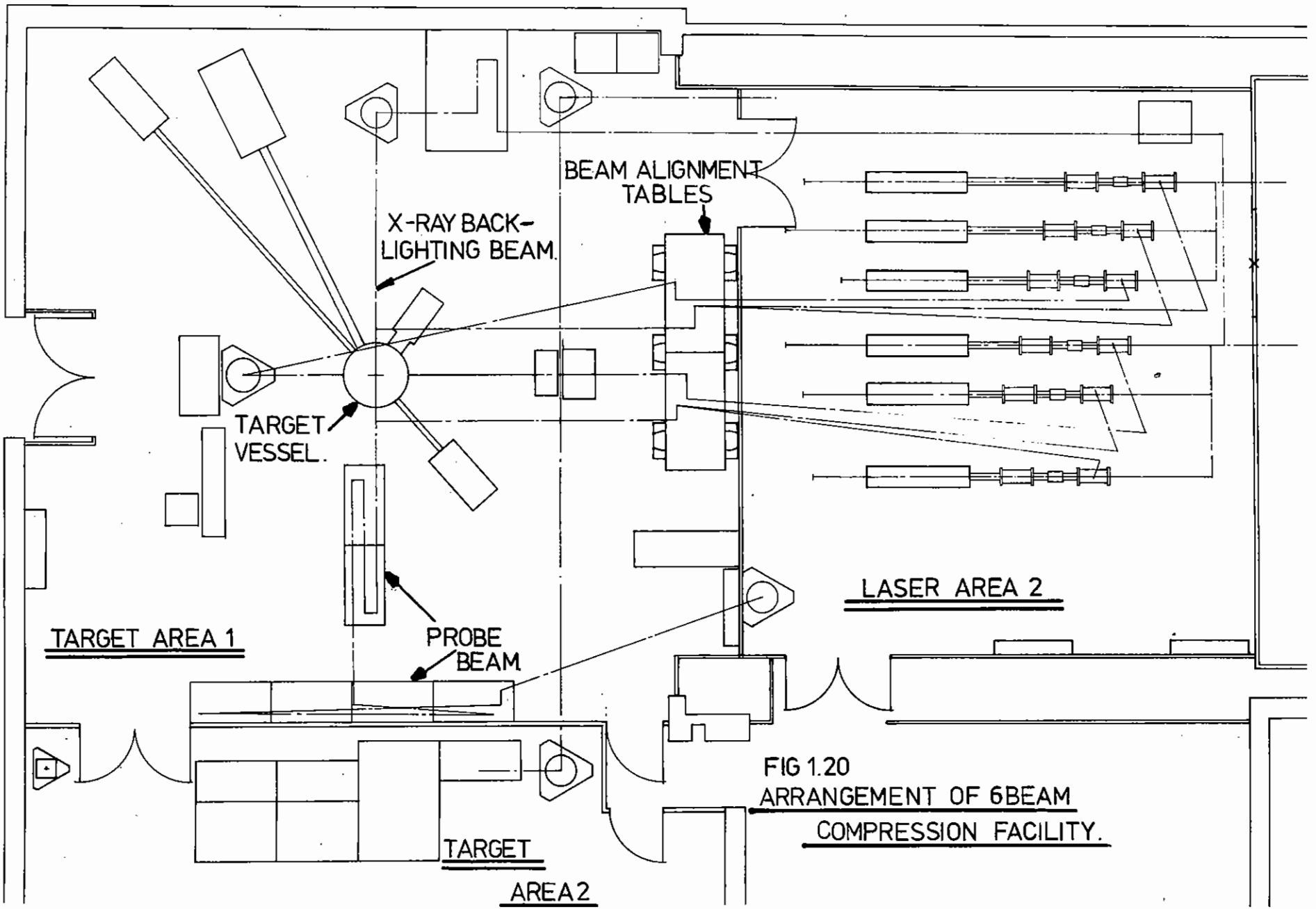

FIG 1.20
ARRANGEMENT OF 6 BEAM COMPRESSION FACILITY.

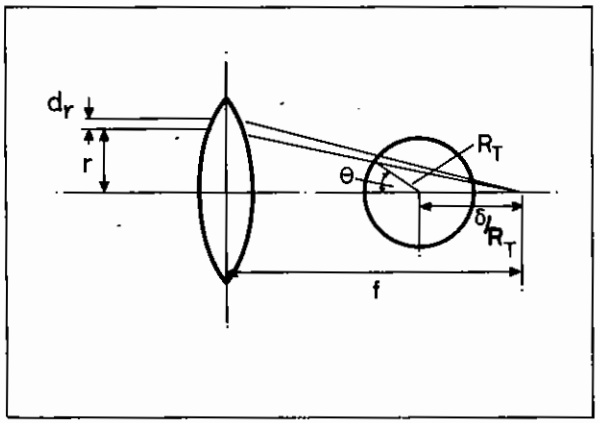

FIG 1.21 IDEALISED LENS ILLUMINATION

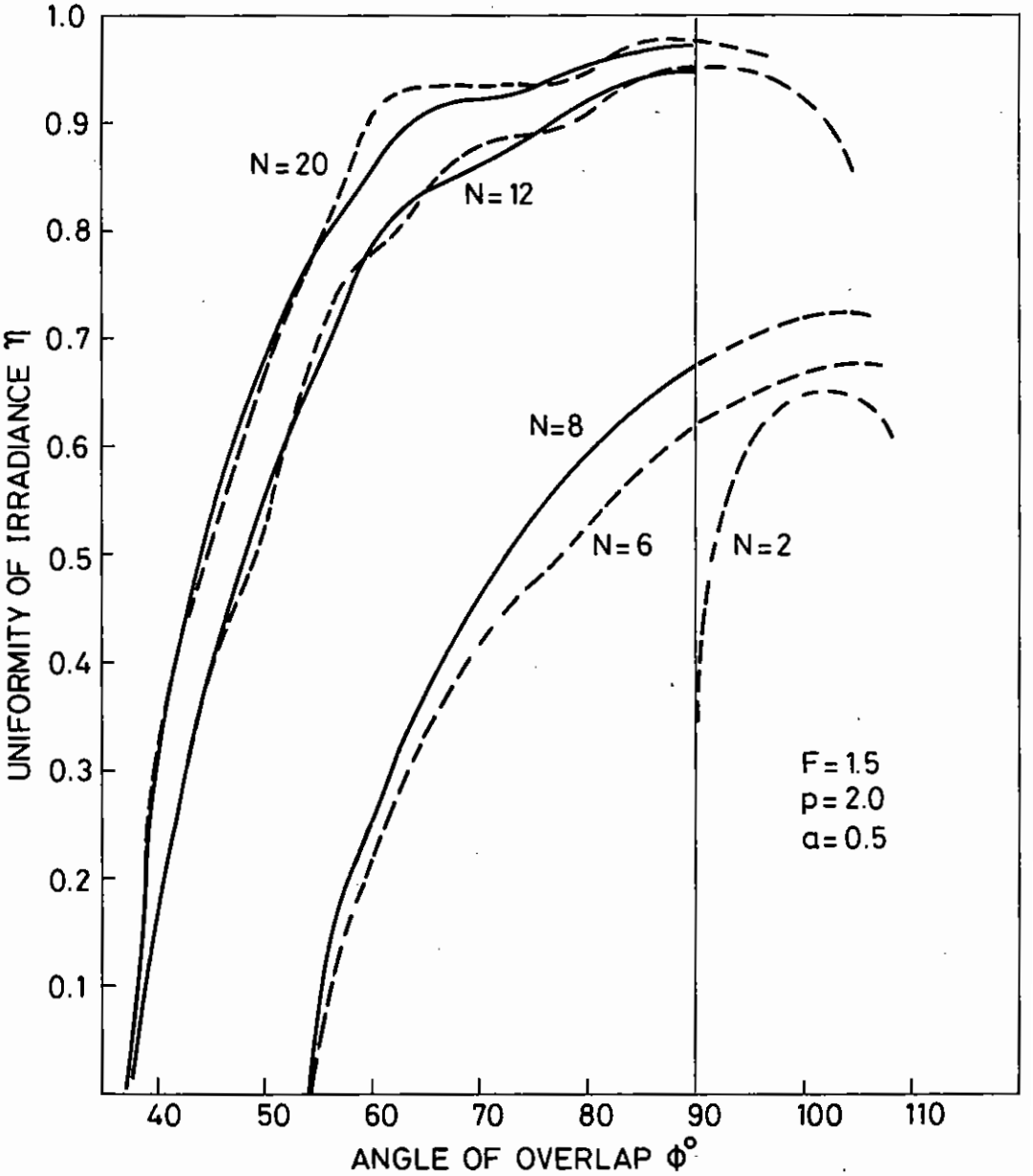

FIG 1·22 UNIFORMITY OF IRRADIANCE FOR MULTILENS IRRADIATION SYSTEM

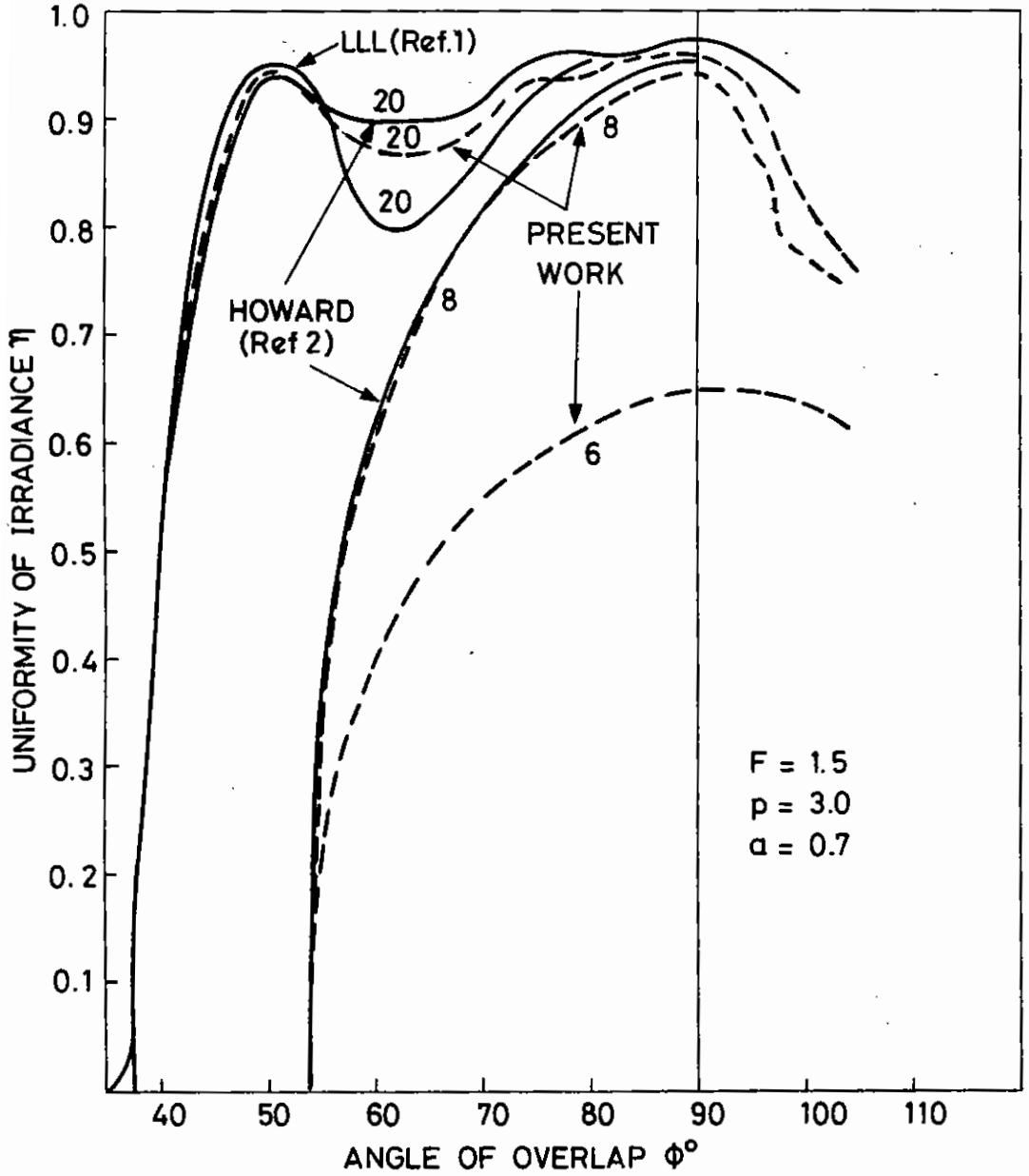

FIG 1·23

UNIFORMITY OF IRRADIANCE – A COMPARISON OF DATA

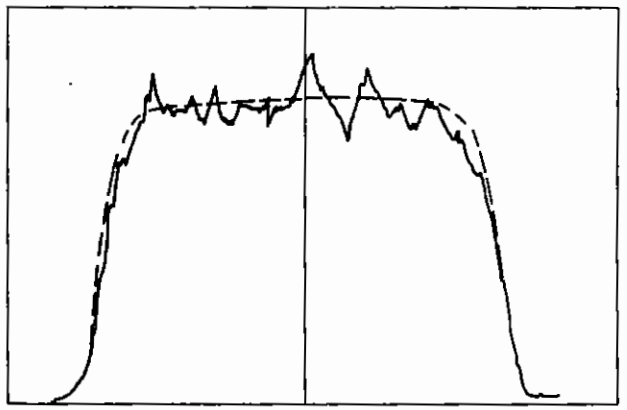

FIG 1.24 TYPICAL LASER BEAM PROFILE (WEST BEAM EXPANDER)

The above calculations were repeated with this "fitted" beam profile for both six and two beam systems with F/1.0 lenses as currently proposed. Fig.1.25 shows the results and indicates a somewhat improved distribution of illumination over the target surface.

We define a quality factor for the overall distribution of irradiance in terms of the variance ξ given by

$$\xi = \frac{\langle I^2 \rangle - \langle I \rangle^2}{\langle I \rangle^2}$$

which gives the weighted average distribution in intensity over the surface area. However, it should be pointed out that instabilities in the spherical compression are driven by terms like κ and in the discussion of these instabilities, which appears later, it is the results as presented previously that may be more relevant.

In Fig.1.26 the ξ variable is plotted for cases of interest to us. As would be expected, this provides a more optimistic view of the uniformity of illumination. Such a presentation of the results influences the data obtained for the smaller number of laser beams to a larger extent than to the larger number of beams. In fact the effect of this interpretation becomes progressively smaller as the number of beams considered increases, with almost zero effect for the 32 beams and above.

As far as assessing the relative performance of two illumination systems is concerned, a direct comparison of say a six F/1 lens system against an eight F/1 lens system has limited usefulness since the eight lens system will occupy a greater solid angle and on this account alone should produce a more uniform illumination. As far as practical choice of systems is concerned it is therefore more useful to compare a six beam F/1 system with an eight beam system which occupies the same solid angle. It turns out in practice that such an eight beam system will have an F number of 1.21. Fig.1.27 shows such a comparison indicating that whilst the eight beam system is still capable of higher uniformity of illumination the improvement is only $\sim$9%.

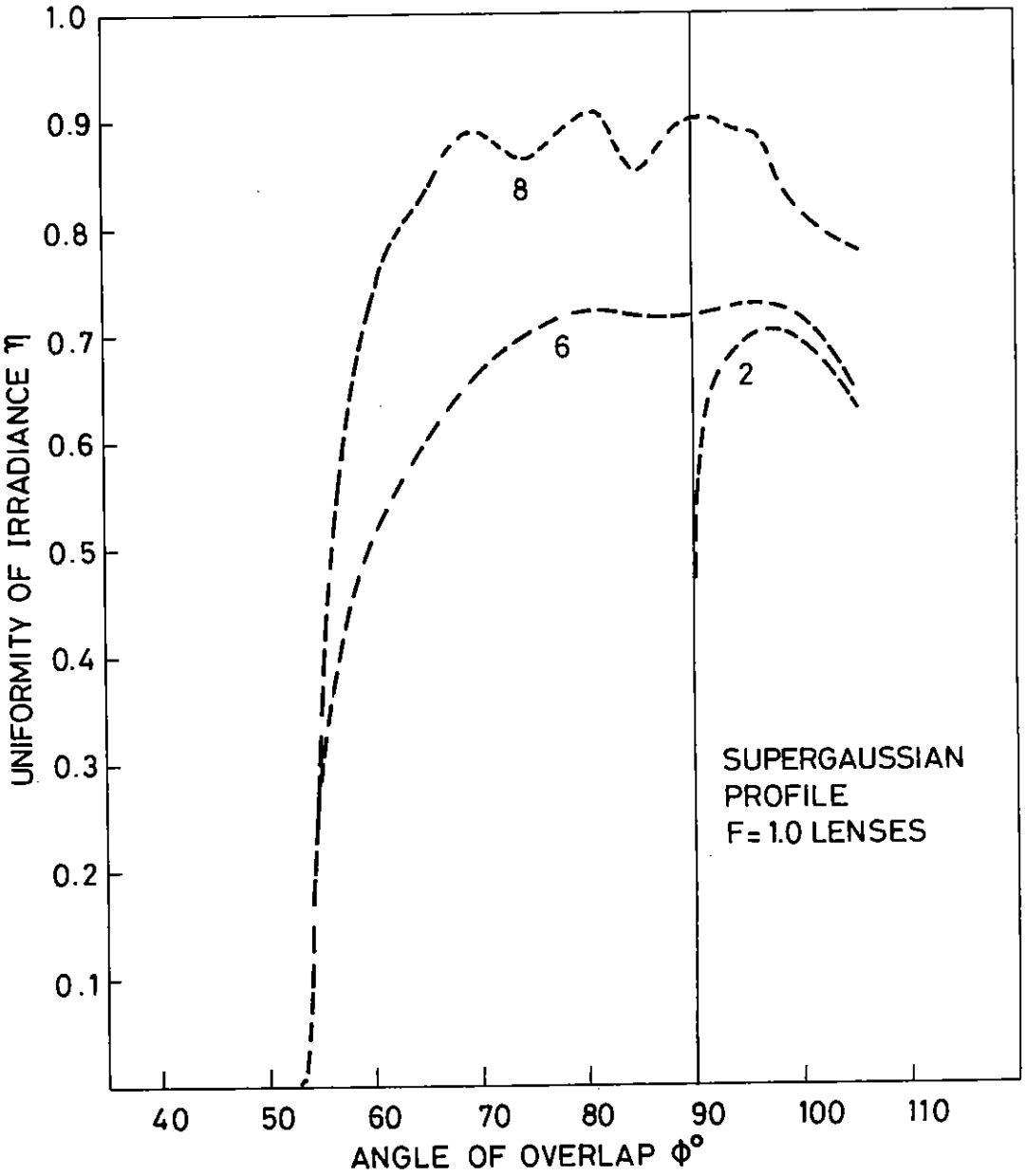

FIG. 1·25 UNIFORMITY OF IRRADIANCE – SUPERGAUSSIAN PROFILE

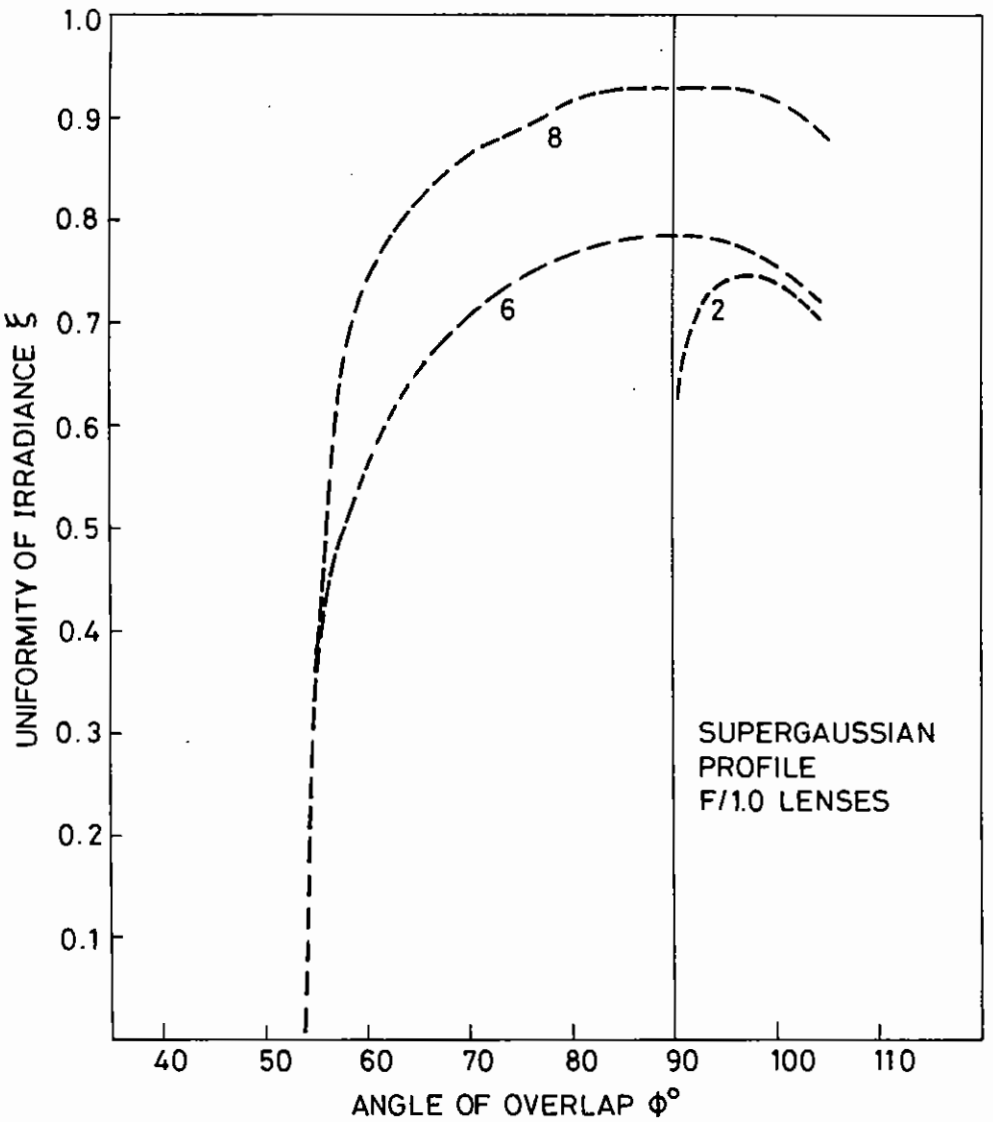

FIG 1·26 UNIFORMITY OF IRRADIANCE - WEIGHT MEAN COMPARISON

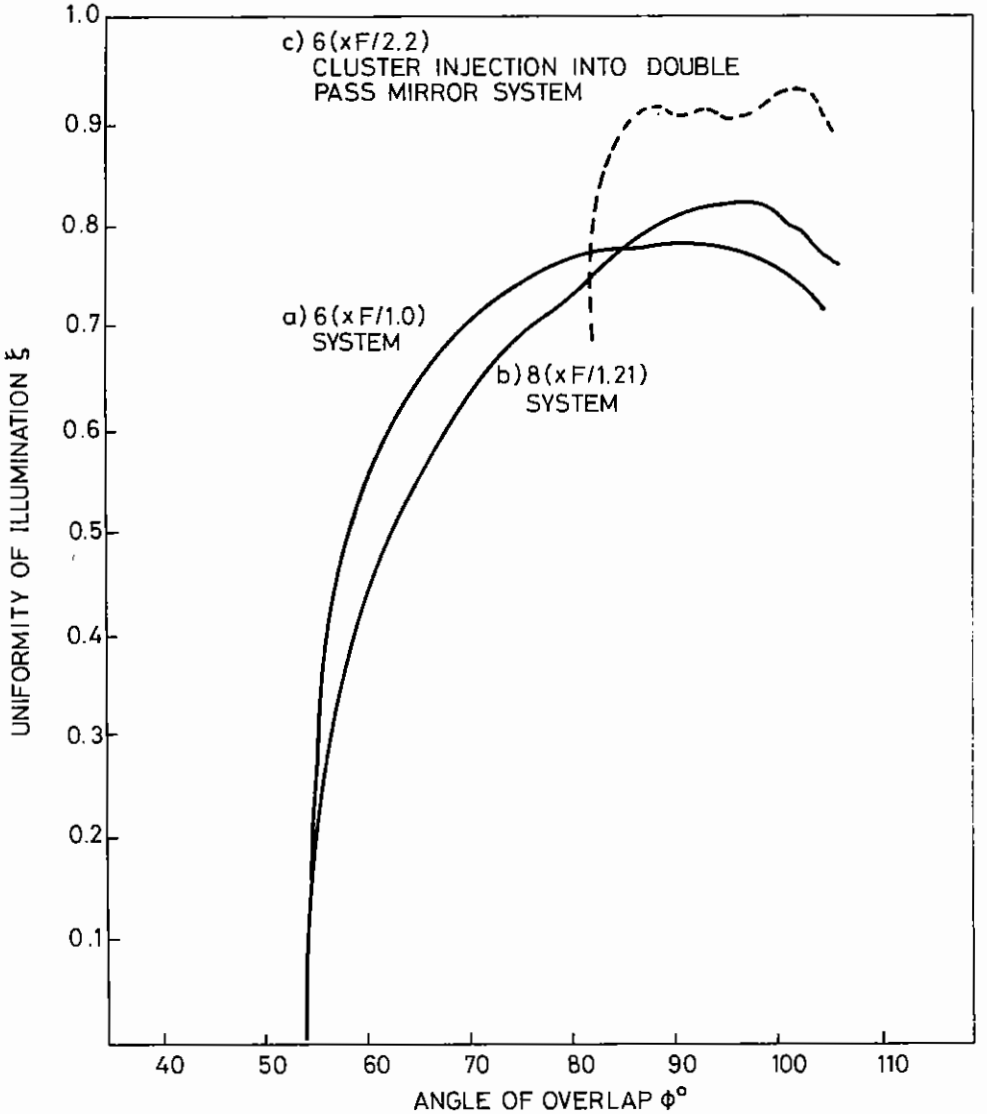

FIG1·27

a) & b) SIX AND EIGHT BEAM SYSTEMS WHICH INTERCEPT THE SAME SOLID ANGLE. c) SIX BEAM F2/2.2 CLUSTER INJECTION SYSTEM.

1.5.3(b) Effects of Illumination Asymmetries on Compression

The asymmetry of energy absorption around the surface of a spherical target will affect the symmetry of the implosion core in two ways: (a) the implosion velocity is a function of energy absorbed, (b) the asymmetry will drive the Rayleigh Taylor instability.

1.5.3(c) Implosion Velocity

We consider the implosion of a spherical shell, initial radius R_o thickness ΔR initially at rest. Under the action of the laser pulse the shell is uniformly accelerated and implodes at time $_{impl}$ with a final radius R_{impl}. The imploded configuration may not be spherical because of nonuniform illumination and the variation in imploded radius will be called ΔR_{impl}. We suppose that the pattern of non-uniformity of the illumination can be described by some harmonic series with "wavelengths" L and peak to peak amplitudes ΔI. The temperature non-uniformity produced by non-uniform illumination with a 'wavelength' L will persist for a time

$$t_{th} = 1.6 \times 10^{-14} \frac{(L/2)}{T^{5}/_{2}} \text{ sec.}$$

see for instance Ashby (1.13) where L is in microns and T in keV.

As a simple model we assume that the hotter parts of the target are accelerated at a rate $a + \Delta a$ for a time t_{th}, and then for the remainder of the implosion time $(t_{impl} - t_{th})$ they are accelerated at the same rate 'a' as the rest of the target.

Then from elementary dynamics

$$\frac{\Delta R_{impl}}{R_o} = \frac{2\Delta a}{a} \left\{ \frac{t_{th}}{t_{impl}} - \frac{1}{2} \left(\frac{t_{th}}{t_{impl}}\right)^2 \right\}$$

We require for a tolerably symmetric implosions that $\frac{\Delta R_{impl}}{R_{impl}} \lesssim \frac{1}{2}$

then

$$\frac{\Delta a}{a} \lesssim \frac{1}{4} \frac{R_{impl}}{R_o} \left\{ \frac{t_{th}}{t_{impl}} - \frac{1}{2} \frac{t_{th}}{t_{impl}} \right\}^2$$

In general the acceleration can be taken as propotional to $I^{\frac{1}{2}}$

so $\frac{\Delta I}{I} \lesssim \frac{1}{2} \frac{R_{impl}}{R_o} \left\{ \frac{t_{th}}{t_{impl}} - \frac{1}{2} \left(\frac{t_{th}}{t_{impl}}\right)^2 \right\}^{-1}$

if $t_{th} = t_{impl}$, ie we neglect the effect of heat conduction then we obtain $\frac{\Delta I}{I} \lesssim \frac{R_{impl}}{R_o}$ ie the maximum radial compression is about equal to the fractional non-uniformity of illumination.

1.5.3(d) Rayleigh-Taylor Instability

The imploding shell is unstable to the Rayleigh-Taylor instability while the dense shell is accelerated by the tenuous corona, the growth rate of the mode of wavenumber $k = 2\pi/L$ being $\gamma = \sqrt{ka}$ where a is the acceleration.

In general the Rayleigh-Taylor instability will grow out of "noise" but certain modes will also be driven by the non-uniform illumination. The temperature difference associated with the illumination non-uniformity is again assumed to exist for a time t_{th} as in section 1.5.3(c) and during this time the R-T modes corresponding to the pattern of non-uniformity in the illumination will be accentuated.

To a first approximation it can be argued that the R-T growth due to the non-uniform illumination will grow independently of any other modes arising from microscopic structure of the target. Thus the growth constant due to the illumination is

$$\gamma t_{th} = \sqrt{ka} \times 1.6 \times 10^{-14} \frac{(L/2)^2}{T^5/2}$$

According to the theory of Kidder (1.12) the non-uniform illumination $\Delta I/I$ is equivalent to an initial perturbation of the target surface ΔR given by $\delta R/\Delta R \approx 1/5 \Delta I/I$ where ΔR is the thickness of the shell. This perturbation will grow by the factor $\exp(\gamma t_{th})$ and in order to avoid the catastrophic break-up of the shell we must have

$$\delta R \exp(\gamma t_{th}) \lesssim \frac{1}{2} \Delta R$$

$$\text{ie } \Delta I/I \lesssim \frac{5}{2} \exp(-\gamma t_{th})$$

In order to determine γ we need to specify the acceleration 'a' which initially we take to correspond to a uniform implosion of a 100 μm radius target in 1nsec, ie

$$v = 10^{-4}/10^{-9} = 10^{5} ms^{-1}$$
$$a = 10^{14} ms^{-2}$$

Converting L in the formula for γ into microns we obtain

$$\gamma = 2.5 \times 10^{10} L^{-\frac{1}{2}} s^{-1}$$
$$t_{th} = 1.6 \times 10^{-14} \frac{(L/2)}{T^{5/2}}$$

and $$\Delta I/I \lesssim 5/2 \exp(-\gamma t_{th})$$

If t_{th} is longer than the implosion time t_{impl} then we must restrict the Rayleigh-Taylor growth at this point

ie $$\gamma t_{th} \lesssim \gamma t_{impl}$$

It must be pointed out that this argument only considers the specific Rayleigh-Taylor modes which are excited by the non-uniform illumination. Modes of large k will grow from 'noise' and may cause the break-up of a thin shell even for perfect illumination uniformity.

The numerical evaluation of the formulae obtained in sections 1.5.3(c) and 1.5.3(d) has been performed for the specific case of a moderately large target, R_o = 100 μm of unspecified thickness, imploded in $t_{impl} = 10^{-9}$ sec to an imploded radius $R_{impl} = 0.1\ R_o$.

The results of these calculations are shown in Fig.1.28 and Fig.1.29 representing the restrictions described in sections 1.5.3(c) and 1.5.3(d) respectively. The calculations have been performed for four values of the coronal temperature 100eV, 250eV, 500eV and 1 keV. The effects of changing: R_o to 50μm and t_{impl} to 5×10^{-10}s are shown in Figs.1.30 and 1.31 the case of R_o = 50μm, $t_{impl} = 10^{-9}$s leaves Fig. 1.28 unchanged but the effect on the 'Rayleigh-Taylor' restriction is shown as the chain line in Fig.1.32.

1.5.3(e) Discussion

Numerical values of $\Delta I/I$ as a function of the non-uniformity 'wavelength' are shown in figures 1.28 and 1.29. Fig.1.28 shows the restriction on uniformity if the implosion velocity is to be uniform, the left hand scale assumes that the desired radial compression

$R_{impl}/R_o = 0.1$, and the right hand scale shows the more general quantity

$$Q = \frac{\Delta I/I}{R_{impl}/R}$$

The horizontal cut off at Q = 1 corresponds to no thermal conduction, ie $t_{th} \gtrsim t_{impl}$.

Fig.1.29 shows the requirements to limit the growth of Rayleigh-Taylor modes corresponding to the pattern of non-uniform illumination. The asymptote at $\Delta I/I = 2.5$ is somewhat non-physical since it corresponds to a zero growth constant of the Rayleigh-Taylor mode and the equations used are not valid for $\gamma t_{th} \lesssim 1$. The parts of the curves with $\Delta I/I \gtrsim 1$ are best ignored and Fig.1.28 should be used to determine $\Delta I/I$ in this region.

Fig.1.32 shows the more restrictive condition taken from Fig.1.28 and Fig.1.29, with the above proviso that regions of Fig.1.29 with $\gamma t_{th} \lesssim 1$ are ignored. Only the data for T = 100eV are plotted since at the higher temperature the 'implosion velocity' restriction is always more severe than the 'Rayleigh-Taylor' restriction. It is clear that if the coronal temperature is as low as 100eV, or if the thermal conduction in a hotter corona is inhibited so as to produce a similar conductivity, then there is a range of wavelength around 30μ where Rayleigh-Taylor instabilities are likely. If the corona is significantly hotter than 100eV and classical heat conduction can be assumed then the most demanding requirement on the illumination is at very long length scales $\gtrsim$ 60 μ where a uniformity of 10% is required. In particular this means that each beam of a mult-beam illumination system should be within 10% of the mean energy. In the range of scale lengths 20μ - 60μ the required uniformity of illumination is critically dependent on the heat conduction in the corona and no definite statements can be made from the present analysis. This is clearly a profitable area for experimental study.

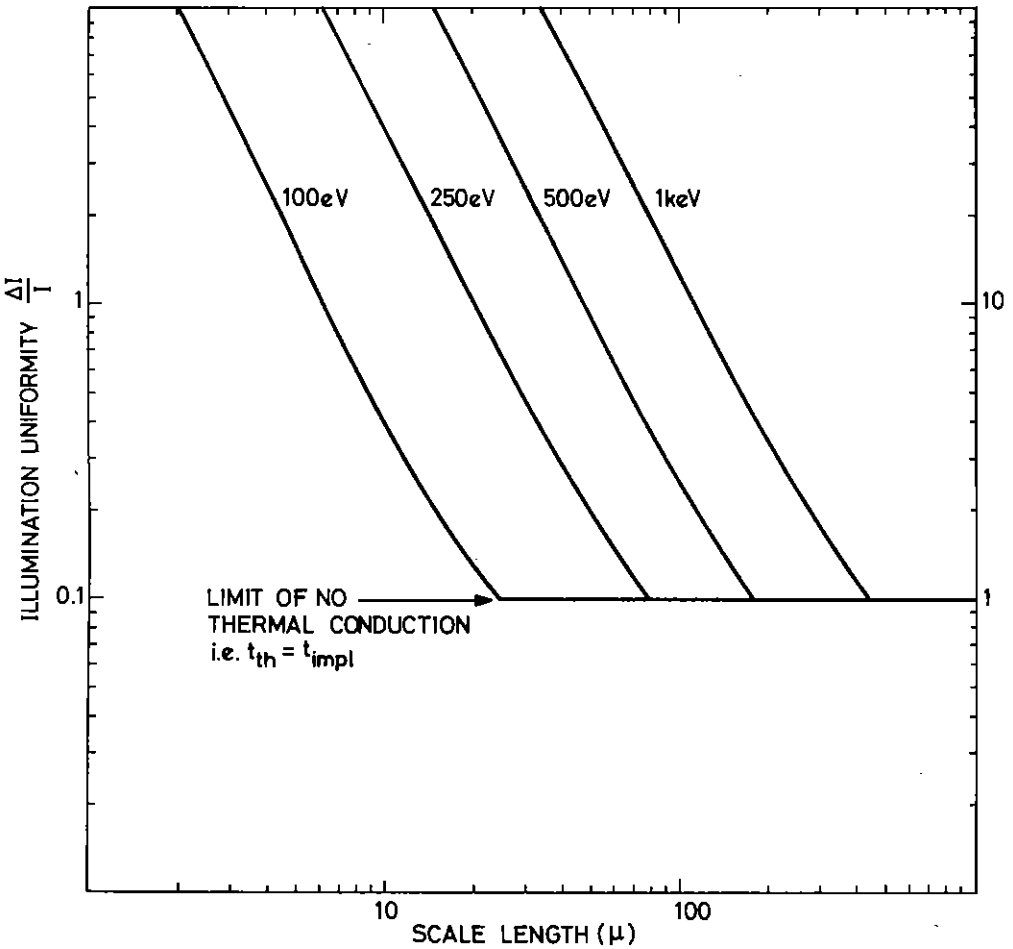

FIG 1·28. "IMPLOSION VELOCITY" RESTRICTION ON ILLUMINATION UNIFORMITY

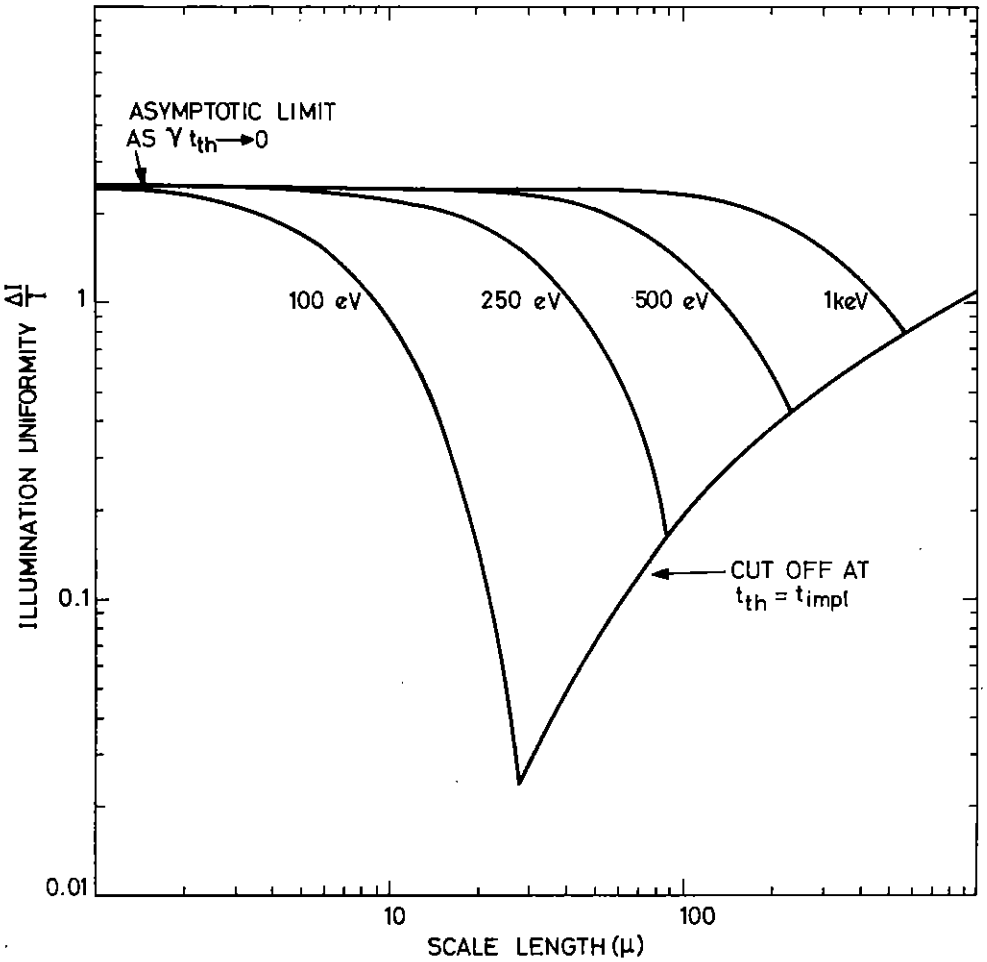

FIG 1·29 "RAYLEIGH-TAYLOR" RESTRICTION ON ILLUMINATION UNIFORMITY

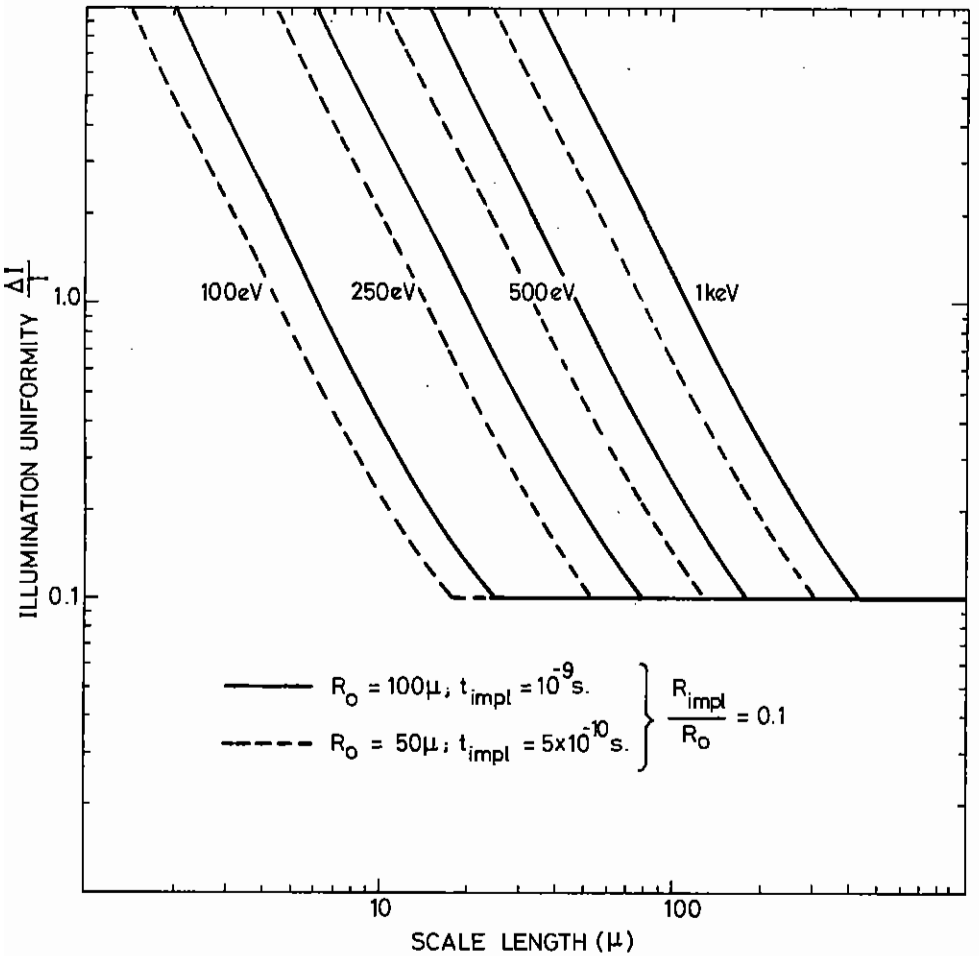

FIG 1·30

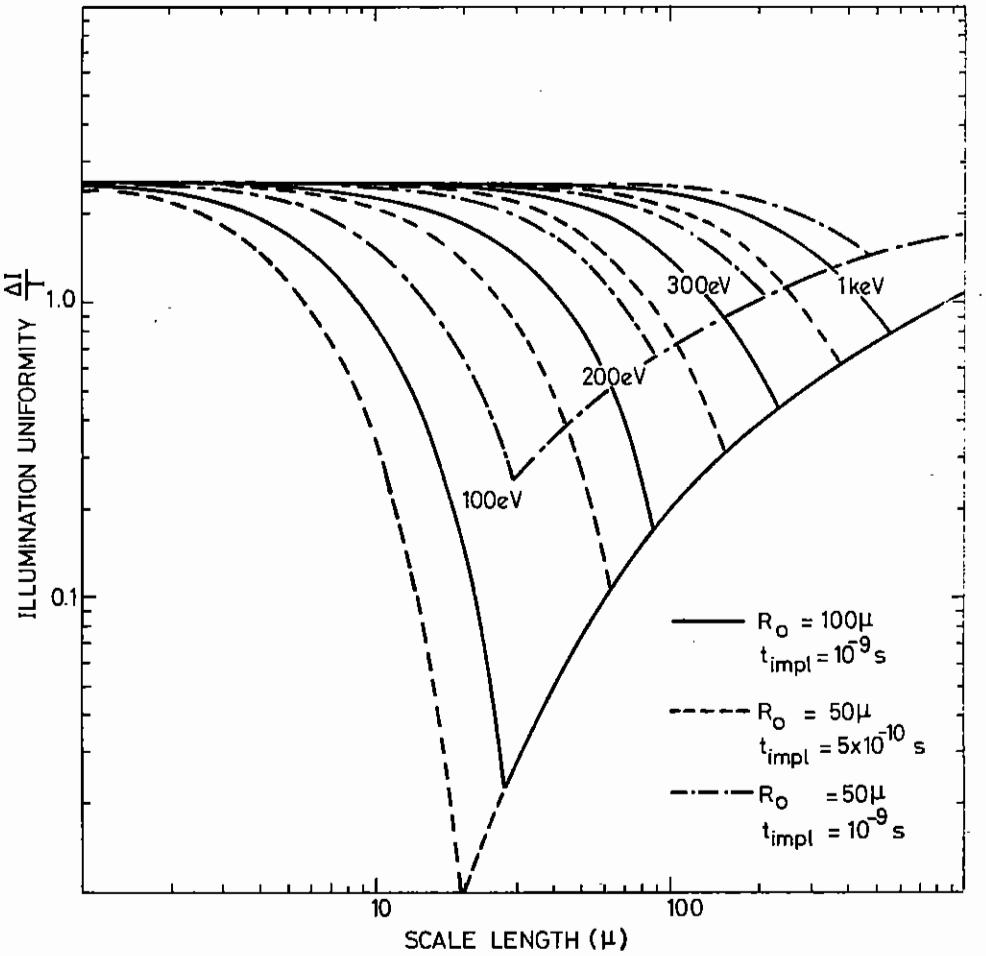

FIG 1·31

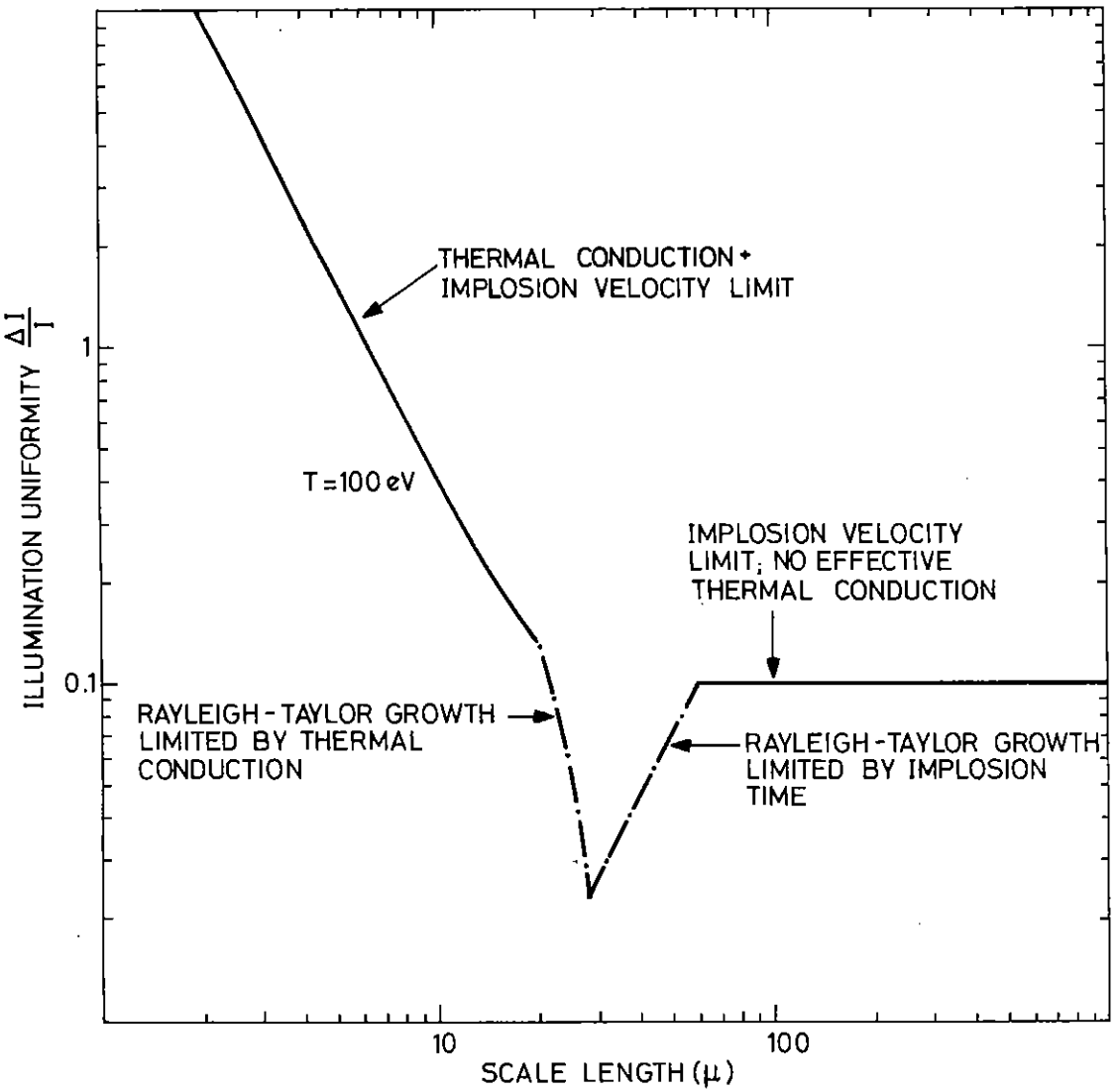

FIG 1·32 OVERALL RESTRICTION ON ILLUMINATION UNIFORMITY

1.5.4 Development of Components

The major effort was directed to the design and development of a lens mount and target positioning mechanism suitable for the six beam target facility.

Both of these components required the following features:

1. Stability of position - free from vibration or movement due to vacuum induced stresses.
2. Positioned control to an accuracy of better than 5 μm.
3. Permanent indication of relative position.
4. Remote control and position indication.
5. Vacuum compatibility.
6. Reliability of components.

The drive systems chosen for both components consist of standard 0-15 mm barrel micrometers driven by a 200 step/revolution stepping motor. This enables a repeatable displacement of 2.5 μm to be obtained for each step. All the normal lubricant is removed from each component, and replaced with a high grade vacuum grease. One assembly was translated over the whole range (0-15 mm) 10^6 times without any serious problems.

The lens mount (See Fig.1.33) incorporates three such drive systems giving control of the lens in 'X','Y' and 'Z' directions. Each of these movements is kinematically restrained and is driven through a 2:1 linkage, thus giving a movement of 1.25 μm for each step of the motor. The lens mount also has manual adjustments for tilt in the 'X' and 'Y' planes.

The target mechanism (See Fig.1.34) also incorporates three drive systems, giving 'X','Y' and 'Z' motions, each of which is restrained to move by cross roller slides, and is directly coupled to the drive system. Each drive system is fitted with a precision linear potentiometer to give permanent relative position.

Both of these components have been designed as complete subsystems, so that they can be assembled, tested and calibrated before assembly into a target vessel.

To update the original target chamber, when it was moved into the new single beam target area (TAII), it was decided to incorporate three of the new lens mount assemblies (two main beams, and a backlighting beam) and a new target positioning mechanism. This has enabled these devices

to be operationally tested before setting up the six beam system. Suitable control and indication systems have been developed and tested. The control system used in the single beam target area (TAII) enables any one motion of the twelve 'X','Y' & 'Z' motions to be selected and operated either at the central panel Fig.1.35 or from a remote hand box on a flexible lead at the target chamber. Operation of either the forward or reverse buttons gives a single step command to the drive motors, but if the button is held depressed for longer than 0.6 sec then the motor is continuously driven until either the button is released, or the motion reaches its limit switch, in which case a buzzer sounds until the motion is reversed. Each step of the motor is recorded on a digital counter, added for forward movement, subtracted for reverse. In addition the relative position of each motion is monitored from the precision linear potentiometers with a digital voltmeter.

The other major improvement made during the move to target area TAII was to the vacuum system of the target vessel. The vessel now pumps down to vacuum below 10^{-2} torr in 4 mins irrespective of the degree of contamination from experimental apparatus containing film etc., whereas previously pump times of 30-60 mins had been required to reach these pressures. This has been accomplished by having separate mechanical roughing and backing systems, the roughing system consisting of an Edwards EM1200 mechanical booster pump backed with a GK547 Kinney Pump. The booster is run for a preset time of 4 mins, the diffusion pump system cuts in automatically during this sequence. The let-up system has also been improved by the provision of a matched volume tank filled with clean dry nitrogen at high pressure. This is connected to the tank and the pressure equalises between the two volumes to atmospheric pressure thus preventing over pressure in the vacuum vessel. This enables the vessel to be let up in $\sim$2 mins when previously $\sim$10 mins was required.

1.6 Target Fabrication

1.6.1 Target Requirements

Production and measurement of microsphere type targets has once again been the major activity of the target preparation group. The experimental programme has called for targets of much greater variety and complexity than previously.

This year has seen the commencement of ablative type compression experiments which require targets with considerably greater wall thickness (up to 15 μm) than the simple thin walls ($\sim$ 1 μm) microspheres used for exploding pusher experiments. Consequently various coating techniques for building up the wall thickness of microspheres have been evaluated and developed. Targets with coatings of plastic up to 12 μm thick can now be routinely produced.

Compression experiments diagnosed by X-ray shadowgraphy techniques have been conducted this year and have required targets of greater complexity (as shown in Fig.5.05(b)). Mounted characterized targets have to be transferred to special brass supports and carefully aligned with one face which acts as an X-ray source behind the imploding target when irradiated with a laser beam. Such targets each require several hours to fabricate. Many simple thin walled, gas filled microspheres have been processed, measured and mounted for use in two-beam compression experiments, interaction physics experiments and for alignment purposes. In addition numerous hollow and solid spheres of various other materials (eg polythene, magnesium, manganese/nickel alloy, tungsten carbide and uranium) in sizes from 50 to 300 μm diameter have been supplied for various experiments.

Production of multi-layered flat foil targets for transport experiments has continued. Additional material layers have been incorpoirated (eg Au, KCl and Ti0) and targets now contain up to 7 layers with thicknesses between 0.1 and 4 μm.

Numerous thin ($\sim$ 0.1 μm) polystyrene and cellulose nitrate foils have been cast for laser beam burn through type experiments. In addition these foils have been used as ultra thin substrates onto which layers of either gold or aluminium have been deposited to make sensitive photocathodes for the X-ray streak camera or soft X-ray filters for spectrometers.

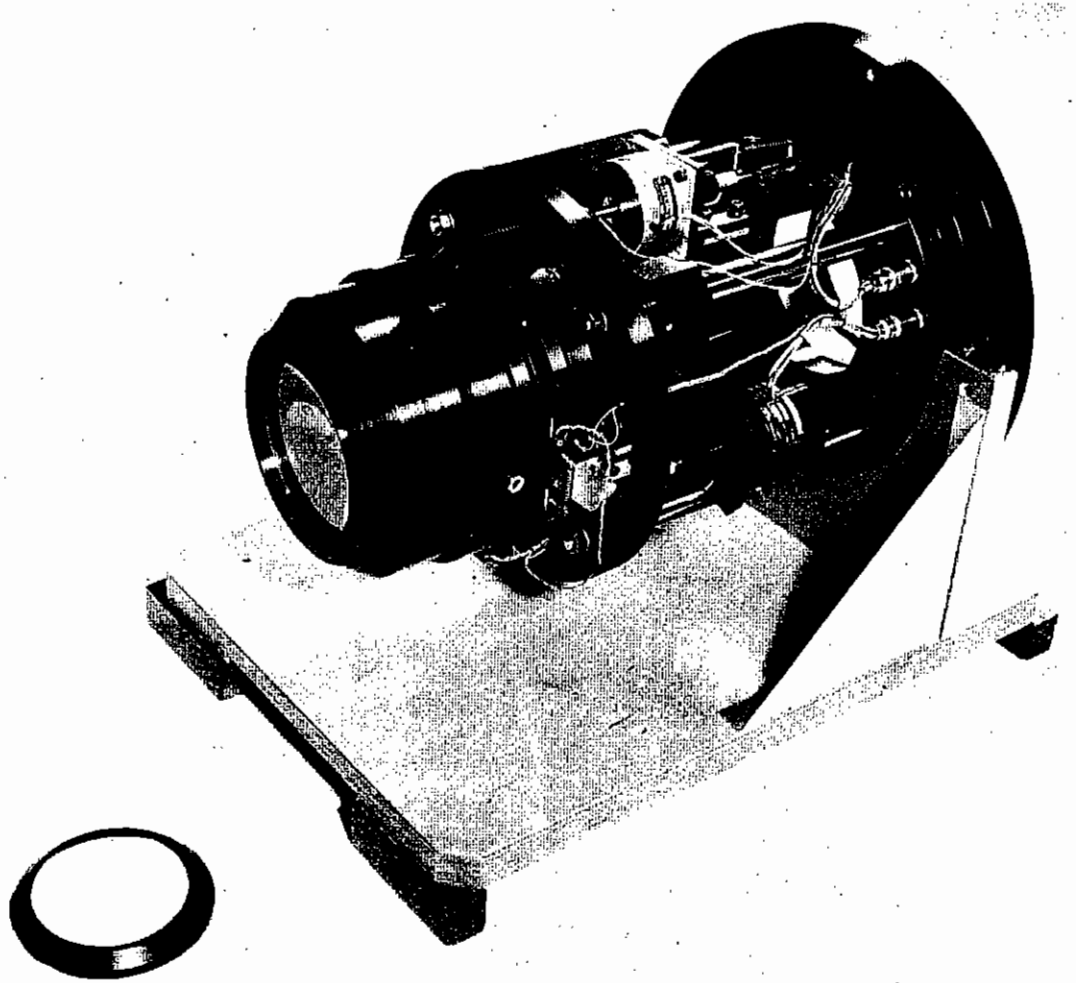

FIG 1.33 MOTORISED LENS MOUNT.

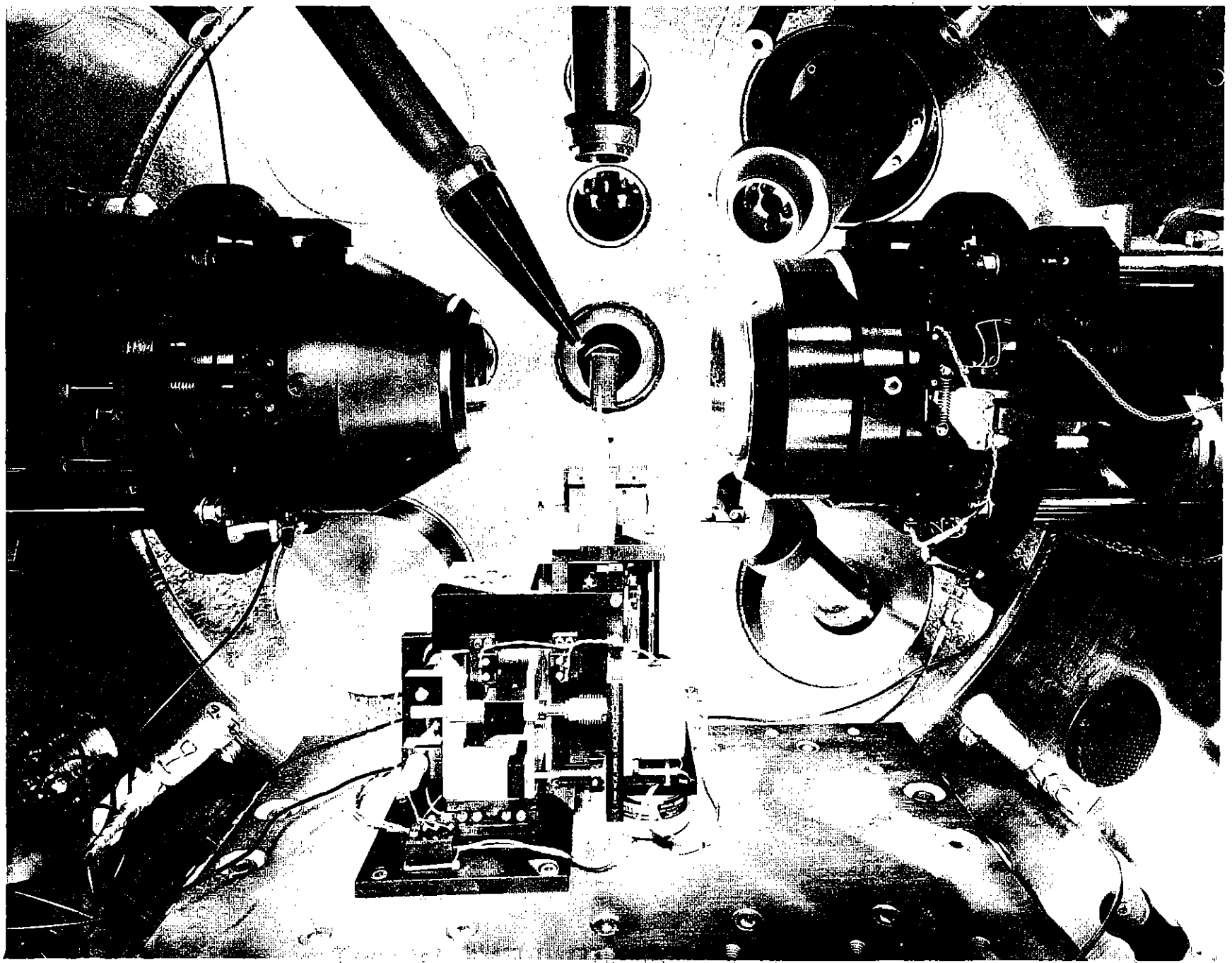

Fig. 1.34

TAII Target chamber showing 2 lens mounts, target system & various diagnostics

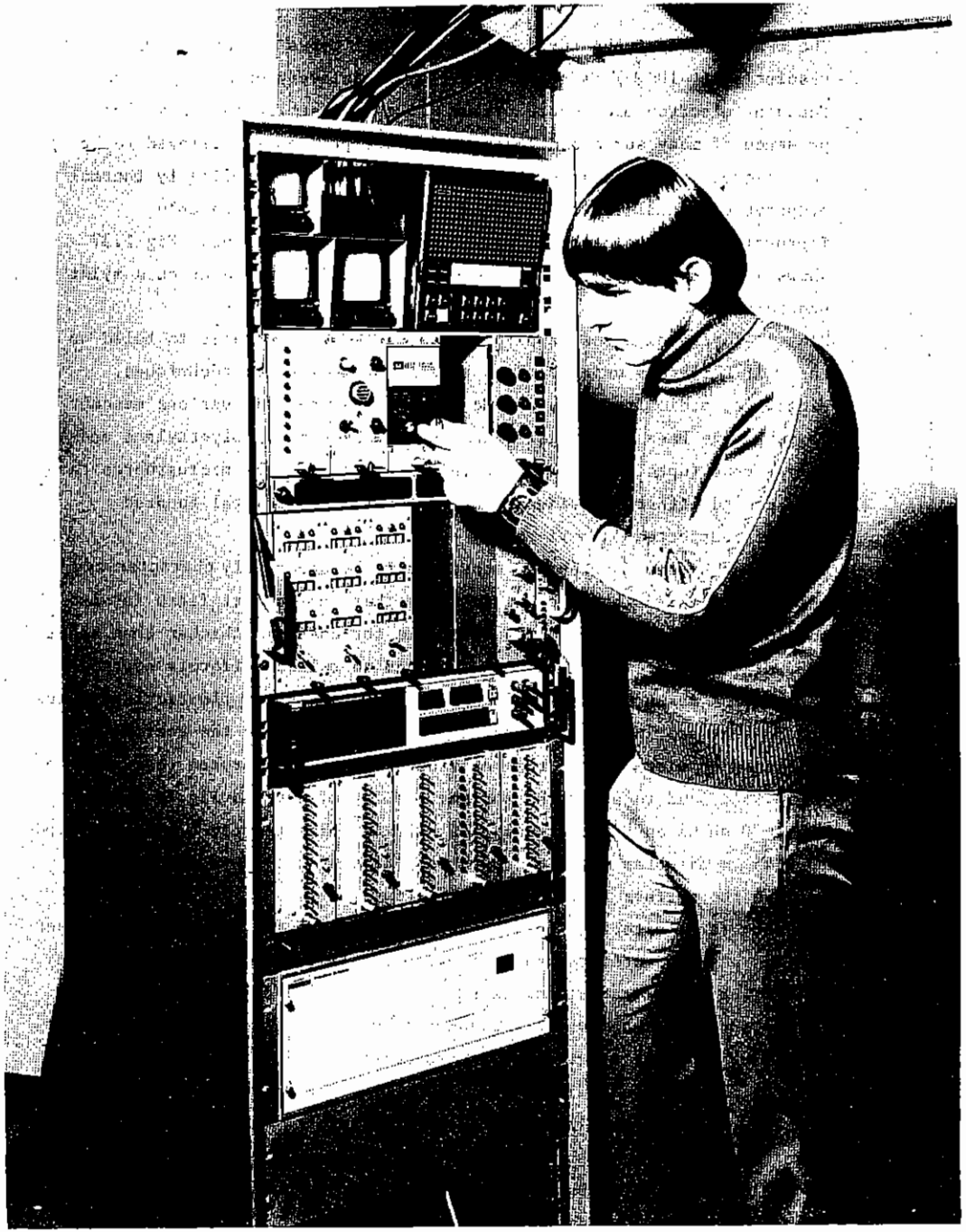

Fig. 1.35
TAII Remote Control Panel

As well as acting as microsphere supports, carbon fibres have been incorporated into complex targets for use in experiments studying possible X-ray laser schemes. For this type of experiment the target consists of an 8 mm length of thin fibre stretched across a gap so that it can be irradiated with the line-focussed laser beam. A tungsten plate, glued close to one end of the fibre, is irradiated during the expansion phase of the cylindrical carbon plasma by means of a delayed laser pulse. The plasma formed acts as an X-ray source to probe the expanding plasma to detect population inversion and gain at a wavelength of 18.2 nm. The Materials Development Group at AERE Harwell has processed extremely small diameter (3 to 4 μm) fibres for these targets. Experiments designed to study spontaneously generated magnetic fields in laser produced plasmas have involved the manufacture of another type of fibre target. These consisted of 125 μm diameter fibres of nylon onto which bands of aluminium of 100 nm thickness were superimposed by coating and masking techniques. With the laser beam focussed on the discontinuity between the aluminium and the nylon such a target geometry is predicted to give rise to spontaneously generated magnetic fields aligned along the discontinuity.,

1.6.2 Techniques

Hollow glass microsphere processing has been improved by the construction of a Freon flotation rig for wall thickness separation. After sieving to a particular diameter miscropheres are loaded into a vessel which can be pressurized with Freon. As the pressure is increased above a few 100 psi the Freon density becomes comparable to the microsphere density and the thinest walled targets float to the top of the vessel where they are collected. This equipment has proved invaluable for the production of targets of both high and low aspect ration ($R/\Delta R$).

Microsphere measurement techniques have been improved by the acquisition of a Nomaski type interference microscope to supplement the present Twyman-Green system. With this new equipment the wall thickness and uniformity of glass microspheres can be checked with much greater accuracy both before and after mounting on a support fibre. Fig.1.36 shows an interferogram of a mounted glass microsphere target obtained with this equipment.

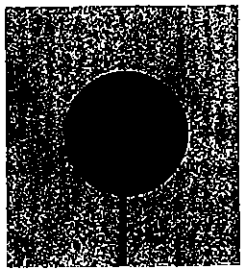

Fig. 1.36

Interferogram of mounted plastic coated glass microsphere target.
ϕ 250 μm Total wall thickness 2 μm.

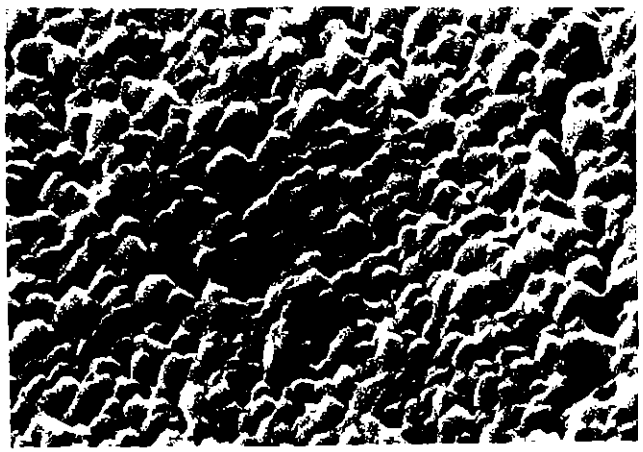

Fig. 1.37

Surface of a 3 μm thick Kα layer applied to a mylar substrate.
Magnification x5000

The examination of the surface finish of all types of targets with high resolution (~ 100 Å) is now possible since delivery of a very versatile scanning electron microscope system. Such inspection has shown the presence of many surface defects on targets previously believed to be satisfactory. For example study of material layers applied by thermal evaporation techniques to foil targets has led to considerable improvements in choice of material and coating conditions. Fig 1.37 shows a micrograph of the surface of a 3 μm thick KCl layer on a mylar subtrate.

Plastic layers have been applied to microsphere substrates to build up the wall thickness using various plasma polymerization techniques. Microwave, audio frequency and dc discharge systems in various manomer vapours have been investigated and uniform layers of polyethylene and polystyrene (upto 12 μm thick) have been applied. The microspheres have been coated either individually after mounting or several hundred together supported on a vibratory pan.

The former system enables the substrate to be accurately characterized before coating but has the disadvantage that the support fibre is also coated. The latter system is preferable for coatings thicker than about 1-2 μm. Interference techniques are used to select uniformly coated targets and measure wall thicknesses since the applied plastic layers are transparent and in addition the SEM is used to measure the coating thickness on microspheres that have been mounted and broken (as shown in Fig.5.05(a))and to study the surface quality of targets Fig.1.38. Fig.1.40 shows an SEM photograph of a 12 μm thick plastic coating applied to a 45 μm diameter glass microsphere. Efforts are now being made to improve the surface finish of such coatings.

A system for monitoring the tritium content of DT filled exploding pusher targets has been constructed. The β-particles emitted during the decay of tritium in the target strike the glass wall and cause characteristic X-rays to be produced which are counted by two gas proportional counters. Fig.1.39 shows the spectrum of X-rays emitted. The total X-ray count is a function of target wall thickness and diameter and calibration is carried out by monitoring various measured targets which are subseqnetly burst under oil to measure the total gas content. With this equipment several targets with abnormally low X-ray counts due to gas leakage have been identified and eliminated.

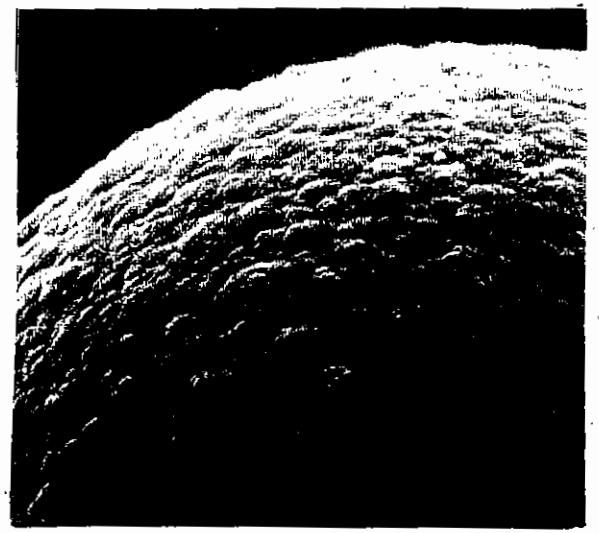

Fig. 1.38

Surface of glass microsphere coated with 12 μm of polyxylene.
Magnification x 2250

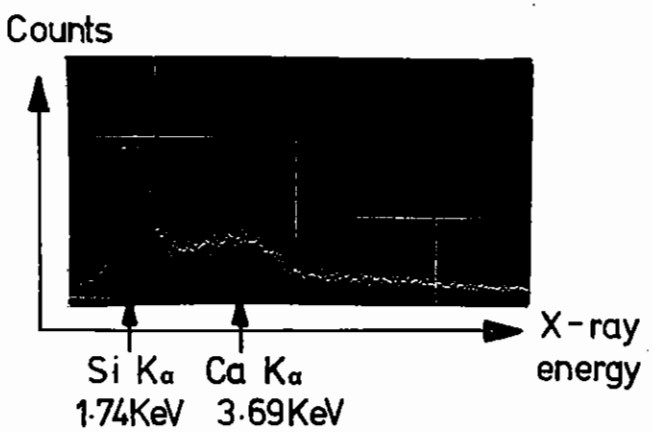

Fig. 1.39

Spectrum of X-rays emitted from a DT fillted glass microsphere

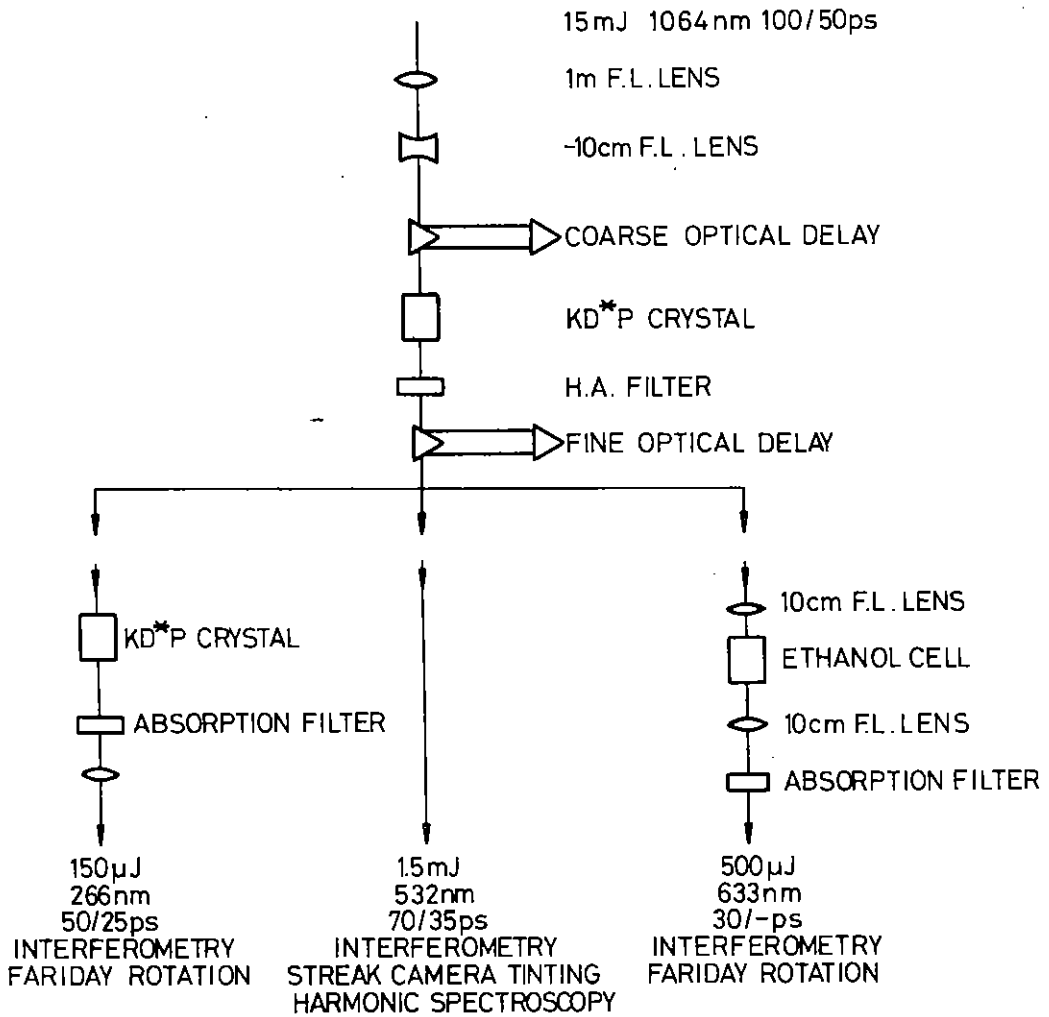

FIG1.40 ARRANGEMENT OF OPTICAL PROBE BEAMS

1.6.3 Target Production (Statistics)

The number of targets produced during the year has risen considerably above last year's figure. Over 600 microsphere targets have been processed measured and mounted ready for compression and interaction experiments. In addition several hundred other types of targets such as thin foils, multi-layer foils, lollipop targets and carbon fibre targets have been supplied for interaction physics and other experiments.

1.7 Diagnostic Development

1.7.1 Optical Probe Beams

Optical probing beams, derived from the main laser harmonics, have been generated to suit the requirements of the experimental programme. Probe wavelengths of 532 nm (2nd harmonic) 633 nm (Raman shifted second harmonic) and 266 nm (4th harmonic) have been used, the latter two being derived from the second harmonic by further frequency conversion stages. The main uses of these probe beams are:

1. 532 nm: Interferometry
   S-20 streak camera timing
   Calibration harmonic spectroscopy experiment
   Drives for other probe beams

2. 633 nm: Faraday rotation
   Interferometry

3. 266 nm: Interferometry
   Faraday rotation

The arrangement to generate the probe beams is shown in Fig.1.40. In general, the particular system needed is assembled specifically for an experiment and is subsequently dismantled. A portion of the main beam is split off after the vacuum spatial filter by a partially transmitting turning mirror. The beam at this point is of well defined divergence irrespective of changes in the pumping of the laser rods. The 60 mm diameter split-off beam is reduced to a 6 mm diameter, and passed through an optical delay to achieve approximate synchronisation with the main beam at the target chamber. The beam at this point is approximately 15 mJ giving an intensity of $10^{9}Wcm^{-2}$ at the first frequency doubling crystal. This is a 30 mm long KD*P (deuterated potassium dehydrogen phosphate) crystal cut for Type I critical phase matching. At maximum input energy approximately 10% energy conversion to the second harmonic is achieved. The unconverted 1064 nm light is absorbed in a heat-absorbing glass filter leaving 1.5 mJ of green light which is either used directly or for driving further frequency conversion stages.

For Faraday rotation experiments, where second harmonic emission from the plasma can prove troublesome, the second harmonic is shifted in frequency by stimulated Raman scattering (Ref.1.14) in ethanol. This gives a red output beam at the 1st stokes frequency which is coincident with the He-Ne laser line and hence facilitates alignment. After a further optical delay to allow timing adjustments of the probe beam at the target, the green light is focussed by a 10 cm focal length lens into a 7.5 cm long cell of ethanol. The beam travels through the cell as a self-focussed filament and is collected at the output by a further 10 cm focal length lens. The output beam is filtered by an absorption filter to give 500 μJ of red light which, since scattering is in the transient regime (Ref.1.15), is also pulse shortened by a factor 3 to 30 ps.

To generate the fourth harmonic (266 nm) the second harmonic beam is passed directly into a Type I non-critically phase matched short (4 nm) KD*P crystal. The wide temperature ($\pm$ 10°C) and angle ($\pm$ 10 mrad) tuning ranges of the short KD*P crystal result in very non-critical alignment. In practice setting the crystal normal to the beam line, using the back reflection of a HeNe laser from the crystal face, and setting the temperature controller to 40°C is found to be sufficient to achieve optimal conversion efficiency. Conversion from the second to fourth harmonic is achieved with 10% efficiency giving 150 μJ of UV output.

The systems used so far suffer from two disadvantages namely (1) The repetition rate is limited to that of the front end of the main laser to two minutes which can make alignment tedious and (2) The pulse input is tied to that of the main laser. For the two new target areas, these problems are being overcome by having separate probe beam systems driven from the oscillator. This allows greater flexibility in generating for example a short probe pulse and long main pulse by pulse stacking or regenerative amplification methods and a high repetition rate for alignment (20 pps). A fraction of the oscillator pulse will be split-off after spatial filtering and amplified up to a maximum of 100 μJ in a high repetition rate amplifier. The beam will then be passed via a multipass delay line to one of the two target areas where a fine optical delay and further spatial filtering will occur before the relevant frequency conversion stages. It is hoped to be able to provide probe beams at all times as a standard diagnostic tool by this method.

1.7.2 X-Ray Imaging

1.7.2(a) Grazing incidence X-ray microscope

A grazing incidence X-ray microscope has been built and tested at Queen's University, Belfast. The instrument has a measured resolution of $\sim 4\ \mu m$ and therefore offers improved resolution over existing pinhole imaging systems.

The refractive index of all materials is less than unity in the X-ray region of the spectrum, therefore, X-rays incident on a smooth surface are totally reflected if the angle of incidence is less than a certain critical angle; given by;

$$\theta_c = \lambda(Ne^2/\pi mc^2)$$

N_e = electron density in the solid

For gold $\theta_c = 7 \times 10^5 \lambda$ (λ in cm)

The scheme proposed by Kirkpatrick and Baez is shown in Fig.1.41. A concave spherical mirror produces a line focus with a focal length given by:

$$f = \frac{R_i}{2}$$

R = radius of curvature of mirror and

i = glancing angle of incidence

The severe astigmatism is removed by placing a second mirror, orthagonal to the first such that radiation reflected from both mirrors forms a point to point image of the source.

The resolution of the microscope is limited mainly by spherical aberration and can be expressed as:

$$s = \frac{3}{2}\ \frac{r^2}{R}$$

where r is the radius of the mirror aperture.

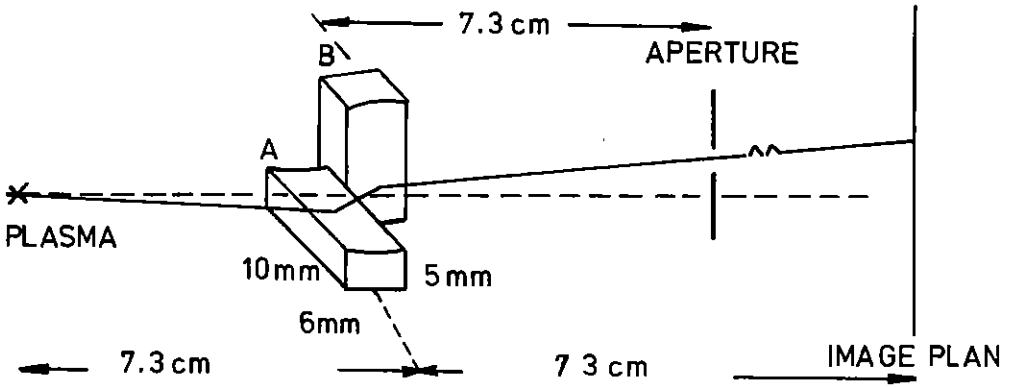

GRAZING INCIDENCE
X-RAY MICROSCOPE

Fig 1·41

INSTRUMENT DESCRIPTION

Object distance	7.3cm
Magnification	10
Grazing angle	1.5°
Radius of curvature of mirrors	5m
Coating	Gold
Resolution	~3 μm
Solid angle	2×10^{-6} sr

X-RAY IMAGE

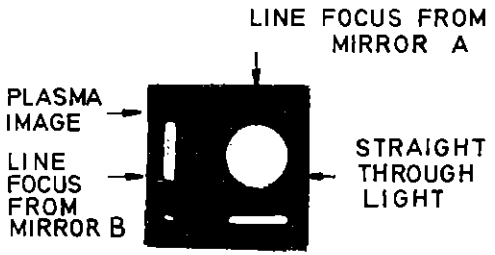

Fig 1·42

For the Queen's University design shown in Fig.1.42:

$s = 3\mu m$

The resolution of the microscope was measured by using the X-ray radiation from a laser-produced plasma to backlight a fine copper mesh placed in the object plane of the mirrors. The grids consisted of 20 μm wide copper bars separated by 5 μm. Fig.1.43 shows a microdensitometer trace of a grid image, recorded on INDUSTREX C X-ray film, from which a resolution of ~ 4 μm can be inferred.
The microscope has ben used successfully for several experiments at the Laser Facility and shown in Fig.1.44 is a typical microscope picture of a microballoon implosion.

A measurement of the resolution of the instrument with a magnification of x15 has also been made and it is planned to couple the microscope, in the times 15 mode, to the X-ray streak camera.

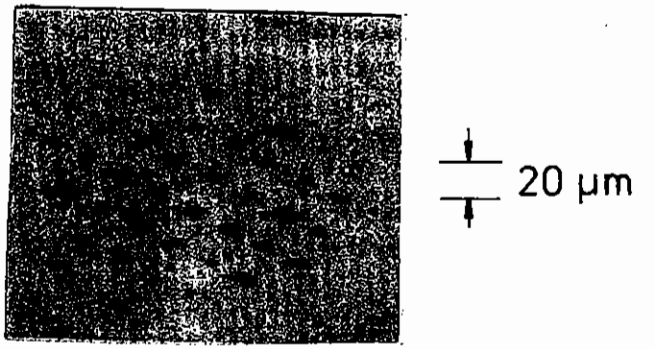

X-RAY IMAGE OF GRID

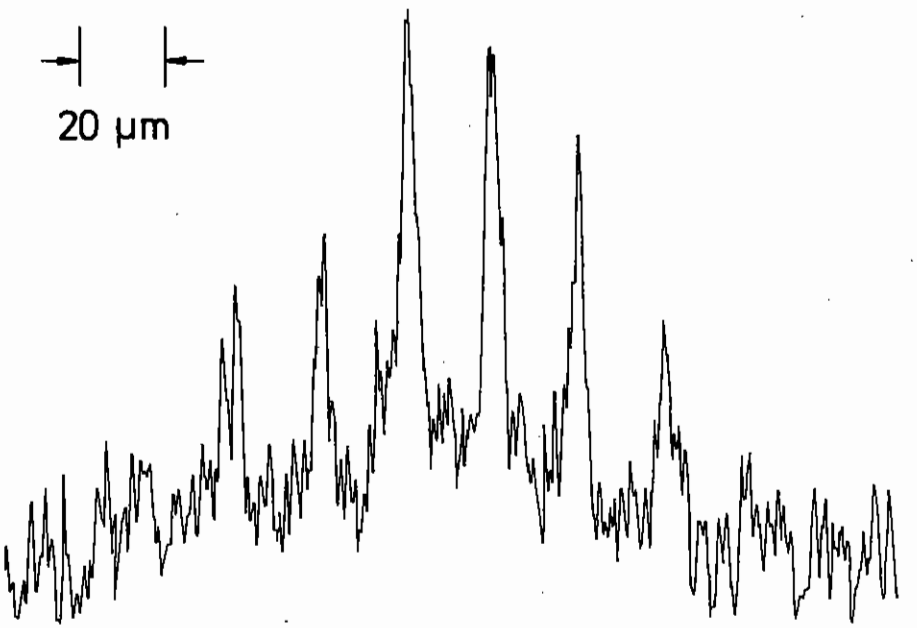

FIG 1.43

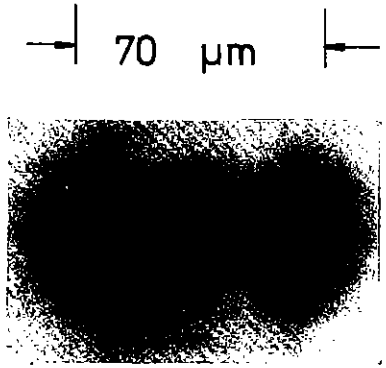

X-RAY MICROSCOPE IMAGE

FIG 1.44

1.7.2(b) Toroidal grazing-incidence mirror

To collect radiation adequate to record a grazing incidence X-ray spectrum, the spectrograph slit is normally placed as close as possible to the source to obtain as bright an astigmatic image of the slit in the focal curve as possible. However the space constraints due to other instrumentation inside the Laser Facility's target chambers make the placing of a bulky slit assembly close to the plasma difficult and antisocial. The problem has been solved for the GML5M grazing incidence spectrograph (section 1.7.5(b)) by imaging the target onto the spectrograph slit, placed about 76 cm away, using a grazing-incidence toroidal mirror placed midway between the two in such a position that the slit and plasma are on the mirror's Rowland circle (circle diam = mirror major radius). (This mirror is in fact a blank for one of the toroidal gratings described in Section 1.7.5(b). It forms a small part of the surface of a torus of 5m major radius and 25 mm minor radius, the section being approximately 5 cm long x 1 cm wide and taken normal to the major torus section). Used in this mode the torus produces a xl magnified image on the slit matched approximately to the f/no of the GML5M, and therefore, by the well-known brightness theorem of optics, relays the maximum amount of useful light into the instrument. The torus is currently being used in this 'collection lens' mode in the carbon VI laser gain experiments (Section 7.2.2).

Experiments by D Turner and R J Speer at the Blackett Laboratory, Imperial College, have shown that it is also possible to use the torus in the magnifying mode to produce images magnified up to 20x or more without serious aberrations, contrary to what had previously been expected from the properties of grazing incident optics. Such a simple X-ray microscope system would be useful both on its own and in conjunction with an X-ray streak camera for laser plasma and implosion studies; work to develop such a system has been proposed as part of the Universities' research programme associated with the Laser Facility.

1.7.2(c) X-ray microfocus source

With increasing demands on glass laser time and increasing complexity of X-ray optical systems, the need has arisen for a separate test facility for evaluating the performance of such systems.

A small but highly efficiency X-ray microfocus source has been developed by D J Pugh and P D West (Ref.1.16) (at the National Physical Laboratory for microradiography and X-ray Optics (eg for X-ray astronomy) testing, and forms the basis for a test system under construction at the Rutherford Laboratory. The triode electron gun in conjunction with a special single pole Mulvey magnetic lens is capable of focussing a 5 μA beam of 25 keV electrons into a 2 μm spot on any selected conducting target approximately 5mm from the lens snout. Associated with the electron source is a focussing detection system which permits simple optimisation of the spot size, and a scanning system enabling the beam to be magnetically scanned over an area approximately 500 μm x 500 μm around its central position. The electron source is sufficiently small and adaptable that its use to produce an X-ray source 'in situ' in the target chamber is anticipated, to enable X-ray microscopes and other devices to be lined up 'CW' without using laser shots. As an external test facility it will be used in the development of the grazing incidence optics systems described here and in section 1.7.5.

1.7.3 Xray Detectors

1.7.3(a) Caesium Iodide X-ray Photocathodes

During the year significant advances have been made in X-ray recording by using CsI photocathodes which were developed at the Laboratory.

The caesium iodide (CsI) X-ray photocathode consists of a layer of CsI evaporated onto a suitable substrate (typically a thin beryllium foil) in such a way that a layer of spongy solid is produced with a density of (typically) 5% of the crystalline form of the material. X-rays absorbed by the atoms of the material generate photoelectrons which in turn generate a cloud of a few hundred electrons. With suitable extraction electric field strengths a large proportion of these electrons can be made available in free space for subsequent amplification.

The cathode is a development of the low density alkali halide dynodes used in image intensifiers and integrating television camera tubes (for example the Westinghouse SEC tube). The main differences are the use of CsI instead of KC (in order to obtain higher X-ray absorption cross-sections) and thicker, more dense layers. A cathode may be anywhere from 20 to 200 μm thick depending on the required X-ray energy range.

The performance of the cathodes follows from known physical parameters. Thus the spatial resolution is determined by the lateral spread of the photoelectrons in the cathode. This is easily shown to be ~ 20 μm at low keV X-ray energies. The time resolution is governed by the transit time of the secondary electrons in the cathode and for a 100 μm layer is of the order of 100 ps. The sensitivity depends on the product of the quantum efficiency of the absorption process ($\sim$ 100%) for few keV X-rays and the secondary emission gain (50-100).

A more detailed description of the X-ray photocathode is to be found in the Proceedings of the 7th Symposium on Photo-Electronic Imaging Devices (Imperial College 1978).

1.7.3(b) Xray streak camera with CsI photocathode

Protoype CsI photocathodes have been used in our X-ray streak camera. Their sensitivity (for ∿50 μm thickness on 15μmBe substrates) has been compared directly to that of a gold photocathode (∿ 200A° gold on 15μmBe). Tests have been carried out at QUB with a fibre optic coupled image tube and Mullard 50/40 microchannel plate intensifier. X-rays were generated with 4J, 100ps pulses focussed on solid carbon targets. The X-ray continuum was filtered with an additional 50μmBe foil to give ∿ 2 keV photons. Using extraction fields of 2kV/cm a x20 enhancement of sensitivity was observed for the CsI cathodes. This agrees with indirect comparisons made at the CLF during the streak shadowgraphy experiment, see section 5.4, and the implosion time experiment, see section 5.2, using pinhole camera images for normalisation. This additional sensitivity (which can be increased with higher extraction fields) has also made it possible to streak X-ray spectral lines using crystal dispersion. Time resolved line profile measurements were obtained in this way, see section 4.76.

The time resolution of the CsI photocathode has been shown to be ∿ 95 ps with an extraction field of 12 Kev/cm. Streaks of pulsed Xray emission from Cu targets with a Be filter of e^{-1} transmission at ∿ 1 Kev were recorded with Au and CsI photocathodes. The pulsed Xrays were generated by laser pulses of 190 ps separation and 25 ps duration and streak records showed pulse half widths of 50 ps and 70 ps for the first two pulses in the train with a gold photocathode and 107 ps and 114 ps with CsI. Gaussian deconvolution suggests a CsI response time of 95 ps. The technical time resolution (slit width/streak velocity) was 6 ps. The absolute sensitivity of the camera system with the CsI photocathode was ∿ 50x relative to Kodirex film substituted for the photocathode.

1.7.3(c) Sealed off microchannel plate Xray intensifier with a CsI photocathode

A sealed off Xray intensifier is necessary because micro channel plates (mcp) can only be used at high gain at low pressures, of the order of 10^{-6}T. At higher pressures ion feedback during use causes damage to the mcp as well as to CsI photocathodes.

The first tube made surmounted some of the technical details of sealing off a tube with an Xray window. The body was constructed of glass. There was a 12 μm beryllium window which was brazed in hydrogen to a copper flange. To 'wet' the beryllium it had to be copper plated. At the back of the tube there was a mcp proximity focussed to a P11 phosphor, which was coupled to optical film by a fibre optic face plate. The brightness of the device was estimated by comparison with KODIREX which is one of the fastest Xray films. Using the fastest optical film comparable film densities were obtained with an exposure of about one tenth of the exposure on KODIREX.

However, defects which arose from the mounting of the mcp made it impractical to use this device in experiments. Also the small increase in speed over KODIREX did not warrant the effort required for use.

All of these drawbacks have been overcome in the second design. It is shown in Fig.1.45. The principal change is to use low density CsI photocathodes which have been recently developed for Xray use at the Rutherford Lab. These cathodes have a high quantum efficiency and high gain. However the density, and area density of the deposited CsI has to be optimised in a trade off between gain and spatial resolution for different regions of the X-ray spectrum. Electrons from the cathode are proximity focussed onto a mcp. The accelerating voltage was 500V over 0.5 mm and of course can now be easily gated. The back of the mcp is coupled as before onto film.

One further advantage is that the body of the tube is made out of ceramic tubing, which ensures high accuracy of the mounting of the components, as well as great physical strength.

A well characterised electron beam was focussed onto thin foil targets producing Kα Xrays. By obtaining similar film densities to KODIREX it was established that the exposure required for this device was 10^3–10^4 less than that of KODIREX. This vast increase in the speed

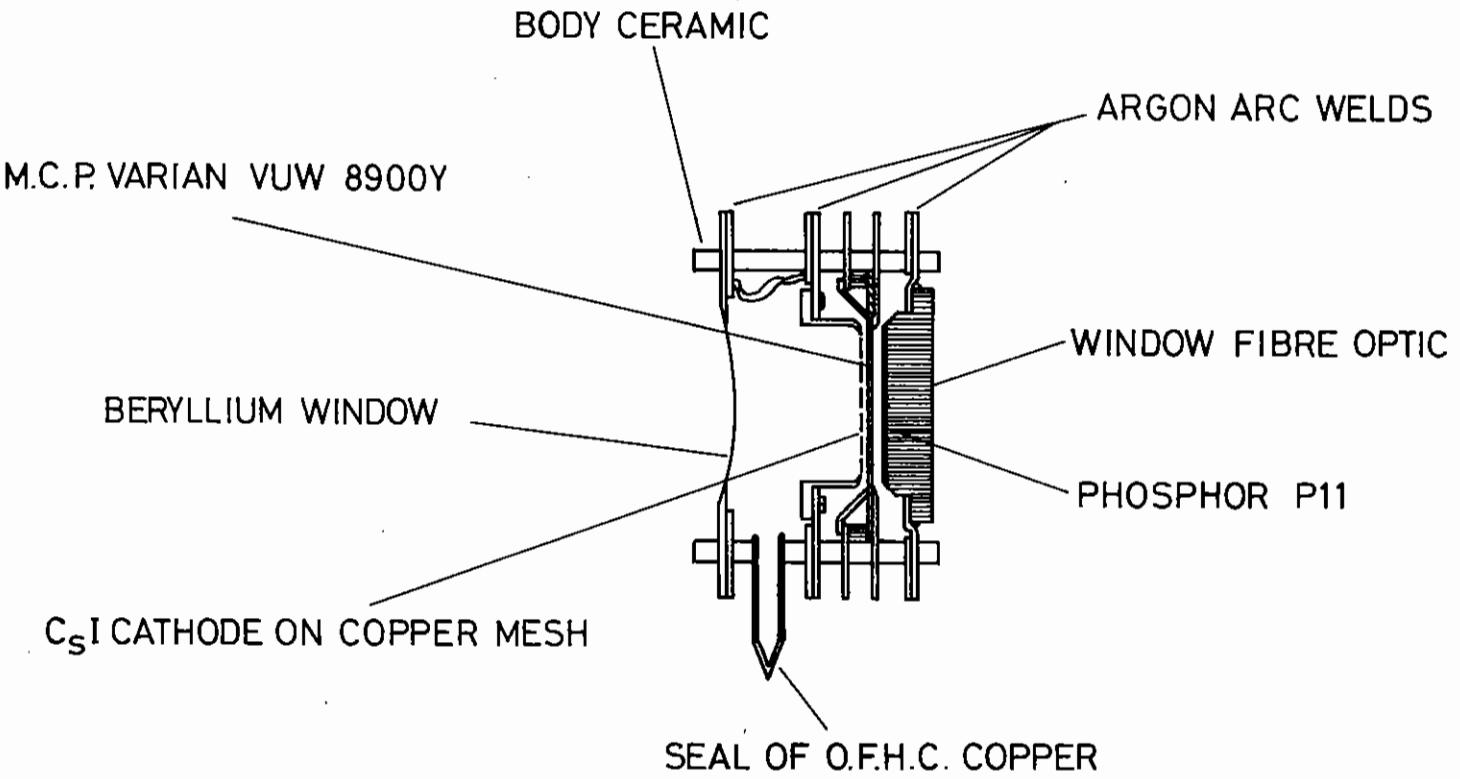

HIGH GAIN 'X' RAY INTENSIFIER

FIG 1.45

makes it worth the effort required to use the device, as a gate voltage pulse of 5ns duration can easily be achieved using a krytron switch. The spatial resolution we could achieve is illustrated in Fig.1.46. This was obtained with a cathode that was 20% of solid density and 50 μm thick. The resolution shown is better than 100 μm.

1.7.3(d) Detection of Xray images with a phosphor/intensifier s

Detection of X-rays (∿ 1 KeV) using phosphor screen coupled to visible image intensifiers promises to be a sensitive technique. In tests at QUB a range of phosphor types and thicknesses have been studied. It was found that ∿ 5mg/cm^2 of P11 was a suitable optimised phosphor screen having a sensitivity 100x better than direct X-ray detection using Kodirex film. (Comparison made at 0.9D on Kodak 2485 and Kodirex films.) This method allows direct observations of X-ray emission ex-vacuo (eg at QUB x20 magnification pinhole images and RAP crystal dispersed Cu spectra from 8-13A^o have been recorded on polaroid film using single shot 2J, 100 psec pulses). Using an Al filter step wedge across a Cu spectrum (∿ 0.7 KeV) has shown the phosphor to respond linearly over two orders of magnitude incident flux. An on-line system planned for the CLF will incorporate a fibre optic plate window in the target chamber with one side having an aluminised phosphor and the other directly coupled to a standard Mullard 50/40 microchannel plate image intensifier.

Fig 1·46

Scale 4× actual size.

X-RAY SHADOWGRAPH OF RESOLUTION CHART TAKEN WITH C_sI INTENSIFIER.

1.7.4 Particle Detectors

1.7.4(a) Faraday cup detectors

Arrays of Faraday cup ion detectors have been used for routine monitoring of the ion emission characteristics with both compression experiments and plane target experiments. Up to 10 channels have been used on various experiments with signals recorded by two methods.

Signals with bandwidths much greater than 20MHz have been recorded photographically on fast oscilloscopes followed by digitization on the graphics tablet linked to the GEC 4080 computer. This data has then been processed to yield mass and energy recovery rates and ion velocity distributions for each probe. Such manual digitization is time consuming and consequently has only been carried out for selected shots.

In order to remove this limitation and to enable all signals to be rapidly processed a multichannel digitising unit has been designed and built which is capable of receiving the signals from the Faraday cups and feeding the digital data directly to the computer for analysis. This system has been purpose built for this application and contains analogue memories based on charge coupled devices. It can process 10 channels at 10MHz or 5 channels at 20 MHz sampling rate, has a total recording time of 10 μs and can handle a large dynamic signal range (50 mV - 1v).

Most Faraday cups used are situated on the inner wall of the vacuum chamber at a distance of 40 cm from the target. At this position the fastest ions arrive in a time (50-100 ns) which is comparable with the resolution time of the digitiser. Consequently a Faraday cup of large aperture (50 mm diameter) has been constructed and placed on a side arm of the vacuum chamber at a distance of 120 cm from the target in order to resolve the fast ion signals. Fig 1.47 shows the information derived from this detector for an exploding pusher compression shot, recorded via the digitizing unit and presented to the experimenter at the computer terminal.

1.7.4(b) Thomson parabola ion analyser

A Thomson parabola ion analyser has been constructed and used in various experiments. Initially the instrument has been used to obtain information on the fast ions generated in laser-plasma interactions at high irradiance. Cellulose nitrate track detector foils, which are

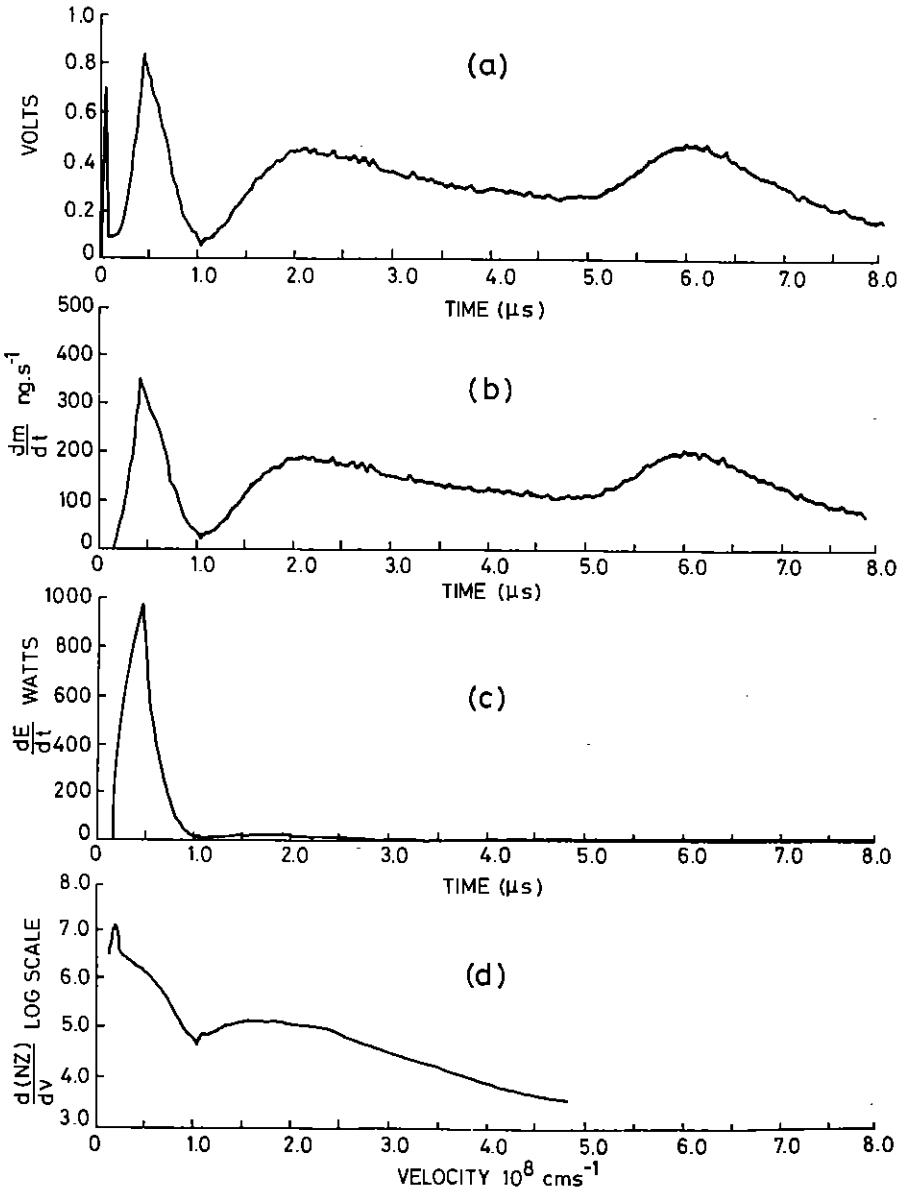

Fig. 1.47

Output from Faraday cup in detector situated at 120 cm from the target has an exploding pusher shot after automatic digitization and processing

sensitive to ions with velocities greater than about $2 \times 10^8 cm.sec^{-1}$, have been used as the recording medium. With this system the instrument produces on each laser shot experimental data which is anlysed to give complete velocity distributions for each fast ion species. A novel feature of the instrument's design is that a very wide range of ion energies can be observed by utilizing a film plane of adjustable position rather than a variable magnetic field.
Consideration has been given to using a channel multiplier plate as the recording device rather than CN foil. This would enable ions of lower velocity to be detected and analysed though the instrument would become less quantitative.
A portable vacuum system has been constructed to pump the Thomson parabola detector (and other available analysers) down to pressures of order 10^{-6} torr. Previous experiments have shown that it is necessary to achieve this pressure for ion charge exchange collision effects along the 100 cm flight path to be negligible. An interlocked, automatically operated, gate valve isolates the instrument from the main target chamber to enable detector foils to be removed.

1.7.4(c) Neutron Measurements

The neutron counter used to measure fusion reaction yields consists of a cylindrical organic scintillator 15 cm in diameter and 10 cm thickness, viewed by two 56 AVP photomultipliers whose outputs are recorded on oscilloscopes. A large dynamic range is obtained by setting one tube for high gain, the other for low gain, and recording the signals independently. A time marker from a photodiode which sees a fraction of the incident laser pulse is also recorded. The counter is usually operated at a distance of 1.5 m from the target where time-of-flight is adequate to identify 14 MeV neutrons from Xrays. Once the X-ray timing has been established a lead shield is placed between the target and counter. A typical shot with both X-ray and neutron signals is shown in Fig.1.48.

Cosmic Ray Calibration

Since the neutron has no charge its detection results from the ionization produced by the charged products of its interaction with the nuclei of the scintillator, predominantly carbon and hydrogen. The cross-section for these processes, the energy distributions of the reaction products and the relative efficiency with which ionization is converted into scintillation light are all sufficiently well known to compute the ratio of the average light output per neutron to the light output of a singly charged relativistic particle traversing the counter, by the Monte-Carlo method, Refs(1.18,1.19,1.20). Cosmic ray Mu-mesons can then be used to calibrate the counter in terms of pulse-height per singly charged relativistic particle.

Fig.1.49 is a schematic diagram of the cosmic ray calibration system. Coincident signals from the counters above and below are used to open the gate of an ADC on the passage of a penetrating particle which traverses the full diameter of the counter and deposits on average 30 mev of ionization energy. The event rate is $\sim$ 1 per minute.

The pulse area data is transferred event by event to a histogramming programme in the 4080 and the mean is evaluated. A typical calibration histogram is shown in Fig.1.50. The width of the histogram is due

SHOT NUMBER 7

TARGET NUMBER 675

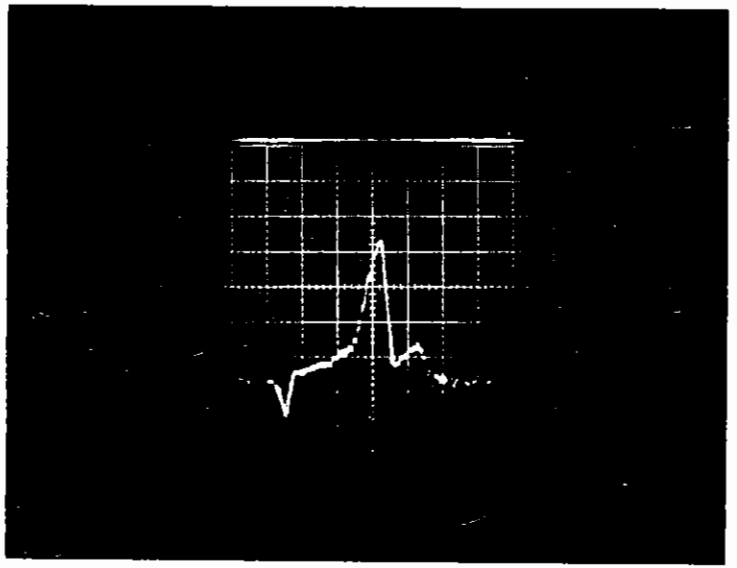

TARGET DIAMETER 71·28 μm

TARGET WALL 0·58 μm

EAST BEAM 26·6 j

WEST BEAM 26·7 j

NEUTRON YIELD $(1.1 \pm 0.11) \times 10^5$

ELECTRON TEMPERATURE 439±89ev
(FROM CORE SPECTROSCOPY)

FIG 1·48 OSCILLISCOPE TRACE OF THE PULSES FROM THE NEUTRON DETECTOR.

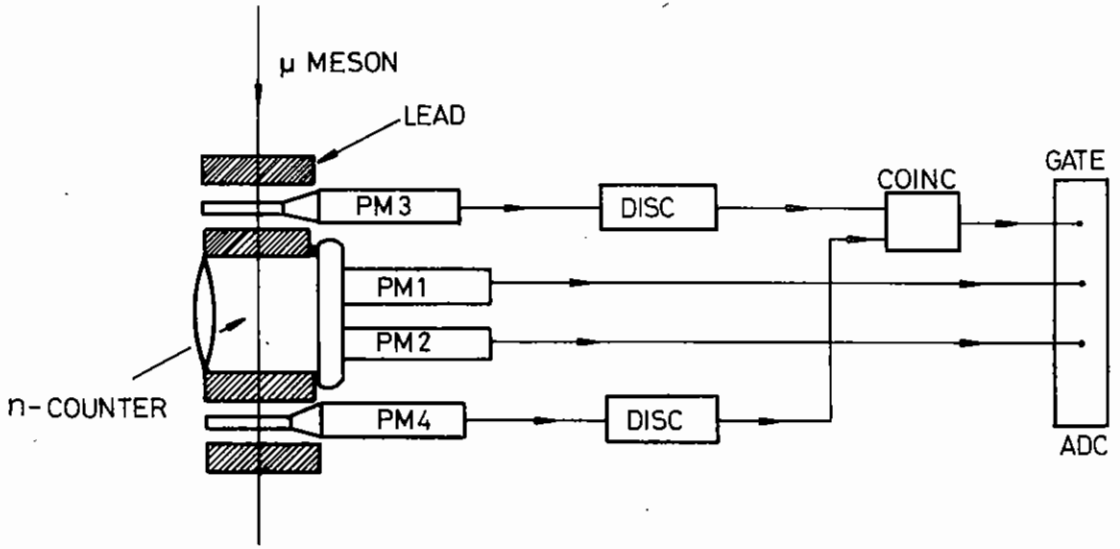

FIGURE 1.49. SCHEMATIC DIAGRAM OF THE COSMIC RAY SYSTEM.

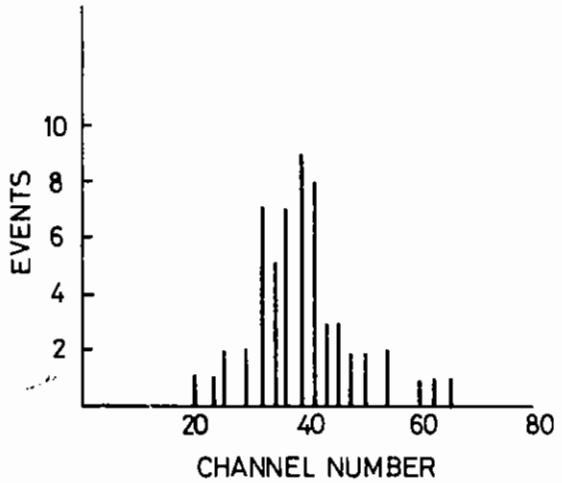

FIGURE 1.50. HISTOGRAM OF COSMIC-RAY PULSE-HEIGHTS.

in part to photoelectron statistics and in part to variation in the muon trajectories through the counter. The calibration was initially made for a wide range of voltages. Checks are made before and after each run.

Efficiency Monte-Carlo

A Monte-Carlo program has been written and used to calculate the average light output for each neutron interacting in the scintillator. In the programme, neutrons are generated with an isotropic distribution in a cone substantially larger than the cone subtended by the counter. They are tracked towards the counter through the target chamber window and the x-ray shielding. Loss by absorption and loss and gain by scattering are taken into account. The neutrons are tracked through the counter until they interact or leave. The light output from all charged reaction products is evaluated in terms of equivalent electron energy deposition. The scattered and secondary neutrons are in turn followed until they interact or leave. The tracking process is continued through several generations until all the energy has been deposited or all the products have left the counter. The following interactions are taken into account:

a) $np \longrightarrow np$ elastic

This interaction dominates the detection mechanism for neutrons with energies of interest. The differential cross-section in the CM system is isotropic (1.21). The light output is given (1.18) by:

$$L(Ep) = -10.68\,(1 - \exp(-0.07\,Ep^{0.89})) + 0.929\,Ep$$

mev electron equivalent

where Ep is the KE of the recoil proton in the Laboratory. At the moment it is assumed that the energy is deposited locally. Since the maximum energy recoil proton has a range of only 2.7 mm, the edge effect correction is small for our detector.

b) $nc \longrightarrow nc$ elastic

The assumption that the neutrons are isotropically scattered by the carbon nuclei in the cm systems is good for neutrons with energies of interest. The light output from a carbon recoil with energy (Ec) is:

$$L(Ec) = 0.017E_c \text{ Mev electron equivalent}$$

c) $nc \rightarrow \alpha + {}^{9}Be$

This is a two-body isotropic interaction and the light output from an alpha particle of energy (E_α) is given by:

$$L(E_\alpha) = 0.046\ E_\alpha + 0.007E_\alpha^2 \text{ Mev electron equivalent}$$

d) $nc \longrightarrow n + 3\alpha$

It is assumed that the reaction products have a four-body phase-space distribution. The light output for each alpha is found as in reaction (c). A histogram of the light outputs from individual neutrons is shown in Fig.1.51. Second and subsequent scatterings are included. The neutrons pass through an aluminium window (ie the target chamber window) and three cms of lead used as Xray shielding before they enter the scintillator, so we considered the following interactions in the programme:

e) $n\ Al \longrightarrow n\ Al$

where we have absorption and elastic scattering of the 14 mev neutrons by the Al nuclei. The elastic scattering is considered as isotropic.

f) $n\ pb \longrightarrow n\ pb$

As in the case of aluminium we have absorption and elastic scattering. We evaluate the elastic scattering of the neutron from the pb nuclei according to the black-disc model.

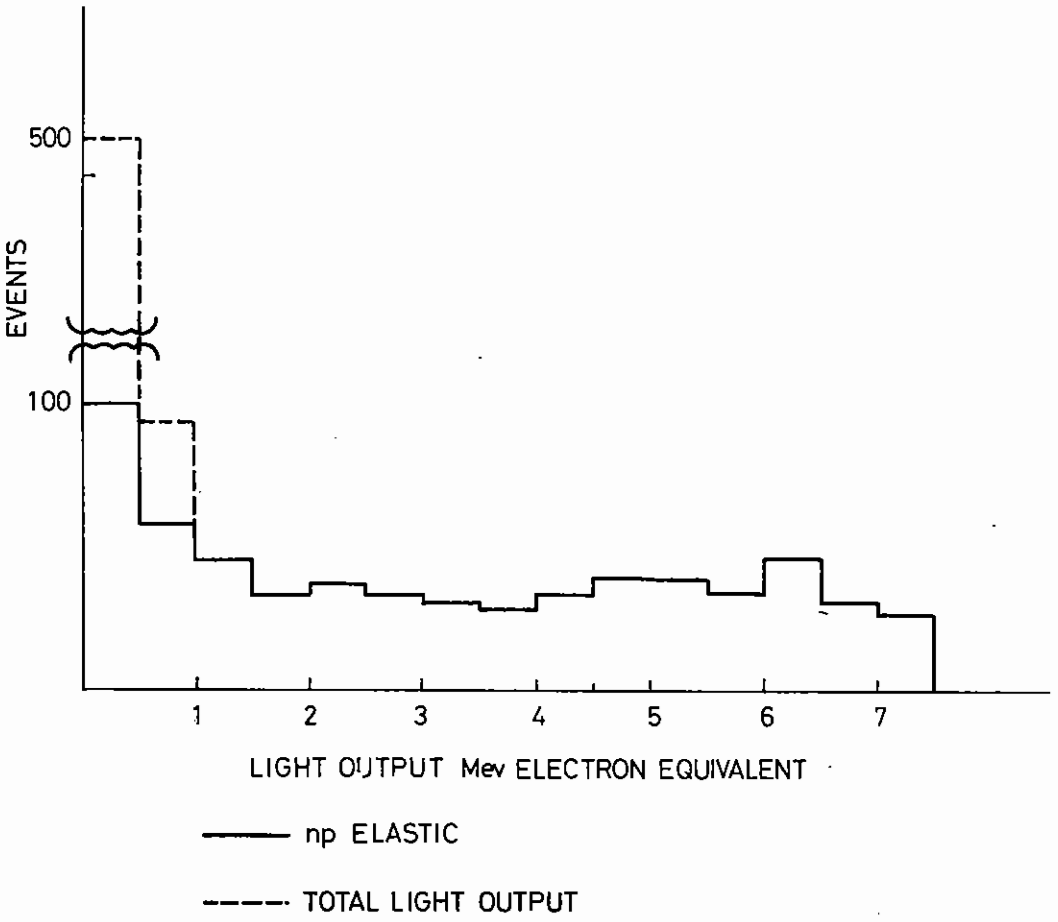

FIGURE 1·51. LIGHT OUTPUT DISTRIBUTION

TABLE 1.03	MARK I	MARK II	MARK IV
SPECTRAL RANGE	3 - 8.3 Å	3 - 8 Å	3 - 8 Å
SPECTRAL RESOLUTION (For a 15 μ Imploded core)	1300 (@ 8.3 Å) 5500 (@ 3 Å)	1000 (@ 8 Å) 4200 (@ 3 Å)	1500 (@ 8 Å) 5200 (@ 3 Å)
RELATIVE LUMINOSITY (W.R.T MK I @ 3 Å) 8Å 3Å	5.156 1.00	1.996 0.867	2.721 0.930
MAGNIFICATION 8A 3A	3.8 10.9	7.7 11.7	6.6 11.3

THESE FIGURES ARE FOR A TARGET - SLIT DISTANCE OF 5 MM AND USING A P E T CRYSTAL (2d - 8.74 Å)

TABLE 1.04

% Absorbed in the Al	% Absorbed in the Pb	% Do not interact in the scintillator
5.7	18.3	49.7

Table 1.04 gives the percentage of neutrons absorbed in the aluminium window and the lead shield as well as the percentage of neutrons which pass through the scintillator without interacting.

1.7.5 Spectroscopy

1.7.5(a) Instrumentation for X-ray crystal diffraction spectrometry

In recording space resolved X-ray spectra at laser intensities greater than $\sim 10^{15} Wcm^{-2}$, using a spectrometer of the design reported in Ref.1.17, it was found that the recording film was fogged, especially at the long wavelength end which is closest to the plasma. One component of this spurious radiation was found to be fluorescence from the foil covering the slit. This problem was overcome by moving the film plane further away from the slit assembly; and in another design by tilting the Bragg crystal such that the film did not have a direct view of the slit assembly. A more serious contribution to the fogging was found to be due to hard X-rays emission, at energies greater than 20 kev, which was transmitted by the 1 mm Aluminium plate that formed the slit holder. This source of fogging was supressed by a cladding of 60 μm of Tungsten.

To diagnose quasi ablative targets, where the X-ray emission from the core is likely to be less than that from exploding pusher targets, a spectrometer of sensitivity greater than that achieved in Ref.1.17, is required.

The sensitivity can be increased, at the expense of spectral range, by using a concave crystal, such that emission at each wavelength is collected from a range of angles greater than the width of the rocking curve of the crystal and focussed on the detector. From a technical point of view the configuration due to Johann (1931) is the easiest to implement. Secondly the sensitivity of detection can be increased above that provided by photographic film as discussed in section 1.7.3.

Space resolved spectroscopy on targets irradiated in the proposed six beam configuration requires a modified form of spectrometer. The design of the Mark IV Xray spectrometer (Fig.1.52) is based on the use of crystals from previous spectrometers but avoids interference with the 6 laser beams while giving acceptable values of luminosity, spectral resolution, range, etc. The front of the spectrometer is reduced in size to enable the crystal to be placed close enough to the plasma to give the properties shown in Table 1.03. Here it is compared with spectrometers in current use. Most of the front cover and film holder is made of brass to reduce the hard Xray flux.

1.7.5(b) Spectroscopy with the GML5M

In the spectral region below 25Å crystals of various types are commonly used as dispersers and above 300Å near-normal incidence concave spherical grating spectrographs can be used, but the intermediate range of wavelengths is accessible only to grazing incidence concave spherical grating spectrographs, because of the limitations on crystal lattice spacing (although crystals have been developed which will reach 100Å) and the poor reflection coefficients of grating materials at all but large incident angles below 300Å. Grazing-incidence spectroscopy is notorious for its difficulty, since if a resolving power equal to that theoretically available with a particular slit and grating is to be obtained, the slit, grating and photographic plate must be aligned on the Rowland Circle to a precision of the order of microns, and the angular attitude of the grating must also be precisely set. Obtaining the optimum focus for such an instrument may take weeks of careful work and many X-ray plates. Further, the acceptance solid angle of the instrument is so small that even alignment with the source can require great care. Understandably therefore, exchange of gratings, alteration of the grazing angle or even movement of the instrument to a different experiment are operations usually performed reluctantly.

The Laser Facility has recently acquired an instrument in which most of the above disadvantages have been obviated, and interesting new spectroscopic techniques made possible. This is the GML5M, a 5 metre f/120 instrument made by Grating Measurements Ltd, in which the grating, slit and plateholder are mounted in modules which locate precisely on rails lapped to a radius of curvature of 245 cm within a tolerance of a few microns, the rails being incorporated in a rigid Meehanite beam 1 metre long. The module construction ensures that wherever a module is clamped on the rails, the element it contains is positioned accurately on the 250 cm Rowland Circle at the correct attitude. The angle of grazing incidence and spectral region recorded may be simply altered by changing the relative position of the modules, and gratings may be changed easily by substitution of another module, all modules being interchangeable between different instruments.

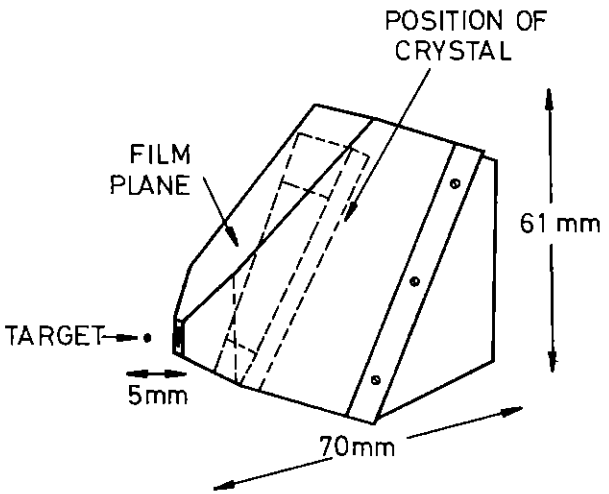

MARK IV MINATURE X-RAY SPECTROMETER

Fig1·52

The latter facility not only makes possible the selection of a concave spherical grating suitable for the work to be done, but also permits the use of special-purpose gratings such as the toroidal type currently under development by Dr R J Speer and Mr D Turner (who were responsible for the development of the GML5M) and their group at the Blackett Laboratory, Imperial College. They have also been responsible for the setting up of a grating test facility which permits characterization of existing available gratings to aid in the choice of one for a particular purpose as well as evaluation of development gratings constructed by novel methods.

The torus mentioned in section 1.7.2 is in fact the blank for a toroidal grating, which is capable of stigmatic imaging over a selected small range of wavelengths, in contrast to the almost total astigmatism parallel to the grating rulings obtained with a spherical grating. Work is in progress in collaboration with the IC group to develop a system combining the GML5M with a toroidal grating and the toroidal relay mirror to permit spectral observations spatially resolved to within 10 μm. This would enable studies to be made of the subcritical density ablation plasma from solid target laser-produced plasmas by measuring Doppler shifts and widths, pressure broadened linewidths and line intensity ratios.

The GML5M is currently being used with a spherical grating and the toroidal relay mirror in experiments designed to measure gain on the Balmer α line at 182A in expanding carbon fibre plasmas (Section 7.2.2).

1.7.6 Automated Data Processing

1.7.6(a) Graphics Tablet

Experimental data in the form of line traces (eg densitometer output, oscilloscope traces, interferometric data etc) can be digitised into the GEC 4080 computer via a Tektronix 4956 Graphics Input Tablet which has a resolution of 100 μm. A typical task involves manually digitising the fringe positions of an interferogram. This can then be subsequently processed interactively to display the original interferogram with and without the background fringes removed (Fig.3.02) and analyse the corresponding density profiles. Other processing covers analysis of oscilloscope traces, X-ray backlighting data and film curve deconvolution in a variety of data.

1.7.6(b) Scanning Densitometer

The present 1-D film densitometer is to be supplemented by a 2-D scanning densitometer of similar design. Control of the scanning and data acquisition will be through the local GEC4080 computer and the GRACES intepretive language. Data can be analysed and displayed on a local graphics terminal or can be transferred to the dual IBM 360/195 for more sophisitcated processing and display through the FR80 precision graphics facility. Data processing programmes have been developed and tested and include simple contour plotting and 2-D digital filtering routines locally and a variety of colour/black and white data representation programmes on the IBM 360/195.

CHAPTER 1 REFERENCES

1.01 P W Smith Proc IEEE 60 422 (1972)

1.02 D C Hanna, B Luther-Davies and R C Smith, Elect.Letts. 8 369 (1972)

1.03 W Seka and Bunkenburg, J.Appl.Phys. 49 2277 (1978)

1.04 D J Kuizenga, Opt.Comm. 22 156 (1977)

1.05 University of Rochester, Laboratory for Laser Energetics, Annual Report 1977

1.06 ILL Annual Report, UCRL-50021-74 (1974)

1.07 J E Howard, Applied Optics, 16 2764 (1977)

1.08 C E Thomas, Applied Optics, 14 1267 (1975)

1.09 D J Nicholas et al, Applied Optics, 17 3368 (1978)

1.10 D J Nicholas and R G Evans, Rutherford Lab Report, RL-78-017/A (1978)

1.11 D J Nicholas and W T Welford, Rutherford Lab Report, RL-76-147/B (1976)

1.12 R E Kidder, Nuclear Fusion, 161 3 (1976)

1.13 D E T F Ashby, Nuclear Fusion, 15 993 (1975)

1.14 R S Adrain, E G Arthurs, W Sibbett, Opt.Comm. 15 290 (1975)

1.15 R L Carman, F Shimizu, C S Wang, N Bloemberger, Phys.Rev.Lett. A2 60 (1970)

1.16 D J Pugh, P D West, Electron Microscopy and Analysis (Inst.Phys.Conf.Ser.No.36) 29 (1977)

1.17 M H Key et al, Rutherford Lab Report, RL-77-122/B (1977)

1.18 N R Stanton, COO-1545-92 (Ohio State University, 1971, unpublished)

1.19 R J Kurz, UCRL-11339 (University of California, 1964, unpublished)

1.20 R Batchelor et al, Nuclear Inst and Methodes 13 70 (1961)

1.21 M D Goldberg, V M May and J R Stehn, Angular Distribution in neutron-induced reactions, BN1400, 2nd edition, vol 1 (Brookhaven National Lab, 1962, unpublished)

CHAPTER 2 GAS LASER DEVELOPMENT

I N D E X

CHAPTER EDITOR: F. O'Neill

CONTRIBUTORS: F.S. Gilbert, C.B. Edwards, M.J. Shaw, M.W. McGeoch, D.J. Nicholas.

Chapter 2 GAS LASER DEVELOPMENT

2.1 Introduction

During the year being reviewed by this report there has been considerable progress in the gas laser development program. Construction of the program's main piece of experimental equipment, the ELF electron-beam machine, has been successfully completed and the device has been fully commissioned. The machine was used for its first laser experiment (excitation of a large KrF laser) in March 1979. The electrical characteristics of the ELF machine have been extensively investigated and the device now reliably produces a high energy (> 3KJ), 50 nsec, electron-beam pulse at a voltage of 1.4 MV. A computer program has been written to describe the interaction of high voltage electron beams with thick gas targets. The program can be used to calculate the rate of electron-beam energy deposition in various types of laser gas mixtures thus allowing accurate, quantitative laser efficiency measurements to be made in future studies.

Experiments related to a high power selenium laser project have also progressed. The aim of this project is to operate a high energy selenium atom laser which is excited by an electron-beam-pumped ArF laser. Laser action in atomic selenium is initiated by the photolysis of carbonyl selenide (OCSe):

$$OCSe + h\nu(UV) \rightarrow Se(^1S_o) + CO$$

This photolytic process is followed by laser action from the $Se(^1S_o)$ state on either of two transitions:

$$Se(^1S_o) \rightarrow Se(^3P_1) + h\nu_{laser}(489\ nm)$$

or

$$Se(^1S_o) \rightarrow Se(^1D_2) + h\nu_{laser}(777\ nm)$$

Our experiments will be mainly aimed at obtaining laser emission on the first of these transitions. The large laser cell for this experiment is presently being constructed and will be used on the ELF machine during 1979.

In the meantime some small scale OCSe photolysis experiments have been carried out using a discharge excited ArF laser. These experiments have been performed to test the effectiveness of 193 nm ArF laser radiation as a means of photolytically producing $Se(^1S_o)$ atoms from OCSe. The outcome of these experiments has been very encouraging showing that about 25% of the absorbed ArF photons produce selenium atoms in the ^1S_o upper laser level.

A small scale OCSe production facility has been set up which can now generate and purify the gas at a rate of 50 cm^3 atm. per day. This facility will be capable of supplying enough OCSe for experiments being planned over the next 1-2 years.

During the reporting year a new research program on potential metal vapor excimer lasers has been initiated. Present experiments are concentrating on the cadmium-mercury system using excitation mechanisms based on optical pumping of cadmium and mercury vapor mixtures. The 266 nm fourth harmonic of a Nd:YAG laser has been used as a pump source and significant progress has been made towards understanding the kinetics of optically pumped cadmium-mercury mixtures. An argon ion laser has been used to probe for gain or loss in a metal vapor cell following excitation by an energetic 266 nm laser pulse. Results to date have been encouraging, suggesting the possibility of gain at some wavelengths in the $CdHg^*$ emission spectrum, and more refined experiments in this area are planned for the next reporting year.

The research projects outlined above are discussed in more detail in the following sections.

In the meantime some small scale OCSe photolysis experiments have been carried out using a discharge excited ArF laser. These experiments have been performed to test the effectiveness of 193 nm ArF laser radiation as a means of photolytically producing Se(^1S_o) atoms from OCSe. The outcome of these experiments has been very encouraging showing that about 25% of the absorbed ArF photons produce selenium atoms in the ^1S_o upper laser level.

A small scale OCSe production facility has been set up which can now generate and purify the gas at a rate of 50 cm^3 atm. per day. This facility will be capable of supplying enough OCSe for experiments being planned over the next 1-2 years.

During the reporting year a new research program on potential metal vapor excimer lasers has been initiated. Present experiments are concentrating on the cadmium-mercury system using excitation mechanisms based on optical pumping of cadmium and mercury vapor mixtures. The 266 nm fourth harmonic of a Nd:YAG laser has been used as a pump source and significant progress has been made towards understanding the kinetics of optically pumped cadmium-mercury mixtures. An argon ion laser has been used to probe for gain or loss in a metal vapor cell following excitation by an energetic 266 nm laser pulse. Results to date have been encouraging, suggesting the possibility of gain at some wavelengths in the $CdHg^*$ emission spectrum, and more refined experiments in this area are planned for the next reporting year.

The research projects outlined above are discussed in more detail in the following sections.

2.2 ELF Electron-Beam Machine

2.2.1 Machine Construction

The ELF electron-beam machine was designed to produce a high energy (few KJ) electron pulse for laser excitation experiments. The electron beam pulse is produced by a cold cathode, field emission diode which is powered by a 50 nsec co-axial Blumlein. The Blumlein is pulse charged by a D.C. charged 12 stage Marx bank. The components of the ELF machine are shown in the block diagram in figure 2.01 and design details of these components are listed below.

Marx Generator

12 stage Marx. 100 KV, 0.5μF capacitors.
Marx erected capacitance = 42 nF
Output voltage = 0.96 MV at ± 80 KV charge
Voltage gain into Blumlein = 1.35
Marx erection time < 200 nsec
Spark-gap column composed of mid-plane gaps pressurised with SF_6 or Air
Marx stored energy = 19.2 KJ at ± 80 KV charge
Maximum energy = 30 KJ at ± 100 KV charge
Marx insulation, transformer oil(k =2.3)

Marx Trigger

Trigger voltage to mid-plane gaps = 200 - 250 KV (negative)
Trigger pulse energy = 400 J
Pulse rise-time = 80 nsec
Trigger generator based on a high voltage pulse transformer

Blumlein

Dielectric, transformer oil (k = 2.3). Common with Marx bank. Total volume ≃ 3200 gallons.
Blumlein cylinder radii: Inner (28 cm), Intermediate (34 cm), Outer (40.5 cm).
Length = 500 cm.

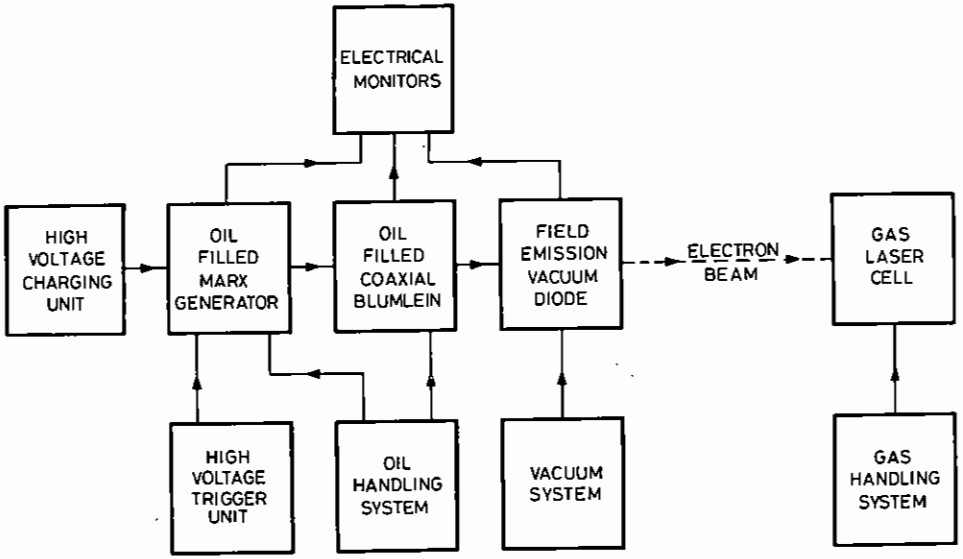

FIG 2.01 ELECTRON-BEAM-PUMPED LASER FACILITY (ELF) BLOCK DIAGRAM.

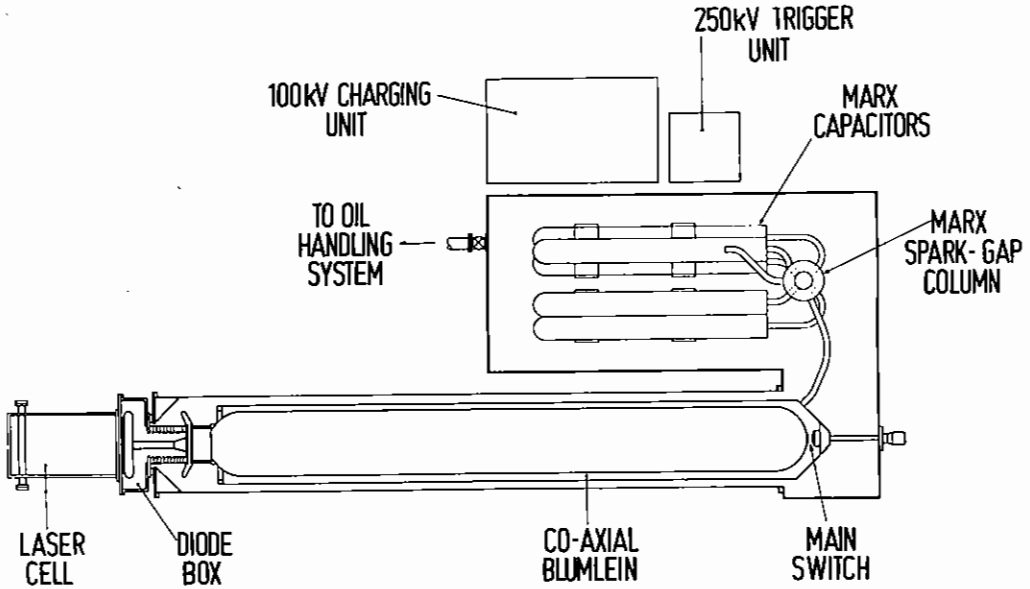

FIG 2.02 ELECTRON BEAM MACHINE LAYOUT.

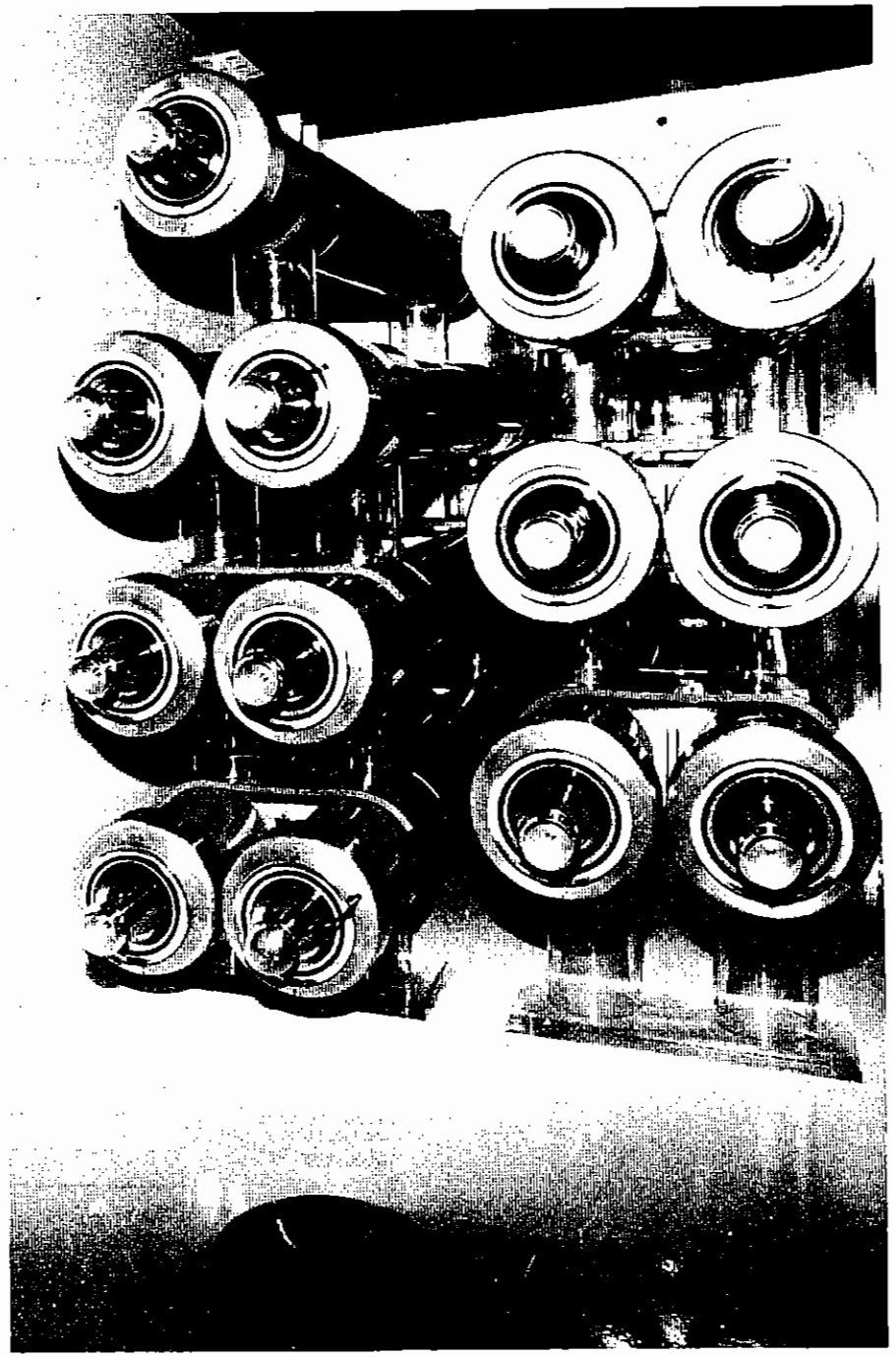

FIG 2.03 ELF MARX BANK DURING MACHINE CONSTRUCTION. THE SPARK-GAP COLUMN STANDS ON THE ROUND PLATE IN THE BOTTOM FORE-GROUND

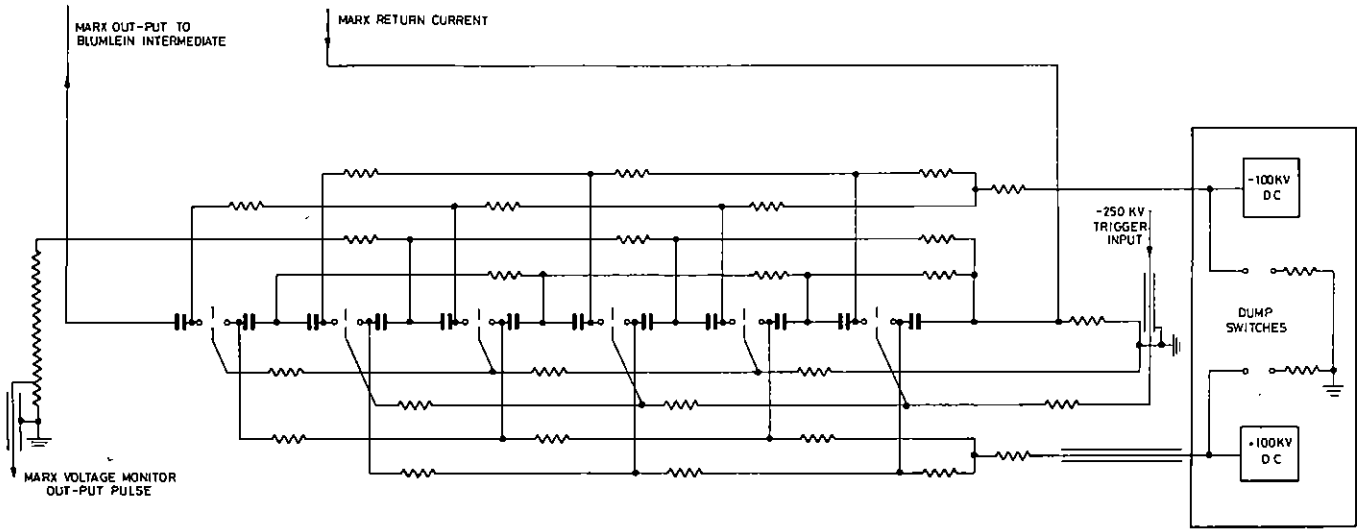

FIG 2.04 THE ELF MACHINE MARX GENERATOR AND HIGH VOLTAGE D.C. CHARGING UNITS.

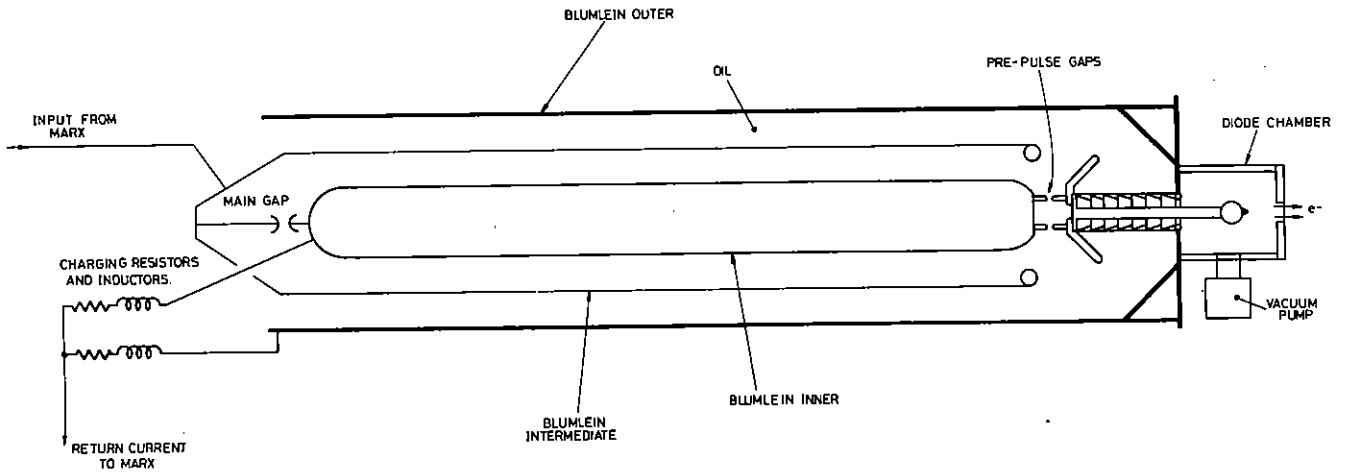

FIG 2.05 ELF BLUMLEIN PULSE FORMING LINE.

The capacitor pairs are separated vertically by supports, made from perspex tube and sheet, which are designed to withstand the voltage gradient between stages when the Marx erects. The Marx charging is carried out using a dual high voltage power supply with output variable up to ± 100 KV.

The Marx bank is erected by six spark-gaps mounted in a single perspex column which is situated in front of the Marx capacitors as noted in figure 2.03. The capacitors are connected to the spark-gaps using 2½" diameter stainless steel tubing. The Marx charging and triggering units are connected to the machine using resistor chains made from PVC tubing filled with copper sulphate solution and with copper electrodes. The spark-gaps all have a mid-plane trigger electrode and are mounted closely together in the perspex column to increase UV and capacitance coupling between stages.

The output from the Marx bank is used to charge the Blumlein pulse forming line which consists of three co-axial steel cylinders. The outer cylinder is integral with the Marx tank thus forming one complete insulation oil, containment vessel. The intermediate and inner lines are supported on polythene feet for radial location with nylon tie rods at one end giving axial location. The inner cylinder has hemispherical ends one of which carries one of the main gap electrodes. The pulse output is taken from the other end of the inner via the pre-pulse limiting spark-gaps. The switch end of the intermediate cylinder is conical and carries the connection to the Marx output. The inner and outer cylinders of the Blumlein are connected to the low voltage side of the Marx by inductors and copper sulphate resistors. The Blumlein spark-gap is adjustable from outside the Marx tank thus enabling continuous variation of the Blumlein output voltage.

The trigger pulse for the Marx bank is derived from a high voltage autotransformer. The input pulse to the autotransformer is supplied by a 40 KV, 0.5 μF capacitor switched by a low inductance, low jitter, Pulsar spark-gap. This spark-gap is itself triggered by a 25 KV pulse from a Krytron switched miniature Marx bank which is in turn triggered by the out-put from an avalanche transistor chain. The high voltage autotransformer has a gain of 6 and an out-put voltage of 250 KV has been measured with a rise-time of 80 nsec. The out-put pulse energy is approximately 400 J.

The electrical circuits of the machine are shown in figures 2.04 to 2.06.

2.2.2 Commissioning of ELF

Following construction, commissioning of the electron-beam machine began in November 1978. A series of test firings were carried out to calibrate voltage (Blumlein charge voltage and diode voltage) and current (diode current) monitors and to compare actual machine parameters with calculated ones. The Marx spark-gaps were tested using SF_6 and air as the dielectric. For each gas the voltage hold-off and minimun trigger voltage was measured as a function of gas pressure and the results are shown in figure 2.07. Some effort was also spent on obtaining clean monitor signals from the machine. The monitor signals from the machine are attenuated and then fed into Tektromix oscilloscopes which are placed in a screened room. Considerable attention was given to reducing the level of electrical noise (caused by firing ELF) inside this screened room because it is planned to use the same room for monitoring laser signals in future experiments.

At its highest operating voltage, 1.5 MV, the machine produces a considerable X-ray pulse when it is fired. Measurements of the X-ray level around the machine were taken and concrete shielding was located, as required, for operator protection. The final lay-out of the ELF laboratory area is shown in figure 2.08. By the end of the reporting period about 300 shots had been logged on the machine without the occurrence of any major problems.

2.2.3 Diode Studies

The ELF electron-beam machine was designed to produce a 1.5 MeV, 60 KA, 50 nsec electron-beam pulse for laser excitation. In addition, for initial laser experiments, it was decided to configure the machine diode to provide a spatially uniform electron-beam with dimensions $(5 \times 50)cm^2$. Following machine commissioning, as described in the previous section, a program of electron-beam diode studies was initiated which was aimed at achieving the operating characteristics described above.

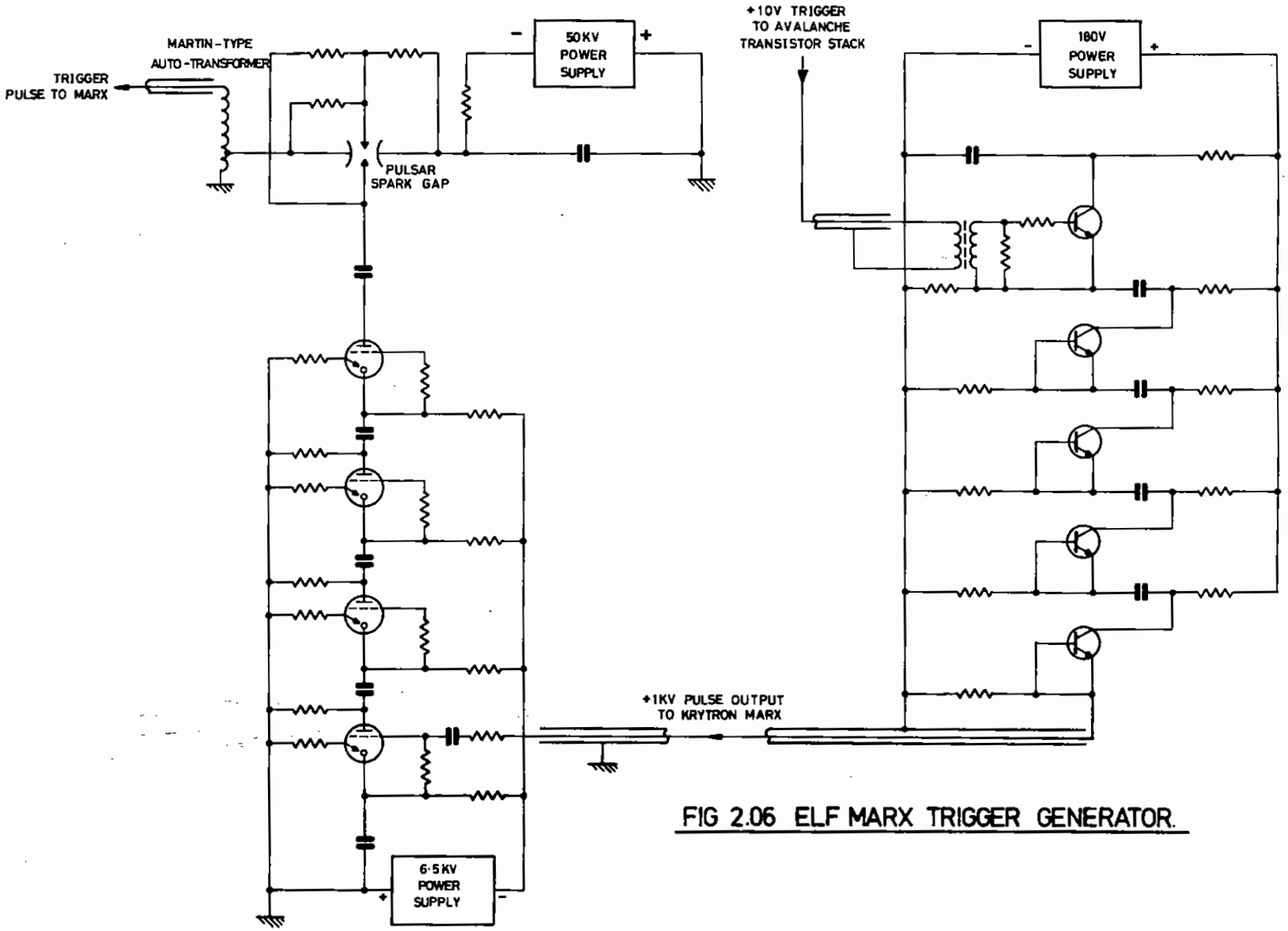

FIG 2.06 ELF MARX TRIGGER GENERATOR.

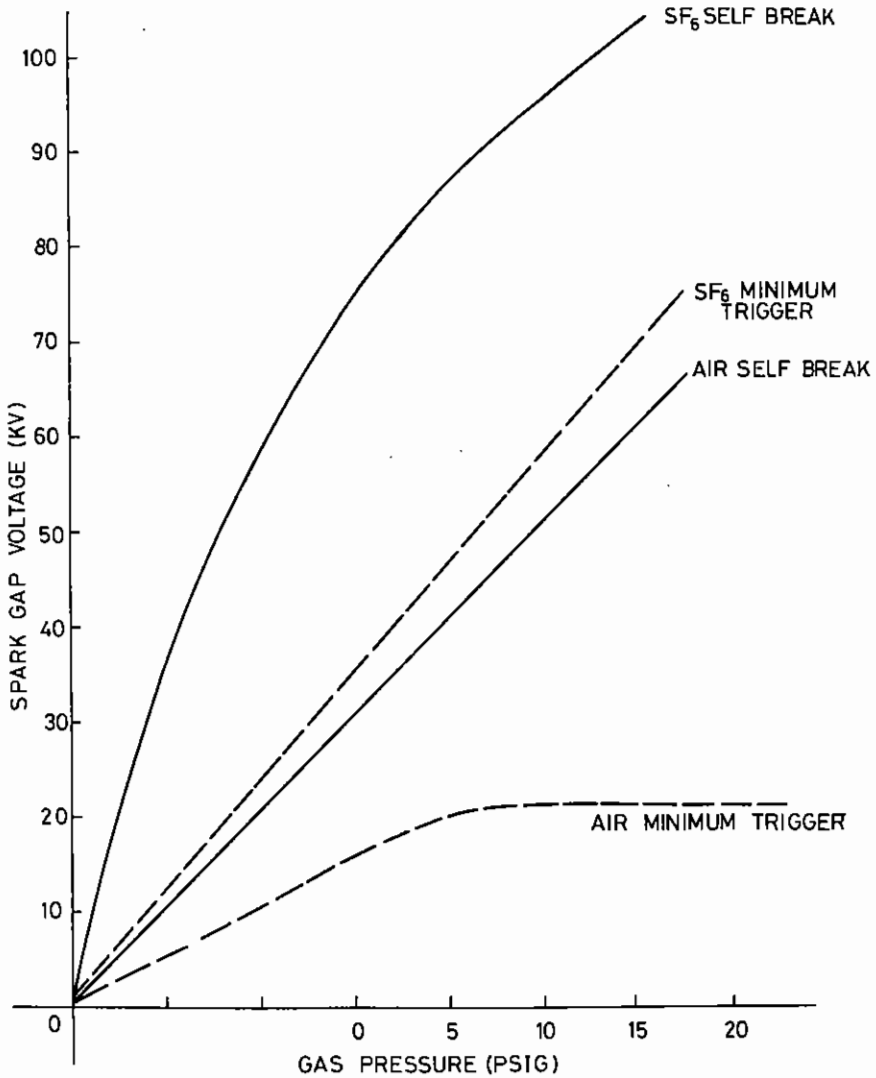

FIG 2.07 VOLTAGE HOLD-OFF AND TRIGGERING CHARACTERISTICS OF THE ELF MARX SPARK-GAP COLUMN.

A diagram of the ELF diode chamber is shown in figure 2.09. The field-emitted electron-beam is obtained from a V-shaped, fine-grain, graphite cathode which is held in a cigar shaped aluminum holder. Monitors were attached to the machine to measure diode current (i_D) and the output voltage of the Blumlein (V_{OB}). A computer program has been written to correct the Blumlein output waveform for inductive effects to yield the true diode voltage (V_D). This program can also integrate the diode energy and calculate power and impedance profiles thus allowing rapid comparisons of different diode configurations to be made. A typical set of gun electrical traces are shown in figure 2.10.

The useful output from the machine is obtained through a (5 x 50)cm^2 aperture in the steel anode plate. The vacuum to gas interface in this aperture is maintained by a 50 μm titanium foil. This foil is supported by a metal hibachi structure and it is also protected from low voltage electrons by a 25 μm titanium prefoil. The energy transmitted through the anode aperture has been measured using an aluminum block calorimeter and the spatial uniformity of the beam has been measured using cellophane dye dosimetry (2.01). On each shot the transmitted beam energy can be compared with the calculated internal diode energy to yield a transmission efficiency for the particular diode geometry being used. The cellophane has also been placed on the anode plate inside the diode box to measure the internal distribution of the high voltage electrons.

Using the diagnostics described above, we have evaluated a number of different diode configurations. The main variables in these experiments were the Marx charge voltage (to vary V_D), the emitter to anode plate separation (to vary the gun impedance Z_L, and therefore V_D and i_D), and the emitter shape and protrusion distance from the holder (again to vary Z_L). While the main effect of changing the emitter position is to change V_D and i_D, it also changes the energy transmitted through the anode aperture due to the divergence of the accelerating field within the diode chamber. The peak diode voltage, V_D, is related to the Blumlein charge voltage, V_{CB}, the Blumlein impedance, Z_o, and the diode impedance, Z_L, by the equation:

$$V_D = \frac{g_o V_{CB} Z_L}{Z_L + Z_o}$$

In this expression g_o is the Blumlein open circuit voltage gain (measured as 1.6 for ELF) and Z_o is the total Blumlein impedance (15 Ω). Attainment

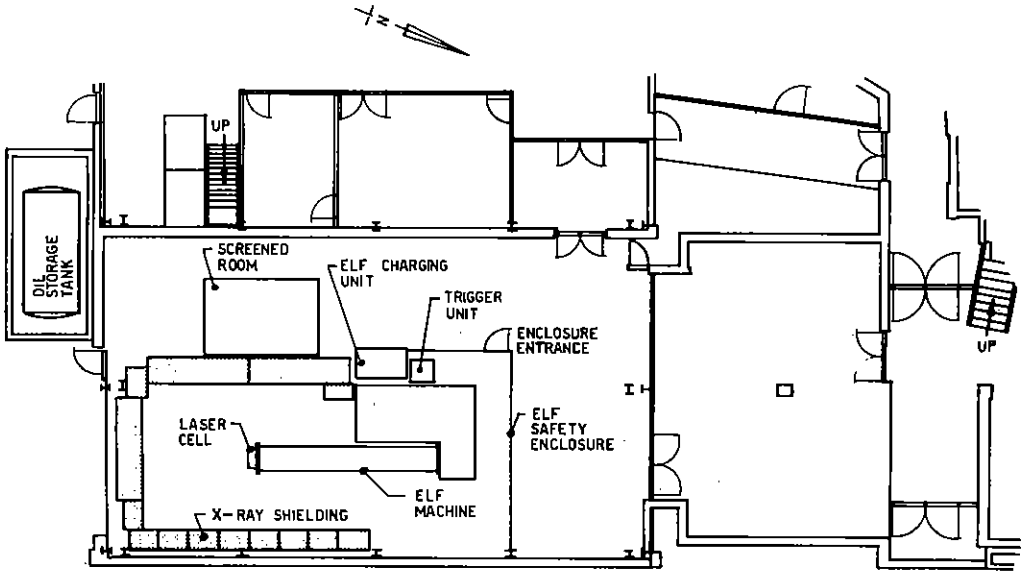

FIG 2.08 FINAL LAYOUT OF ELF LABORATORY AREA IN THE RUTHERFORD LABORATORY BUILDING R2

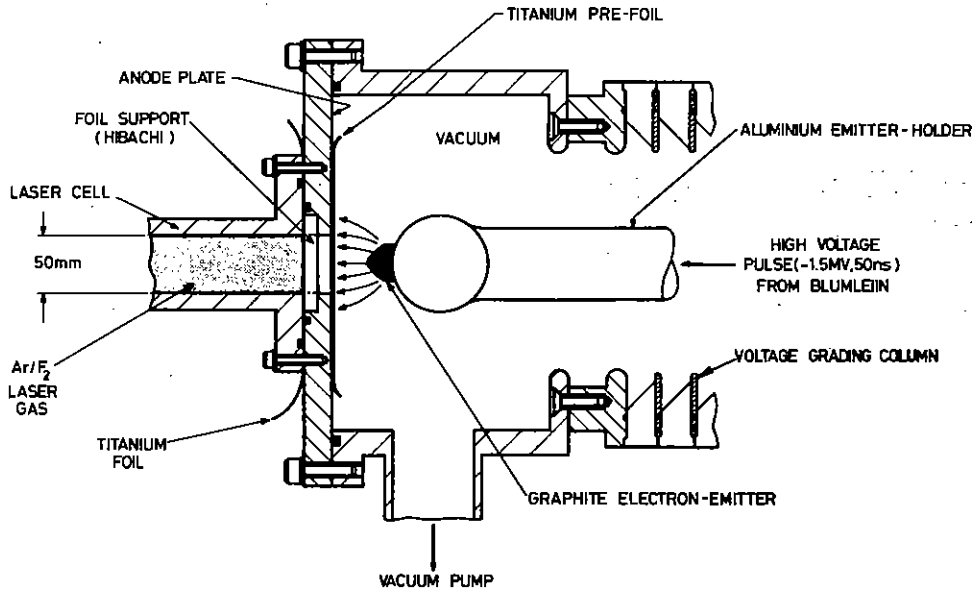

FIG 2.09 THE ELF ELECTRON BEAM MACHINE DIODE CHAMBER.

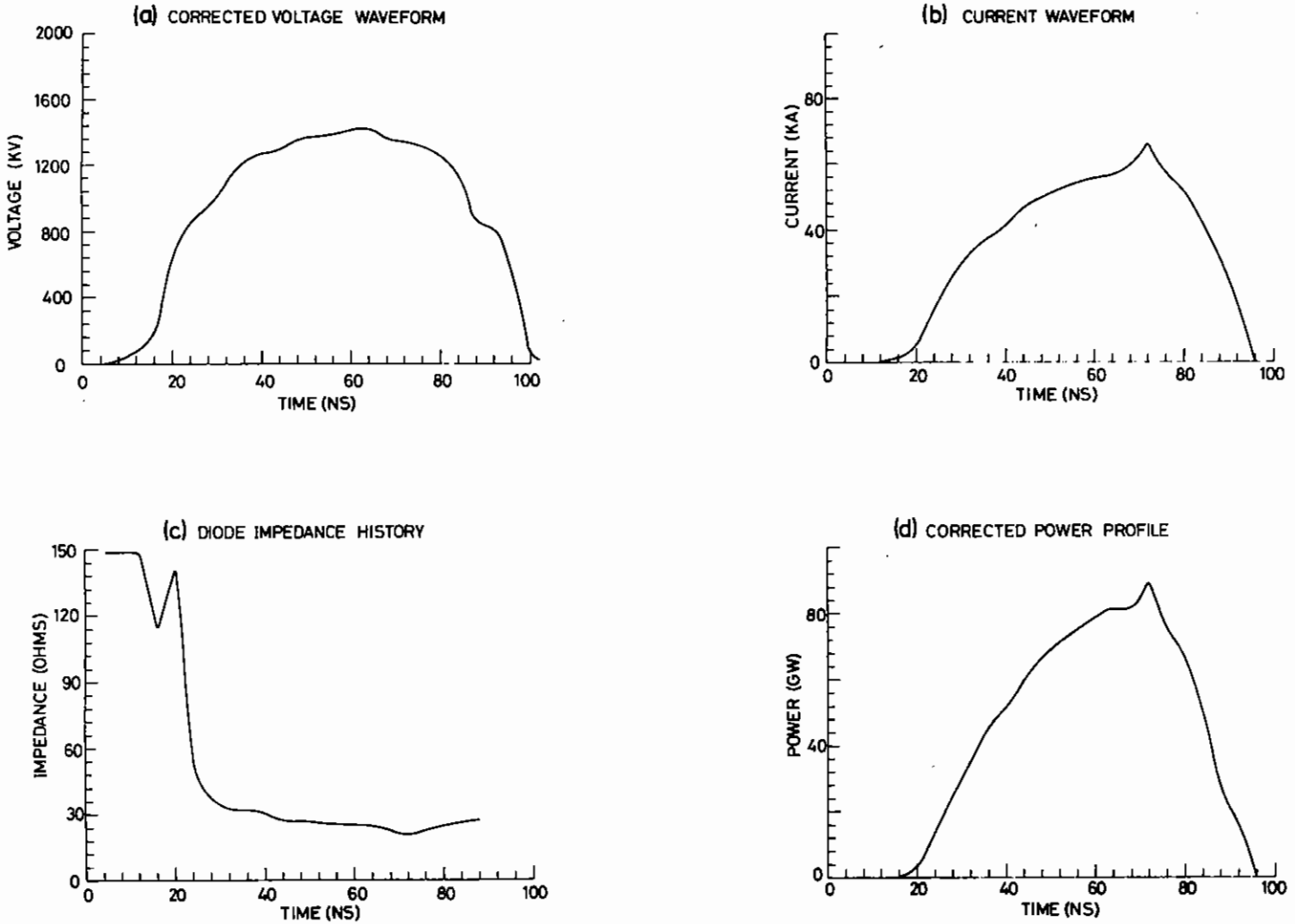

FIG 2.10 ELF ELECTRICAL TRACES.

of the 1.5 MV output voltage requires Z_L to be approximately 25 Ω for the maximum charge voltage of 90 KV which is applied to the 12 stage Marx bank used to pulse-charge the Blumlein.

A diode voltage of 1.6 MV has been obtained using a 90 KV Marx charge voltage and an emitter to anode plate separation of 51 mm. For this shot the peak diode current was approximately 60 KA and the integrated internal diode energy was 4.2KJ. However, because of the large diode spacing used (51 mm), only 36% (1.5 KJ) of this energy was transmitted through the anode aperture and measured by the aluminum calorimeter. Better overall performance was obtained by using a diode spacing of 26 mm at a Marx charge voltage of 90 KV. Under these conditions a diode voltage of 1.4 MV was achieved for a peak current of approximately 80 KA and an integrated internal diode energy of 5.2 KJ. However at this reduced spacing 65% (3.4 KJ) of the energy appeared as useful output from the machine. This is considerably better performance than was obtained under the higher voltage conditions of the previous settings. Output beam uniformity measurements under conditions of high output coupling have shown the beam to be uniform to ± 10% over the total (5 x 50) cm^2 beam area.

While the performance of the electron-beam machine is now very close to its original specification, it is expected that further improvement can be made and experiments towards this end will be carried out over this next year. These experiments will concentrate on detailed shaping of the graphite emitter and on the use of focussing electrodes in the diode chamber. It has also been found necessary to use ± 90 KV Marx charging (rather that the anticipated ± 80 KV charge) to obtain a high voltage output on the diode. The reasons for this are not completely clear and this point will require some investigation.

2.3 Selenium Laser Experiments

2.3.1 OCSe Production

Selenium ^1S_o atoms can be produced in high concentrations by UV photolysis of a suitable selenium bearing fuel. The number of potential fuels for selenium atoms is rather restricted and to date the majority of work has concentrated on the molecule carbonyl selenide, OCSe.

OCSe is a colourless gas at room temperature which condenses to a colourless liquid at -22^oC and freezes to a white solid at -123^oC. OCSe is a relatively unstable compound and is thus not available commercially. When prepared it may, however, be stored indefinitely at liquid nitrogen temperatures. As a gas at room temperature it appears to have a decomposition lifetime of several hours for most common dry vacuum materials. Its decomposition rate on wet surfaces is, however, appreciably faster.

An initial sample of OCSe was prepared for our use by Dr S Craddock of the University of Edinburgh, and he also advised us on the setting up of our own production rig. The on-site production facility was set up with the collaboration of the Rutherford Laboratory Chemical Technology group and it is located in building R34 where suitable fume cupboards and waste disposal services exist.

The preparation of OCSe involves the direct reaction of carbon monoxide and selenium at high temperature viz: CO + Se → OCSe. The reaction vessel is a silica tube, 30 mm in diameter, which passes through two furnaces. In the first furnace, selenium is vapourised from a boat at about 500^oC and in the second it is reacted with CO carrier gas at 650^oC. The products are passed through a glass wool trap to remove selenium and are condensed at liquid nitrogen temperature. The pressure of CO is maintained below 300 Torr, to avoid condensation in the trap, and the optimum flow rate was about 100 cm^3 atm per minute. The yield of OCSe from this reaction is very low being about 50 cm^3 atm per hour.

The major impurities are CO_2, CSe_2, Se and H_2O which are removed by distillation at low temperature using toluene (-96^oC) and iso-pentane (-130^oC) slush baths. CO_2 is the most troublesome impurity requiring some 5 or 6 distillations for complete removal. The purity of the sample is checked

using an IR spectrophotometer. The vibrational frequencies of OCSe are ν_1 = 2021 cm^{-1}, ν_2 = 466 cm^{-1}, ν_3 = 642 cm^{-1} and the most prominant bands in order of strength are ν_1, ν_3, $\nu_1 + \nu_3$ and $2\nu_2$. The CO_2 impurity level is checked using the CO_2 ν_3 band at 2349 cm^{-1}.

The OCSe is stored in glass containers as a solid under vacuum at liquid N_2 temperatures. Using the present rig it is possible to produce OCSe for about four hours per day to allow for the heating and cooling times of the apparatus and for gas purification. This 4 hour working day results in the production of approximately 50 cm^3 atm of pure OCSe gas.

2.3.2 Quantum Yield Measurements

Previous measurements by Black et al (2.02) have indicated that the quantum yield of Se(^1S_o) atoms from photolysis of OCSe was 100% at 170 nm and 30% at 190 nm. The use of the ArF laser at 193 nm for photolysis of OCSe is attractive because this wavelength is less than the photoionization threshold of Se(^1S_o) and thus electrons, which rapidly de-excite the ^1S_o atoms will not be produced, at least not by single photon processes.

It was thus decided to investigate the ArF laser photolysis of OCSe in order to

1) re-determine the ^1S_o quantum yield using an entirely different techinque from that of Black et al.
2) determine the yield for the other selenium levels likely to be produced in photolysis
3) investigate some of the kinetic processes leading to the decay of the excited atom populations.

The apparatus used is shown schematically in figure 2.11 and consists of a glass pipeline cross piece fitted with fused silica windows and connected to a diffusion pumped vacuum station and gas filling rig. The cell is non-bakeable and the ultimate vacuum is about 10^{-5} Torr. OCSe and other gas pressures are measured using an absolutely calibrated M.K.S. Baratron gauge.

The OCSe is photolysed by an Oxford Lasers KX2 discharge excited excimer laser which gives about 100 mJ output on ArF. The laser beam entered the measurement region through a 30 mm x 6 mm slot in a baffle plate to provide a well defined beam profile. Typically the laser fluence was between 2 and 10 mJ/cm^2 at the center of the cell in a pulse of 20 ns duration.

The excited atom concentrations are determined from absorption measurements on atomic lines emitted from a selenium discharge lamp. The transitions used are given in table 2.01.

Initial measurements were made with a sealed lamp of the type described by Little (2.03) but this lamp was difficult to operate under conditions where line reversal was not evident. This was replaced by a flowing lamp where selenium vapour was carried into the lamp in a flowing helium stream. The lamp was excited by a microwave discharge of 10-15 watts power. The discharge was struck in a 2 mm internal diameter spectrosil capillary which was surrounded by a 12 mm outside diameter spectrosil vacuum jacket. Light was taken out through the capillary and vacuum jacket walls. Because of the very small optical depth of this lamp self reversal was not a problem under widely varying operating conditions.

The light from the lamp was collimated and passed through baffles which ensured that all the probe light passed through the photolysed region. The spectral line of interest was selected by a small monochromator and detected on a photomultiplier. The absorption signals were recorded as a function of time on an oscilloscope.

The absorption, A, is related to the absorption coefficient k_o by the relation

$$A = \frac{k_o l}{\sqrt{1+\alpha^2}} - \frac{(k_o l)^2}{2!\sqrt{1+2\alpha^2}} + \cdots + \frac{(-1)^{n-1}(k_o l)^n}{n!(1+n\alpha^2)^{\frac{1}{2}}}$$

where α is the ratio of the doppler line width of the emitter to that of the absorber. This ratio was inferred on the assumptions that the absorber was at 300°K for $t > 10$ μs and $p > 10$ Torr and the emitter was at 650°K since this temperature was measured for helium lines emitted by the lamp in the visible. With the value of α so obtained it was possible by inverting the above series to obtain k_o and thus the atom concentration, N, by the relationship

$$k_o = \frac{2}{\Delta\nu_D}\sqrt{\frac{\ln 2}{\pi}}\frac{\pi e^2}{mc} Nf$$

where $\Delta\nu_D$ is the absorber doppler width and f is the oscillator strength of the line and the other symbols have their usual meaning. Values of f were initially taken from the work of Lawrence (2.04) but it was discovered that the $^1S_o - {}^1P_1$ (199.5 nm) value was in error by a large factor. The values given by Gruzdev (2.05) appear to be more reliable and are in agree-

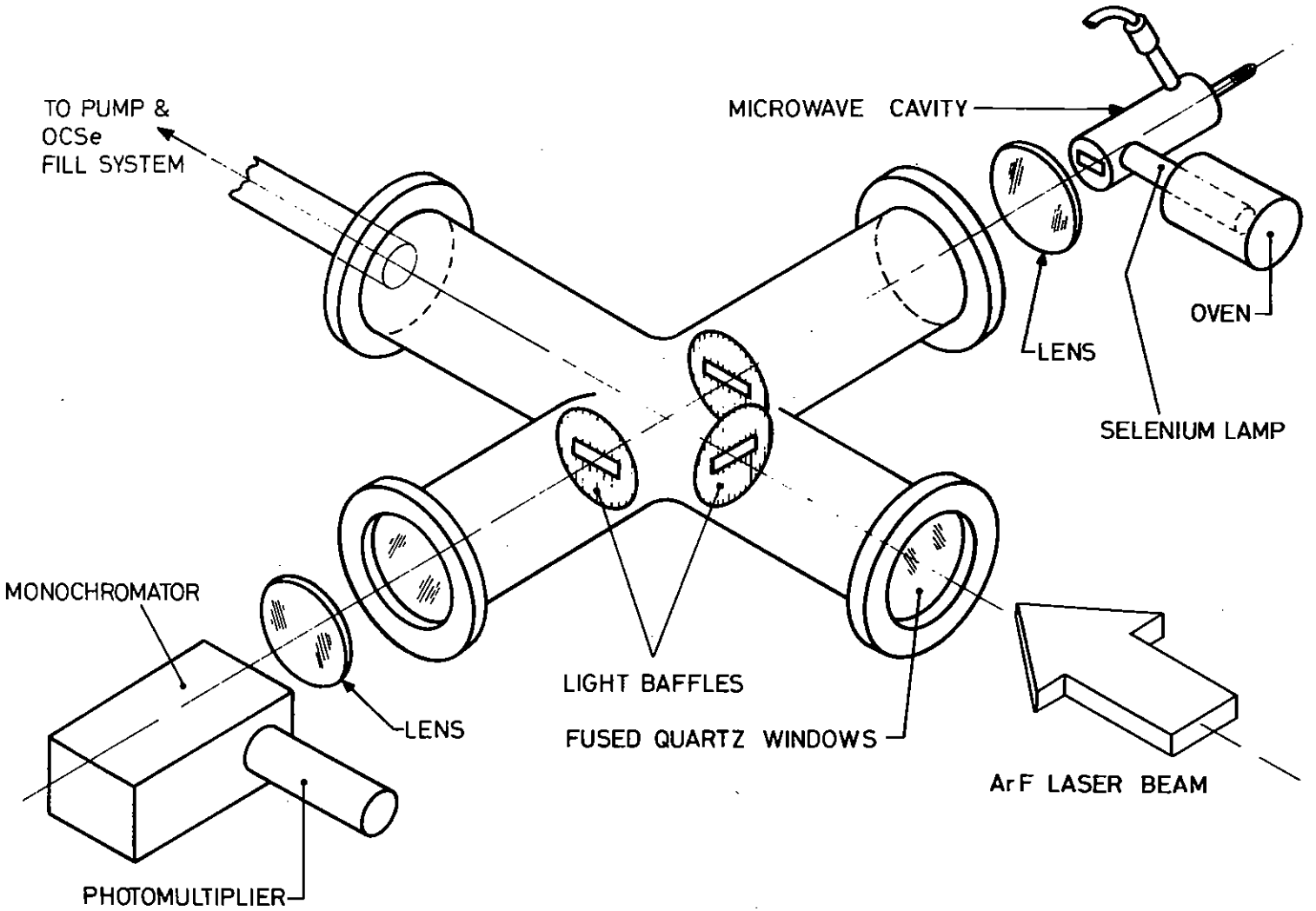

FIG 2.11

LASER PHOTOLYSIS AND ATOMIC ABSORPTION APPARATUS

TABLE 2.01

State	Transition	Wavelength nm	f value	Quantum Yield %
$^1S_0$	$^1S_0 - {}^1P_1$	199.5	0.17	25
$^1D_2$	$^1D_2 - {}^1D_2^0$	185.5	0.13	10
$^3P_0$	$^3P_0 - {}^3S_1$	206.3	0.054	5
$^3P_1$	$^3P_1 - {}^3S_1$	204.0	0.054	25
$^3P_2$	$^3P_2 - {}^3S_1$	196.0	0.062	35

ment with some recent calculations by Weiss (2.06).

Figure 2.12 shows typical decays of all of the five levels in the ground configuration of selenium. The quantum yields given in table 2.01 are obtained from the expression:-

$$QY = \frac{[Se^*(t=0)]\ h\nu}{[OCSe]\ \sigma_a\ F}$$

where $[Se^*(t=0)]$ is the measured atom concentration at t = o, $[OCSe]$ the OCSe concentration, σ_a the absorption cross section at the laser frequency ν. F is the laser fluence in J cm^{-2} and this expression is only valid for optical depths much larger than the cell dimensions and laser fluences much less than the saturation fluence.

The rapid decay of ^1S is due to quenching by OCSe:-

$$Se(^1S) + OCSe \xrightarrow{k_1} Se_2^* + CO$$

k_1 was found to be $1.5 \pm 0.5 \times 10^{-10}$ $cm^3 s^{-1}$.

The high yield of $^3P_1$ is undesirable since this is the lower laser level and methods of efficiently removing this state were investigated. Rate coefficients for the processes

$$Se(^3P_1) + CO \rightarrow \text{Products}$$

and

$$Se(^3P_1) + CO_2 \rightarrow \text{Products}$$

have been determined and are $1.0 \times 10^{-11} cm^3 s^{-1}$ and $1.6 \times 10^{-11} cm^3 s^{-1}$ respectively. The importance of these results is that CO and CO_2 are likely to be present in the laser cell and have very small de-excitation rates ($k \simeq 10^{-16} cm^3\ s^{-1}$) for $Se(^1S)$. CO is produced in the photolysis process and CO_2 is likely to be present as an impurity in OCSe.

The conclusions which may be drawn from these measurements are as follows:-

1) The ArF laser may be used to photolyse OCSe and yields $Se(^1S_o)$ atoms with an efficiency of about 25%.
2) The ^1S_o atom decay is dominated by quenching from OCSe and hence the OCSe must be bleached in any practical laser system.
3) High concentrations of the lower laser level are produced in

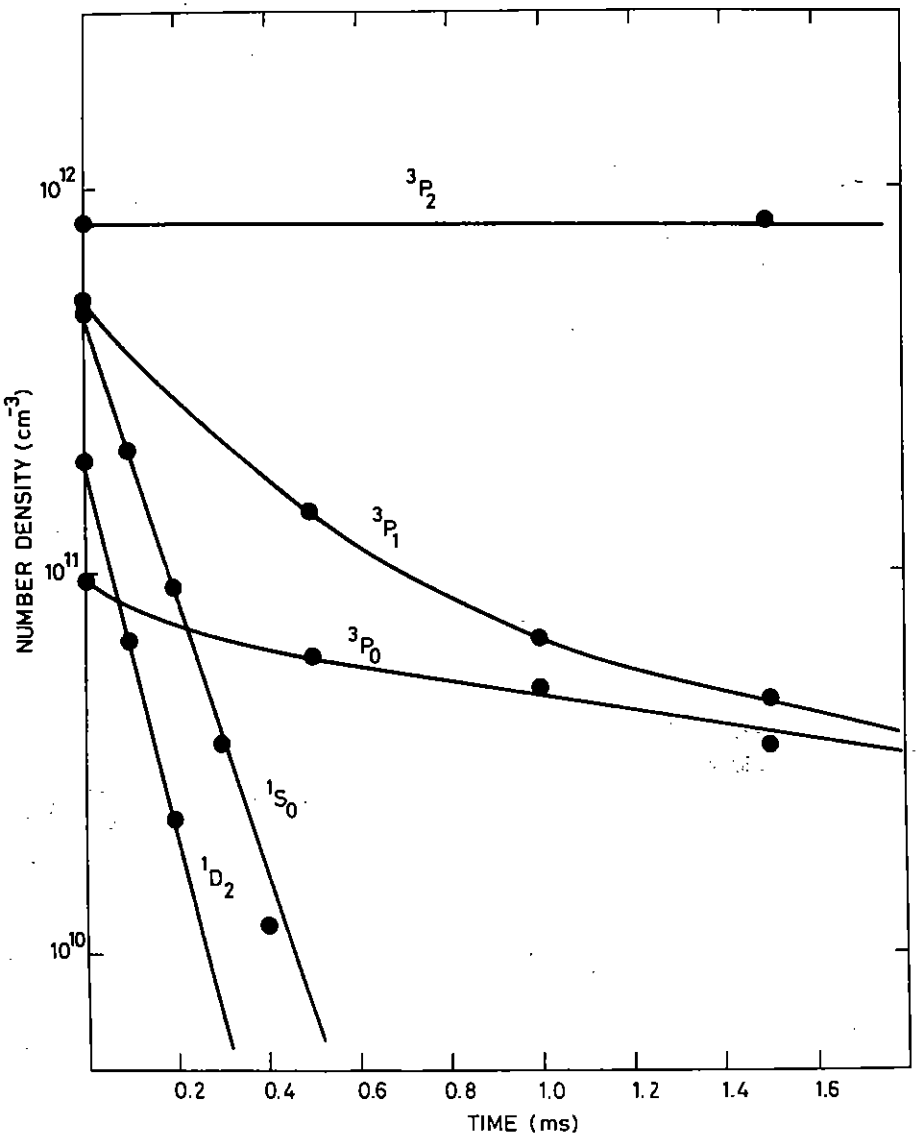

FIG 2.12 SELENIUM ATOMIC LEVEL DECAYS

photolysis but may be removed efficiently by the addition of CO or CO_2.

2.3.3 Laser Cell Progress

Based on the photolysis measurements described in the previous section it was clear that it should be possible to operate a high power 489 nm selenium atom laser using an ArF pump source. A large ArF laser cell has therefore been designed for use on the ELF electron-beam machine and this laser cell is presently under construction. For preliminary experiments, a small high pressure laser cell has been constructed and has been used on the ELF machine to obtain laser action on KrF at 248 nm. An output of 5 Joules has been obtained for an estimated e-beam energy deposition of 250 Joules. This cell will now be used to investigate the operation of a short pulse ArF laser as a preliminary experiment for the ArF-pumped selenium laser project.

2.4 Cadmium-Mercury Excimer Studies

2.4.1 Optical Pumping at 266 nm: Energy Transfer Processes

The optimum mode of excitation for the cadmium-mercury excimer system is an electron-beam-controlled discharge (2.07). As a preliminary to this type of experiment, a more thorough knowledge of the system kinetics, in the absence of ionisation, has been obtained by optically pumping cadmium-mercury mixtures at 266 nm. At this wavelength one may either pump the $^1\Sigma_u$ band of Hg_2 or the $^1\Sigma_u^+$ band of Cd_2. The absorptions depend on the square of the atomic density. New measurements have been made of both cadmium and mercury molecular absorptions throughout the 200 nm to 350 nm band and the absorption constants at 266 nm are 2.9×10^{-38} cm^5 (Cd) and $7{\cdot}0 \times 10^{-40}$ cm^5 (Hg). Depending upon the relative concentration of each metal the excitation pathway in a metal mixture may either be through molecular Cd or molecular Hg.

At relatively high Hg and low Cd concentrations, a new formation route for CdHg molecules has been observed:-

$$Hg_2^* + Cd \rightarrow CdHg^*(a) + Hg$$

with a forward rate coefficient of 5×10^{-10} cm^3/sec. The precise identity of the parent mercury state has yet to be established. Present data suggests that it is either the $Hg_2(0_g^{\pm})$ reservoir states or Hg_3. The product

state has a decay lifetime of 3.5 μsec and a fluorescence spectrum identical to that previously observed for CdHg(a) (2.08) in an optical pumping experiment at 326.1 nm. As the Cd density is increased, a change in spectrum and decay time indicates that a second CdHg state is forming. One process which may be present is

$$CdHg(a) + Cd \rightarrow CdHg(b) + Cd$$

with a rate of $2.6 \times 10^{-11} cm^3/sec$. However, another possible route is via the $Cd_2(^3\pi_g)$ state as shown in figure 2.13. The emission spectrum of CdHg(b peaks at 460 nm and its decay lifetime has been inferred indirectly to be 150 nsec.

At relatively high Cd and low Hg concentrations the 266 nm excitation enters the $Cd_2(^3\pi_g)$ and Cd_3 states with only about 10% efficiency. Most of the energy is radiated in the $Cd_2(^1\Sigma_u^+ \rightarrow {}^1\Sigma_g^+)$ continuum band within a few nsec. As the Hg concentration is varied to zero the pure Cd_2 fluorescence is observed (2.09). A kinetic explanation has been found for the Cd_2 fluorescence which gives a good fit to the data of (2.09) using the most simple state system compatible with theoretical cadmium potentials. It involves a cadmium dimer reservoir level at an energy of 0.89 eV below the $Cd(^3P_1)$ level and a Cd_3 species 0.82 eV below the reservoir as shown in figure 2.13. At Cd concentrations of $\sim 1 \times 10^{18}/cm^3$ the reservoir and trimer are assumed to be in equilibrium and radiation is from the $Cd_2(^3\Sigma_u^+)$ state which is populated via the $Cd(^3P_1)$ level by collisions:-

$$Cd_2(^3\pi_g) + Cd \rightarrow Cd(^3P_1) + 2Cd(^1S_o)$$

$$Cd(^3P_1) + 2Cd \rightarrow Cd_2(^3\Sigma_u^+) + Cd.$$

The rate constant for the first process is 4.6×10^{-10} exp $(-0.89(eV)/kT)$ cm^3/sec.

As Hg is added, the fluorescence band changes into that of CdHg(b) and the system decay time decreases. A good fit to experiment has been obtained using the process

$$Cd_2(^3\pi_g) + Hg \rightarrow CdHg(b) + Cd$$

with a rate constant of $3.8 \times 10^{-14} cm^3/sec$. This has a resemblance to

the CdHg(a) formation discussed above.

The major conclusions from this kinetic study are that

(i) CdHg(a) may be produced with unit quantum efficiency using optical excitation at 266 nm.

(ii) The Cd_3 state lies very deep and may be populated at quite low Cd densities.

(iii) The CdHg(b) state has a rapid radiative decay and does not normally hold a high proportion of the excitation.

2.4.2 Excited State Absorptions at Ar^+ Laser Wavelengths

The CdHg(a) band is centred at 470 nm, has a half width of 80 nm and a theoretical stimulated emission cross section of 2×10^{-19} cm^2 at the band centre. The corresponding figures for CdHg(b) are: 460 nm, 70 nm and 5×10^{-18} cm^2. Using a pump energy of 5 mJ at 266 nm in a collinear geometry of cross section 5×10^{-2} cm^2 the maximum gain predicted for CdHg(a) is 1.5% and that for CdHg(b) is 40%. An experiment has been performed using Ar^+ laser lines as a monitor of gain or loss in conditions where the excited population is almost completely in the CdHg(a) state. It was found necessary to employ a collection angle of 100 mrad for the transmitted beam in order to reduce the acoustic beam distortion effects to a level of about 1%. The results of this measurement are shown in figure 2.14. At 5×10^{16} Cd atoms/cm^3, more than 90% of the excitation is in CdHg(a). At increasing [Cd], the kinetic model predicts an increasing $Cd_2(^3\pi_g)$ and Cd_3 population and also a small fraction ($\lesssim$ 10%) of CdHg(b) at the highest [Cd]. The absorption which is observed has a cross section of at least 1×10^{-18} cm^2 at 456 nm and is most probably associated with molecular Cd species. The experimental error of $\pm$ 1% corresponds to approximately $\pm$ 1×10^{-19} cm^2 cross section for gain or loss. The apparent small gain to the red of 500 nm is not significantly above the experimental noise.

For comparison, the absorption of pure mercury molecular species under identical excitation is shown in figure 2.15. The peak absorption cross section is $\gtrsim 5 \times 10^{-19}$ cm^2.

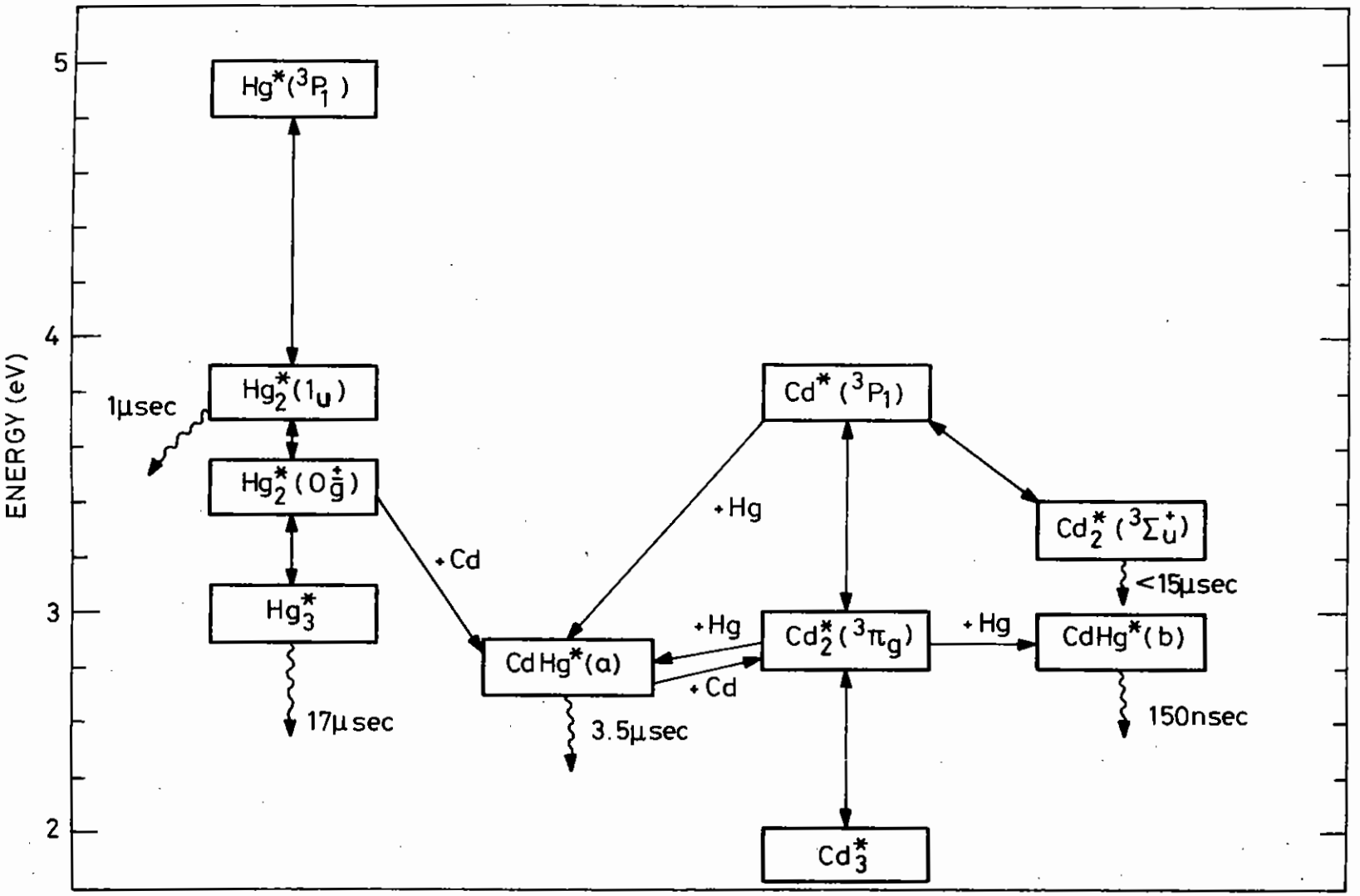

FIG 2.13 ENERGY PATHWAYS IN THE CADMIUM-MERCURY SYSTEM.

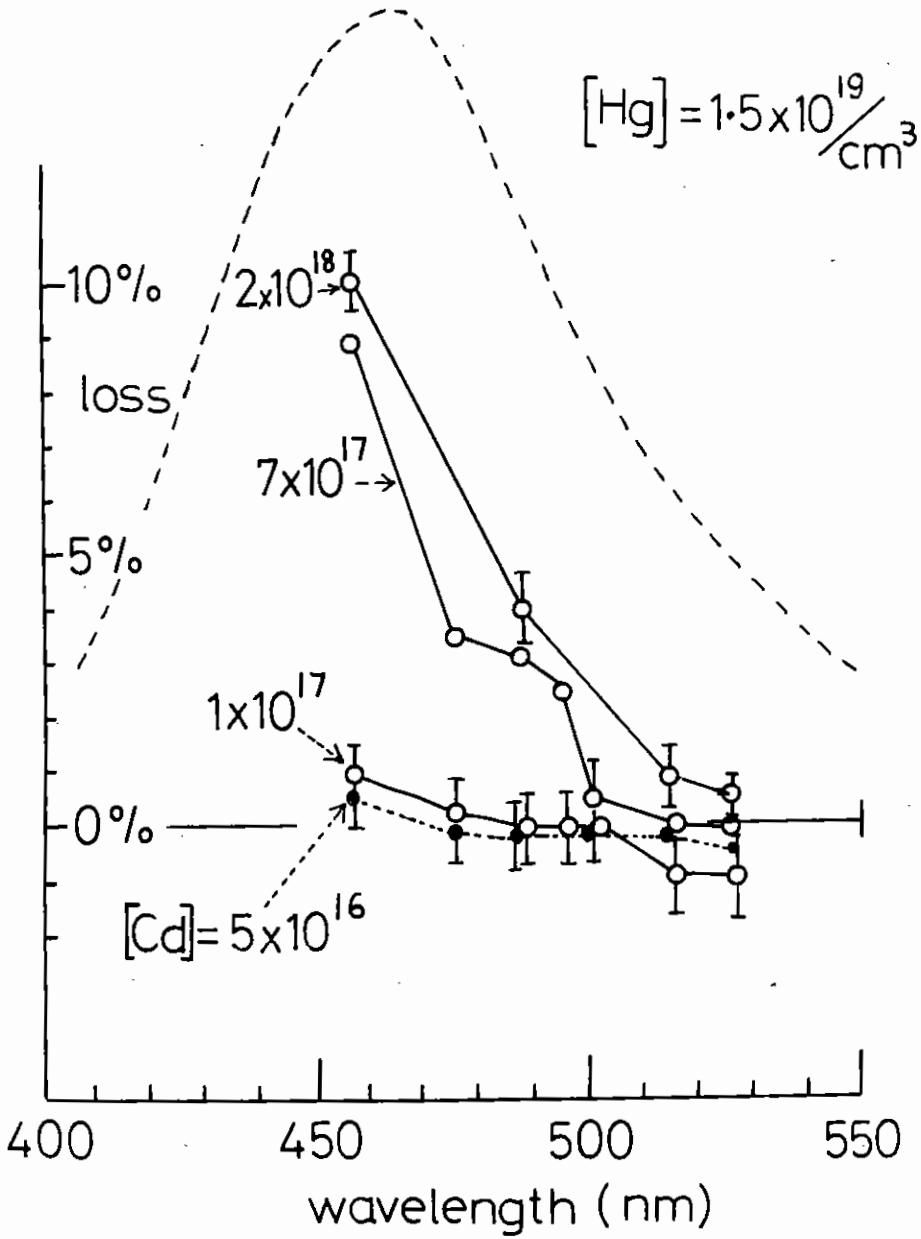

Fig.2.14

Transmission of Ar^+ laser lines through a 5 cm cell of cadmium-mercury pumped collinearly by 5 mJ at 266 nm The dashed curve is the reversed stimulated emission profile in arbitrary units.

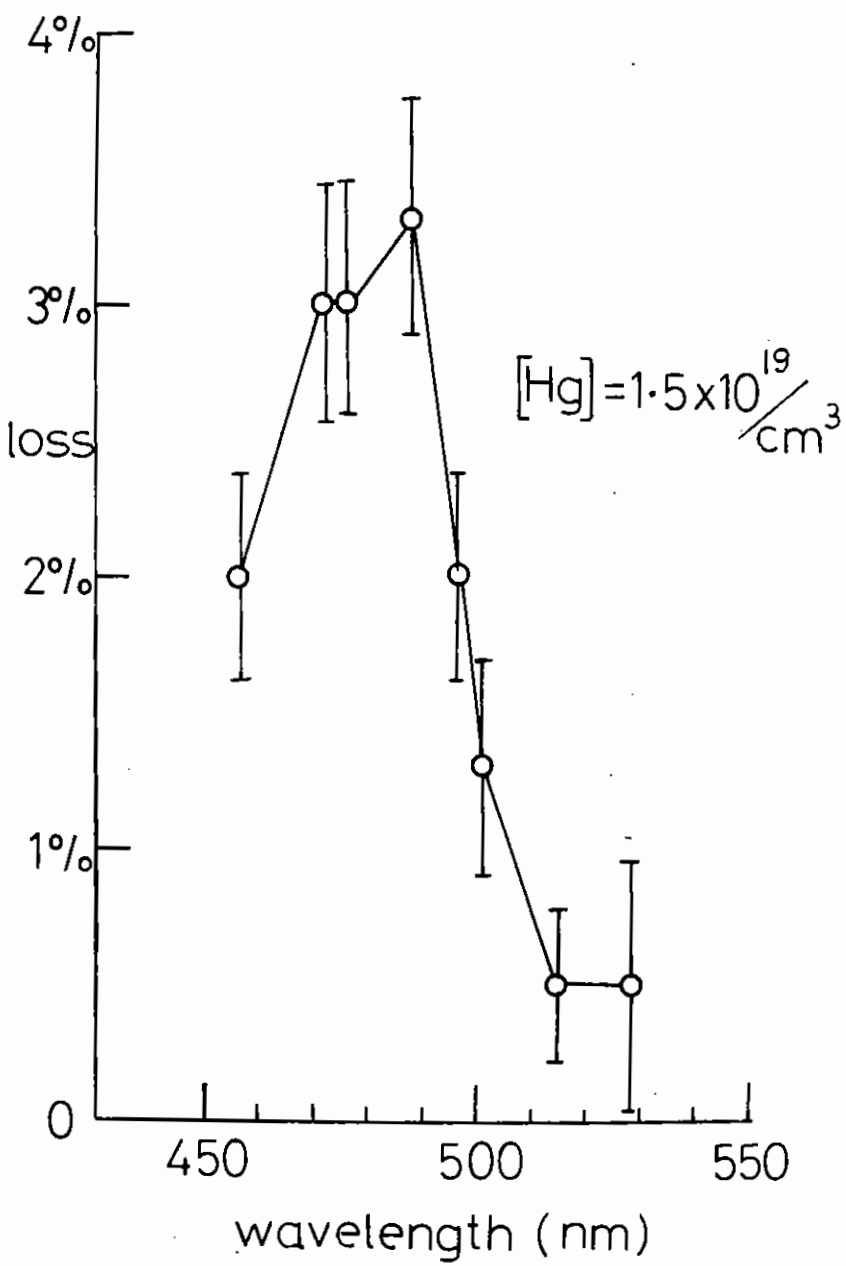

Fig.2.15

Transmission of Ar^+ laser lines through a 5 cm cell of mercury only, pumped collinearly by 5 mJ at 266 nm

2.4.3 Laser Implications of Kinetic Model

The experiments completed to date have not been adequate to distinguish net gain or loss on the CdHg(a) band. The molecular cadmium and mercury absorptions both overlap the CdHg bands and have to be accounted for in the CdHg measurements. It is necessary to establish whether there is intrinsic gain on the CdHg bands before the overall laser efficiency can be predicted. It is possible that there may not be net gain for small signals (such as the Ar^+ probe beam) due to the presence of a small proportion of highly absorbing molecules, but that there could be net energy gain for saturation energy pulses.

In conclusion, the present experimental data still allows the possibility that the CdHg(a) state may be a highly efficient laser with ideal characteristics for high power and high energy operation. Further transmission experiments with a 30 mJ, TEM_{oo} pulse at 266 nm are expected to increase the experimental resolution to $\pm$ 2 x 10^{-20} cm^2.

2.5 Electron Energy Deposition Calculations

A computer program (EPIC) has been written to describe the way in which an electron beam penetrates and causes ionisation in thick gas targets. This program will be used to calculate energy deposition in laser cells so that laser efficiency measurements can be made. During the initial development of the program, comparisons were made between EPIC calculations and published theoretical data for electron beam penetration in the energy range 200 kev to 500 kev. These comparisons showed excellent agreement between EPIC calculations and published data. Unfortunatly very little published data exists for the voltage range 1.0 Mev to 1.5 Mev which is of most interest in our work with the high voltage ELF electron-beam machine. It was decided therefore to compare high voltage EPIC calculations with experimental results for the ELF beam propagating in air. This is of course the simplest e-beam deposition experiment to perform since it is necessary only to extract the electron beam into the laboratory air.

The spatial characteristics of the energy deposition of the ELF electron beam have been investigated using cellophane dosimetery as a monitor of deposited energy. Since the energy stopped in the cellophane (25 μm thick) is a small fraction of the total beam energy, the propagation of the beam

in the open air is largely unaffected by the presence of the detector. Consequently it is possible to sample the beam at many positions in space simultaneously, accumulating the required data from one pulse and thus eliminating any averaging due to shot to shot variations. In addition since the experiment consists of firing the electron-beam through a widely spaced array of cellophane in air, backscatter of electrons between detectors (pieces of cellophane) is eliminated thus greatly simplifying the interpretation of experimental results.

The measured energy deposition versus distance of a nominally 1 Mev electron beam in air is shown in figure 2.16. For this shot the peak electron-beam diode current was measured to be 120 KA in a pulse with a 50 nsec flat top and a full width half maximum (FWHM) of 70 nsec As can be seen the distribution is peaked at about 50 cm from the foil and then falls off gradually at larger distances as the electron-beam diverges and is attenuated. The energy deposition predicted by EPIC is shown in the figure for comparison. The solid line is the result obtained by running the code in its 1-D configuration with the electrons emerging normal to the diode foil as a parallel beam of uniform current density and with an energy of 980 Kev. The peaked energy profile at 50 cm is not exhibited. It is interesting to try to interpret the peaked energy profile in terms of two beam fractions, one diverging (at 0.1 radian) and one converging (due to self pinch) such that the sum of these components is normalised to the 1-D simulation. This was carried out with EPIC operating in its 2D mode. The contribution of the two fractions is shown (hatched lines) in figure 2.16. A two component beam would have characteristics similar to an emerging parallel beam which is exhibiting self magnetic pinching. This was most probably the case for the 120 KA beam obtained in this shot.

The above results show that the EPIC code can predict some of the features observed on the penetration of the ELF electron beam into air. Further tests will be carried out to try and obtain quantitative agreement so that EPIC can in the future be used for laser calculations.

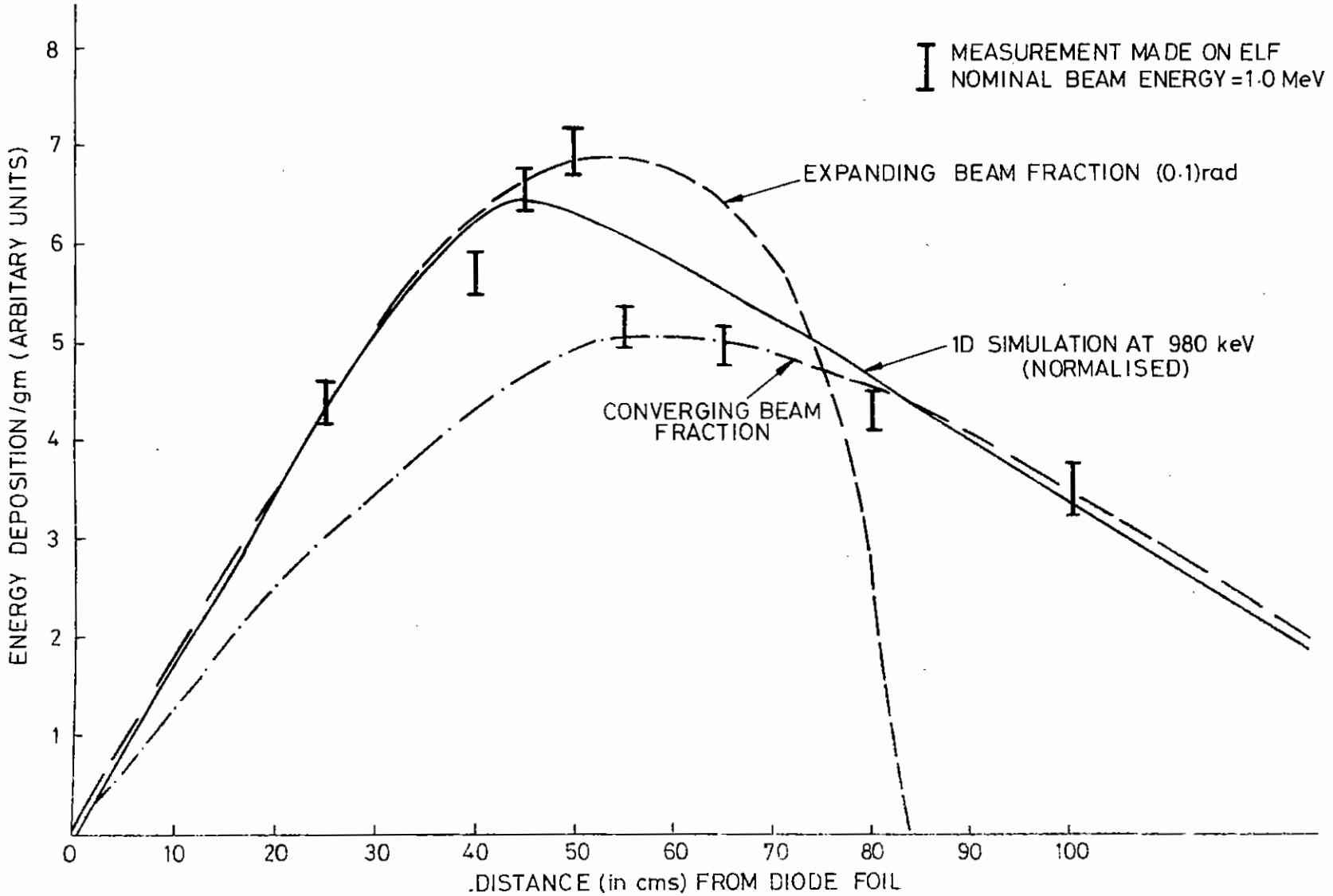

FIG 2.16 ELECTRON ENERGY DEPOSITION IN AIR AT 1·0 MeV

CHAPTER 2 REFERENCES

2.01 Nucleonics 12, 62 (1954)

2.02 G. Black, R.L. Sharpless, and T.G. Slanger, J. Chem. Phys. 64, 3985 (1976)

2.03 D.J. Little, Ph.D. Thesis, University of Edinburgh (1974).

2.04 G.M. Lawrence, Astro. J. 148, 261 (1967).

2.05 O. Gruzdev, Optics and Spec. 27, 479 (1969).

2.06 A.W. Weiss, Private Communication.

2.07 G.R. Fournier and M.W. McGeoch, J. Appl. Phys. 49, 2651, (1978).

2.08 M.W. McGeoch, G.R. Fournier, and P. Ewart, J. Phys. B. 9, L121 (1976).

2.09 R.E. Drullinger and M. Stock, J. Chem. Phys. 68, 5299 (1978).

CHAPTER 3 LASER PLASMA INTERACTIONS

INDEX

CHAPTER EDITOR D J Nicholas

CONTRIBUTORS B Ahlborn, H C Barr, P D Carter, A J Cole, R G Evans, D R Gray, T P Hughes, J Murdock, A Raven, S M L Sim, W T Toner and O Willi.

CHAPTER 3 LASER PLASMA INTERACTIONS

3.1 Introduction

The laser time available for interaction studies during the year was very limited, and so it was decided to concentrate on carrying out a small number of experiments. Several valuable new results have been obtained concerning electron density distributions, Brillouin scattering and harmonic generation. These are summarized below and described in detail in the following sections (3.2-3.4). They were made possible largely through the development of improved techniques for high-resolution ultra violet interferometry and its analysis; and for time-resolved spectroscopy using streak cameras.

Good progress was made during the year towards bringing together theoretical and experimental work on interactions: the theoretical contributions by Barr and Cairns referred to in Sections 3.2 to 3.4 are described in Chapter 8.

Most of the experiments used ∿50 ps laser pulses giving focussed irradiances of $\sim 10^{16}$ W cm^{-2}. Density profiles in plasmas from small microballoon targets were measured interferometrically with excellent resolution (∿ 1μm) upto twice the critical electron density for the main laser pulse. Steepening of the density gradient near n_c during the pulse was found to vary with the incident irradiance in good agreement with Kidder's model (3.07) of an isothermal plasma with sonic flow through the critical density surface. The subsequent development of the density structure was followed and interpreted as a transition to supersonic flow with a temperature step near n_c resulting from inhibition of thermal conduction, possibly due to the growth of ion acoustic waves. Density profiles were also obtained in plasmas from essentially plane targets where large magnetic fields were observed previously. They showed the expected effect of the magnetic field in pushing the plasma into a shell structure with an off-axis density depression.

Time-resolved spectra of backscattered radiation near harmonics of the laser frequency ω_o were obtained for the first time using microballoon targets with a time resolution of 10 ps and a spectral resolution of 1Å, using a streak camera to record the output of a grating spectrometer. The $2\omega_o$ spectrum showed intense bursts of radiation, of duration and bandwidth no greater than the resolution limits of the system, over a total spectral breadth of about 30Å. The $\frac{3}{2}\omega_o$ spectrum with similar time resolution but with 15Å spectral resolution also showed very brief bursts of emission: they occurred with both red and blue shifts simultaneously, the separation of the components being initially about 300Å but decreasing towards the end of the laser pulse. A comparison of the forward and backward scattered $\frac{3}{2}\omega_o$ radiation from thin foil targets, without time resolution, showed differences which have yet to be fully understood: in general the forward scattered light had a stronger blue-shifted component. In general the $\frac{3}{2}\omega_o$ results appear to be consistent with the theoretical model of Avrov et al (3.17), though the pulsation of the emission requires further explanation, possibly involving soliton formation.

Long (1.6 ns) laser pulses of energy $\sim$ 100J were used in another series of experiments with microballoon targets. Time-resolved spectra were obtained of the backscattered radiation, ascribed to Brillouin scattering near the laser frequency ω_o; and of the $2\omega_o$ harmonic radiation. The Brillouin scattered light persisted during most of the laser pulse. The interpretation of the spectrum in terms of the ion acoustic wave frequency and hence (since $\kappa_{ia} = 2\kappa_o$) of electron temperature is complicated by the Doppler shift due to the motion of the ablating medium. At irradiances below 10^{14} W cm^{-2} the second harmonic radiation consisted of a single narrow component about 2Å wide, consistent with the occurrence of resonant absorption: at higher irradiances the spectrum broadened to $\sim$20Å and showed a structure resembling that obtained with short (50 ps) laser pulses.

3.2 Density profile measurements

The effects of radiation pressure on the density profiles formed during the interaction of intense laser light with plasmas have been recently

reported in the regime where the radiation pressure P_r is a fraction (0.2) of the plasma pressure P_c at critical density (3.01). Three types of profile modification have been discussed theoretically (3.02) of which one type is consistent with numerical studies (3.03) and favoured by stability. An interferometric study at λ = 266 nm has been made of the time evolution of density structures produced at irradiances of 10^{16} W cm^{-2} where $P_r > P_c$. Initial steepening of the profile with a step height scaling of $\Delta n/n_c \propto I^{0.16 \pm 0.01}$ is observed followed by the development at later times of supercritical density structures. Structures are also observed that are attributable to the high magnetic field pressure ($B^2/8\pi nkT \sim 0.5$) in the low density corona.

The targets consisted of small 40 μm diameter hollow glass microballoons or 1 mm diameter aluminium wires. The former were chosen to facilitate probing to high densities (3.01). Irradiation of these targets was with single pulses of 50 ps duration at half maximum intensity and energies between 0.5 and 2.5J in a 15 μm focal spot, giving irradiances on target of up to 10^{16} W cm^{-2}.

A portion of the main 1.06 μm irradiating beam was split off and frequency quadrupled in two successvie KD*P crystals to generate a probe beam at 266 nm (Fig.3.01). The probe pulse of 150 μJ in 25 ps was used to illuminate the target from the side. Timing with respect to the main beam was to within 15 ps as measured by an EPL streak camera. An f/2.5 x 10 ultraviolet microscope objective was used to image the target. Protection of the objective from target debris and scattered 1.06 μm light was achieved by the use of a 100 μm thick quartz pellicle with a dielectric mirror coating on the front surface. The interferometer was of the Nomarski type (3.04) and used a quartz Wollaston prism and a calcite Glan-Taylor prism mounted coaxially behind the microscope objective. Interferograms were recorded on Kodak HP5 film. Alignment and focussing were carried out in He-Ne light with the interference fringes switched off: an empirically determined focal length correction was then applied to focus the image in 266 nm light. A focal accuracy of 10 μm, which is

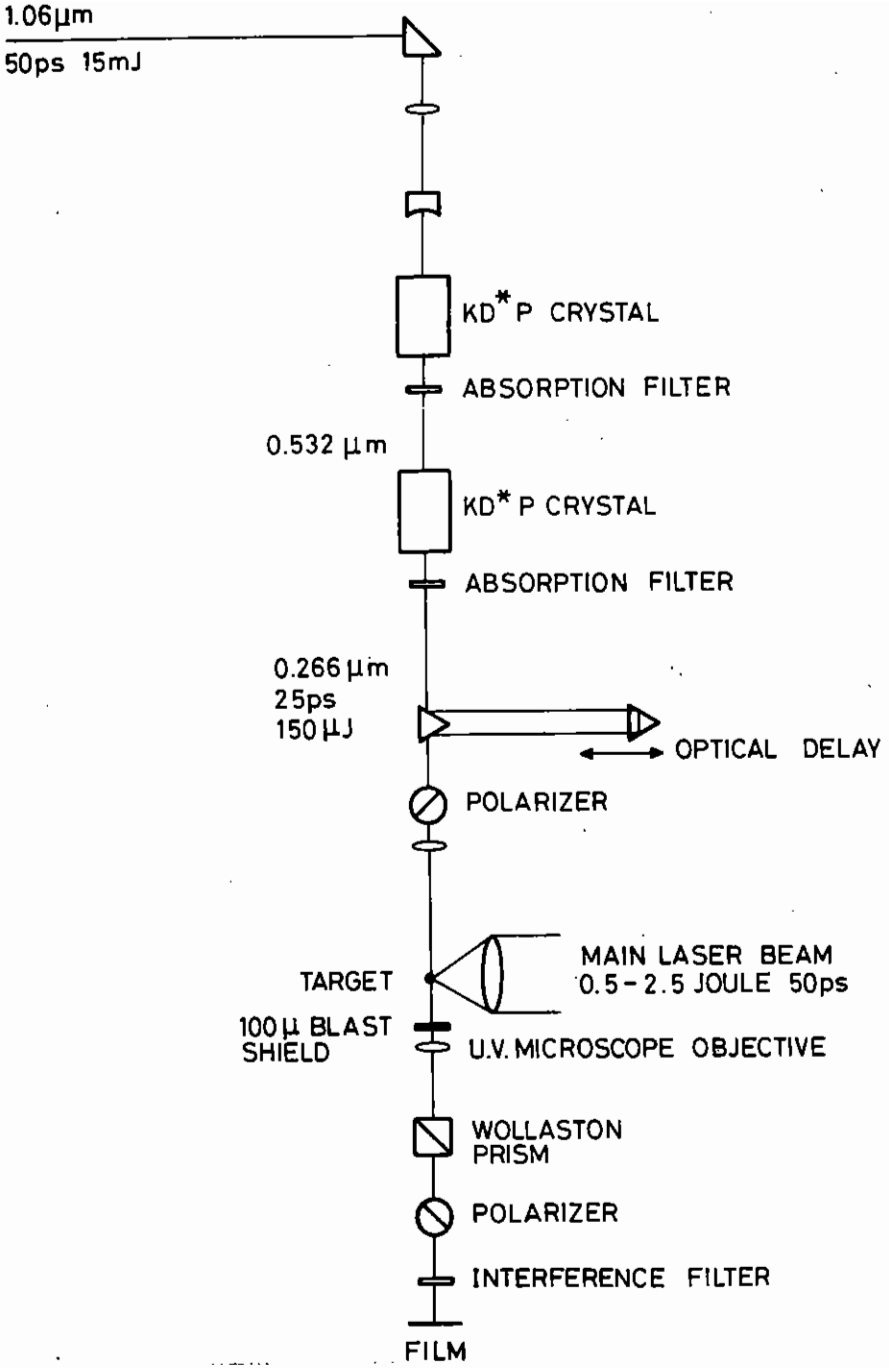

Fig.3.01

Experimental system for 4th harmonic interferometry.

necessary for the accurate analysis of the density profiles of the strongly refracting plasma (3.05) was achieved.

The interferograms (3.02) were enlarged and fringe position data were digitised with a computer-linked graphics tablet. Abel inversions (3.06) were performed along lines normal to the main laser beam and the central values of such inversions, taken every 0.5 μm, were used to obtain the axial (z) electron density profiles.

Measurements on spherical targets during the main heating pulse (3.03) at an intensity of 10^{16} W cm^{-2} show a steepened profile with upper and lower density shelves at 1.8 n_c and 0.4 n_c respectively (n_c is the critical density for 1.06 μm = 10^{21} cm^{-3}). The scale length of the steepened section is limited by the optics resolution and plasma motion to 0.5 μm. These results are very similar to those observed by Attwood (3.01) at the lower intensity of 3×10^{14} W cm^{-2} with the exception that the upper density shelf is, as expected, at a higher density. Measurements made at an intensity of 2.5×10^{15} W cm^{-2} show the step height to be reduced to 1.1 n_c and these, together with the results of (3.01), indicate an intensity scaling of the step height of $\Delta n/n_c = 4.0 \times 10^{-3}\, I^{0.16} \pm 0.01$ with I in W cm^{-2}.

Kidder (3.07) on the basis of an isothermal plasma with sonic flow through the critical surface has estimated the density step to be proportional to $(P_r/P_c)^{\frac{1}{2}}$ for $P_r/P_c \ll 1$. Experiments (3.09) (3.12) have shown the electron temperature is related to the incident intensity by $T \propto I^{2/3}$ and consequently the density jump can be estimated to scale as $\Delta n/n_c \propto (I/cnkT)^{\frac{1}{2}} \propto I^{0.17}$. This is in very close agreement with the measured scaling despite the limitations of the theoretical model.

After the main heating pulse a complex density structure develops (Fig. 3.04). In particular a supercritical density bump is seen and considerable low density structure appears. Several shots were taken at each delay time and all show qualitatively the same density structures. At late times (t = 285 ps, 385 ps), the low density

structure relaxes to a smooth two scale length profile as has been observed before (3.10). The positions of the profiles are referenced with an accuracy of 1 μm to the original target surface and allows the velocity of the critical surface to be determined as $6.3 \pm 0.8 \times 10^6$ cms^{-1} (Fig.3.05). This is consistent with estimates of $v_c \lesssim 5 \times 10^6$ cms^{-1} obtained from the visibility of the interference fringes and the plasma motion limit on the measured scale length of the steepened profile.

The supercritical density bump in Fig.3.04 is similar to the supersonic profile discussed by Max and McKee (3.02) and numerically modelled by Virmont et al (3.03). The analysis (3.02) was carried out for an isothermal plasma with a local momentum deposition at the critical surface due to the light pressure and it led to either a D (step) front for subsonic plasma flow or an R (compression front) for supersonic flow. It was suggested that when driven by light pressure a shock plus D front may be more stable than an R front for supersonic flow. In a laser produced plasma at high irradiance the incident energy flux due to absorption at or below critical density is greater than can be assimilated by thermal conduction to the more dense plasma. This inward heat flux is further inhibited by for example ion acoustic turbulence and results in the low density corona thermally decoupling (3.11, 3.12) from the more dense plasma with a steep temperature step around critical density (3.08, 3.12). Under these conditions the steady state solutions of Ref.3.02 can be remodelled in terms of a non-isothermal plasma (with or without light pressure) and leads to similar flow conditions and density structures that now depend on the temperature ratio $\alpha^2(>1)$. Omitting light pressure effects equations 4 and 5 of Ref.3.02 now become

$$\frac{\rho 1}{\rho 2} = \frac{(1 + M_1^2) \pm \{(1 + M_1^2)^2 - 4M_1^2\alpha^2\}^{\frac{1}{2}}}{2M_1^2}$$

with $M_1 > M_R \equiv \alpha + \sqrt{\alpha^2 - 1}$

or $M_1 < M_D \equiv \alpha - \sqrt{\alpha^2 - 1}$

where ρ_1, and M_1 are the upper density and Mach number and ρ_2 is the lower density. The effect of this non-isothermality has been observed in numerical simulations (3.08) where the D-front density jump was found to be dependent on the flux inhibition factor applied.

After the laser has switched off, the corona will be considerably hotter than the more dense plasma and will drive a heat wave travelling against the outflow of colder plasma from the target. This heat wave can be of the subsonic (D-front) or supersonic (R-front) type depending on the local flow conditions. The type that exists will depend on the ratio of the thermal (burn) wave velocity V_{HW} to the sound velocity C_s where

$$V_{HW} = \frac{W}{\rho_1 h_2} \; ; \; C_s = \left(\frac{\gamma Z k T_2}{A m_p}\right)^{\frac{1}{2}} \text{ and } \; h_2 = \frac{\gamma - 1}{\gamma}\left(\frac{Z k T_2}{A m_p}\right) = (\gamma - 1) C_s^2$$

W is the heat flux and h_2 the enthalpy of the low density region 2. If the thermal wave velocity exceeds the sound velocity the flow must be supersonic with respect to the density step. For an initially subsonic front this can only occur if the cooling behaviour of the plasma is such that T_2 decreases more rapidly than $W^{2/3}$. This seems reasonable since hydro and radiation cooling will decrease T_2 faster than by thermal conduction alone.

The transition from sub to supersonic flow can be more readily seen in the "universal" plane of T_2-W/ρ_1 (Fig.3.06). In this plane one can draw families of curves, for constant values of various parameters (3.13), which are consistent with the equations of conservation of mass, momentum and energy, so that cross correlations between measured and unknown parameters can be made. From other experiments (section 4.3) the net power input to the ablation plasma during the laser pulse is known. This together with the density ratio of $\rho_2/\rho_1 = 0.2$ and the upper shelf density ρ_1 measured during the laser pulse allows a point to be fixed in the plane representing the initial conditions. This then indicates a subsonic D-type profile modification and a coronal temperature of 10 to 20 keV which is not inconsistent with the measurements of Rosen et al (3.12). The role of the

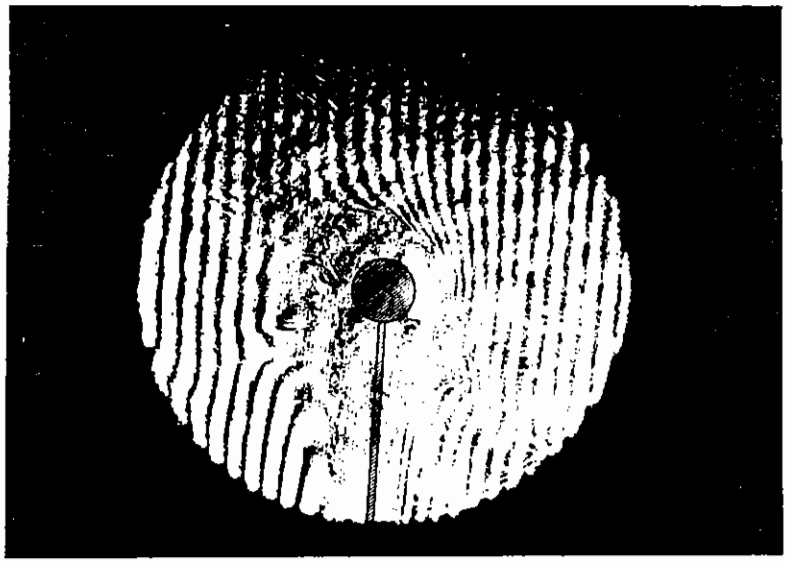

INTERFEROGRAM

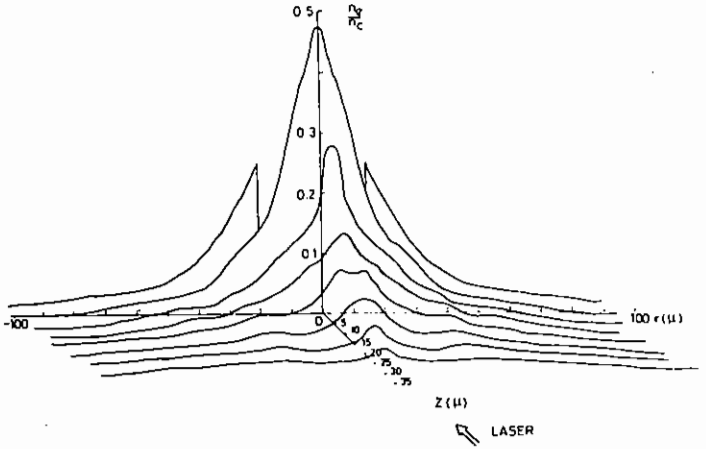

DENSITY PROFILE

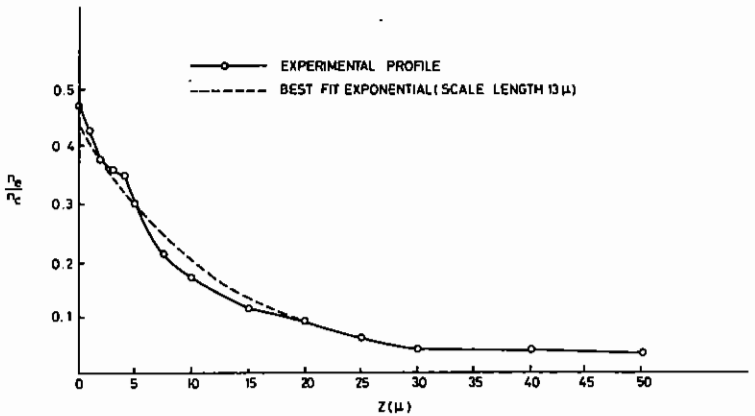

AXIAL PROFILE

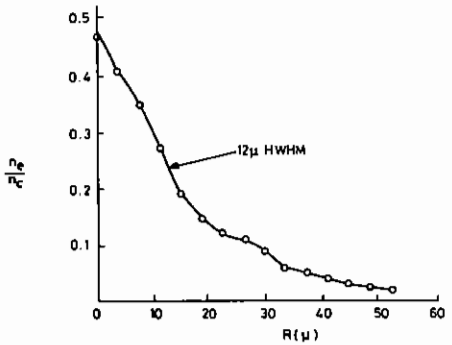

RADIAL PROFILE

TIME: 400ps AFTER THE PEAK OF THE PULSE 5×10^{15} Wcm

Fig.3.02

An example of an interferogram and electron number density profiles deduced from it for a 45 μm diameter microballoon target irradiated with a 50 ps pulse.

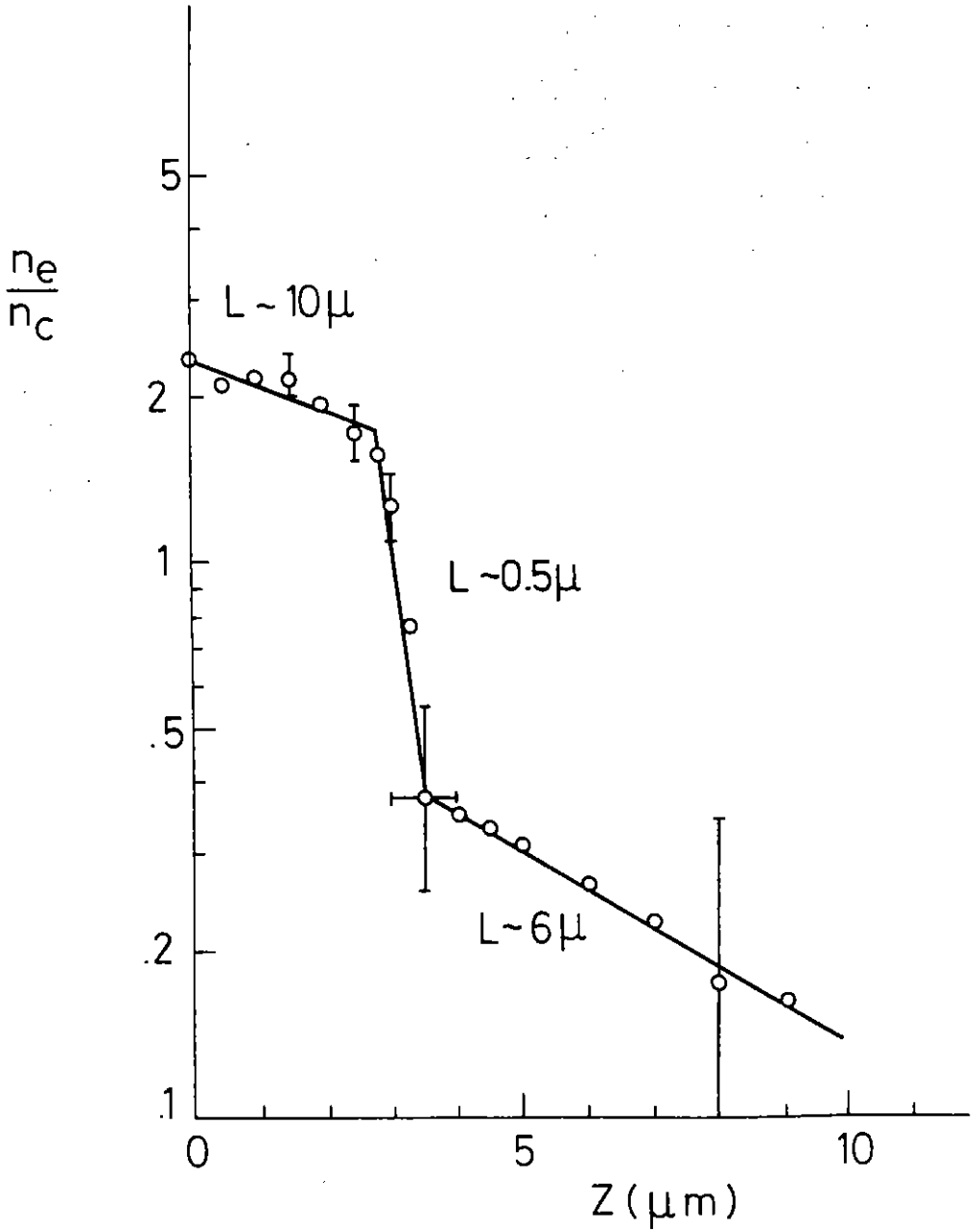

Fig.3.03

Radiation pressure steepened density profile during the main heating pulse of 10^{16} W cm^{-2} irradiance. Solid lines are best fits to exponentials of the form $e^{-z/L}$.

radiation pressure has not been fully evaluated in relation to these thermal flux arguments, and its addition may well lower this temperature estimate somewhat. At a later time ($t \sim 200$ ps) computer simulations and estimates of the expansion cooling from the measured profiles indicate corona temperatures of about 500 eV. The density ratio is now measured to be 1.1 and indicate a value of W/ℓ_1 of 8×10^{14} W cm/g. Since ρ_1 is approximately 4×10^{-3} g cm^{-3} at this time, a power flux of 3×10^{12} W cm^{-2} results. If this power flux is expressed in terms of the temperature and density on the hot side and a flux limit factor f as

$$W = f\, n_2 kT_2 \left(\frac{kT_2}{M_e}\right)^{\frac{1}{2}}$$

f can be calculated to be 0.03 for a temperature of 500 eV. The local power flux is therefore consistent with flux limited heat flow still occurring at this time.

Measurements on the wire targets were made 85 ps after the peak of the main heating pulse. At this time strong magnetic fields of order 2MG have been measured in the low density ($\sim 0.1\ n_c$) corona (3.06, 3.14) and have subsequently been shown to extend to higher densities using a similar fourth harmonic probing system (section 4.2). A typical density profile at an intensity of 10^{16} W cm^{-2} is shown in Fig.3.07. The profile at high density shows the familiar hollowing by the incident radiation pressure to a half width equal to the focal spot radius, and a density minimum equal to that of the lower shelf density on spherical targets. In lower density plasma this changes to a double hollow structure with minima off axis at the focal spot radius. This correlates well with the measured position of the magnetic fields (3.06). The field pressure in this low density region can be estimated at approximately 50% of the thermal pressure of the plasma in agreement with the observed 50% depletion of the local plasma density. At still lower densities, this profile reverts to the low density shell type structure measured previously (3.06) that rings the field region. The role of the magnetic field in pushing the plasma out into a shell structure and creating an on-axis density

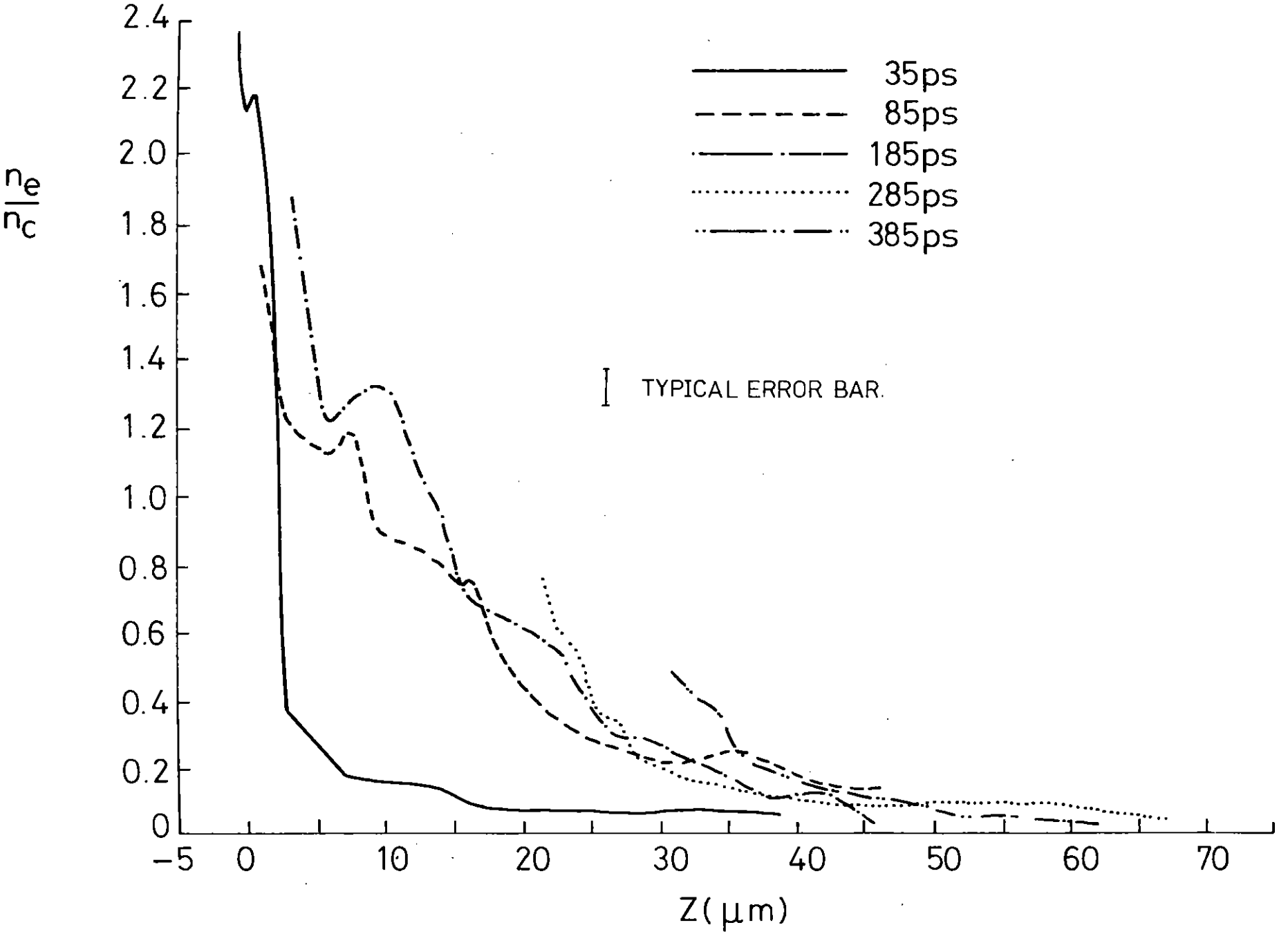

Fig.3.04

Time development of electron density profiles after the main heating pulse of 10^{16} W cm^{-2} irradiance. Profiles at 285 ps and 385 ps are taken with a second harmonic probe. Other profiles are with 4th harmonic probe.

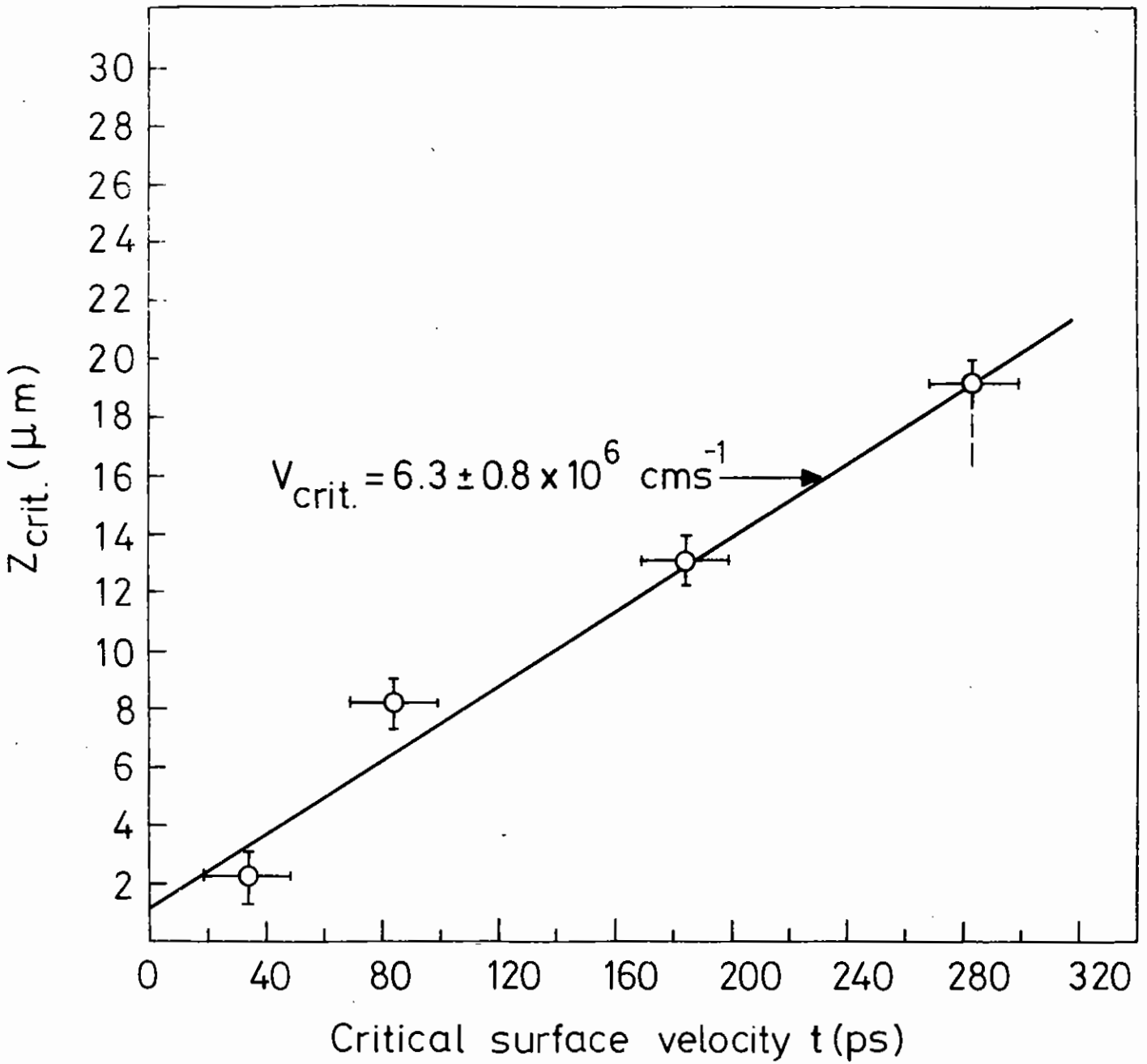

Fig.3.05

Critical surface position with time. Position at 285 ps is an extrapolation from the measured profile and represents an upper limit.

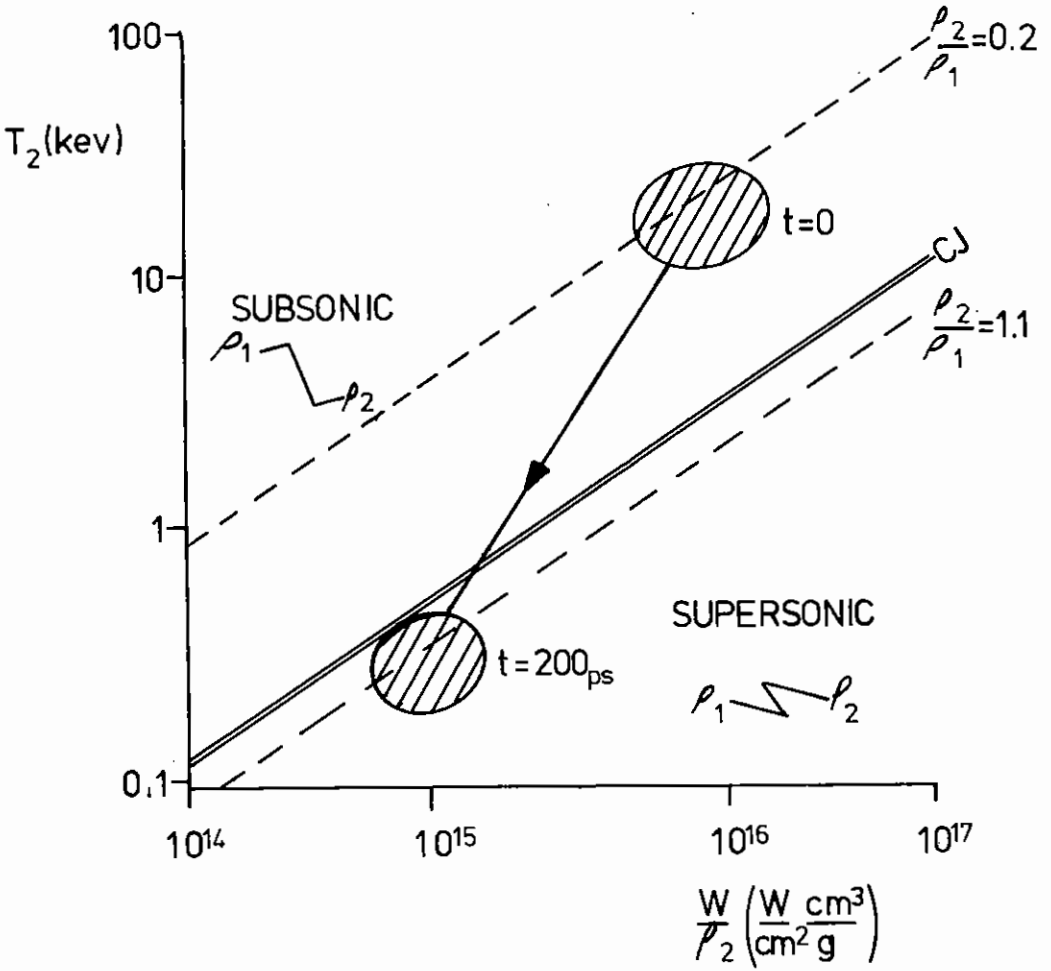

Fig.3.06

Plasma response plane showing sub and supersonic regions separated by the Chapman-Jouguet line (CJ). The experimental parametric regions are indicated by the shaded areas and are identified from the measured values of ρ_2/ρ_1 and W/ρ_1.

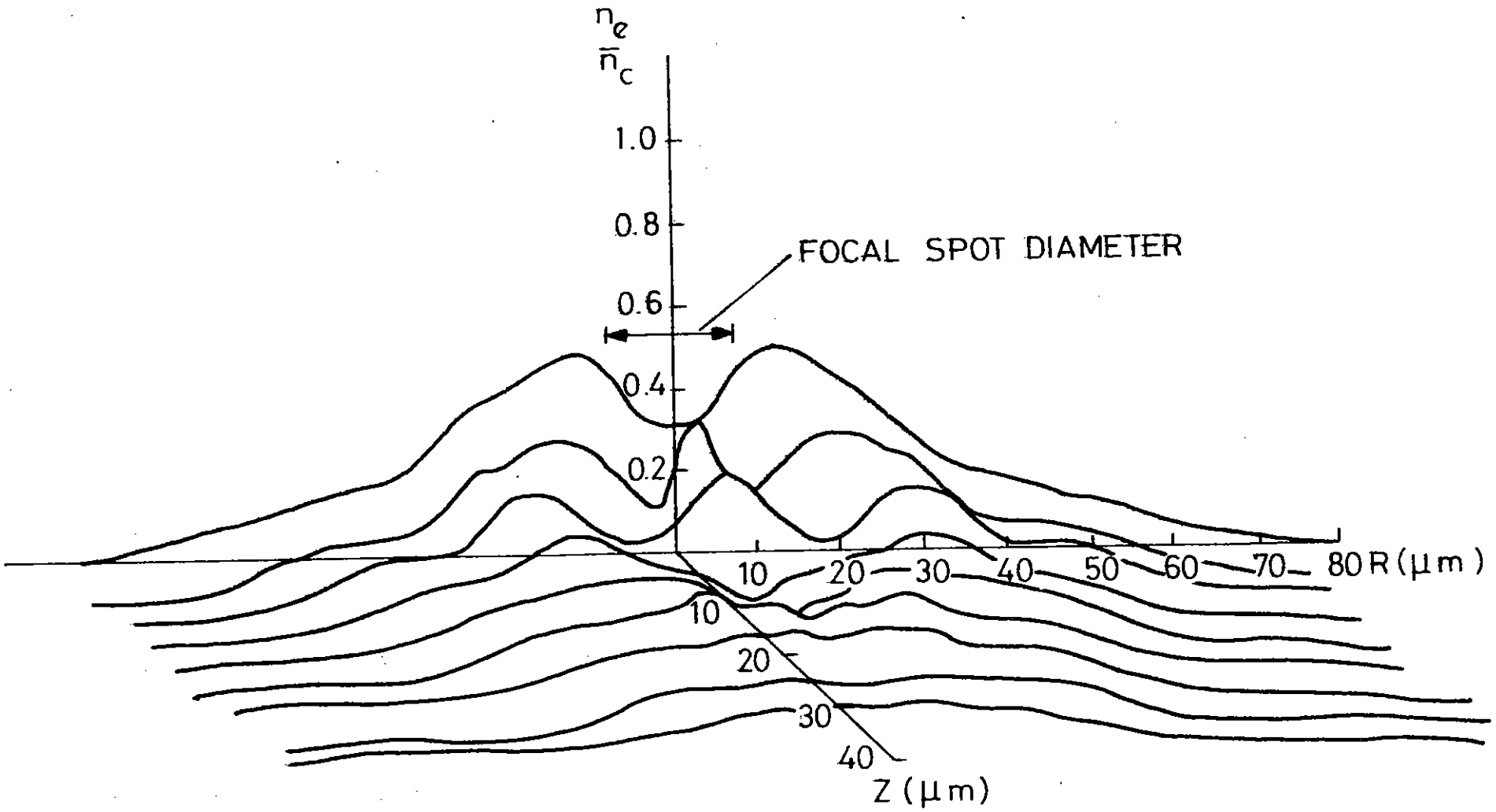

Fig.3.07

Density profiles on plane target 85 ps after the peak of the laser pulse. Irradiance is 10^{16} W cm^{-2} and the focal spot diameter is 15 μm. The off-axis density depression due to the magnetic field pressure is clearly evident on the profiles at z = 5 μm and z = 10 μm.

maximum is clearly evident. The profiles measured on the spherical targets showed no such structures and are further evidence for no significant fields on this type of target (3.06).

3.3 Harmonic emission from plasmas generated by short (∿ 50 ps) laser pulses

3.3.1 Space resolved spectroscopy

The latest work on spatially resolved harmonic spectroscopy has concentrated on the generation of the 3/2 ω_o harmonic emission. At the quarter critical density surface, both stimulated Raman scattering (3.15) and the two plasmon decay (3.16) can produce $\omega_o/2$ plasmons and so both can give rise to the emission of 3/2 ω_o harmonic radiation. Two generation mechanisms have been proposed: it is thought that either an incident photon interacts with a parametrically excited plasmon, or three plasmons coalesce to give 3/2 ω_o emission

$$\omega_o + \frac{\omega_o}{2} \rightarrow \frac{3\omega_o}{2}$$

$$\frac{\omega_o}{2} + \frac{\omega_o}{2} + \frac{\omega_o}{2} \rightarrow \frac{3\omega_o}{2}$$

From the previous work, the spectral distribution of this harmonic is typically a double peaked structure, with a blue shifted peak and a more intense red shifted one (Fig.3.08). The formation of this spectrum has been explained by Avrov (3.17) as follows: the red shifted photons are directly backscattered at the $\frac{n_c}{4}$ surface, while blue-shifted photons are forward scattered and then reflected at the $\frac{9n_c}{4}$ surface. As some absorption occurs at the latter surface, the blue shifted peak appears less intense than the red shifted one.

The time difference between the two peaks is too small to be resolved on a streak record, so to verify the Avrov theory, it was proposed to image the forward and backward directions of a thin foil target simultaneously onto the same 3/2 ω_o spectrograph. For one-sided irradiances above threshold, only the blue peak should appear in the

forward scatter direction and the usual double peak structure in the backscatter direction. Already, experiments in underdense plasmas, where $n_e < n_c$, have shown only a red shifted component (3.18).

The experimental layout is shown in Fig.3.09. The backscattered harmonic emission was collected by the F1 singlet lens used to focus the laser light on target. This was then optically relayed to form a x 25 magnified image on the slit of the 0.5m, 600 line mm^{-1} grating spectrograph. The forward scattered harmonic emission was collected by the F1 doublet lens and then optically relayed to form a X10 magnified image on the slit of the same spectograph. The Nd glass laser beam provided an irradiance of 3×10^{15} W cm^{-2} in an ∿ 100 ps pulse on polystyrene foil targets ranging in thickness from 0.1 μm to 2.0 μm. The burn through energy was monitored with a calorimeter and simultaneous streak records of the incident ω_o, reflected $2\omega_o$ and burn through ω_o, emission were obtained on the Electrophotonics streak camera with an S-1 photocathode.

One of the results obtained is shown in Fig.3.10. It shows a slightly more intense blue shifted peak in the forward scattered direction and only a red shifted component in the backscattered direction. The more intense blue shifted peak in the forward direction is typical of the results obtained for foils of thickness 0.3-0.4 μm. For the rest of the range of foil thicknesses investigated, the forward scattered spectra always displayed a double peak structure with both peaks of equal intensity. It is more difficult to comment on the backscattered spectra due to the extremely poor imaging qualities of the F1 singlet lens at red wavelengths. However, the observations showing a more intense blue component for the first time in the forward scattered direction, does tentatively support the Avrov hypothesis. A further investigation at a foil thickness of 0.3-0.4 μm, with better imaging quality in the backscattered direction would probably be more conclusive.

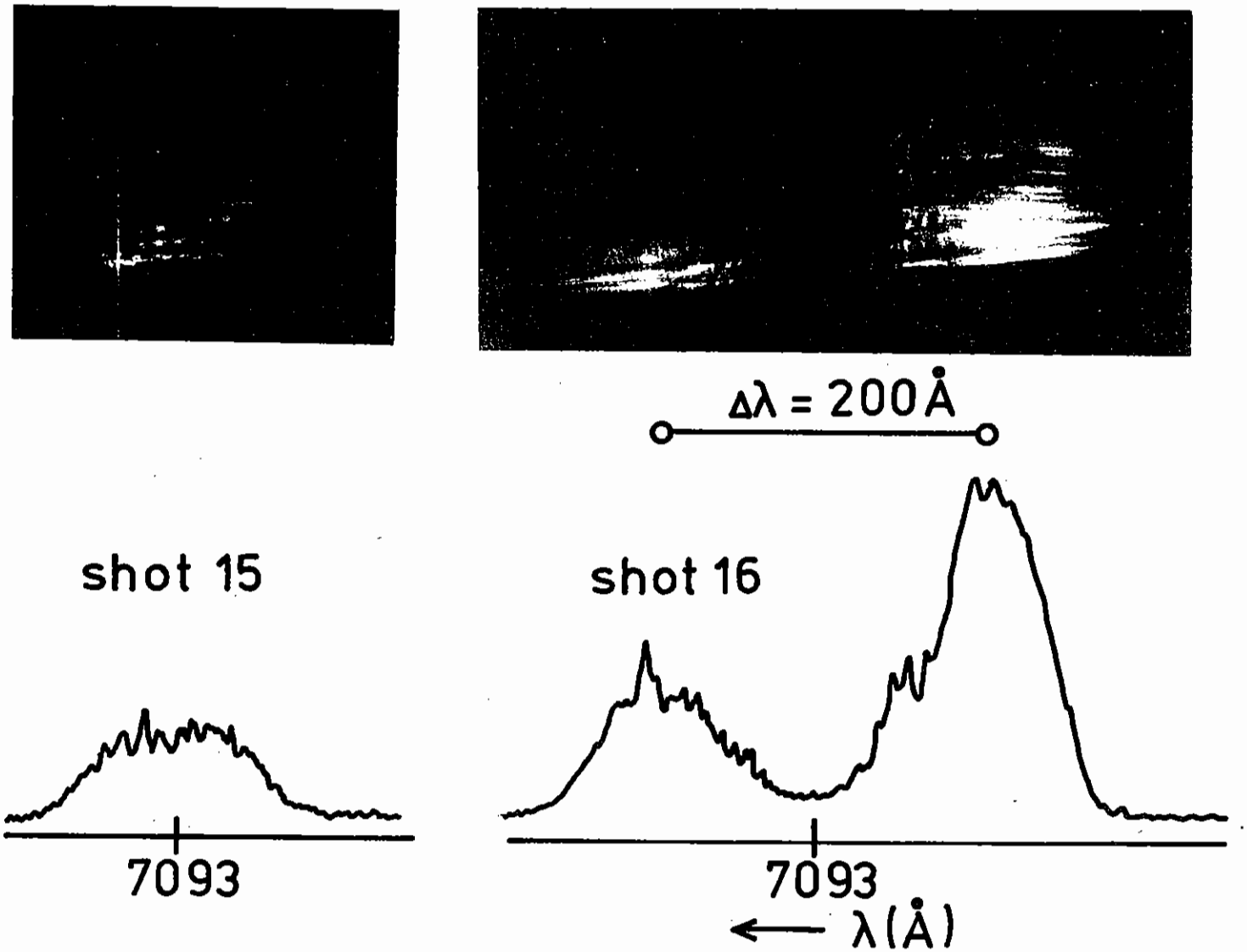

FIG 3.08 SPACED RESOLVED $\frac{1}{2}$ ω_o SPECTRUM

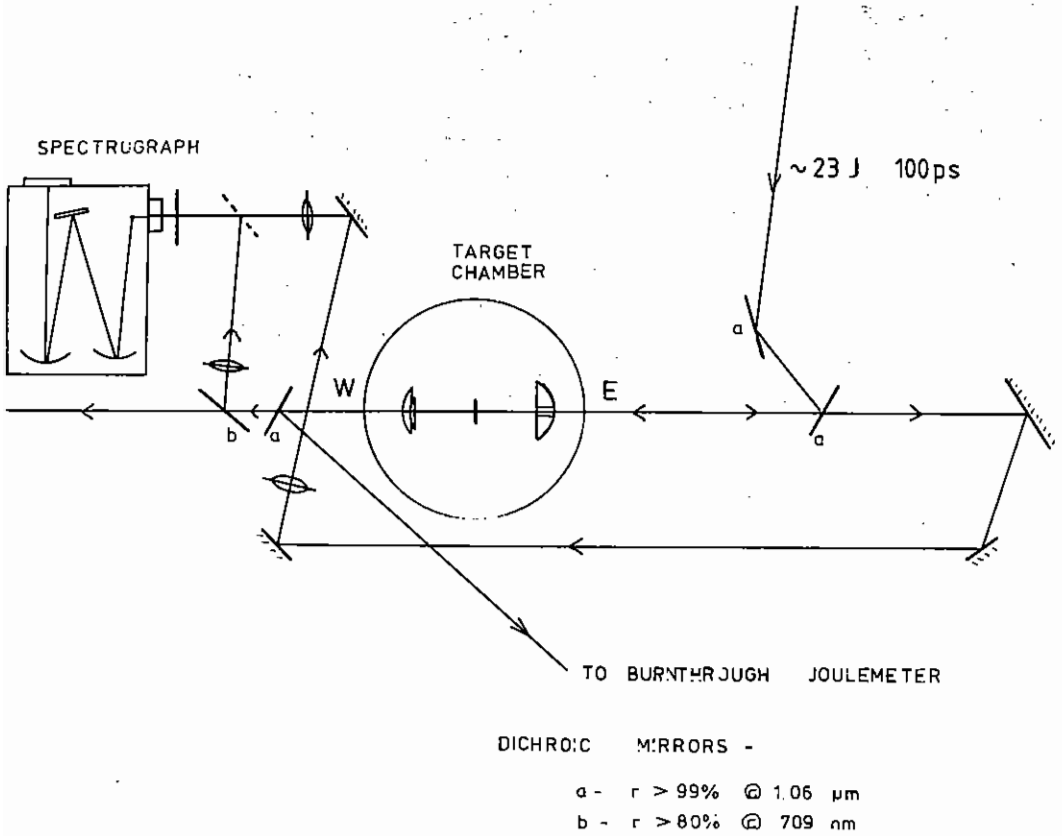

fig.3.09

experimental set-up for observing forward & backscattered $^3/_2\,\omega_o$ emission from thin-foil targets.

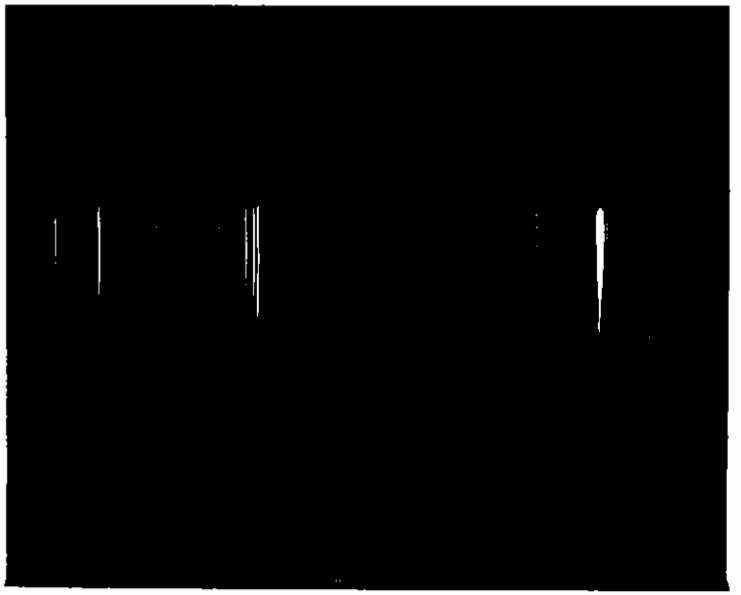

Fig.3.10

$^3/_2\,\omega_o$ emission from thin foil targets

Another interesting result of this experiment was the extent of foil thickness for which burn through of the laser pulse was obtained. Even for a foil thickness of 0.7 μm, a strong forward scattered spectrum was obtained and it was only at a foil thickness of 2.0 μm that no forward scattered emission was observed. This is corroborated by the streak cameras pictures (Fig.3.11), which show burn through for the laser pulse on all the observations except for the 2.0 μm foil.

3.3.2 Time resolved harmonic spectroscopy, and interpretation of observations

The earlier work performed by this group (3.19), concerning the study of harmonic emission from the plasma, concentrated on time-integrated observations at the $2\omega_o$ and $3/2\omega_o$ spectra, with the emphasis on spatial and spectral resolution. Also, as it is generally believed that the $2\omega_o$ emission is produced at the critical density surface some time-resolved work was done, streaking the sidescattered second harmonic light to give an indication of the movement of the critical density surface.

Towards the end of this period, it was decided that various interesting features of the time-integrated spectra might be better examined by the use of high-speed photography techniques with sufficient time resolution to study the evolution of the harmonic spectra. Hence, an exploratory experiment was carried out to streak the $2\omega_o$ emission spectrum. This produced a few results, which were encouraging enough to prompt a more exhaustive study this year with the possibility of attempting to streak the $3/2\omega_o$ emission spectrum as well.

The typical time-integrated $2\omega_o$ spectrum obtained in our earlier work is shown in Fig.3.12. It features a red-shifted peak with a broad red wing, exhibiting periodic fine structure. The appearance of this red wing has been explained by the excitation of ion accoustic waves (3.20). If this is the case, the shift to the red should develop in time and so the theory would be verified by time-resolved studies.

Fig.3.13 shows the experimental layout for streaking the $2\omega_o$ spectrum. The Nd glass laser beam provided an irradiance of $\sim 10^{16}$ W cm^{-2} in a $\sim$100 ps pulse on D-T filled glass microballoons of $\sim$ 80 μm diameter. The backscattered harmonic emission was collected by the F1 aspheric doublet lens (3.21) used to focus the laser light incident on the target, then optically relayed to give a 55x magnified image at the 0.5 m, 1200 lines mm^{-1} grating spectograph. The image from the spectrograph was, in turn, optically coupled to the Electrophotonics streak camera, which was fitted with an S-20 photocathode and operated at a speed of 500 ps cm^{-1}. This arrangement gave a spectral resolution of $\sim$1Å determined by the 70 μm slit width of the spectrograph, and a temporal resolution of $\sim$10 ps which was limited by the range of path lengths in the spectrograph grating, as the streak camera had a time resolution of 5 ps determined by its entrance slit width.

Photographic recordings of the streak data were made on Kodak 2485 film. Separate exposures of the 5461 Å Hg line were taken with the spectrograph at different settings to obtain the spectral calibration. The temporal calibration was made in an auxiliary experiment using a 50% reflectivity air-gap etalon and a mode-locked dye laser.

Three of the results obtained are shown in Fig.3.14. While the streaks show the expected development of the red wing with time, the most striking feature is the presence of intense spots. These indicate that the second harmonic is emitted in bursts, whose spectral width is less than the 1Å spectral resolution of the system and whose duration is less than the 10 ps temporal resolution. The majority of the spots are clustered near the position of the nominal $2\omega_o$ ie 5320 Å, so if the streaks were time-integrated the previous results would be duplicated, where a red-shifted peak and a broad red wing was obtained. The spectral width of the streak ($\sim$ 30Å) corresponds to the shot obtained in the time-integrated data too.

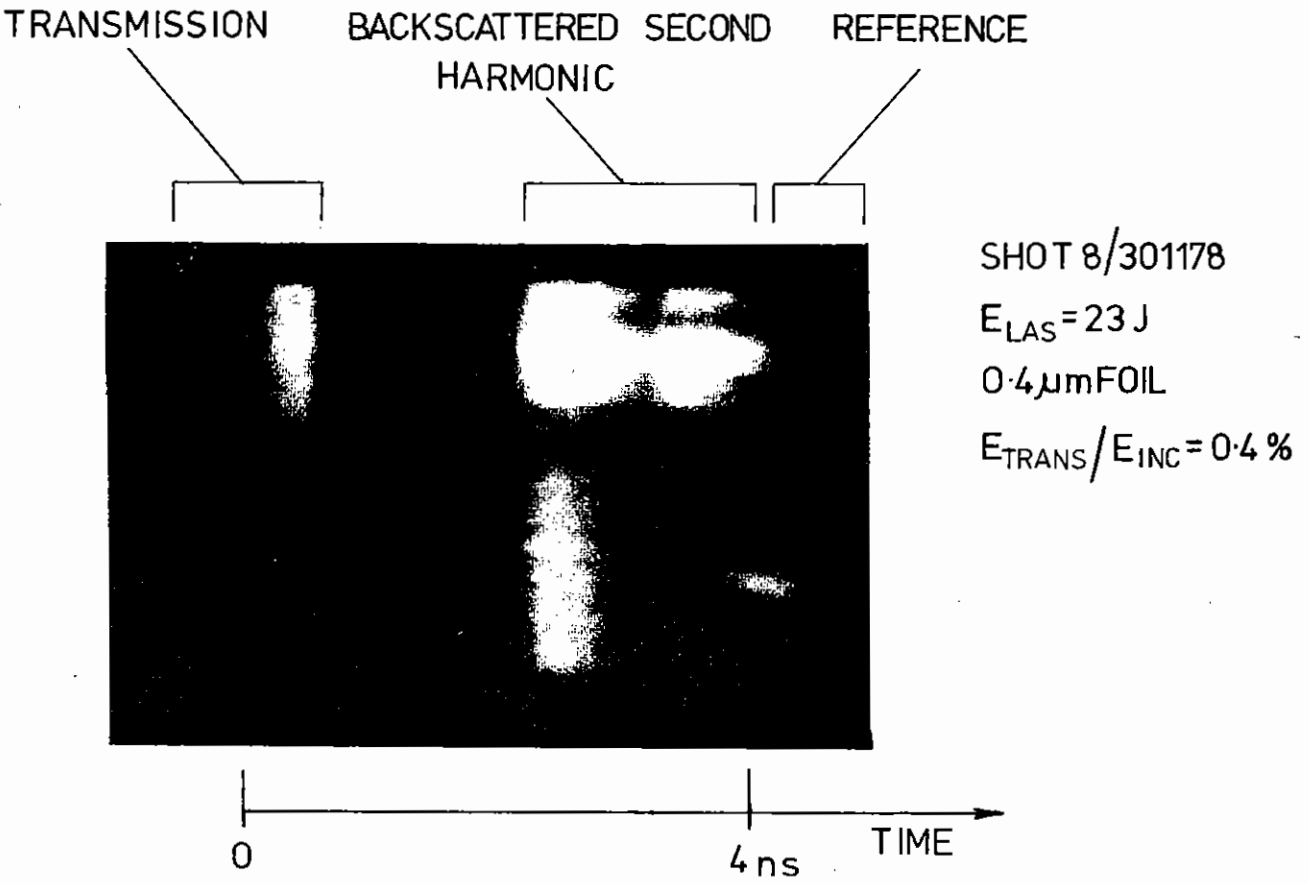

Fig.3.11

Streak photograph showing burn-through laser pulse. (original supplied J. Murdock)

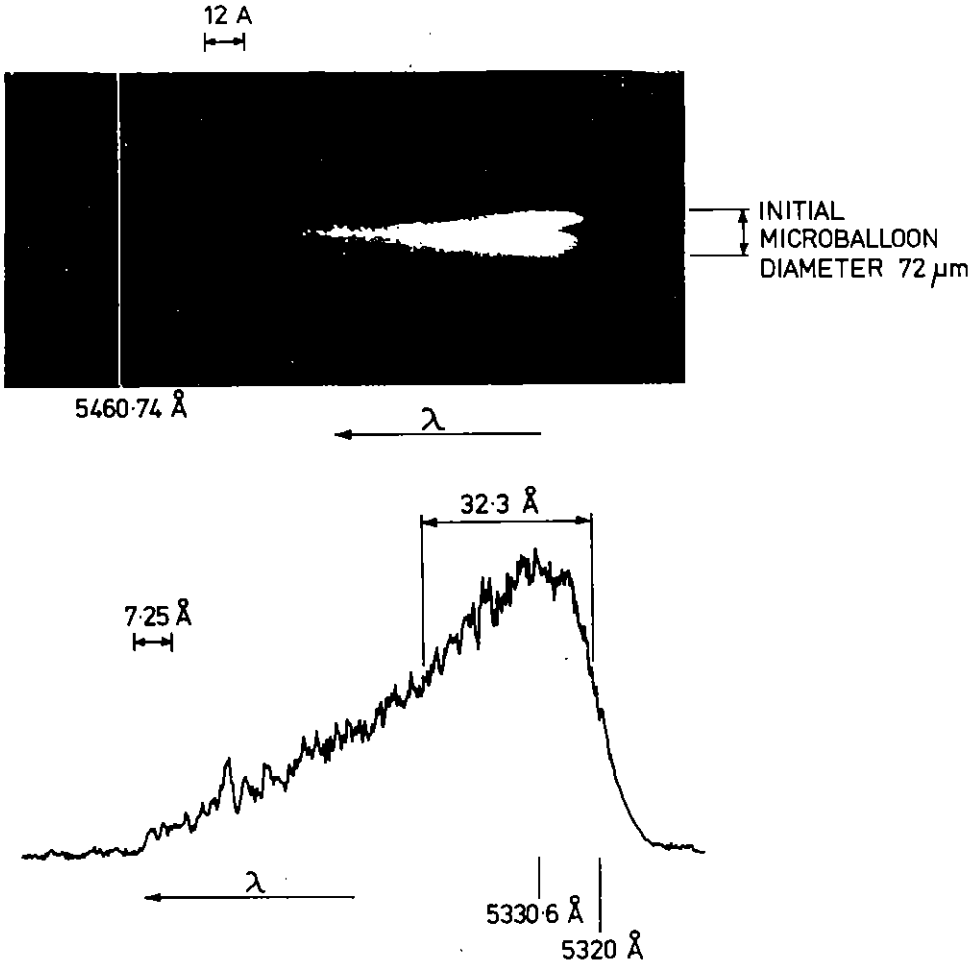

Shot 16

SPACE RESOLVED $2\omega_o$ SPECTRUM

FIG 3.12

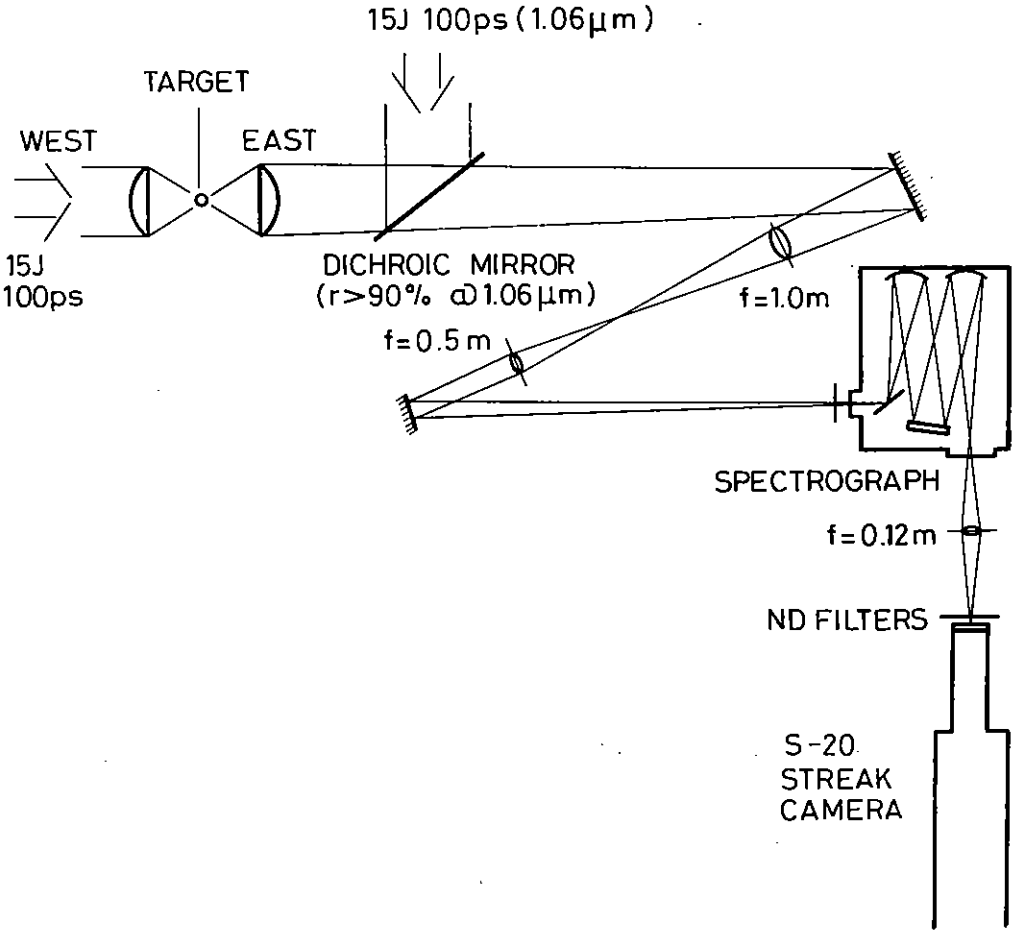

EXPERIMENTAL LAYOUT

Fig.3.13

Experimental layout for streaking $2\omega_o$ spectrum.

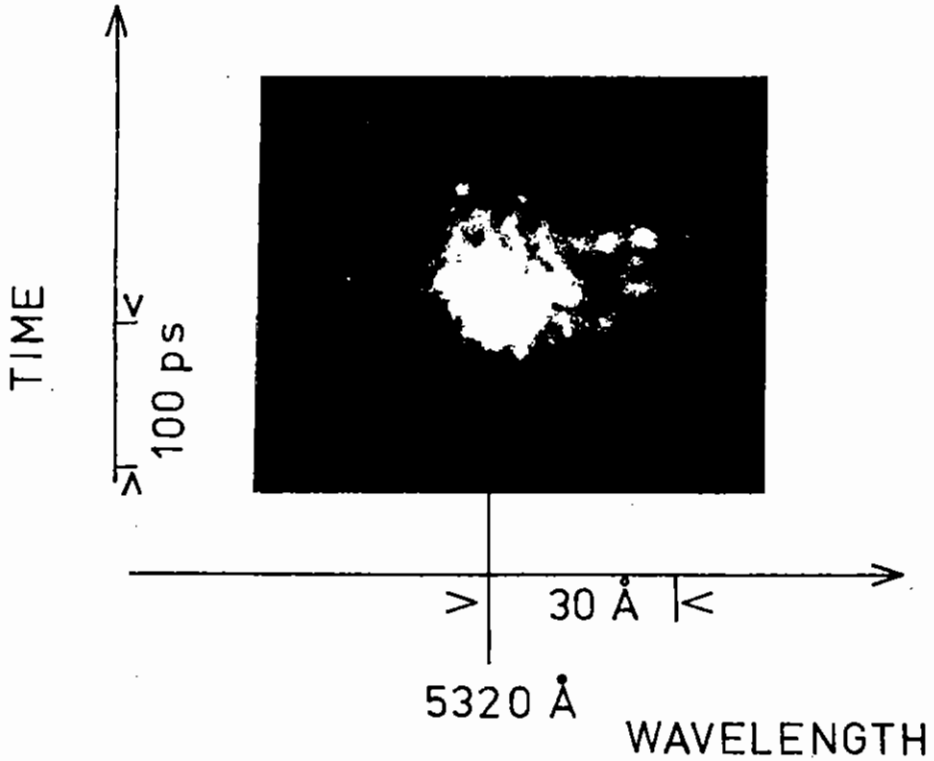

time dependence of second harmonic emission. ($E_i \sim 15J \times 2$)

microballoon target 80 μm diam.

Fig.3.14(a)

Time Resolved 2 ω_o Spectrum

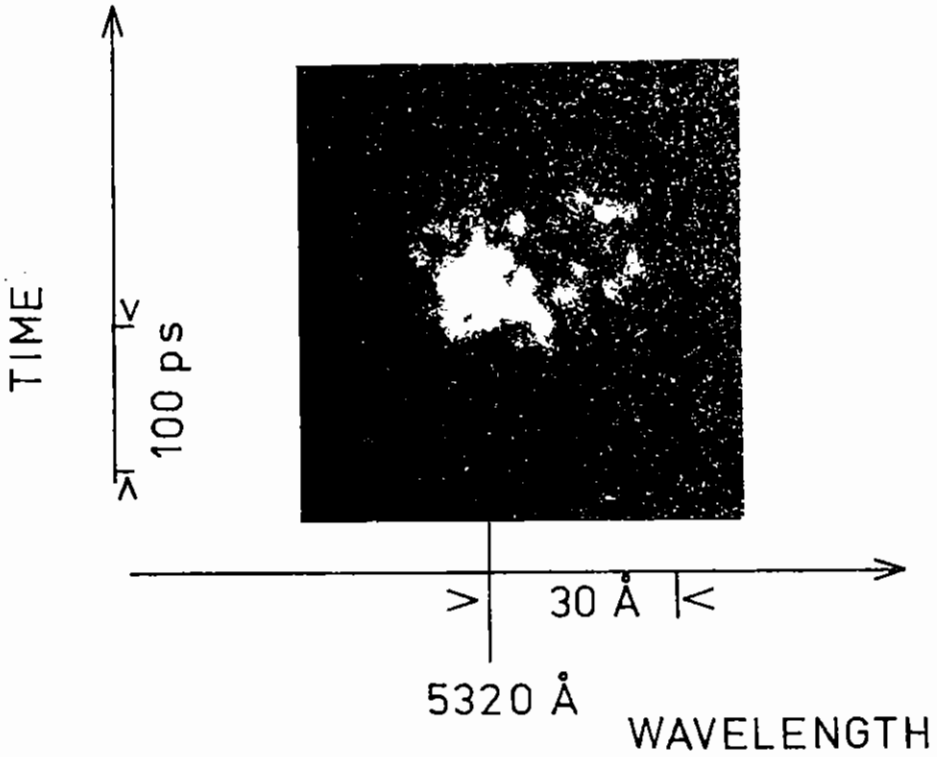

time dependence of second harmonic emission. ($E_i \sim 15J \times 2$)

microballoon target 80 μm diam.

Fig.3.14(b)

Time Resolved 2 ω_o Spectrum

These observations may be interpreted in various ways. The existence of the spots cannot be simply attributed to Doppler shifts, unless the plasma flow is oscillatory due to some hydrodynamic instability eg ponderomotive force. They might also be due to the spatial motion of several discrete emitting regions through the source area observed, with a speed $\geq 10^8$ cms^{-1} but this is not corroborated by the sidescattered spatial images obtained earlier by Raven et al (3.19). These show small bright spots which if they were due to fast moving regions of emission would be blurred out to appear as streaks.

More likely, the pulsed nature of the $2\omega_o$ harmonic emission is due to individual plasma waves growing on a picosecond timescale, with the fastest growing mode being the one with the largest K that is not Landau damped ie $K\lambda_D < 0.25$. Further growth will be limited by detuning effects such as particle trapping. The Landau damped plasma waves will produce hot electrons (3.22) which then produce Landan damping at larger phase velocities

$$K\lambda_D = \frac{v(\text{thermal})}{v(\text{phase})}$$

This reduces $K\lambda_D$ and so effectively increases the threshold.

The increasing temperature in the plasma causes an increase in the ion wave frequencies so that the harmonic emission is shifted to the red, although at the same time there will be a blue shift of ~ 4Å due to the Doppler effect.

Further data analysis is in progress. Meanwhile, it was decided to proceed with streaking the $3/2\ \omega_o$ harmonic emission. Fig.3.08 shows a typical time-integrated $3/2\ \omega_o$ spectrum. Its main features are two peaks, symmetrically blue and red shifted from the nominal $3/2\ \omega_o$ wavelength (ie 7093 Å), where the emission is a minimum. The temporal evolution of these peaks is obviously of interest.

Some slight changes were made in the experimental layout, shown in Fig.3.15, mostly to accommodate the substitution of the Hadland Imacon streak camera. This was preferred as it had different streak electronic circuitry which resulted in practically negligible jitter performance, even at its fastest streak speed. The dove prism was then necessary to rotate the image from the 0.5 m, 600 lines cm^{-1} grating spectrograph, so that wavelength would be dispersed along the streak camera slit. For simplicity, only the F1 doublet lens was used to form an image at the spectrograph, which was operated in both first and second orders in this experiment. The Nd glass laser beam provided an irradiance of 2×10^{16} W cm^{-2} in an $\sim$100 ps pulse on empty glass microballoon targets of 50-90 μm.

The new arrangement gave a spectral resolution of $\sim$30Å in first order ($\sim$15Å in second order) determined by the 1 mm slit width of the spectrograph, and a temporal resolution of $\sim$20 ps in second order, which, again, was limited by the range of pathlengths in the spectrograph grating, as the streak camera had a time resolution of $\sim$3 ps determined by its entrance slit width. Both spectral and temporal calibrations were performed as before.

Two of the results obtained in this manner are shown in Fig.3.16, where Fig.3.16(a) was taken with the spectrograph in first order and Fig.3.16(b) was taken in second order. Both spectral streaks show that $3/2\ \omega_o$ harmonic emission has a pulsed nature, where the duration of the pulses is less than the 10 ps temporal resolution of the system. Although the blue shifted and red shifted peaks appear simultaneously in each burst, their separations vary in time. The spectra with decreasing separations, as in Fig.3.16(a), were obtained when the laser prepulse level was very low (less than 10^{-5} times the main pulse energy) while the spectra which exhibit an increasing and then decreasing separation, as in Fig. 3.16(b), occurred when a large prepulse level, or double pulse, was recorded. The blue shifted peaks appear more intense than the red shifted peaks, which is the reverse of the time-integrated observations, but this is probably due to the spectral response of the S-20 photocathode which falls off rapidly in the red.

Models linking the separation between the peaks with the local plasma electron temperature have been proposed by Avrov et al (3.17) and Barr (3.23). Both models assume the 3/2 ω_o emission is generated by the two plasmon instability (3.16) since Raman scattering in an inhomogeneous plasma has a much higher threshold (3.16). The 3/2 ω_o emission can then be produced either by the coalescence of three plasmas or a photon and a plasmon. Although the first of these mechanisms is a nonlinear process of high order of smallness, it may contribute more significantly in a number of experiments, as the phase matching conditions are difficult for the latter process.

The Avrov model considers contributions from both processes and gives a shift for the red and blue satellites of

$$\Delta\lambda = \pm 22.7\ Te\ |\cos\sigma|\ \text{Å}$$

where σ is the angle between the vectors k 3/2 and k_o, and Te is in Kev.

Both processes in the Barr model give rise to the same frequency shift as a function of the scattering angle σ

$$\Delta\lambda = -33.8\ Te\ (\cos\sigma - 0.92)\ \text{Å}$$

Due to the angular distribution of the emission, the blue shifted photons travel forward into the region of greater density and are reflected at the $9n_c/4$ layer, while the red shifted photons are directly reflected at the $n_c/4$ layer. The separation of the peaks is given by

$$\Delta\lambda = 67.6\ Te\ |\cos\sigma|\ \text{Å}$$

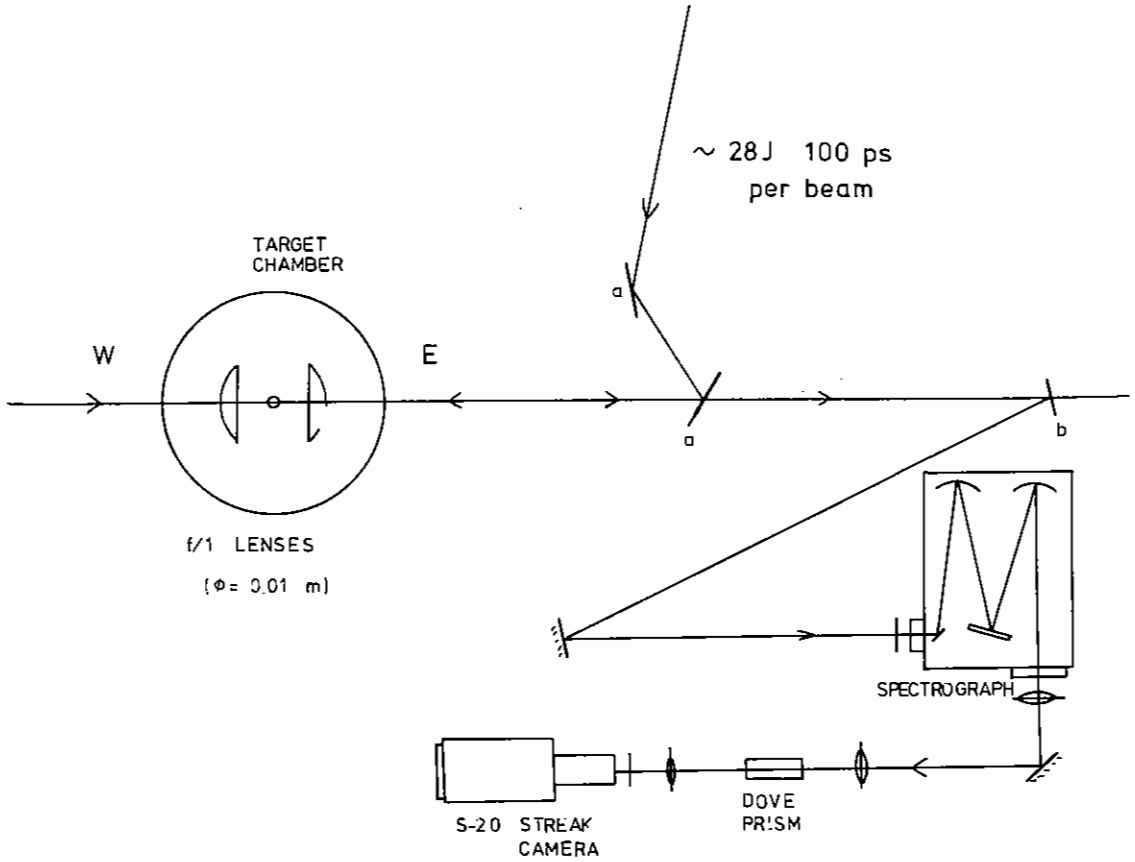

fig.3.15

experimental arrangement for $^3/_2\ \omega_o$

temporal dependence

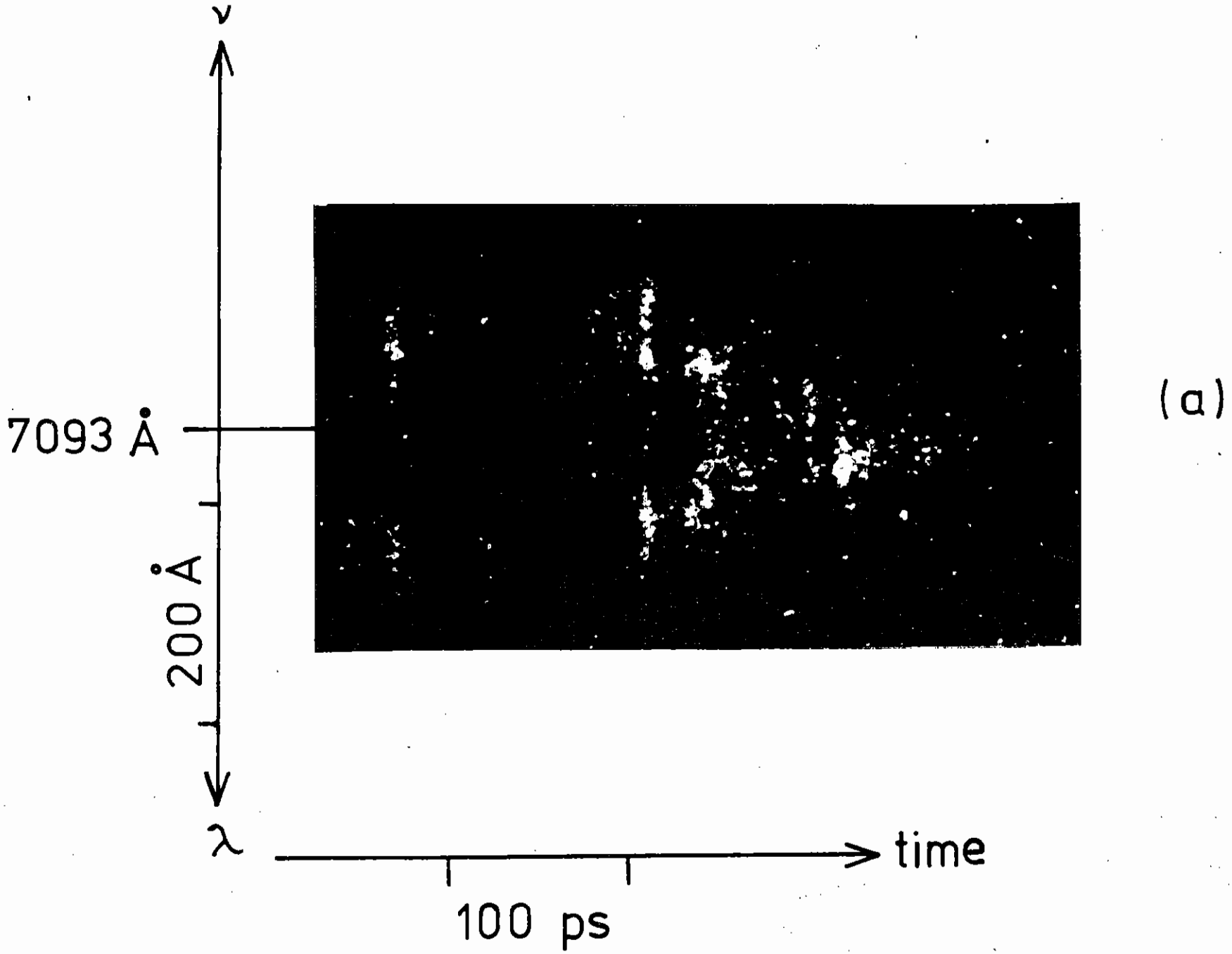

Fig.3.16

Time Resolved $^{3}/_{2}\ \omega_{o}$ Spectrum

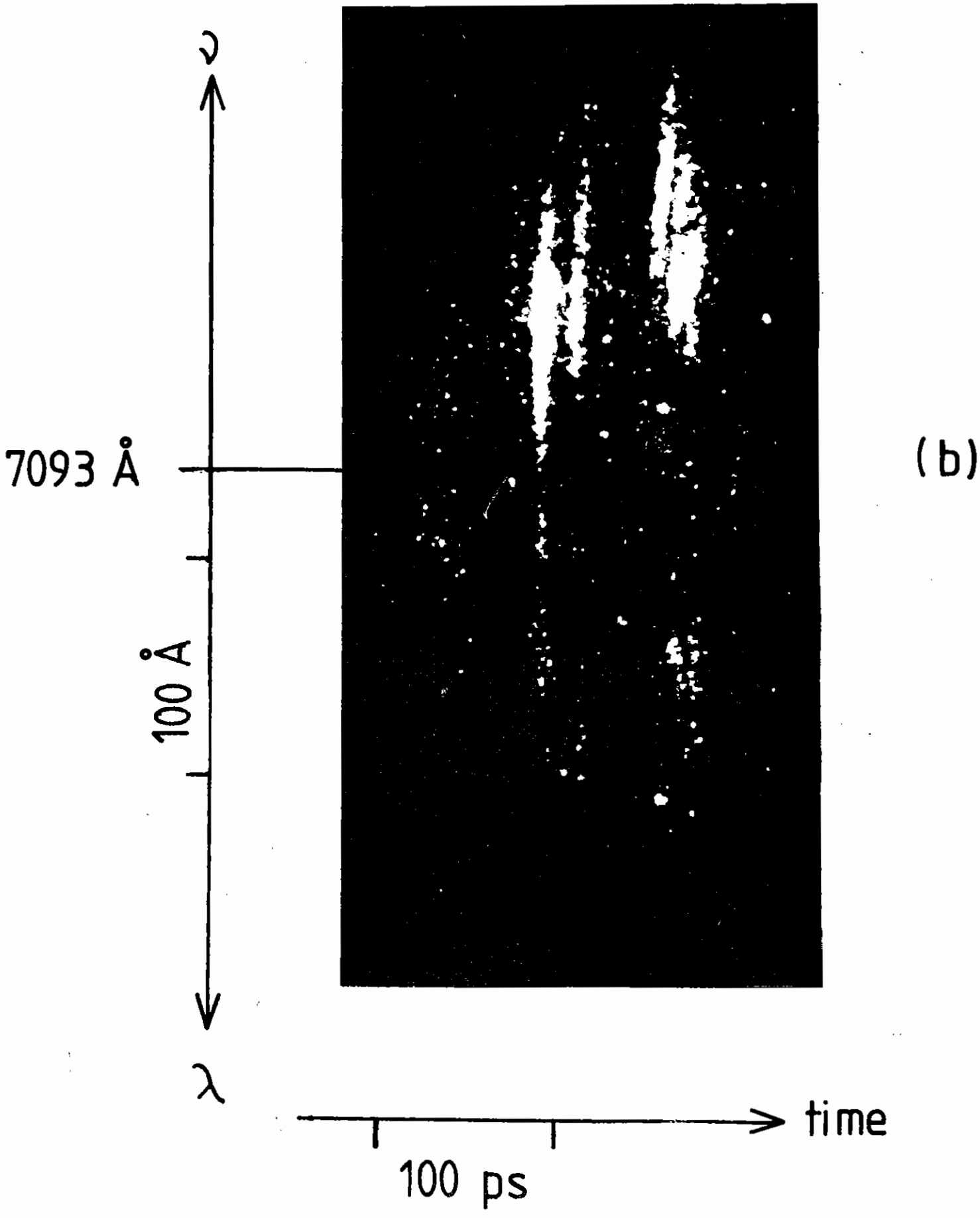

Fig.3.16

Time Resolved $^{3}/_{2}\ \omega_{o}$ Spectrum

The observed separation of ~ 300 Å corresponds to an electron temperature of 6.6 KeV for the Avrov model and 4.5 KeV for the Barr model. These seem high but may reflect the weighted mean of the "cold" and "hot" electron temperatures at quarter critical density. The Barr theory also predicts that the red shift from nominal 3/2 ω_o is much greater than the blue shift, but this is not observed. Instead, there appears a more symmetrical distribution such as that predicted by the Avrov theory, although because of the Doppler effect, some asymmetry will occur.

However, both theories account for the two types of time-resolved spectra observed. In the case of low prepulse, the density scale length is very short on the rising part of the laser pulse and the threshold for the two plasmon decay is exceeded only near the peak of the pulse. The decreasing separation of the red and blue peaks is then a reflection of the decreasing electron temperature during the latter half of the pulse. With a significant prepulse, the density scale lengths are longer and threshold is exceeded earlier, so the spectral separation then follows the electron temperature which rises and falls with the laser intensity.

The interpretation of the pulsed nature of the emission is more speculative. Raven et al (3.19) have also obtained static images showing that 3/2 ω_o emission occurs from localised spots of very high intensity and size less than the resolution limit of the optics. The expansion of the quarter critical density surface would blur the emission over an area greater than the observed spots, so the pulses of $\leq$ 10 ps duration in our data would be consistent with small spatial zones of emission.

It may be that the pulsed nature of the 3/2 ω_o emission is due to density profile modifications caused by the ponderomotive force of the plasma waves. Profile modification at the quarter critical density surface has been observed by interferometry (3.24) and predicted in plasma simulations (3.25). The appearance of solitons has been proposed by Chen and Liu (3.26) as a saturation mechanism for the two plasmon decay.

The growth rate for the formation of a soliton has been shown to be fractions of a picosecond and the saturation time for the instability (about 30 e-folding periods) is consistent with our observations. At saturation, the soliton will travel down the density gradient and eventually produce a new quarter critical density layer at which the instability will reform.

3.4 Brillouin Scattering and Second Harmonic Emission from Plasmas Generated by Long (1.6 ns) laser pulses

Brillouin scattering is one of the parametric instabilities of the laser plasma interaction processes which is very detrimental to the efficient absorption of laser energy and hence to the prospects of laser fusion. The incident laser wave at ω_o couples to an ion wave at ω_{ia} and a scattered electromagnetic wave at ω^1 such that both energy and momentum are conserved.

$$\omega_o = \omega^1 + \omega_{ia}$$
$$k_o = k^1 + k_{ia}$$

The energy of the ion acoustic wave is very small compared with the photon energy so very little of the laser energy is coupled into the plasma. The Brillouin instability may occur anywhere in the underdense plasma but is most likely at densities of a few tenths of the critical density (3.22).

The characteristic signature of Brillouin scattering is the frequency shift to the red of the scattered radiation near ω_o and a convenient means of investigating Brillouin scattering is to study the temporal evolution of the light backscattered through the focussing lens (3.28, 3.29).

The experimental arrangement is shown in Fig.3.17. The main laser beam contains up to 110J in 1.6 ns at 1.06 μ, and is focussed onto microplane and microballoon targets by an aspheric doublet f/1 lens. The back-scattered ω_o radiation is directed onto a 1m MONOSPEK grating spectrograph and the dispersed output is optically coupled onto an Electro Photonics SI streak camera. The wavelength and time resolutions are approximately 2.0 Å and 20 ps respectively. Simultaneously with

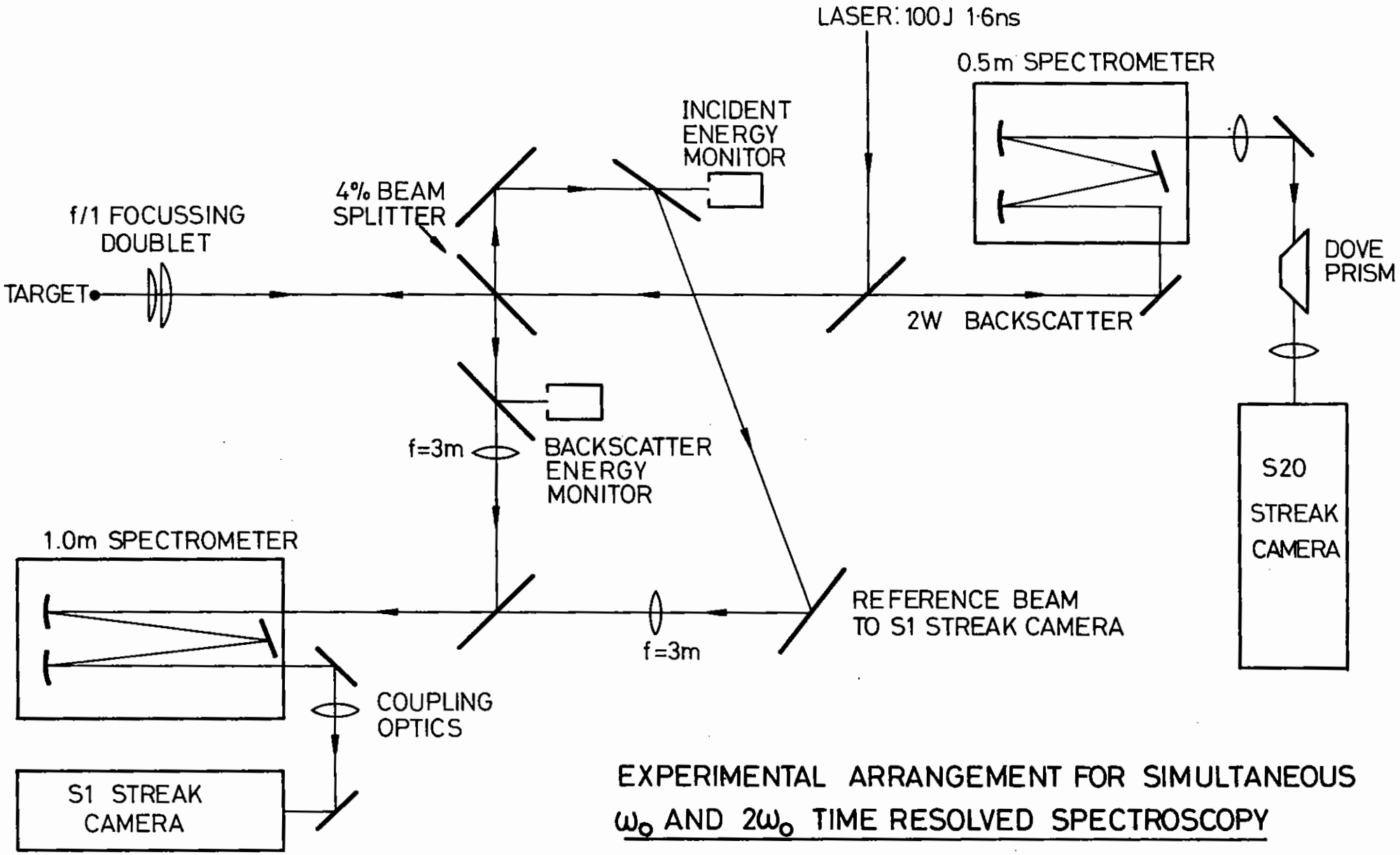

EXPERIMENTAL ARRANGEMENT FOR SIMULTANEOUS ω_o AND $2\omega_o$ TIME RESOLVED SPECTROSCOPY

FIG 3.17

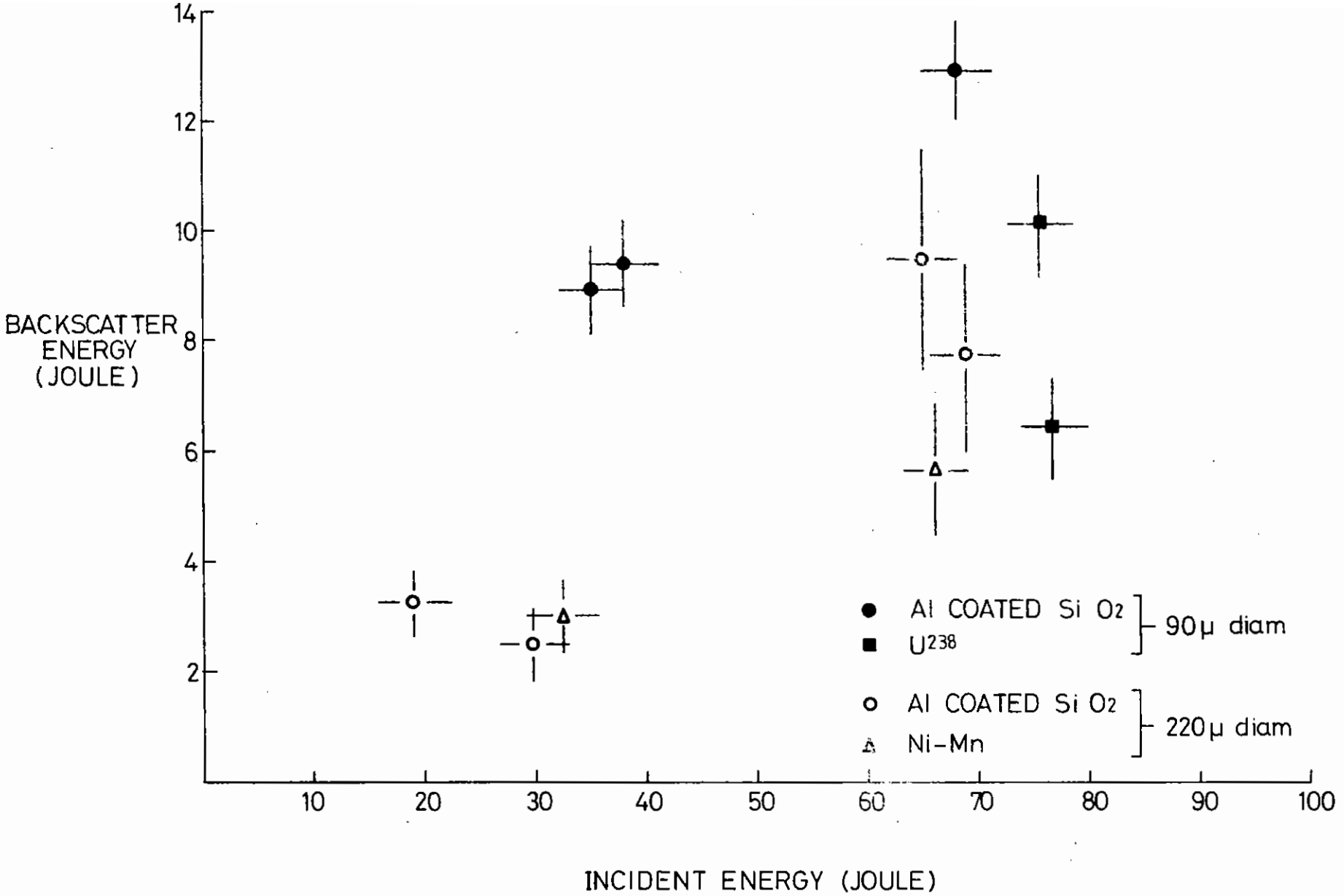

Fig.3.18

Incident and Backscattered energies for various microballoon and microsphere targets.

the ω_o spectroscopy the backscattered $2\omega_o$ radiation is taken via a dichroic mirror to a 0.5 m SPEX grating spectrograph and an IMACON S-20 streak camera. Since the slit of the IMACON is vertical a dove prism is used to rotate the image by 90^o. The wavelength and time resolution at 2ω are about 1.0 Å and 10 ps respectively.

The incident and reflected energies at 1.06μ are monitored by two calorimeters as shown.

The targets for this investigation were microspheres and microballoons in essentially two different sizes, small targets of ∿ 70 μm to 90 μm diameter and 'large' targets of 210 μm to 240 μm diameter. A range of Z was used, from plastic polymer, to U^{238} in the small targets and from plastic to Manganese-Nickel alloy in the larger size.

The range of parameters which may be varied in an investigation of Brillouin scattering is considerable and for this experiment the duration and shape of the laser pulse (1.6 ns FWHM) were unchanged. The focussing of the laser radiation by the f/1 lenses was on to the centre of the spherical targets so that all rays were close to normal incidence. On the small targets the irradiance on target for a beam energy of 100J was 4×10^{15} W cm^{-2} and on the larger targets the corresponding irradiance was 5.2×10^{14} W cm^{-2}.

3.4.1 Calorimetry

The variation of backscattered energy with target type and laser energy is summarised in Fig.3.18. For a fixed target type the fraction of laser energy which is backscattered into the focussing lens remains fairly constant over the limited range of irradiance that was studied although there is some suggestion that the backscatter might be saturating for the highest irradiances on Al coated microballoons (3.30).

With both small and large microballoons the higher Z materials have less backscatter (about 30%-40%) compared with the Al coated microballoons and this is attributed to the lower coronal temperatures and consequently shorter density scale lengths of the high Z materials.

The larger microballoons would also be expected to have larger density scale lengths on geometric arguments but this may be more than offset by the lower coronal temperature due to the reduced irradiance.

3.4.2 ω_o Spectra

Some typical time resolved spectra of the backscattered ω_o radiation are shown in Figs.3.19 to 3.22 . One of the characteristics of the spectra is the initial burst of ω_o emission which is separated from the continuous emission carrying on throughout the laser pulse. On all the spherical targets the ω_o backscatter persisted throughout essentially all of the laser pulse in contrast to the results of the Osaka group (3.31) who observed that at irradiances of ∿ 2×10^{14} W cm^{-2} the Brillouin backscatter cut off about half way through their 1 nsec laser pulse. During some alignment tests on flat brass targets the results of Fig.3.23 were obtained where the backscatter turned off in a manner very similar to the Osaka results. They have suggested ion heating due to the large amplitude ion acoustic wave as a mechanism for turning off the Brillouin scattering but why this does not occur on the spherical targets is not understood.

The red shift of the backscattered radiation during most of the laser pulse is consistent with Brillouin scattering but the frequency shift also contains a component $\Delta\lambda_D$ due to the Doppler shift of the ablating material.

We can write the Doppler shift $\Delta\lambda_D$ as

$$\Delta\lambda_D/\lambda_o = -2v_a/c = \frac{-2Mv_{ia}}{c}$$

where v_a is the ablation velocity, v_{ia} is the ion acoustic phase velocity $v_{ia} = \sqrt{\frac{ZkT_e}{M_i}}$, and M is the Mach number of the flow.

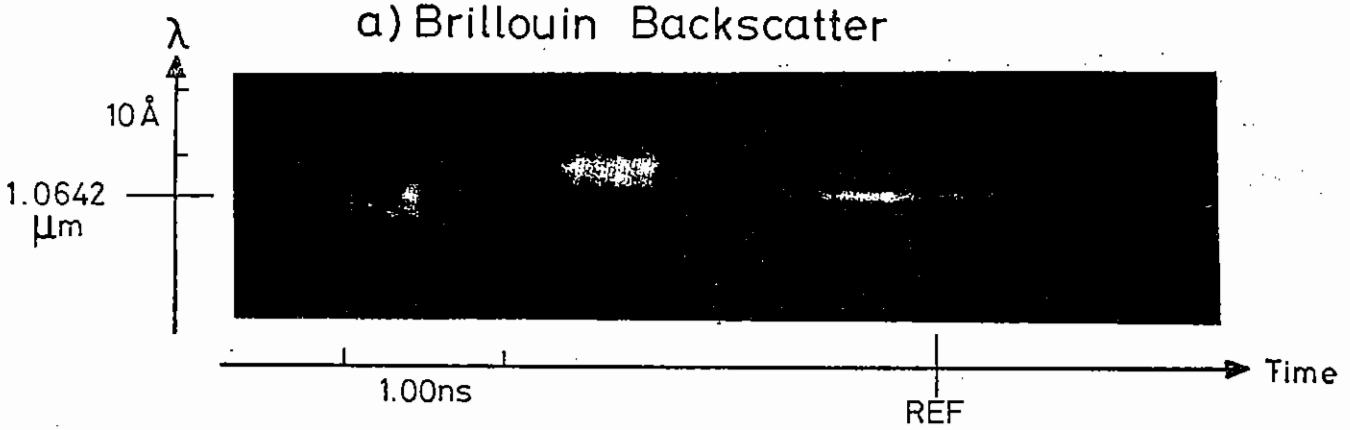

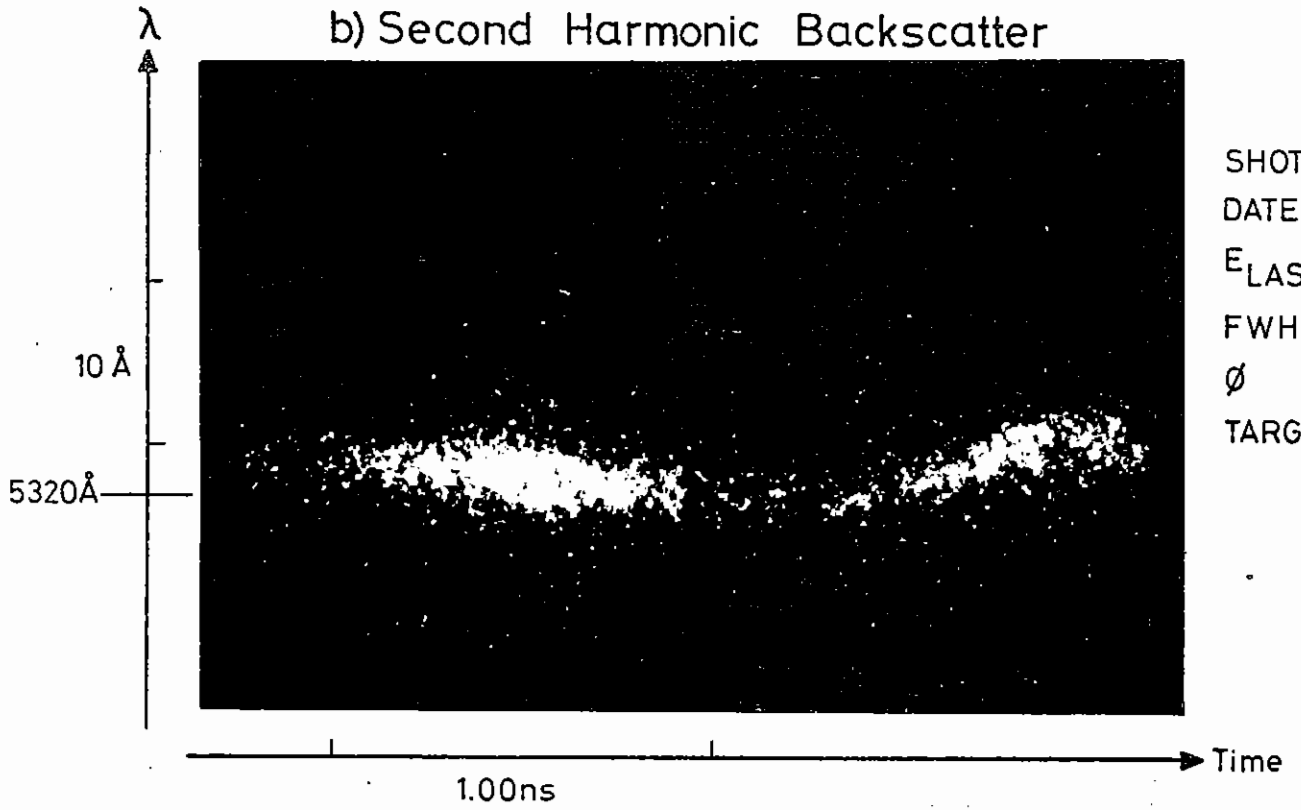

SHOT No.: 13
DATE : 13 /2/79
E_{LAS} : 47 J
FWHM : 1ns
Ø : 6×10^{14} watts cm^2
TARGET : 250μm Al coated glass

Microballoon

Fig.3.19

Fundamental and Second Harmonic Time Resolved Spectra

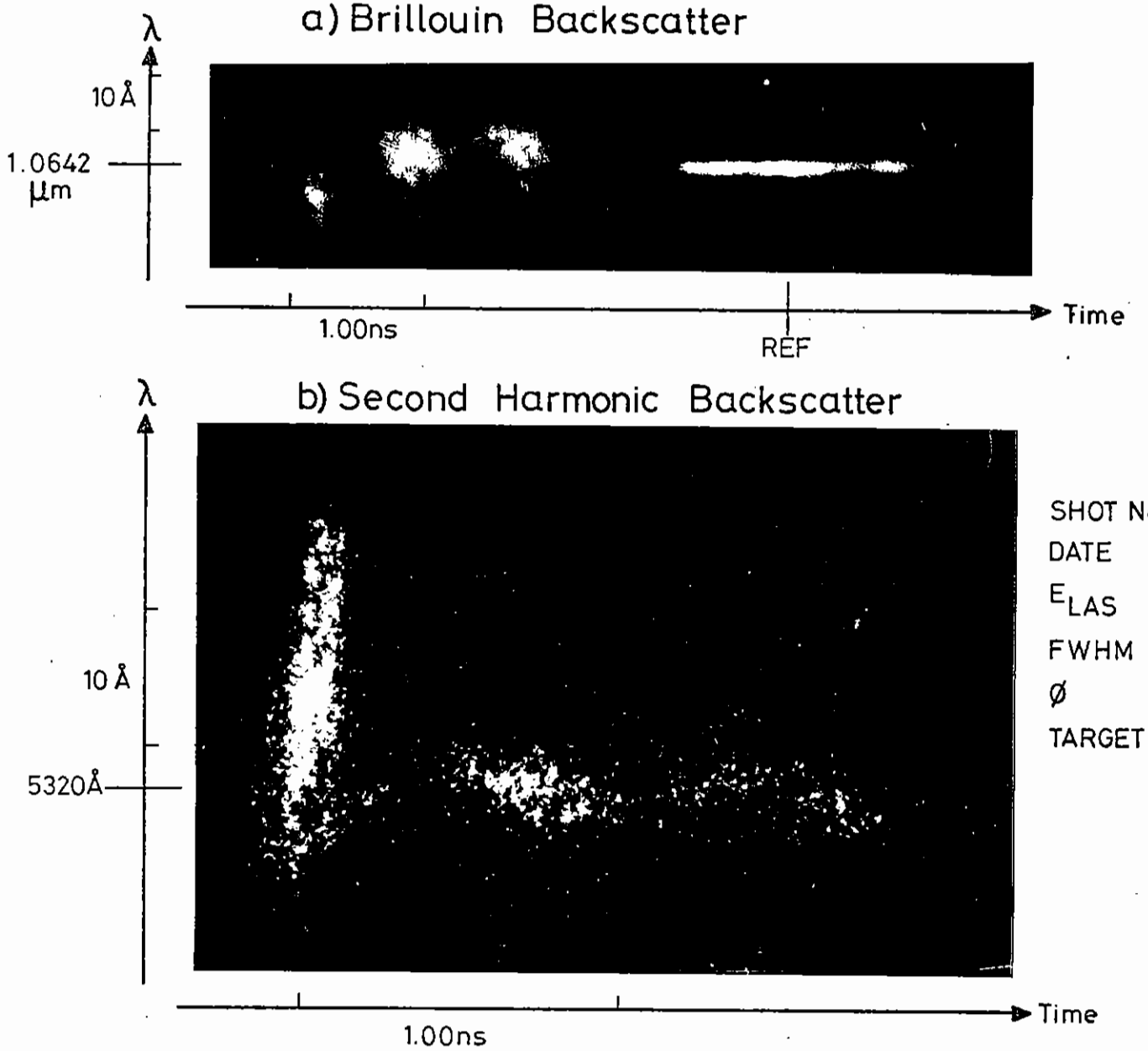

Fig.3.20

Fundamental and Second Harmonic Time Resolved Spectra

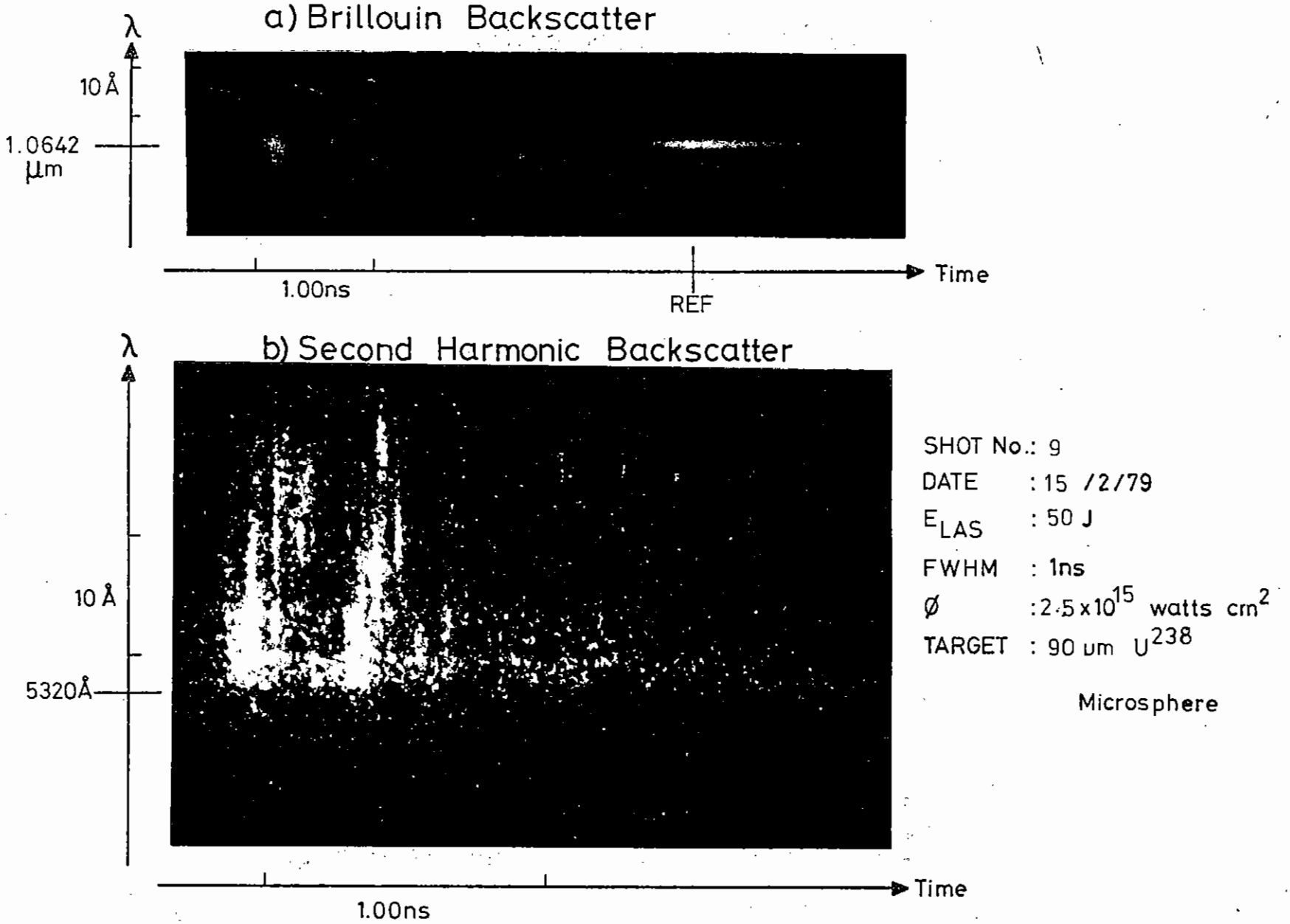

Fig.3.21

Fundamental and Second Harmonic Time Resolved Spectra

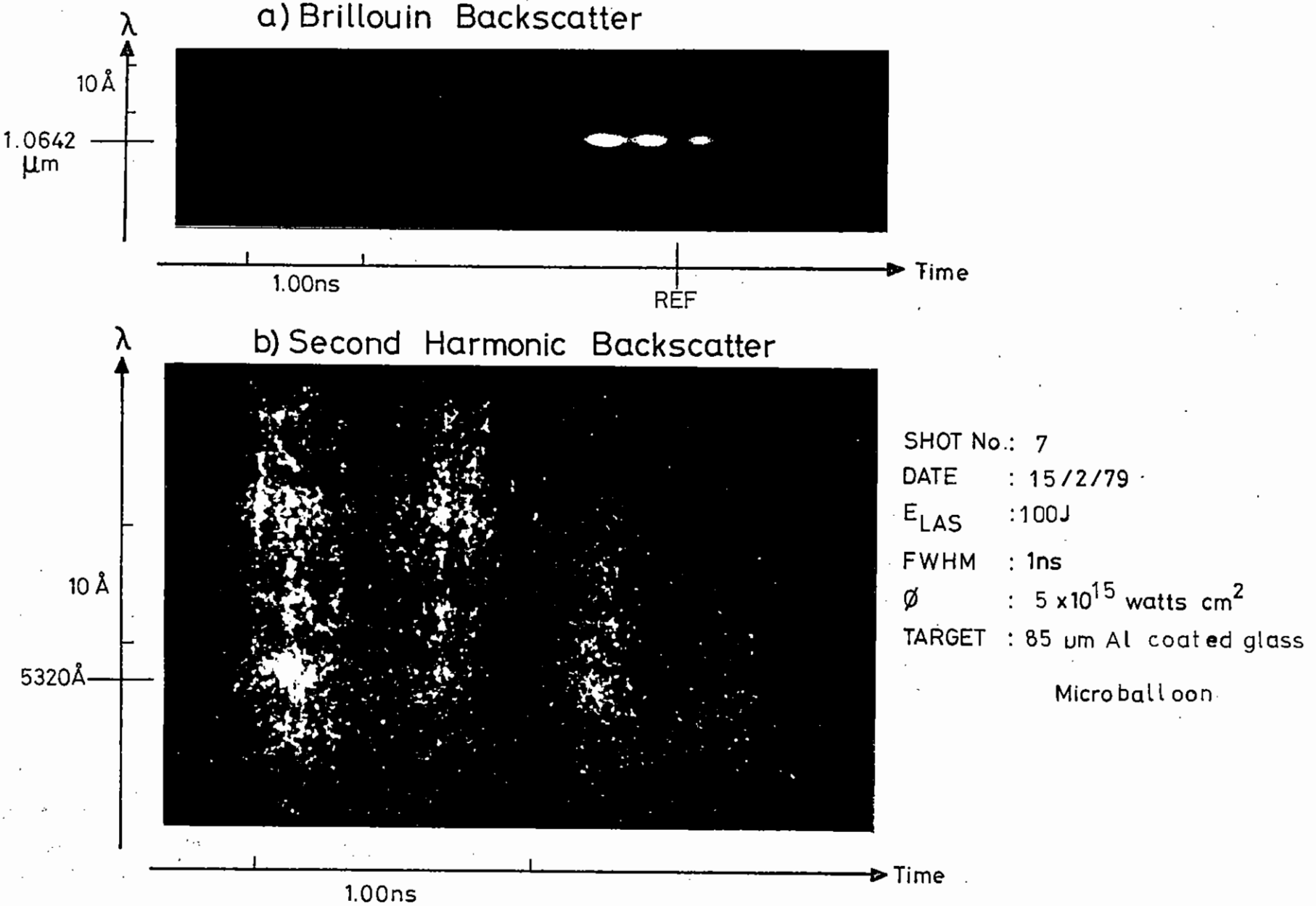

Fig.3.22

Fundamental and Second Harmonic Time Resolved Spectra

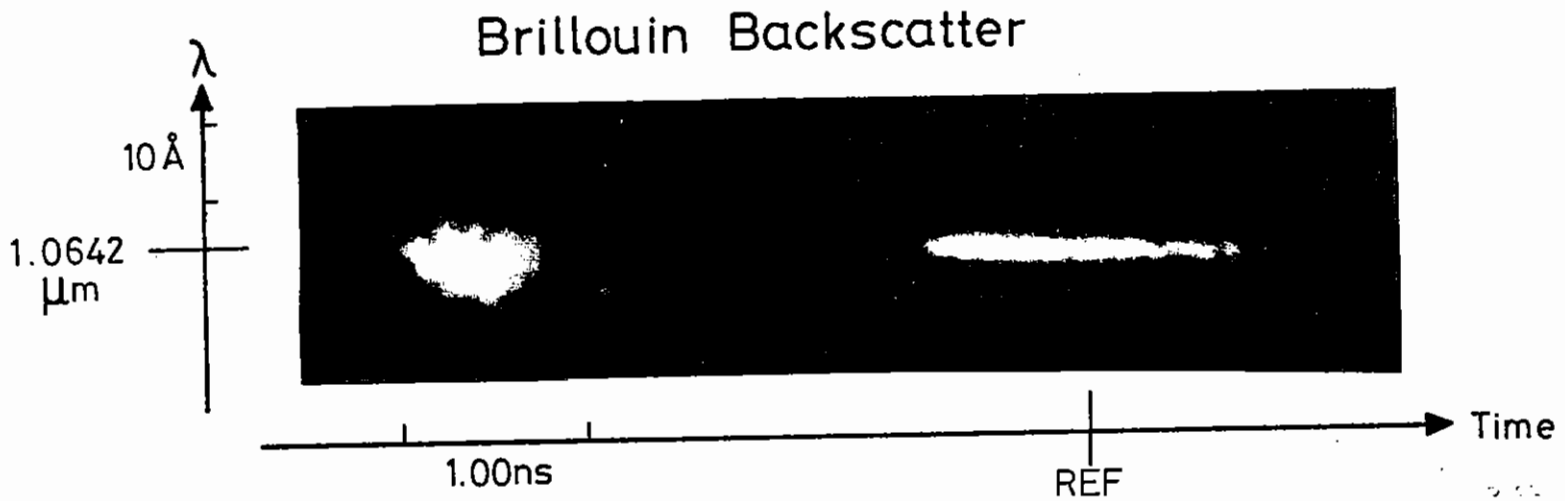

Fig.3.23

Time resolved backscatter spectrum from plane brass target, laser energy 10 J in 1.6 ns pulse.

The red shift due to the ion acoustic wave generated by Brillouin scattering will be

$$\Delta\lambda_{\beta}/\lambda_o = \frac{\omega_{ia}}{\omega_o} = \frac{2k_o v_{ia}}{\omega_o} = \frac{2v_{ia}}{c}$$

where we have used the result that the wavenumber of the ion acoustic wave has modulus $\sim 2k_o$.

The net red shift is then

$$\Delta\lambda/\lambda = \frac{2v_{ia}}{c} (1 - M)$$

showing that the shift is to the red if the flow is subsonic and to the blue is the flow is supersonic.

In their experiments on high Z disk targets the Livermore group (3.32) have shown that the Brillouin and Doppler components of the frequency shift may be separated, at least approximately, by tilting the target by 45^o. The Doppler shift is then reduced by cos 45^o while the Brillouin shift is essentially unchanged. Their results, at irradiances of 3.10^{14} W cm^{-2} and 3.10^{15} W cm^{-2} with a 1 ns pulse on a gold target show that the flow Mach number M is about 0.8 and 0.84 respectively. Unfortunately this shows that a measurement of the reflected ω_o spectrum is not a good indicator of the electron temperature in the under dense plasma because of the close cancellation of the two contributions to the wavelenght shift. If we use the value of the Mach number of M = 0.82 and take $\Delta\lambda = 5$ Å for the high irradiance shots on Al coated microballoons ($\phi \sim 4.10^{15}$W cm^{-2}) then

$$v_{ia} = \frac{c\Delta\lambda}{2\lambda(1-M)} = 4 \times 10^7 \text{ cm s}^{-1}$$

also $v_{ia} = \left(\frac{ZkT_e}{Amp}\right)^{\frac{1}{2}}$ where A is the ion mass number and mp the proton mass. Thus if $M_z \gtrsim 2$, Te $\gtrsim$ 13 keV.

On the spectra which are somewhat well exposed eg Fig. 3.19 the ω_o backscatter is seen to possess short time scale structure extending both to the red and to the blue of the 'normal' Brillouin backscatter.

The possible instabilities which might lead to those short burst of emission are being considered.

3.4.3 $2\omega_o$ spectra

Some typical $2\omega_o$ time resolved spectra are shown in Figs.3.19 to 3.22. At low irradiances, $< 10^{14}$W cm^{-2} the $2\omega_o$ emission is spectrally narrow and moves continuously in wavelength presumably due to a Doppler shift. The spectral narrowness of the emission, $\lesssim 2$Å, would suggest that this emission is due to a 'resonant' effect at the critical density without the mediations of any electron plasma waves or ion acoustic waves. At slightly higher irradiances the $2\omega_o$ emission begins with a burst of spectrally broad emission, ~ 20Å, and then continues as the spectrally narrow emission as on the lower irradiance shots. At higher irradiances, $> 10^{15}$ W cm^{-2} the broad emission persists throughout much or all of the laser pulse and appears as a series of discrete temporal pulses. Each pulse is close to the instrumental limit of time resolution and in many cases the pulses also break up into a set of fairly regular 'spots' in the spectral direction. The reasons for this small scale structure are being investigated.

The difference between the spectrally narrow and broad emissions appears to correlate with steep density gradients near critical density. At moderate irradiances $\lesssim 5.10^{14}$W cm^{-2}, the ponderomotive pressure of the laser beam is not sufficient to cause steepening of the density profile but a steep profile will exist in the initial part of the laser pulse before significant hydrodynamic motion has occurred. At higher irradiances, when the ponderomotive pressure is important the steep density profile will persist throughout the laser pulse. In the presence of the steep density profile resonance absorption is enhanced and is known to produce many fast electrons: the cold electron return current needed to maintain charge neutrality can drive ion acoustic turbulence. This is probably responsible for the spectrally broadened $2\omega_o$ emission since large amplitude ion waves can induce a spectrum of electron plasma wave frequencies as shown by Cairns in section 8.3.6 of this report.

Conclusions

This work has shown that the target material can significantly change the amount of Brillouin backscatter high Z materials producing less backscatter. Further work is needed to make these conclusions more quantitative and also to establish the variations of Brillouin backscatter with target radius and laser irradiance.

The time development of the backscattered fundamental frequency shows that the backscatter persists for the whole of the laser pulse but also exhibits very short duration modulations which are yet unexplained.

The nature of the second harmonic emission suggests that the spectral broadening is associated with fast electron production through the ion turbulence set up by the fast electron return current.

CHAPTER 3 REFERENCES

3.01 D T Attwood et al, Phys.Rev.Lett. 40 184 (1978)

3.02 C E Max and C F McKee, Phys.Rev.Lett. 39, 1336 (1977)

3.03 J Virmont, R Pellat and A Mora, Phys.Fluids 21, 567 (1978)
K A Brueckner and R S Janda, Nuclear Fusion 17, 451 (1977)

3.04 R Benattar, C Popovics and R Sigel - A polarised light interferometer for Laser Fusion studies - CNRS Report (1978)

3.05 C M Vest, Appl.Optics 14, 1601 (1975)

3.06 A Raven, O Willi, P T Rumsby, Phys.Rev.Lett. 41, 554 (1978) and in J Stamper, Naval Research Laboratory Report 3872 (1978)

3.07 R E Kidder, 'Proceedings of Japan - US Seminar on Laser Interaction with matter', Tokyo (1975)

3.08 J T Larsen and J Harte, Bull.Am.Phys.Soc. 20, 1061 (1977)

3.09 N Minyanaga and K Tanaka, Osaka University Report No ILE-APR-77 (1977)

3.10 H Azechi et al Phys.Rev.Lett. 39, 1144 (1977)

3.11 R E Kidder and J W Zink, Nuclear Fusion 12, 1325 (1972)

3.12 M D Rosen et al, Lawrence Livermore Laboratory Report UCRL 82146 (1978)
P M Campbell et al, Phys.Rev.Lett. 39, 274 (1977)

3.13 B Ahlborn and S Ariga, Phys.Fluids 20, 18 (1977)

3.14 J A Stamper, E A McLean and B H Ripin, Phys.Rev.Lett. 40, 1177 (1978)

3.15 D Biskamp and H Welter, Phys.Rev.Lett. 34, 312 (1975)

3.16 C S Liu and M N Rosenbluth, Phys.Fluids 19, 967 (1976)

3.17 A I Avrov et al, Sov.Phys.JETP 45, 507 (1977)

3.18 Offenberger (to be published)

3.19 Annual Report to the Laser Facility Committee 1978, Rutherford Lab Report No LD/78/04

3.20 R A Cairns (Section 8.3.6 of this Report)

3.21 D J Nicholas, C Pataky and W T Welford, Appl.Opt. 17 3368

3.22 J Albritton and P Koch, Phys.Fluids 18, 1136 (1975)

3.23 H C Barr (Section 8.33 of this Report)

3.24 H A Baldis, J C Sampson and P B Corkum, Phys.Rev.Lett. 41 1719 (1978)

3.25 A B Langdon and B F Lasinski, Laser Program Annual Report (1975) LLL Report UCRL 50021-75 (1976) 309

3.26 H H Chen and C S Liu, Phys.Rev.Lett. 39, 881 (1977)

3.27 D W Forslund, J M Kindel, E L Lindman, Physics of Fluids 18, 8 p1017 (1975)

3.28 B H Ripin, J M McMahon, E A McLean, W M Mannheimer and J A Stamper, Phys.Rev.Lett. 33 11, p634 (1974)

3.29 L M Gorbenor, Yu S Kasyanov, V V Korabkin, A N Polyanicher, A P Shevel'ko, Soviet Physics JETP 27 4 p242 (1978)

3.30 A Ng, L Pitt, D Salzman, A A Offenberger, Phys.Rev.Lett. 42 5 p307 (1979)

3.31 H Azechi, H Fujita, K Imasaki, Y Izawa, Y Kato, Y Kawamura, M Matoba, K Mima, S Miyamato, Y Mizumato, T Mochizuki, S Nakai, K Nishikara, H Nishimura, T Norimatsu, T Sasaki, H Takabe J J Thomson, K Yoslida, T Yamanaka, C Yamanaka, Paper IAEA-CN-37-M-4 Conference on Plasma Physics and controlled Nuclear Fusion Research Innsbruck August 1978

3.32 M D Rosen, D W Phillion, V C Rupert, W C Mean, W L Krier, J J Thomson, H N Komblum, V W Slivinsky, G J Caparaso, M J Boyle, K G Tirsell, Lawrence Livermore Laboratory preprint UCRL 82146 (1978)

CHAPTER 4 TRANSPORT AND PARTICLE EMISSION

I N D E X

CHAPTER EDITOR W T Toner

CONTRIBUTORS A Ahlborn, D J Bond, A Cole, R G Evans, D A Gray, T Goldsack, J D Hares, C Hooker, J D Kilkenny, M H Key, R Illingworth, R Lee, J G Lunney, A Moore, J Murdoch, A Raven, P T Rumsby, S Sartang, J A Stamper, R K Thareja, W T Toner, S Veats, O Willi.

CHAPTER 4 TRANSPORT & PARTICLE EMISSION

4.1 Introduction

The transport of energy is crucial in determining the properties of any implosion: once laser energy is absorbed by a plasma the way in which it is transported determines the ablation pressure. In an ablative mode, energy is absorbed near to the critical density surface, and remains near this region. Unfortunately for compression, the other extreme, where most of the energy is transported large distances by fast electrons appears a more realistic model at high laser intensities. Some of the complex physical phenomena which result are investigated in this chapter.

In section 4.2 experiments using Faraday rotation and interferometry to study magnetic field generation at the critical density surface are discussed. Large fields are observed for plane targets in the low density region and the transition to small microballoon targets where fields are low is studied. A coherent pattern emerges from apparently contradictory results in different laboratories.

In section 4.3 observations of the Xray emitting region of layered microballoons are used to measure the coupling of energy into the ablation plasma, and the transport of energy away from this plasma. It is found that the absorption is very low. The majority of the energy goes into fast electrons and experiments demonstrating this are presented in section 4.4. The fast electron energy is measured using targets with layers of tracer materials which detect the fast electrons by the K_α radiation they produce. It is found that the hot electron temperature T_H, scales as $I^{0.5}$ in the intensity region around 10^{15} Wcm^{-2}. Measurements at 1.06 μm and 10.6 μm have suggested that T_H scales as $(I\lambda^2)^\alpha$. To confirm this, experiments with a frequency doubled 1.06 μm laser beam have been performed and preliminary results are presented in section 4.5.

Experiments on the burn through of thin plastic films are presented in section 4.6. These experiments suggest that previous interpretations of the burn through of plastic foils are incorrect in that the foil only becomes transparent when the plasma density is well below critical. Otherwise there is heavy absorption by ion acoustic turbulence.

The experiments on exploding pushers are described in section 4.7. The spectroscopic diagnosis of the core is described in some detail because of recent advances in the method of analysis. An attempt is made to correlate the measured density, temperature and neutron yield from several shots.

4.2 Magnetic Field Measurements

Faraday rotation techniques have been used recently to observe the presence of magnetic fields in the megagauss range generated in plasmas produced by high intensity laser irradiation of solid targets (4.01,4.02). Such fields are of great concern to designers of targets for laser fusion schemes since they may cause the transport of thermal energy into the target to be severely inhibited (4.03) leading to such effects as high coronal temperatures and fast ion production. All the magnetic fields observed in Nd laser experiments so far have been of toroidal geometry consistent with a thermoelectric source term driven by an axial electron density gradient and a radial electron temperature gradient ($\frac{dB}{dt} \alpha \nabla n \Lambda \nabla T$). It is important to know whether such large fields will still exist in the case of symmetrically illuminated spherical pellets and also if magnetic fields due to other $\nabla n \Lambda \nabla T$ topologies are produced by such effects as target composition discontinuities (4.04). Fig.4.01 shows in schematic form the toroidal and discontinuity generated fields.

Measurements relevant to these problems have been made in a series of Faraday rotation experiments in which the effects of target size and composition structure on the generation of thermoelectrically driven magnetic fields in laser produced plasmas were studied.

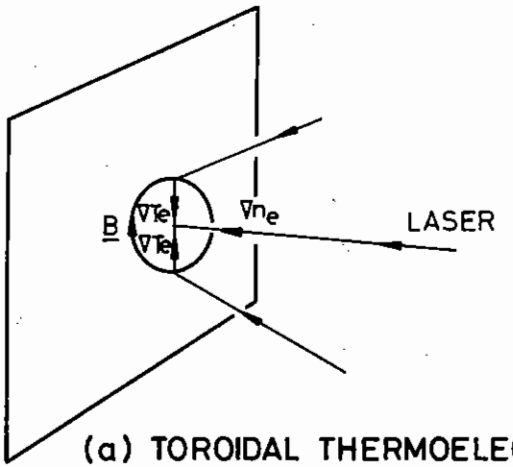

(a)

(a) TOROIDAL THERMOELECTRICALLY DRIVEN FIELD

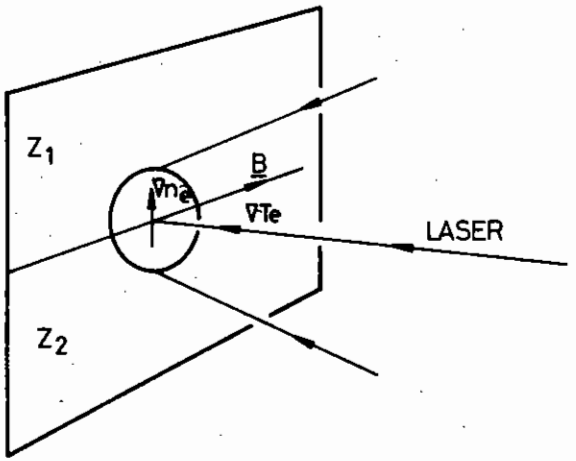

(b)

(b) DISCONTINUITY DRIVEN FIELD.

FIG. 4.01

Experiments were conducted using a single beam of the Rutherford Laboratory neodymium glass laser producing up to 10J in a single 100 ps duration pulse. Using an f/1 focusing lens, irradiances up to a few x 10^{16} watts cm^{-2} were achieved over a focal spot of diameter 15 μm. Observations were made on a range of targets using Faraday rotation and interferometry techniques with either a Raman shifted 2nd harmonic probe beam (λ = 633 nm) or a UV 4th harmonic probe beam (λ = 266 nm). More details of the experimental arrangements are available in reference 4.02 and sections 3.2 and 1.7.1 of this report.

4.2.1 Spherical Targets

Previous magnetic field measurements with similar laser systems and irradiances have produced diverse results. At Lawrence Livermore Laboratory (4.05) no magnetic fields above a detection threshold of 100 KG were observed (266 nm probe beam) on 100 μm diameter glass microballoons and 300 μm diameter plastic disc targets. Similarly, at the Rutherford Laboratory (4.02), no fields above 100 KG were observed (633 nm probe beam) on 45 μm diameter microballoons but fields of up to 2 MG were observed in large plane targets. On the other hand, the Naval Research Laboratories (4.01) have observed large magnetic fields on 120 μm diameter solid polystyrene spheres and on plane targets. These magnetic fields were enhanced by the presence of a prepulse (4.01). To clarify the situation a series of Faraday rotation and interferometry experiments were carried out to study the effect of target size and composition structure on the generation of thermoelectrically driven magnetic fields. Experiments were carried out on hollow and solid spherical targets ranging from 40 μm to 250 μm in diameter and on solid plane targets.

A number of techniques were used for detection of Faraday rotation and for interferometry with a 30 ps probe beam pulse of wavelength 633 nm (Raman shifted 2nd Harmonic) or 266 nm (4th Harmonic). Faraday rotation was detected with a polariser set at an angle less than 10^{o} to the position for total extinction of unrotated radiation. Electron density measurements were made with either one of two large-aperture interferometers. For each interferometer a microscope objective imaged the target plasma onto film and a beamsplitter was used to make probe

beam radiation that had passed, undeviated, in front of the plasma interfere with radiation that had passed through the plasma. A phase shift caused by the plasma gave rise to a shift in position of the interference fringes. In one case a Wollaston prism combined with a Glan-Taylor polariser was used as the beam splitter. In the other case Fresnel Mirrors or a Fresnel biprism were used as beam splitters. Faraday rotation and interferometric measurements were simultaneous for the visible probe beam but were made separately for the UV probe beam.

Fig.4.02 shows typical Faraday rotation (probe wavelength 633 nm) photographs obtained with a 15 μm focal spot, 60 ps after the peak of the main pulse of ∿10J in 100 ps. The analyser-polariser angle relative to the polarisation of the input beam was $+80^{\circ}$. The targets are (a) a 100 μm diameter solid polystyrene sphere, (b) a 250 μm diameter hollow glass microballoon and (c) a 1 mm aluminium wire. The 250 μm sphere and the plane target show strong Faraday rotation showing up as bright and dark regions above and below the axis and indicating the presence of a toroidal magnetic field. Simultaneous interferograms confirm that the magnetic fields occur in regions of the coronal plasma with electron density between $0.1n_c$ and $0.3n_c$, where n_c is the critical density ($10^{21} cm^{-3}$). There is marginal evidence for magnetic fields above 100 kG on the 100 μm spherical target. No magnetic fields were observable on smaller spherical targets, diameter 40 μm.

The results from a number of such shots can be summarised as follows: (1) Magnetic fields were only detected on spherical targets with diameters greater than 100 μm. (2) The presence or absence of a detectable field was independent of the wall thickness of the spherical targets. (3) The magnitude of the magnetic field for spherical targets was dependent on the ratio of target to focal spot diameter (D/d) with fields only observable if $D/d \geq 5$. (4) Large plane targets showed very strong fields but plane targets consisting of small discs (4.05) with $D/d >> 5$ showed no field.

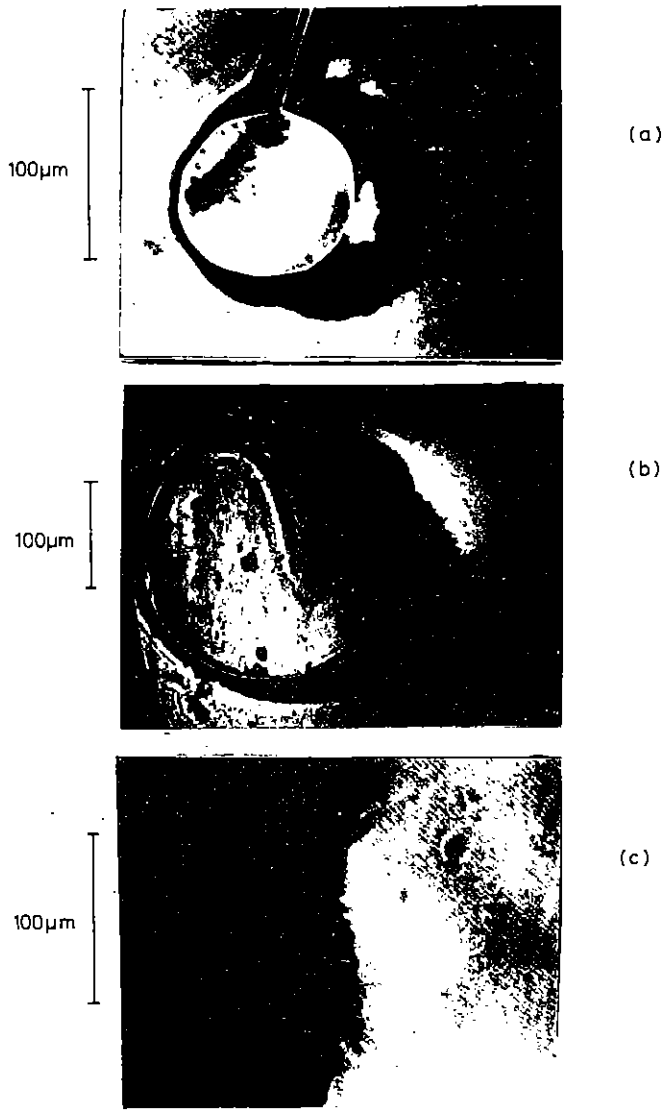

FIG 4.02. FARADAY ROTATION PHOTOGRAPHS TAKEN 60ps AFTER PEAK OF 100ps PULSE.

To account for these observations we suggest that the main factor that determines the magnitude of the magnetic field produced by a given laser beam is not the ratio D/d but is the electrical capacitance of the target ($2\pi\varepsilon_o D$ for a spherical target). Electrons leaving the plasma will leave the target positively charged with respect to earth (4.06). The resulting electric field will oppose the electric field in the plasma responsible for driving the current that generates the toroidal magnetic field. The magnitude of the inhibiting electric field will be proportional to $1/D^2$, ie will be important for small targets but will be small for large targets. This explanation may also account for the rapid disintegration of the target mounting stalk previously observed for low capacitance targets. If the target became charged to a high positive potential with respect to earth the large potential difference along the length of the stalk would drive a return current from the target to earth. The application of a large positive potential to targets to suppress magnetic fields has been suggested previously (4.07).

All the above observations are encouraging for laser driven fusion schemes as they indicate that even for very non-uniform illumination, for small targets the magnetic fields generated will be low.

4.2.2 Plane Targets

Experiments are now moving away from short 100 ps pulses towards longer 1 ns pulses. Accordingly, the effect of a prepulse on magnetic field generation by a 100 ps pulse may be relevant to future long-pulse work.

With a prepulse of 20% of the total energy 1.0 ns before the main pulse on plane targets, the Faraday rotation pattern showed the same overall toroidal field pattern but of much larger spatial extent and with considerable structure along a direction normal to the laser beam axis. Such structure is similar to that observed in CO_2 laser produced plasmas (4.08) although the overall toroidal nature indicates thermoelectric rather than other sources for these structured fields, in the low density corona at least. Such complex field structures seem to be associated only with long slow rise high intensity laser pulses and very large prepulses as they were not observed for prepulse of $\sim$3% (4.01). The shaped pulses required for adiabatic compression schemes may well give rise to this type of phenomenon.

The toroidal fields so far measured have all been associated with the low density plasma where thermal conduction effects are not important. To observe the fields at the critical density surface where these effects are important, and to investigate the possibility of fields driven by other $\nabla n \Lambda \nabla T$ topologies as for example in multilayered targets, a fourth harmonic probe beam and special targets having a step discontinuity in Z, the atomic number, across the focal region were used. Such targets have been predicted (4.04) to give rise to large magnetic fields directed along the line of the discontinuity (Fig.4.01b).

A number of discontinuity targets (Aluminium/polystyrene, tungsten/polythene and Aluminium/beryllium) were studied using simultaneous Faraday rotation and interferometry at 633 nm. No evidence for Faraday rotation associated with a magnetic field near the discontinuity could be detected although interferograms showed density steps of magnitude up to 30 ($\pm$ 10)% extending out to less than 0.1 n_c (mean density at discontinuity) with step widths less than 10 μm. This absence of Faraday rotation is consistent with earlier, less detailed, observations (4.02). To overcome the possibility that the visible probe beam was being deflected away from the region of magnetic field by large refractive index gradients at the discontinuity, and to investigate magnetic fields occurring in the region of the critical surface, Faraday rotation measurements were made using the 266 nm probe beam. Interferometric measurements on similar but unstructured targets had shown that the critical density could be probed with this wavelength.

The targets were 125 μm diameter nylon fibres overplated with 100 nm thick bands of aluminium. On such targets conclusive evidence was observed for thermoelectric magnetic fields at critical density and magnetic fields along the discontinuity. Fig.4.03 shows a contour plot of the Faraday rotation image for such a target with the polariser set at an angle of 2^o to that at which total extinction of the unrotated probe light was obtained. The bright/dark pattern as a signature of thermoelectric fields can be clearly seen above and below the beam axis and is shown more clearly in the section CC[1]. From the background level of the probe light the rotation is estimated at

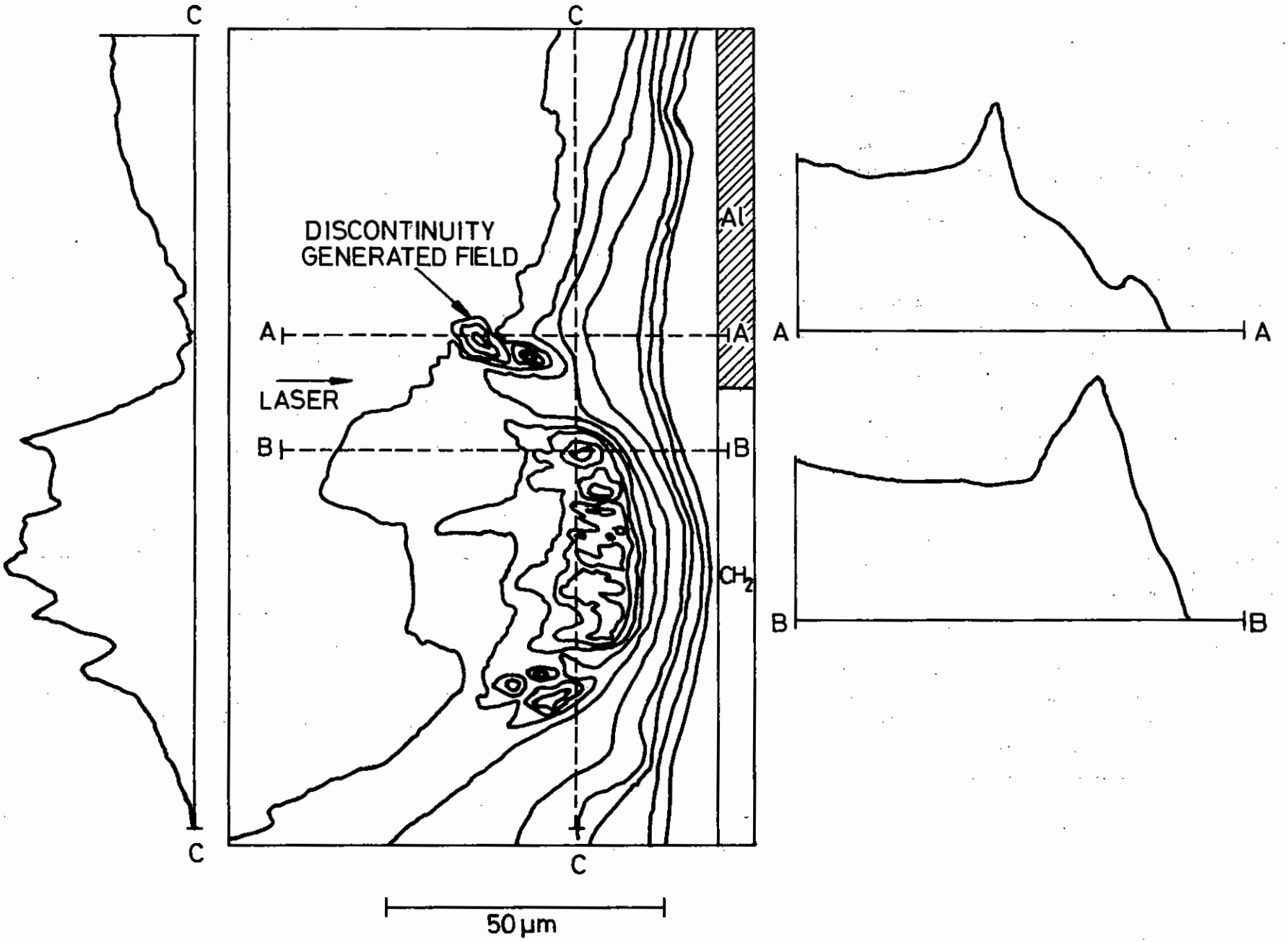

FIG. 403: FARADAY ROTATION IMAGE USING 266 nm PROBE.

$\sim \pm 1^{o}$ for this field. The field due to the target discontinuity is also seen as a line of high rotation of about 5 μm width in the low density plasma and corresponds to the peak on the section AA^{1}. The time is 30 ps after the peak of the main pulse.

Because of the assymmetric nature of the Faraday rotation, Abel inversion and detailed comparison with electron density measurements is not possible. However, comparison with interferometric data (266 nm) from similar but unstructured targets permits some approximate estimates (4.01) of magnetic field magnitudes (See Fig. 4.04) to be made. The magnetic field in the outer regions of the plasma well away from the discontinuity is approximately 0.6 ($\pm$ 0.3) MG at the critical density, increases to a maximum of 3($\pm$ 2) MG at $0.2n_c$, and decreases to zero at approximately $0.1n_c$. These estimates are in agreement with previous more accurate measurements of magnetic fields in the low density corona and are in qualitative agreement with the numerical modelling of Colombant and Windsor (4.09) in that the maximum field occurs in the low density plasma well away from critical density. The effect of such a field on thermal transport at the critical layer is expected to be small based on an estimate of $(\omega_{ce}\tau_e)^2 \sim 0.5$. This compares with a value of $(\omega_{ce}\tau_e)^2 \sim 500$ at a density of $0.2\ n_c$.

The peak magnetic field at the discontinuity was estimated to be 1.5 ($\pm$1)MG with the direction of the field consistent with ∇n_e directed from the polystyrene (Low Z) into the Aluminium (High Z) plasma. This field was only observed in the low density corona ($n < 0.1\ n_c$), but the absence of observable Faraday rotation at larger densities may be limited by the deflection of the 266 nm probe beam by the larger refractive index gradients occurring in the region of the discontinuity close to the critical surface. As mentioned previously, 633 nm interferometer measurements provided clear correlation of the discontinuity with an electron density gradient directed across the discontinuity.

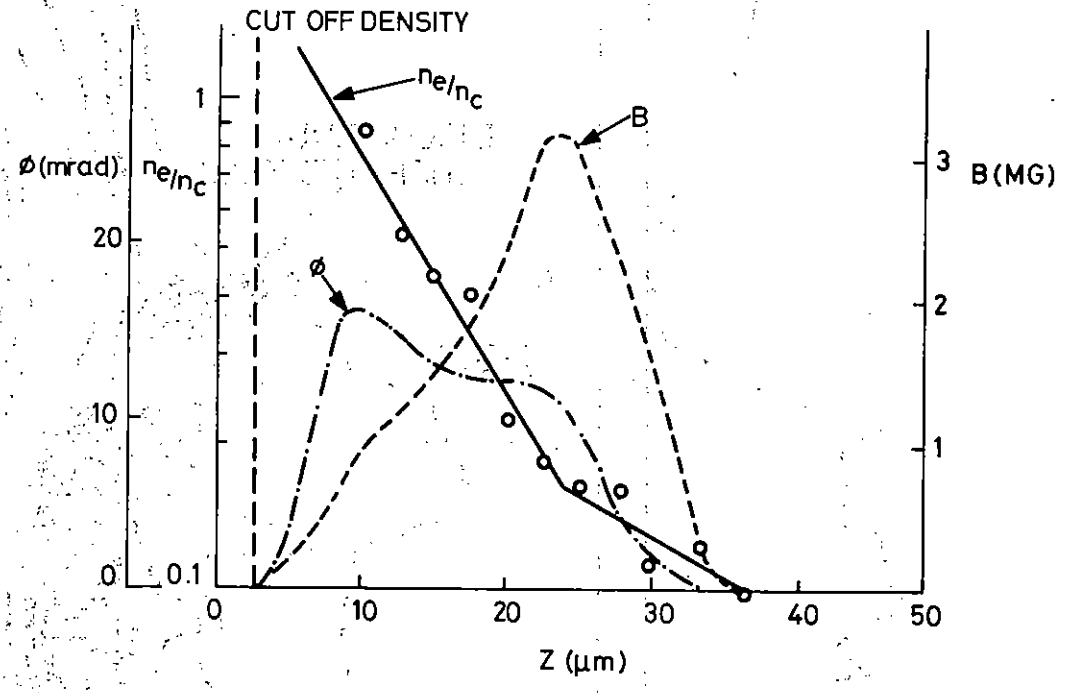

FIG. 404: ESTIMATE OF MAGNETIC FIELD STENGTH AT THE EDGE OF FOCAL SPOT, FROM DATA OF FIG. 402

Conclusions

1. Magnetic field measurements on a variety of spherical targets have been performed. Magnetic fields are not observed when the target diameter is less than $\sim$ 100 μm irrespective of the target material or the degree of focusing of the Nd glass laser on the target. It has been proposed that due to the small electrical capacitance of such targets, a very large electric field may be generated close to the target that opposes the electric field driving currents in the plasma. The observations show that previous apparently contrary results from different laboratories actually fit into a coherent pattern.

2. When a large prepulse is present, the magnetic fields are enhanced and strongly structured.

3. Measurements on discontinuous plane targets up to the critical surface showed that the magnetic field is strongest in the low density region. The existence of an electron density step across the discontinuity has been proved and the magnetic field associated with the discontinuity has been detected.

4.2.3 Magnetic probe measurements

In a previous Faraday rotation experiment (4.02) measurements were simultaneously made with a number of inductive probes which showed two field components. These were a slow component consistent with the direction of a thermoelectric field and a fast reversed component correlated with the production of fast ions. The dependence of the slow component on the laser intensity and the target mass number, and the radial scaling of the fields were measured. A threshold is seen in the intensity dependence.

The targets were irradiated with a single beam of the Rutherford Nd-glass laser in a single pulse of between 5 and 40 Joules in 100 ps. The targets used were polythene, aluminium, copper and tungsten wires of 1 mm diameter. The magnetic fields were measured using a coil 4 mm

in diameter with ten turns, encapsulated in an aluminium coated glass tube of 6 mm diameter. The aluminium coating was earthed at the target chamber to prevent electrostatic noise pick-up. The photographically recorded probe signals (α dB/dt) were digitised into a computer linked graphics tablet and then integrated to obtain a magnetic field B.

Fig.4.05(a) displays a typical recorded $\frac{dB}{dt}$ probe signal for an aluminium wire target. The integrated magnetic signal B (Fig.4.05(b)) is made up of two well defined components B_1 and B_2. The first component B_1 has the polarity of an equivalent current flowing from the target ie is reversed relative to a thermoelectric field and is only observed when fast ions are recorded with a Faraday cup detector. The arrival time of this fast component at the probe is consistent with the velocity of fast ions (2×10^8 cms^{-1}) observed from such plasmas (section 4.8.1). The polarity of the second signal B_2 agrees with the direction of a thermally generated magnetic field and is consistent with the expansion velocity of the thermal plasma (a few x 10^7cms^{-1}).

By increasing the laser intensity from 0.3 to 2.10^{16} Wcm^{-2} a sharp increase in the magnitude of the slow component B_2 over the small intensity range from 0.5 to 0.7 10^{16}Wcm^{-2} is seen (Fig.4.06). The error bars in Fig.4.06 represent the shot-to-shot variations in amplitude. This is in quantitative agreement with the results of Faraday rotation measurements carried out simultaneously with these experiments (4.02). This sudden increase of the magnetic field may be due to hot electrons gaining in importance as a thermoelectric source at such high intensities (4.10) or to the thermal-magnetic instability (4.11).

By varying the probe to target distance(r) over the range from 1.5 cm to 6 cm the radial dependence of the magnetic field B_2 was measured to be $r^{-2.45 \pm 0.37}$. By extrapolating this back to the focal spot region, fields of the order of 100 MG would be obtained in disagreement with Faraday rotation results (4.02). This implies that the scaling law breaks down close to the target surface.

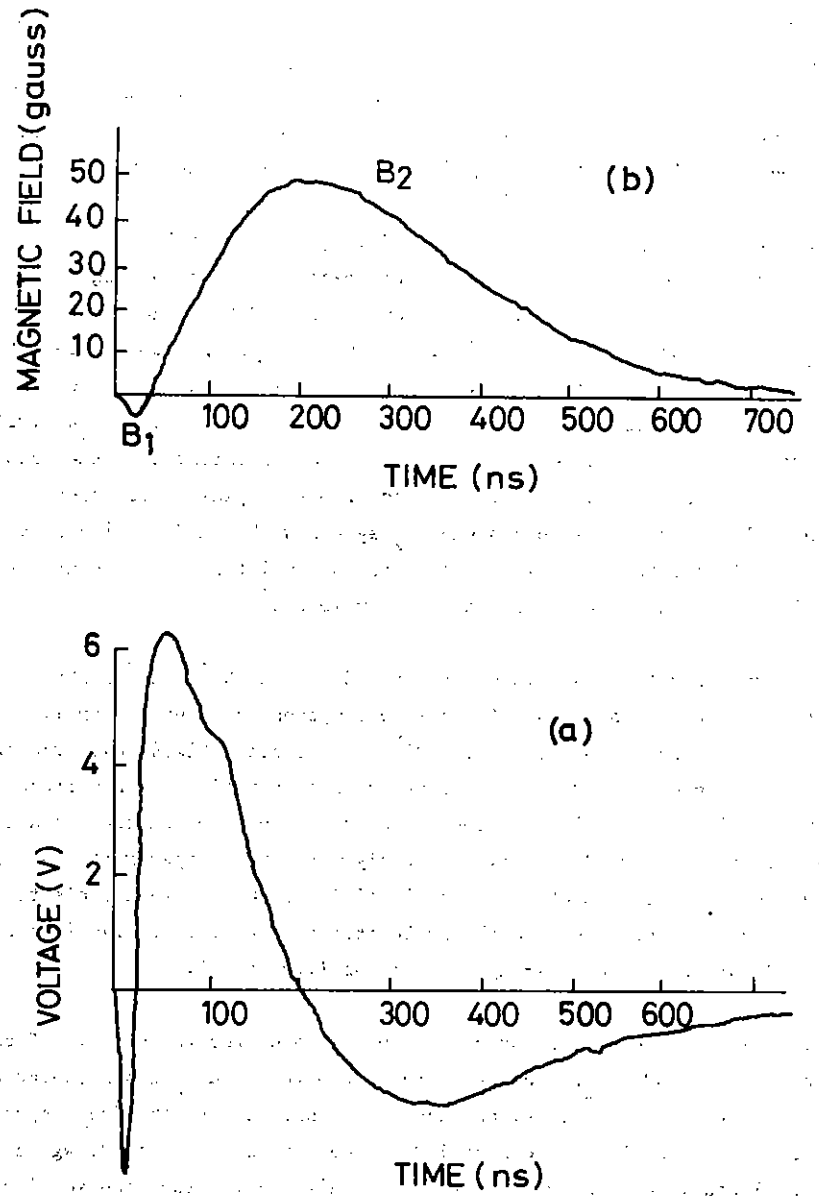

FIG. 4.05: MAGNETIC PROBE SIGNAL, PROBE 1·5cm FROM BEAM AXIS AND 1·5cm FROM TARGET SURFACE.

The maximum value of the magnetic field B_2 is found to decrease with increasing atomic number (Fig.4.07). From aluminium to tungsten B_2 is proportional to $m^{-0.46 \pm 0.05}$. This may be due to the magnetic field being partly diffused when reaching the remote probe. The plasma resistivity increases with the ion charge Z (4.12) and therefore the assumption that the magnetic field is frozen into the expanding plasma may not be valid for higher Z plasmas.

4.3 Transport Inhibition Experiment at 1.06 μm

There have been several experiments purporting to indicate transport inhibition in plane targets (4.13,4.14,4.15). However the interpretations of these experiments have neglected the effect of fast electrons and have been complicated by the possible presence of magnetic fields. In this experiment, which has been previously reported in a preliminary form (4.16) these drawbacks are partially overcome. A measurement of the laser energy absorption into the ablation plasma is made and a configuration is used in which independent measurements of magnetic field (see section 4.2) show that it is less than 100 kg.

4.3.1 Experimental Arrangement

The two beam laser was used to irradiate microballoons which were coated uniformly with various thicknesses of aluminium. The laser pulse was 100 ps long and the irradiance was $2\ 10^{15}$ W cm^{-2}. It was found important to keep the prepulse low, less than 10^{-5}, otherwise the aluminium coatings were partially removed before the main laser pulse. The Xray emission of the ablation plasma was then observed with a space resolving PET crystal spectrometer. Three parameters were obtained from the spectra: the electron temperature of the Xray emitting region; the burn depth of the ablation plasma by comparing intensities of aluminium and silicon (from the glass) emission lines and the density from both the Stark broadening of the lines and the intensity of the recombination continuum.

4.3.2 Experimental results

The electron temperatures are shown in Table 4.01 for several different laser shots. Note that it was usually 500 eV.

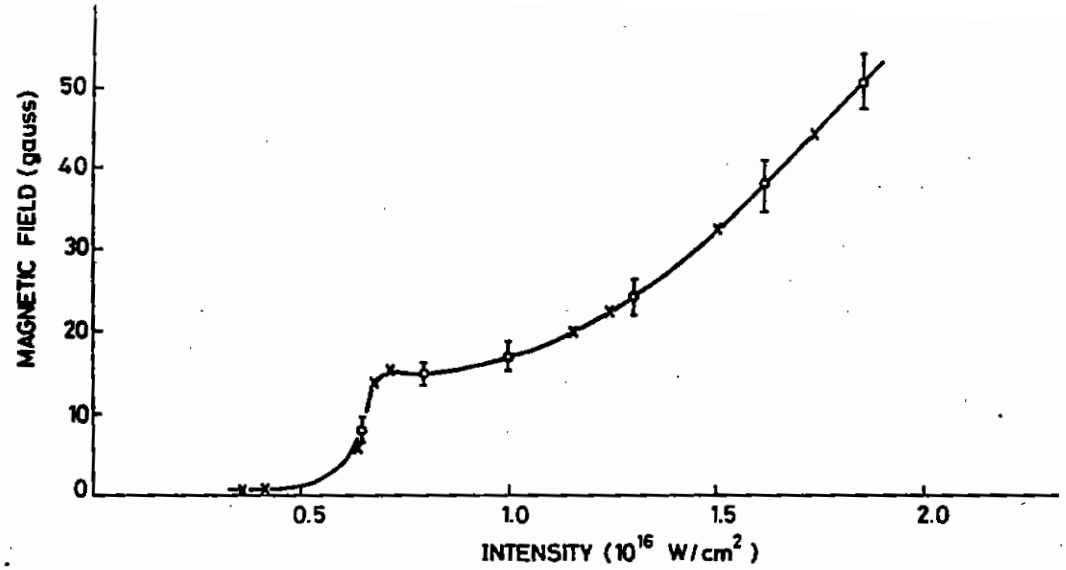

FIG. 406. PEAK FIELD AS FUNCTION OF INTENSITY.

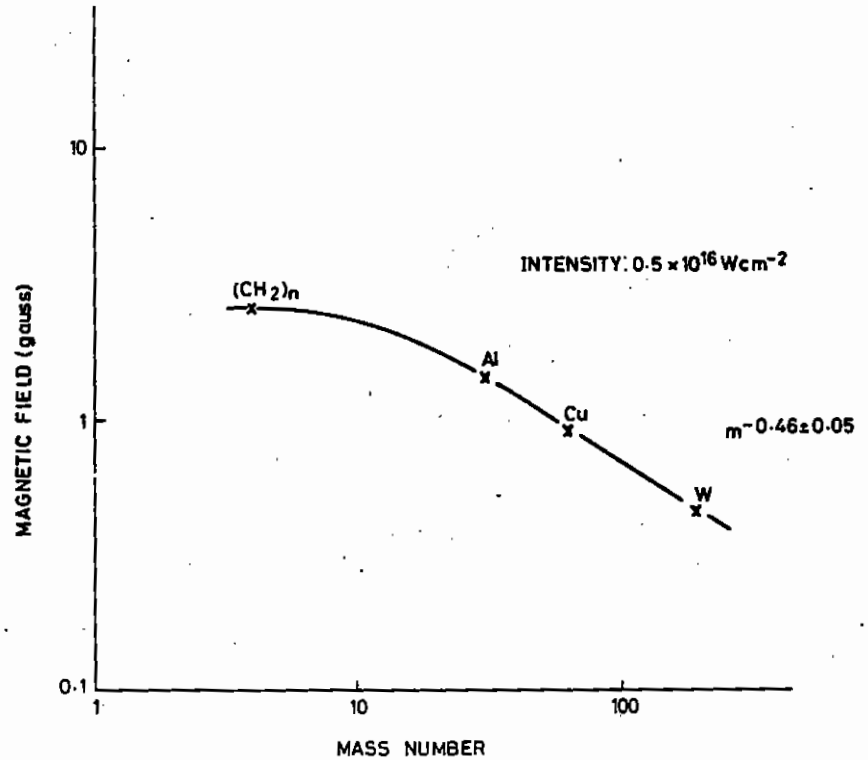

FIG. 407. PEAK MAGNETIC FIELD AS FUNCTION OF ATOMIC MASS.

TABLE 4.01

Electron Temperature of the Ablation Plasma in Microballoons

Shot	Line Ratio Used	N_B/N_H	T_e(eV) Collisional radiative	T_e(eV) recombination continuum
31	Aℓ L_β/Aℓ 1^1S_o-3^1P_1	0.11	455	430 ± 40
167	Aℓ L_γ/Aℓ 1^1S_o-4^1P_1	0.22	510	650 ± 50
180	Aℓ L_γ/Aℓ 1^1S_o-4^1P_1	0.11	455	-
184	Aℓ L_γ/Aℓ 1^1S_o-4^1P_1	0.10	450	420 ± 50
	Aℓ L_γ/Aℓ 1^1S_o-4^1P_1	0.18	495	500 ± 30
209	Si L_β/Si 1^1S_o-3^1P_1	0.10	540	

TABLE 4.02

Saturation K_α yields for various elements

Fluor Element Z	Comment	Atomic density(cm^{-3})	Max Z for small shift	Te from (eV)	Sat K_α yield per atom (eV)
Ne (10)	10B gas	2.7×10^{20}	1.5	8	0.017
Si (14)	Solid SiO	6×10^{22}	4.5	66	0.43
Cl (17)	Solid KCl	1.6×10^{22}	7.5	90	1.7
K (19)	Solid KCl	1.6×10^{22}	9.5	125	3.2

The burn depth of the plasma was characterised by taking the ratio of the Aℓ XII 1^1S_o-4^1P_1 line to the Si XIII 1^1S_o-3^1P_1 line. Results are shown in Fig.4.08. There is a very pronounced burn depth of 0.08 μm of Aℓ.

The electron density of the Xray emitting region was obtained by fitting the Aℓ XIII L_α, L_β, L_γ and L_δ lines. Some details of the method are given in section 4.7.1. A fit to the Aℓ XIII L_δ line is shown in Fig.4.09. However, one experimental profile can fit a theoretical profile for many values of n_e and n_1 (the ground state density of the line, which is proportional to the opacity). By considering the lines of best fit for the four spectral lines in the n_e, n_1 parameter space, values of n_e and n_1 in the overlap region were found which consistently fit all four lines. Thus the electron density of the Xray emitting region is $1.10^{22} cm^{-3}$. This disagrees with other work (4.17) where a value of $n_e \sim 1.10^{21} cm^{-3}$ was ascribed to the density of the Xray emitting region.

The intensity of the Aℓ XII and Aℓ XIII recombination continuum was measured in absolute units. At $h\upsilon$ = 2.52 keV the intensity was $8.8\ 10^{-4}$J/st/keV. Assuming an emission time of 100 ps this implies a value of $n_e^2 V$ of $6.6\ 10^{36} cm^{-3}$ where V is the emitting volume of the plasma.

4.3.3 Simulation of the properties of the ablative plasma

This experiment has been modelled by the code MEDUSA. Although this code has been modified to include in a simple manner the effect of fast electrons, this feature of the code was not used because the range of the fast electrons (Fig.4.24c) is much larger than the observed burn depth (Fig.4.08) and so their specific energy deposition is low compared with the energy density in the ablation plasma. There are two free parameters left, the fractional absorption of laser energy into the ablation plasma η, and the degree of inhibition of the (cold) electron thermal flux. The thermal flux is inhibited by simultaneously reducing the Spitzer (4.18) thermal conductivity and the free streaming flux limit by the same factor, f.

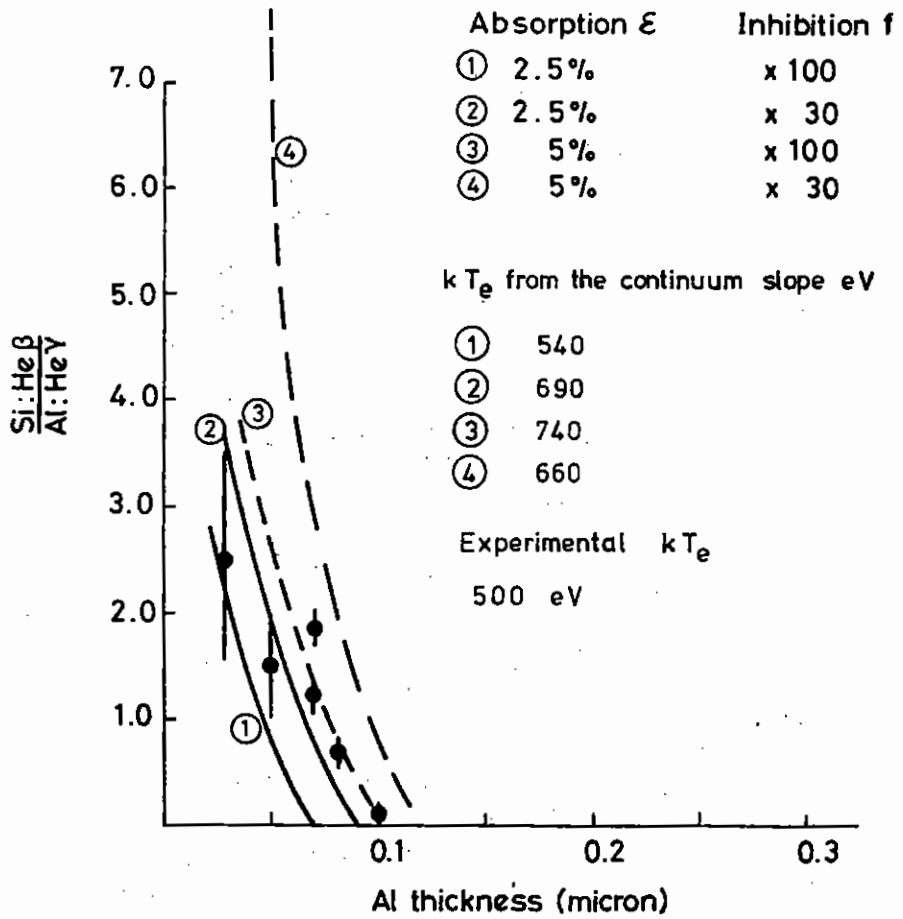

FIG 4.08

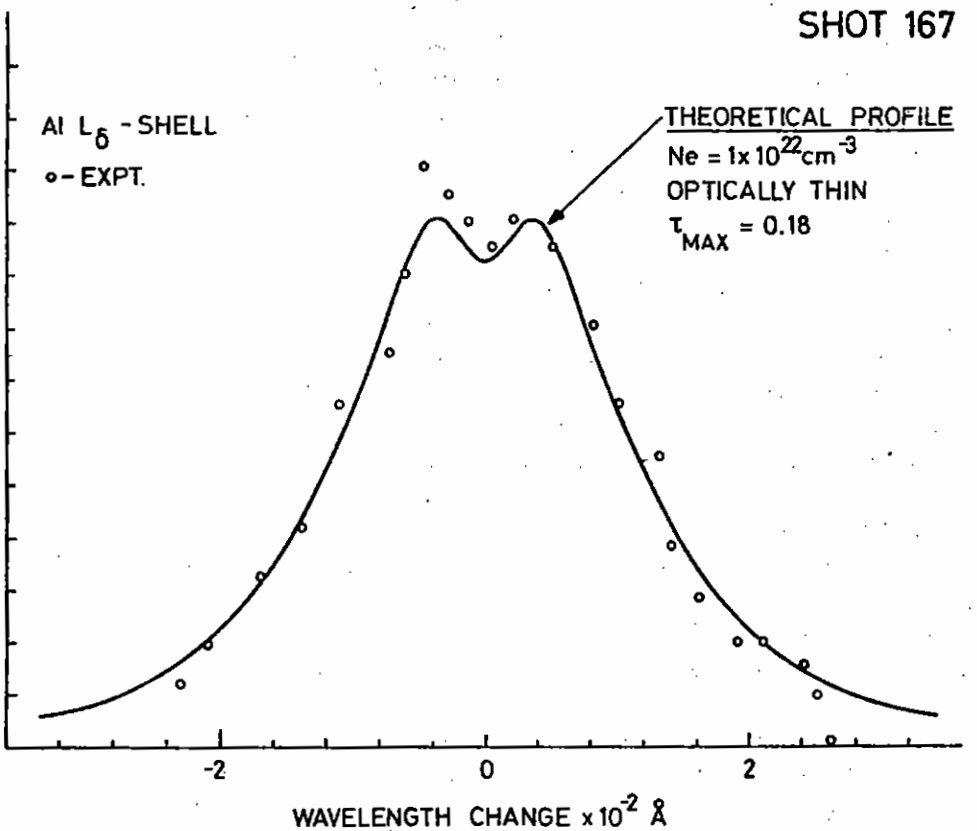

FIG 4.09

At each time step the code then calculates the ionisation equilibrium (4.19) and post processes these results to obtain the space and time integrated line emission. It is assumed that the upper levels are in LTE with the ground state of the next higher stage of ionisation. Space and time averaged values of the recombination continuum radiation are also calculated for comparison with the experimentally measured T_e.

Many runs of the code have been made covering a matrix of values of η and f, as shown in Fig.4.10. Increasing the absorption fraction η increases the burn depth and temperature, whereas increasing the flux inhibition f reduces the burn depth and increases the temperature. But because there are three experimental parameters to be fitted, unique values for η and f can be obtained. This is shown in Fig.4.10. The best fit is with $\eta = 0.025$ and $f = 30$. Runs with $\eta = .0125$ and $f = 3$ or $f = 10$ predict burn depths and temperatures in rough agreement with this experiment but the emission is from a very low density plasma.

4.3.4 Discussion

Let us first consider the absorption. It is well known that the total absorption fraction in laser plasma interaction at $\sim 10^{15}$ Wcm^{-2} is about 30%. Yet here we observe only 2.5% absorption into the ablation plasma. This is consistent with measured absorption into other plasma components. It is shown in section 4.4 that a much larger fraction of the energy is absorbed and transported by fast electrons. The fraction of 1.06 μm light absorbed into the ablation plasma is very low.

The flux inhibition measured here cannot be caused by magnetic field inhibition. It is shown in section 4.2 that with spherical targets the magnetic field is small, yet similar burn depths are measured here as for the plane targets of ref 4.15. This lends support to the suggestion that ion acoustic turbulence causes the transport inhibition.

Data were obtained from MEDUSA on the local values of λ, the 90° electron deflection mean free path, and the temperature scale length, L. In the ablation front region $10^{21} < n_e < 10^{22}$, $\lambda/L \leq 10^{-1}$. Because $Z \sim 11$ then ZT_e/T_i was ~ 20 and the condition (4.20) for heat flux driven ion acoustic turbulence is exceeded. An additional phenomenon likely

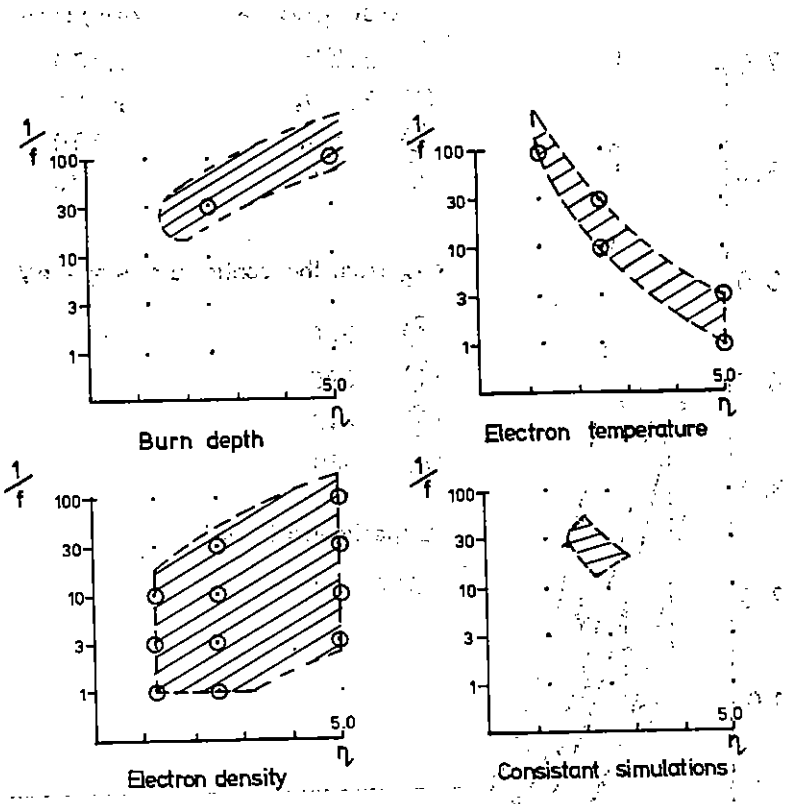

Fig.4.10

Computer simulations of the X-ray emission from Aluminium coated microballoons. The points indicate the individual runs, and the circles indicate the runs which agree with the experimental parameter at the foot of each diagram. The fourth diagram indicates the region where all experimental parameters are reproduced.

to increase the growth rate of an ion acoustic instability is the return current of the fast electrons (section 4.4). This is under further investigation.

It therefore seems possible on theoretical grounds that turbulent ion waves cause the observed transport inhibition. This would be independent of magnetic fields, and consistent with the observation of similar inhibition in both plane and spherical targets.

4.4 Fast Electron Preheat in Layered Targets

4.4.1 Introduction

This section describes experiments performed during four weeks of single beam operation on plane layered targets. The object of these experiments was twofold. The fast electron preheat was to be measured by using the K_α yields from 'tracer' layers in targets to measure the velocity spectrum of fast electrons. This objective has been achieved: the fast electron spectra have now been measured over a range of intensities giving values of T_{HOT} which agree roughly with Xray diode measurements and moreover measure the amount of energy in the fast electrons which has not been measured by Xray diodes. In learning how to do this experiment, many misconceptions of previous experimenters have been eliminated.

The second objective was to examine the properties of the ablation plasma as in section 4.3 (burn depth) but for a plane target. Although target fabrication difficulties foiled this objective, the cold electron temperature, and some evidence for a spatial ring structure and for population inversion was obtained. Lastly, a novel type of experiment, X-ray absorption spectroscopy, was performed to examine the structure of the silicon K shell absorption edge in preheated targets.

When high intensity laser radiation is incident on a solid it is well known that the resulting plasma has both a thermal (cold) and a hot component in its electron velocity distribution and that a large fraction of the absorbed laser energy couples into the hot electrons (4.21, 4.22, 4.23). Fast ions are accelerated by the hot electrons, and

the temperature of the hot electrons T_H has been inferred from the ion velocity spectrum (4.24). A substantial fraction of the hot electron energy is transferred to the ions, and the remainder is deposited in the target causing preheating of the solid, X-ray continuum emission and K line emission.

The hard Xray (5–50 keV) continuum slope has been widely used to estimate the hot electron temperature (4.21, 4.23, 4.25). However the experimental method is not amenable to spatial resolution, and the total energy inferred in the hot electrons is sensitive to the model electron distribution function (4.26).

We report the first experiments using K_α radiation from laser produced plasmas to measure the magnitude of preheating of the solid by hot electrons, with radiation induced K_α emission and saturation of the K_α emission due to ionisation eliminated. The range and degree of the preheating, and the form of the hot electron velocity distribution are also measured. Direct measurement of this preheating has not previously been obtained. It is of importance for laser fusion target design.

Earlier work (4.27, 4,28) has attributed K_α emission to fast electrons and in a detailed study (4.29) their range and effective temperature were deduced for 10.6 μm radiation at 3×10^{13} Wcm^{-2}. Target preheating was estimated in (4.28) but consideration of ionisation effects below suggests that the conclusions of the experiment were invalid.

4.4.2 Experiment

The experiment was performed using the Rutherford neodymium glass laser in single beam mode. The laser was normally focused with a f/1 lens onto multilayered targets constructed as in Fig.4.11. The functions of the layers in Fig.4.11(a) are as follows. The aluminium and silicon layers isolate the front fluor from the thermal plasma whose burn through depth is only 0.1 μm in 100 ps. The K in KCl and Ca in CaF_2 are K_α fluorescent elements or fluors acting as fast electron detectors and the mylar is a variable thickness electron filter. Information on the fast electron energy spectrum is deduced from the Ca and K K_α yields for different mylar thickness. Some shots were fired onto targets as shown in Fig.4.11(b). There are three fluor materials present:

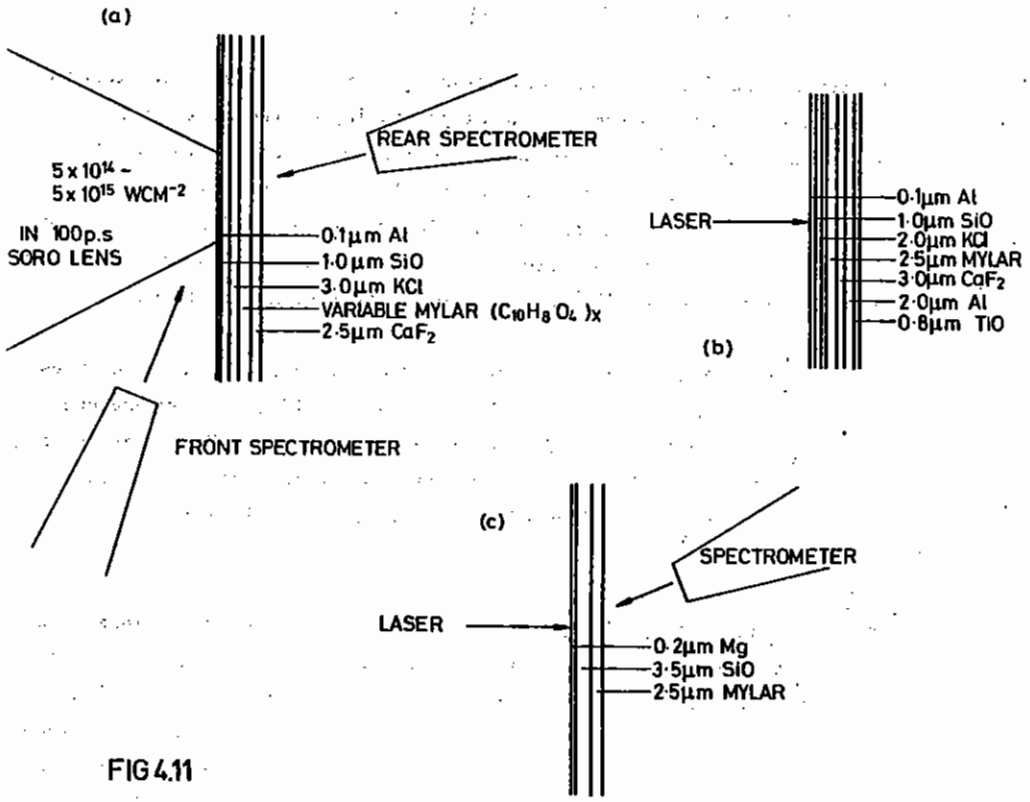

FIG 4.11

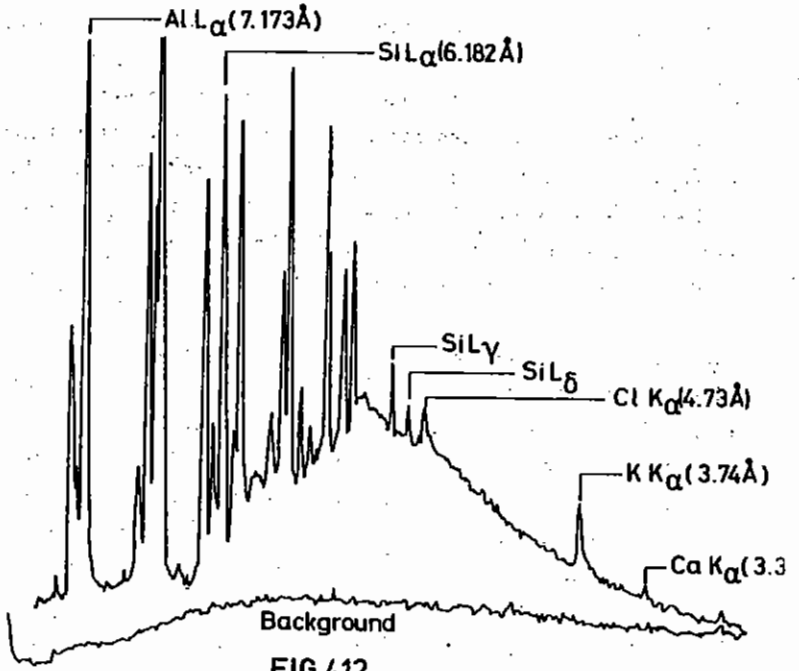

FIG 4.12

K in KCl, Ca in CaF_2 and Ti in TiO. The aim of these three fluor layer targets was to obtain more reliable electron spectrum information on a single shot basis.

In designing these targets it is important to minimise target Xray self absorption. To this end contiguous elements in the periodic table are used. With the lowest Z element at the front of the target, minimum absorption is obtained for viewing through the rear of the target. The targets were made by vacuum deposition. Even though care was taken to outgas the salt before deposition, an irregular finish was obtained for targets which contained KCl. Thus for these targets it was important to separate the fluors by a layer of mylar.

The targets were irradiated by 20J of 1.06 μm radiation in 100 ps. The minimum focal spot size is less than 50 μm but the focusing was varied to give a variable power density. The extent of the equivalent focal plane was photographically measured and this coupled with the X-ray pinhole picture and incident energy gave the intensity. A detailed study was made on the electron distribution produced with a 100 μm focal spot ($\sim 2 \times 10^{15}$ Wcm^{-2}). The laser prepulse level was monitored on each shot and an acceptable pre-pulse level was taken as not greater than 2×10^{-5} of the main pulse energy.

Xray spectra were recorded with two flat crystal spectrometers which were sensitive enough to give single shot exposures. The reflectivities of the crystals have been measured (4.30) and the spectrometers are hence absolutely calibrated. The spectrometers were positioned as shown in Fig.4.11(a). The front spectrometer was space resolving by a means of a 12 μm or 25 μm entrance slit. A typical microdensitometer tracing of a spectrum taken by the rear, spatially integrating spectrometer, using a PET crystal (2d = 8.74 Å), is shown in Fig. 4.12. The K, Ca and Cl K_α emissions are seen together with ionised aluminium and silicon lines and the silicon recombination continuum. Subsidiary diagnostics were an Xray pinhole camera and an Xray diode array.

4.4.3 Factors affecting the K_α yields from laser plasmas

(a) The production of K_α lines

Two important Z related effects in the fluor are now discussed. Firstly, a judicious choice of fluor material must be made. Ionisation of the fluor gives rise to a shift in the spectral position of the K_α emission (4.31). When this shift is large the K_α emission is not detected as such. The bulk of the energy deposited by electrons goes into heating and ionising the fluor and only a small fraction (eg about 1% for Ca and E_e = 20 keV) goes into K ionisation. A saturation level of the K_α yields is therefore reached and is defined by the fluor becoming sufficiently ionised to produce a large shift. Large shifts occur only when electrons are removed from the L shell so to maximise the K_α yield a fluor whose Z is appreciably larger than ten is needed. The saturation energy for a Z-10 ionised fluor is:-

$$U_s = Na\left(\sum_{n=1}^{Z-10} E_i^{\,n} + 1.5k((Z-10)T_e + T_i)\right)$$

where $E_i^{\,n}$ is the ionisation potential of ionisation stage n and Na is the number of fluor atoms under the focal area. This is the total electron energy deposition. The instantaneous ratio of energy deposited into K shell ionisations (which can be liberated as K_α photons) to total energy deposition, R(E) is given by

$$R(E) = \frac{\sigma_K(E)\, E_K}{m_A \; {}^1/\rho \; \partial E/\partial S}$$

where $\sigma_K(E)$ is the K ionisation cross-section (4.32), m_A is the fluor atomic mass, and ${}^1/\rho \; \partial E/\partial S$ is the linear electron stopping power. R(E) is well approximated by

$$A \;\; \ln(E/E_{K_I})/\ln(2 \times E/E_I)$$

where E_I is the mean excitation energy, E_{K_I} is the K ionisation potential and A is a constant for the fluor.

For electron energies greater than about 15 keV and for $19 \leq Z \leq 22$ R(E) is nearly constant with electron energy and is around 1% (Fig.4.13). The saturation K_α yield for the unshifted line is thus $U_s R\omega$ joules where ω is the fluorescence yield.

In our calculations of saturation yields an LTE equation of state was assumed to obtain the electron temperature (4.33). In Table 4.02 the saturation K_α yields per atom for various elements and densities are shown together with Z and Te. Notice that the saturation yields are much larger for $Z \sim 10$ than for Si or Ne.

In previous work (4.28), this saturation effect has been ignored. It has been reported that both Ne K_α and Si K_α have been observed from irradiation of thin wall microballoons. However using the method described above we estimate the saturation energy of electron pumped Ne K_α to be 5.0×10^{-7}J (for their 10^{14} atoms) compared with the reported observed yield of 2.0×10^{-4}J.

In microballoon work at the Rutherford Laboratory neither Si K_α nor Ne K_α lines have ever been observed. In some microballoon targets the glass of the microballoon has been coated with 1 μm of CaF_2 (section 4.7). A microdensitometer tracing of this spectrum is shown in Fig.4.14, in the region of the Ca^{18+} $1^1S_o - 2^1P_1$ resonance line. The Ca K_α line is just visible and in the region in between an enhanced continuum is seen indicative of K_α like transitions from highly ionised states of Ca.

The K_α lines are only just seen in this case because we have used a high Z fluor. The saturation yield for the amount of Ca on this target is 0.9 10^{-5}J/st compared with the observed 0.7 10^{-5}J/st. The Si K_α line would not be observable as the saturation yield is an order of magnitude lower.

There is a second reason for using a high Z fluor. Significant energy is carried by the soft X-ray (2Å - 10Å) continuum. X-rays of energy greater than E_{K_I} are very efficient at producing K ionisations. If Z is too low there is a danger that the observed K_α emission is dominated by radiation pumping. It is thus desirable that E_{K_I} be greater than kT_C the cold continuum temperature, but not so high that E_{K_I} is comparable with kT_H. In our experiment the fluors used are Cl, K, Ca and Ti with E_{K_I} = 2.82, 3.62, 4.04 and 4.97 keV respectively. The chlorine was included to observe radiation pumping. A specific calculation of radiation pumping is presented below.

(b) The observation of saturation and radiation pumping

The saturation and radiation pumping effects described above were demonstrated experimentally. Figure 4.15 shows a microdensitometer tracing of the K K_α emission coming from the front fluor layer. Here the energy deposition is greatest. Short wavelength shifted components are clearly seen. The energy in the unshifted, shaded, component is $1.4 \pm 0.1 \times 10^{-5}$ J sr^{-1} and the energy in the shifted component is $0.8 \pm 0.3 \times 10^{-5}$ J sr^{-1}. The calculated saturation energy for a 100 μm by 3 μm deep emitting volume of KCl is 2.0×10^{-5} J sr^{-1}, in fair agreement with the measured, unshifted yield. The observed peaks should be compared with the predicted positions of the K_α like emissions from (4.31). The 3/2 NkT-electron energy was included in this calculation.

To demonstrate radiation induced K_α emission a 25 μm mylar target with KCl on the rear was irradiated with a larger focal spot and hence a lower flux density. The less energetic fast electrons were unable to penetrate to and activate the rear fluor layer. This was corroborated by the absence of K K_α emission. However the Cl K_α yield was measured to be $1.3 \pm 0.1 \times 10^{-6}$ J sr^{-1}. The soft Xray continuum was virtually the same as with the higher flux density and was measured to be $I(\nu) = I_o e^{-h\nu/kT_c}$ where $kT_c = 500 \pm 100$ eV and $I_o = 6.0 \pm 1.0 \times 10^{-5}$ J sr^{-1} eV^{-1}. The induced K_α emission due to this continuum is calculated as follows (see Fig.4.16). If the continuum intensity is $I(\nu)$ J sr^{-1} eV^{-1} then the number of photons emitted into $dh\nu\, d\theta = (I(\nu)/h\nu)dh\nu d\Omega = I(\nu) \sin\theta \cdot 2\pi/h\nu\, dh\nu d\theta$. These are attenuated in the layers by

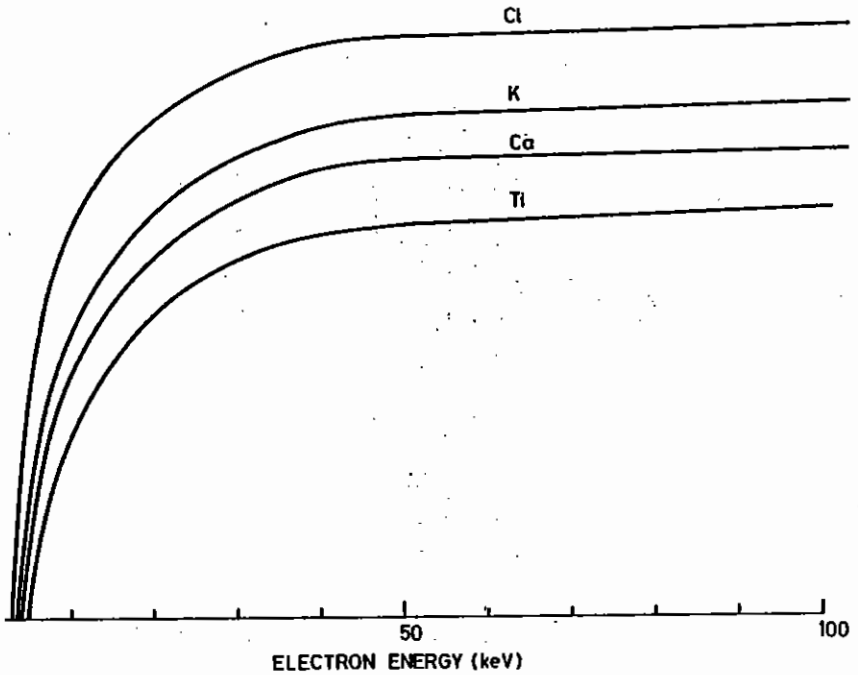

FIG.413.R(E) AS A FUNCTION OF ELECTRON ENERGY

FIG. 414. Ca XIX $1^1S_0-2^1P_1$ AND Ca Kα FROM CaF_2 COATED SHELL OF MICROBALLOON. LASER ENERGY=30J SHOT 248

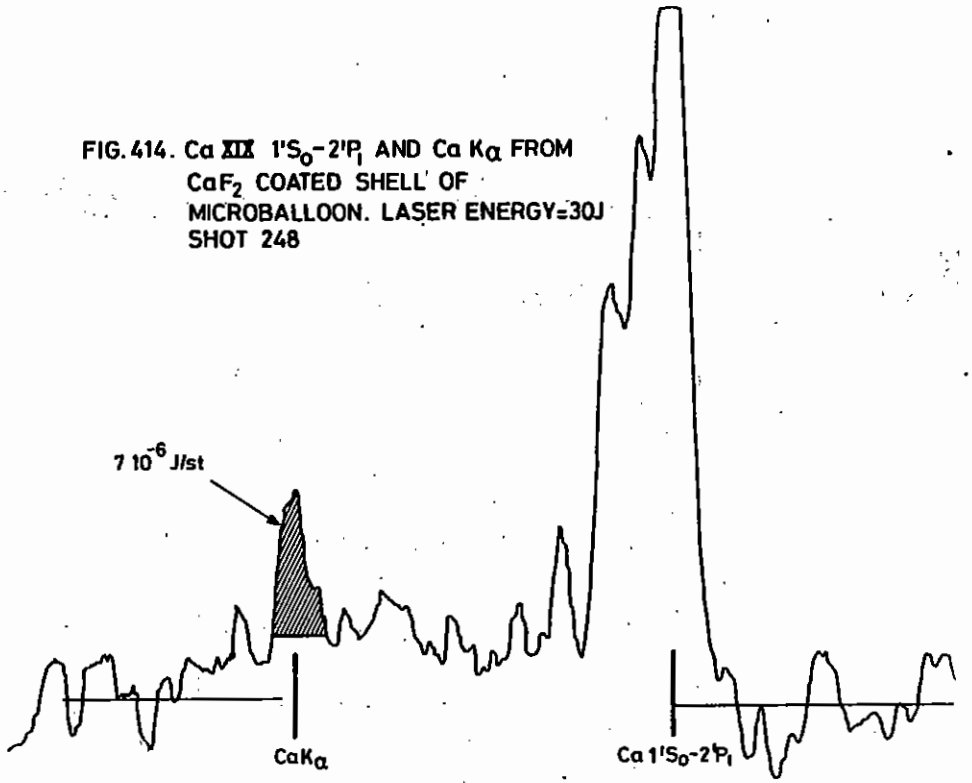

FIG 4.14

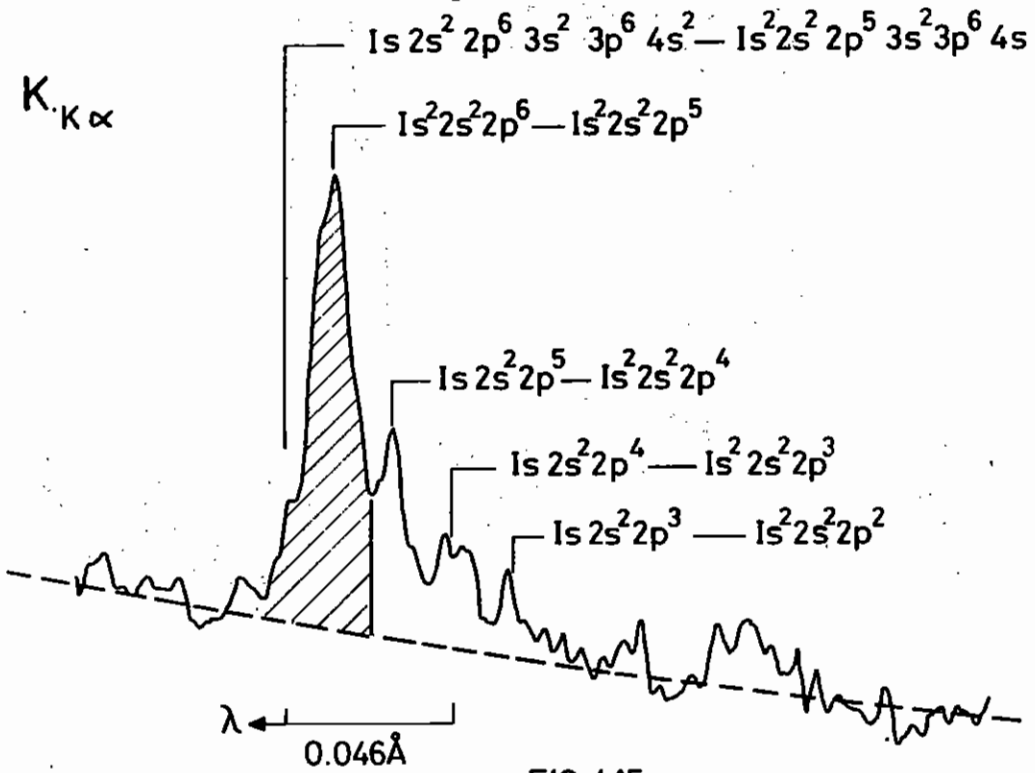

FIG 4.15

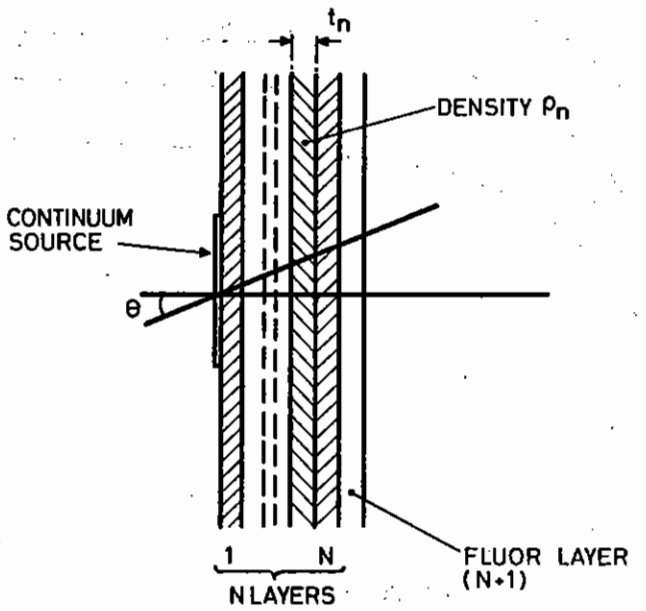

FIG. 4.16. GEOMETRY OF RADIATION PUMPING

$$A(h\nu, \theta) = \exp\left(-\sum_{n=1}^{N} (t_n \mu_n(h\nu) / \cos\theta)\right)$$

A fraction, F, is then absorbed

$$F(h\nu, \theta) = 1 - \exp\left(-t_{N+1}\mu_{N+1}(h\nu) / \cos\theta\right)$$

The total number of photons, sufficiently energetic to cause K ionisation, absorbed in the fluor, is

$$N_p = \int_0^{\pi/2} \int_{E_{K_I}}^{\infty} A(h\nu,\theta)F(h\nu,\theta)I(\nu)\sin\theta \cdot 2\pi/h\nu \, dh\nu \, d\theta$$

A fraction, B, of these photons cause K ionisation events

$$B = \left(1 - \frac{1}{J_R}\right) \cdot \mu_1/(\mu_1 + \mu_2)$$

where J_R = attenuation coefficient jump ratio at the K absorption edge and $\mu_1/(\mu_1 + \mu_2)$ is the fraction of the absorbed photons going into the fluor element. This fraction is nearly constant with $h\nu$ (incident) for $h\nu > E_{K_I}$. Each K ionisation event liberates $\omega . E_{K_\alpha}$ joules into 4π steradians, and therefore the total radiation pumped K_α yield is

$$Y = N_p B \, \omega E_{K_\alpha} / 4\pi \quad J\ sr^{-1}$$

The calculated Cl K_α yield induced by this continuum emission was 1.7×10^{-6} J sr^{-1}, in fair agreement with the experimentally observed $1.3 \pm 0.1 \times 10^{-6}$ J sr^{-1}. It should be noted that the predicted radiation pumped K K_α yield is only 0.3×10^{-6} J sr^{-1} which is small compared with the lowest observed yield of 2.0×10^{-6} J sr^{-1}. The radiation pumped Ca and Ti emissions are completely insignificant.

(c) Calculation of K_α yields for various electron distributions

To obtain the fast electron energy spectrum the K_α yields for various electron energy distributions must be theoretically predicted. Spencer (4.34) has made extensive computational calculations on electron

energy deposition in plane targets and these are the basis of our calculations of the K_α yields. We have also checked the calculation by measurements on a low current electron beam.

Spencer's calculations were performed only for single material targets and must be applied to multiple layers. The energy deposition in the target due to an incident electron of energy E_o in a layer dx can be expressed as

$$\left(\frac{\partial E}{\partial x}\right)dx = \left.\frac{\partial E}{\partial s}\right|_{\substack{x=0 \\ E=E_o}} \cdot f(x) \cdot g(x) \cdot dx$$

where f(x) is the ratio of actual path length of the electron passing through dx to dx, and g(x) is the linear electron energy deposition rate in dx divided by the initial energy deposition rate at E_o.

The non-relativistic linear energy deposition rate as given by the Bethe Bloch formula(4..35) is, $\left(\frac{\partial E}{\partial s}\right) \sim K \ln\left(\frac{2V}{V_i}\right)$. Thus if E(x) is the average electron energy in dx then,

$$g(x) = \frac{K \ln E(x) - \ln V_i}{K \ln E_o - \ln V_i}$$

and if $E(x) > V_i$

$$g(x) = \frac{\ln E(x)}{\ln E_o}$$

It is now assumed that the scattering (f(x)) and average energy (E(x)) in the target can be approximated by taking an average Z throughout it. This is reasonable since the scattering and stopping power of the target is not a strong function of Z and the overall effect on the fluor is the cumulation of scattering and energy deposition in each layer. Our targets have $\bar{Z}$ in the range 7 → 18.

Thus the energy deposition in a multilayer target by an incident electron is

$$dE = \left.\frac{\partial E}{\partial s}\right|_{\substack{Z \\ E_o \\ x=0}} \cdot g_{\bar{Z}}(x) \, f_{\bar{Z}}(x) \cdot dx$$

which in Spencer's notation is

$$dE = \frac{1}{\rho} \left(\frac{\partial E}{\partial s}\right)_{r_{Z^o}} \cdot J_{\overline{Z}} \left(\frac{x}{x_{o_{\overline{Z}}}}\right) \rho_Z dx$$

$x_{o_{\overline{Z}}}$ = integrated linear Bethe-Bloch range.

Of the energy deposited by the electron a fraction R(E) goes into K shell ionisation. The ratio R(E) as a function of electron energy E is shown in figure 4.13. It should be noted that for energies above 15 keV the ratio is nearly constant.

Of the energy going into K ionisations a fraction ω reappears as K_α radiation, where ω is the fluorescence yield. The K_α yield per electron is given by

$$Y(E) = \frac{1}{4\pi} \frac{1}{\rho} \left(\frac{\partial E}{\partial s}\right)_{E_{Z^o}} J_{\overline{Z}} \left(\frac{x}{x_{o_{\overline{Z}},E_o}}\right) \rho_Z \, dx \cdot R(\overline{E}) \cdot \omega \; J \; sr^{-1} \; e^{-1}$$

The average electron energy $\overline{E}$ was assumed to drop linearly to zero over the residual range. This assumption leads to inaccuracy only at low electron energy, since R(E) is constant for energies over 15 keV.

To find the K_α yields at low energies reliably and verify the calculation at high energies an electron beam was focused onto duplicate targets. The K_α energies were measured using the crystal spectrometer from the laser experiment. The electron beam supplied 0.1μ A at 15 to 50 keV into a 200μ diameter spot. The response of each fluor layer to monoenergetic electrons was measured over this voltage range. Again because the spectrometer is absolutely calibrated the absolute K_α yields per incident electron were obtained. The full K_α yields constructed from the calculation and calibration for the variable mylar targets used are shown in Fig.4. 17. Note the good absolute agreement between the calculation and calibration, adding confidence to the absolute energy calibration of the spectrometers.

The K_α yield for a given model electron energy distribution can then be calculated from

$$\text{Yield} = \int_0^\infty Y(E) \; n(E) \; dE$$

where n(E) is the electron distribution passing into the surface of the target. As a further check on the calculations the K_α yields were calculated for a solid Ti target and compared with the results of (4.36) for an incident electron energy of 29 keV. The yields are shown in Fig.4.18. The good agreement adds further confidence to the above method of calculation.

4.4.4 Results

(a) Ablation plasma

In some of our early experiments the spectrometer viewing from the front was used in a space resolving mode. A print and microdensitometer scans of a plate from this spectrometer are shown in Fig.4.19. The viewing direction for this spectrometer was at an angle of 70° to the incident laser direction and so there is good axial spatial resolution. The plate shows the helium and hydrogen like lines of Al and Si (except Al XII $1\,^1S_o - 2\,^1P_1$) recombination continuum and, faintly, Ca K_α. The temperature of the ablation plasma can easily be obtained from such spectra. The most reliable way is to use the slope of the recombination continuum (4.37). Alternatively the ratio of high order members of the spectral series can be used to measure ground state densities of the next stage of ionisation (4.38). A collisional radiative equilibrium model of ionisation then gives the electron temperatures. In Fig.4.20 the results of this analysis are presented giving T_e as a function of intensity; the intensity variation here was achieved by defocusing the target. Notice that the temperatures achieved at $I \sim 10^{15}$ W/cm^2 are the same as the temperatures measured in the ablation plasma of microballoons at the same intensity (section 4.3) implying similar transport inhibition in plane targets as in microballoons. Also note that the dependence on intensity is very weak.

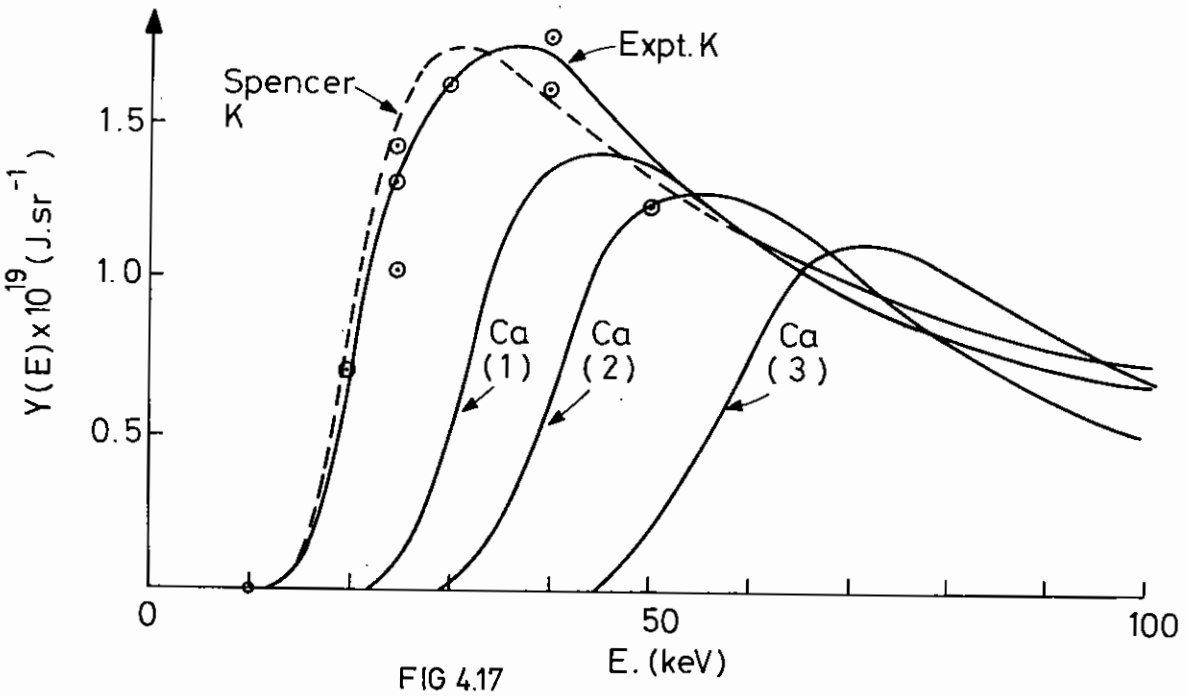

FIG 4.17

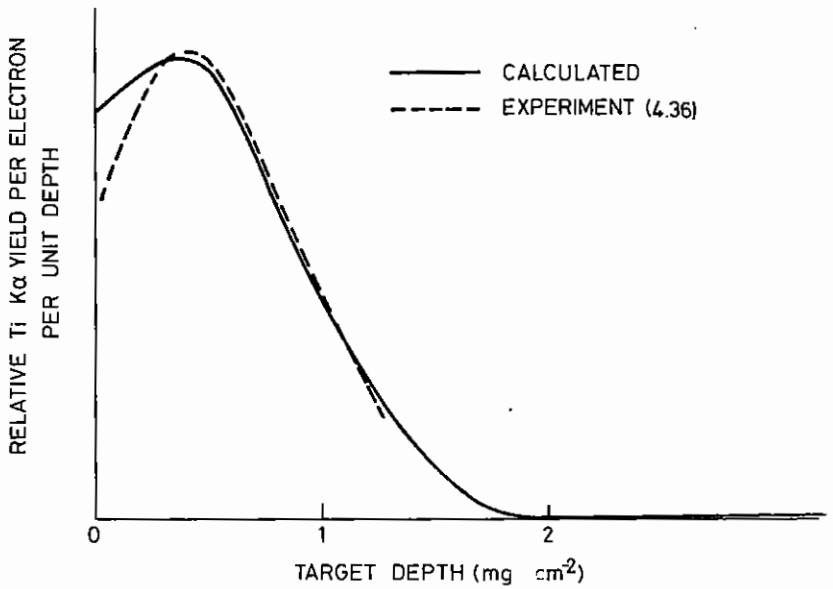

FIG. 4.18. EXPERIMENTAL AND PREDICTED Ti Kα YIELD AS A FUNCTION OF DEPTH FOR E_e = 29keV

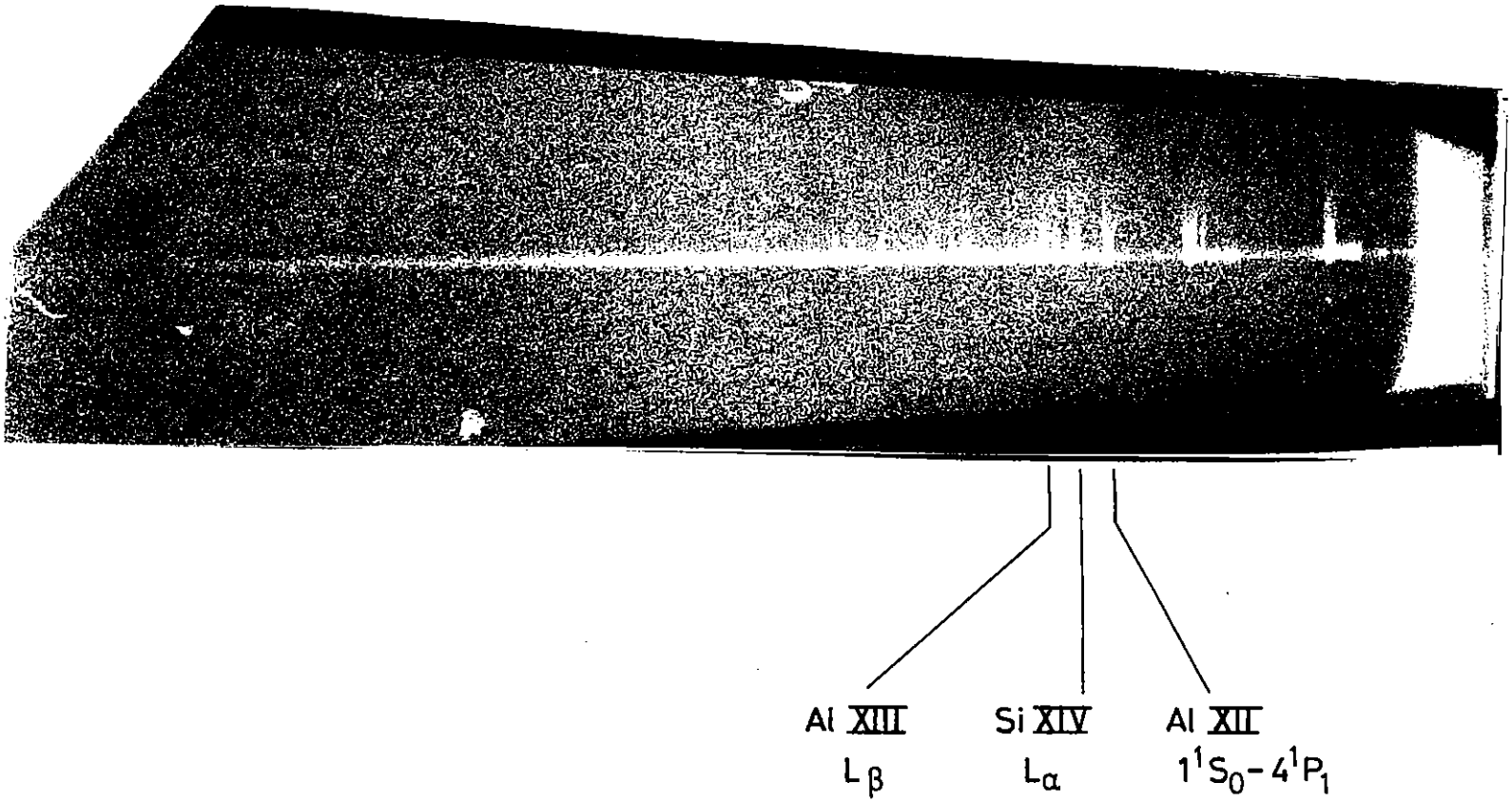

FIG 4.19(a) SHOT 137 25J, 150μm

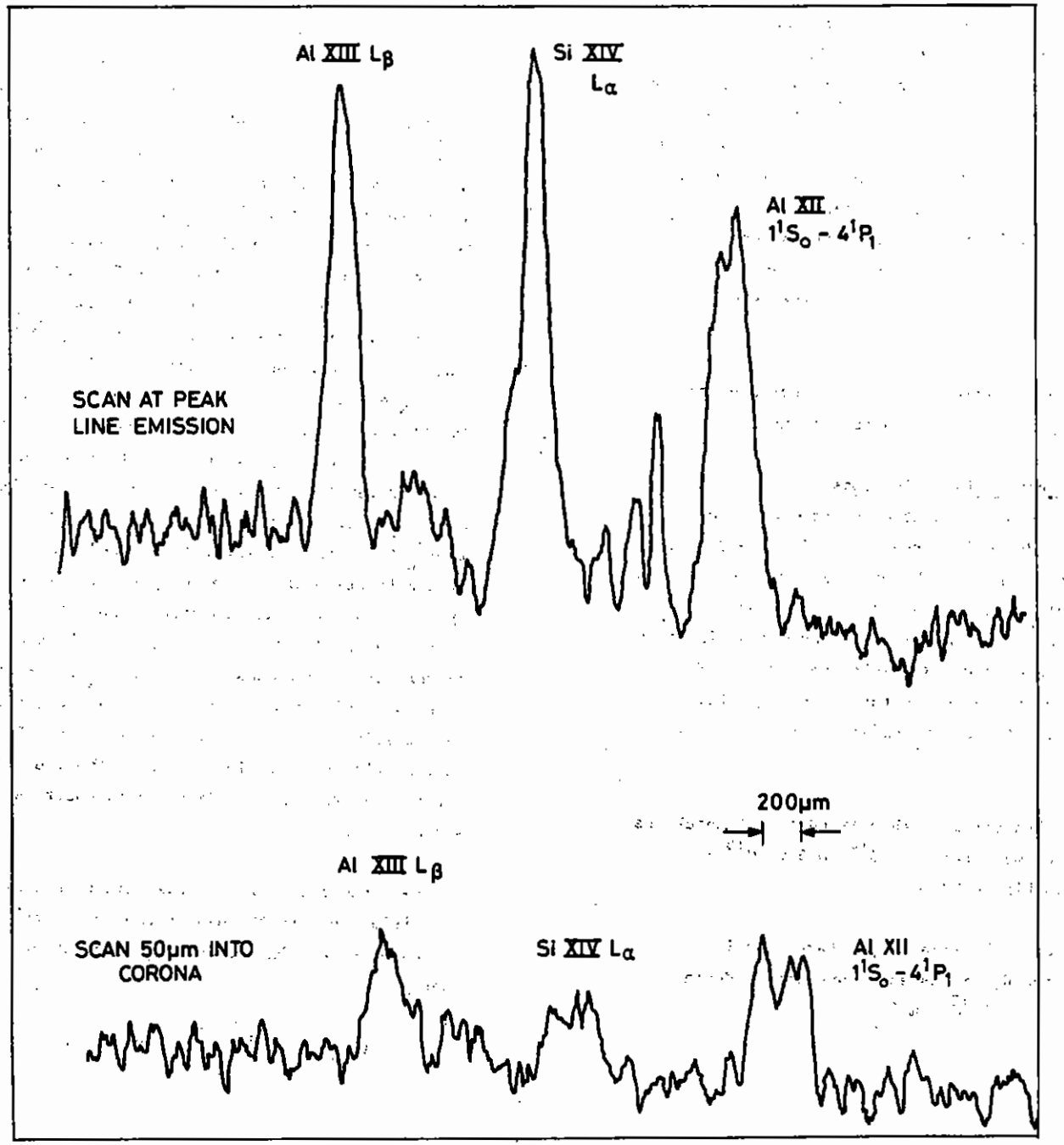

FIG 4.19 (b) MICRODENSITOMETER SCANS OF 4.19 (a)

The plate in Fig.4.19 also shows evidence of a ring structure of line emission in the expanding plasma. The spectral line broadening is small compared with the broadening caused by the finite size of the emitting region. Thus a scan in the spectral direction across any one line is equivalent to a spatial scan across different chords of the expanding plasma plume. The emissivity clearly has a dip in its centre as the plasma expands away from the surface. A similar phenomenon has been observed in other laboratories (4.15) and has been attributed to magnetically produced hot spots (4.39). However, in our series of experiments this phenomenon was not reproducible. On most shots a ring structure was not evident.

The last observation to be made concerning Fig.4.19 is evidence for population inversion in the expanding cooling plasma plume.

(b) Experimental measurements of fast electrons

The fast electron energy spectrum and preheat were measured as a function of laser intensity and depth in target. Initially a detailed study with fixed focusing conditions, and hence incident intensity, was made to investigate the form of the distribution. The intensity on the target was $2.0 \pm 0.5 \times 10^{15}$ wcm^{-2}. The mylar thickness was varied from 2.5 μm to 50 μm and the absolute Ca and K K_α yields were recorded. These are shown as a function of depth in the target in Fig.4.21. 50 μm of mylar was sufficient to stop any K_α emission from the rear fluor.

The focusing conditions were then varied with a fixed target thickness. The intensity range investigated was from 5×10^{14} to 5×10^{15} W cm^{-2} and the yield ratio is shown in Fig. 4.22.

Several shots were then fired onto the three layer target as in Fig. 4.11(c). Fig.4.23 shows the K_α yields as a function of depth in target for an intensity of 2.2×10^{15} ωcm^{-2}.

(c) Fast electron spectrum

The form and temperature of the electron distribution was determined by fitting K_α yields produced by various model electron energy distributions, calculated as in section 4.4.3(c), to the measured yields. It is not immediately clear what the model electron energy distribution should be. Hard Xray continuum measurements indicate a Maxwellian like distribution (4.21, 4.22, 4.23, 4.25, 4.26) but it is not known if the distribution acts as a source, in which case a velocity term enters into the preheating spectrum. This is a reflection of the controversy in the mechanisms for fast electron production. For this reason a general distribution of the form $\frac{\partial n(E)}{\partial E} = A E^{N/2} \exp(-E/kT_H)$ was chosen and values of N from 0 to 3 were tested. The yields for the targets with varying mylar thickness have been calculated for N = 0 to 3 and kT_H = 5 to 25 keV. Some of these results are shown in Fig.4.21. The hard Xray continuum was recorded by an Xray diode array in the range 10-20 keV. This radiation is produced dominantly by electrons of energy several times greater than kT_H. At these energies the behaviour of the distribution function is dominated by the exponential factor in $\frac{\partial n(E)}{\partial E}$ so the temperature inferred from the diode signals is not a strong function of N. The K_α yields, however, are produced by electrons of lower energy so the inferred temperature is a strong function of N. It is reasonable, therefore, to choose N such that the hard continuum temperature is consistent with the K_α temperature. Moreover, as can be seen in Fig.4.21, the yields for different values of N do not fit the experimental data equally well. The value of N which gives the best fit is the same N which makes the two values of T_H consistent. For the analysis of the variable intensity shots this value of N(N = 3) was assumed.

The absolute energy in the fast electron distribution and the energy deposition density throughout the target has also been calculated. The values of A and kT_H are determined as above and the total preheat energy is

$$E_{TOT} = A \int_0^\infty E\left(\frac{N+2}{2}\right) \exp\left(-E/kT_H\right) dE$$

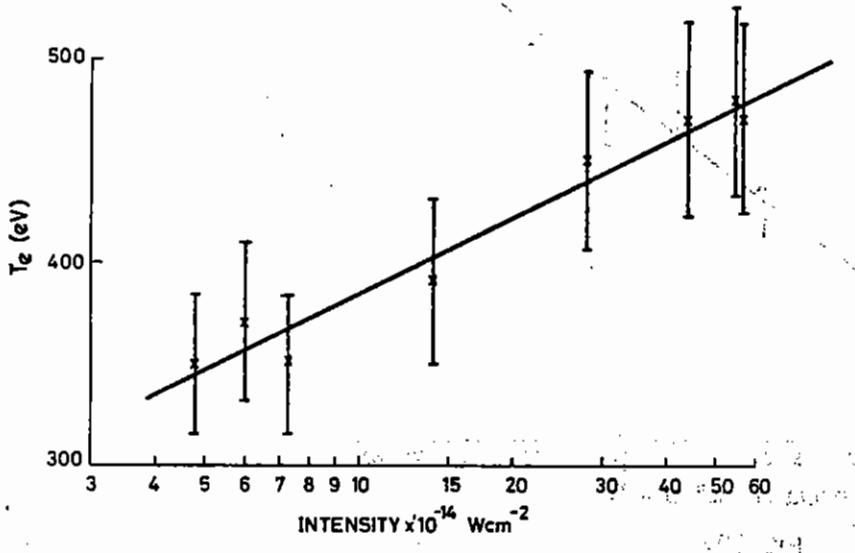

FIG. 420. COLD ELECTRON TEMPERATURE AS A FUNCTION OF INTENSITY

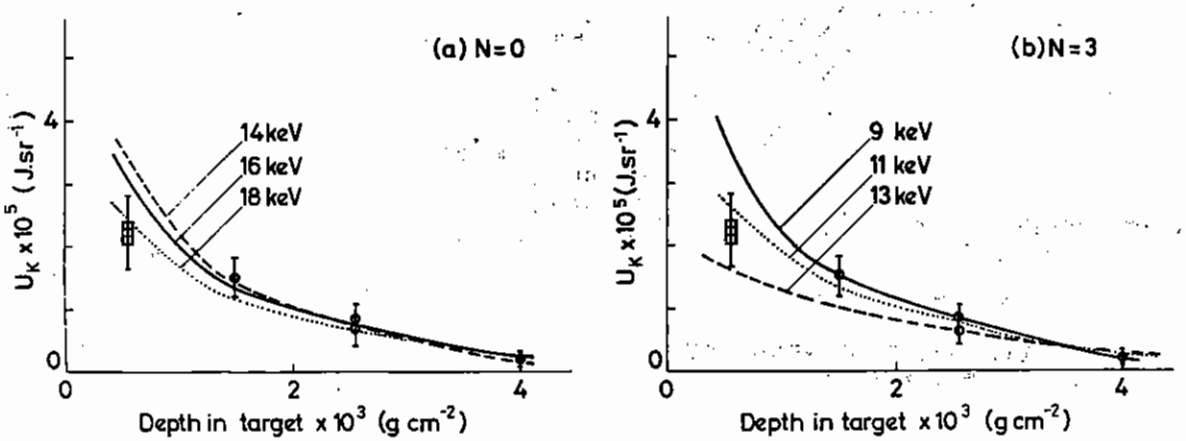

FIG 4.21

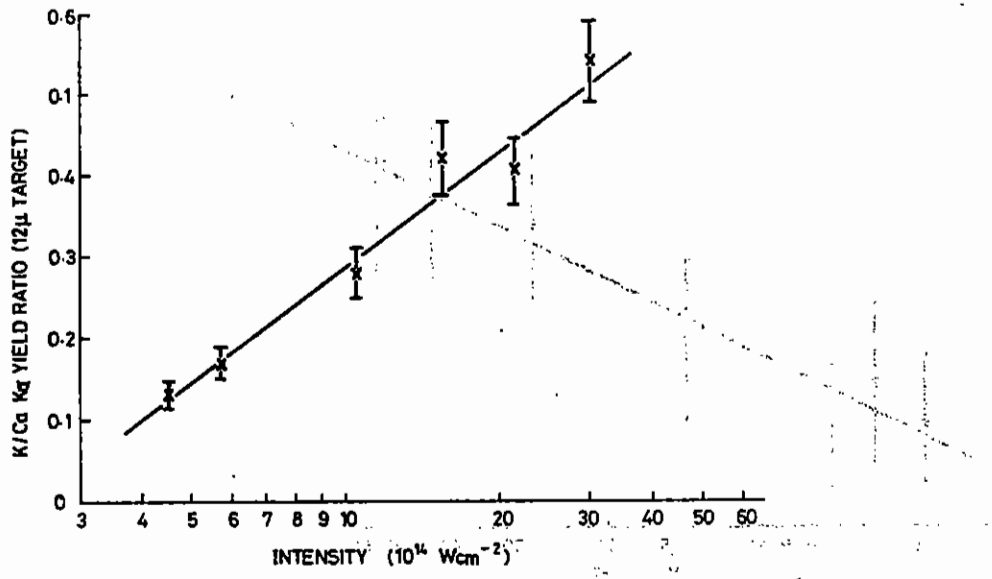

FIG 4.22

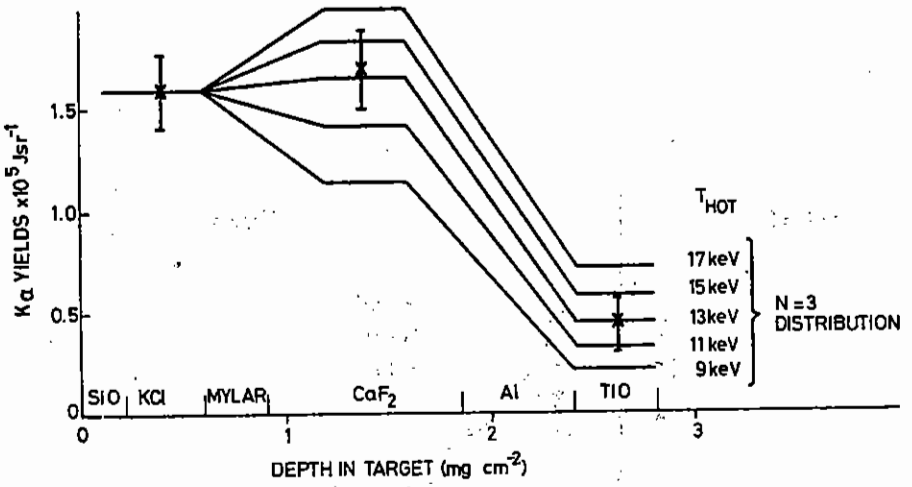

FIG.4.23. THEORETICAL AND EXPERIMENTAL Kα YIELDS FOR THREE FLUOR LAYER TARGET

It should be pointed out that E_{TOT} is almost independent of N. This is because R(E), the ratio of total energy deposition to energy into K ionisation, is almost constant and the energy deposited in the fluor is well approximated by $4\pi Y_{K_\alpha}/(\omega\bar{R})$. The energy deposition densities have been more accurately calculated using a R(E) averaged over the known energy spectrum. (See Table 4.03).

A guide to the depth to which fast electrons cause preheat is given by the characteristic preheat range, r_o which is calculated by assuming energy deposition of the form;

$$\frac{\partial E}{\partial x} = \frac{\partial E}{\partial x}\bigg|_{x=0} e^{-x/r_o}$$

Almost all the preheat energy is deposited in a depth of $2r_o$.

An electron distribution was fitted to the three fluor layer target. Predicted yields for T_H = 9 - 17 keV and N = 3 are shown with the experimental yields in Fig.4.23. As for the two-fluor targets, $T_H = 11 \pm 2$ keV.

The hot electron temperature determined from the K_α yields, the fraction of the incident energy going into fast electrons and the characteristic preheating range are shown as functions of the incident intensity in Figs.4.24(a), 4.24(b) and 4.24(c) respectively.

As is evident from Fig.4.24(b) there is no very clear trend in the variation of the fractional energy coupling into fast electrons with intensity, although it is possible that the coupling is better at high intensity. The average coupling of ∿12% is consistent with the overall expected energy balance with 35% (4.23) of the incident energy absorbed, 60% (4.22) of that going into fast ions, a small fraction going into the ablation plasma and the remainder appearing as fast electron preheat.

TABLE 4.03

Total energy deposition in fluor compounds

Fluor layer (Mylar thickness)	Depth in target mgm cm^{-2}	Deposited energy Joules	Deposited energy density J cm^{-3}
KCl (top)	0.56	0.40	1.4×10^7
CaF_2(2.5 μm)	1.58	0.24	1.0×10^7
CaF_2(12.5 μm)	2.81	0.12	5.1×10^6
CaF_2(25 μm)	4.50	0.04	1.7×10^6

TABLE 4.04

Target potential as a function of time

Time (ps)	Potential (eV)
5	138*
15	235
25	226
35	217
45	201
55	200

* used cut off of ln Λ at 1/8
(if value of 1 used potential would be higher)

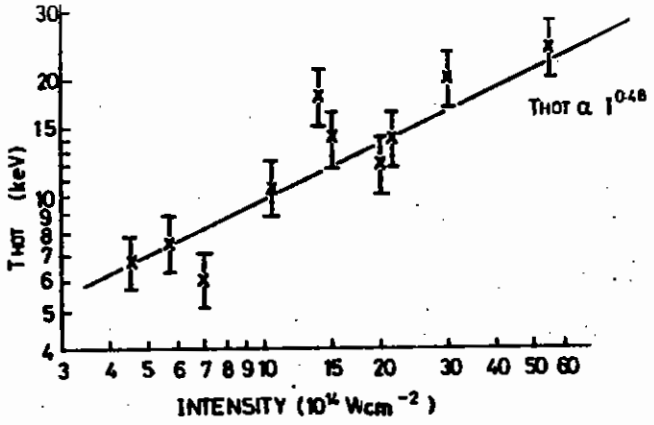

FIG 4.24(a)

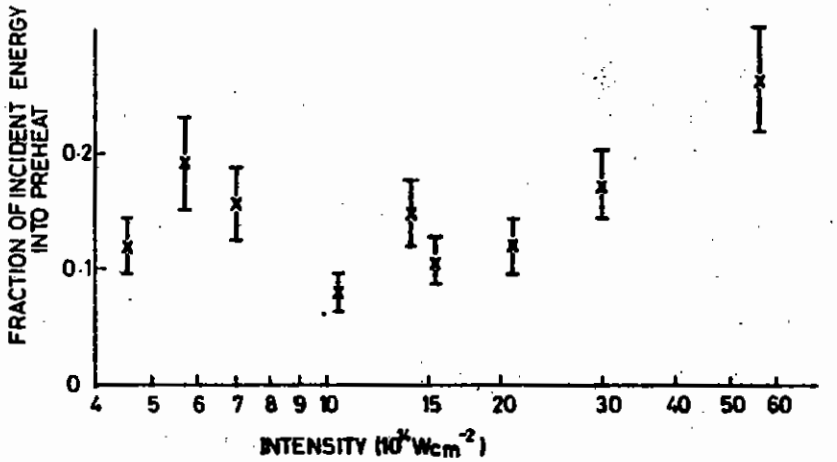

FIG 4.24(b)

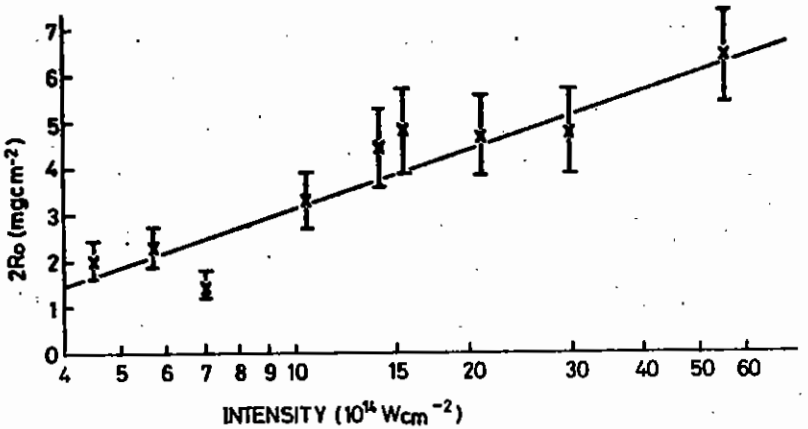

MEASURED RANGE OF PREHEATING AS A FUNCTION OF INTENSITY.

FIG 4.24(c)

The variation of T_H with intensity shown in Fig.4.24(c) agrees well with independent measurements of the Xray continuum (4.21).

(d) Spatial extent

The K_α emission was spatially resolved by the front spectrometer, by means of a slit. A spatial tracing of the K_α emission from the rear of the target is shown in Fig. 4.25 together with a tracing of the pinhole picture at the same magnification. The spatial resolution from the spectrometer was poor because of the oblique viewing angle. The front and rear emitting regions are clearly the same size. The pinhole images the thermal plasma whereas the K_α tracing images the extent of the fast electrons at the rear of the target. Since the extent of the fast electrons at the rear is the same as their source the distance at which reflexing of outward travelling electrons in their self-consistent electric field occurs must be small compared to the focal diameter.

(e) The spectral positions of the K shell absorption edge in preheated targets

As described above the spectral position of the K_α line is a good diagnostic of the state of ionisation of a target. As the K_α transitions are inner shell transitions they are insensitive to outer shell ionisation. In contrast, the position of the K shell absorption edge is sensitive to outer shell ionisation, although its usefulness as a diagnostic is reduced because of the plasma depression of the ionisation potential.

An experiment was performed using the layered target shown in Fig.4.11(c). A layer of SiO was deposited on a mylar substrate. To observe the Si K edge, a layer of Mg was deposited on the SiO, and was irradiated with 20 J of laser energy in a 150 μm spot. A spectrum was taken viewing through the target and is shown in Fig. 4.26. The Mg helium-and-hydrogen-like lines are seen, together with the Mg recombination continuum through the SiO. The nearby Mg Lγ and Si XIII $1^1S_o - 2^1P_1$ emission lines show that the wavelength of this edge is 6.65 ± 0.03 Å (cf 6.73 Å, the position of the K edge of Si).

Theoretical values for the spectral position of the K edges can be obtained. If the state of ionisation of an isolated Si atom is k then the energy of configuration is

$$E_i = -\sum_k^{13} I_k$$

This is the initial state for a K shell ionisation event; the final state is of the form $1s2s^s2p^6$ ... and its energy is given in the tables by House (4.31). The difference corresponds to the position of the K edge. There is a slight error in House's calculations, which is allowed for by matching the theoretical value for SiI to the measured value. The resultant values of the position of the edge are shown in Fig. 4.27. As expected with increasing state of ionisation it becomes harder to remove inner shell electrons and the energy of the absorption edge increases. The shift is in fact some fraction (about $\frac{1}{2}$) of the appropriate ionisation energy.

Using the observed position of the absorption edge from Fig. 4.26 the state of ionisation of the SiO would be SiIII. However, from the experiments on the K_α lines a much higher state of ionisation is expected because of fast electron preheating. This could be consistent with the position of the K_{abs} edge if the depression of the ionisation were included. This depression would be large for a high density, low temperature, plasma and would tend to cancel out the shift due to the increasing ionisation.

4.4.5 Discussion

Our analysis of electron energy deposition is not exact. The electron stopping material is not solid as in Spencer's formulation, so there will be some deviation from the Bethe-Bloch stopping formula due to ionisation. Electric fields generated in the target will also modify the electron energy deposition. To investigate the shortcomings of our 'linear' analysis (ie no electric fields) a Monte Carlo electron penetration and energy deposition program has been written (section 8.4).

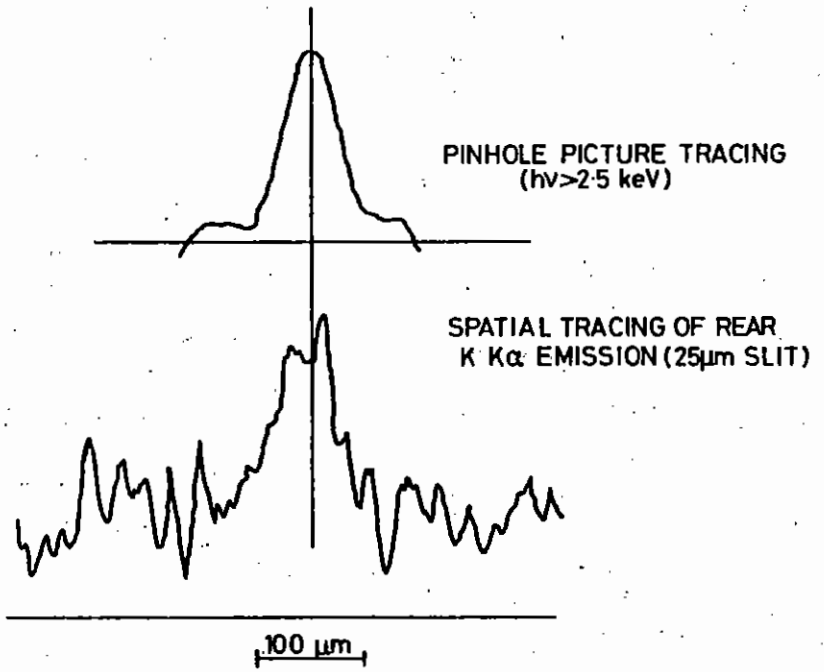

FIG 4·25

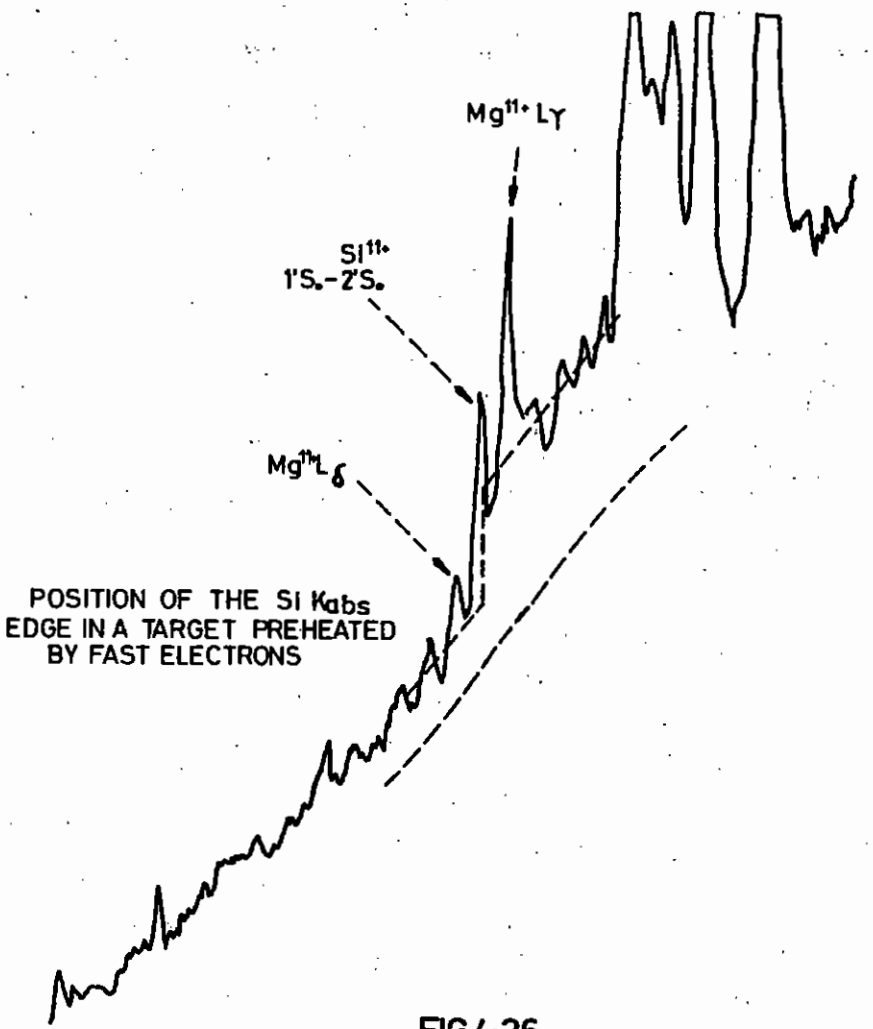

FIG 4·26

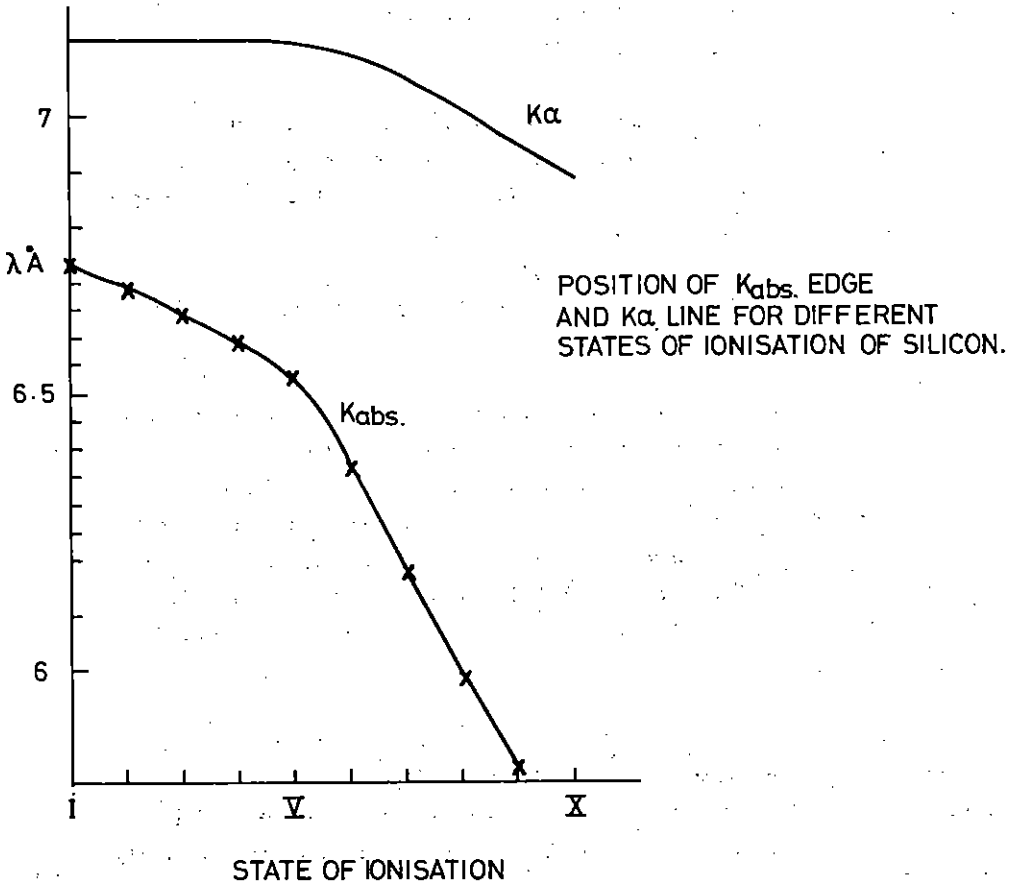

POSITION OF $K_{abs.}$ EDGE AND Kα LINE FOR DIFFERENT STATES OF IONISATION OF SILICON.

FIG 4·27

An incident electron flux of the form $AE^3/2\ \exp(-E/kT_H)$ was used with T_H = 11 keV and A chosen such that 2 joules was deposited in a 100 μm spot in 100 ps. The target was solid density carbon and a LTE equation of state was assumed (4.33). Initially the target was taken to be uniformly at 10eV with z = 0.3. The electrostatic potential across the target as a function of time is given in Table 4.04. The ES potential developed across the target was small compared with the fast electron energy so the electric field makes only a small contribution to the electron energy loss. The solid Bethe-Bloch energy deposition rate was then compared with a more realistic computational calculation taking into account Coulomb friction, energy loss to plasma oscillations in the wake of suprathermal electrons (4.40) and modification of average ionisation potential in the Bethe-Bloch formula. It was found that the simple Bethe-Bloch form as used by Spencer was accurate to 10%.

Another potential source of error is the assumption that the fluorescence yield, ω, does not change with ionisation. Competing de-exitations, ie the emission of Auger electrons, reduce ω from unity so the removal of electrons from the outer shell might be expected to increase ω. Auger electrons originate dominantly from the L shell for K ionisations where Z is < 30 (4.41). This is clear since ω steadily increases as Z^{-4}, as does the spontaneous transition rate, down to Z=10(neon) with no electrons outside its L shell. Thus one would expect outer shell ionisation to effect ω only if the shift in L shell ionisation potential it produces is comparable to the energy of the emitted Auger electron. This energy is the difference between the K and L shell ionisation potentials. It turns out that this condition is close to the saturation condition and does not effect our analysis.

4.5 Green beam experiment

A trial experiment using a frequency doubled laser beam has shown some interesting results on the properties of the ablation plasma. These are that the burn depth of the ablation plasma is considerably greater for 0.53 μm than for 1.06 μm, the temperature of the plasma is roughly the same, and the plasma densities are similar. The results described below are in preliminary form. In particular numerical modelling has not yet been attempted.

The experiment was performed in Target Area 2 (section 1.5.1). The second harmonic crystal (section 1.2.3) was placed in the 1.06 μm beam at the position indicated in Fig.1.17 (section 1.5.1). The crystal angle was optimised using low power pulses.

The green beam was taken to the target chamber by four dielectric mirrors which gave an overall rejection of $x10^6$ at 1.06 μm and was focused on target with an f/1 ICOS doublet lens (4.42). In order to facilitate the changeover from fundamental to second harmonic irradiation the lens element spacing was left at the optimum for 1.06 μm. As a result, the distribution of the focal spot of the green beam was dominated by spherical aberration. It was calculated to be $.56 \times 10^{-4}$ cm^2 in area (4.43) which agrees with data from pinhole camera images of the plasma.

Target focusing and alignment were carried out using an expanded beam from a .528 μm argon-ion laser. Incident and backscattered green energies were monitored with calorimeters and the back-scattered green spectrum was obtained on several shots.

The targets used for this experiment were either glass microballoons coated uniformly with Aℓ, or plane layered targets. In addition to plane targets with Ca and K fluors to detect fast electrons (or radiation) as described in Section 4.4, simpler targets with variable thicknesses of Aℓ coated on 0.5 μm of SiO on top of a 3.5 μm mylar substrate were also used. The latter plane targets had a good enough surface to use for a burn depth experiment.

The main diagnostics for the experiment were two Xray crystal spectrometers. One spectrometer viewed the targets from the front at 70° to the laser axis. The crystal used was PET which enabled the Si XIII and XIV and Aℓ XII and XIII lines and recombination continuum to be recorded. This was usually used in a space integrating mode. The rear spectrometer usually had a Ge crystal allowing recording for $\lambda < 3.7$Å. The Bragg reflection integrals for Ge and PET are similar at 3.5Å but because of the geometry of the spectrometers the sensitivity at ∿3Å with Ge was 3x greater than with PET.

Shorter wavelength Xray emission was observed with a calibrated array of four Xray diodes. The light backscattered from the plasma was spectrally resolved and recorded on TRIX together with a reference split off from the incoming green beam.

The following properties of the laser plasmas produced by a green beam are evident from the preliminary analysis.

The burn depth with a green beam is two to three times larger than with 1.06 μm. Fig. 4.28 shows the ratio of Si XIII $1^1S_o - 3^1P_1$ to Aℓ XII $1^1S_o - 4^1P_1$ for 1.06 μm on microballoons (section 4.2) and for 0.53 μm on both microballoons and plane targets. The green beam energies onto target were all 3-5J compared with 6J for the infra-red; yet the burn depth is 0.25 μm of Aℓ compared with 0.1 μm of Aℓ for 1.06 μm. This confirms the results of Ref.4.44, but using a different and more direct method.

The cold electron temperature has been obtained from the slope of the recombination continuum. The spectral intensity I_ν is shown in Fig. 4.29, from which a temperature of 440 eV can be deduced. This is similar to our measurements of Te for 1.06 μm at the same intensity.

The hot electron temperature is indicated by the hard Xray continuum. In the region up to $h\nu$ = 12kV the spectrum of I_ν indicated a temperature of 5kV although the reproducibility was poor. The $h\nu$ 22kV value indicated a higher temperature. Unlike (4.44) the signal at $h\nu$ = 22 kV was only a factor of 10 smaller than obtained with a 1.06 μm beam at similar intensities.

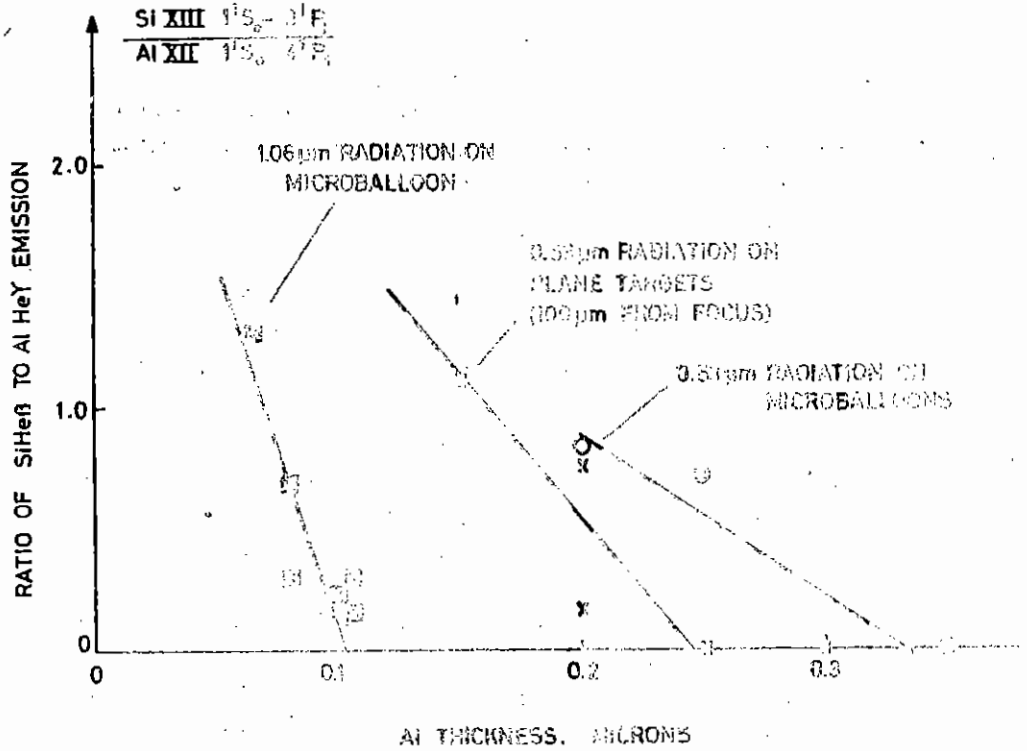

FIG 4(a) BURN DEPTH FOR 0.53μm AND 1.06μm BEAMS

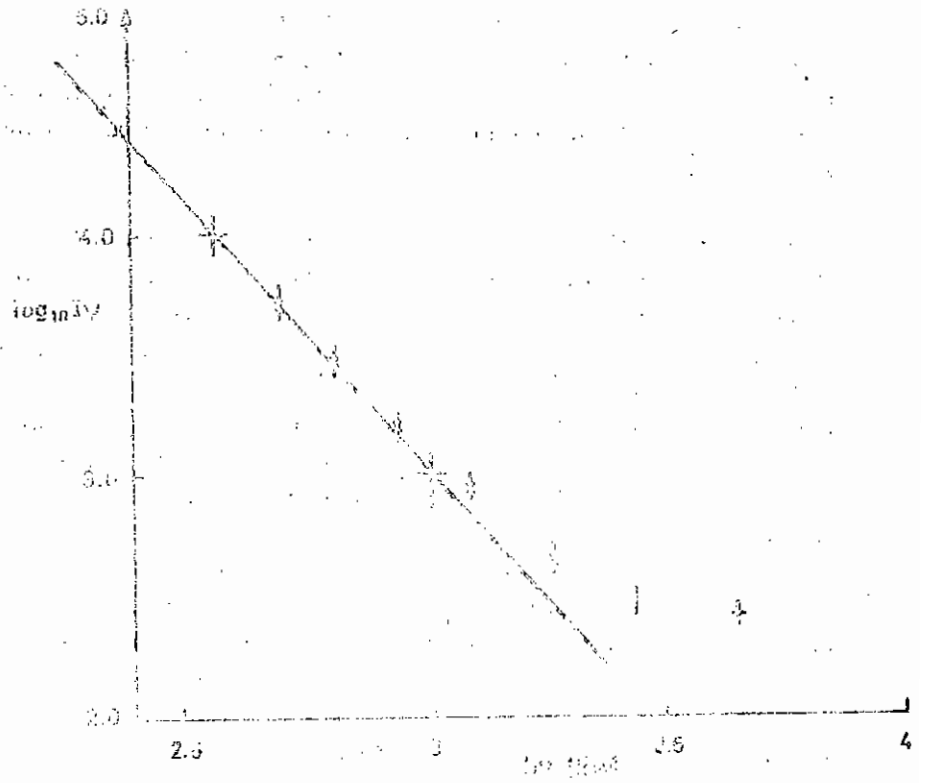

FIG 4(b) Al PROPAGATION CONTINUED FOR 0.53μm
SHOT 706

The density of the Xray emitting region was obtained by fitting the Aℓ XIII L_δ line using the technique discussed in section 4.7.1. assuming that it is optically thin. The fit is shown in Fig.4.30. Note that the deduced density is similar to the case with 1.06 μm (Sec.4.3). However, the intensity of the recombination continuum is much greater than for a plasma produced with a 1.06 μm laser. With the green beam onto a plane target the Aℓ recombination continuum was 9.9 10^{-4} J/st/keV at 4.6Å, for 4J on target. This should be compared with 3 10^{-4} J/st/keV on a similar plane target (3 10^{15} Wcm^{-2}) for 1.06 μm. This continuum intensity should be proportional to n_e^2 V δt where V is the volume of emitting plasma. If, as suggested by the line broadening, n_e is similar, then the volume of emitting plasma must be larger for .53 μm than for 1.06 μm.

A consequence of the high radiation field is radiative preheating of the target. Experiments using the KCℓ and CaF_2 targets described in section 4.4 show K_α emission. Fig.4.31 is an example of such a spectrum, recorded with the rear spectrometer. The Ca and K K_α lines shown are emitting 1.7 10^{-6} J/st and 4 10^{-6} J/st respectively. The plasma recombination continuum is also evident above the background and because the plasma is being viewed through the target the K shell absorption edges are visible. This figure graphically illustrates the radiation pumping. Because of the energy absorbed above the K_{abs} edge an appreciable fraction (ω_e = 0.16 and 0.14 for Ca and K respectively) should appear as K_α radiation. In fact the calculation of the expected radiation pumped K K_α yield (section 4.4) gives 5.6 10^{-6} J/st. in agreement with the measured yield.

The spectrum of backscattered green light is shown in Fig. 4.32. The peak of the backscattered light is shifted about 5Å to the blue. If this were solely a Doppler shift it would imply a velocity of 1.5 10^7 cm s^{-1}. Any shift due to Brillouin backscatter would increase the implied velocity.

The fraction of the incident light backscattered into f/1 is 10%, significantly lower than the 30% we observe at 1.06 μm from thick CH foils (section 4.6).

In conclusion, a preliminary analysis of this experiment has shown that the burn depth for the green beam is larger than for 1.06 μm. However it is puzzling that the ablation pressure determined spectroscopically by n_e and T_e seems the same as for 1.06 μm. Further analysis of this data is in progress.

4.6 Transport Processes in thin films

In this section we discuss an experiment to study transport processes in plasmas formed by irradiating thin polystyrene films with 100 psec pulses from a Nd-Glass laser at intensities of the order of 10^{16} W/cm^2. Data taking was completed this year.

The concept of the experiment is as follows. The incident laser pulse creates a dense, hot, plasma at the surface of the foil. The hot region spreads radially and in depth at rates depending on the thermal transport properties; the depth penetration of the thermal front may also depend on the rate at which material is ablated from the surface or on fast electron transport. As the hot material expands the plasma density drops, ultimately creating a radially expanding sub-critical density hole through which light may be transmitted.

Previous experiments with thin foils have relied on time and space integrated measurements of the fractional transmission (4.45, 4.46), of the ion fluxes from the front and back of the foil (4.47, 4.48) or of the Xrays generated in the foil (4.49). The data has been explained by invoking anomalously low thermal conductivity (445-448) or inhibition of ablation by the ponderomotive force (4.49, 4.50) with no flux inhibition.

In the present experiment time and space resolved data were obtained in addition to integrated data. Our measurements of the radial growth rate of the underdense hole show that it develops later and grows more slowly than MEDUSA or Laser B simulations predict. The time-

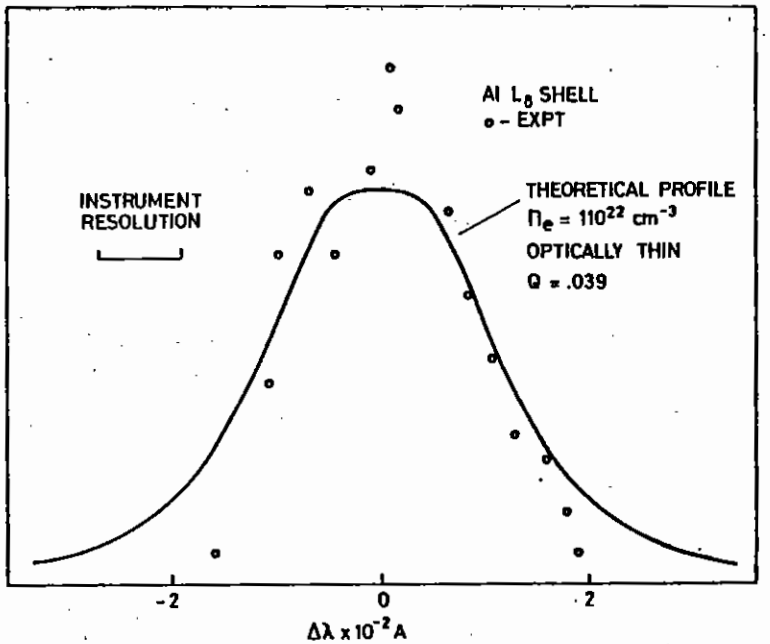

FIG 430 SHOT G133

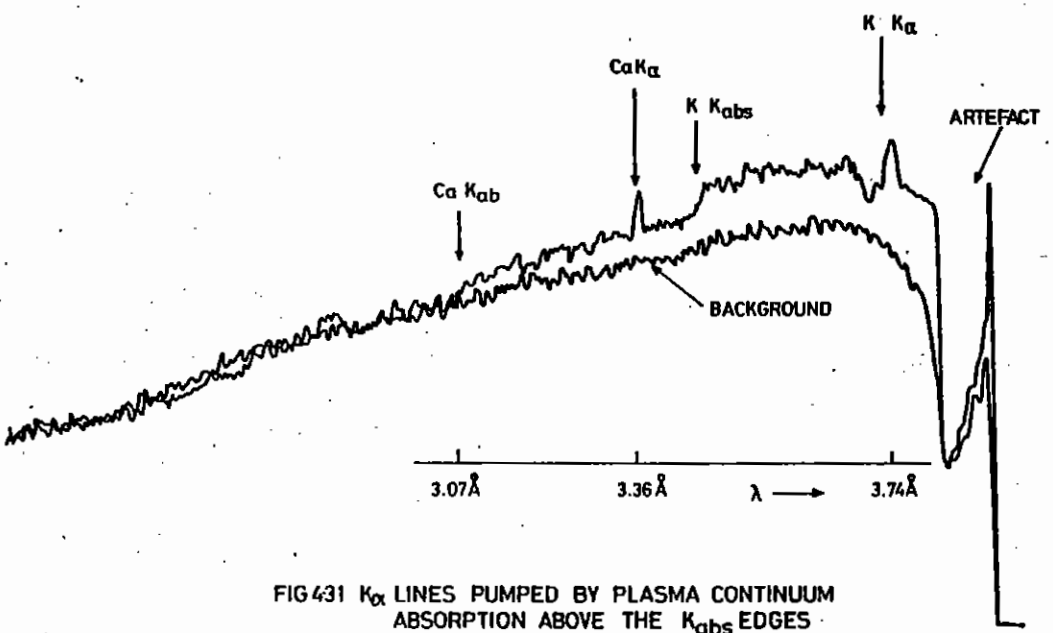

FIG 431 K_α LINES PUMPED BY PLASMA CONTINUUM ABSORPTION ABOVE THE K_{abs} EDGES SHOT 134, 2J, GREEN

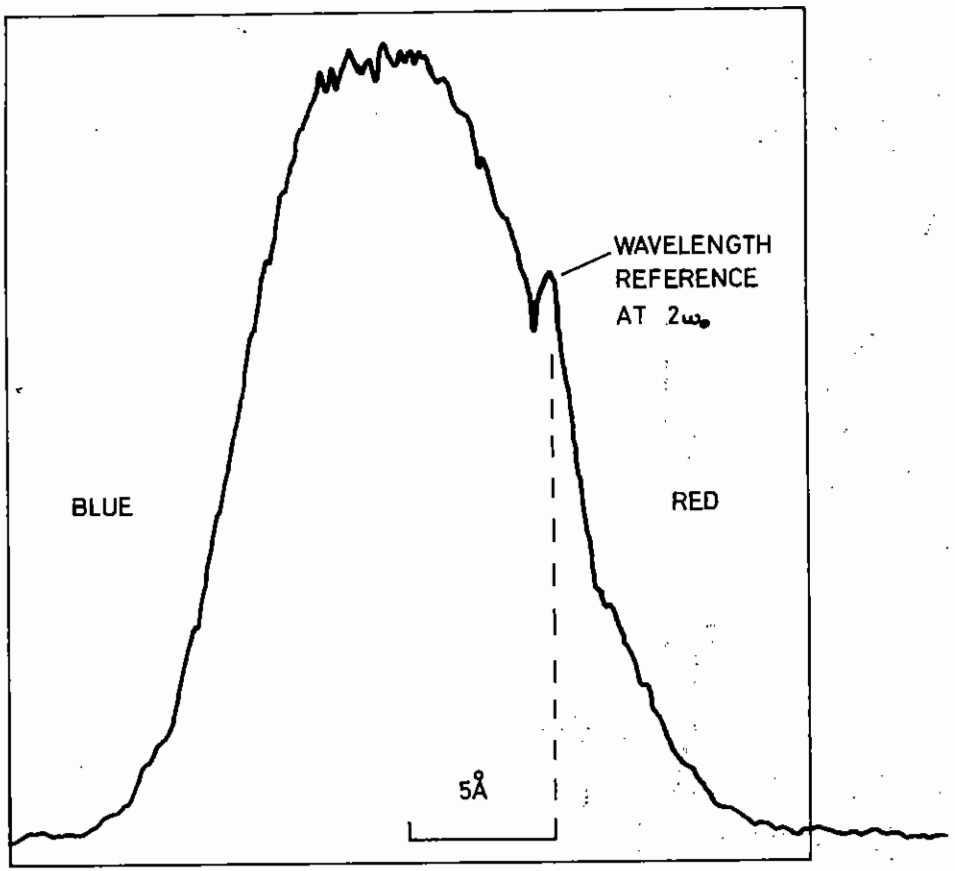

FIG 4.32 BACKSCATTER GREEN LIGHT SPECTRUM
SHOT 835 PLANE TARGET

resolved measurements of the reflection and transmission of the incident 1.06 μm beam show that substantial reflection and absorption continues after the plasma is underdense. Ion turbulence leading to low thermal conductivity and anomalous absorption may explain these observations.

The results are presented in section 4.6.2 with a discussion in section 4.6.3.

4.6.1 Experimental arrangement

Polystyrene (CH) foils of thickness 0.05–0.18 μm were irradiated at normal incidence by 100 ps FWHM neodymium laser pulses of energy 2–12J (Fig.4.33). The beam was focused to a 30 μm diameter spot by a 10 cm focal length f/1 doublet to give measured power densities up to $\sim 10^{16}$ Wcm^{-2}. Prepulse energy was typically 2.10^{-6} E_{inc}. An EPL S1 streak camera measured the incident, transmitted and back-reflected power as a function of time, collecting over 0.66 sr (f/1) with temporal resolution of $\sim$ 15 ps. The radial extent of the underdense plasma was measured by backlighting the target with a ruby probe beam ($n_c = 2.35 n_c(1.06)$). The foil was imaged at an Imacon S20 streak camera to give transmission measurements at 0.69 μm with temporal and spatial resolution of 5–20 ps and $\sim$ 10 μm respectively.

Further time-integrating diagnostics (calorimetry, light diodes, ion probes, Xray diodes) were also used.

4.6.2 Results

All diagnostics showed a great sensitivity to the level of prepulse. Except where noted below we have rejected data with prepulse >5 x 10^{-6}Einc.

(a) Backlighting measurements at .69 μm

The behaviour of foil targets when irradiated at $\sim 10^{15}$ Wcm^{-2} is displayed most clearly by the backlighting pictures shown in Fig. 4.34. The foil is initially transparent; time-structure on the probe beam is due to mode-beating. With the arrival of the main pulse, the foil becomes opaque on axis and later at larger radii (zero ruby transmission as measured by the streak camera corresponds to an attenuation of > x 5 to > x 20, depending on the signal level). At a later time, the

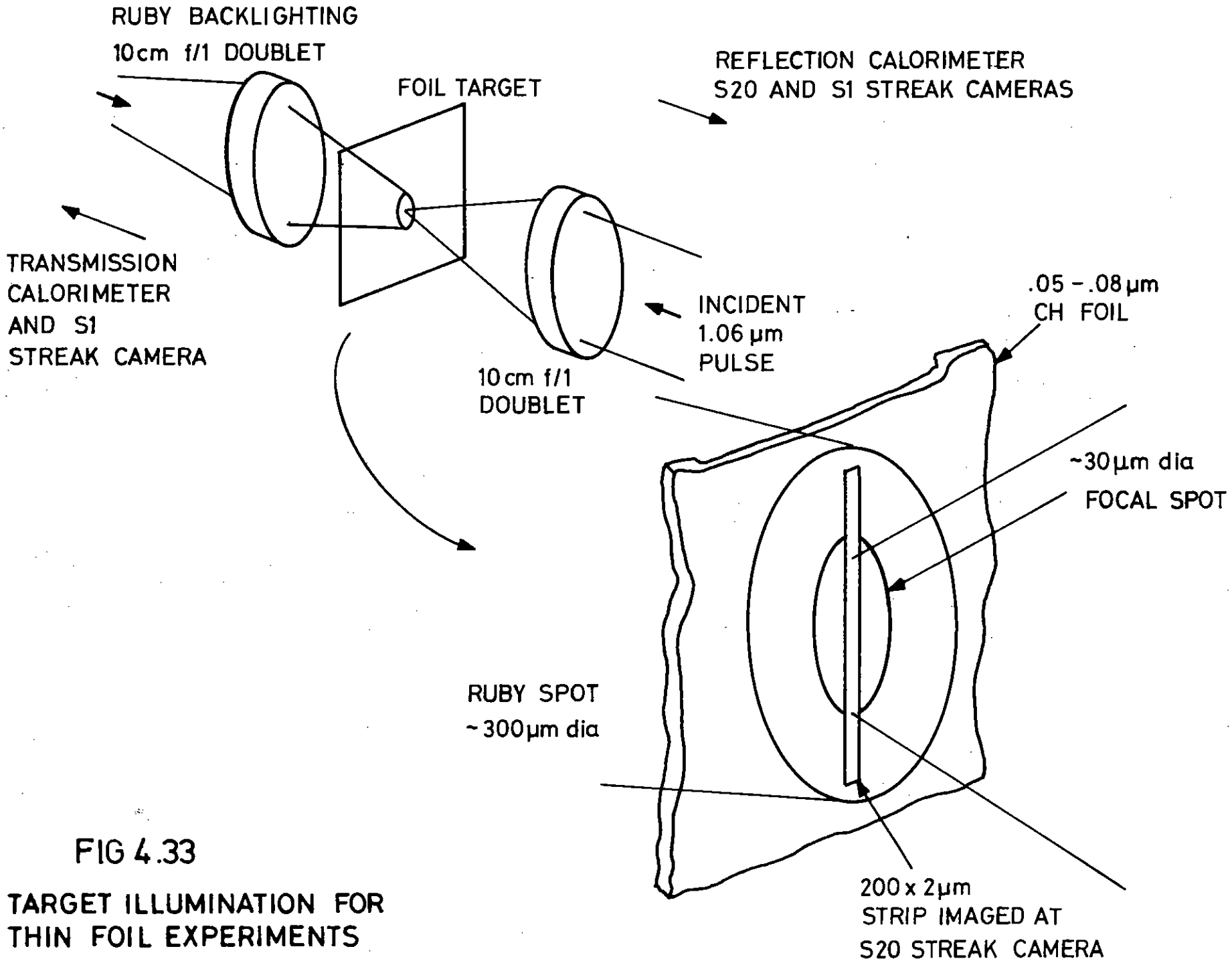

FIG 4.33

TARGET ILLUMINATION FOR
THIN FOIL EXPERIMENTS

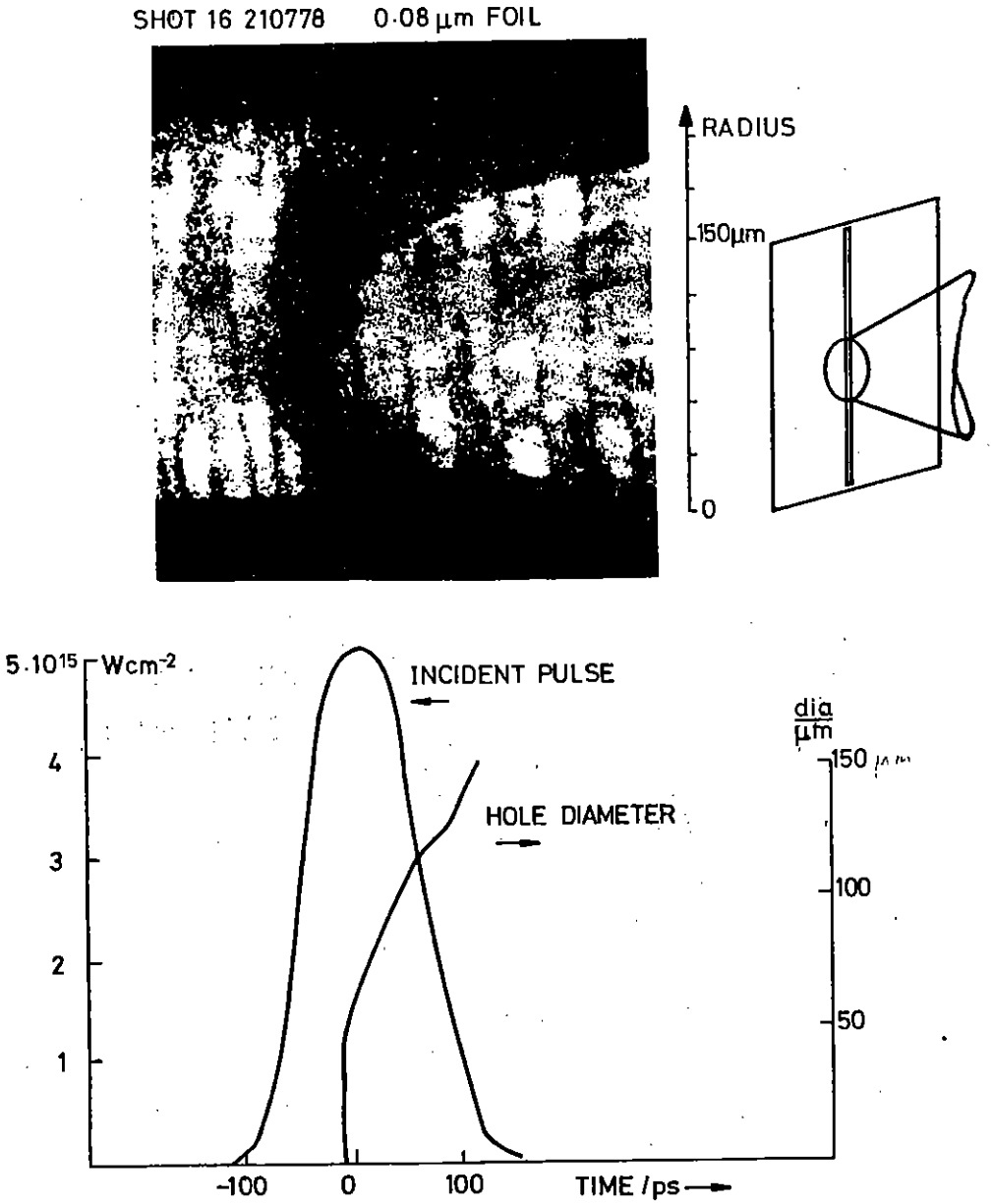

EXAMPLE OF S20 STREAK CAMERA DATA

FIG 4.34

foil begins to transmit on axis. The burnthrough hole then spreads radially at a rate dependent upon the foil thickness (Fig. 4.35). In case of the thicker foils, cold dense plasma was still present at a radius of ∿ 100 μm at the end of the observation time window, 1 ns later. The times at which a foil becomes opaque and transmits on axis are also dependent on foil thickness as shown in Fig. 4.36. The effect of varying incident power and prepulse level are illustrated in Table 4.05.

(b) Time resolved transmission and reflection at 1.06 μm

The 1.06 μm light transmitted and reflected into the f/1 lenses was time-resolved by the S1 streak camera. Data from a typical shot is shown in Fig. 4.37. The radial extent in the focal plane of back-scattered and transmitted light showed no substantial changes from test shots, suggesting that refraction effects do not change the focal plane distribution. It is found that the foils generally transmit only 10-20% of the incident power immediately after burn through. Often the transmission remains at this level out to the latest observable time. The backscattered fraction is very high (∿ 90%) early in the incident pulse just after the foil has become overdense, and then drops but is still present at the 10-20% level after transmission has been resumed. The time of onset of transmission at 1.06 μm shows the same dependence on foil thickness as the ruby laser data. We cannot distinguish the two burn through times within the experimental uncertainties of ± 20 psec. Thick(0.34 μm) foil shots allow observation of transmitted 1.06 μm light before the plasma becomes ionized. A very sharp cut off was observed at a time consistent with the ruby measurements, within the experimental uncertainties.

(c) Time-integrated measurements

The energy transmitted and reflected into the f/1 lens cones is shown in Fig. 4.38 as a function of foil thickness; data from a similar experiment (4.46) is also shown for comparison. The effect of variations in incident power and prepulse level is illustrated in Table 4.06.

TABLE 4.05 STREAK SHADOWGRAPHY DATA

Shot Number	FOIL μm	Imax $W.cm^{-2}$	Epp E_{inc}	Onset of Opacity	Transmission	Duration of opacity
				TIME in ps with t = 0 at incident pulse peak		
(i) Variations of incident pulse power						
8/200778	0.14	3.10^{15}	2.10^{-6}	-116	82	198
10/200778	0.14	1.10^{16}	3.10^{-6}	-140	-8	132
8/210778	0.05	$3.4.10^{15}$	9.10^{-6}	-90	-24	66
11/210778	0.05	$3.5.10^{15}$	4.10^{-6}	-91	-40	51
13/210778	0.05	1.10^{16}	6.10^{-6}	-151	-89	62
(ii) Variation of prepulse						
17/210778	0.08	3.10^{15}	2.10^{-6}	-76	12	88
20/210778	0.08	4.10^{15}	3.10^{-5}	-73	44	117
22/210778	0.08	4.10^{15}	1.10^{-4}	-66	60	126
21/210778	0.08	3.10^{15}	$1.2.10^{-4}$	No opacity		0

TABLE 4.06 CALORIMETER DATA

Shot Number	FOIL μm	Imax $W.cm^{-2}$	Epp E_{inc}	Epp μJ	TRANS into F/1 cones (per cent)	REFL	ABS
(i) Variation of incident pulse power							
8/200778	0.14	3.10^{15}	2.10^{-6}	5	6	∿ 30	44
10/200778	0.14	1.10^{16}	3.10^{-6}	26	9	5	57
8/210778	0.05	$3.4.10^{15}$	9.10^{-6}	22	31	5	-
11/210778	0.05	$3.5.10^{15}$	4.10^{-6}	10	39	2	40
13/210778	0.05	1.10^{16}	6.10^{-6}	50	34	small	47
(ii) Variation of prepulse							
17/210778	0.08	3.10^{15}	2.10^{-6}	5	12	12	45
20/210778	0.08	4.10^{15}	3.10^{-5}	81	12	11	42
22/210778	0.08	4.10^{15}	1.10^{-4}	290	19	6	39
21/210778	0.08	3.10^{15}	$1.2.10^{-4}$	276	50	∿ 0	27

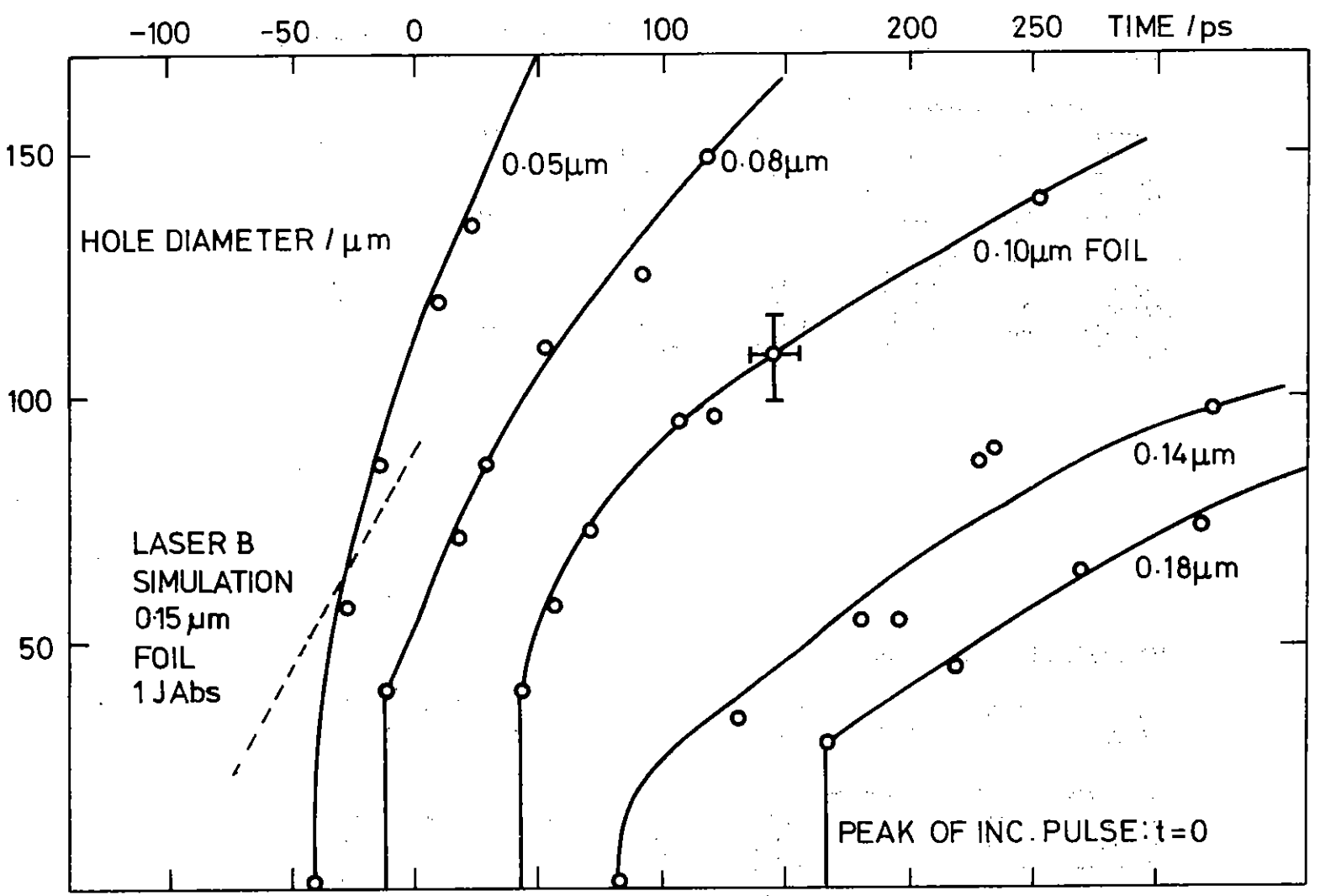

FIG 4·35 DIAMETER OF HOLES HOLES BURNT IN THIN POLYSTYRENE FOILS AS A FUNCTION OF TIME, ~30μm DIAMETER FOCAL SPOT, $I \sim 2.10^{15}$ Wcm^{-2}.

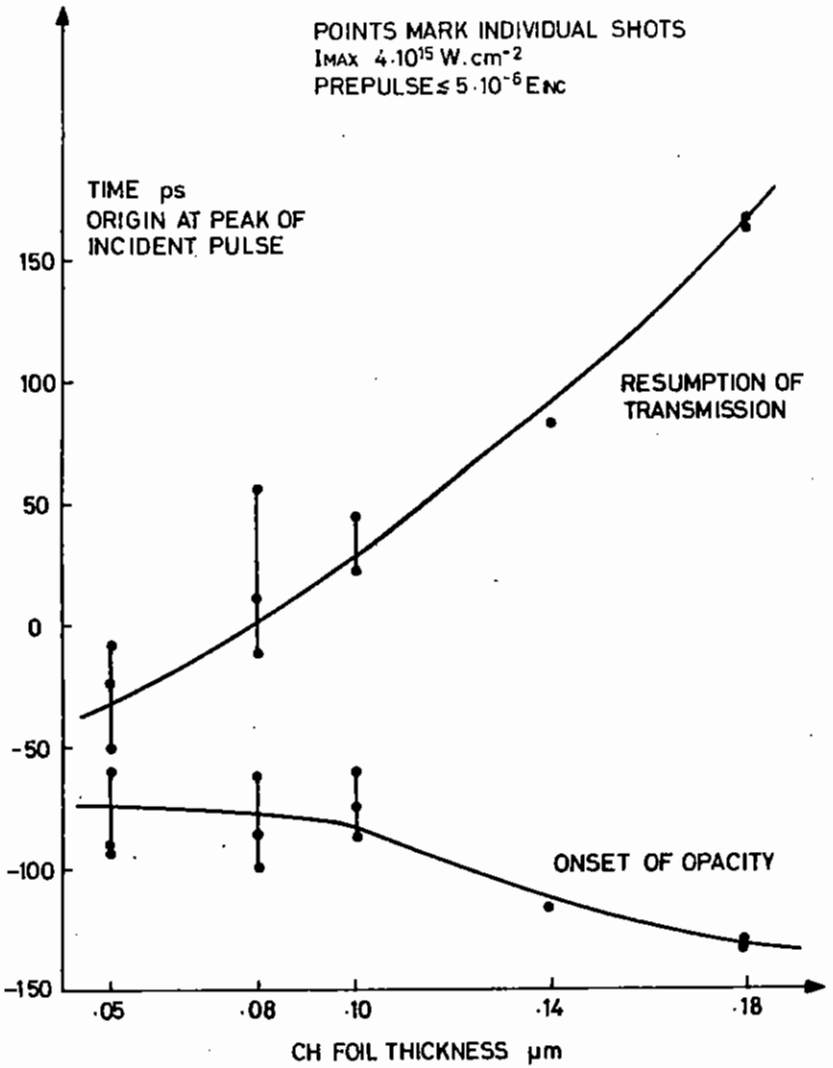

DURATION OF HIGH OPACITY TO RUBY BACK LIGHTING AS A FUNCTION OF FOIL THICKNESS

FIG 4·36

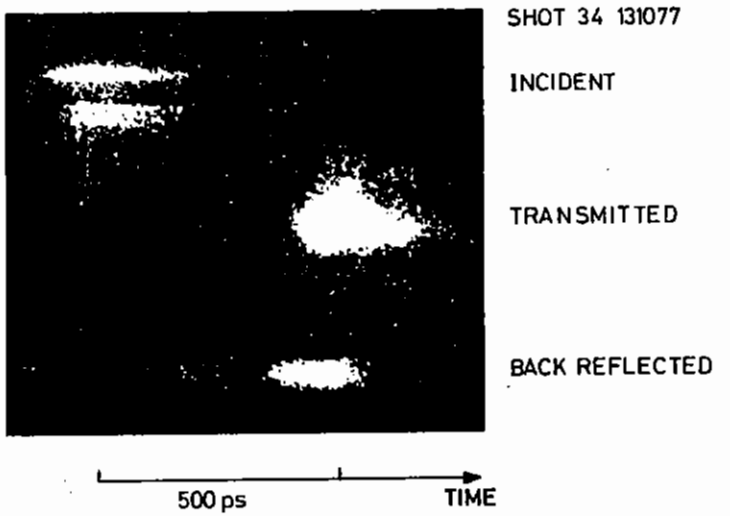

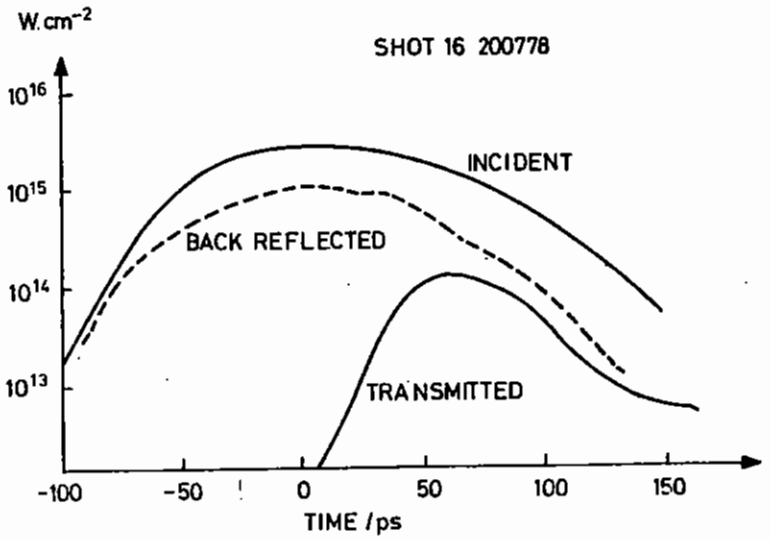

EXAMPLE OF SI STREAK CAMERA DATA

FIG4·37

Fig.4.38

Fractional transmission (●) and reflection (○) as a function of foil thickness. $I \sim 2 \times 10^{15}$ W cm^{-2} prepulse $< 5 \times 10^{-6}$
— — — — — — — — — Ref 4.4 ($I = 2 \times 10^{14}$ W cm^{-2})

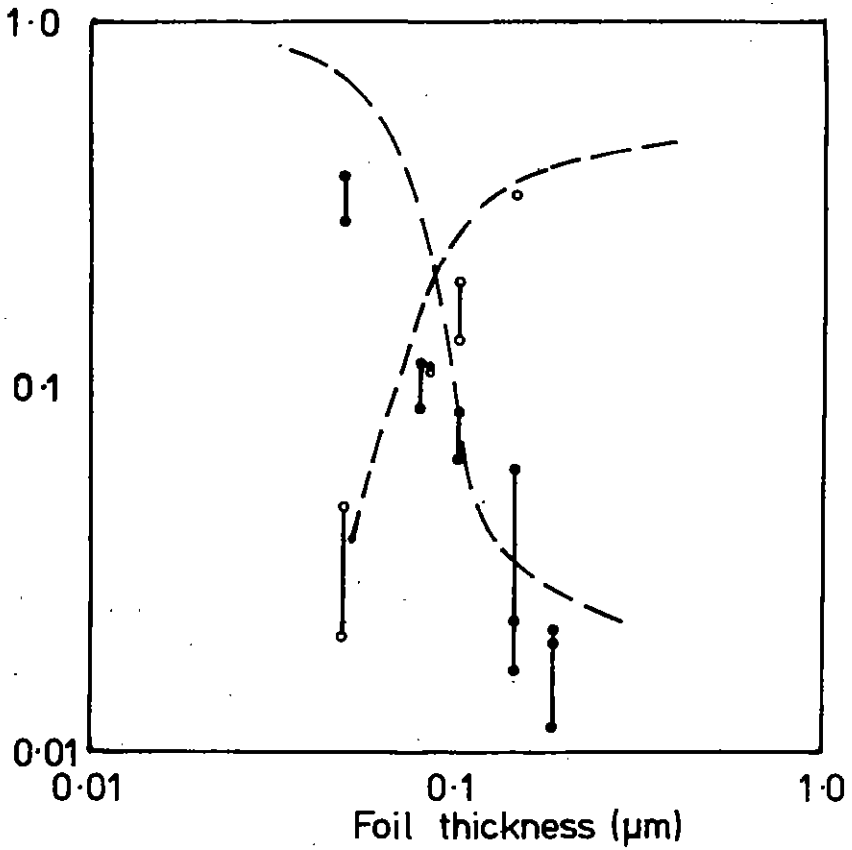

In order to obtain consistent data we found it necessary to exclude any shot with prepulse $>10^{-5} E_{inc}$.

An example of the scattered light distribution (Fig. 4.39) displays the azimuthal dependence typical of resonance absorption (4.51). This feature is not present in the distribution in the rear f/1 lens (Fig.4.40). Integration of the scattered light leads to a measurement of the absorption; variation with power and prepulse is illustrated in Table 4.06. Absorption is generally 50-60% for 0.10 - 0.14 μm foils and 30-50% for thinner foils. Xray diodes gave an electron temperature of 2 keV for $I \sim 10^{15}$ Wcm^{-2} and ~ 5 keV for $I \sim 10^{16}$ Wcm^{-2}. Ion blown off signals show a fast and slow component on both sides of the foil. Integration of the fast component, assuming M/Z = 1.75, implies that the suprathermal ions originate from a 40 μm diameter area of the target.

4.6.3 Discussion

Although our time integrated data shows the same general trend as results obtained by other workers, we generally observe less transmission for thin ($\sim$ 0.05 μm) foils (4.45, 4.46). The present work indicates that calorimeter measurements are particularly sensitive to prepulse energy and this could explain the difference in the observations. We also note that models which assume 100% transmission immediately after burn through are not consistent with our time-resolved transmission data.

Simulations using the 2D Eulerian code LASERB indicate that the burn through hole is expected to grow faster than experimentally observed. Reduction in the thermal conductivity results in better, through not perfect, agreement with experiment. The predicted transmission in a 0.15 μm foil is shown on Fig. 4.37 as a dashed line.

The experiment has been compared with the 1D, Lagrangian code MEDUSA which predicts that the plasma should expand at approximately the sound speed and go underdense earlier ($\sim$ 40 ps before the incident pulse peak with a very weak dependence on foil thickness) than we observe transmission of either ruby or 1.06 μm light.

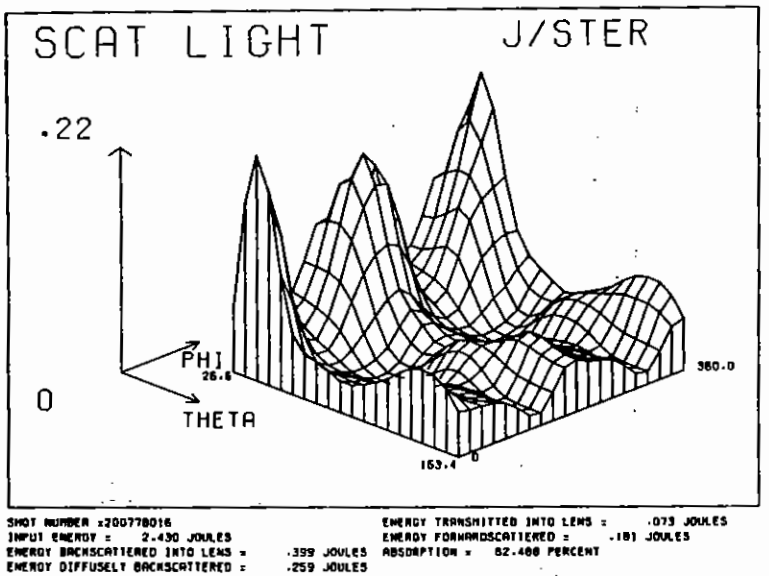

FIG 4.39 Intensity of scattered light vs angle.

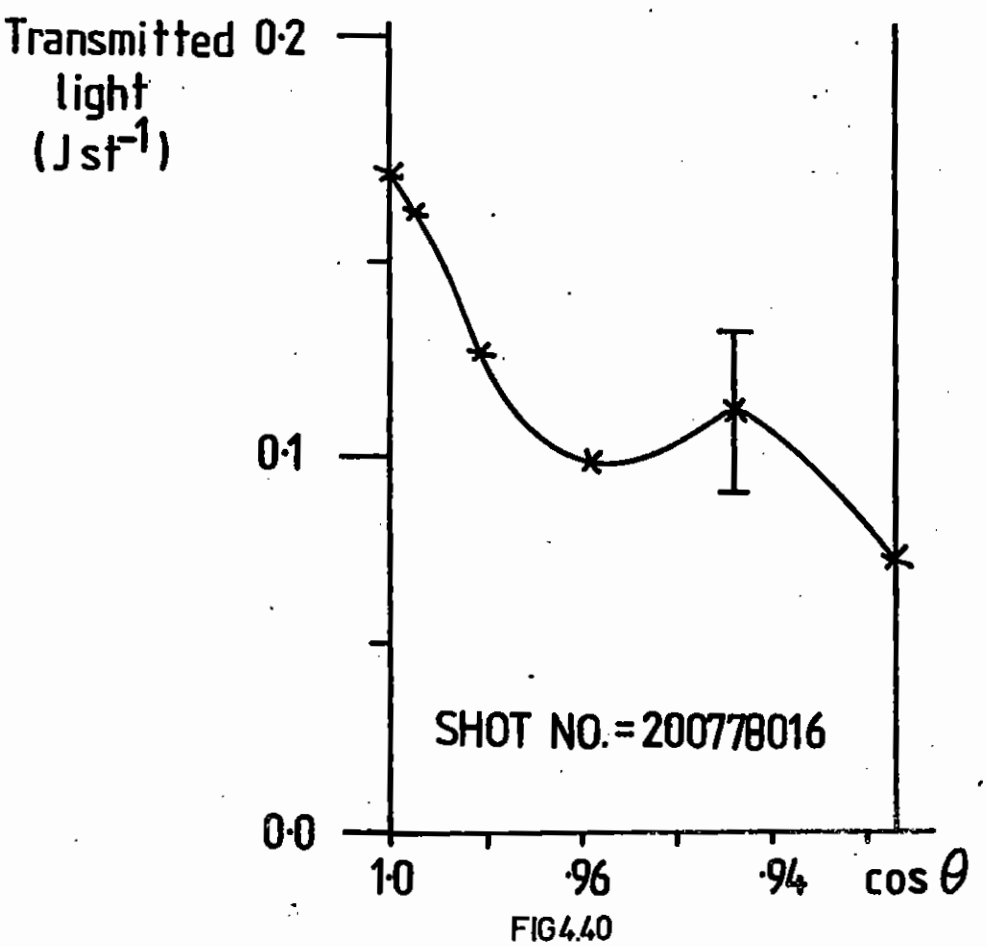

FIG 4.40

Reflection of 1.06 μm radiation was observed after the onset of transmission. This cannot be attributed to reflection from the edge of the hole since at this time the hole is larger than the focal spot. (Fig.4.35). This reflectivity is therefore attributed to Brillouin backscattering from ion turbulence in the underdense plasma. A saturation level for ion-acoustic waves of $\delta n/n \sim 20\%$ is calculated from ion trapping (4.52). This turbulence level is consistent with a reflection coefficient of 30-50% for a 50 μm long plasma (4.53). The length of the plasma at the time the foil goes underdense is given very roughly, by

$$\ell = n_{solid} \times \text{foil thickness}/n_{crit}$$
$$\simeq 35\ \mu m \text{ for a } 0.1\ \mu m \text{ foil}$$

Fig. 4.41 shows the absorption length (with enhanced absorption due to an ion fluctuation level of 20% (4.52) and inverse bremsstrahlung (4.54) in a 1 keV, Z = 3 plasma) as a function of plasma density. There is enhanced absorption mainly due to the turbulence until the density falls below $n_{crit/3}$. The dashed line in Fig. 4.41 also shows the length of plasma for an initial foil thickness of 0.1 μm, assuming 1 dimensional cylindrical expansion. Transmission at 1.06 μm is not expected until the absorption length is longer than the plasma.

In conclusion, the time-integrated data for shots with low prepulse show less transmission through thin foils than observed by other workers. Inclusion of time resolved measurements indicates that inhibition of the radial conductivity and anomalous absorption processes are both present. It has been proposed, on the basis of the observed Brillouin backscatter, that the presence of ion fluctuations driven by Brillouin backscattering may be responsible for these processes.

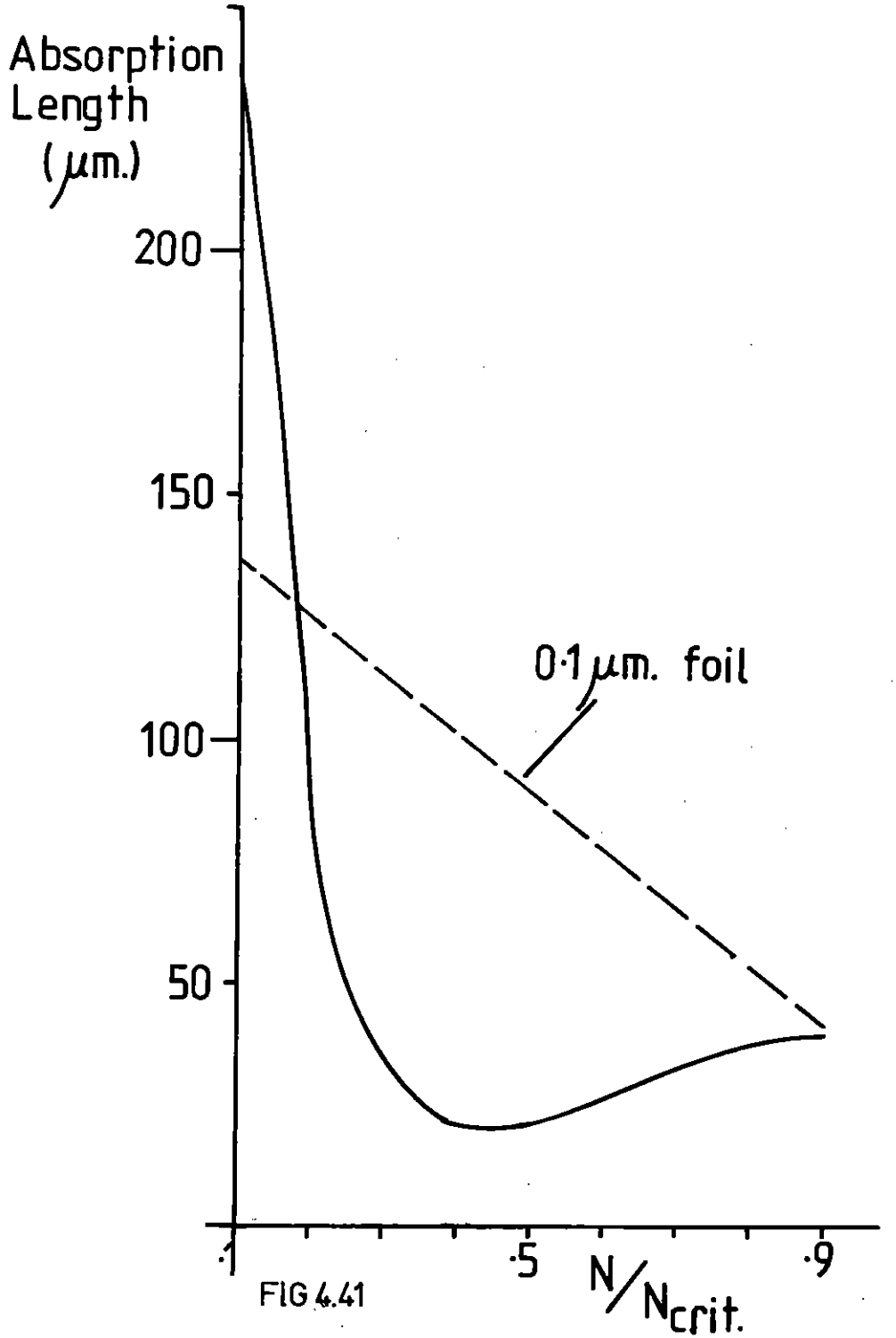

FIG 4.41

4.7 Exploding Pushers

This section covers a number of investigations of exploding pusher implosions with two-beam f/1 illumination. Significant improvements in the X-ray spectroscopic analysis of implosion cores are discussed in 4.7.1 and applied to a number of shots.

Neutron yield measurements are presented in 4.7.2 and discussed in relation to the spectroscopic data and to scaling law models. Some comments on the models are given in 4.7.3. The application of MEDUSA in the exploding pusher regime is described in 4.7.4. We reported previously (4.55) on the observation of Aℓ line emission from implosion cores. A more complete set of measurements confirming this result is discussed in 4.7.5.

Finally, in 4.7.6 we report preliminary data on time-resolved X-ray spectroscopy.

4.7.1 The diagnosis of core properties by Xray spectroscopy

The major diagnostic tools for measuring the core properties of exploding pushers are the space-resolving crystal spectrometers. Time averaged values of electron density, electron temperature, the number of atoms in the core and the size of the core can all be obtained by this diagnostic (4.56). We describe the methodology involved in obtaining these parameters from the raw data, discussing two examples in some detail. One shot illustrates the diagnosis of the glass in the core, another illustrates the diagnosis of the compressed gas.

The results from a number of shots are summarised in 4.7.1.4.

4.7.1.1 The preparation and comparison of theoretical emission line profiles with the experimental profiles

(a) Optically thin profiles

Optically thin profiles were taken from the line shape calculations of Lee. (Section 8.4.5). Two different sets were generated which we refer to as the

standard and the full sets of line profiles. For the standard set the electrons are treated dynamically and the ions are treated quasistatically. These profiles are similar to those calculated by Kepple and Griem (4.57). For the full set of profiles the ions are treated dynamically, the first order shift and broadening functions which arise from the charge on the emitter are included, and the fine splitting is included.

The main differences between the full and the standard profiles are as follows. First, the full calculations provide a somewhat broader profile which is most noticeable on the α transitions. Second, the full profiles will be damped in the central regions of the lines, which will make the central region of the line narrow. After Doppler broadening the central intensity will be decreased. The suppression of the central peak will be most noticeable for the γ lines. Finally, the full theory predicts shifts in the line profiles; however, shifts are difficult to observe with a crystal spectrometer.

It is necessary to examine the way in which the line widths of the various transitions depend upon the plasma parameters. Fig.4.42 shows the variation of the full width half maximum with electron density for the standard calculation of Si. It should be emphasised that these widths are without any Doppler, opacity or instrument broadening. The variation of the half width with the electron temperature is weak: At $n_e = 1.5\ 10^{23}\ cm^{-3}$ and with T_e about $5\ 10^6\ ^oK$, the scaling is $\delta\lambda_{\frac{1}{2}} \alpha\ T_e^{0.2}$. The scaling at lower number densities with more particles in a Debye sphere will be even weaker.

We conclude that the major variable upon which the width of the optically thin profiles depend is n_e. Thus a large set of standard line profiles was generated for various values of n_e. The value of T_e used was $5.2\ 10^6 K$, as suggested by the experimental observations. Because of their expense a limited number of full profiles were calculated.

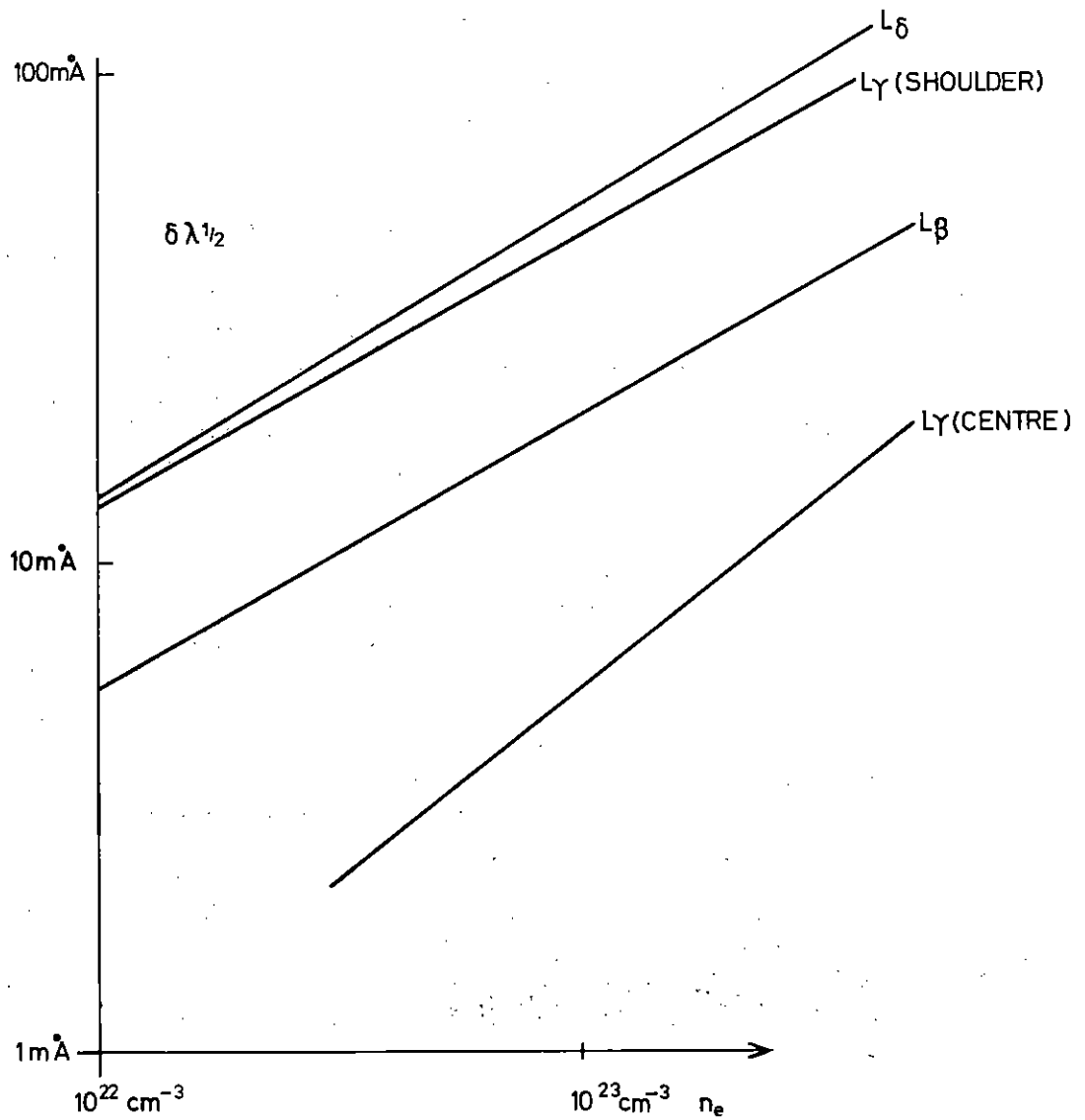

FIG 4.42

FULL WIDTH HALF MAXIMUM OF HYDROGEN-LIKE TRANSITIONS IN SILICON

Te= 5.2 10^6K, NO DOPPLER BROADENING.

(b) Broadening the optically thin profiles

Before comparing with experiment the optically thin profiles are processed (broadened) in the same order in which further broadening processes actually occur.

The profiles are first Doppler broadened by an amount corresponding to the electron temperature. They are then opacity broadened according to the simple formula for a uniformly emitting and absorbing slab.

$$B_\nu(\ell,\nu) = (1-\exp(-\tau(\nu,\ell)))\, B_\nu$$

where $\tau(\nu,\ell)$ is the optical depth at frequency ν due to a slab of length ℓ and B_ν is the source function.

Other algorithms for opacity correction are discussed in Section 8.4.5.

(c) Fitting the theoretical profiles to experimental profiles

Experimental data is prepared by microdensitometering the plates and converting to intensity using the calibration curve (4.58) for KODIREX. Theoretical profiles are then fitted to the experimental points using an interactive graphics routine which is only available on the Imperial College CDC 6400. The broadened theoretical profiles are shifted in wavelength to best coincide with the experimental profile. The intensity scale of the theoretical profile is then adjusted so that the areas under the theoretical and experimental curves are equal. To characterise the quality of this fit a normalised sum of squares parameter is used: this is:

$$Q = \Sigma(y_{exp}-y_{th})^2/\Sigma\, y_{th}^2$$

where the sum is over all the digitised experimental points. In practice a quality of fit Q = .01 is good whereas Q=0.1 is poor. Examples will be shown in Section 5.

(d) The idealised fitting procedure

The two major variables in determining the width of the observed emission line are n_e and n_l. The gross width of any line is not a unique function of n_e and n_l. The details of a line shape may be a unique function of n_e and n_l, but it is only the coarse features that are observables. If the theory is compared with an experimental profile, then for low opacity the line width will be only a function of n_e. If the line of best fit is plotted on graph of n_e versus n_l as in Fig. 4.43 the theory will fit the experiment anywhere along the horizontal part. As the opacity (n_l) is increased the same total theoretical width can be obtained with a smaller n_e. Thus the fit line curves downwards. Ideally a line of best fit could be obtained for several transitions. They would intersect at one point in the n_e, n_l plot, which would be the value of n_e and n_l in the slab. In fact the region of fit is an area, which may be defined by the constraint that Q must not be more than twice its minimum value.

There is an additional constraint on the allowed region in the (n_e, n_l) parameter space. If T_e is known the state of ionisation can be predicted by either a coronal model (4.59) or a collisional radiative model (4.60). The relationship between n_e and n_l, the ground state of a particular state of ionisation will then be known. For example at $T_e \simeq 500$ eV, 50% of aluminium atoms would be Aℓ XII, and for this state of ionisation, $n_e \sim 20\ n_l$. The exact ionisation equilibrium may also be influenced by the opacity at resonance lines and non-steady state equilibrium.

4.7.1.2 Fitting the compressed gas plasma

The Xray diagnosis of the compressed gas plasma can be illustrated by shot 242. The target was a 102 μm diameter, 0.58 μm wall thickness microballoon filled with 2B of Ne. It was imploded by a 16J, 100 ps laser pulse. The pin-hole photograph is shown in Fig. 4.44. A space integrated spectrum was recorded with a TlAP crystal spectrometer and a space resolved spectrum was recorded with a PET crystal spectrometer. A tracing from the TlAP crystal spectrometer is shown in Fig.4.45. This figure shows NeIX and NeX lines together with Na lines from the glass. The space resolved spectrometer shows very little Si line

emission from the core, but does show strong core continuum emission from the Ne IX and Ne X recombination continuum.

Core Electron Temperature: From the slope of the Ne X and Ne IX recombination continuum T_e was found to be 300 ± 50 eV. The observed intensity ratio Ne X L to NeIX $1^1S_o \rightarrow 3^1P_1$ was 1.50. Assuming the upper states of these lines are in LTE with the ground state of the next stage of ionisation, this ratio implies $n_B/n_H = 1.3$. Here n_B and n_H are the number densities of Ne XI and Ne X respectively. Optically thin collisional radiative equilibrium (4.60) requires an electron temperature of 350 eV to achieve this state of ionisation.

Core size: On this shot it is evident from the pin hole photograph, Fig. 4.44. that the core is not spherical. This is a result of the large size of the microballoon and the double beam irradiation. From the pin hole photograph the larger dimension of the microballoon is 27 μm. The transverse size of the core is best obtained from the space resolved PET spectrometer and is 12 μm. The intensity of the neon recombination step implies $n_e^2 V$ is $2\ 10^{36}$ cm^{-3} assuming an emission time of 80 ps. With the above core dimensions this gives $n_e \sim 2\ 10^{22}$ cm^{-3}.

Core Electron Density: The electron density is obtained much more accurately by the line fitting. The Ne X Lα, Lβ and Lγ lines were fitted to the theoretical profiles as described in 4.7.2.1. Good fits, with $Q \sim 0.01$ were obtained for the Lα and Lβ line. A Lγ line 'fit' is shown in Fig. 4.46. It shows that the central feature of the theoretical profile is not seen experimentally, resulting in a poor quality fit, Q = .036. The lines of best fit for all three lines are shown in Fig. 4.47. The effect of using the full theory for the line broadening (section 8.4.5) is not very pronounced. Also shown is the line $n_l = 0.05\ n_e$, which represents 50% of the neon atoms being NeX. From the intersection of the L_β, L_α and state of ionisation lines, n_e is $2.8 \pm 0.5\ 10^{22}$ cm^{-3}, and n_l is $1.4 \pm 0.4\ 10^{21}$ cm^{-3}.

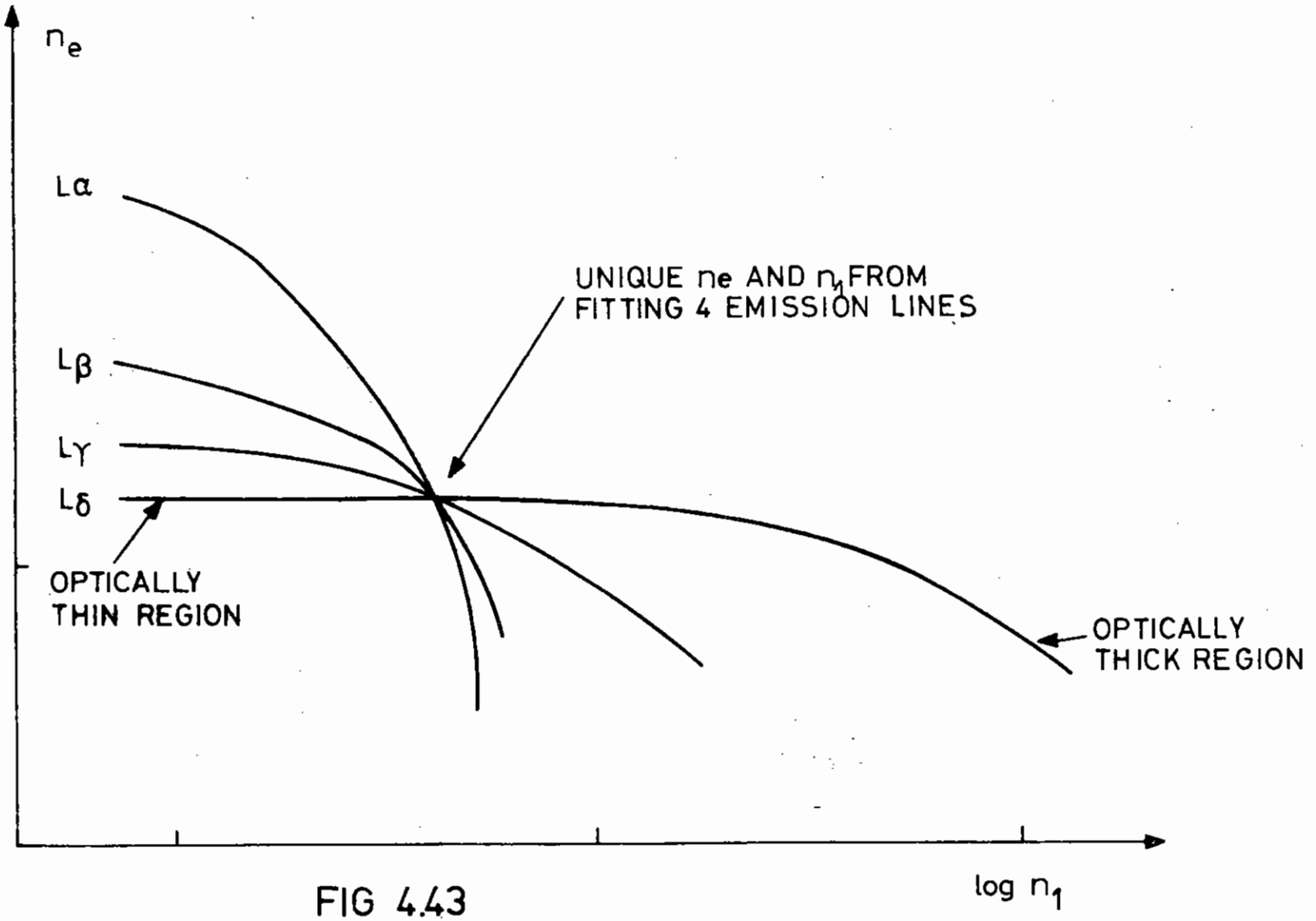

FIG 4.43
IDEALISED LINE OF BEST FIT FOR SEVERAL SPECTRAL LINES

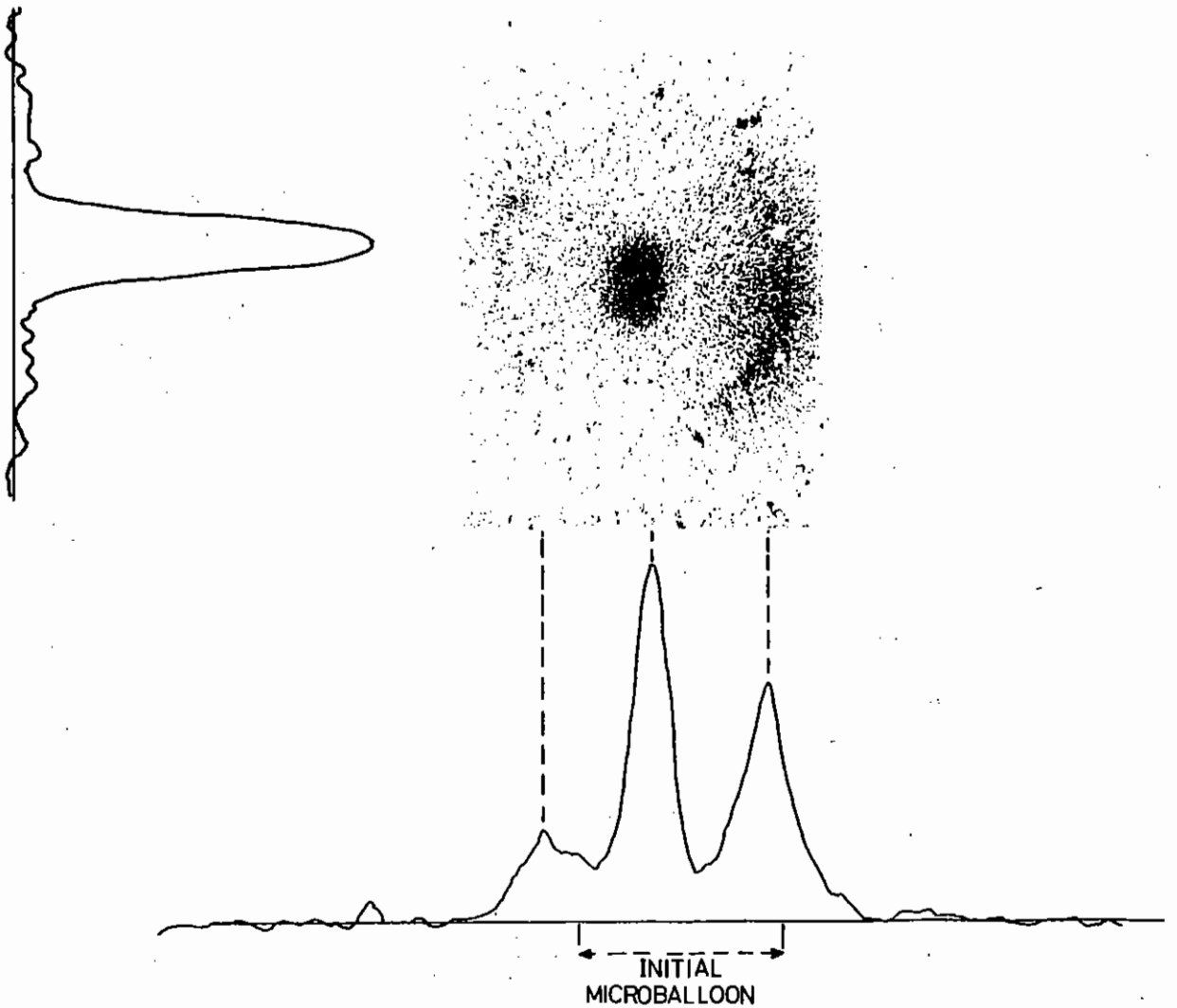

FIG. 444. PIN HOLE PHOTOGRAPH AND MICRODENSITOMETER SCANS
SHOT 242

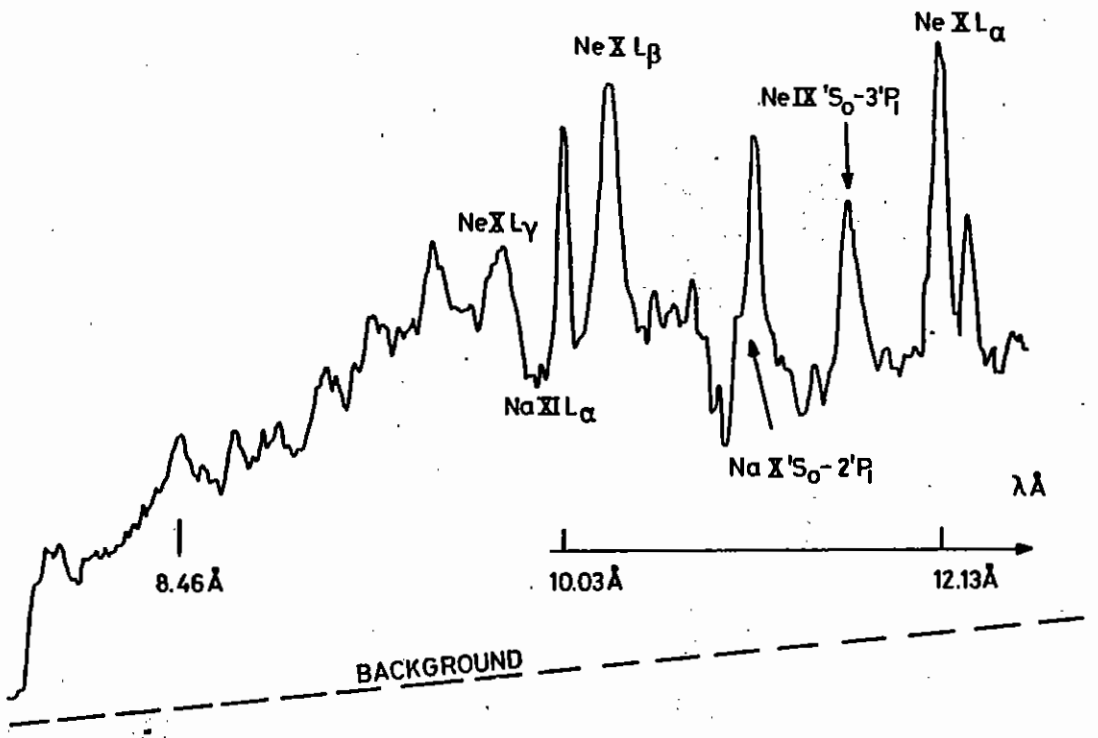

FIG. 4.45. SPACE INTEGRATED SPECTRUM SHOT 242

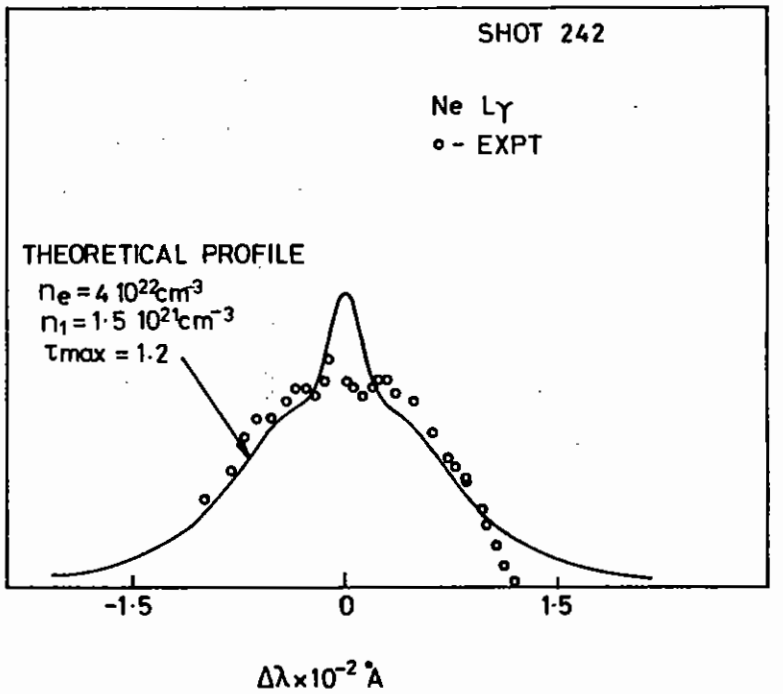

FIG 4.46

The above core dimension gives a volume of 4 10^{-9} cm^{-3}. If n_e = 2.8 10^{22} cm^{-3} with Z = 9, then the number of neon atoms in the hot core is 1.2 10^{13} compared with the initial 2.8 10^{13} neon atoms. It is difficult to estimate confidence limits on the former figure.

4.7.1.3 Fitting the compressed glass plasma

Shot 209 is a good example of the diagnosis of the properties of the compressed glass in the core. The microballoon target for this shot was 66 μm diameter, 0.75 μm wall thickness and was filled with approximately 0.3 B of argon. It was imploded with a 22J laser pulse. A space resolved spectrum was obtained with a PET crystal spectrometer and part of the spectrum is shown in Fig.4.48. The core is distinct from the Xray emitting shell regions, and shows emission from Aℓ XII, Si XIII, Si XIV and Aℓ XVII and Si recombination continuum.

Electron Temperature: From the recombination continuum the intensity I_ν as a function of photon energy is shown in Fig. 4.49. In the range $2.5 < h\nu < 3.2$ the slope indicates T_e = 430 ± 40 eV. The Si XIV L to Si XIII $1\,^1S_o - 4\,^1P_1$ line ratio was 0.42 ± .08. Assuming that the upper states of these lines are in LTE with the ground state of the next state of ionisation this ratio implies n_B/n_H = 0.13 ± .03 where n_H is strictly the ion number density in the ground state of Si XIV. Optically thin collisional radiative equilibrium requires T_e = 560 ± 20eV to achieve this state of ionisation. A lower temperature would be required for a model with an optically thick L_α line. From a coronal model of ionisation this ratio of n_B/n_H implies that 25% of the silicon atoms are Si XIV.

The Core Size: By tracing the silicon recombination continuum in the spatial direction the diameter of the silicon emitting region was found to be 22 ± 2 μm.

The intensity of the Si recombination continuum step implies that $n_e^2 V$ = 4 10^{37} cm^{-3} assuming an emission time of 50 ps. Because of the low filling pressure of argon most of the core is glass and so the volume V of Si emission is taken as a sphere of diameter 22 μm. The electron density is then estimated to be 9 10^{22} cm^{-3}.

The Core Electron Density: Inspection of Fig.4.48 indicates a high density. There is considerable broadening of the high order members of the series, and the dielectronic satellites of Si XIV L_α are almost as intense as the Si XIV L_α line.

The Si XIV L_α, L_β and L_γ lines were compared with the theory. The lines of best fit in n_e, n_1 parameter space are shown in Fig. 4.50. Good fits to the Si L_α transition can be obtained with Q as low as 0.017.

A fit to the Si L_β transition is shown in Fig.4.51. It is noticeable that the theoretical dip at the line centre is absent from the experimental profile. For optically thin fits such as Fig.4.51, Q is low because of this mismatch at the line centre. Fits with increasing opacity reduce the relative size of this dip, and thus increase the quality of the fit.

A fit to the Si L_γ transition is shown in Fig.4.52. As before the central feature with characteristic shoulders of the theoretical profile is not seen experimentally. The quality of the optically thin fits is even worse at 0.04. Even at quite high values of n_1, such as 1.5 10^{21} cm^{-3} this profile is hardly affected by opacity broadening and the quality of the fit remains poor.

Using the full theory for this case causes a significant change. The central feature of Si Lγ is suppressed, and this is shown in Fig.4.53. for the same conditions as Fig.4.51. But the most significant change is on the Si L_α transitions. Because the optically thin profile is considerably broader than with the standard theory the best fit is attained with a lower n_1 which is consistent with the other emission lines, as shown in Fig.4.50.

The state of ionisation line is also shown in Fig.4.50. Assuming that the core is SiO_2 and that 25% of the Si is Si XIV then $n_1 = 0.009\ n_e$. It can be seen that a consistent fit can be obtained only with the full theory and then $n_e = 1.51 \pm \begin{matrix}.4\\.2\end{matrix}$ 10^{23} cm^{-3}, n_1 = 1.2 ± 0.4 10^{21} cm^{-3}.

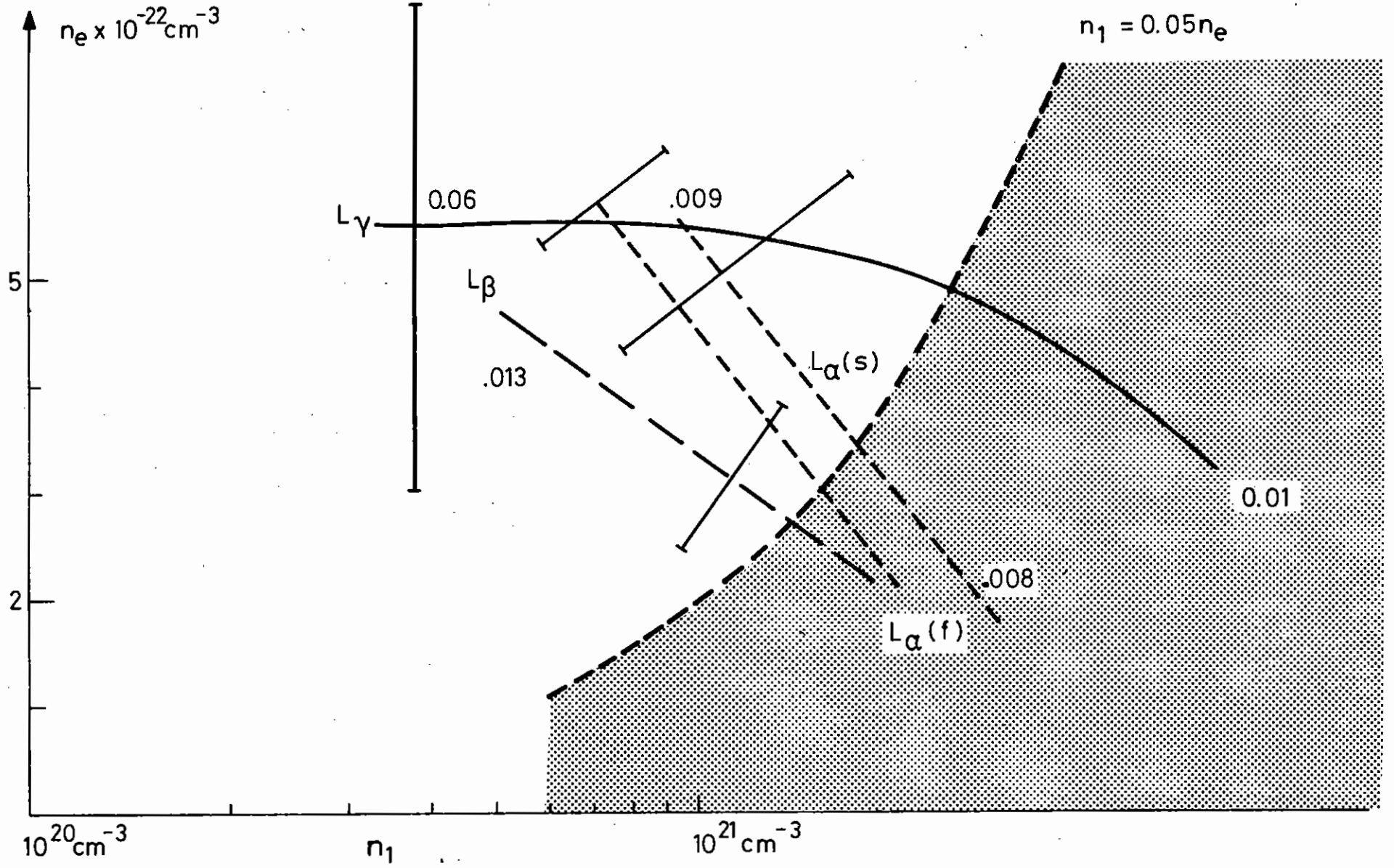

FIG. 4.47. LINES OF BEST FIT FOR NEON LYMAN LINES FROM THE CORE ($l = 30 \mu m$, SHOT 242)

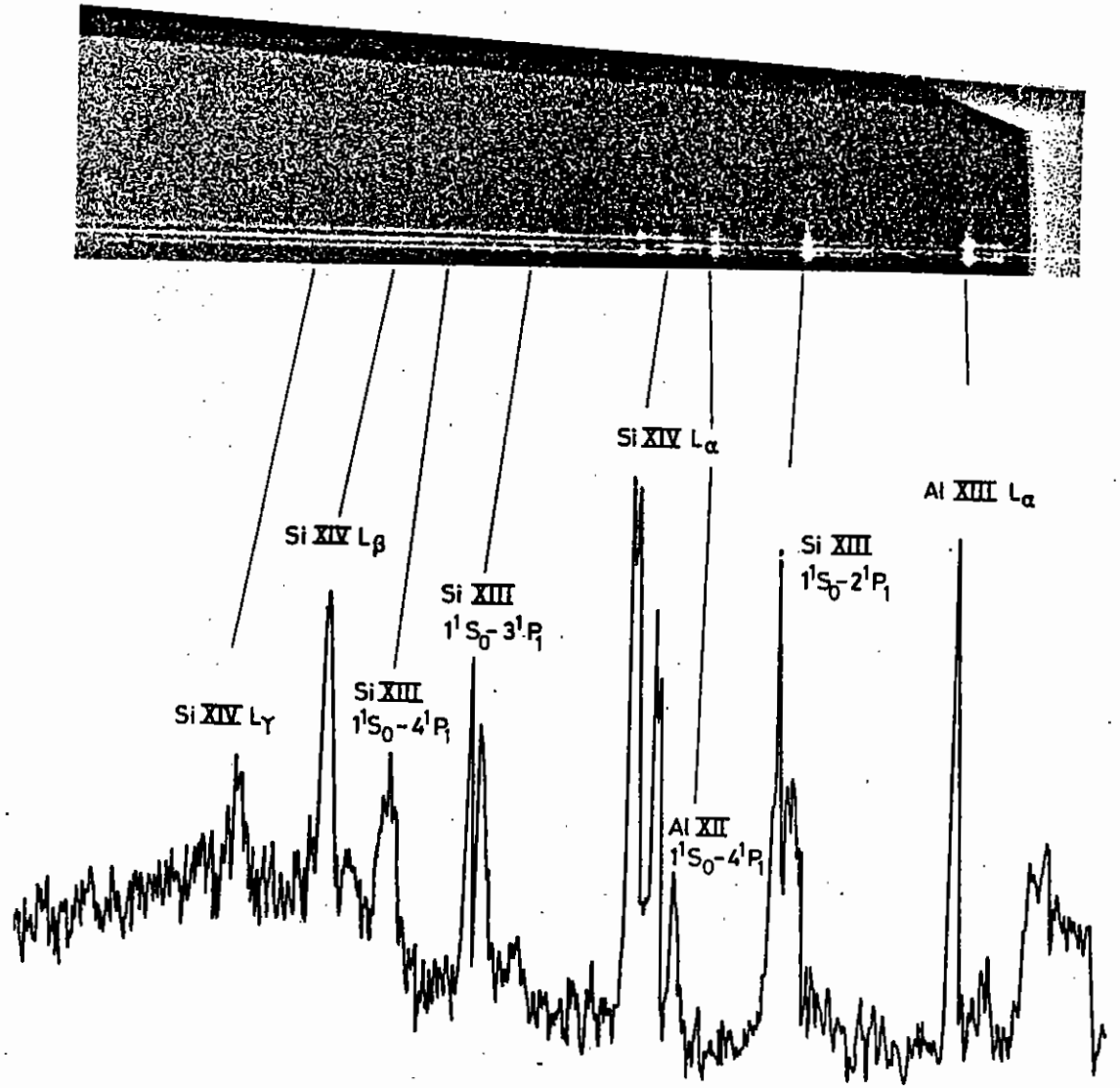

FIG4.48 CORE SPECTRUM. SHOT 209

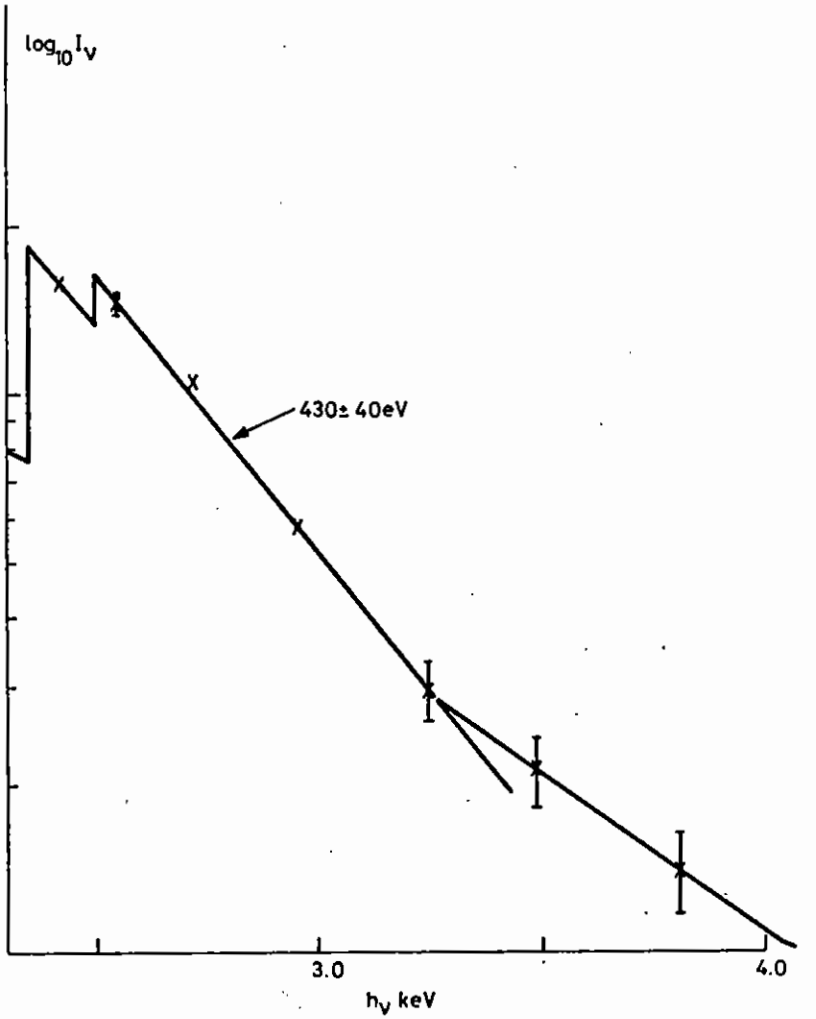

FIG. 4.49. INTENSITY OF Si XIII AND XIV RECOMBINATION CONTINUUM FROM THE CORE. SHOT 209

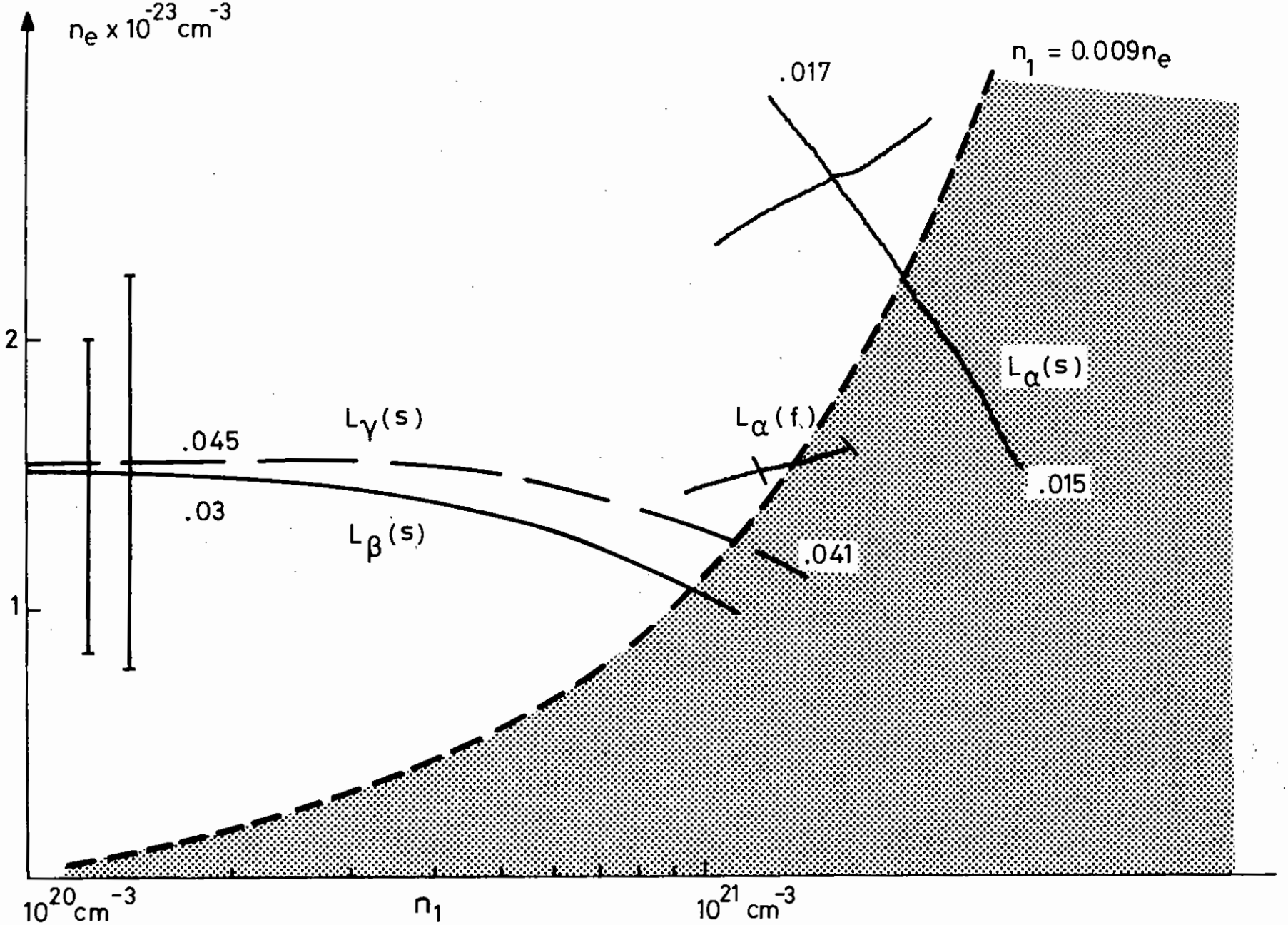

FIG. 450. LINES OF BEST FIT FOR SILICON LYMAN LINES FROM THE CORE ($2r = 24\mu m$, SHOT 209)

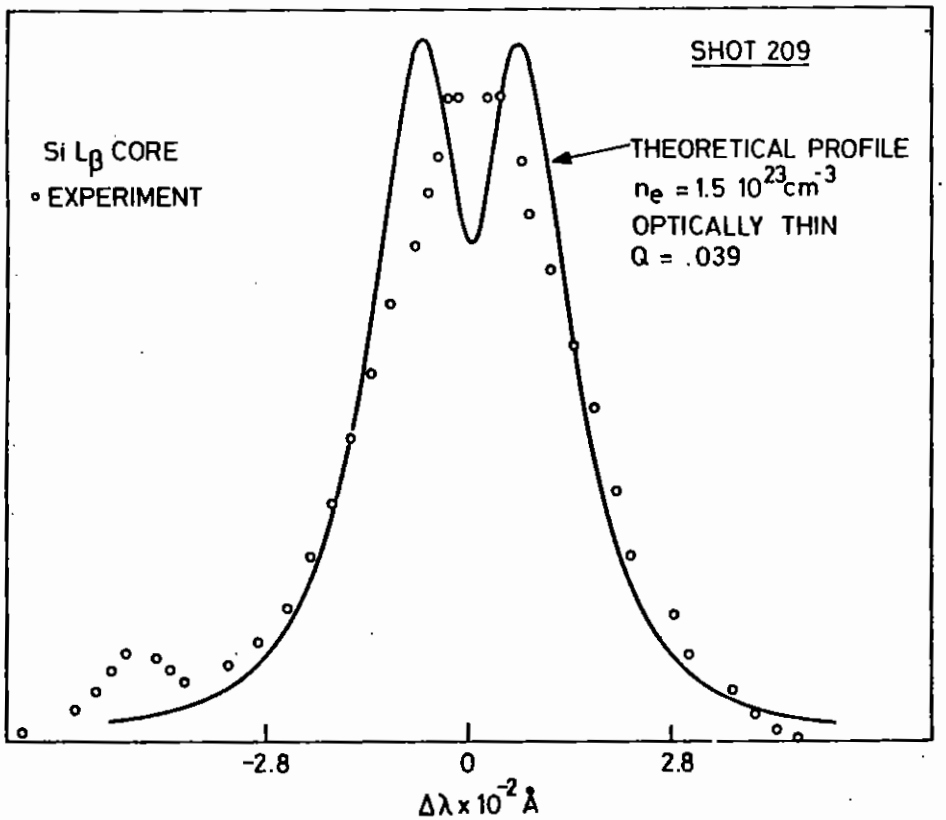

FIG 4.51

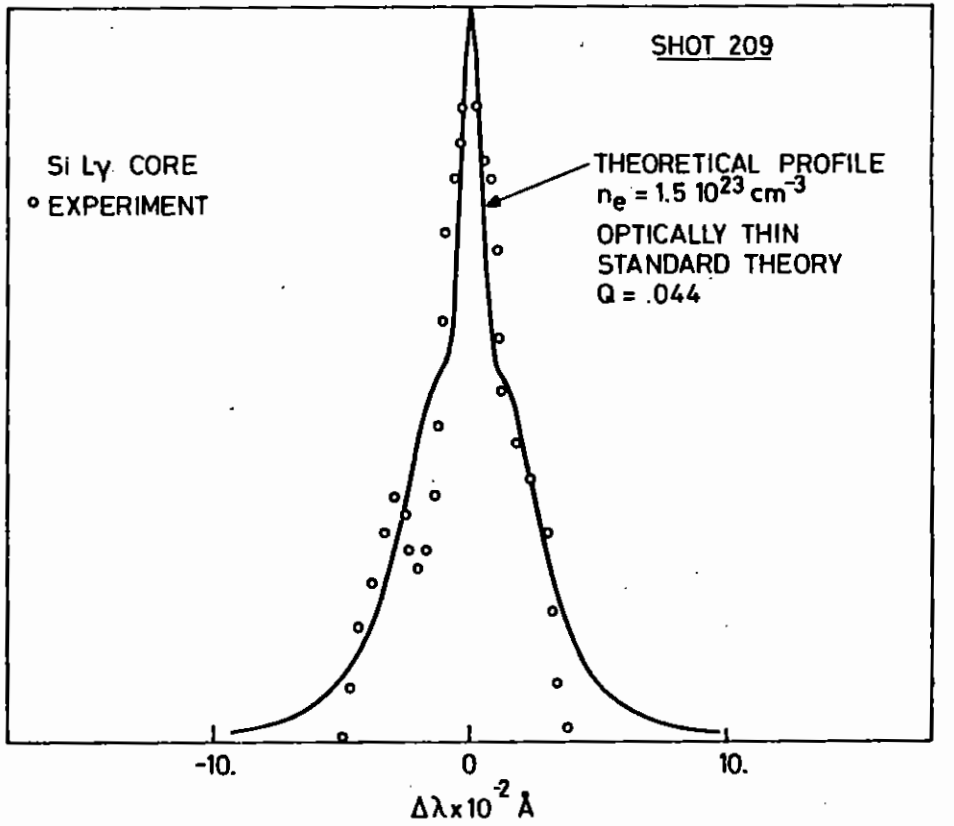

FIG 4.52

The Si XIII series can also be fitted. The Si XIII $1\,^1S_o - 3\,^1P_1$ core line is particularly interesting and is shown in Fig.4.54. A very high electron density is needed to fit the experimental line. A high opacity will not give a good fit because this has the effect of equalising the two peaks of the theoretical profile. Also note that the dip in the centre of the experimental profile is much larger than in the theoretical profile. This must be due to absorption of cool low density in the outer region of the shell.

One further completely novel aspect of this shot is the presence of broadened argon lines. The spectrum showed A XVII $1\,^1S_o - 2\,^1P_1$ and A XVII $1\,^1S_o - 3\,^1P_1$ lines both of which are broadened beyond the instrument width. A fit to the theory for the latter line is shown in Fig.4.55. These lines have not yet been alaysed in detail: it is very important to use the full theory for these lines because of the high Z of the emitter.

4.7.1.4 Results of Core Spectroscopic Analysis

We have so far analysed the data from ten exploding pusher shots using the methods discussed above. The results are given in Table 4.07. Some comments on individual shots are given below:

Notes to Table 4.07

Shot 28: Fit using Ne IX $1\,^1S_o - 3\,^1P_1$ and $n_{NeIX}/n_e = 0.27$ (coronal)

Shot 30: Density from Si XIV L_α, L_β, L_γ; T_e from recombination continuum. The continuum shows an absorption edge close to SiK edge in Fig.4.56 presumably due to cold material around core

Shot 31: Fit using Si XIV L_α, L_β. Te from recombination continuum.

Shot 102: T_e from Si XIII and Si XIV line ratio. Density from Si XIII and Si XIV

Shot 105: Density from NeX L_α, L_β. T_e from line ratio of Ne X and Ne XI : coll. rad. eqm 310 eV; coronal eqm, 385 eV.

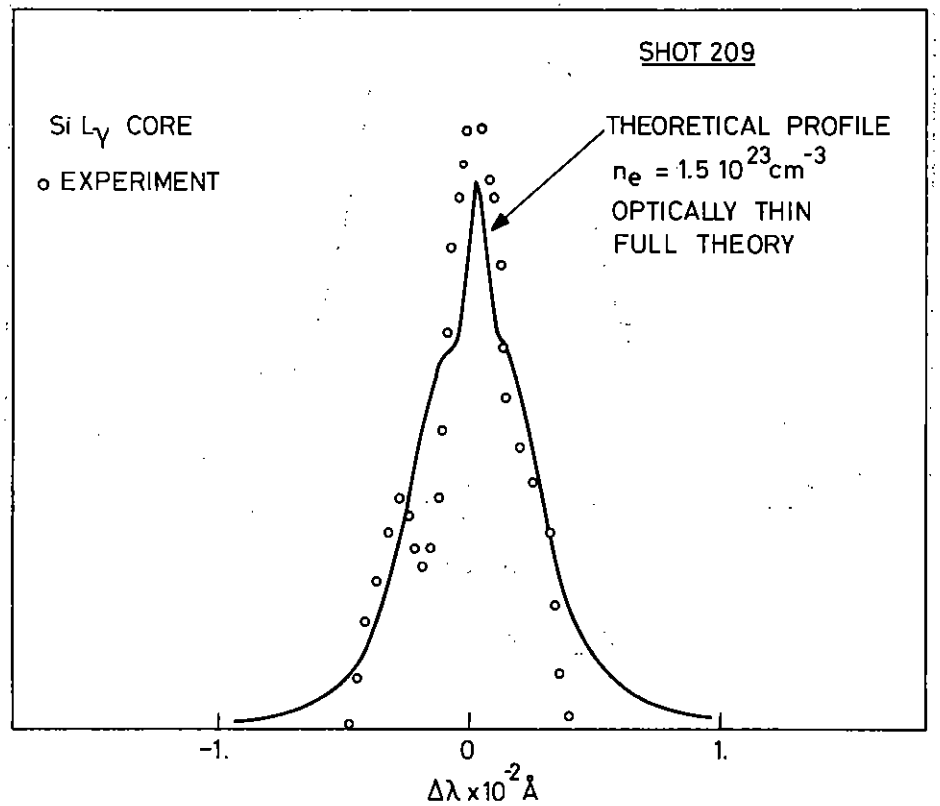

FIG 4.53

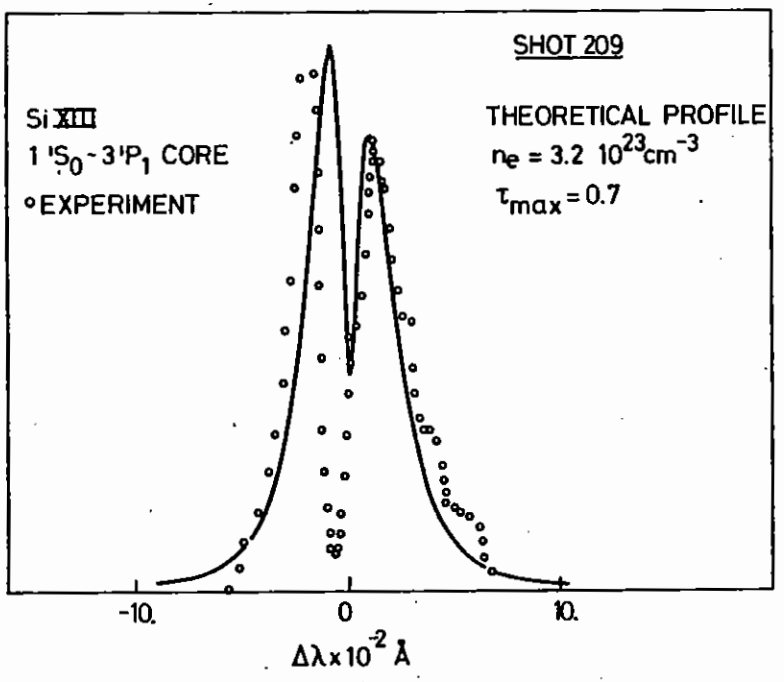

FIG 4.54

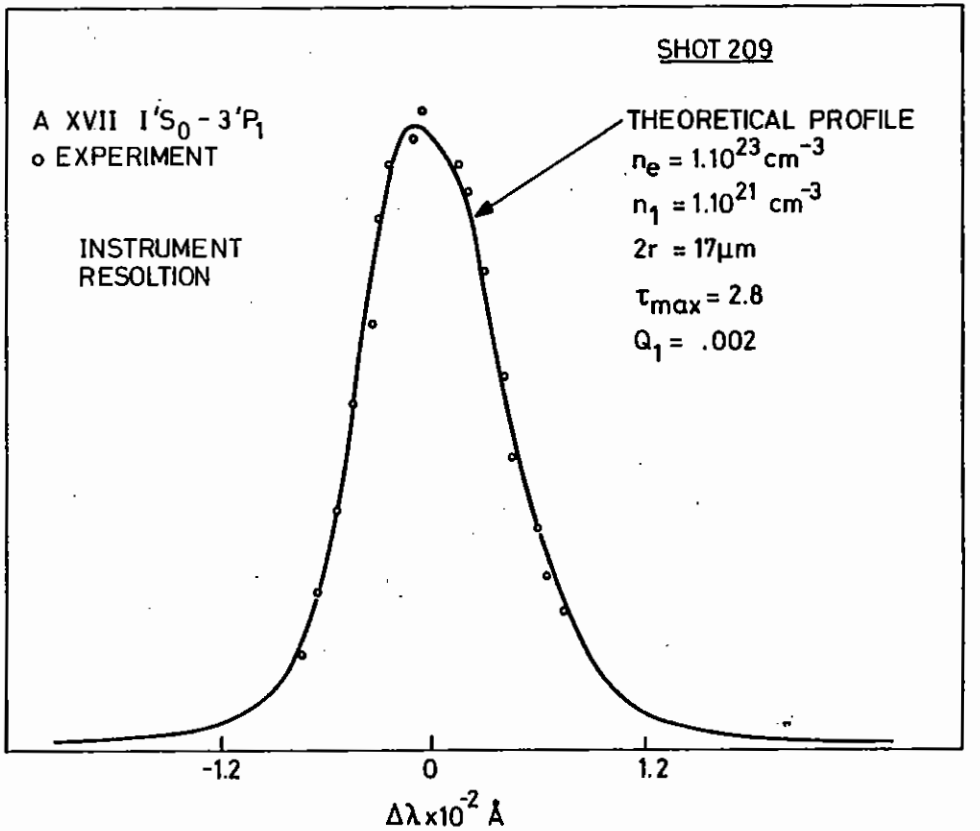

FIG 4.55

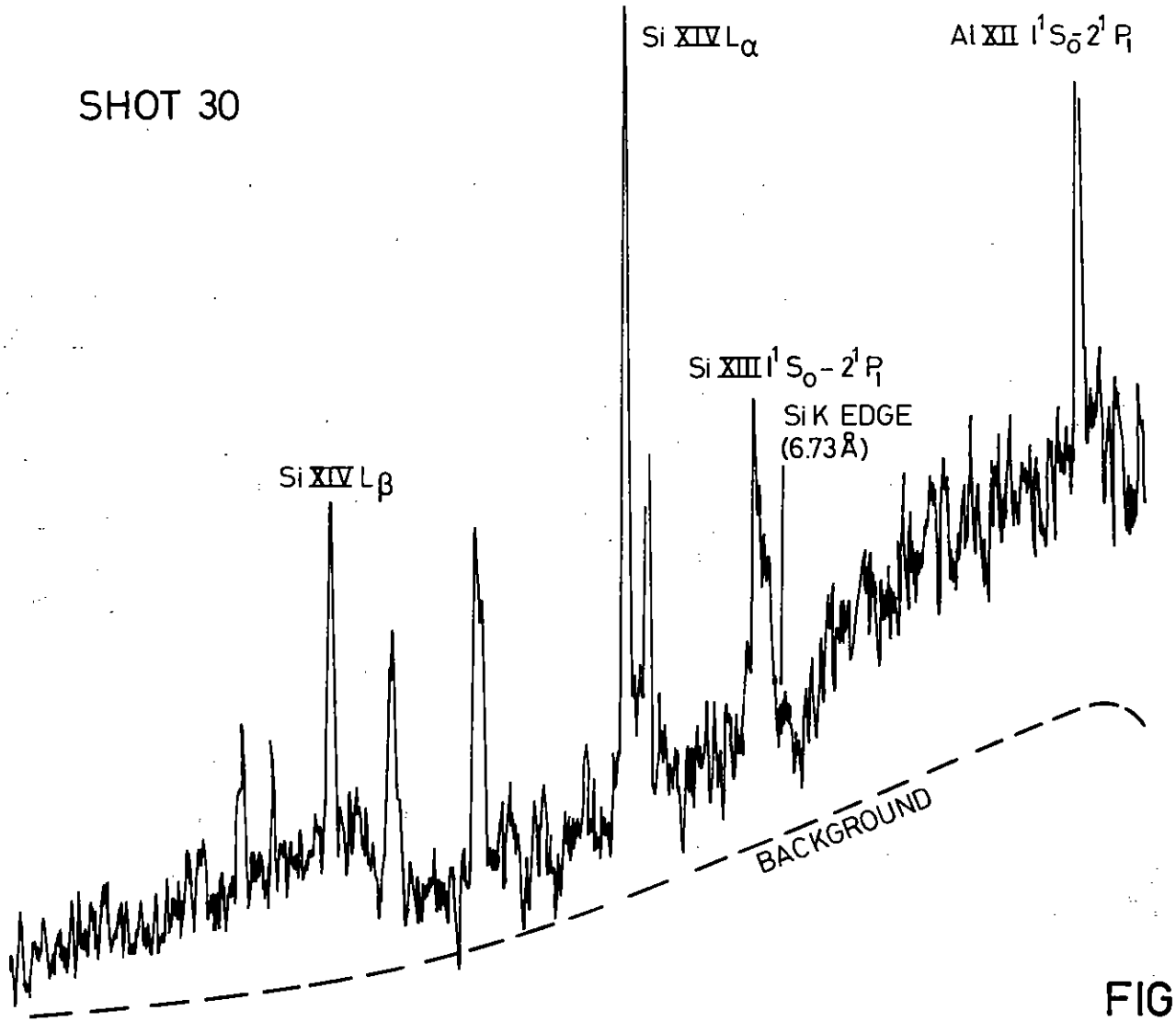

FIG 4.56

CORE SPECTRUM SHOWING Si K EDGE ABSORTION

TABLE 4.07 IMPLOSION CORE DENSITY, TEMPERATURE AND SIZE BY X RAY DIAGNOSIS

Shot Number	Balloon Diam. µm	Shell Thickness µm	Laser Energy J	Gas Fill	Electron Density gm cm^{-3} ±20%	Mass Density gm cm^{-3} ±20%	Core Diameter µm	Te (eV)	$\rho = \frac{8,6\Delta r}{r}$ gm cm^{-3} (Storm et al)
28	70.5	0.96	18.2	Neon 8 Bar	4×10^{22}	0.15	17.0	400 ± 100	0.23
30	69.5	0.82	15.5	Neon 8 Bar	6×10^{22}	0.23	25.8	450 ± 50	0.203
31	70.0	0.92	13.7	Empty	6×10^{22}	0.23	19.5	450 ± 50	0.226
102	88	0.88	15.3	$D_2 + T_2$ 10 Bar	6×10^{22}	0.23	16.5	470 ± 50	0.17
105	84.1	0.91	16.3	D_2 5%Ne 11 Bar	2.8×10^{22}	0.09	24.5	340 ± 30	0.19
106	70.5	1.1	15.9	Neon 2.5 Bar	8×10^{22}	0.30	14.5	-	0.268
209	66.0	0.75	22.0	Argon 0.33 Bar	1.5×10^{23}	0.58	22	430 ± 40	0.195
242	102	0.58	16	Neon 2 Bar	2.8×10^{22}	0.11	27 x 27 x 12	300 ± 50	0.097
322	50	0.6	15.3	$D_2 + T_2$ + 10% Ne	6×10^{22}	0.23	20	510 ± 80	0.206
331	50	0.5	33	$D_2 + T_2$ +10% Ne 10 Bar	4×10^{22}	0.15	37	560 ± 50	0.17

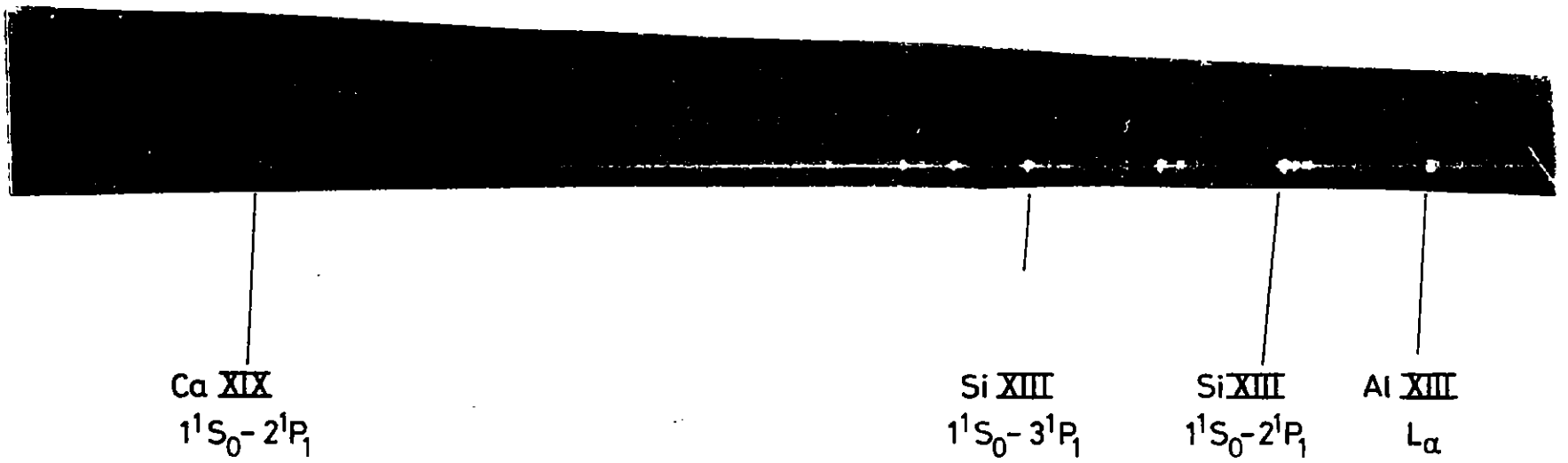

FIG 457 SPACE RESOLVED SPECTRA SHOT 322
50μm x 0.5μm, 10B D.T. TARGET

Shot 106: Density from NeX L_α, L_β and 50% of Ne hydrogenic. Measured Ne atoms in core 1.4 10^{13}; initial Ne in fill: 1.2 10^{13}.

Shot 209: See section 4.7.1.3. Note differences from shots 30, 31

Shot 242: See section 4.7.1.3

Shot 322: Small microballoon with high energy; core emission dominates spectrum, no distinct shell emission seen (Fig.4.57). Density from Si XIV L_α, L_β; also with Si XIII $1'S_o-3'P_1$ and $1'S_o-4'P_1$. T_e from Si recombination continuum.

Shot 331: Large core again dominates spectra as for shot 322. Difficult fitting Si XIV L_α, L_β, L_γ and L_δ uniquely. T_e from Si recombination continuum.

4.7.1.5 Discussion

Core densities scatter by up to a factor of 5 and display no obvious correlation with shot parameters. There is, however, some measure of agreement with the predictions of Storm et al (4.61) although we have explored only a limited range of parameters.

Electron temperatures are around 450 eV, vary very little from shot-to-shot and correlate neither with shot parameters nor with ion temperature (Section 4.7.2). We note that for the few shots where the temperature of the Ne fill gas has been measured, the temperature is somewhat lower. This suggests that some mechanism such as radiative cooling is determining the electron temperature.

4.7.2 Core ion temperatures from neutron yields

The temperature of the ions in the implosion core as distinct from that of the electrons may be obtained from the yield of the nuclear fusion reactions. The reaction rate is a very strong function of ion temperature ($\sim T_i^5$ in the region of interest) but is only moderately sensitive to the compression ratio ($\sim \eta^{2/3}$).

4.7.2.1 Neutron Data

In several runs, microballoons filled with an equimolar deuterium-tritium mixture with the addition of a small percentage of neon were imploded and the 14 MeV neutrons from $d + t \rightarrow n + \alpha$ were detected in a plastic scintillation counter. Details of the method and calibration procedure are given in section 1.7.5 of this report. A yield of $\sim$ 5000 neutrons corresponds to one detected neutron. The most obvious feature of the early data was the large shot-to-shot variation in neutron yield. A more carefully controlled experiment was performed at the end of 1978. Prepulse monitoring was better and a large number of shots with the same laser parameters were made on targets whose diameters ranged from 50 to 95 μm. The targets were individually tested for tritium content by counting Xrays from the microballoon walls (4.62).

The neutron data from all runs are listed in Table 4.08. Shots where this were abnormal beam properties, prepulse or a low tritium count have been omitted. Core spectroscopic data obtained on some shots is included in the table.

4.7.2.2 Analysis

If the core is assumed to have a uniform temperature and density and is confined for a time determined by the ion sound speed, we can write

$$Y \propto R_o^4 \, \rho_o^2 \, \eta^{2/3} \, \frac{\overline{\sigma v}}{T_i^{\frac{1}{2}}}$$

where Y is the neutron yield; R_o, ρ_o the initial radius and density of the fill gas; η is the volume compression, T_i is the ion temperature of the compressed gas and $\overline{\sigma v}$ is the Maxwell-average cross-section-velocity product.

We show in Table 4.08 an ion temperature computed on this basis with the further assumption that the compression is 75 for all shots. (A factor of 2 error in compression would change the inferred ion temperature by only 10% at $T_i \sim 700$ eV). Values of T_i deduced in this way are compared with the results of a scaling model (4.61) in Fig.4.58, where it has been assumed that 25% of the power on target is absorbed. Although there is a wide scatter of data points, the data and the model do correlate. In particular, the data from the more recent runs show values which are roughly half the model predictions. It may well be that beam quality and focusing though consistent within the run, were poorer than before and resulted in a smaller absorbed fraction and thus a smaller ion temperature.

4.7.3 Scaling models for exploding pusher targets

Neutron yield, electron temperature and maximum compression are important parameters for laser compression and laser fusion experiments. In order to assess how these parameters would be optimised by the choice of the free parameters of the experiment (laser intensity, target radius, R, wall thickness, ΔR, and fill gas density, ρ_o) scaling laws were developed and improved by Storm et al 1977 (4.61) Rosen and Nuckolls 1977 (4.63) and Storm (4.64). These laws claimed success for the prediction of neutron yield for moderate fill gas pressures ($\rho_o \sim 10$ atm) but do not properly describe experiments carried out for $\rho_o > 10$ atm.

A recently developed shock compression model (Ahlborn and Key 1979) (4.65) describes this high fill gas pressure region more appropriately. Tables 4.09 and 4.10 compare the various assumptions and give the results derived with the different models, for maximum density ρ_f, and electron and ion temperature T_e and T_i. Figs.4.59 and 4.60. compare the model predictions with experimental data.

Discussion of density scaling

Fig.4.59 gives the maximum density ρ_f as a function of the initial fill gas density ρ_o. In this representation the variation of ρ_f with $R/\Delta R$ can not be shown and the available data points range from $30 \leq R/\Delta R \leq 80$ with an average of $R/\Delta R = 50$. In the range of typical exploding pushers $2 \lesssim \rho_o \lesssim 8$ mg/cm^3 the experimental data for ρ_f scatter widely and do not favour any one of the 3 scaling laws. The spectroscopic data of RL, LASL and LLE yield generally lower densities. The data from KMS lie considerably above the rest. This could be a systematic difference due to the photographic diagnostic technique used or it could be a genuine effect caused by the better symmetry of the KMS target irradiation system. No direct data are available for low ρ_o where the models differ widely, except for some experiments with "empty" shells, where the imploded glass density was ~ 0.2 g cm^{-3}. These would support the Storm model. At high fill gas densities the RL results obtained with Xray shadowgraphy and the KMS measurements tend to favour the AK model. The Rochester results in this fill gas range are inconclusive since they only yield a lower limit for the electron density.

Discussion of temperature scaling

All three models yield ion temperatures which scale proportional to E/M but the effective energy E differs since it is obtained by integrating the laser energy upto different cut off times. The different effective energies of the models must become the same value in the limit that the laser pulse duration is shorter than any one of the cut off times. Hence experiments with short laser pulses and relatively low E/M have been compared with the models. Table 4.11 gives the temperature predictions for RL shot 102 where $R/\Delta R = 50$ $\Delta R/\rho_o R = 9$, $\rho_o = 2.2\ 10^{-3}$ g/cm^3 and the total absorbed energy E divided by the shell mass is $E/M = 6.10^{-2}$ J/ng.

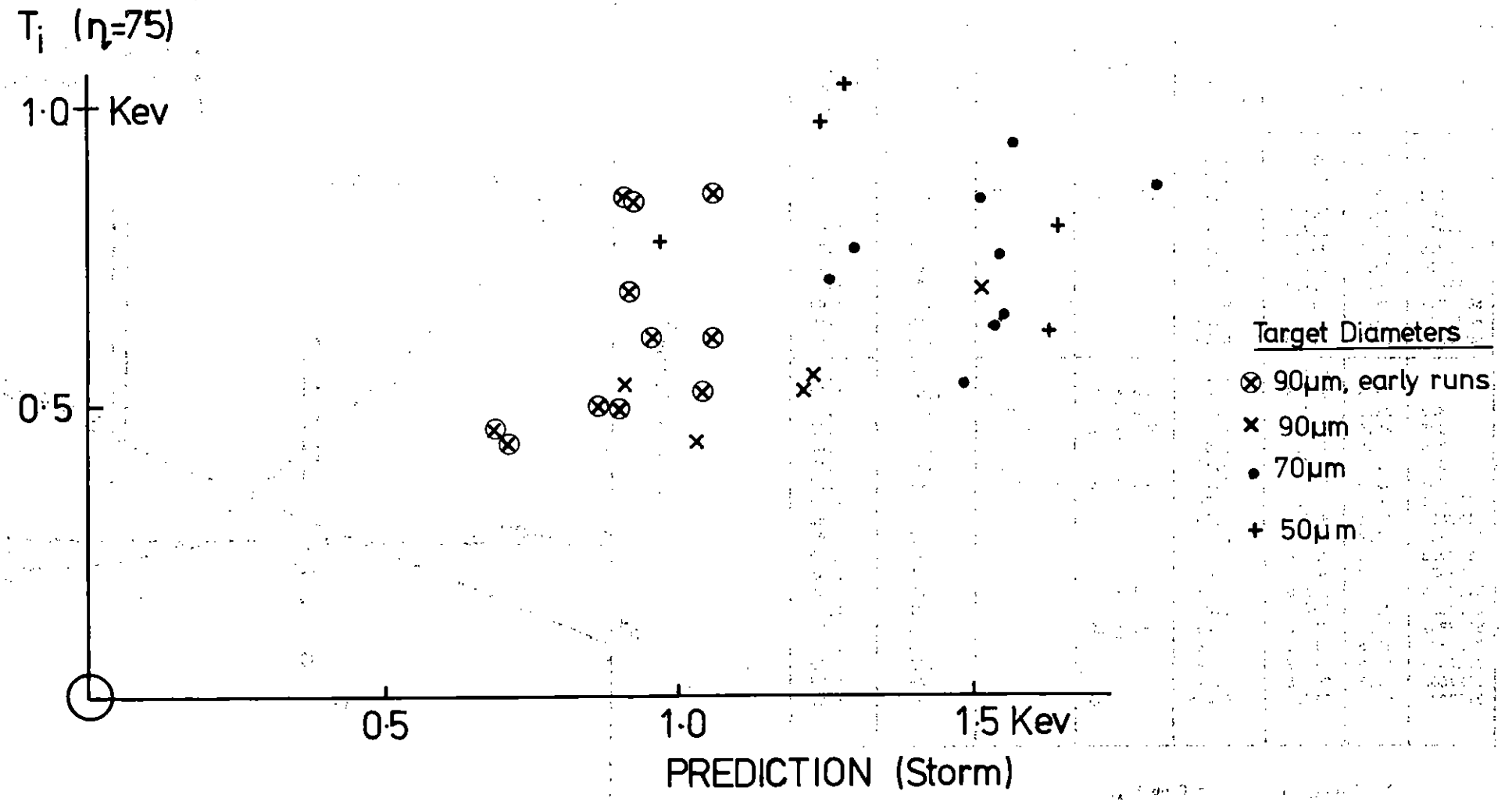

FIG 4.58 ION TEMPERATURE vs PREDICTION

TABLE 4.08

Shot	E_{LAS} *	2R/ΔR	Neutron Yield (10^5)	Core Spectroscopy		T_i (η=75) Kev	T_i (Storm) Kev
				T_e	η_e		
75	31.6	88/.8	1.0			.62	.96
76	29.0	83/.8	1.8			.70	.92
102	22.8	88/.9	.16	470 ± 50	6×10^{22}	.47	.69
103	24.0	90/.9	.12			.44	.71
5077817	38.0	88/.8	1.1			.62	1.06
5077818	29.0	90/.7	7.1			.85	.93
5077819	30.0	90/.7	7.5			.86	.91
6077806	34.0	85/.7	6.0			.86	1.06
6077807	34.0	83/.7	0.3			.52	1.05
6077808	26.	88/.8	0.27			.50	.90
6077810	31.	94/.8	0.35			.50	.87
318	17.2	51/.5	0.50			.78	.97
321	29.3	51/.5	2.4	440 ± 70	–	1.05	1.29
322	22.9	50/.5	1.7	510 ± 80	6×10^{22}	.99	1.25
325	48.5	71/.6	2.7	590 ± 60	–	.85	1.52
326	54.0	70/.6	3.0			.87	1.82
327	41.5	70/.5	0.17			.54	1.49
331	49.0	50/.5	0.11	560 ± 50	4×10^{22}	.62	1.63
5127801	46.6	96/.7	0.54			.53	1.22
5127804	48.4	82/.6	1.75			.70	1.52
5127805	29.9	90/.8	0.45			.53	.91
6127803	37.0	70/.6	1.6			.77	1.30
6127804	53.3	70/.7	1.4			.75	1.55
6127805	54.4	70/.6	.65	452 ± 30	–	.66	1.55
6127806	32.5	70/.6	1.0			.71	1.26
6127807	54.4	71/.6	.48	395 ± 20	–	.63	1.54
7127802	43.8	51/.5	.56			.80	1.65
7127805	47.5	91/.7	.54			.55	1.23
7127806	37.3	90/.8	.11			.44	1.03
7127807	53.3	71/.58	4.4**	439 ± 50	–	.94	1.57

* Energy on target = 0.66 E_{LAS}

** Corrected for D_2-rich fill

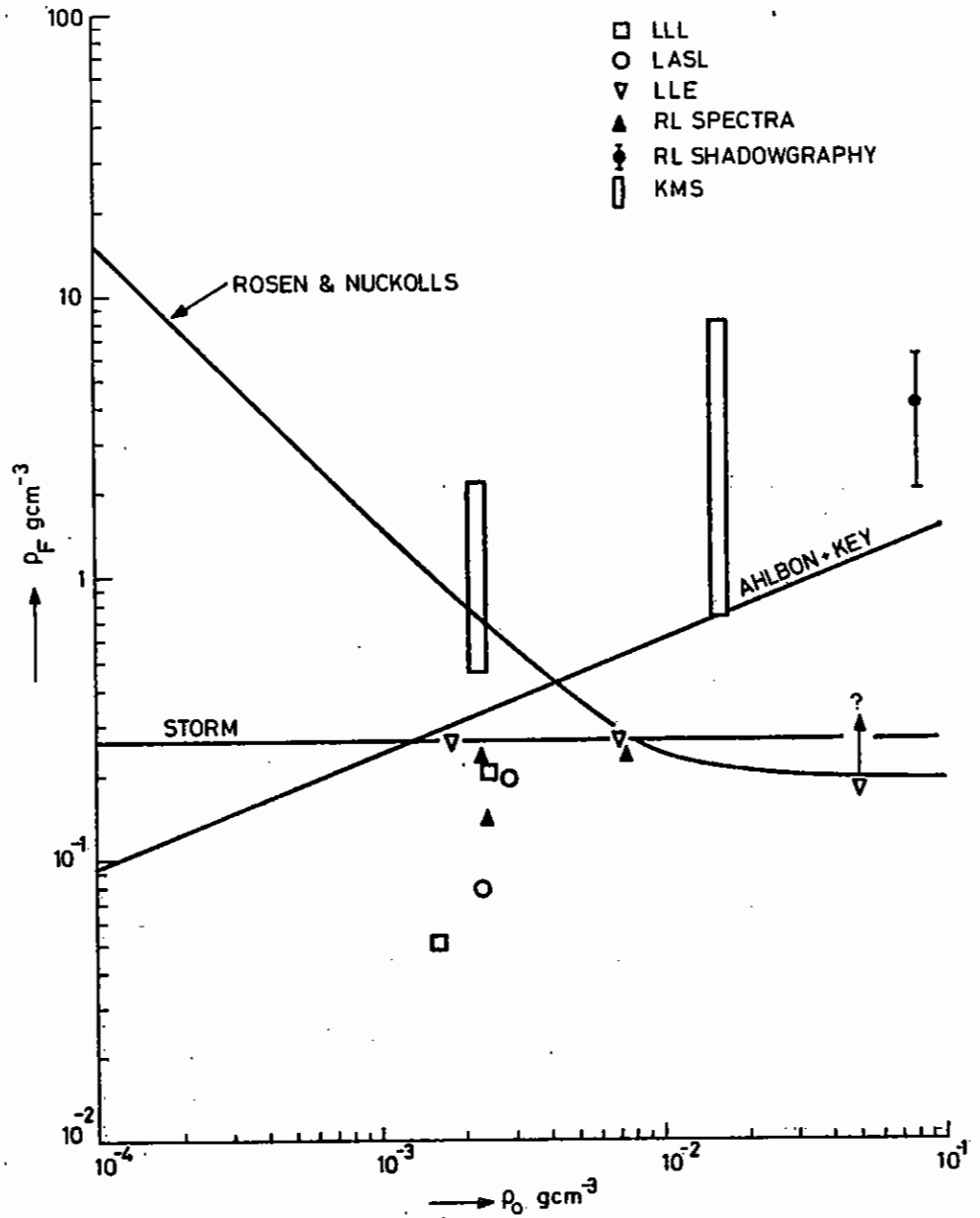

FIG 4.59

TABLE 4.09

DENSITY SCALING LAWS FOR EXPLODING PUSHER TARGETS

Model	Result	Assumptions
Storm (1978)	$\rho_f = 13 \frac{\Delta R}{R} \quad (\rho_p = 2.5)$	empirical constant α obtained from fitting experimental data
Rosen & Nuckolls	$\rho_f = (1+1.9\frac{\Delta R}{R\rho_o})^2 \rho_o$	at peak compression glass shell density ρg is distributed as 1) $\rho_g(r=R_F) = \rho_f$ 2) $\rho_g(r) = \rho_f\left(\frac{R_F}{r}\right)^{3/2}$ 3) $\frac{1}{4}$ of shell mass inside R_o
Ahlborn & Key (1979)	$\rho_f = 3.8\ \rho_o^{0.4}$	contact surface velocity u_2, peak pressure p_f related to specific absorbed laser energy E/M_p as u_2^2, $p_f \sim E/M_p$

TABLE 4.10 TEMPERATURE SCALING LAWS FOR EXPLODING PUSHER TARGETS

Model	Result	Assumptions
Storm	$T_i = 14 \frac{E_c/Mp\ (J/ng)}{(1+1.3\frac{R\rho_o}{\Delta r})}$ $Te = 0.2\ T_i$	obtained from energy balance Mp = pusher mass. The fraction of laser energy E_c useful for compression is absorbed before the time t_c when the contact surface has moved inwards to 0.66 R.
Rosen and Nuckolls	$T_i(keV) = 3.3 \frac{E'}{Mp} (1+1.9 \frac{\Delta R}{R_o\rho_o})^{4/3}$ $Te = 3.56 \frac{E''}{Mp\ (ng)}$	obtained from adiabatic + shock compression. The fraction of laser energy E' useful for compression is absorbed up to the time t_E when the first ingoing shock has reached $\frac{1}{4}$ of the DT target gas inside. E'' is the absorbed energy up to the time of stagnation.
Ahlborn and Key	$T_i = T_e = \frac{8.7\ \alpha\ E}{M_p\ \rho_0^{0.4}}$	obtained from $P_f = P_f(E/M)$ and ρ_f E is the total absorbed laser energy. Best experimental fit for $\alpha = 0.09$.
Ahlborn and Key Revised Storm Model	$Te = \frac{E_c/Mp}{11 \frac{}{1+0.9 \frac{R\rho_o}{\Delta R}(1+f)}}$	$f \simeq T_i/Te$ increases from 1 (in the limit of low temperature). Proportionality constant 11 from normalization against experiments.

TABLE 4.11

	T_i	T_e
Experiment	0.7 keV	0.45 keV
Storm	0.73	0.15
Rosen & Nuckolls	9.5	0.21
Ahlborn & Key (a)	6.0	-
Ahlborn & Key*(b) (Storm modified)	-	0.51

Best agreement is obtained with Storm's model for T_i and Ahlborn & Key's modification of Storm's model for T_e. The dependence of T_i on $\Delta R/\rho_o R$ is shown in Fig.4.60 for E/M = 0.1 J/ng. The models differ widely in the limit of large $\Delta R/\rho_o R$, but most experiments are carried out for $\Delta R/\rho_o R \sim 10$, with a shell aspect ratio $\Delta R/R = 50$ and 10 bar $D_2 + T_2$ fill gas. In order to compare the experiments (which were carried out with different values of E/M) with the model curves (calculated for E/M = 0.1J/ng) the experimental temperatures were scaled as $T_i = T_{ex} \frac{0.1 J/ng}{(E/M)}$. The data points agree in magnitude best with Storm's predictions. However it is noted that the AK model would fit the slope of the data points well. It is quite clear that the AK scaling model which does not yet have an adjustable parameter overestimates the temperature because it assumes instantaneous energy absorption
If one makes allowance for a finite absorption time, the glass shell has time to expand, which lowers the maximum pressure ($P_F \sim E/M$) and hence the temperature. In practical terms one can introduce a scaling factor α to reduce P_F and hence T_i to a more realistic value. The dashed line in Fig.4.60, obtained with $\alpha = 0.09$, fits all experiments better than the other scaling laws.

In summary the scaling laws for temperature and density vary widely, however the data points have a fairly wide scatter as well and they do not have a sufficient distribution in the range of ρ_o and $\Delta R/R$ to give unique preference to any one of the models.

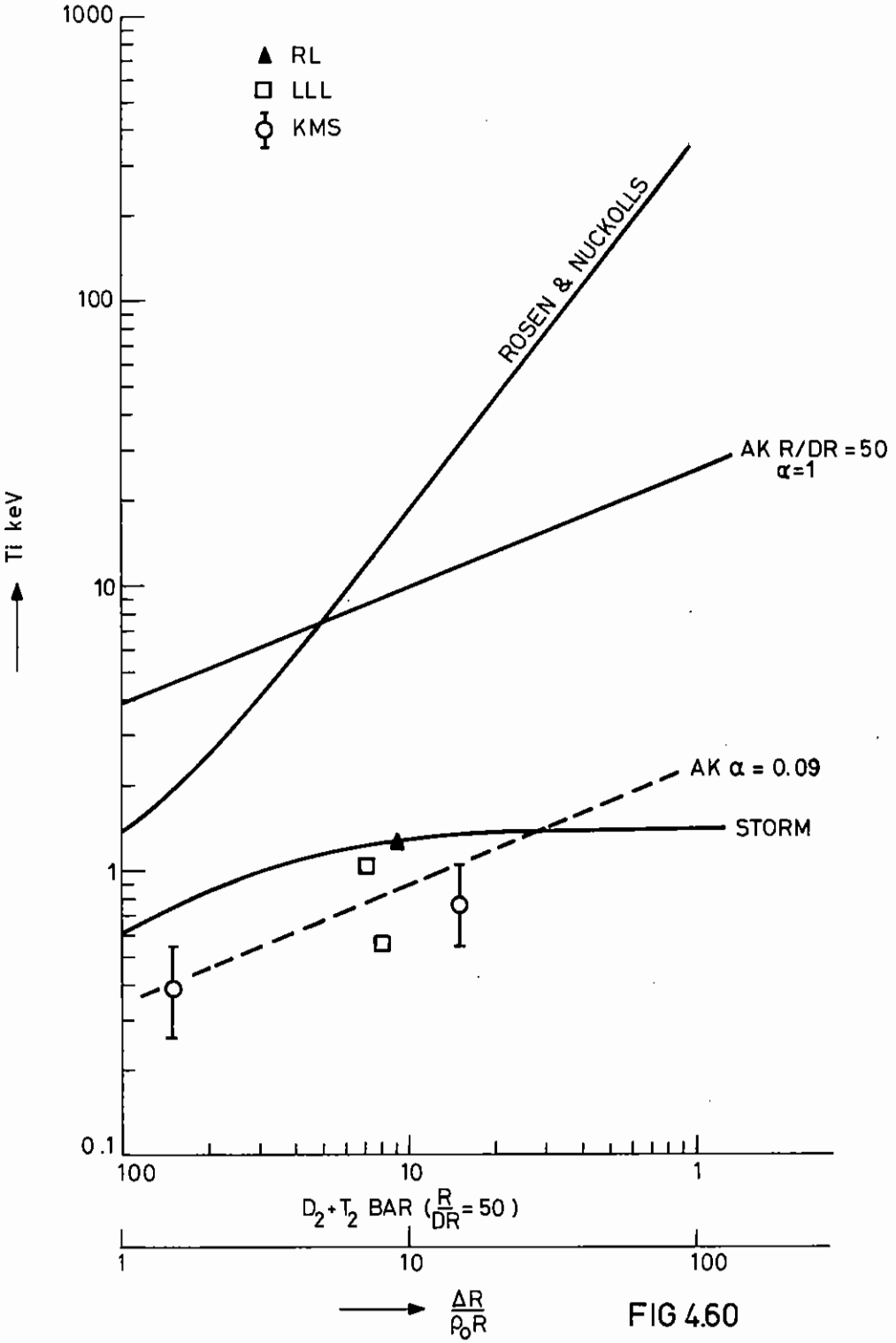

FIG 4.60

4.7.4 Computer Simulations of Exploding Pushers

(a) Core density and temperature

The particular conditions of some of the exploding pusher implosions described in section 4.7.1 have been modelled with our 1D Lagrangian fluid code MEDUSA, including energy transport by suprathermal electrons. The main adjustable parameter in the code is the partitioning of the absorbed laser energy between the thermal and suprathermal, or 'hot', electrons. Best agreement with observed values (Table 4.07, Section 4.7.1) is obtained by assuming that virtually all (ie $\sim$ 90%) of the laser energy which is absorbed at the critical density surface is used to create 'hot' electrons. Only in this case does the implosion show the exploding pusher behaviour in which the centre of the shell remains almost stationary during the implosion. In order to compare with experimental data, values of electron density and temperature were calculated by a post processor atomic physics routine that calculates time integrated X-ray line and continuum emission and these are reduced in exactly the same manner as the experimental spectra. The maximum densities and temperatures in the computer model are higher than these average values by almost a factor of two. For 18J incident on a 70 μm diameter microballoon with a .96 μm wall, filled with 8.5 m g cm^{-3} of neon, the compressed neon density was computed to be .29 gm cm^{-3} and the glass density somewhat higher at .45 gm cm^{-3}. Electron temperatures were computed to be 620 eV (neon) and 610 eV (Glass) somewhat higher than the mean observed values.

(b) Implosion time

The code has also been used to model the experiments described in section 5.2 where the implosion times of exploding pusher implosions were measured for a range of values of the specific energy E/M. The code was used to model the effects of changing the shell thickness and the laser energy independently, since the simple theory of exploding pushers would predict that the implosion time should scale as $(E/M)^{-\frac{1}{2}}$ where E is the useful absorbed energy (4.61) and M is the shell mass.

The results of the computer modelling shown in Fig.4.61 show that the implosion time can usefully be described by the single parameter E/M but that the implosion time measured from the peak of the laser pulse does not scale as $(E/M)^{-\frac{1}{2}}$. This is simply due to the fact that the peak of the laser pulse is not a good time reference for different values of E/M and it is better to measure the implosion time from the time when the inner wall of the shell has moved about 10% of its initial radius. With this definition of implosion time the scaling with E/M is much closer to the expected behaviour.

In Fig.4.62 we show the comparison between the MEDUSA predictions (measured from the time of peak laser power) and the measured implosion times. In order to account for differences in shell radii the implosion times have been scaled linearly with shell radius, normalised to 44 μm. It may be seen that there is a qualitative agreement with the code predictions but an absolute discrepancy of a factor of about 2 in the values of E/M.

The code assumes absorption of laser energy by a 10% dump at the critical density to simulate resonance absorption, together with inverse bremmstrahlung. The total effective absorption in the code is about 12%. In this particular experiment the absorption fraction was not measured but other measurements (4.66) would suggest a figure of 17%. Another factor which may account for the discrepancy between theory and experiment is that the illumination of the microballoon is strongly concentrated at the two poles to about twice the mean and the polar regions will be expected to implode faster than the equator, although the heating by fast electrons will tend to alleviate this asymmetry since they dominate the energy transport in exploding pusher implosions.

For the sake of completeness we have included in Fig.4.62 the computer calculations for purely classical heat conduction and also for the case where the classical conduction is inhibited by a factor of 30 as suggested by some "burn through" experiments. Clearly these cases which do not include fast electron energy transport show implosion times much longer than those observed experimentally.

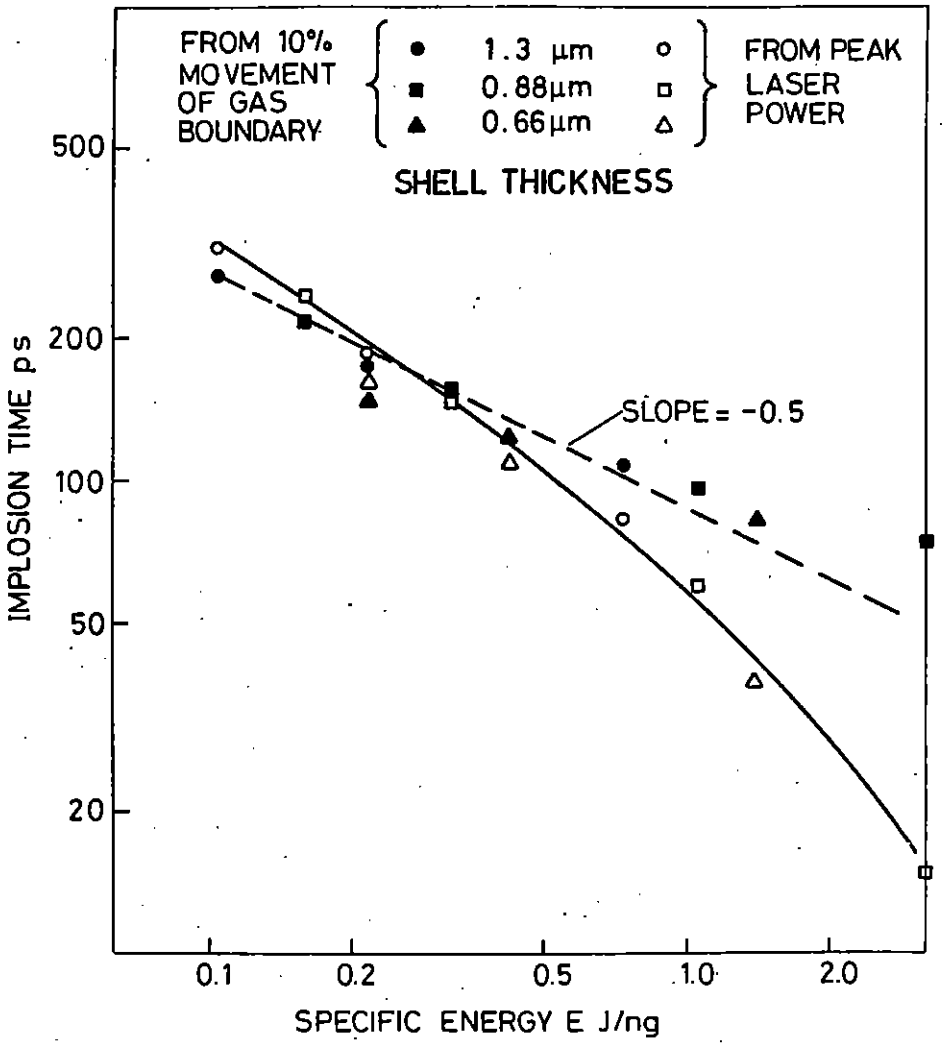

FIG4.61 VARIATION OF IMPLOSION TIME WITH SPECIFIC ENERGY

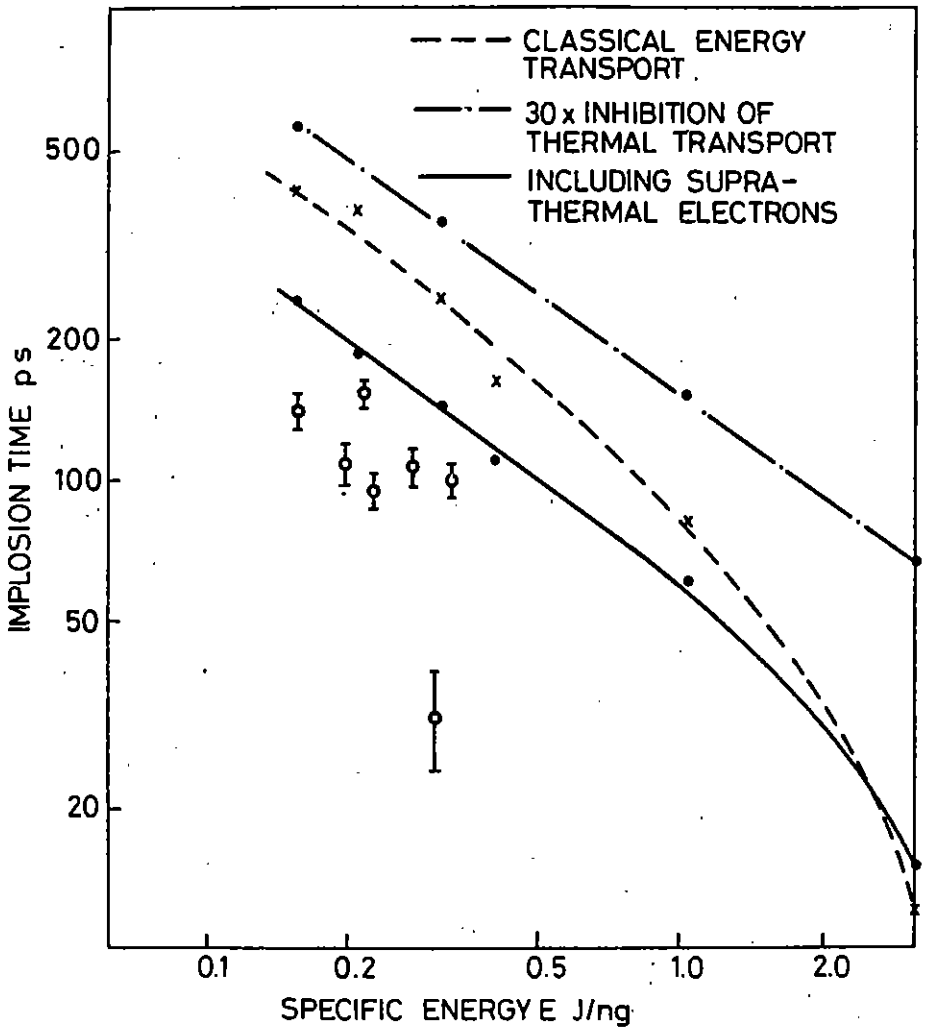

COMPARISON OF MEASURED AND PREDICTED
FIG4.62 IMPLOSION TIMES FOR DIFFERENT DESCRIPTIONS OF ENERGY TRANSPORT

4.7.5 Instabilities in exploding pushers

All of the targets used for exploding pusher work are coated with a thin (~ 1000 Å) layer of Aℓ to facilitate alignment. The space resolving crystal spectrometer used on most exploding pusher experiments resolves the shell emission and the core emission (eg Fig.4.63). In last year's report we showed that Aℓ appeared to be emitted from the core, despite being coated only on the surface of the microballoon. This observation is completely contrary to expectations. During the past year further evidence has strengthened this observation.

Central aluminium emission has been observed on many shots. Fig.4.64 illustrates two particularly good examples shots 208 and 209. On shot 208 Aℓ XIII Lα and Aℓ XII 1^1S_o-3^1P_1 were distinctly seen in the centre. On shot 209 Aℓ XII 1^1S_o-3^1P_1 and 1^1S_o-4^1P_1 are clearly seen.

There are several possible systematic errors to be considered before concluding that observations such as in Fig.4.64 are due to core emission.

First, there exists the possibility that the shell is emitting from its equator. This would cause emission to appear from the centre in space resolved spectra. But if there were uniform shell emission the central emission would not be distinct from the poles of shell as it clearly is in Fig.4.64. Furthermore on shot 208 the microballoon was only coated on the poles and so there could not have been emission from the equator.

Secondly, there exists the possibility of the central emission coming from the support stalk of the microballoon. On shot 208 this possibility was guarded against by remounting the microballoon on a clean support stalk after it had been coated. Furthermore, the spectral position of the lines indicates the spatial position of the sources. The separations of the central emissions of Si XIII 1^1S_o-2^1P_1 and Aℓ XII 1^1S_o-3^1P_1 can usefully be used because of their close spectral positions. If these lines come from a common source, their separation on the plate should be 100 μm. On shots 208 and 209 the separations were 90 and 95 μm respectively. This discrepancy is much less than the 42 μm displacement to longer wavelength expected if the Aℓ XII 1^1S_o-3^1P_1 emission had come from the support stalk.

One further possibility is that the aluminium comes from impurities in the glass. For shot 208 the glass was B18, but for shot 209 it was FI grade. The ratio of Aℓ/Si for these two glasses is $.7\ 10^{-3}$ and $1.3\ 10^{-3}$. This is very much less than the intensity ratio of Aℓ XII 1^1S_o-4^1P_1 and Si XIII 1^1S_o-4^1P_1 on shot 209, which was 1/4.

Completely independent evidence for core emission is obtained by fitting the Aℓ XII 1^1S_o-4^1P_1 to theoretically broadened profiles (section 4.7.1). A fit is shown in Fig.4.65. In fact the density must be higher than the value shown on the fit ($n_e = 2\ 10^{22}$ cm^{-3}). The ratio of $n_e/n_1 = 1/20$ is unrealistic and could only be obtained if the core were all Aℓ. Assuming only 1/4 of the core is Aℓ then a fit can only be obtained for $n_e = 4\ 10^{22}$ cm^3. This density is much higher than the density of the ablation plasma ($1\ 10^{22}$ cm^{-3}, section 4.3) yet is less than the core density of Si XIII on shot 209.

A fit on Aℓ XIII Lα in the core is shown in Fig.(4.66). This line appears to show plasma satellites.

In conclusion, there now appears strong evidence that Aℓ initially coated on the outside of microballoons gets to the implosion core, although it appears at a different time or in a different place to the glass emission.

4.7.6 Time resolved Xray line widths from microballoon implosions

In a recent experiment the time variation of Xray line widths from microballoon targets has been observed for the first time.

The method used was similar to that in earlier work where the time variation of Xray resonance and satellite line intensities from solid Aℓ targets was studied (4.67). The apparatus in this earlier work was of insufficient sensitivity to record the weaker spectral lines which are significantly broadened and provide a density diagnostic (4.68) in microballoon implosions. However, the development of CsI Xray photocathodes (Section 1.7) sufficiently enhanced the Xray streak camera sensitivity to allow a study of the line widths of SiHeβ and Ne Lyβ by Xray streak spectroscopy.

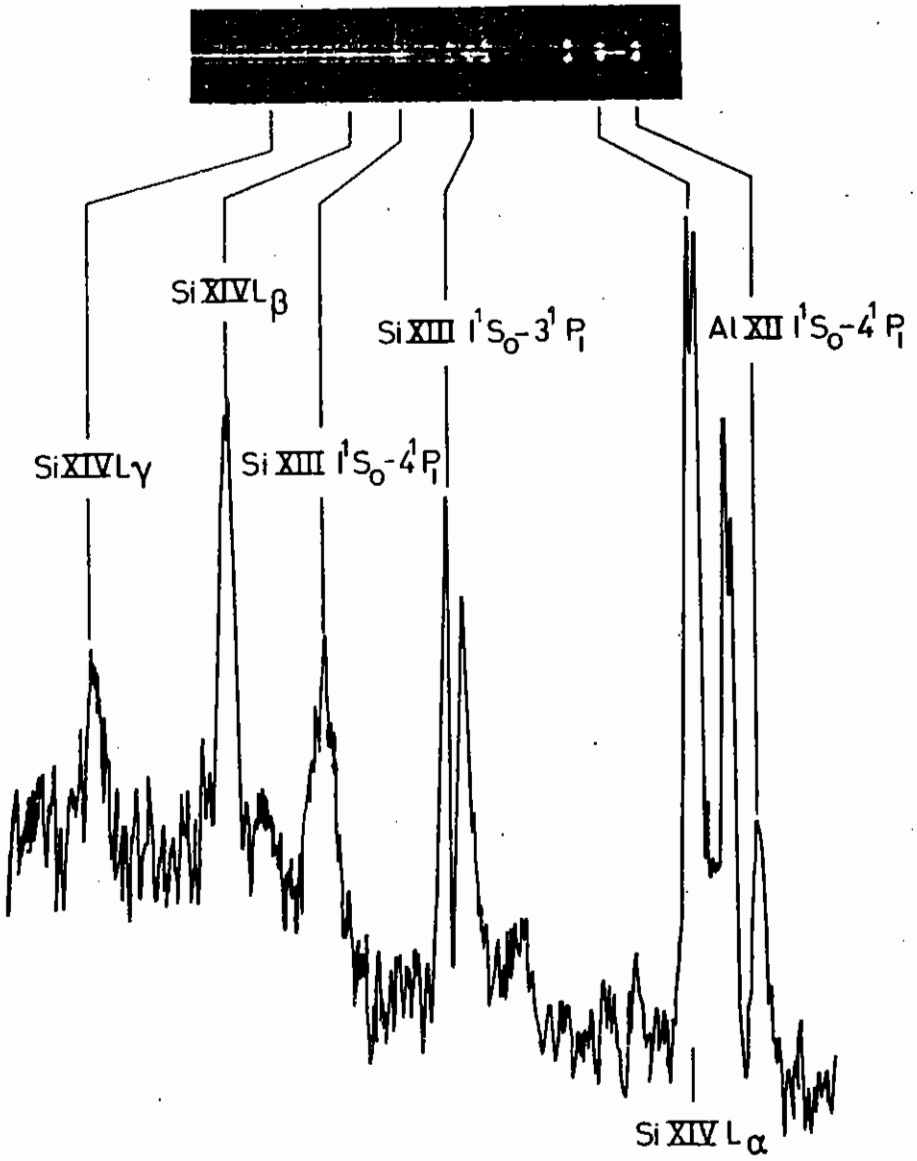

BALLOON RADIUS = 33 μm
WALL THICKNESS = 0.75μm
GAS FILL = 0.33 BAR ARGON

FIG 4.63

CORE SPECTRUM SHOT 209

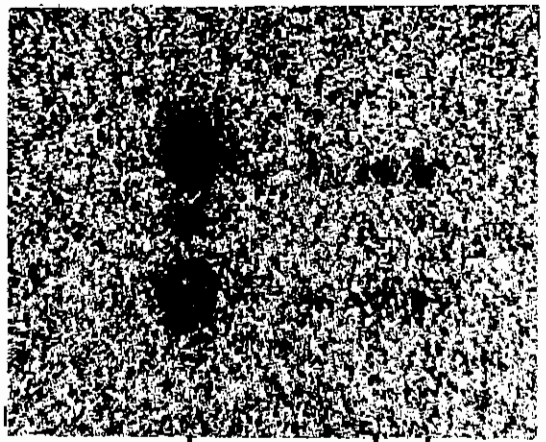

Al XIII
Lα

DIELECTRONIC
SATELLITES

INITIAL
DIAMETERS

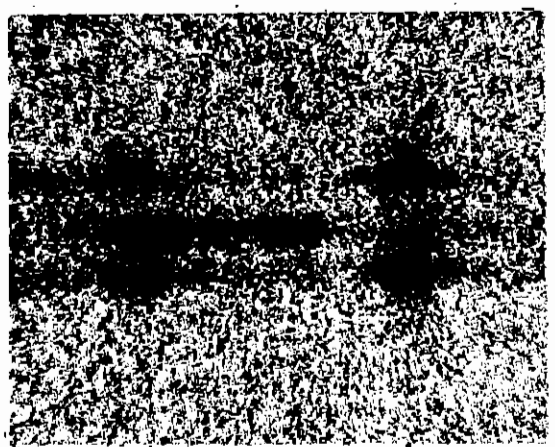

Si XIV
Lα

Al XII
$1s^2\,{}^1S_0 - K4p\,{}^1P_1$

OPTICAL DENSITY

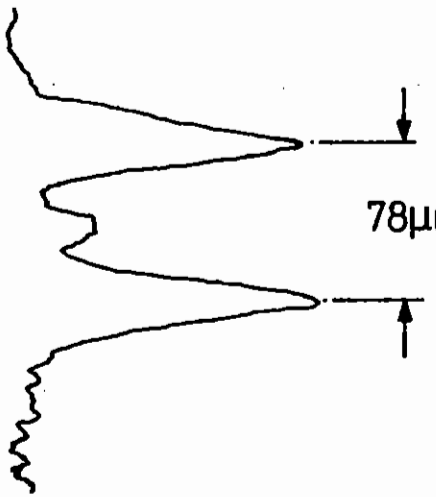

78μm SHOT 208

MICRODENSITOMETER
TRACE

SHOT 209

SPACE RESOLVED X-RAY
SPECTRA

1μm WALL THICKNESS ALUMINIUM
COATED MICROBALLOONS, SHOWING
EVIDENCE OF Al XII AND Al XIII
IONS IN THE IMPLOSION CORE.

FIG 4.64

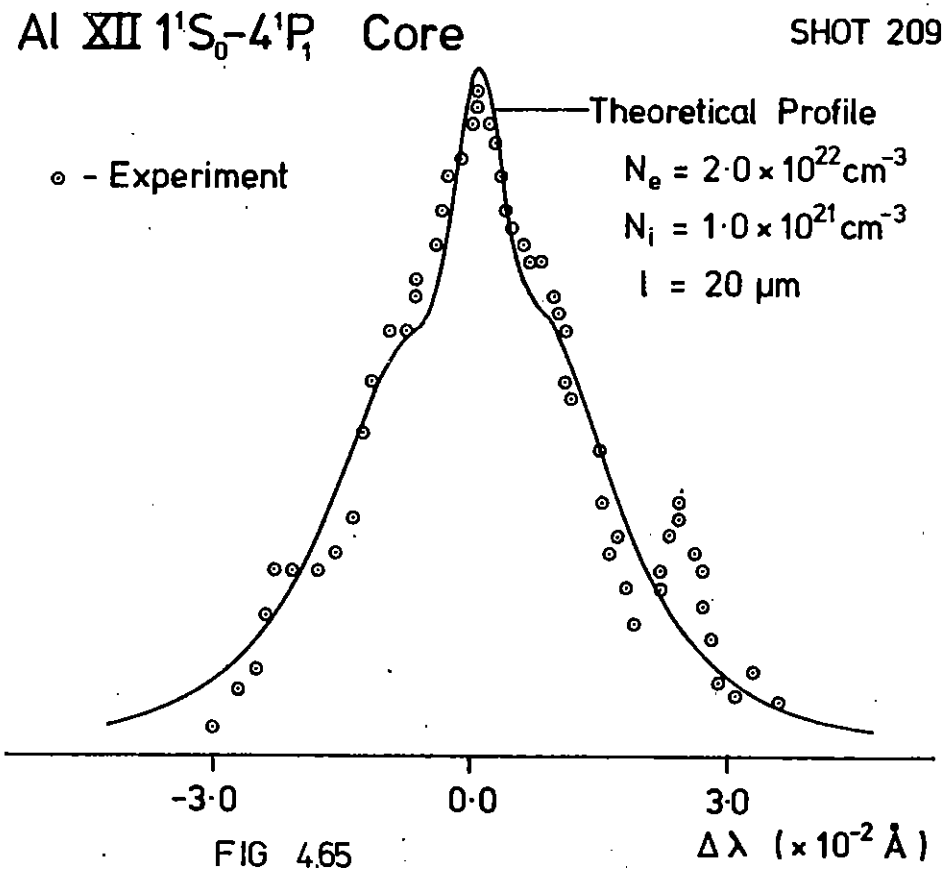

FIG 4.65

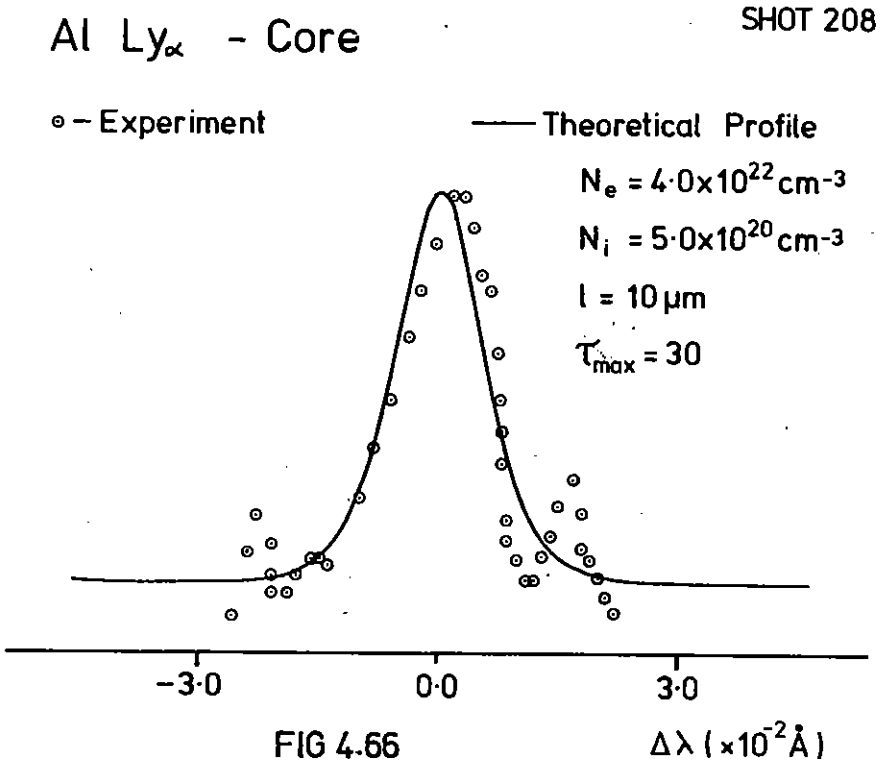

FIG 4.66

The apparatus is shown schematically in Fig.4.67. Bragg reflection from a crystal of T&AP or PET dispersed the microballoon Xray spectrum on the photocathode of the Xray streak camera. Spectral resolution was limited by the spatial resolution of the streak camera/intensifier system which was $\Delta S \sim 200$ μm at the photocathode. The spectral resolution was thus $\Delta\lambda = \Delta S \frac{2d \cos^3\theta}{L}$ where d is the crystal plane spacing and L is the plasma to photocathode distance in Fig.4.67. Thus Ne Lyβ ($\lambda = 10.24$ Å) was recorded with 22 mÅ resolution using a T&AP crystal ($2d = 25.75$ Å) and, Si Heβ ($\lambda = 5.68$ Å) with 4.3 mÅ resolution using a PET crystal ($2d = 8.74$ Å). This instrumental resolution is smaller than the line widths of these transitions im emission from implosions (4.68) which are typically 30 mÅ for Si He and 150 mÅ for Ne Ly β.

The recorded wavelength was controlled by translation of the crystal to vary θ in Fig.4.67 and the recorded spectral range was limited by the 1.4 cm field of the streak camera tube at its photocathode. It was 0.3 Å and 1.5 Å for recording Si Heβ and Ne Lyβ respectively.

Temporal resolution was limited by the streak speed and the length of the spectral lines perpendicular to the dispersion axis. The latter was controlled by the 1100 μm slit in Fig.4.67. Point projection through the slit from the plasma gave a 340 μm length which was convolved with the imaging via the slit of the 100 μm microballoon plasma with 2 x magnification. The combined effect gave ∿ 20 ps time resolution for a streak speed on the recording film of 3×10^9 cms^{-1}. This was adequate to resolve the typically 100 ps implosion time of the microballoon targets (4.69, 4.70).

The apparatus also included filters to suppress radiation at long wavelengths (the photocathode substrate was 15 μm Be and additional filters of 15 μm Be and 1.5 μm A were placed in front of the slit in recording Si Heβ and Ne Lyβ respectively) and a baffle shown in Fig. 4.67 to suppress fluorescence from the filters.

Si Heβ emission is known from space resolved spectroscopy studies to be emitted both from the ablation plasma and from the implosion core of

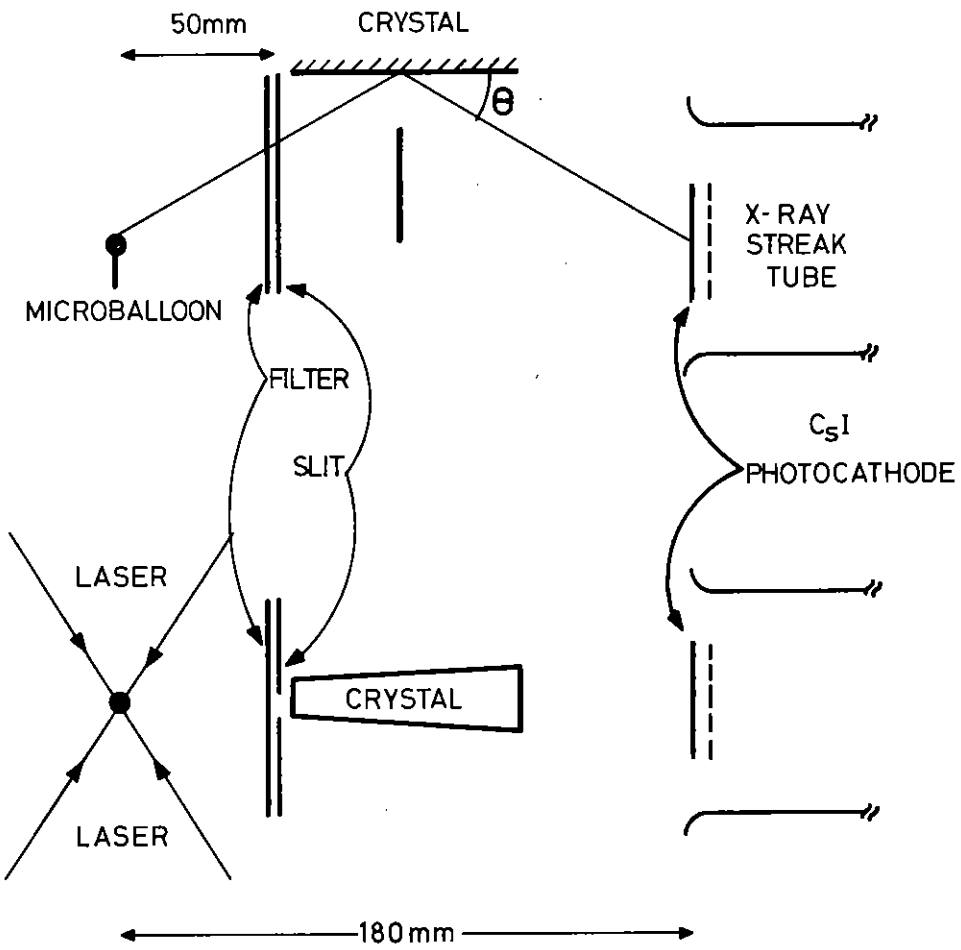

FIG 4.67 Apparatus for time resolved X-ray spectroscopy

microballoon targets (4.68) and its generation has been used as an indication of ablation burn through depth in Aluminium coated microballoons (4.69).

Time resolution of its emission thus offers the possibility to observe
- time variation of line width, particularly narrow line 'after glow' emission which might change the interpretation of time integrated spectra from the ablation plasma
- time difference due to 'burn through' delay between Si Heβ emission and Aℓ Lyγ emission from Aℓ coated targets (since Aℓ Lyγ at 5.739 Å could be recorded simultaneously with Si Heβ at 5.683 Å).
- time and linewidth difference due to implosion delay between ablation plasma and implosion core emission.

Neon Lyβ emission is known from space resolved spectroscopy to be emitted from the implosion core of microballoon targets and to provide a good core density diagnostic (4.68).

The available spectral range allowed recording of the sequence of spectral features Na Heα, Ne Lyβ, Na Lyα, Ne IX continuum edge, Ne Lyγ and Na Heγ.

Features of potential interest in time resolving this spectrum include:
- determination of implosion time from the time delay between NaLy α emission in the ablation plasma and Ne Lyβ emission in the implosion core
- observation of any time variation in Ne Lyβ line width (particularly narrow line after glow) which might affect interpretation of time integrated spectra.
- observation of any difference in emission duration between Ne line and Ne continuum radiation (as is characteristically seen in solid target studies with the other elements (4.71)) which would affect the interpretation of line/continuum ratios in time integrated spectra.

Experimental results were obtained with two beam f/1 lens irradiation of microballoons with energy on target of typically 10J per beam in a 100 ps pulse with a prepulse level of $\sim 10^{-5}$ which was higher than the 10^{-6} usually achieved. Targets had diameters from 50 to 90 μm, wall thickness from 0.5 to 1.2 μm, aluminium coating from 0.04 to 0.4 μm thick and gas fill of 0.5 to 2 bar Ne or 10 bar deutrium plus tritium. Preliminary consideration of the data shows qualitatively at this stage several interesting features.

Ablation plasma Si Heβ emission was recorded from targets where simultaneous space resolved spectra showed negligible implosion core emission. With very thin Aℓ layers (0.04 μm) the Si Heβ line was very strong relative to underlying continuum and broadened to $\sim$9 mÅ. It was observable $\sim$ 30 ps sooner than the continuum and had a considerable after glow emission with narrowing line width continuing for upto 200 ps after the $\sim$ 100 ps pulse of continuum emission.

Thicker Aℓ (0.2 μm) made the Aℓ Lyγ line just observable relative to the continuum but still weak relative to Si Heβ (see Fig.4.68 (a)). With 0.4 μm of Aℓ, Si Heβ and Aℓ Lyγ were of approximately equal intensity and both were not much above the continuum level. The Si Heβ line was surprisingly emitted with no time delay relative to the continuum and Aℓ Lyγ line. The latter showed some after glow emission. The interpretation of this last observation in terms of a simple ablation burn through is difficult since a delay of the order of the pulse duration would be expected when the burn through just reaches the SiO_2. However the ablation burn depth was larger than reported in section 4.3 and this may be due to the 10^{-5} prepulse for these shots. Where small targets with $\sim$ 50 μm diameter were imploded to give strong implosion core emission as in Fig.4.68(a) the Si Heβ streak showed a sudden appearance of $\sim$ 18 mÅ wide line wing after $\sim$ 2/3 of the continuum emission duration. This can be associated with the implosion time delay $t_3 - t_1$ in Fig.4.68.

Implosion of targets with neon gas fill and observation of the spectral features around He Lyβ showed that He Lyβ was emitted with a delay relative to He Lyα (Fig.4.68(b)). The line was strongly broadened to

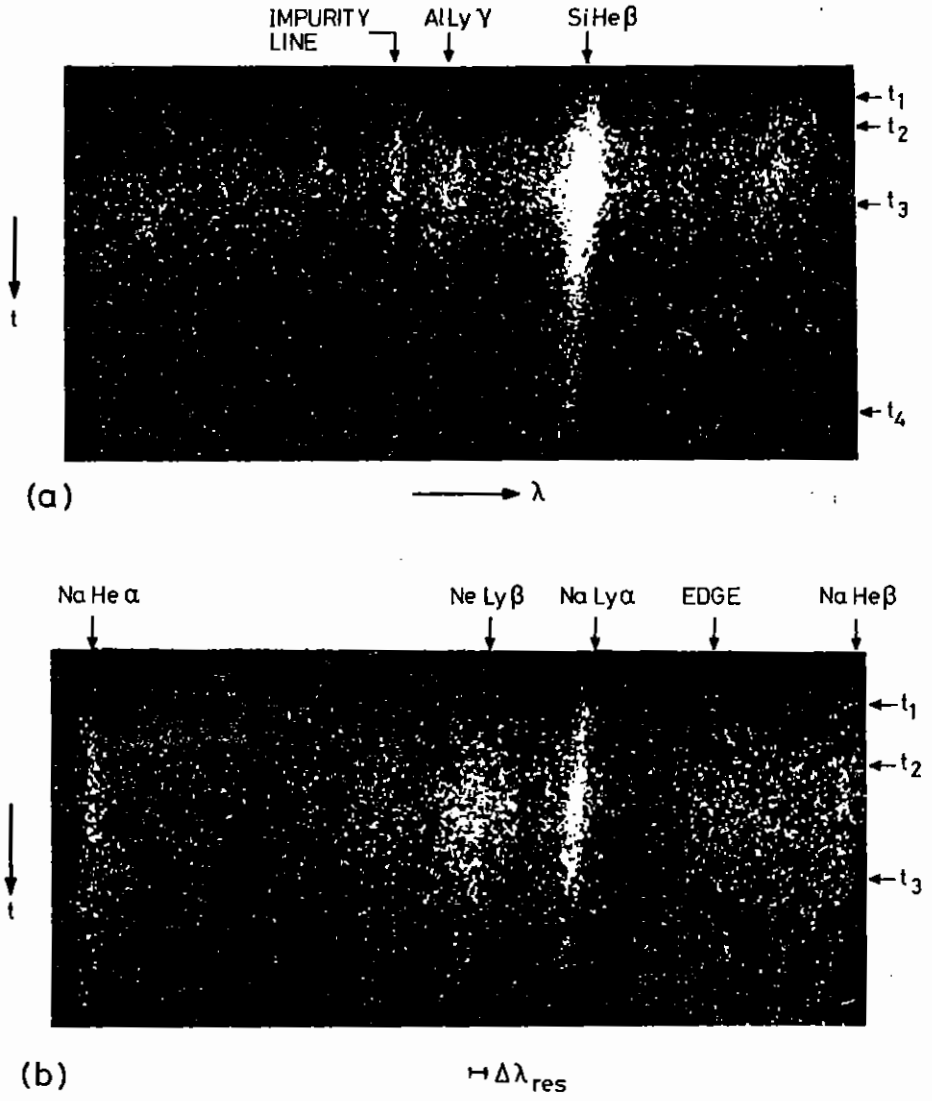

FIGURE 4.68

$\sim$ 14 mÅ and much wider than the almost instrument limited Na Lyα line. The emission pulse duration was short ($\sim$ 100 ps) and there was no obvious after glow emission or change of line width during the emission. The He IX continuum was seen to be emitted at the same time as the Lyβ ie delayed by the implosion time relative to Na Ly α. Variation of implosion delay time from $\sim$ 50 ps to $\sim$ 100 ps with change of target diameter from 64 to 93μm was noted.

The Na Ly_α and the He_α lines were both emitted for $\sim$ 200 ps. The emission was a super position of that from the ablation plasma and implosion core with the former dominating due to its larger volume. Observation of a sudden 2 x increase in the line width of Na Heα at about the end of the He Lyβ emission may be evidence of a peak density in cool imploded glass occurring later than the peak density in the Neon.

CHAPTER 4 REFERENCES

4.01 J A Stamper and B H Ripin, Phys Rev Lett 34, 138 (1975)
J A Stamper, E A McLean and B H Ripin, Phys Rev Lett 40, 1177 (1978)

4.02 A Raven, P T Rumsby and O Willi, Phys Rev Lett 41, 554 (1978)

4.03 C E Max, W M Manheimer and J J Thomson, Phys Fluids 21, 128 (1978)

4.04 D A Tidman, Phys Rev Lett, 32, 1179 (1974)

4.05 D T Atwood, private communication

4.06 J S Pearlman and G H Dahlbacka, Appl Phys Lett 31, 414 (1977)
R F Benjamin, G H McCall and A W Ehler, Phys Rev Lett 42, 890 (1979)

4.07 D A Tidman and J A Stamper, Appl Phys Lett 22, 498 (1973)

4.08 B Grek et al Phys Rev Lett 41, 1811 (1978)

4.09 D G Colombant and N K Winsor, Phys Rev Lett 38, 697 (1977)

4.10 R J Mason, Phys Rev Lett 42, 23 (1979)

4.11 D A Tidman and R A Shanny, Phys Fluids 17, 1207 (1979)

4.12 S I Braginskii, Reviews of Plasma Physics p 205

4.13 R C Malone, R L McCrory, R L Morse, Phys Rev Lett 34, 721 (1975)
F C Young et a, Appl Phys Lett 30, 45 (1977)

4.14 NRL, Appl Phys Lett, 77

4.15 B Yaakobi, T C Bristow, Phys Rev Lett 38, 350 (1977)

4.16 M H Key et al, XII European Conf. on Laser Interaction with Matter Moscow, December 1978 R1-79-014

4.17 B Yaakobi, A Nee, Phys Rev Lett 36, 1077 (1976)

4.18 L Spitzer, 'Physics of fully ionised gases', Interscience, New York 1956

4.19 C Jordan, Mon Not R Astr Soc (1969) 142, 501

4.20 D W Forslund, J Geophys. Res, 75, 17 (1970)

4.21 D W Forslund, J M Kindel, K Lee, Phys Rev Lett 39, 284 (1977)

4.22 P M Cambell et al, Proc VI IAEA Conference on Plasma Physics and Controlled Nuclear Fusion Research, Vol I, Vienna, 1977

4.23 E K Storm et al, UCRL 50021-76 p 5,85 - 5.126 (1977)

4.24 L M Wickens, J E Allen, P T Rumsby, Phys Rev Lett 41, 243 (1977)

4.25 J W Shearer et al, Phys Rev A6, 764 (1972)

4.26 K A Brueckner, Nuclear Fusion, 17, 1257 (1977)

4.27 A Zigler, H Zmora, J L Sczwab, Phys Lett 63A, 275 (1977)

4.28 B Yaakobi, I Pelah, J Hoose, Phys Rev Lett 37, 836 (1976)

4.29 K B Mitchell, R P Godwin, J Appl Phys 49, 3851 (1977)

4.30 Rutherford Lab Central Laser Facility Annual Report 1978, RL-78-039

4.31 L L House, Astrophys. J Suppl 18, 21 (1969)

4.32 Handbook of Spectroscopy, Vol I, CRC Press, Ohio 1974

4.33 Ya B Zel'dovich, Yu P Raizer, Phys of shock waves and high-temp hydro phenomena, p 201, Academic Press 1966

4.34 L V Spencer, NBS Monograph 1, 1959

4.35 N A Dyson, X-rays in atomic and nuc phys Longman (1973)

4.36 A Vignes and G Dez (1968) Brit J Appl Phys (J Phys D)

4.37 H Greim, Plasma Spectroscopy, McMillan (1964)

4.38 D R Bates, A E Kingston, R W P McWhirter, 1962 Proc Roy. Soc A, 267 297 (part 1)

4.39 R S Craxton, M G Haines, Phys Rev Lett 35, 1336 (1975)

4.40 D Pines, D Bohm, Phys Rev 85, 338 (1952)

4.41 W Bambynek et al, Rev Mod Phys 44, 716 (1972)

4.42 See section 8.6

4.43 D Nicholas (private communication)

4.44 F Amiranoft et al, 7th Int Conf on Plasma Physics and Controlled Thermonuclear Fusion Research, Innsbruck 1978 paper IAEA-CN-37-D-4

4.45 R.C Malone, R L McCrory, R L Morse, Phys Rev Lett 34, 721 (1975)

4.46 (Ref.4.44)

4.47 J S Pearlman, J P Anthes, Appl Phys Lett 27 (11) 581 (1975)

4.48 J S Pearlman, J J Thomson, Appl Phys Lett 32 (11) 703 (1978)

4.49 S J Gitomer, D B Henderson, Phys Fluids 22 (2) 364 (1979)

4.50 D B Henderson, Los Alamos Report LA-UR-77-1442 (1977)

4.51 Shay et al, Phys Fluids 21 (9) 1634 (1978)

4.52 R J Faehl, W L Kruer, Phys Fluids 20 (1) 55 (1977)

4.53 D W Forslund, J M Kindel, E L Lindman, Phys Fluids 18 (8) 1002 (1975)

4.54 T W Johnston, J M Dawson, Phys Fluids 16 (5) 722 (1973)

4.55 M H Key et al, Rutherford Lab Reports
RL 77 122 1 13 1977
RL 78 020 Q 1978
RL 79 014 1979
J Phys B 12 L213 1979
RL 78 039

4.56 B Yaakobi, D Steel, E.Thorsos, A Hauer, B Perry, Phys Rev Letts 38 1526 (1977)
K B Mitchell, D B Van Husteyn, G H McCall, P Lee, Phys Rev Letts 42 232 (1978)

4.57 P C Kepple, H R Griem, NRL Memorandum Report 3382, Naval Research Lab, Washington D C 1976

4.58 M C Hobby, N J Peacock, J Phys F, 6, B4 (1973)

4.59 C Jordan, Mon Nst R Astr Soc (1969) 142, 501

4.60 D R Bates, A E Kingston, R W P McWhirter, Proc Roy Soc A, 267, 297 (1962)

4.61 E K Storm, J T Larsen, J M Nuckolls, M G Ahlstrom, K R Manes, UCRL preprint 79788 Nov 1977

4.62 We would like to thank E J Bateman for assistance.

4.63 M D Rosen, J M Nuckolls, UCRL preprint 81343 July 1977

4.64 E K Storm, private communication

4.65 B Ahlborn, M H Key, Rutherford Lab report RL 79033 (1979)

4.66 H G Ahlstrom, Lawrence Livermore Laboratory Report No. UCRL 79819 (1977)

4.67 Annual Report to the Laser Facility Committee 1978 RL 78 039 p 2/A

4.68 M H Key, J G Lunney, J M Ward, R G Evans, P T Rumsby, J Phys B 12 6213

4.69 M H Key et al Review of recent progress... RL 79 014 1979

4.70 M H Key, M J Lamb, C L S Lewis, A Moore, R G Evans, Appl Phys Letts (in press)

4.71 M H Key, C L S Lewis, M J Lamb, Opt. Comm 28 331 (1979)

CHAPTER 5 ABLATIVE COMPRESSION STUDIES

INDEX

CHAPTER EDITOR P T Rumsby

CONTRIBUTORS L Cooke, R G Evans, T A Hall, M H Key, M J Lamb, C L S Lewis, J G Lunney, A Moore, J M Ward

5.1 Introduction

All compression experiments carried out prior to 1978 were of the so called exploding pusher type where hot ($T \sim 10^7$ ^oK) but relatively low density ($Ne \sim 10^{23}$ $cm,^{-3}$ or ~ 0.3 gm cm^{-3}) core plasmas are produced. The dynamics of this type of implosion are dominated by energy transport throughout the thin wall of the glass shell target and preheating of the fill gas by the hot electrons produced by laser absorption processes.

Attainment of significantly higher core densities, a major scientific objective, is only possible by moving away from this type of implosion and changing to the so called ablatively driven mode. To achieve this it is necessary for the target shell thickness to be increased to be greater than the hot electron range with the result that only the outside of the glass shell wall is heated by the laser. As a consequence the target behaves somewhat like a spherical rocket with the outside of the shell being ablated away by the laser and the inner region being accelerated inwards. For most efficient compression the laser pulse length must be increased to match the implosion time. This requirement calls for laser pulse lengths of order 1 ns compared with the 50-100 ps pulses used for exploding pusher experiments. Whether or not such ablatively driven shells are seriously subject to potential damaging Rayleigh-Taylor type instabilities is of major scientific interest at the moment as such behaviour could lead to shell break up and limit the densities achievable.

Over the year the experiments performed have shown a transition from short pulse exploding pusher to long pulse ablative type compressions. X-ray streak camera studies of exploding pusher implosion times

were continued involving development of diagnostic methods suitable for high densities. Further pulsed X-ray shadowgraphy experiments were carried out with exploding pusher targets designed to produce high density cores, using an improved backlighting arrangement. Finally streaked X-radiography observations of truly ablative type implosions were performed in an initial attempt to study the dynamics and stability of such events.

5.2 X-ray streak camera study of implosion time

In last year's report (5.1) we gave details of an X-ray streak camera study of implosion time in 'exploding pusher' targets. This produced results of the type illustrated in figure 5.01.

This work has been extended by obtaining data at lower values of laser energy/target mass (E/M) using a new ultra soft X-ray sensitive photocathode in the camera. The photocathode was a 150A gold layer on a 1000 A polymer substrate.

The range of conditions studied is given in Table 5.01 and in figure 5.02 the implosion time is plotted as a function of E/M.

Comparison with computer modelling with MEDUSA is also shown in figure 5.02 and the conclusions that have been made are that:

(a) The implosion time varies as (E/M)

(b) The calculated and observed implosion times agree in magnitude only if the absorbed energy in the calculations is assumed to go initially into 'hot' electrons with a temperature related as observed experimentally to the laser intensity (5.2), and if the intensity used in the one dimensional spherical model calculation is the local intensity at the irradiated poles of the microballoon. This is 2.5 higher than the intensity averaged over the sphere and shifts the data by the factor on the E/M axis of figure 5.02.

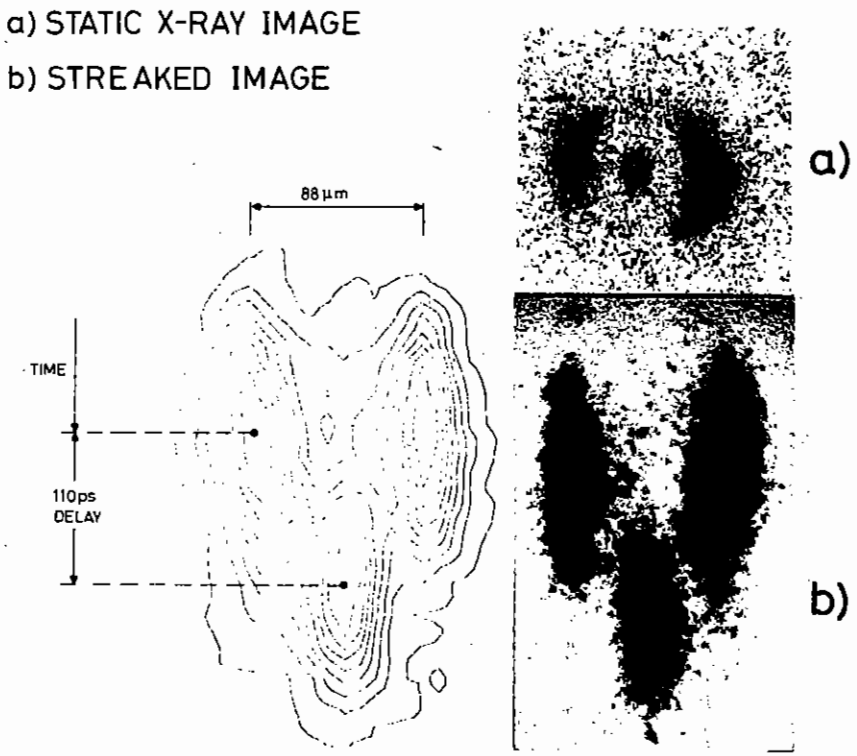

TIME AND SPACE RESOLVED X-RAY EMISSION FROM IMPLOSION OF 10 BAR $D_2 + T_2$ FILLED GLASS MICRO-BALLOON

Figure 5.01

An example of an Xray streak record of an implosion showing the time delay of the implosion core emission for the shot 081177/102 in Table 1.

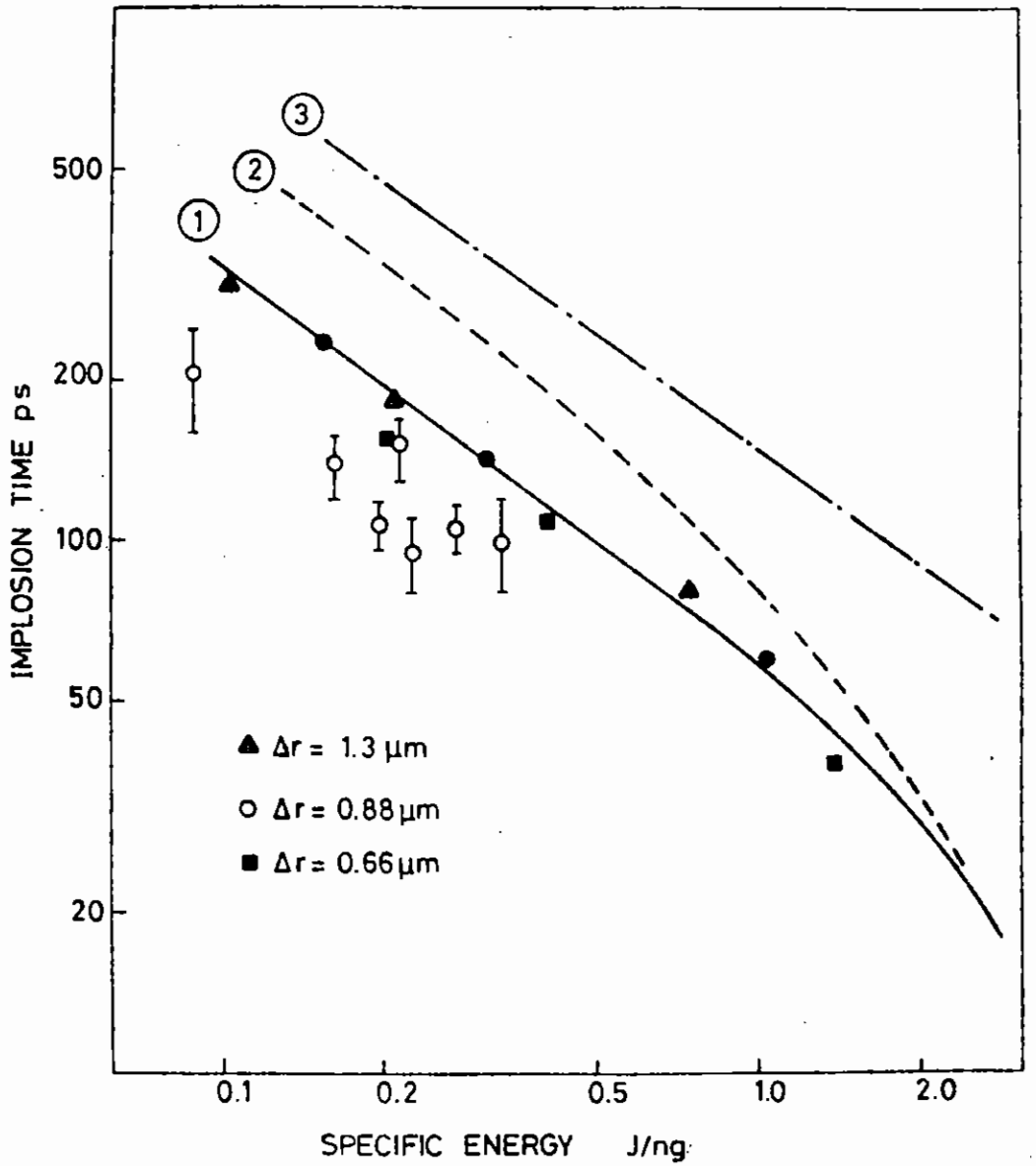

Figure 5.02

Experimental results showing implosion time as a function of laser energy/target mass (termed specific energy). One dimensional simulation results are also shown (1) in which it is assumed that 10% of the energy reaching the critical density surface is absorbed and creates Maxwellian hot electrons with 10 x the critical density electron temperature; (2) shows the result where the 10% absorbed energy is added to the thermal energy at the critical density and classical flux limited thermal conductivity is assumed; (3) shows the case as in (2) but with 30 x inhibited flux limited thermal conductivity.

TABLE 5.01 TABULATED TARGET, LASER PULSE AND X-RAY STREAK RECORD PARAMETERS

Shot Number	Laser Energy J	Target Diameter μm	Target Wall Thickness μm	Gas Fill	X-Ray Cut-off Energy KeV	Implosion Time ps	Specific Energy J/ng
021177/087	8.4	74	1.12	Empty	1.4	120	.17
071177/094	16.8	70	1.28	Empty	1.0	79	.34
071177/096	5.4	70	0.64	Empty	1.0	122	.22
081177/100	8.7	84	0.77	$D_2 + T_2$ 10 Bar	1.0	104	.20
081177/102	15.2	88	0.88	$D_2 + T_2$ 10 Bar	1.0	110	.28
081177/103	13.2	90	0.88	$D_2 + T_2$ 10 Bar	1.0	97	.23
160878/256	2.5	90	0.55	Ne 2 Bar	0.03	210	.07

The experiment observes the implosion on the axis between the irradiated poles where there is a more rapid implosion than perpendicular to it.

A further improvement of the X-ray streak camera has been the use of a photocathode formed from CsI at 5% of solid density. Such photocathodes have been shown recently (5.3) to be capable of giving quantum efficiencies $\sim$ 50% for photon energies up to 10 KeV and to yield a large number of electrons per detected photon. ($\sim$ 30 with a 3 KV/mm field at the photocathode).

The photocathode is believed to function as an electron multiplier with secondary multiplication occurring as electrons are accelerated across voids in the low density medium. Yield therefore depends on the field at the photocathode and, with 0.9 kV/mm as the normal field between cathode and mesh in the streak camera, simple substitution of the CsI photocathode gave $\sim$20 x improved sensitivity over the more usual gold photocathode in tests at photon energy of 2 to 2.5 KeV.

Time resolution limitations of the photocathode are believed to depend on its thickness and estimates (5.3) suggest $\sim$40 ps for a 50 μm layer which is efficient for photon energies up to several KeV.

Time resolution tests are in progress.

The availability of this additional sensitivity was a significant factor permitting experiments on streaked X-ray shadowgraphy of ablative implosions described in section 5.4 below.

5.3 Pulsed X-radiography of dense cool laser - imploded plasma

In last year's report (5.1) we gave details of an experimental study of the laser driven implosion of 87 bar Neon filled glass microballoon targets using a new Xray shadowgraphy diagnostic technique which is suitable for cool dense implosions from which there is no significant X-ray or thermonuclear reaction product emission.

Experiment (a) in Table 5.02 specifies the main parameters of the experiment which yielded core densities in Neon of 4 ± 2 gcm^{-3}.

A limitation of the above work was the need to assume negligible transmission in the zone of peak opacity in order to evaluate the opacity in the presence of observable emission from the imploded target ablation plasma. Moreover the system used to form the 'backlighting' X-ray source plasma was inflexible in not allowing independent focussing of the beam on the 'backlighting' target.

An experiment was therefore set up as shown in figure 5.03 with 2 pinhole cameras one of which produced the shadowgraphy images with the second one producing separated images of the 'backlighting' plasma source and the imploded microballoon. In addition a 3 beam 3 lens configuration was used to eliminate the focussing limitation.

Experiment (b) in table 5.02 was essentially a repeat of (a) with this improved apparatus. The apparatus also allowed shadowgraphs to be recorded at earlier times in the implosion than previously and an example is shown in figure 5.04 where a very clear ring structure of the absorption region is seen due to the imploding glass shell 250 ps after irradiation.

The experiment (b) confirmed the results obtained from (a) in Table 5.02. It may be noted from the table that the ratio of the scale lengths of

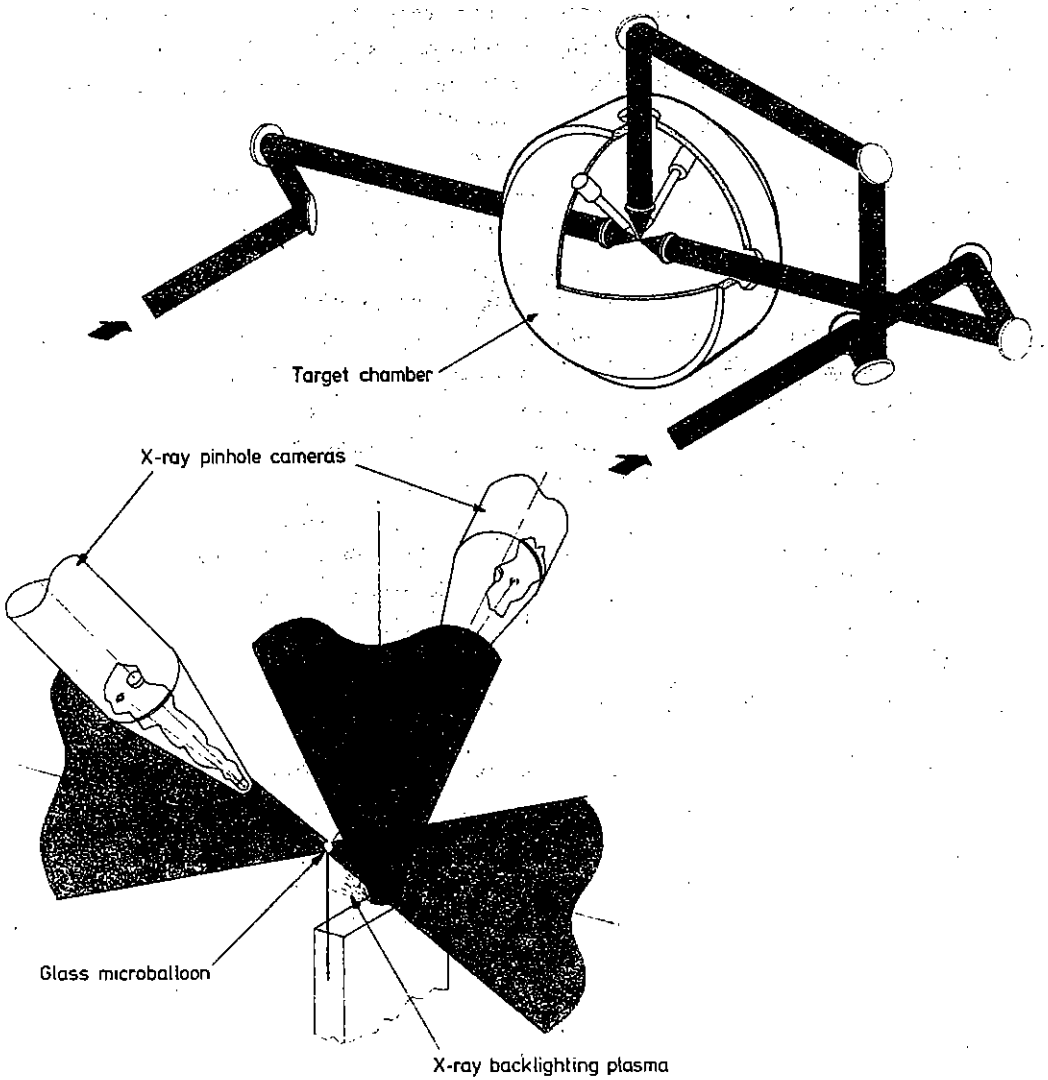

Figure 5.03

Improved system for pulsed X-ray shadowgraphy with an independent 3rd beam and focussing lens for the 'backlighting' source plasma.

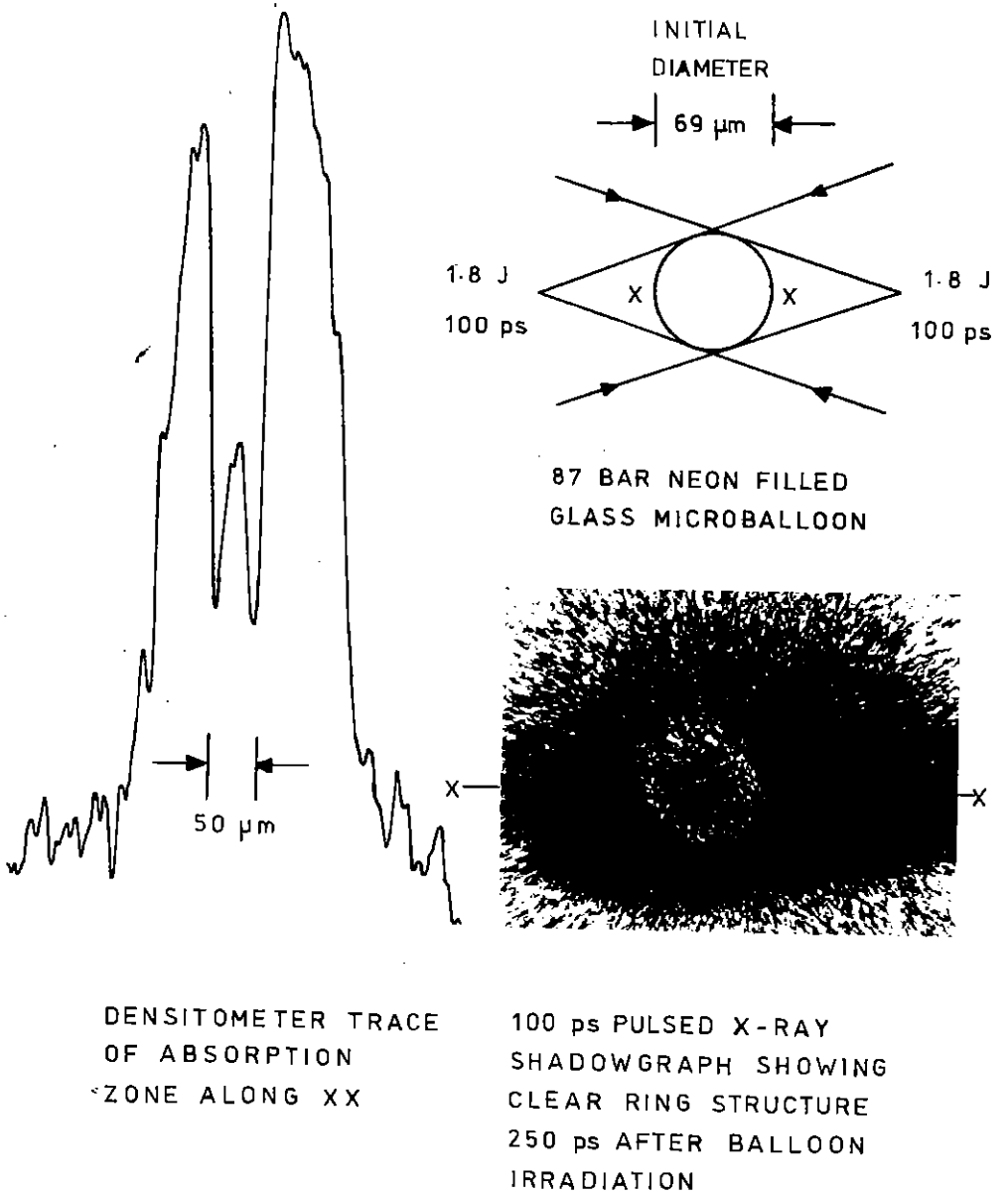

Figure 5.04

An example of a pulsed X-ray shadowgraph obtained with the system shown in Figure 5.03 with experimental conditions as specified in experiment (b) in Table 5.02. Note the transmission of X-rays through the centre of the target shown in the densitometer tracing.

TABLE 5.02 X-RAY SHADOWGRAPHY EXPERIMENTS

Experiment	TARGET				LASER			ENERGY TRANSPORT			IMPLOSION		SHADOWGRAPHY				
	Target diameter μm	Glass shell μm	Polymer layer μm	Fill gas bar	Pulse length ns	Energy per beam J	Intensity $W cm^{-2}$	Hot* Electron KT_H KeV	**Range λ_H μm	Ratio range shell $\lambda/\Delta r$	Time ns	Peak density $g\ cm^{-3}$	Laser Pulse J	X-ray filter KeV	Recording System	Time res' ns	Brightness ratio Backlight: Implosion
a)	65	1.3	none	Ne 87	0.1	2	5×10^{14}	5	8	2.5	0.5	Ne ++ 4 ± 2	5	1.8	1 phc	0.1	5
b)	65	1.3	none	Ne 87	0.1	1.7	5×10^{14}	5	8	2.5	0.5	Ne ++ 4	3.3	1.8	2 phc	0.1	7
c)	*** 95	1.7	2.8	none	0.1	12	2×10^{15}	10	30	5	0.6	glass 3+	4.6	1.8	2 phc	0.1	> 11
d)	*** 95	1.7	2.8	none	1.6	17	1.5×10^{14}	3	2	0.3	0.9	glass 6+	5.5	1.5	streak + 2 phc	0.09	5
e)	+++ 240	1.4	variable 1 to 6	none	1.6 to 2.5	20 to 35	4×10^{13}	2	1	0.5 to 0.1	2 to 3	glass ~ 10+	16 to 25	2.2	streak + micro scope	0.2	2 to 10

* Inferred from the intensity and target material using data in ref (5.02)

** Approximate range in polymer assuming $\lambda \alpha (kT_H)^2$ and using the value 30 μm for $kT_H \sim$ 10 KeV found in the data shown in figure 4.23.

\+ Calculated

++ Experiment

*** Targets supplied by J Fries of the Los Alamos Scientific Laboratory

+++ Target glass substrates supplied by J Fries of the Los Alamos Scientific Laboratory

hot electron preheating (λ) to the glass shell thickness (Δr) is large ensuring 'exploding pusher behaviour' of the shell. The high Neon density in the compressed core was found to be the result of compression by the glass shell material in which signifcant radiation cooling of the high Z Neon plasma dissipated internal energy and lowered the pressure for the final phase of near adiabatic compression. This radiative enhancement of compression was mentioned earlier (5.4) and has been recently invoked as a deliberate strategy to enhance compression core density (5.5).

The laser energy in experiments (a) and (b) in table 5.02 was deliberately kept low relative to the energy in the 'backlighting' beam to give a strong ratio of backlighting intensity relative to the intensity from the microballoon ablation front plasma.

A desirable relaxation of this constraint was possible by suppressing the X-ray emission from the microballoon by coating it with a low Z polymer.

The first such targets were generously made available to us by J Fries of the Los Alamos Scientific Laboratory, and an electron microscope picture of a broken section of such a target is shown in figure 5.05. The target parameters are given in Table 5.02 as experiment (c).

It was possible to increase the laser energy on target by $\sim$ 6 x without changing the energy in the backlighting beam and still have an X-ray intensity from the microballoon that was significantly smaller relative to the backlighting intensity than in experiments (a) and (b). See Table 5.02.

These targets were not gas filled and the 'exploding pusher' mode of operation evidenced by the ratio $\lambda/\Delta r >> 1$ in Table 5.2 led to implosion of the glass shell material which formed a dense X-ray absorbing core.

A sequence of pulsed X-ray shadowgraphs at various delay times in the implosion showed the absorption zone contracting in a manner similar to that published in last year's report (5.1) and Ref (5.5). However the greater mass of high Z material in the core prevented observation of on axis transmission through the target of the type seen in figure 5.04.

The minimum absorption core diameter occurred 600 ps after the peak of the irradiating pulse and its diameter at an opacity of 2 was 60 μm.

Modelling the implosion with Medusa in a manner similar to that which we used for other exploding pusher targets (5.1) and (5.6) showed that the Xray absorption was mainly due to the glass which reached an average density $\sim 3 g cm^{-3}$ at maximum compression. The computed time of maximum compression was 670 ps after the laser pulse peak and the diameter of the absorption zone at that time was $\sim$60μm. There was therefore general agreement between the MEDUSA calculations and the experiment but the experiment did not permit a direct density determination from measurement of the Xray transmission in the centre of the implosion core.

Some effort was directed to achieving a high enough backlighting Xray energy to enable such a direct observation but technical difficulties prevented the measurement on this occasion. In future work it is expected that this will be achieved.

5.4 Streaked X-radiography of ablative implosions

A major current objective of laser compression research is to exploit ablatively driven implosion of shell targets to obtain compression to high densities in near Fermi degenerate conditions.

To date there has been only limited experimental study of implosions of this type in which the range of hot electron preheating is less than the shell thickness. The 'Kalmar' experiments in the USSR (5.7) and

a)

SECTION THROUGH POLYMER ABLATOR COATED TARGET WITH 2 µm POLYMER LAYER

Figure 5.05

(a) Electron microscope picture of a broken segment of a polymer coated microballoon (see Experiment (c) Table 5.02. This target was supplied by J Fries of the Los Alamos Scientific Laboratory.

b)

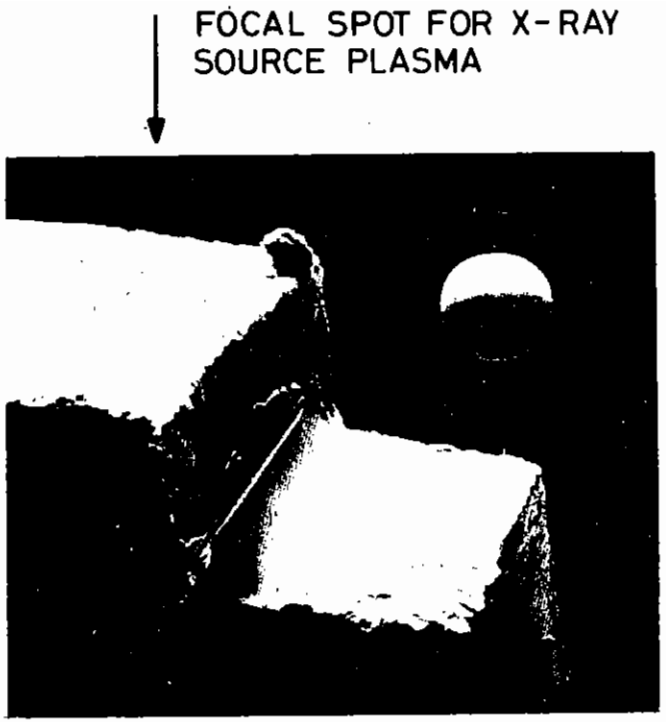

240µm MICROBALLOON WITH 5µm POLYMER ABLATOR MOUNTED FOR X-RAY RADIOGRAPHY

Figure 5.05

(b) Polymer coated microballoon target manufactured by P T Rumsby at the Rutherford Laboratory and mounted for streaked X-ray shadowgraphy (experiment (e) Table 5.02).

'Iris' experiments at the CEA Limiel Laboratory in France (5.4) have produced most data in this field, but have not yielded the direct information on the implosion dynamics afforded by X-ray shadowgraphy.

A simple estimate of the scaling behaviour of ablative implosions and of the realisation of the ablative mode of implosion is afforded by the consideration that the hot electron temperature T_H is an experimentally known function of the laser intensity I with a scaling of the form $T_H \sim I^{1/3}$ (5.2). The range λ of electrons of energy kT_H in matter of density ρ scales roughly as $\rho\lambda \alpha T_H^2 \alpha I^{2/3}$ and the more quantitative scale length for hot electron preheating has been determined as discussed in section 4.4. The ablation pressure has been studied extensively for low intensities (5.8) and may be adequately represented as $p \alpha I^{3/2}$.

Ablative acceleration 'a' of a thin shell of mass per unit area $\rho\Delta r$ over a distance r in the limit of negligible mass change yields a velocity 'V' given by $V^2 \alpha ar \alpha \rho r/\rho\Delta r \alpha I^{2/3} r/\rho\Delta r$

Ablative implosion will be achieved only when $\rho\lambda < \rho\Delta r$ and a constraint for maximum velocity can be expressed in the form $\rho\lambda \alpha \rho\Delta r \alpha I^{2/3}$ so that $V^2 \alpha rI^0$.

The power of I depends on the exact power exponents defined above but is clearly small and the expression depends on the assumption that $\rho\Delta r$ is scaled in relation to the laser power which for a fixed laser power implies $\rho\Delta r \alpha r^{-1/3}$.

Such a scaling implies a desirable increase of implosion velocity with increasing radius but with the aspect ratio $r/\Delta r$ increasing very rapidly too. The scaling will be limited by either the ablation depth exceeding the shell thickness, or by fluid instability of the accelerated shell, with the latter prevailing if the majority of theoretical predictions are correct.

These predictions suggest (5.9) that the classical Rayleigh Taylor instability growth rate $\gamma = (Ka)^{1/2}$ is applicable to the growth of surface perturbations of wave number K in the ablation front. The model becomes invalid for $K > 2\pi/\Delta r$ beyond which the growth is suppressed. This leads to the conclusion that the most unstable wavenumber is $K \sim 2\pi/\Delta r$ and with the above simple model for shell acceleration, that the total growth exponent $\gamma t \alpha (r/\Delta r)^{1/2}$.

These considerations supported by one dimensional fluid code modelling with MEDUSA led us to investigate implosions with the parameters listed as experiments (d) and (e) in Table 5.02 where $\lambda/\Delta r \ll 1$ and the implosions are clearly ablative.

Diagnosis of these long pulse ablative implosions by X-ray shadowgraphy required a means of time resolving the evolution of the shadowgraph since the backlighting pulse and implosion duration were similar. The X-ray streak camera was adapted for the purpose.

With the microballoons mounted relative to the backlighting target as shown in figure (5.05) and the system irradiated with 3 beams as in figure (5.04) the streak camera was used to view the shadowgraph image as in figure 5.06. Multiple (2 or 3) images were projected onto the streak camera slit, and an angle θ in figure (5.06) between the slit and pinhole array axes facilitated alignment and gave additional data on the alignment.

The conditions chosen for the first such experiment are given as experiment (d) in Table 5.02. Rather low energy X-rays (33 μm Be filter in the X-ray shadowgraph) were used and a small fraction of the laser power (4 GW of 20 GW) was used for the backlighting.

The intensity of the backlighting relative to the emission of the microballoon seen in X-ray pinhole camera images was ~5:1. However the brightness of the streak image (figure 5.07) was rather low

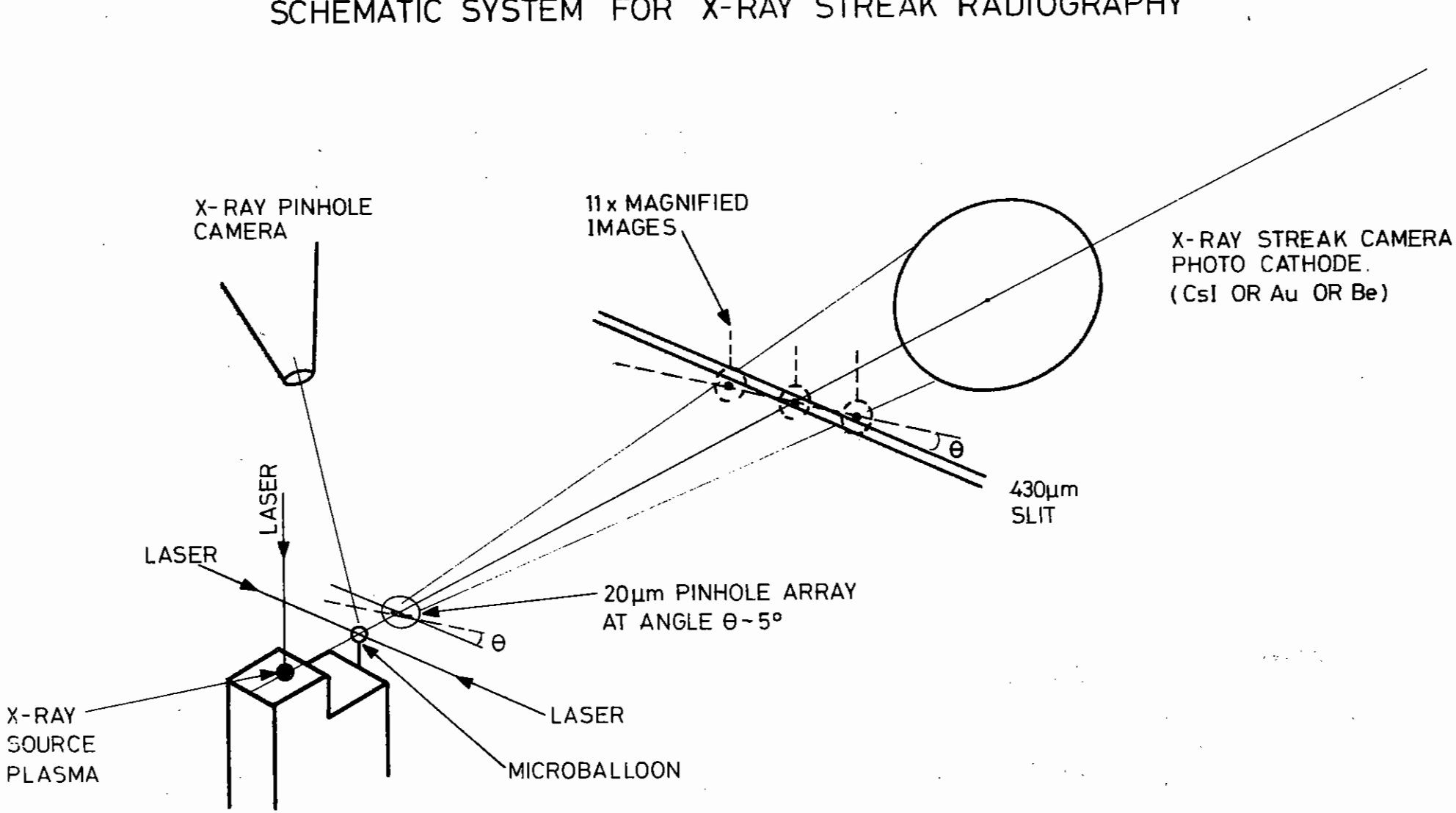

Figure 5.06

Schematic system for streaked X-ray shadowgraphy using a 3 pinhole imaging system (experiment (d) Table 5.02).

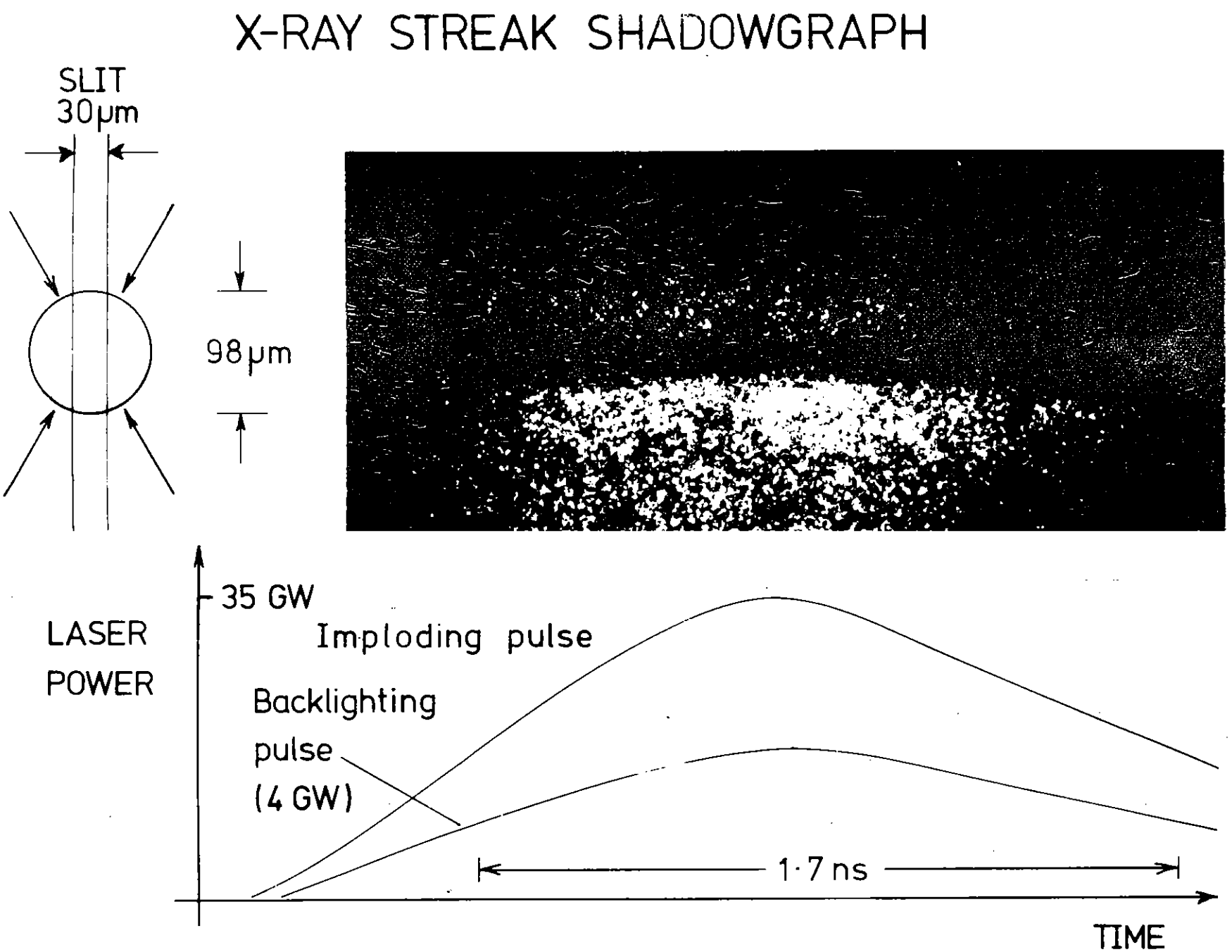

Figure 5.07

The first streaked Xray shadowgraphy data using the LASL polymer coated targets. (Experiment (d) Table 5.02). The streak record shows the formation of an absorption zone of minimum diameter coincident in time with the peak laser power. Xray filter cut off energy 1.5 KeV.

with the simple gold photocathode being used for the experiment. The 98 m microballoon with 1.7μm glass wall and 2.8μm polymer coating was seen (figure 5.07) to implode to a minimum absorption source diameter of ∿ 30 μm at the time of peak laser power.

The implosion was again modelled with the MEDUSA code using assumptions which are discussed in more detail below in the context of interpreting experiment (e) in 5.02.

The modelling predicted, in agreement with the experiment, that maximum compression would coincide with the peak power of the laser pulse. The implosion was clearly ablative in character as indicated by the estimated ratio of range of preheating λ to target shell thickness Δr which was ∿ 0.3 Table 5.02. This was corroborated by the computer modelling which showed the ablation front to have penetrated through only ∿1.5 μm of polymer at the time of maximum compression and it also indicated low temperatures (10 to 50 eV) in the compressed glass.

The rather low intensity obtained in the streak record made any comparison of the observed and computed profile of opacity to x-rays rather inaccurate.

It was therefore preferred to improve the quality of the experimental data by taking advantage of new technical possibilities before making such comparisons.

An increase of both the intensity of the streak record and of the energy of the X-rays used to produce the shadowgraphy image was obtained by substituting the high sensitivity CsI photocathode for the gold photocathode in the streak camera, as discussed in section 5.2, and by increasing the fraction of the laser power diverted into the backlighting beam. In addition a larger 250 μm target diameter was chosen and using our own coating facilities, variable thickness polymer layers in the range 1 to 6 μm were deposited on the 1.3 μm thick glass microballoons. (See experiment 'e' in table 5.2)

The marked improvement in data is shown in figure 5.08 where a strongly exposed streak shadowgraph is obtained with 20 μm diameter pinhole imaging and 15 x magnification at the streak camera photocathode, an effective slit width of 39 μm in the object plane and a sweep speed limited time resolution of 230 ps.

There is strong transmission through the centre of the target (similar to that in the 2 dimensional pulsed shadowgraph in figure 5.04) with the imploding walls seen as dark absorption zones. Increasing compression reduces the transmission in the centre and the backlighting pulse intensity dies away before the time of maximum compression, which occurs towards the end of the laser pulse. Figure 5.08 is purely illustrative being derived from figure 5.09 as explained in its caption but the data in figure 5.10 was obtained under similar conditions and is more suitable for analysis. In this case the target had a thick (6 μm) polymer layer which ensured negligible emission relative to the backlighting source. Densitometry shown in the diagram allowed an estimate of the opacity profile as discussed earlier (5.6). Observations of the implosion at the time of maximum compression were obtained by delaying the backlighting beam by eg 1.8 ns in figure 5.11. Here the X-ray emission of the microballoon itself prior to the backlighting pulse is clearly seen partly because the delay permits this but also because the target had a thinner (1.9 μm) polymer layer. Densitometry shows the form of the absorption zone at maximum compression which occurs approximately 1.8ns after the laser pulse peak. The opacity to x-ray at the time of maximum compression was too large to give recordable transmission in this case.

Numerical simulation of these implosions was again made using the one dimensional MEDUSA code with, for this problem, an approximation of the equation of state of the glass shell material obtained by setting the specific heat ratio $\gamma = 2.2$ and assuming an average ion charge of 10 and an initial temperature of 0.3 eV. This prescription gave a reasonable fit to the Fermi degenerate compression characteristics of SiO_2 obtained from calculations using the Thomas Fermi model (5.10) for pressure above 100 M bar and extrapolated experimental shock compression data for pressure below 1 M bar (5.11).

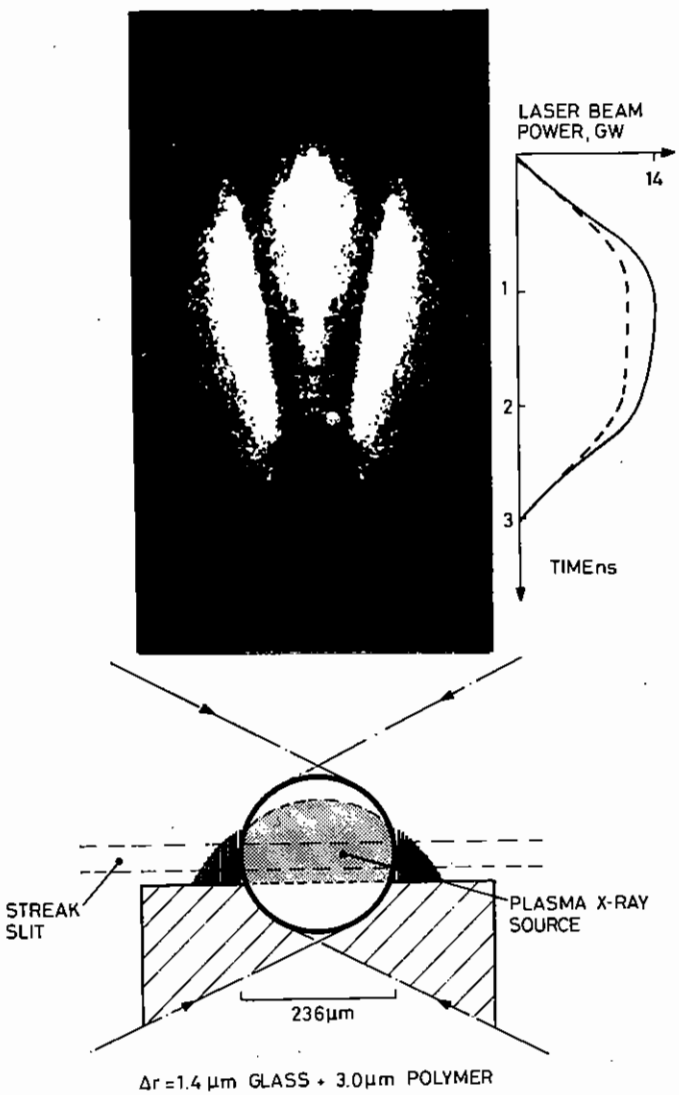

Figure 5.08

An illustration of better quality streaked X-ray shadowgraphy data using the new CsI X-ray photocathode, larger diameter targets and harder X-rays from the backlighting plasma (experiment (e) Table 5.07). The implosion of the target wall is clearly seen as a convergence of the zones of maximum absorption. The polymer layer thickness was 3 m and filter cut off energy was 2.2 KeV.

Incorporation into the model of a calculation of the instantaneous X-ray opacity profile as described previously (5.6) gave predicted opacity profiles developing as shown in figure 5.12.

Comparison with experiment in the initial stage of implosion was possible using the opacity profile derived from the data in figure 5.10 and this is shown in figure 5.13.

There is agreement in the diameter of the absorbing region and in the shape of its opacity profile. But the outer edge is significantly 'softer' than the model predicts and there is a discrepancy in the magnitude of the opacity in the centre with the experimental opacity being lower than calculated by a factor of 3.8. These discrepancies are further considered below.

Analysis of the experimental data (figure 5.14) at the time of maximum compression revealed that instrumental contrast limited the maximum measurable opacity to a value $\sim$1 while the calculated value was up to 10. The only comparison made therefore was of the diameter of the region of opacity 0.5 which was in agreement with the calculation. A lack of sharpness in the boundary of the region of high opacity was seen experimentally in this case too (see figure 5.11).

A better appreciation of the development of the diameter of the absorbing region with time is afforded from the data in figure 5.15, where an over exposure of the streak reveals the implosion of an absorbing wall region (almost saturated in the image) to form an absorbing implosion core.

The very weak emission of the microballoon itself prior to the 666 ps delayed backlighting emission is also seen, illustrating the suppression of target emission relative to backlighting source emission with a 6 μm polymer layer.

Densitometry of the streak record allowed the locus of the outermost point of opacity 0.5 to be plotted as a function of time as shown in figure 5.16 where it is compared with the MEDUSA simulated result.

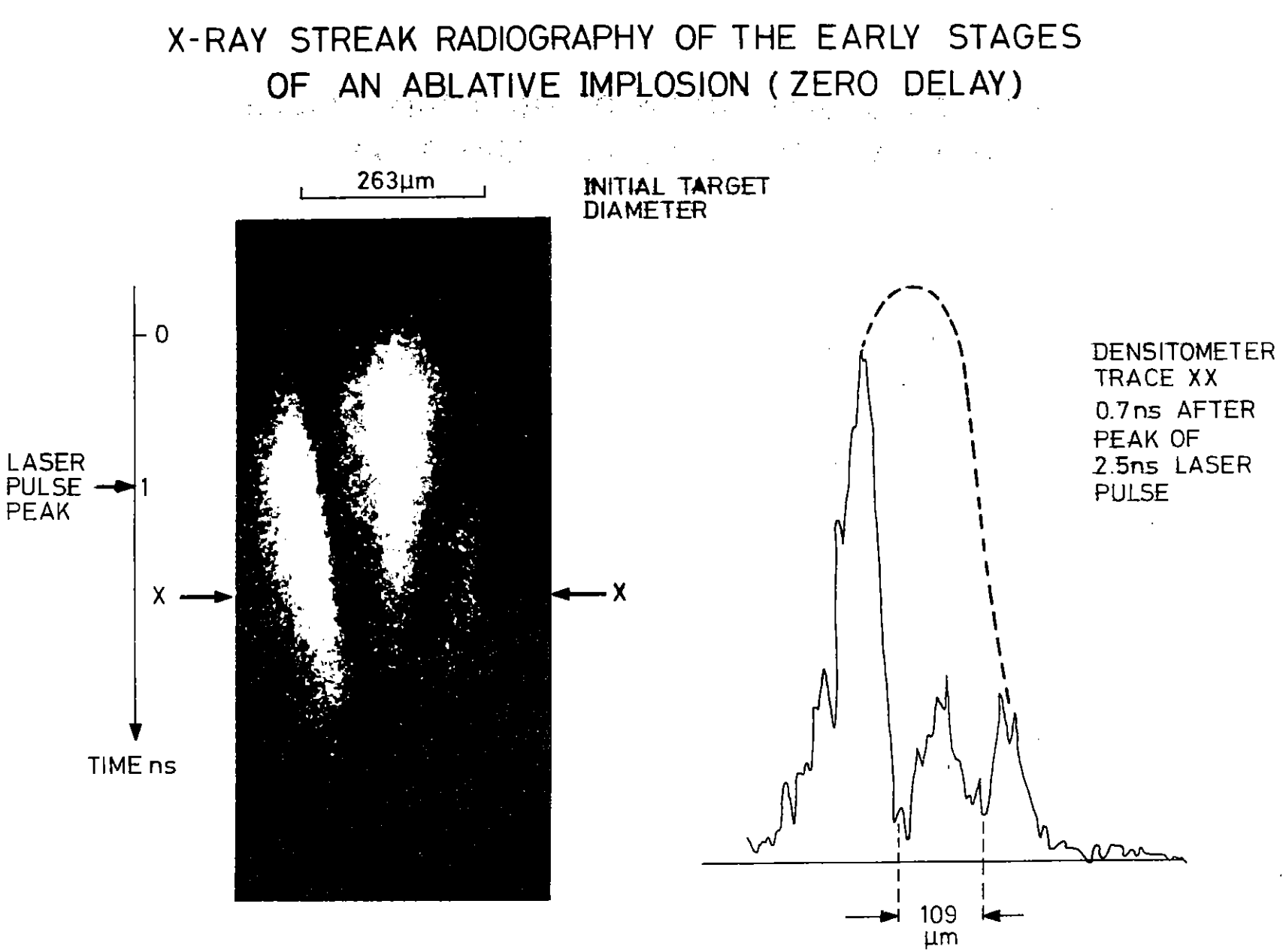

Figure 5.09

The original data from which Figure 5.08 was derived by reflection about the symmetry axis of the imperfectly illuminated shadowgraph record. Densitometry shows the absorption peaks of the imploding shell and transmission at the centre.

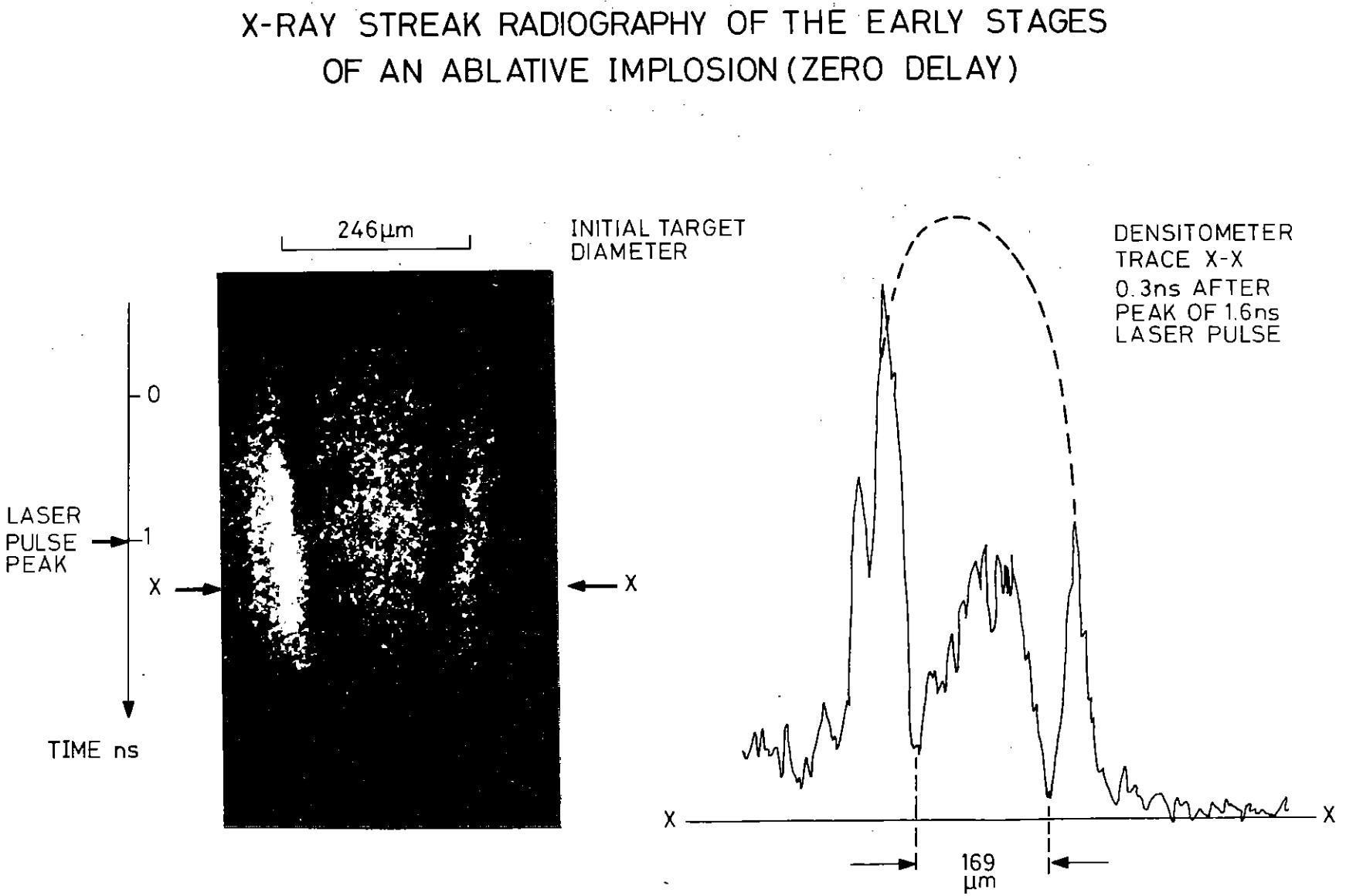

Figure 5.10

A streaked X-ray shadowgraph of a target with a 6 µm polymer coating having negligible emission from the microballoon relative to the backlighting source and showing the early stages of the implosion. The filter cut off energy was 2.2 KeV.

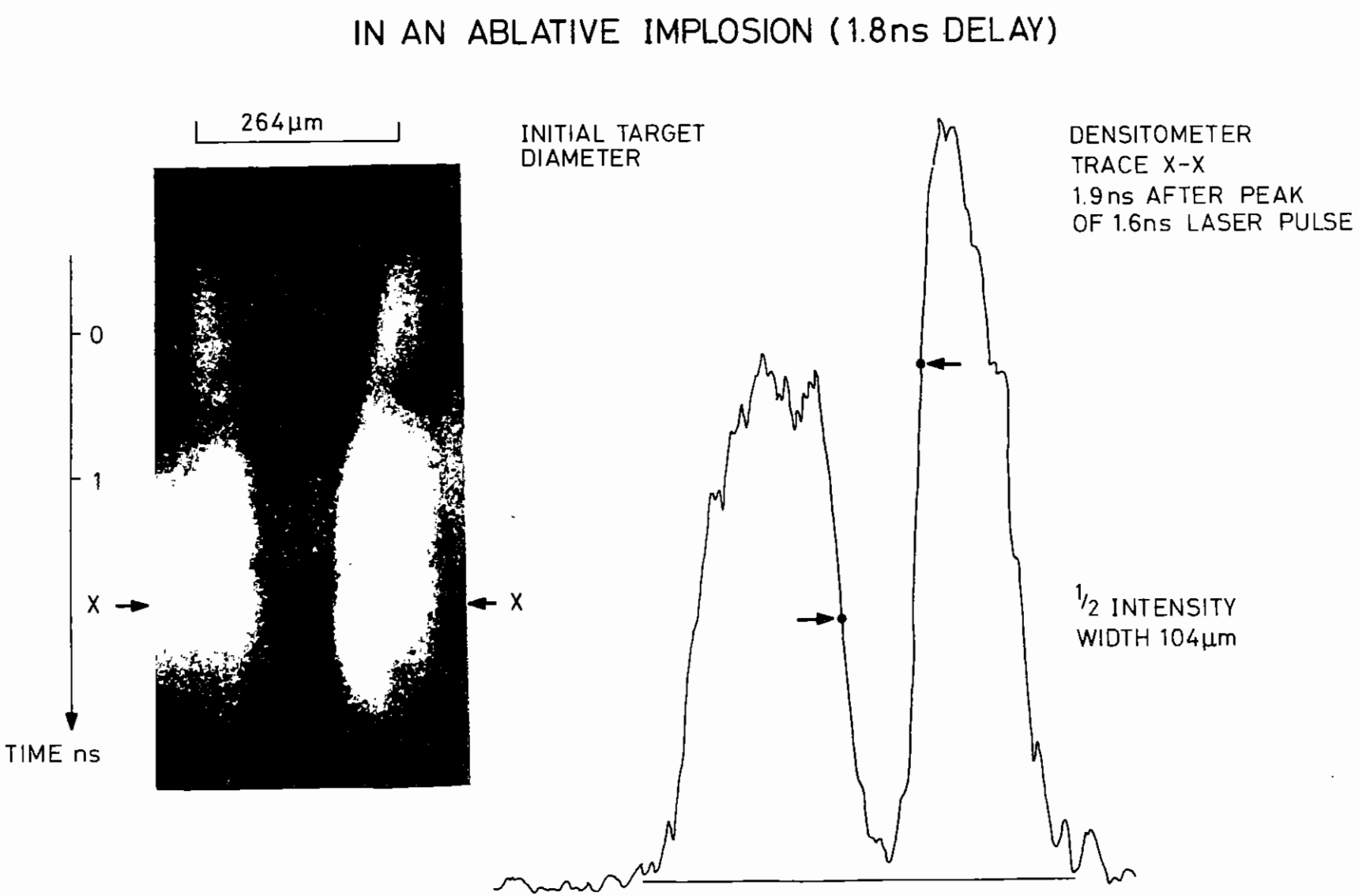

Figure 5.11

As Figure 5.10 but with a 2 µm polymer layer thickness and delayed backlighting showing the maximum compression phase where no transmission is seen and the absorption zone has minimum diameter. Detectable emission from the imploding target precedes the backlighting emission. The filter cut off energy was 2 KeV.

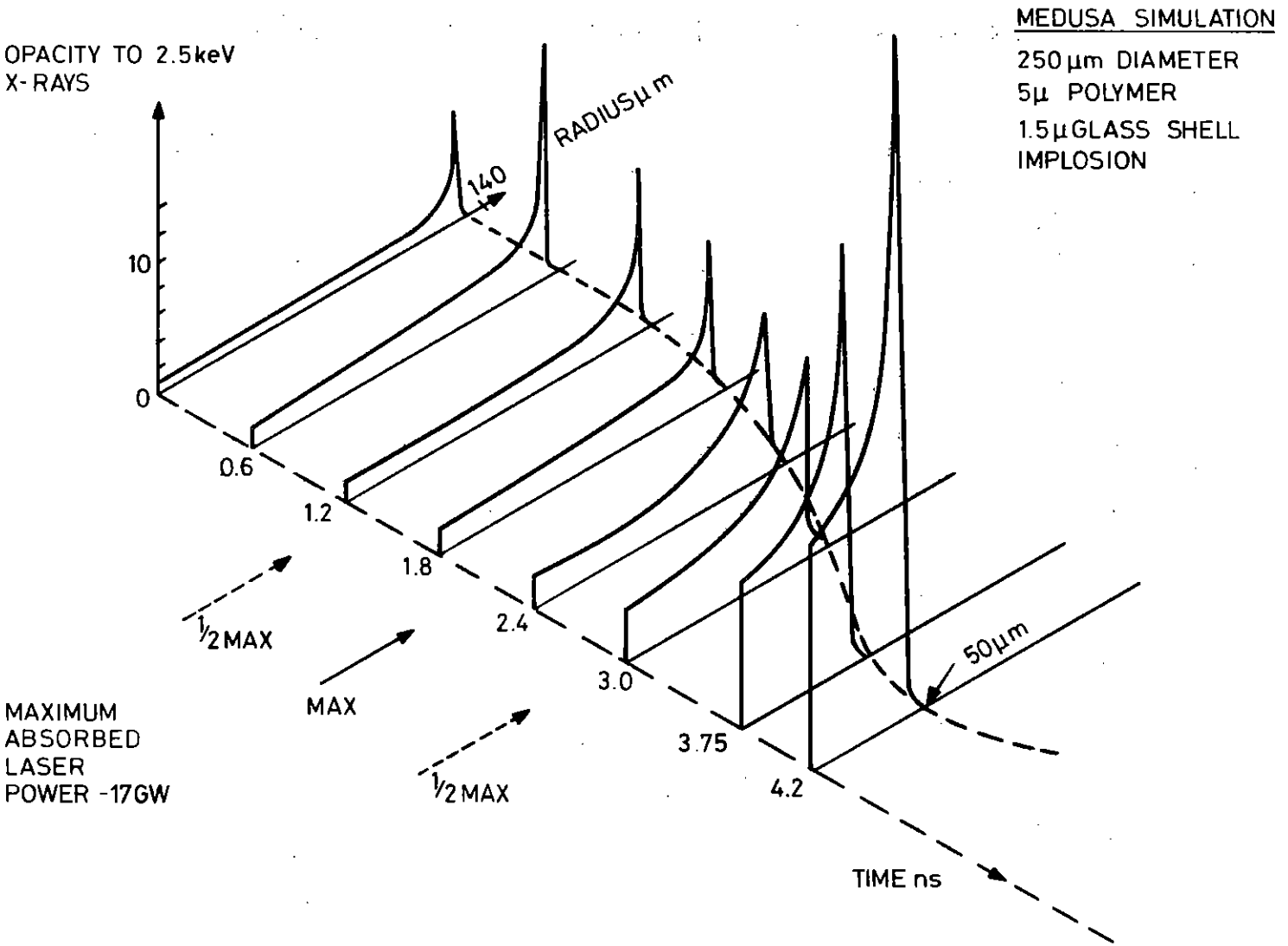

Figure 5.12

Simulation with the one dimensional MEDUSA code of the time development of profiles of opacity for 2.5 KeV X-rays.

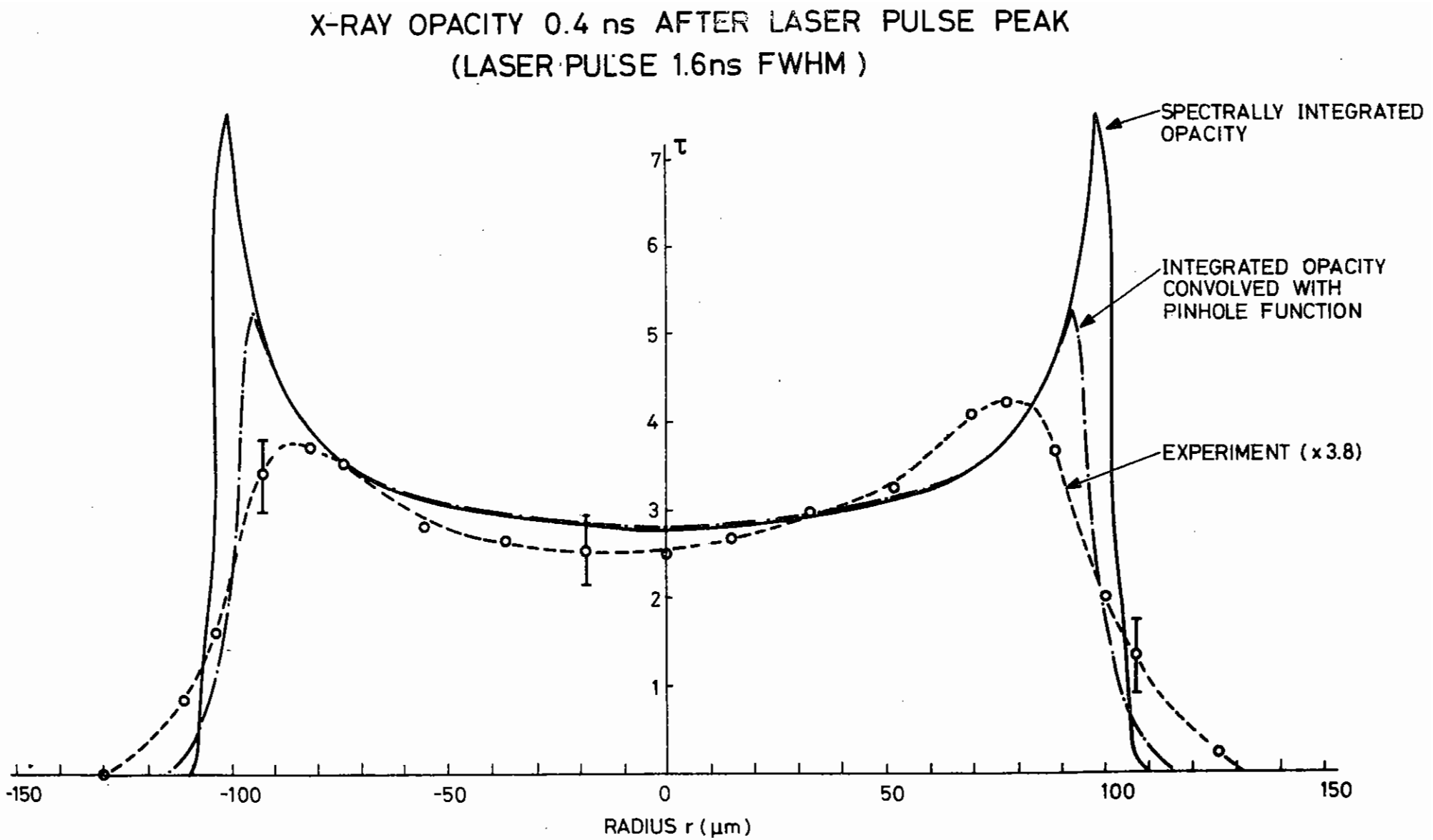

Figure 5.13

Simulated opacity profiles for the conditions corresponding to the densitometer tracing in figure 5.10. The opacity profile has been spectrally averaged and transformed by the finite resolution of the pinhole camera as in Ref 5.6. The experimental opacity profile scaled up by a factor 3.8 is also shown.

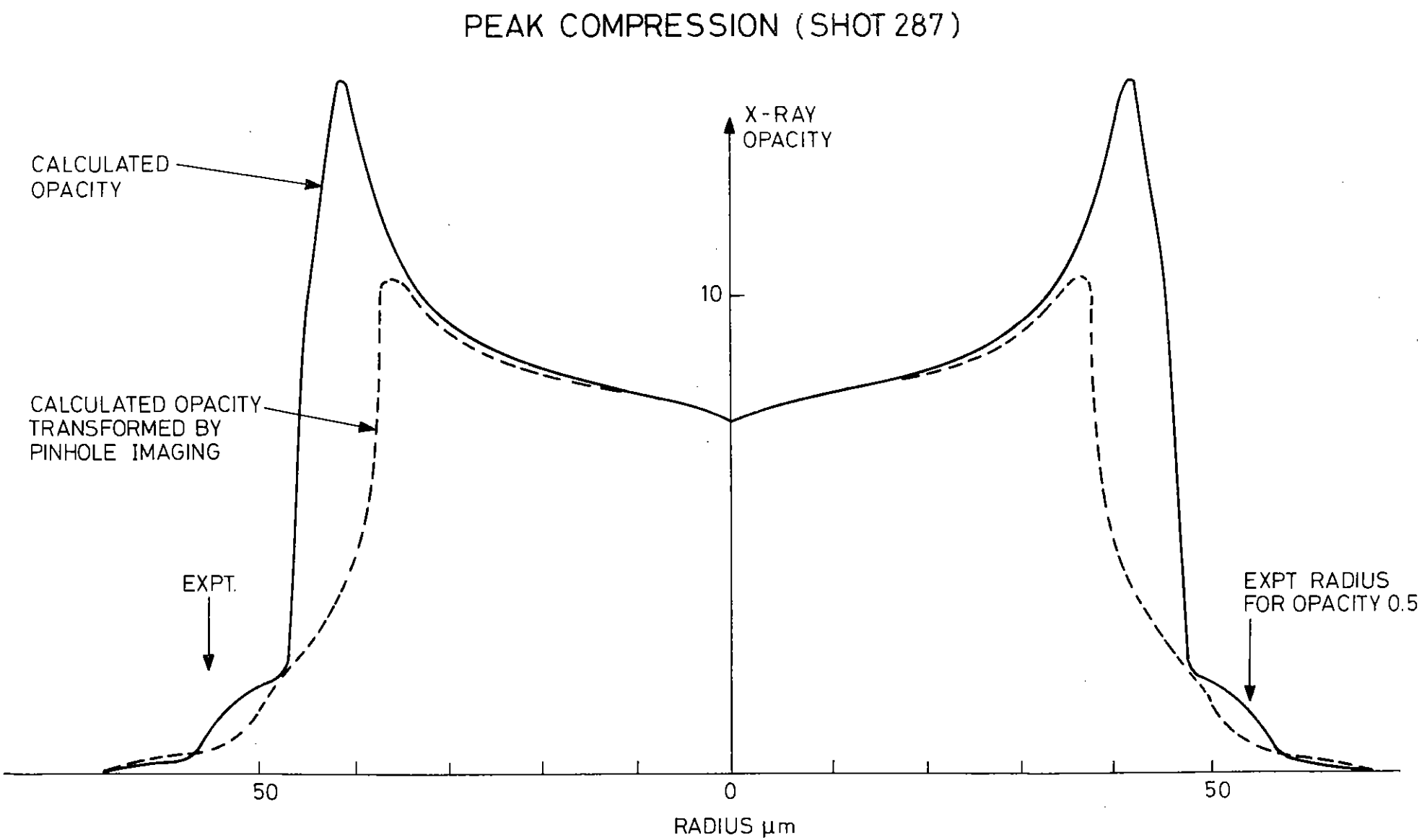

Figure 5.14

Simulated opacity profile for peak compression conditions corresponding to the densitometer tracing in Figure 5.11. The experimentally recorded radius at opacity 0.5 is also indicated.

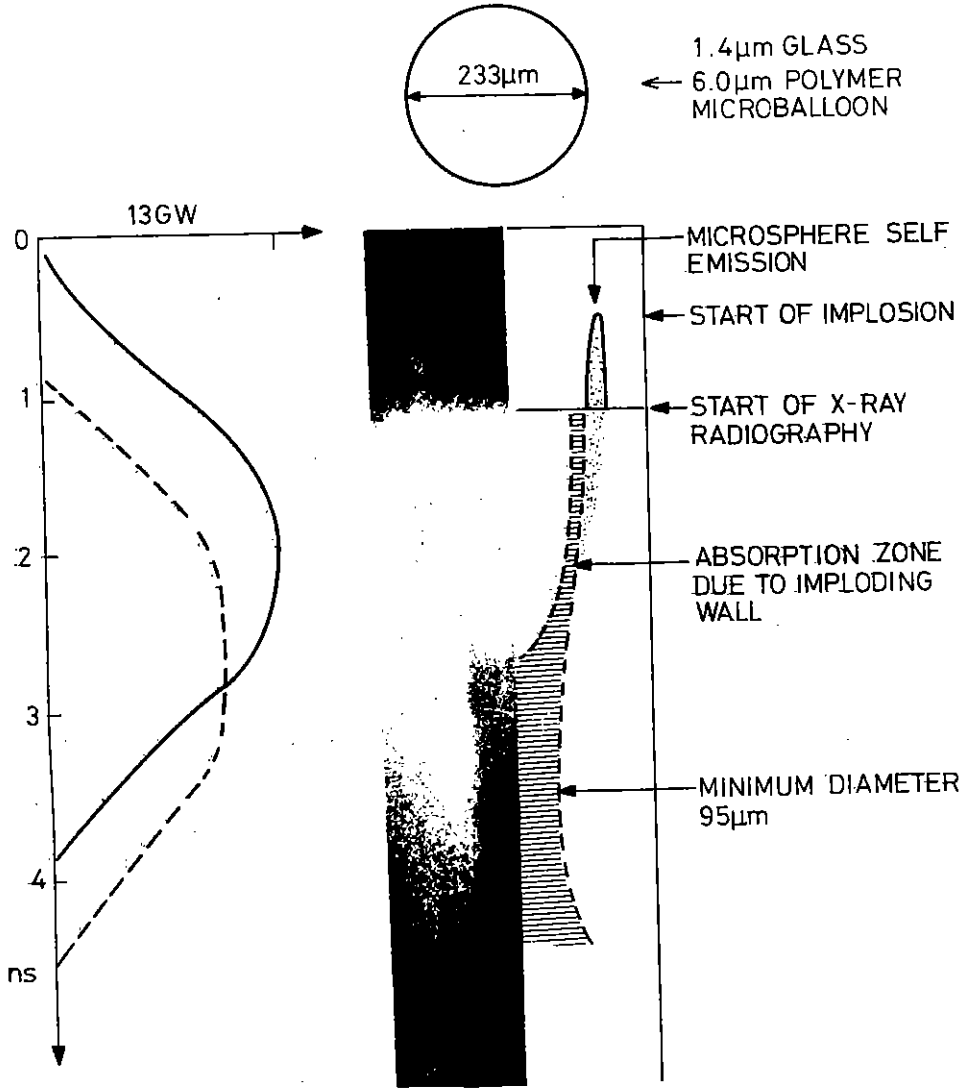

Figure 5.15

Heavily exposed streaked shadowgraphy record for a target with 6 µm polymer coating and delayed backlighting showing schematically how the radius of the outer boundary of the absorption zone can be followed as a function of time. The filter cut off energy was 2.2 KeV.

The simulations assumed classical uninhibited thermal conductivity since the intensity is below the level where hot electron generation and transport inhibition are significant. The absorption fraction was set at 0.3 from data obtained for polymer targets at the same intensity (5.12).

Following our conclusions in section 5.2 from streak implosion studies with resolution along the irradiated pole axis, the laser intensity in the 1D model was set equal to the intensity at the irradiated poles of the target, as determined from the 300 µm defocussing used in the experiment.

The code predicted densities $\sim 10 gcm^{-3}$ in the glass at peak compression and there was general agreement between experimental and calculated data on the radius of the absorption zone as a function of time.

There were discrepancies however as noted above in the sharpness of the absorption zone boundary. This is further illustrated in figure 5.17 where, as shown in the X-ray miscroscope image, one side of the target was irradiated with a small focal spot and the other was more uniformly irradiated with 300 µm defocussing relative to the target pole. The backlighting was delayed by 2.5 ns the self emission of the target is as intense as the backlighting, because the polymer layer was only 1 µm thick.

The streak has clearly one sharply bounded zone of absorption and one diffusely bounded side as shown in the densitometer tracing. The sharp edge corresponds to the point focus on the target. This is therefore an abnormal case which serves only as a resolution test for the camera confirming its capability to reach the resolution expected, from the experimental geometry.

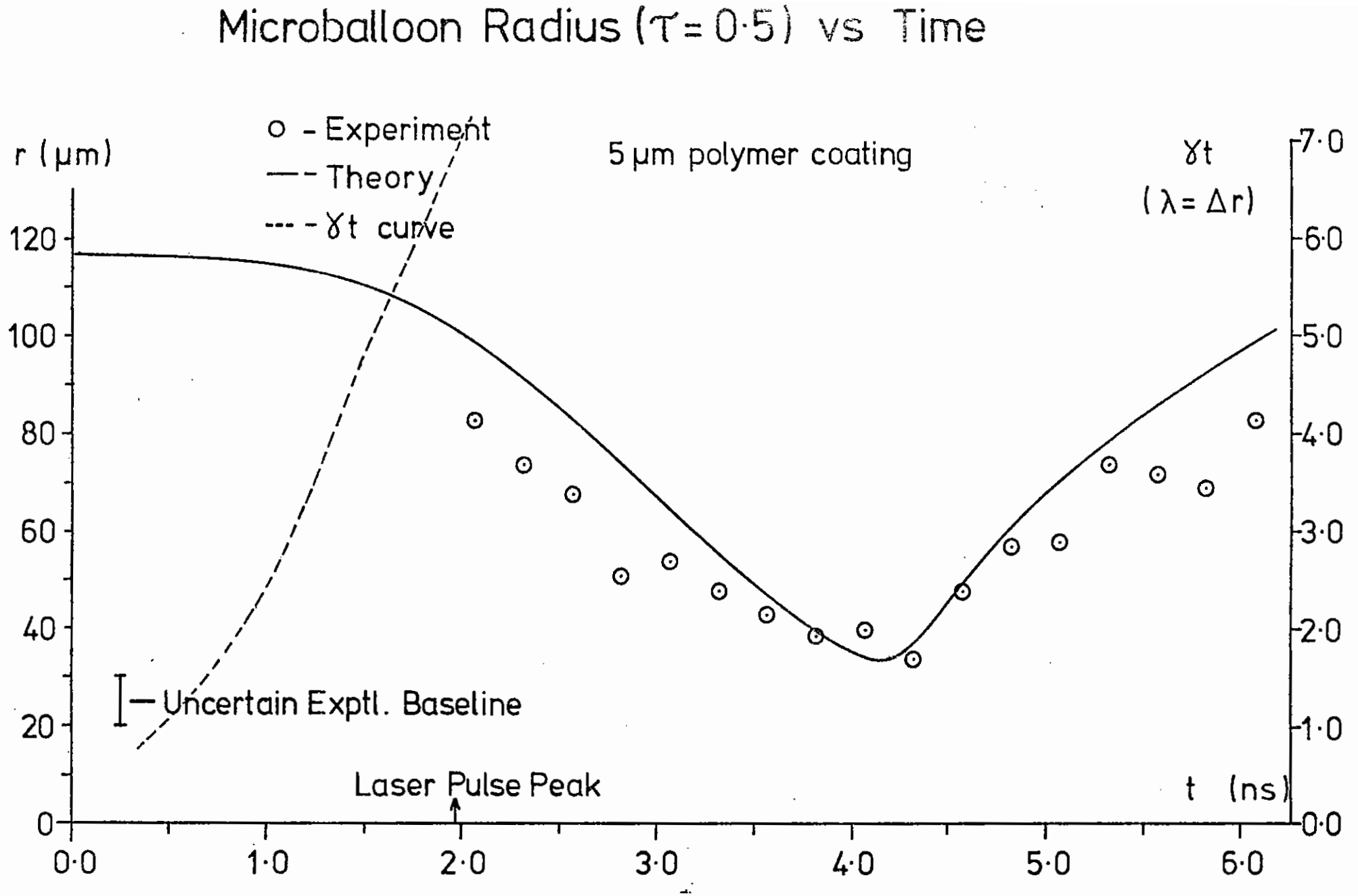

Figure 5.16

Data reduced from Figure 5.15 showing the radius of the outer boundary of the region of opacity 0.5 as a function of time together with simulated results. An upper limit estimate of the growth exponent γt of the most unstable Rayleigh Taylor mode with wavelength equal to the shell thickness Δr is also plotted (dotted line).

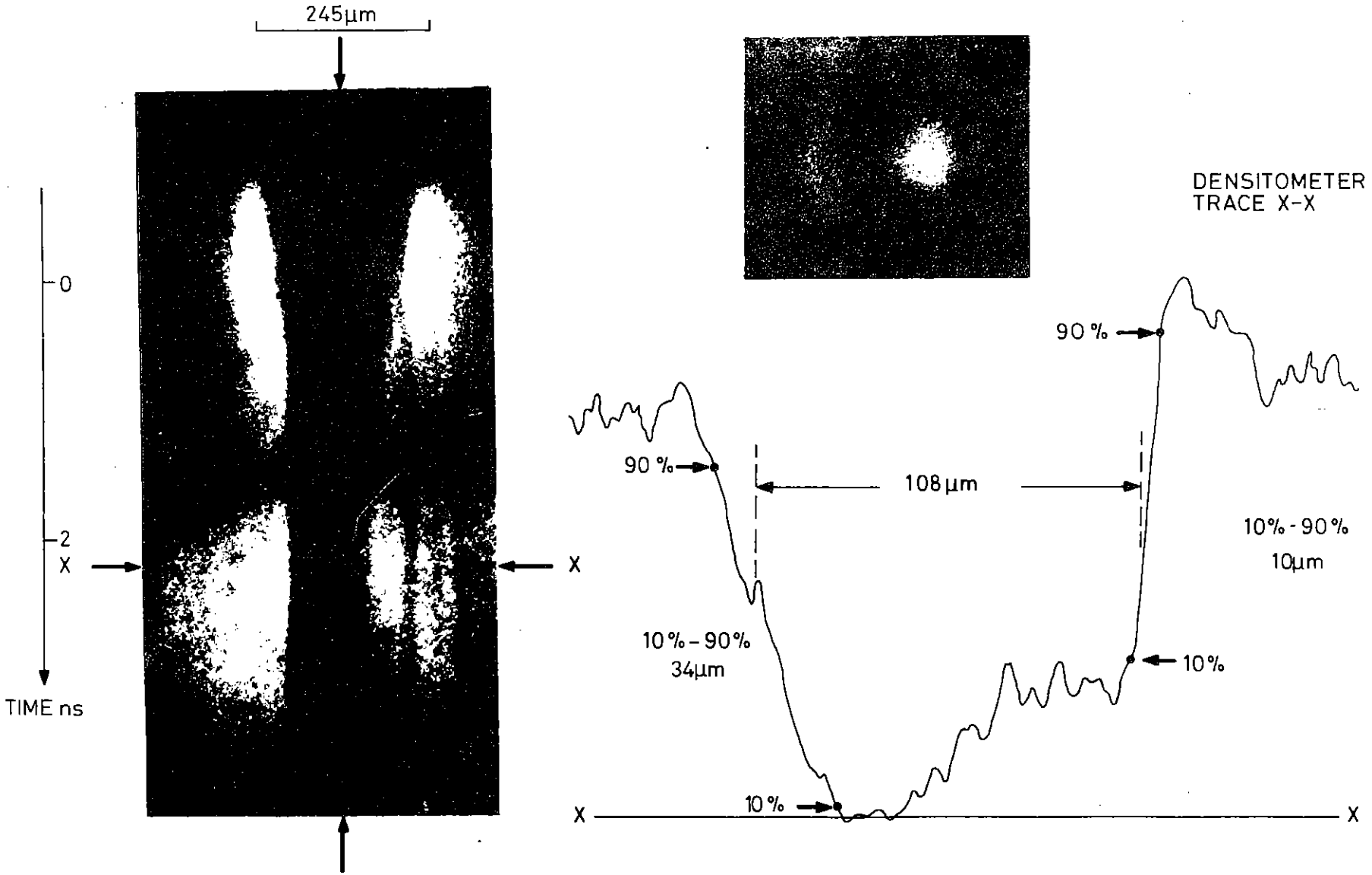

Figure 5.17

An X-ray streak shadowgraph with a 2.5 ns time delay of the backlighting radiation and thin 1 µm polymer layer. The vertical arrows indicate the centre axis of the target and the horizontal bar shows its initial diameter. The horizontal bar axes in the densitometer tracing and the static X-ray microscope image are reversed relative to that in the streak image (ie. the LHS of the streak corresponds to the RHS of the tracing and static image). Distances for a change of intensity from 10% to 90% in the absorption zone boundaries in the streak picture are indicated on the densitometer tracing.

The vertical striations in the streak due to small cathode defects show the streak axis and it can be concluded that the side of the target which was irradiated at low intensity with the normal defocussing exhibits the greatest acceleration and moves relative to the indicated centre line by an amount typical of symmetric implosions. This side of the target shows however a 34 μm diffuse boundary to the zone of high absorption. We conclude therefore that some process causes a diffuseness in the boundary of the zone of high absorption which is much greater than both the resolution of the measurement and the one dimensional simulation.

It may also be noted that there is intense emission from the polymer coated target when the coating thickness is 1 μm (figure 5.17) which decreases systematically with increasing polymer thickness as seen with 2 μm (figure 5.11) and 6 μm (figure 5.15). The modelling, even with the extreme assumption of no transport inhibition, predicted a penetration depth for the high temperature ablation front at the peak of the laser pulse of only 0.6 μm.

Clearly the high X-ray emission intensity is due to the underlying high Z glass penetrating into the ablation front.

One explanation for both the diffuse boundary of high absorption and the anomalously bright emission could be unstable growth of surface perturbations on the shell as seen in figure 5.05, due to the Rayleigh Taylor instability. Calculation of γt by evaluation of $\int_0^t (Ka)^{\frac{1}{2}}\, dt$ with $K = 2\pi/\Delta r$ for the case shown in figure 5.16 clearly indicates that if the simple instability theory is valid the growth could cause mixing of the plastic and the glass since γt exceeds 100 at an early stage in the implosion.

It could also be that the anomalously large transmission of X-rays noted earlier in figure 5.13 is due to the inverse process in which low Z polymer 'bubbles' break through the high Z absorbing glass shell to give anomalously large X-ray transmission.

Certain qualifications are required about these hypotheses since the spectrum of backlighting source was measured only in experiment (a) in table 5.02 and assumed to be similar in calculating opacities in experiment (e). The results are not very sensitive to this assumption but we should like to remeasure the spectrum for the long pulse case before making a definite conclusion about the opacity anomaly* In addition the possibility of prepulse or superfluorescence damage to the polymer coating was not systematically tested though a spot check with a 1 μm coating showed no damage except very locally around a coating defect.

With these qualifications it seems that the experiment shows strong evidence for instability in the ablative implosion of high aspect ratio polymer coated shells.

* These measurements have been made recently and indicate that the transmission is not in fact anomalously high.

CHAPTER 5 REFERENCES

5.1 Annual Report to the Laser Facility Committee, Rutherford Lab Report RL-78-039 (1978)

5.2 D W Forsland, J M Kindel, K Lee, Phys.Rev.Lett. 39 284 (1977)
H G Ahlstrom et al in Laser Interaction and related plasma phenomena
H J Schwartz and H Hora, Eds Vol 4A 437 Plenum Press (1977)

5.3 J E Bateman, R J Apsimon, Adv.Electr.Elec.Phys. 40 (in press) (1979)

5.4 M Bernard, D Billon, P A Holsteain, J Launspach, C Paton, J M Reisse, D Schirmann, CEA Limeil Laboratory Preprint APS Meeting November (1977)

5.5 R L McCrory, S S Skupsky, J Delattres, R A Craxton, XII European Conference on Laser Interaction with Matter, Moscow (December 1978)

5.6 M H Key, C L S Lewis, J G Lunney, A Moore, T A Hall, R G Evans, Phys.Rev.Letts. 41 1467 (1978)

5.7 M G Basov, A A Kologrivov, O M Krokbin, A A Rupasov, G V Skliskow, A S Shikanova, Ya A Zakharenkov, N N Zoirev, P M Lebedev, Physical Inst Preprint M.177 (1976)
and in Laser Interaction and related plasma phenomena, H J Schwartz and H Hora, Eds Vol 4A 479 Plenum Press (1977)

5.8 P T Rumsby, M M Michaelis, M Burgess, Opt.Comm 15 422 (1975)
S Zweigenbaum, Y Gazit, Y Komet, Plasma Phys 19 1035 (1977)

5.9 R A Kidder, Nucl Fusion 16 3, (1976)
Yu V Afanasev et al Zh ETF Pis Red 21 150 (1975)
J R Frieman, M J Clauser, S L Thompson, Nucl Fusion 17 223 (1977)
S E Bodner et al 'Initial confinement fusion at NRL'
Innsbruck, Austria IAEA CM 37 B-3 (1978)

5.10 R M More, LLE Report 56 (1977)

5.11 J M Walsh, M H Rice, R G McQueen, F L Yarger, Phys.Rev. 108 196 (1957).

5.12 H D Shay et al Phys Fluids 21 1634 (1978)

CHAPTER 6 ATOMIC AND RADIATION PHYSICS

INDEX

CHAPTER EDITOR R G Evans

CONTRIBUTORS G E Bromage, L Cooke, B C Fawcett, T P Hughes, R J Hutcheon, M H Key, R W Lee, C L S Lewis A Ridgeley

CHAPTER 6 ATOMIC AND RADIATION PHYSICS

6.1 Introduction

The atomic and radiation physics group is responsible for studying the ultraviolet and X-ray radiation from laser produced plasmas and the attendant atomic physics and radiative transfer processes. This includes for instance the calculation of ionisation, recombination and excitation rates and their potential application to plasma diagnostics. Also the study of spectral line shapes and their use to determine ion velocity distributions or plasma electron densities. An area in which the group has been particularly active in the last year is the study of atomic structure through the classification of emission spectra from laser produced plasmas. These studies have produced new identifications in astrophysically important ions as well as extensions to the analysis of heavy element spectra of great interest as impurity radiation in magnetic fusion research.

6.2 L-Shell Spectroscopy

Developments in high temperature plasma sources, particularly those using high-power lasers, have made it possible recently to extend the systematic survey of ionic L-shell X-ray emission spectra to elements of atomic number higher than 26 (Fe). Burkhalter et al (6.01)(6.02), and Boiko et al (6.03) to (6.06) have discussed the spectra of several such ions in the oxygen-, fluorine- and neon-like isoelectronic sequences. The elements studied are: Cu, Zn, Ga, As, Br, Rb and Sr, of which Ga, As, Rb and Sr have not been analysed previously in the soft-X-ray region. The spectra show many transition arrays, notably from oxygen-, flurine-, and neon-like ions, and also show sodium like satellites $2p^6nl$- $2p^5ndnl$ to the neon-like $2p^6$ - $2p^5$ nd transitions. The analyses reported here cover the neon-like and $2p^5$ - $2p^4 3s,3d$ fluirine-like transitions.

The sources were plasmas formed by focussing the output beam of giant-pulse lasers onto solid targets with planar surfaces. The targets were made by grinding chemical compounds to a 10 μm grain size, adding a little starch as a binding agent, and compressing in a 6 mm radius die at 5 tonnes cm^{-2}. A compound of the element under study was usually mixed with another to provide wavelength calibration via the latter's hydrogenic and helium-like spectra. The mixture consisted of approximately equal numbers of atoms of the relevant elements. The Cu and Zn spectra were obtained using pure metal targets. The spectra were recorded with a convex-crystal X-ray spectrograph (Donaldson et al (6.07)) During this experiment, RAP crystals were often used in place of mica because of their higher reflectivity: a factor of four was demonstrated experimentally. This and other changes in the experimental parameters are summarised in Table 6.1 and related to the spectra thereby recorded. Those listed under (a) and (b) were obtained at Queen's University Belfast (QUB) and those under (c), at the Central Laser Facility. All the recordings involved multiple exposures of five to ten laser shots.

The spectral resolution was source-width limited (6.07) and the densitometry showed line widths on the recording film of 150 to 200 μm, which corresponded to a resolving power at 10A of ∿ 700. Photographs of all the spectra are reproduced in Figure 6.01.

Wavelength Determination

The most satisfactory method of wavelength calibration in this work was the incorporation into the target of elements emitting resonance spectra of hydrogenic and helium-like ions. Garcia and Mack (6.08) have given exact energy levels for the hydrogenic ions and Ermolaev and Jones (6.09) have calculated helium-like ion energy levels to high precision, so that wavelengths accurate to within 1 mA are available in the relevant atomic number range (6.10).

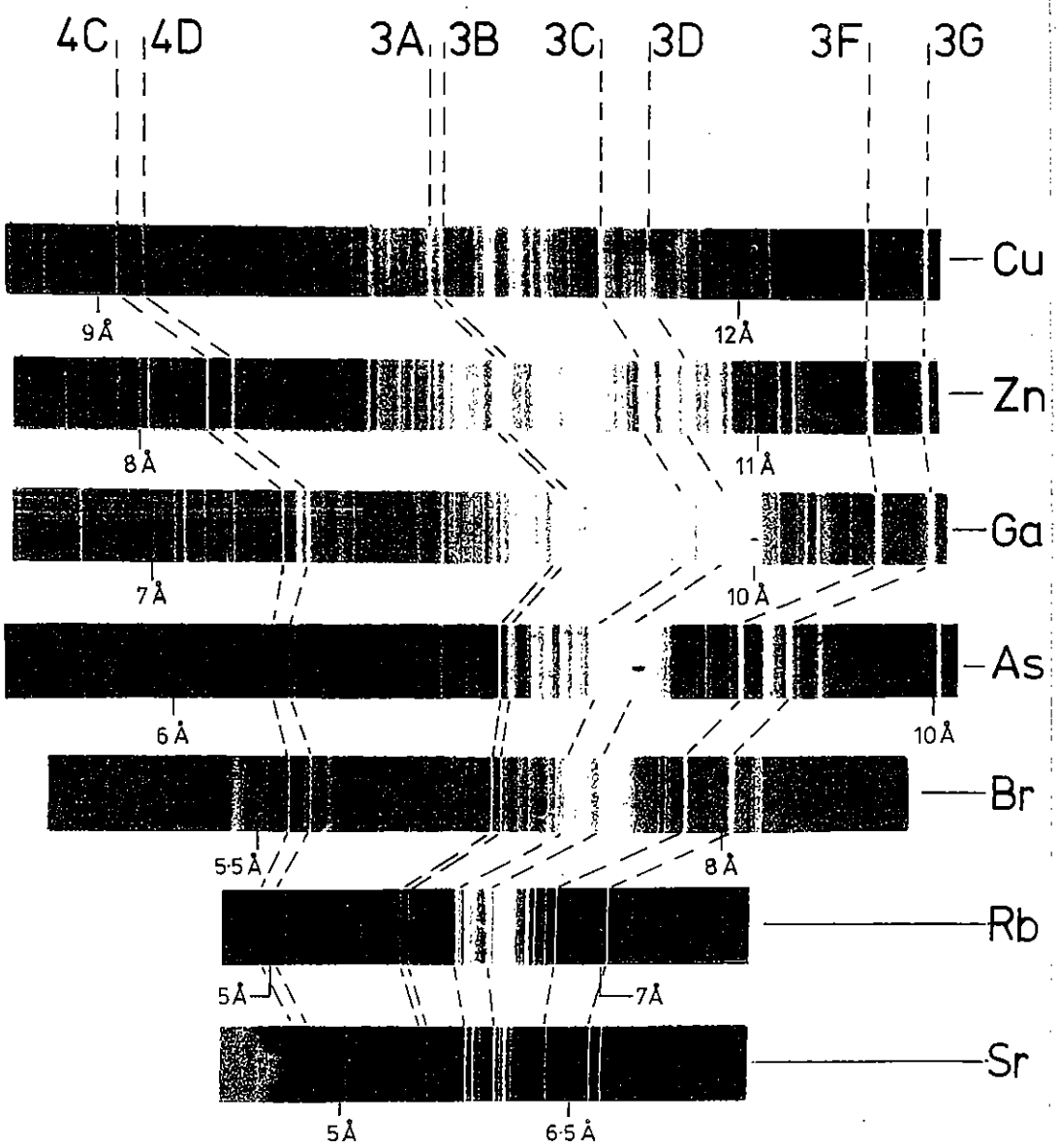

FIG 6.01

TABLE 6.1 EXPERIMENTAL PARAMETERS

Parameter	(a) Ga spectrum	(b) Cu, Zn, Ga, As, Br spectra	(c) Rb, Sr spectra
Laser pulse power (GW)	5	20-40	60
Laser pulse duration (ps)	6000	100	100
Beam diameter (mm)	45	55	100
Effective f-ration of focussing lens	f/2	f/1.5	f/1
Focal spot diameter (μm)	60	60	40
Crystal material	Mica	RAP	T&AP
Radius of curvature (mm)	38.4	150	150
Crystal-plasma distance (mm)	200	175	270
Crystal-film distance (mm) (approx)	80	120	30
Recording film	Kodak SC-7	Kodirex	Kodirex

Identifications in Neon-Like Ions

The recorded spectra each show several lines from neon-like ions. These transitions generate a simple spectrum since they terminate on the single level $^1S_0$ of the ground $2p^6$ configuration. The outer electron transitions ($2p^6$ - $2p^5ns,nd$) and inner shell transitions ($2s^22p^6$ - $2s2p^6nd$) together form only seven Rydberg series of optically allowed $\Delta n \geq 1$ transitions.

The $n = 3 \rightarrow 2$ and $2p \rightarrow 4d, 5d$ lines are generally sufficiently prominent that they can be classified with no risk of misidentification on the basis of agreement between observed and predicted wavelengths. For the same reason they do not appear to be significantly blended. The 3E line is weaker than the two other 2p-3d lines and lies in the same wavelength region as satellites to the 3D line (Burkhalter et al (6.01)).

Identifications in Fluorine-Like Ions

The fluorine-like $2p^5$-$2p^4$3s,3d transition arrays are clearly visible in our spectra up to bromine, and some of the stronger transitions appear on the rubidium and strontium spectra. For the ions considered here the $2p^5$-$2p^4$3s array lies mainly between the 3E and 3F neon-like lines and the $2p^5$-$2p^4$3d array lies between the 3B and 3C lines. Both arrays, with 14 and 34 allowed electric dipole transitions respectively, are much more complex than the corresponding neon-like arrays.

The predicted $2p^5$-$2p^4$3s,3d lines account for virtually all the observed features in the relevant regions of our spectra (see for example, Fig.6.01). The main exception is that the copper, zinc, gallium and arsenic spectra each show one feature at 12.339, 11.340, 10.454 and 8.979 A, respectively, which seem to belong to the same isoelectronic sequence of a $2p^5$-$2p^4$3s line. However the experimental wavelengths differ by at least 30 mA from the theoretical wavelengths of any of the $2p^5$-$2p^4$3s transitions and we therefore give no identification.

The extrapolated wavelength of this feature for bromine (assuming core charges for fluorine-like ions) almost coincide with the 3F line of neon-like Br XXVI but is so much weaker that it should not disturb significantly the observed wavelength for the neon-like line.

Comparison with other Work

The current investigation complements the study of the Ne-like ions Zn XXI, Ge XXIII, Se XXV, Br XXVI and Zr XXXI by Burkhalter et al (6.01), the Ne-like ions Fe XVII to Zn XXI inclusive, Ge XXIII, Se XXV, Y XXX, Nb XXXII and Mo XXXIII by Boiko et al (6.03), the F-like ions Zn XXII, Ge XXIV and Se XXVI by Burkhalter et al (6.02), the F-like ions Fe XVIII and Zn XXII by Boiko et al (6.03), and the F-like ions Y XXVI and Mo XXIV by Boiko et al (6.06).

Comparison with Theoretical Wavelengths

All the experimental wavelengths reported here were compared with theoretical values. The mean values for $\delta\lambda$ = {λ(our experiment) - λ - (theoretical from Boiko et al) lie between 1 and 5 mÅ for the neon-like lines. These differences, although small, are systematically positive and exceed two standard deviations in As, Br and Sr, whereas Boiko et al (6.05) have mean discrepancies for their own data $\delta\lambda$ = {λ (expt) - λ (theory)} of 2±3,0±1, 1±2,-2±2 mÅ for Cu XX, Zn XXI, Ge XXIII and Se XXV respectively.

Although an error of 5 mÅ would not be surprising in the theoretical calculations - which might include unspecified empirical E_{av} shifts we have nevertheless carefully investigated whether our experimental wavelengths might be systematically too long. One possibility is that systematic errors exist in our data reduction, for example, errors introduced by the dispersion curve fitting or in the plate measurement. This possibility is rejected because the derived wavelengths of those higher (and weaker) hydrogenic or helium-like ion lines which are <u>not</u> used as standards generally agree to within 2mÅ of the well established theoretical values.

We conclude that our experimental wavelengths for neon-like spectra are very unlikely to be systematically too long to an extent that would explain the apparent discrepancy of up to 5mÅ discussed above. We therefore attribute the discrepancy to theoretical uncertainties.

6.3 Spectra of highly ionised Iron and Nickel

Li I-like and Be I-like spectra of Ni XXVI and XXV have been classified by means of spectroscopic observations of laser-produced plasmas. Spectral line wavelengths of isoelectronic Fe XXIV and Fe XXIII are also measured. Analysis of the spectrograms was facilitated through comparison of measured wavelengths (between 8 and 13Å) and intensities with wavelengths and oscillator strengths predicted with theoretical 'ab initio' calculations. The microdensitometer traces of these spectrograms illustrated here (see fig 6.02) show many spectral lines which are present in solar flare spectra. The data presented provides an extension to earlier studies of highly ionised spectra in these isoelectronic sequences by Fawcett and Hayes (6.11), Boiko et al (6.05), (6.12) and Bromage et al (6.13).

The experiment

An f/1 aspheric lens was used to focus ∿50J pulses from the neodymium laser onto plane solid targets of iron or nickel with a resulting irradiance near 10^{16}W/cm^2. The duration of the laser pulse was 200ps. Spectra from the ions under investigation were emitted from a region of the laser-produced plasma which extended ∿10 μm from the target surface. The spectrograph, which contained a 5.5 cm long flat beryl crystal, was placed 22 cm from the plasma. Kodirex film, which intercepted the radiation reflected from the crystal, recorded sharp images of the plasma at positions determined by the Bragg angle for reflection of each individual wavelength. Two filters protected the film from stray light. The first was 1.5 μm thickness of aluminium which covered the entrance aperture of the spectrograph and the second was 1.0 μm thickness of polypropylene coated with 0.1 μm of aluminium which

covered the film cassette window. The positions of the spectral lines on the film were measured with an Abbe Zeiss comparator and wavelengths were derived to an accuracy of ±0.006Å by means of a computer interpolation program. The spectral resolving power achieved was 2000 at 10Å. A spectrogram with Ni XIX to XXII lines between 7 and 14Å with accurate wavelength measurements was provided by H Gordon et al (6.14) in advance of publication. Their wavelengths of Ni XIX to XXI lines provided wavelength standards for Ni XXV and XXVI wavelength determination and comparison of the two spectrograms made it possible to distinguish between lower and higher ionisation stages. Wavelength standards for iron were taken from the list of Bromage et al (6.15).

Analysis

The measured wavelengths of nickel were compared with predicted wavelengths calculated with a suite of computer programs (6.10, 6.17, 6.18) provided by Dr R D Cowan of Los Alamos Scientific Laboratory and adapted for the Rutherford Laboratory IBM 360/195 computer by Dr G E Bromage (6.19) and Dr Cowan. For the present work, the Slater parameters involved in the computations were scaled in the following way: the electrostatic (direct and exchange) radial energy integrals were all multiplied by a factor of 0.9, the spin orbit parameters by 0.95 and all configuration interaction integrals by 0.85. These scaling factors are identical to those found appropriate by Bromage et al (6.13) for Fe XXIII. The agreement between the newly measured and calculated wavelengths is about 0.1% which corresponds to the accuracy of the theoretically calculated wavelengths.

The new wavelength measurements for Fe XXIII and Fe XXIV include those corresponding to spectral lines of interest in solar flare studies and are an independent check on the values previously listed by Boiko et al (6.05, 6.12) who published an iron spectrum of excellent quality. Comparison of wavelengths shows good agreement. The spectrum illustrated in this paper contains fewer lines belonging to lower ionisation stages and hence allowed more definitive identifications particularly where a choice was necessary between two lines closely separated in wavelength. The present analysis for iron is in agreement with that of Bromage et al (6.13).

Spectrum of FeXXIII and FeXXIV obtained with a Beryl crystal

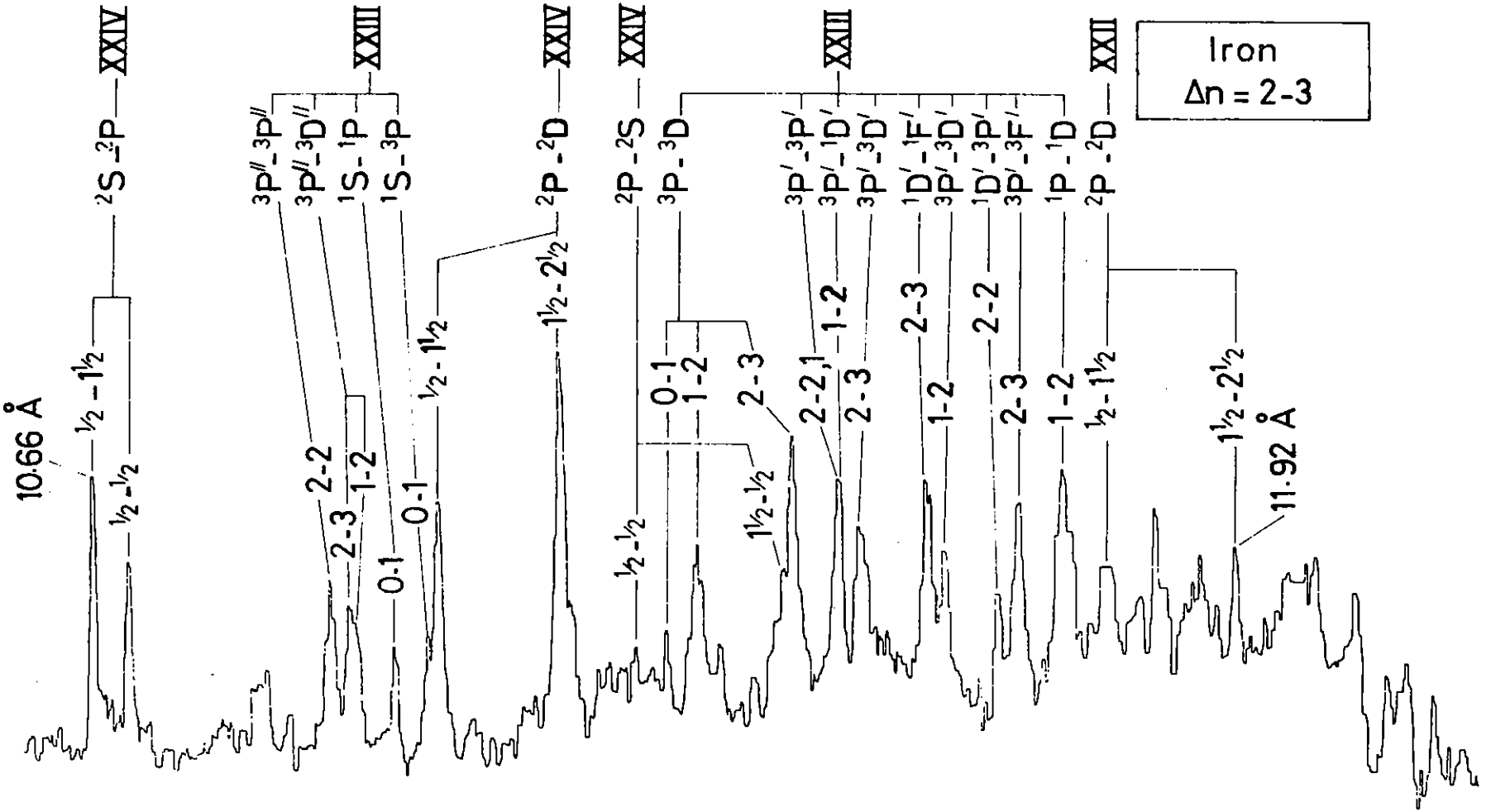

FIG 6.02

The computer program also calculates the composition of levels as a percentage of their LS basis. When substantial mixing occurs it must be accurately determined to calculate accurate oscillator strengths and excitation cross sections. For the ions and configurations involved here mixing in excess of 10% only occurs between levels of the same J value within an individual configuration. Furthermore it is less than 2% between all 2s3d and $2s^2$ levels and less than 5% between 2s2p levels. Mixing between the 2s3p levels is larger but well determined. Because of the low mixing and other theoretical considerations the calculated weighted oscillator strengths (gf) listed in (6.20) for the $2s^2$-2s2p and 2s2p-2s3d transition arrays are likely to be reliable with a probable accuracy of $\pm$ 20%. On the other hand the gf values for the $2p^2$-2p3d and 2s2p-2p3p transition arrays, which have highly mixed levels, can have large errors which are difficult to estimate or reduce without isoelectronic studies. One reason why these errors can occur is because the extent of the mixing within a particular configuration is affected by the scaling factors chosen for the Slater radial energy integrals for that configuration. To add to this, configuration interaction although not contributing directly to a major fraction of the mixing in these specific cases, indirectly affects mixing substantially by altering the interval between mixed energy levels. The extent to which levels mix is critically dependent on their proximity. Fortunately the $2s^2$-2s3p and 2s2p-2s3d transition arrays, for which reliable gf values are listed, are responsible for the n = 2-3 iron and nickel lines likely to be observed in solar flare spectra.

6.4 High Density Effects on Line Profiles

Studies have been carried out in the past year on the physical effects and problems relevant to spectroscopic parameters at very high plasma densities, both from the standpoint of the limits of present theories, and the extent to which experimental evidence of effects is available.

In particular, the possibility that Doppler narrowing can be observed in laser generated plasmas is now under detailed investigation. Doppler narrowing occurs when the mean free path between 90^o deflections λ_{90^o} is of the same order or less than the photon wavelength, λ_{ph}. Dicke (1953) pointed out that when this occurs the nature of the Doppler effect changes drastically. In particular, the Doppler broadening is suppressed and narrowing occurs.

The condition for this to occur in a plasma is approximately

$$\lambda_{ph} = \lambda_{90^o} = \frac{1.29\ K_B T}{Z^4 e^4 n_z \ln\Lambda}$$

where the definition of the 90^o deflection mean free path is derived in Spitzer (1965) and n_z is the number density of the ions of charge z. This implies that

$$n_z > \frac{1.29}{\ln\Lambda} \frac{K_B T}{Z^4 e^4 \lambda_{ph}}$$

for the narrowing to occur. Thus for a given wavelength the critical density can be plotted. In Fig.6.03 we have plotted the Doppler narrowing condition for a number of ions, where we assume $Zn_e = n_z$. The results indicate that pressure narrowing may occur in a laser plasma where the mean charge and the ion charge equal 10 at very low densities. This, it should be carefully noted, has obvious consequences for any scheme to produce X-ray lasers by using laser generated plasmas.

Work is now proceeding to evaluate the effects of the Doppler narrowing and to find the optimum case for study in a laser-generated system.

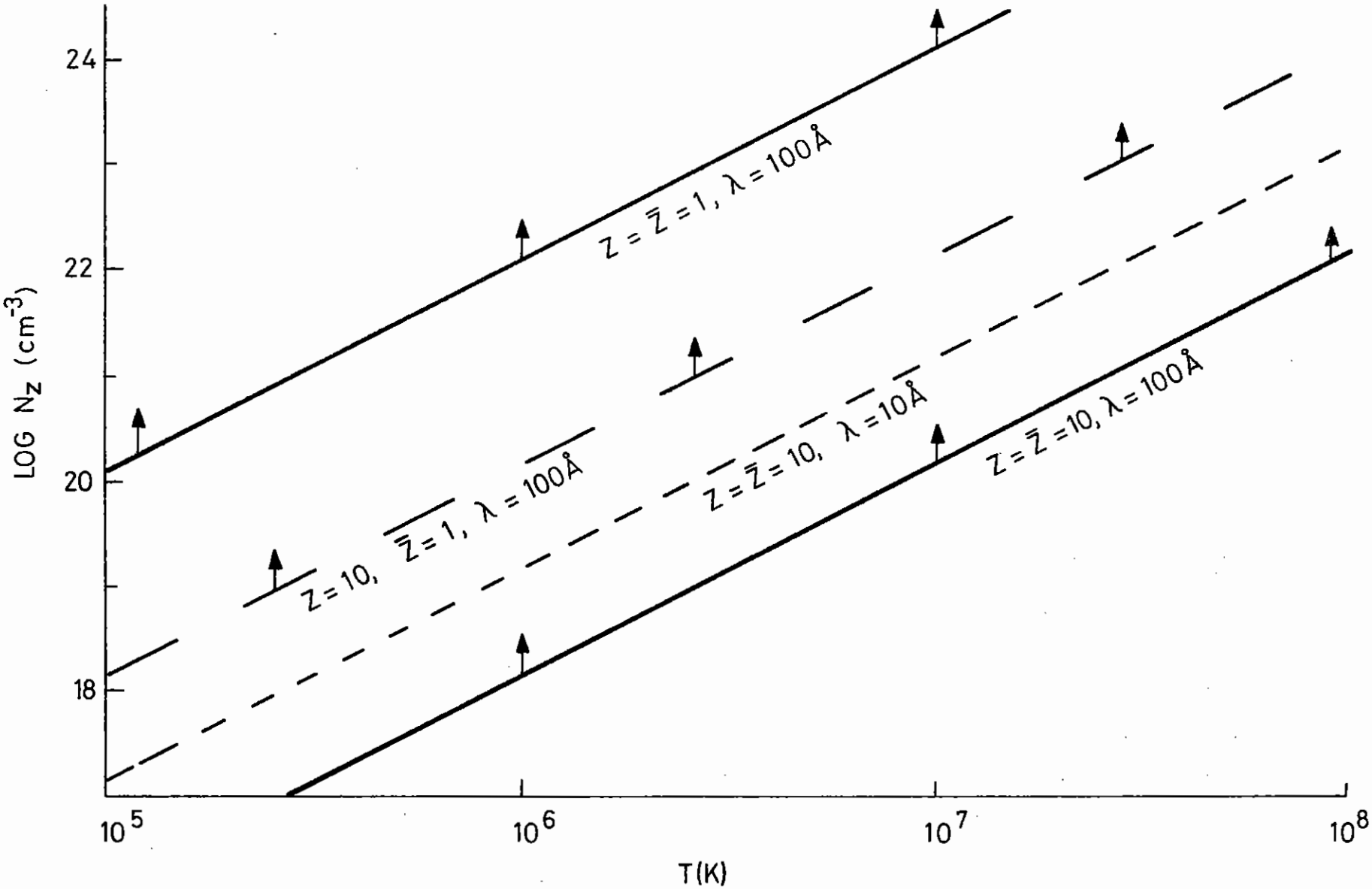

FIG6.03 CRITICAL ION DENSITIES FOR DOPPLER NARROWING ($\lambda_{PH} = \lambda_{90}$)

CHAPTER 6 REFERENCES

6.01 P G Burkhalter, D J Nagel and R D Cowan, Phys.Rev.A11 782-788 (1975)

6.02 P G Burkhalter, G A Doschek, U Feldman and R D Cowan, J.Opt.Soc.Am 67. 741-747 (1977)

6.03 V A Boiko, S A Pikuz, A S Safranova, A Ya Faenov, P O Bogdanovich, G V Merkelis, Z B Rudzikas and S D Shadzuvene, Lebedev Institute Preprint No 175, Moscow, (1977)

6.04 V A Boiko, S A Pikuz, A S Safranova and A Ya Faenov, Lebedev Institute Preprint No 191, Mosow, (1977)

6.05 V A Boiko, A Ya Faenov and S A Pikuz, J.Quant.Spectrosc. Radiat. Transfer, 19 11-50 (1978)

6.06 V A Boiko, S A Pikuz, A S Safranova and A Ya Faenov, J.Phys.B. (Atom.Molec.Phys) 11 L503-506 (1978)

6.07 T P Donaldson, R J Hutcheon, M H Key and R J Urquhart, J.Phys.B. (Atom.Molec.Phys) 9 1645-1655 (1976)

6.08 J D Garcia and J E Mack, J.Opt.Soc.Am. 55 654-685 (1965)

6.09 A M Ermolaev and M Jones, J.Phys.B.(Atom.Molec.Phys) 7 199-207 (1974)

6.10 K D Evans, R J Hutcheon and J P Pye, Space Sci.Instr. 2 339-348 (1976)

6.11 B C Fawcett, R W Hayes, Mon.Not.R.astr.Soc.170, 185-197 (1975)

6.12 V A Boiko, S A Pikuz, U I Safranova, A Ya Faenov, J.Phys.B. Atom.Molec.Phys.10, 1253-63 (1977)

6.13 G E Bromage, R D Cowan, B C Fawcett, A Ridgeley, Jour.Opt.Soc. Am.68, 48-51 (1978)

6.14 H Gordon, M G Hobby, N J Peacock (In preparation and private communication) (1978)

6.15 G E Bromage, R D Cowan, B C Fawcett, H Gordon, M G Hobby, N J Peacock, A Ridgeley, Culham Laboratory Report CLM-R170 (HMSO) (1978)

6.16 R D Cowan, Phys.Rev.163 54-61 (1967)

6.17 R D Cowan, Jour.Opt.Soc.Am.58 808-815 and 924 (1968)

6.18 R D Cowan, D C Griffin, Jour.Opt.Soc.Am.66 1010 (1967)

6.19 G E Bromage, Appleton Laboratory Report AL-R-3 (1978)

6.20 B C Fawcett, A Ridgeley and T P Hughes, Mon.Not.Roy.astr.Soc. (in press)

CHAPTER 7 XUV LASERS

I N D E X

CHAPTER EDITOR: I N Ross

CONTRIBUTORS: N J Peacock, G J Pert, C L S Lewis, D Jacoby, A Raven, L D Shorrock, J M Ward, M H Key, G Tallents.

7.1 Introduction

Experiments aimed at amplification of XUV light stimulated emission using laser-produced plasma as a gain medium have formed part of the programme on the Rutherford Laser Facility during 1978-1979.

While the long term aim of the programme is to investigate the feasibility fo an x-ray laser based on laser-produced plasmas, the immediate task of the present round of experiments is to demonstrate measurable gain by stimulated emission at XUV wavelengths. Some three weeks of the laser operating time have been devoted to carbon fibre irradiation experiments, devoted to the generation of a substantial population inversion between the n = 2 level of CVI and upper levels. The output of Hα (CVI) at 182 Å is expected to be enhanced due to single path stimulated emission preferentially along the fibre axis.

The University of Hull, Queens University, Belfast and the Rutherford Laboratory are collaborating on this project with technical assistance on XUV spectroscopy from Imperial College.

As is noted in section 7.2, computations of the laser-fibre interaction, on which the validity of the scheme is almost entirely based at present, indicate that XUV light gain is only to be expected in a restricted region of operating parameters. The experiment is technically demanding and the interpretation may not be unambiguous. Fibre dimensions and laser intensity are crucial. Using 1 cm long fibres several microns in diameter, the primary laser power required to be absorbed by the target is $\sim$ 1 TW. Thus the experiments are ideally suited to the Rutherford Facility. Subsidiary experiments however, on fibre target interactions at Hull University and optical pumping in the XUV region at the Culham Laboratory have a role to play.

The programme for 1978-1979, discussed in section 7.2, has involved some preliminary experiments on laser-irradiated fibres which are back-lit by XUV continuum from a subsidiary laser-produced plasma. The limited aim of these initial experiments is to measure the time and spatial dependence of

the population inversion and demonstrate XUV light gain by enhancement of the continuum at 182 A.

If these experiments prove successful the scheme will be applied to higher Z targets lasing at even shorter wavelengths. The XUV light gain experiments can be seen therefore as an ongoing programme.

7.2 Carbon VI Experiment

7.2.1 Theoretical Considerations

The development of laser action in the x-ray and XUV spectral regions, places very severe constraints on the power of the pumping system. In view of this it is clear that any such system, if it is to be practically viable, must be made as efficient as possible. In the case of the recombination laser system, it is relatively straight forward to generate population inversions during the expansion of plasma from a solid target irradiated by a high power laser (7.02, 7.03). To construct a working laser using this approach, however, demands extremely large pump laser energies. This limitation on the use of slab targets is associated with the fact that, in order to obtain complete ionisation, we require high temperatures which in turn leads to thermal conduction heating of the bulk, and a relatively large plasma body.

A simple way to overcome this limitation is to restrict the dimensions of the target, i.e. to use a thin cylindrical or foil target. Cylindrical targets have the additional advantages that the transverse dimension is restricted, and also that a two dimensional expansion is more rapid, and therefore more efficient, that a one dimensional one. For these reasons it is believed that the first demonstrations of laser action in the XUV spectral region are likely to be made with expanding fibre targets.

The most suitable target material is carbon. Carbon fibres of about 5μ diameter are readily available. Furthermore, the characteristic laser

pumping requirements for such a system are well matched to values typical of present day laser technology - laser energy ∿ 50 J in a pulse ∿ 100 ps duration.

The charactersitics of carbon fibres under such irradiation have been thoroughly investigated using the similarity computer code "GAIN". This shows that for a given fibre diameter, there are optimal irradiation conditions, and that the gain is relatively sensitive to the change in laser parameters. In particular we find that the gain is relatively insensitive to the laser pulse length, but depends strongly on the absorbed laser energy. Thus in a given experiment there is a relatively small window in parameter space, within which gain can be observed. In particular a variation of a factor 2 in absorbed energy from the value at peak gain may cause a reduction of more than an order of magnitude in the gain.

The scaling of the system at peak gain has been investigated and the following scaling laws found:

$$G \propto a^{-17/11}\, \tau_i^{-6/11}$$

$$E \propto a^{28/11}\, R\tau_a^{-1}\, \tau_i^{-3/11}$$

where G and E are the gain and 'absorbed energy' per unit length respectively, a and R are the radii of the fibre and focal spot respectively, and

$$\tau_a \simeq \tau_p + 2\sqrt{\alpha}\,\tau_d$$

and

$$\tau_i \simeq \tau_p + \sqrt{\alpha}\,\tau_d$$

where τ_p is the laser pulse time-to-peak, and τ_d and α are the pre-pulse delay and fraction absorbed.

It can be clearly seen that the efficiency of the system is greatly improved by the use of thin fibres. The actual values of laser energy required are not very restrictive. Thus, for example, with a 3μ m diameter

fibre, the optimal absorbed laser energy is about 20 J/cm in a 100 ps laser pulse focused into a 50 μ diameter spot giving a gain of about 4/cm. Thus a working laser operating in the XUV region in the amplifier spontaneous emission mode will require about 50 J of laser pump energy.

7.2.2 Experiment to Demonstrate Light Gain by Stimulated Emission at 182 Å

The experimental layout for the CVI recombination laser scheme is illustrated in Figure 7.01. Several millimetres of a 3 μ carbon fibre will be irradiated in a line focus first with a prepulse to shock heat and dissociate the solid fibre and then ≃ 200 ps later with a main pulse to heat the carbon material to several hundred eV at high density ($n_e \simeq 10^{21}$ cm^{-3}). The subsequent rapid expansion phase, during which the inversion develops between n = 3 and n = 2 of hydrogenic carbon ions (7.01), is probed by continuum radiation at 182 Å from an auxiliary high Z plasma source generated by a delayed beam. A xl magnification image relaying toroid is used to collect the backlighting flux travelling axially through the expanding cylindrical carbon plasma and to image the auxilliary source onto the entrance slit of the GML5 5m grazing incidence spectrograph (7.04).

The backlighting source position is arranged spatially to probe the carbon plasma after it has expanded to a radius of ≃ 200 μ when the inversion peaks. This degree of spatial resolution discriminates strongly against the carbon plasma's self-emissivity and any enhancement of the backlight continuum observed at 182 Å may be taken as evidence of gain on the CVI Balmer Alpha transition (H_α).

Preliminary progress towards a full scale experiment may be reported under five headings.

i) Source Continuum at 182 Å

The toroid and GML5 have been successfully aligned and single shot exposures have been recorded on Q-plates using ≃ 5 J, 100 psec pulses to irradiate the carbon and tungsten targets. The carbon spectrum provided a wavelength calibration but definite conclusions about the tungsten continuum at 182 Å was hampered by the possibility of overlapping higher orders from

harder x-rays. This question will be studied further using free standing Al foils (2000-3000 Å) and polymer foils (few microns) to isolate the wavelength bands detected. A suitable choice of grating may also discriminate against harder x-rays.

Source targets other than tungsten will also be investigated to optimise the 182 Å continuum intensity and purity, e.g. ytterbium (7.05). The final requirement on the source continuum to be demonstrated is that a single shot recording can be made with a spectal resolution comparable to the CVI H_α line width which has a Doppler broadened width of ≃ 30 mÅ at the time of inversion. This will give maximum sensitivity for gain detection and implies a slit width of ≃ 5 μ for suitable gratings to be used.

ii) Prepulse Heating Characteristics

5 μ diameter fibres were irradiated with ≃ 0.2 J/mm and the dissociation of the fibre observed using shadowgraphy with a 2 ω probe beam delayed by 200 ps and 500 ps. Results were not conclusive and future investigations will be carried out using 2 ω interferometry. Ideally it should be demonstrated that the prepulse generates a cold plasma of radius ≃ 25 μ and density of $N_e \simeq 10^{21}$ cm^{-3} with which the main pulse interacts.

iii) Uniformity of Irradiation

Ion collectors have been used to show that the plasma expands uniformly in a radial direction. In a full scale experiment x-ray pinhole imaging will show the extent of uniformity along the fibre length.

iv) Cylindrical Optics and Alignment

100 mm diameter cylindrical lenses with focal lengths ranging from 1.5-5 metres are available to cover a wide range of heating conditions. Fibre lengths from 1-10 mm can be irradiated with incident fluxes varying from 40-4 J/mm. The weak cylindrical lenses are situated outside the target vessel and chosen to minimise the increase in power density on the main focusing spherical lenses. The quality of the line focus has been investigated by viewing a CW YAG line focus with an ICOS lens and telemicroscope system. Scanning the lens has shown that the line focus is tolerably

FIG 7.01

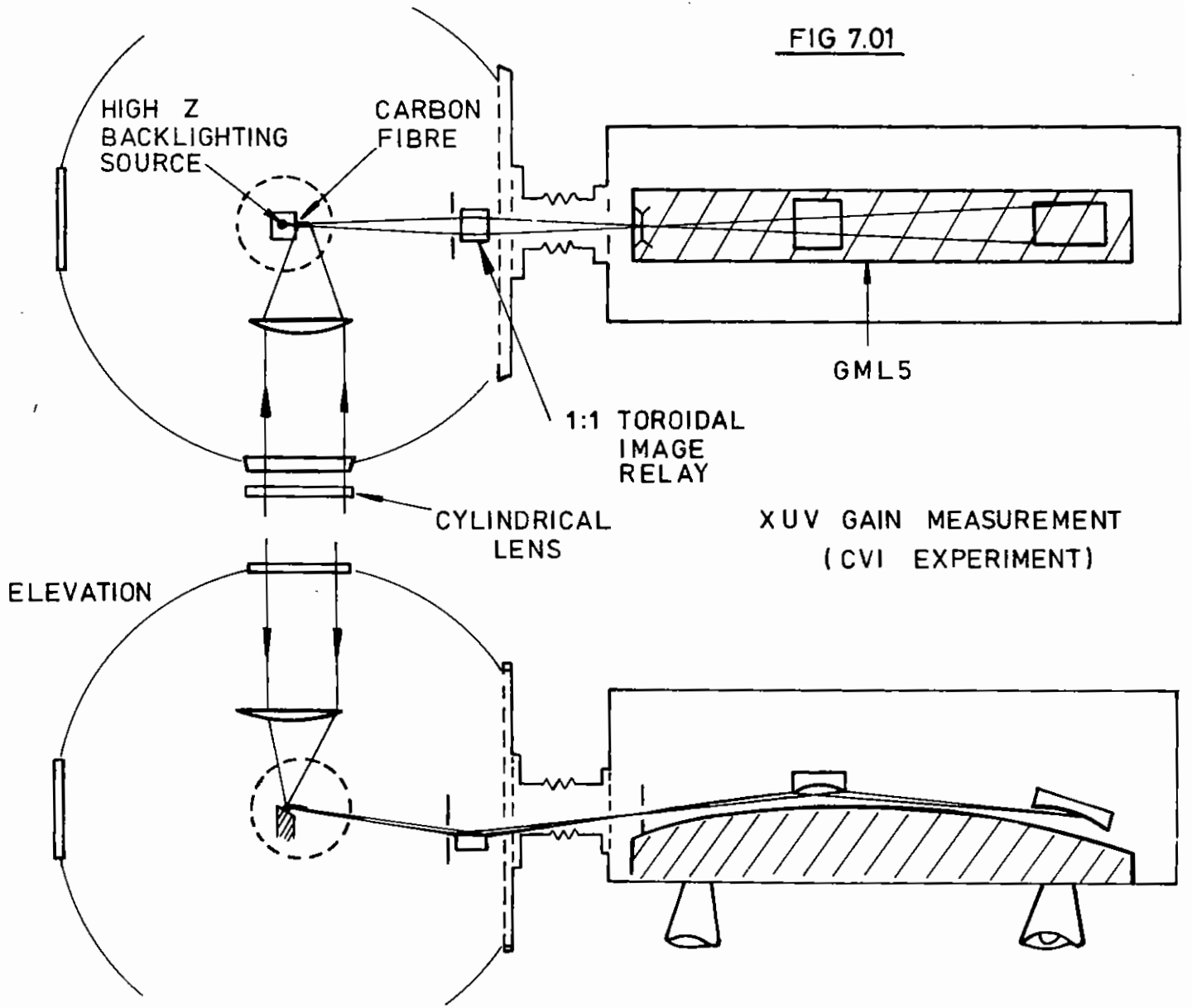

XUV GAIN MEASUREMENT
(CVI EXPERIMENT)

straight over several millimetres with a width of ≃ 50 μ. More quantitative tests of burns on indium foils and film will be made to characterise the focal plane intensity distributions.

v) Recent Evidence on the Source Continuum, Line Focus and Density Profile

In the last two weeks of scheduled laser time further progress was made in establishing the basis of a single shot backlighting continuum exposure at 182 Å, required for a fullscale 'gain' measurement.

Tungsten continuum from a solid target, imaged into the entrance slit plane of the spectrograph by the toroidal mirror, stopped down to 2mm, produced a strong exposure (D > 1.0) in a single laser shot ($E_{o/p}$ ∿ 20 J) with the lens defocused by 250 μm, when recorded on Kodak 101-05 plates. Ilford Q2 plates were found to be too insensitive for single recording.

In subsequent shots, the continuum was filtered with 2000 Å freestanding Aluminium, placed in front of the grating, and revealed the sharp L - edge at 169 Å (see Figure 7.02). This demonstrates that the continuum beyond this edge particularly at 182 Å is first order diffracted and not a superposition of higher orders. Micro-densitometer scans, Figure 7.02, reveal that the continuum appears quasi-continuous with the present instrumental resolution (entrance slit 20 μm, 0.35 Å at 182 Å).

Ultimately, the constraints of recording sensitivity when the entrance slit is reduced to ≤ 5 m for line resolution in the 'gain' measurement, may necessitate the use of active detection and the possibility of incorporating the x-ray streak camera into the GML5 spectrograph is being evaluated. This would provide both significantly increased (static) detection sensitivity with a subsequent option of being able to temporally resolve the 'gain' history.

In the second week of experiments, line focus geometry was used with a - 5 m plano-concave cylindrical lens placed before the main Soro lens, outside the target chamber.

The resulting 'line focus' was observed both in the cw:YAG telemicroscope

system, imaged by the ICOS 12 cm focal length lens, and also from the burn patterns in 1000 Å indium, vacuum deposited on glass. Transmitted and reflected cw:YAG revealed a structured line focus consisting of longitudinal striations, not all of which superimposed in the target plane.

A nominal full-length half energy measurement inferred at 12 mJ, was of a line 1.25 mm long and ∿50 μm diameter, displaying a structure similar to that seen in the cw:YAG telemicroscope.

The remainder of the week was devoted to $2\omega_o$ interferometric observations of expanded carbon fibre plasmas, irradiated in the line focus.

The small fraction (1%) of the main beam transmitted through the primary turning mirror (ω_o vertically polarized) was frequency doubled ($2\omega_o$ horizontally polarized), filtered and attenuated and coupled to an optical delay line before being transmitted through the target plane on the spectrograph axis(West - East) and orthogonal to the main beam axis (North - South).

Single filament carbon fibres of diameter 4 - 5 μm were mounted vertically to observe the radial expansion. On the $2\omega_o$ axis, the fibre was imaged with a X5 microscope objective and recorded on a polaroid back outside the target chamber. Directly behind the objective, a Wollaston prism followed by a linear polarizer sheet were inserted and oriented to produce interference fringes at 45^o to the vertical fibre (see section 3.2).

Figure 7.03 illustrates a typical interferogram for a 4.4 μm fibre (shot 120479/02, $E_{o/p}$ = 24.9 J), where the $2\omega_o$ (∿80 ps) probe beam was delayed by 2.3 ± 0.1 nsec from the main (ω_o, 100 ps) beam. The laser pulse had a ∿ 4% prepulse 200 psec before the main pulse, to optimise the energy coupling to the fibre (7.06). This inteferogram shows a region of plasma surrounding an absorbing core of about 50 μm diameter in which a decrease in the fringe shift is seen. The fringes are continuous through the whole field. This suggest that the core consists of cold absorbing material with the possible presence of unionised material. Abel inversion of the data about the fibre axis shows a density of around 5×10^{19} cm^{-3} with a half-height radius of 50 μm and a strong central hollow due to the fringe reversed at centre. The total number of electrons represented is 10^{16} cm^{-1}

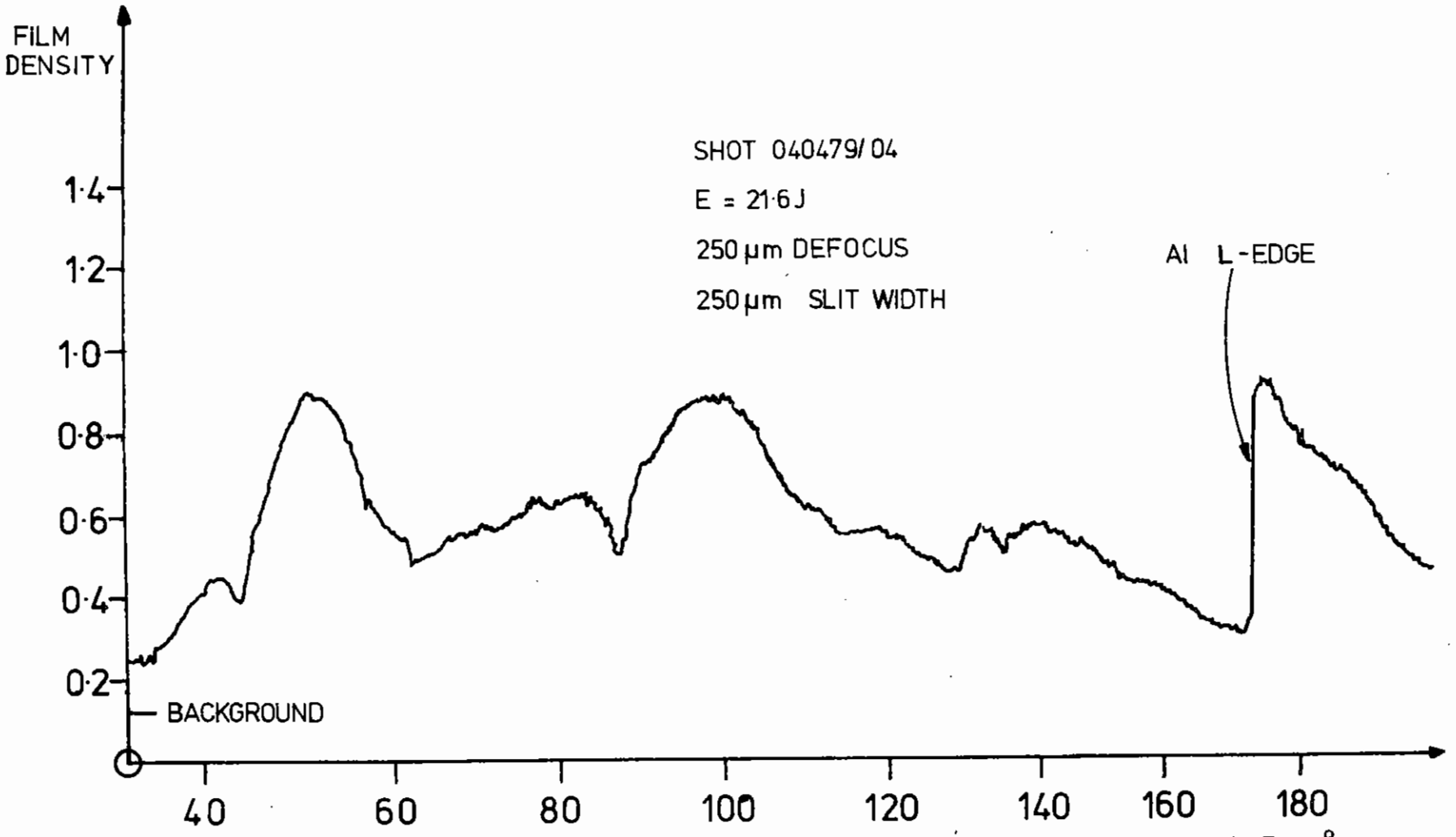

FIG 7.02 TUNGSTEN SOURCE SPECTRUM FILTERED WITH 2000 Å ALUMINIUM

FIG 7.03

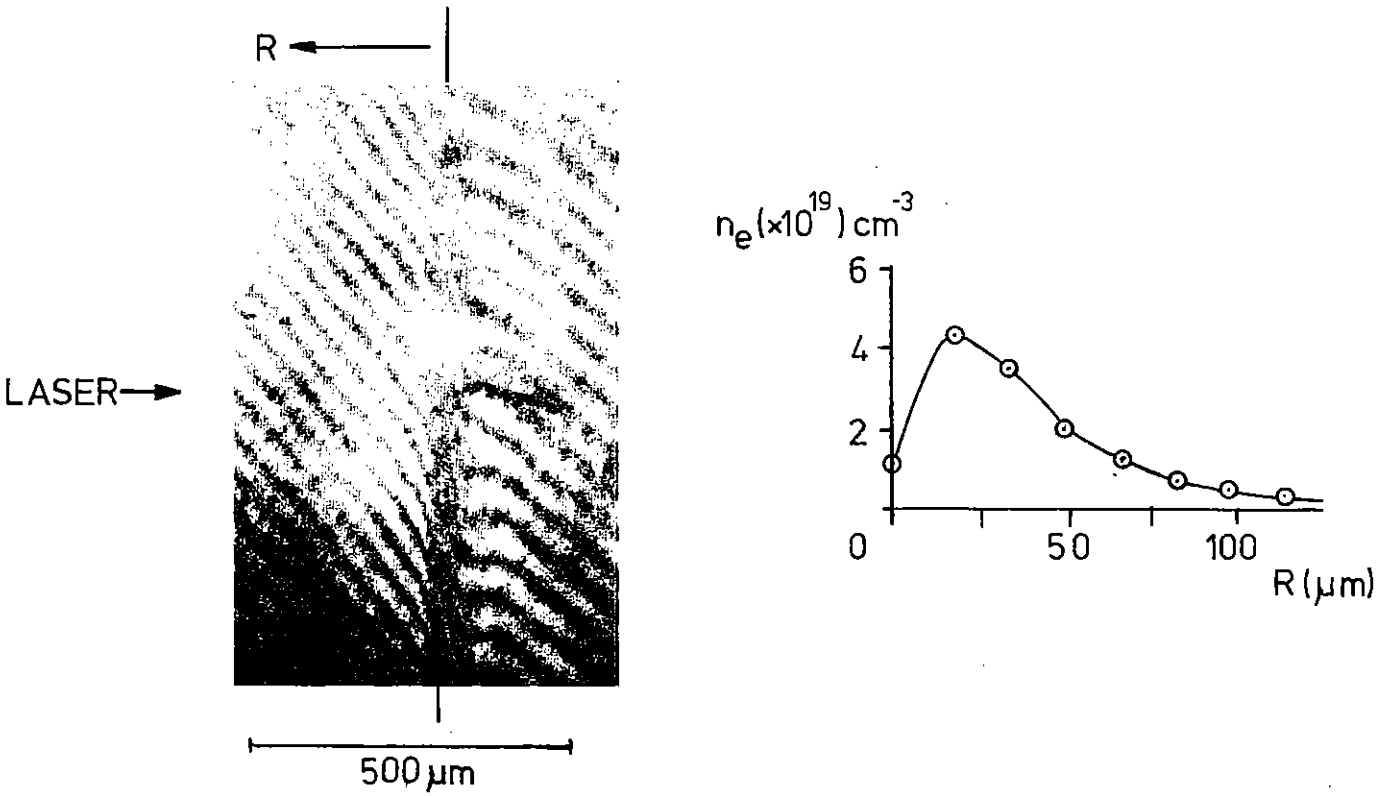

compared with an electron density of 8×10^{16} cm^{-1} of the original fibre. This again supports the view that the plasma is either in a very low ionisation state or there is a considerable amount of neutral material present. The uniformity of the plasma along the fibre was very good (± 10%) despite the non-uniformity of the irradiative beam.

Code modelling assuming optimum coupling suggests that after ∿ 2.0 nsec the plasma front would have expanded to a radius of ∿ 1500 μm and that the electron density at the fibre origin would be - 10^{18} cm^{-3}.

Whilst the coupling efficiency can hardly be expected to correspond to this ideal, earlier work at Hull suggests a figure of ≤ 50%, whereas, micro-balloon studies may put this figure as low as ∿ 10%. There also remains some uncertainty as to the accuracy with which the fibre was both aligned to the line focus axis and placed in the plane of optimum focus at full beam intensities.

Further work is envisaged using this interferometric technique with both spot and line foci, to both improve the target alignment systems and importantly to derive density and size parameters to feed into the code simulations in order that an 'experimental' coupling efficiency can be determined and thus to predict realistic laser energy requirements for the full-scale 'gain' experiments.

CHAPTER 7 REFERENCES

7.01 G.J. Pert, J. Phys. B. Atom. Molec. Phys. Vol. 9, No. 18, pp. 3301-3315 (1976).

7.02 F.E. Irons and N.J. Peacock, J. Phys. B., Atom.Molec. Phys., 7, 1109-1112.

7.03 R.J. Dewhurst, D. Jacoby, G.J. Pert, S.A. Ramsden, Phys. Rev. Lett. 33, pp. 1070- (1976).

7.04 R.J. Speer, Space Science Instrumentation, 2, pp. 463-487, (1976).

7.05 Carroll, UCD, Private Communication.

7.06 D. Jacoby, Ph.D. Thesis, Hull University (1978).

CHAPTER 8 THEORY AND COMPUTATION

I N D E X

CHAPTER EDITOR: C J Webb.

CONTRIBUTORS: R G Evans, S J Abas, D Bond, R A Cairns, G Humphreys-Jones, H C Barr, W T Hewitt, T J M Boyd, M Haines, B Hafizi, R Graham, G A Gardner, D Cooke, N A Tahir, R W Lee, D J Nicholas, P T Rumsby, S Craxton, L Wickens, T D Beynon, J Pert, O Dwyer, E H Smith, D V Bugg, W T Welford, J E Allen.

CHAPTER 8 THEORY AND COMPUTATION

8.1 Introduction

The theoretical and numerical simulation of laser-plasma interactions is being carried out mainly at the Universities, although certain simulations of more direct relevance to particular experiments are carried out at the Rutherford Laboratory.

Hydrodynamic phenomena, especially in spherical symmetry is best followed using the 1-D Medusa code, and this is the main code employed in experimental comparison. Modifications that have been carried out include a simple model of fast electron pre-heat and some atomic physics including radiation transport. More sophisticated modifications, using better fast electron transport for example, are currently in hand.

Plane target and asymmetric compression modelling can be achieved using one of the several 2-D codes, which have the special feature of including magnetic field generation due to $\nabla T \times \nabla n$ effects. The most complete work on this subject in our programme has come from LASER B where hot rings are predicted by the magnetic suppression of the electron thermal conduction, and ultra fast (100 keV) ions have been calculated from the $\underline{J} \times \underline{B}$ force. Future work on 2-D simulation is likely to centre around a more versatile program, CASTOR II, which is still being developed. In this area it would be most useful, and a great saving of duplication of effort, if a direct collaboration with AWRE could be established.

Particle codes are necessary to study the non-linear interaction of the laser radiation with the plasma. Because of limitations of computer power we are at present limited to one dimension in space. Two codes are currently operational; EMPIRE developed at Bangor which has normal incidence e.m. radiation with relativistic effects, the particle velocity being two dimensional; and the PIC code at Imperial College which analytically treats the second dimension so that resonance absorption at arbitrary angles of incidence of radiation is possible. Both of these codes demonstrate ponderomotive zone steepening and fast electron generation. We look forward to when a CRAY or similar computer will be available so that $2\frac{1}{2}$D particle codes can be constructed. Only then will we be able to simulate realistically the rich phenomena in laser-plasma interactions.

Work on such a code has begun.

Despite the need for large scale computing there is still an important role for analytical theory. Here progress has been made on parametric instabilities, on resonance absorption in warm plasmas, and the effect of rippled surfaces in absorption.

8.2 Laser Compression Studies

8.2.1 Hydrodynamic Codes

The 1-D Lagrangian fluid code MEDUSA has been used extensively for simulation of experimental data and also for target design. The code has been continuously improved and new physics has been incorporated as required by the different physical conditions encountered in the simulations.

The atomic physics post processor has been extended to calculate time averaged electron temperatures from the recombination continuum slope and electron densities from time averaged lineshapes. The calculation of these properly averaged quantities has been essential in attaining the excellent agreement with experimental implosion core parameters in section 4.7.3 since the maximum densities and temperatures are about twice the average values.

This code has also been used to calculate implosion times of exploding pushers as described in section 5.2 and here the agreement between code and experiment is less good. It appears that this may be due to some inherently 2-D aspects of the implosions.

As well as x-ray emission from the plasma the code can also calculate line of sight integrated, monochromatic x-ray opacities for the simulation of the x-ray backlighting experiments described in sections 5.3 and 5.4.

As the regime of simulation has changed towards denser, cooler implosions some deficiencies in the original MEDUSA code have been revealed. For instance the experiment of section 5.3 proved to be rather sensitive to radiative cooling of the neon fill gas during the 'coasting' of the pusher before maximum compression. A correct treatment of this would require a description of the radiation transport in the target. A multigroup diffusion model of radiation transport has been written and will be included in the code when suitable radiation opacities have been calculated.

The ablative compression experiments of section 5.4 are in a region where equations of state present some problems and work on including a Thomas Fermi equation of state is in hand. The analysis of section 5.4 used a simple expedient of fitting the experimentally determined equation of state of glass at pressures up to about 1 Mbar with a constant adiabatic index, and adjusting the starting temperature of the code to arrive on the correct adiabat. This technique is justified for the particularly low preheat and low compressed temperature of this target but is not generally applicable.

8.2.2 Predictions of Magnetic Field Profiles from CASTOR

Experimental investigations of magnetic fields generated by thermo-electric sources have continued as reported in section 4.2. Simultaneously, we have employed computer modelling to study the dynamical structure of these fields and their various concomitant effects.

The computer code utilised in these studies is the version 2 of CASTOR (8.01). The code is a two-dimensional (r,z) cylindrically symmetric three temperature MHD code and apart from the usual MHD description the model includes time dependent atomic physics as well as the transport and emission of radiation. Where the classical transport description is appropriate the code solves the equations given by Braginskii.(8.02), but flux limited transport is invoked where necessary constraints on mean free paths electron Larmour radii and collision times are violated. Also, the code allows for simulations of the effects of large amplitude field fluctuations via Bohm or a mixture of Bohm and classical diffusion coefficients.

The original version of CASTOR 2 became available at the Rutherford Laboratory in early October 1978 and tests were begun to compare its predictions with some previously published results on self generated magnetic fields. Also, the code was used to model the experiment of Raven et al (8.03). Initially the code did not perform satisfactorily and numerical difficulties arose when very small scale lengths of only a few microns were encountered. The difficulties were traceable to the limiting form of the amplification factor for the ADI method (8.04) which is the method employed to solve the first stage of the diffusion part of the calculation. To overcome these difficulties, at least until a more rigourous alternative is devised, we employ some artificial smoothing on T_e and B_θ where necessary. The smoothing is made by an explicit diffusion algorithm which

conserves electron thermal energy and magnetic flux but not the magnetic energy. Energy conservation checks are monitored for the error, and a simulation is accepted only if the error in conservation does not exceed a few per cent of the total.

The latest version of CASTOR 2, incorporating smoothing and clipping algorithms and also some other minor modifications, arrived at the Rutherford Laboratory in February 1979. A few bugs connected with rather capricious differences between the ICL 4/70 machine, on which the code was developed, and the IBM 360/195 at Rutherford Laboratory have been, after considerable detective work, discovered and cleared up. However, at the time of writing this report, this latest version of CASTOR is still suffering from some minor transfer problems. We are subjecting CASTOR 2 to extensive comparison tests on the two machines and hopefully the proving and testing period will soon come to an end. We have an extensive program of numerical simulation drawn up for CASTOR, and once our confidence in its predictions is reasonably well established, it should provide us with a growing framework for laser target calculations for several years to come.

We now summarise below the results of one of our simulations, the motive for which was provided by the experiments of Raven et al reported in section 4.2 at Rutherford Laboratory.

We consider an Nd-glass laser beam incident on a plane aluminium target. The cylindrically symmetric simulation region centred around the axis of the beam is defined by $0 \leq r \leq r_{max} = 135$ μm, and $0 \leq z \leq Z_{max} = 78$ μm. The laser beam has a Gaussian profile in space and time with a beam radius of 50 μm and duration (FWHM) 100 psec. The power rises to a maximum of 2×10^{11} W when the peak intensity reaches 10^{16} W/cm^2. 20% of the incident energy reaching the critical surface is assumed to be absorbed. The initial density profile is taken to be only z dependent and rises exponentially to solid density with a scale length of 4 μm.

The equation for the azimuthal magnetic field used in CASTOR 2 is

$$\frac{\partial B_\theta}{\partial t} = \{\nabla \times \left[\underline{u} \times \underline{B} - \frac{1}{\mu_o} \underline{\underline{\eta}} . (\nabla \times \underline{B}) - \frac{1}{\mu_o e} \nabla \times (\frac{1}{n_e} (\nabla \times \underline{B}) \times \underline{B}\right]\}_0 + S,$$

where η is the resistor tensor, the other symbols having their usual meaning.

and the source term S is given by

$$S = \frac{-\kappa}{e\, n_e} \nabla n_e \times \nabla T_e - \frac{\kappa}{c}\, \underline{\beta} \cdot \nabla T_e \ ,$$

$\underline{\beta}$ being the thermoelectric tensor.

The first term on the right hand side provides the 'seed' field and the second term comes into significance when $\Omega\tau \sim 0$ (8.01), where Ω is the electron Larmour frequency and τ is the electron-ion collision time.

In figure 8.01 we have plotted the field at the edge of the focal spot ($r = 60\ \mu m$) and at time $t = 132$ picosec, which is 32 picosec after the peak of the laser pulse. Figures 8.02 - 8.04 show isometric plots of T_e, T_i and B respectively at the same time. Note the formation of hot spots ($\Omega\tau$ effects) in the distribution of electron temperature.

Figure 8.01 also contains plots of n_e/n_c and plots obtained from the experimemts of Raven et al (8.03). As far as the magnitude of the fields are concerned the values predicted by CASTOR are in extremely good agreement, 3.5 MG as compared to 3.2 MG. However, regarding the extent of the field the match is less satisfactory. In the simulation, the field is found to rise sharply around the critical density region at the edge of the focal spot and to maintain a more or less constant value as far as $n_e \sim \cdot 3\ n_c$. Only at later times, when the laser pulse has died out that the fields in the low density corona substantially exceed the fields to be seen at the critical density. Figure 8.05 which shows an isometric plot of B at 198 picosec shows this behaviour. Note also from this figure the penetration of field in the solid region via resistive diffusion.

The findings reported above are preliminary in that a vast amount of data from the most current version of the code has yet to be analyzed. The elucidation of the magnetic field patterns and the understanding of mechanism that give rise to them is an important part of our computer simulation program. It is now clear from the theoretical work published that mega-Gauss fields with scale lengths extending from the scale of the laser spot right down to submicron scales can arise in laser-plasma couplings, and hence the accurate simulation of the important mechanisms is not easy. We are, never-the-less, pursuing this matter vigorously.

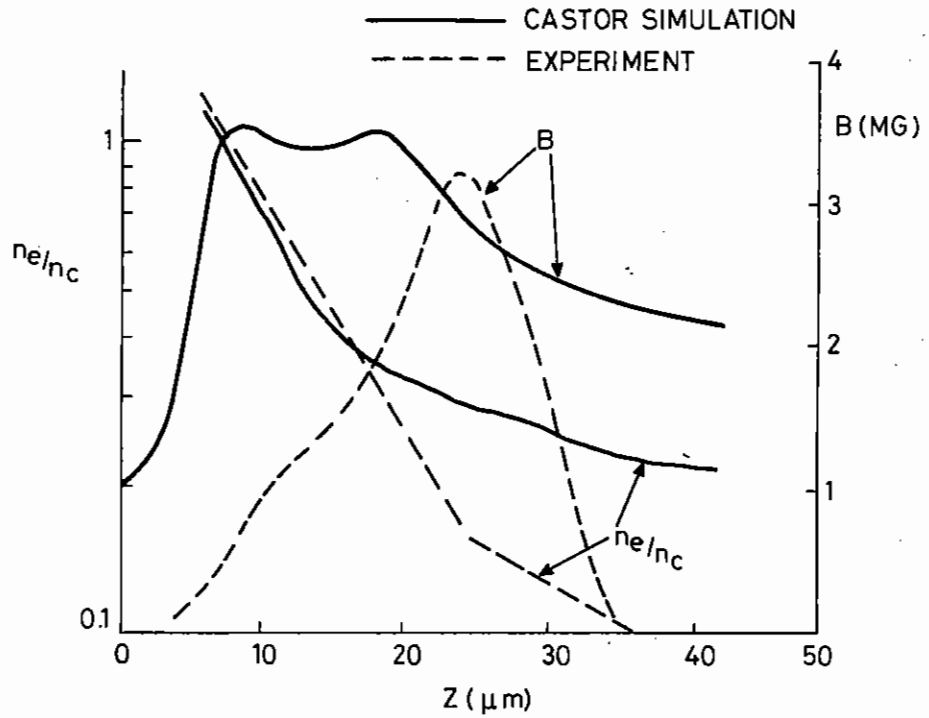

Fig.8.01

Comparison of magnetic field and density profiles at the edge of the focal spot, perpendicular to the target surface.

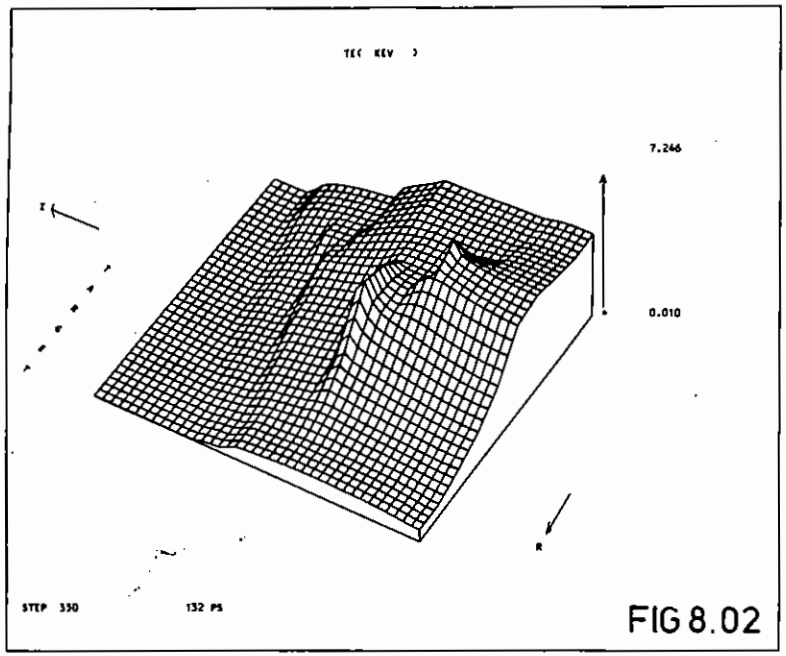

FIG 8.02

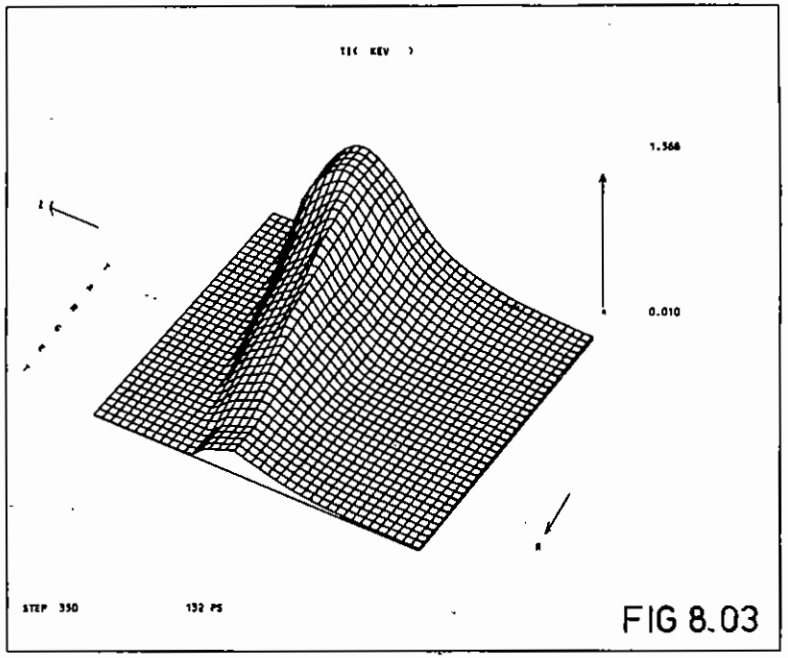

FIG 8.03

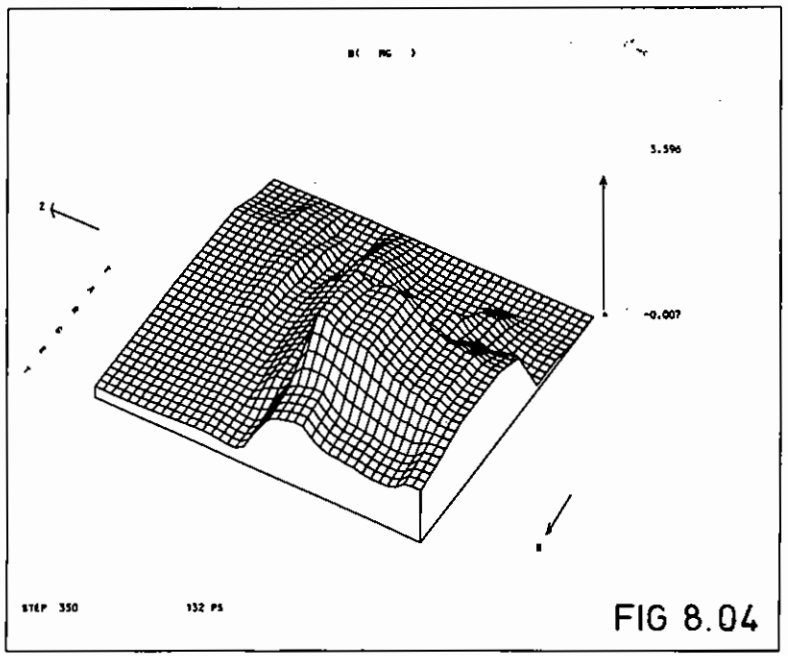

FIG 8.04

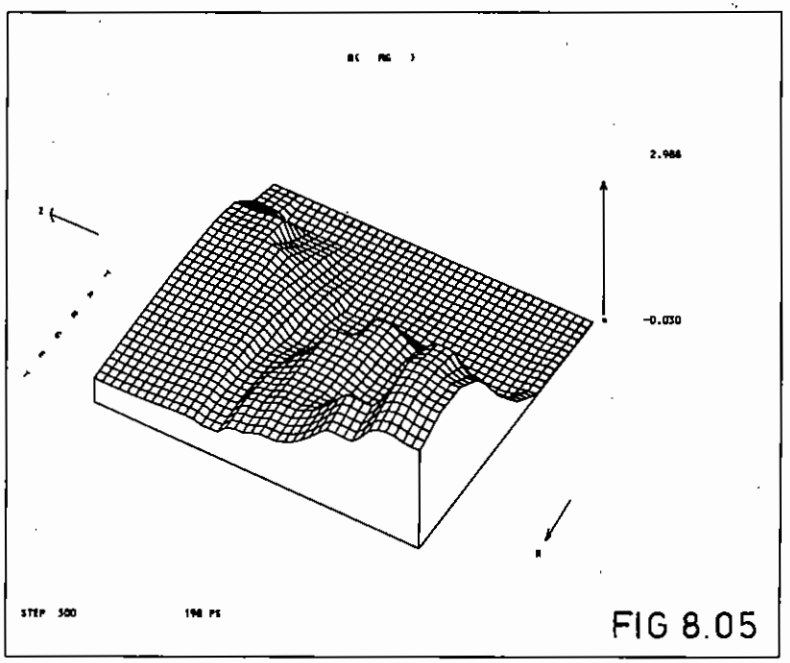

FIG 8.05

8.2.3 Fast Electron Transport

A program has been written to investigate the role of electric fields in the transport of suprathermal electrons in a target. Multi-layered targets can be handled.

The following assumptions are made:-

(1) Timescale for change in properties of target >> suprathermal electron lifetime.
Thus we calculate the steady state suprathermal flux and energy deposition.

(2) Local thermodynamic equilibrium is assumed for the target material.

(3) Spitzer resistivity is assumed for the thermal electrons.
It is probably safe to assume that the true resistivity is greater than the Spitzer resistivity.

(4) One spatial dimension
radius of laser beam >> Penetration depth of suprathermal electrons.

(5) Thermal and radiation transport are ignored.

(6) Hydrodynamic motion is ignored.

A Monte Carlo method is used to calculate the current and energy deposition due to the suprathermal electrons in an assumed electric field. Condensed case histories are used and straggling is ignored. The deflection of the test particles is determined by randomly sampling from a distribution which includes the effect of multiple scattering of the nuclei shielded by the bound electrons and the Debye shielded ions plus a contribution from the deflection of the electron in the electric field. The energy loss includes the effect of inelastic scattering with the ions (non-relativistic Bethe-Bloch formula), Coulomb drag due to the free electrons, the interaction of the suprathermal electron with plasma oscillations in its wake (Pines & Bohm) and energy lost moving in the electric field. The current due to each case history can be weighed to represent any number of real electrons.

Using the resistivity of the target material the electric field needed to give a thermal return current which balances the suprathermal electron current is calculated. The Monte Carlo calculation is then repeated using this electric field. This cycle of calculations is repeated until a self

consistent electric field is found.

The state of the target material is then updated using the energy deposition from the suprathermal electrons and the assumption of L.T.E. The average ionic charge and the Coulomb Logarithm are calculated and used to give the resistivity of the target material.

The program has been used to simulate the experiments of Hares et al (section 4.4) and confirms the authors' views that electric fields are unimportant. It is being used to investigate possible choices of target material and density with a view to increasing the relative importance of electric fields.

8.2.4 Code Development at Hull

The two-dimensional Eulerian and Lagrangian codes have been significantly improved by the use of refined algorithms to improve the conservative properties of the codes.

The inclusion of self-generated magnetic fields introduces two important conservation laws to be simultaneously satisfied within the code - namely magnetic flux and energy. It was found that these quantities were only simultaneously exactly conserved, if the code used time-centred differencing throughout. Since this may unnecessarily strongly restrict the time-step of stiff processes such as diffusion, we have introduced the concept of weak conservation, namely that a quantity be conserved to within errors of $O(Dt^2)$, where Dt is the time-step. In this case since the total time is ΣDt, the error $\Sigma O(Dt^2)$, so that the total error may be restricted to an arbitrary fraction by an appropriate time-step constraint. In the code magnetic flux is exactly conserved, but energy only weakly.

In order to avoid spurious oscillations within the diffusion steps which arise if a centred time difference (Crank-Nicholson) scheme is used with an unconditional time-step, it is necessary to use a fully implicit scheme. We have investigated the nature of permissible matrix approximations to the general diffusion operator in a magnetic field. It is found that the matrix is differential, conservative and extremal, if it is an M-matrix. Furthermore such a matrix can be shown to be unconditionally stable in a general sense, i.e. for arbitrary variation of the diffusivity through the mesh. Considering these equations as stiff, it follows from considerations of A-stability, that only two-step schemes are unconditionally stable. In

practice physical considerations are necessary to constrain the off-diagonal terms of the diffusivity matrix to an M-matrix form.

Considerable improvement in the 2D Eulerian hydrodynamics has been obtained by the use of a flux-corrected donor cell differencing scheme for advection. This has led to a marked sharpening of the profiles in regions of steep gradient - as is indeed to be theoretically expected.

Energy conservation in the 2D Lagrangian code has been found to be markedly improved by the change of the acceleration term from the normal derivative form of Schultz to the integral form used in MAGEE by Browne and Wallick. The nine-point diffusion scheme proposed for LASNEX by Kershaw has been sucessfully implemented in our code.

8.3 Laser Plasma Interactions

8.3.1 Ion Waves and 2nd Harmonic Structure

A theoretical model has been developed to attempt to explain the broadening and shift of second harmonic emission from a laser-produced plasma. It is assumed that this emission is produced by the interaction of a plasmon, produced by resonant absorption of the incoming radiation, with an incoming photon, and that the spread in frequency is due to a corresponding spread in the plasmon spectrum. The latter frequency spread is assumed to occur as the result of propagation of an ion sound wave through the critical surface, leading to coupling of the incident radiation to a series of plasma wave frequencies differing from that of the incident wave by integral multiples of the ion sound frequency.

A one-dimensional model has been considered in which the plasma density near the critical surface is of the form

$$n_{cr}\ (1 - \frac{x}{L})\ (1 + \varepsilon \cos(\Omega t - Kx))\ ,$$

representing a linear density gradient with an ion sound wave propagating outwards from the high to the low density side. To simulate the effect of resonant absorption there is taken to be a high-frequency oscillating field in the x-direction, and its effect on the above density profile is considered. Because of the oscillation of the background plasma, the plasma wave field excited is of the form

$$E = \sum_{\ell} E_{\ell}\ e^{i\omega t + i\Omega t}\ ,$$

where ω is the frequency of the driving field. From the usual equations for the electron fluid, a set of coupled equations for the different frequency components is obtained, of the form

$$\beta \frac{d^2 E_{\ell}}{dy^2} + (y - 2\ell \frac{\Omega}{\omega})\ E_{\ell} = \varepsilon\ e^{-iky} E_{\ell-1}$$

$$+ \varepsilon\ e^{iky}\ E_{\ell+1} + \text{driving term, where } y = x/L \text{ and the}$$

driving term, proportional to the high frequency field amplitude, only occurs for $\ell = 0$ and $\ell = \pm 1$. The parameter β has the value $1.5 \times 10^{-4} T/L^2$, where T is the electron temperature in KeV, and L is the density gradient length scale, in units of the wavelength of the incident light.

The above set of equations (after truncation to include only a finite number of modes) has been solved numerically for various values of the parameters involved. The broadening of the spectrum depends strongly on K, the wavenumber of the ion sound wave, and is a maximum when it is approximately equal to the wavenumber of the plasma wave in the neighbourhood of the critical surface. Some typical spectra, plotted by considering the relative magnitudes of the maximum intensity of each of the frequency components, are shown in figure 8.06, K being the wavenumber of the ion wave in units of 1/L. The explicit dependence on the ion sound wave frequency is very weak, so that details of the ion sound dispersion relation, and possible Doppler shifts due to plasma motion, do not affect these results significantly. What they do affect is the frequency difference between adjacent components and hence the frequency spread expected in the second harmonic due to this mechanism. If a spread in ion sound wavenumbers is present then there might be expected to be some kind of superposition of the effects of monochromatic waves, with the spread in plasma wave frequencies being mainly due to components with values of K which produce substantial broadening when present as a monochromatic wave. The optimum value of K for producing broadening scales as $\beta^{-1/3}$, while the strength of the coupling between modes scales approximately as $\varepsilon\beta^{-1/3}$.

For parameters appropriate to experiments carried out at the Rutherford Laboratory (8.05), the model predicts second harmonic spectra whose width and shape are in reasonable agreement with experiment. Further details of this work may be found in (8.06).

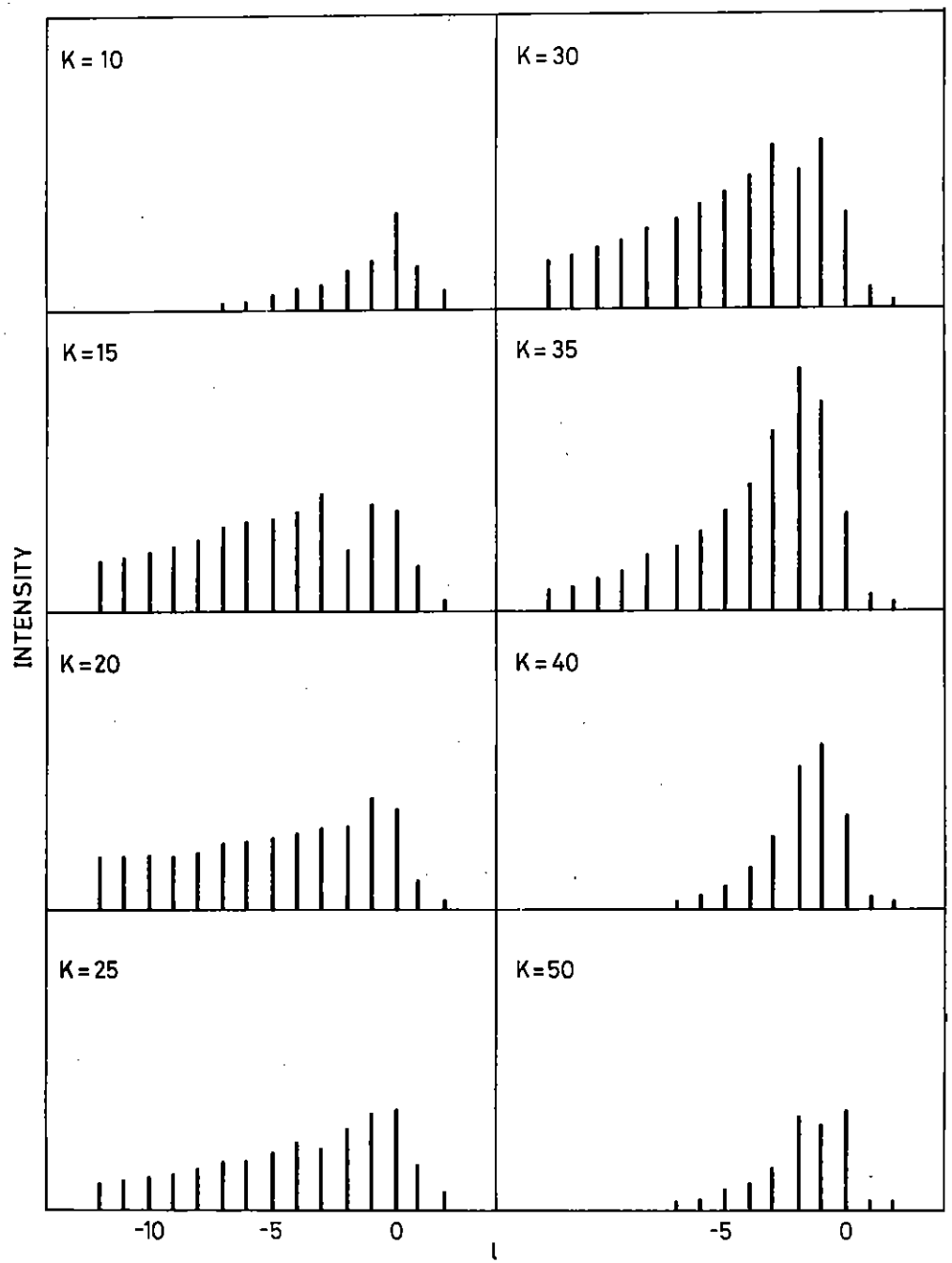

Fig.8.06

Spectra for $\beta = 1.5 \times 10^{-4}$, $\epsilon = 0.1$ and various values of K.

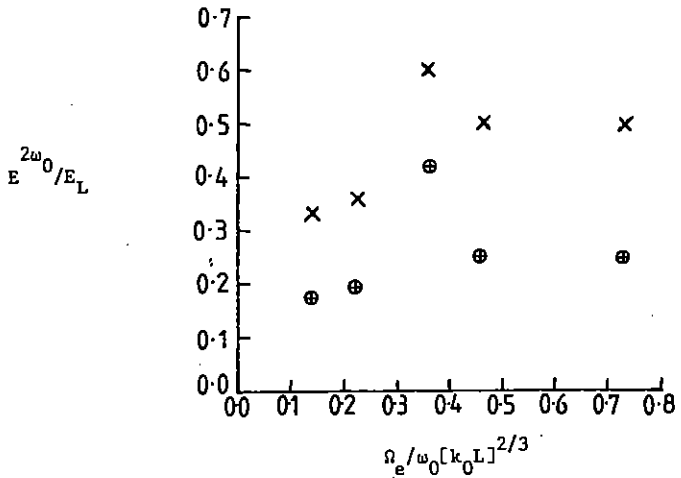

⊕ - Theory ; X - Computation.

Fig.8.07

Variation of the ratio of the electric fields of the second harmonic, and incident pump waves versus the ratio of the distance between the cut-off and the resonance layers and the scale length of variation of the electromagnetic wave near cut-off.

8.3.2 Harmonic Emission from Magnetized Plasmas

Recent observations of self-generated magnetic fields in plane target experiments (8.03) with high powered lasers have prompted us to look again at harmonic emission from magnetized plasmas. It is well known(8.07, 8.08) that second harmonic generation in Tokamak plasmas has not only been observed but has proved to be a useful magnetic field diagnostic. In the experiments by Raven and his co-workers, megagauss fields were measured in the quarter-critical density region, from which one might expect that magnetic field strengths close to critical density would also be very large. In the presence of such strong magnetic fields it has been shown recently that significant absorption of normally incident laser light is possible, together with harmonic generation (8.09, 8.10). We report here a theoretical study of harmonic generation together with results obtained from numerical experiments using a 1½-D code, EMPIRE. The computer experiments, in addition to providing information on harmonic emission, also indicate that a strong quasi-static magnetic field is generated in the neighborhood of the resonance region (cf. Section 8.3.5).

The configuration examined in this work is the following. An electromagnetic wave propagates along Ox and is normally incident on a plasma density ramp. The electric field of the incident wave is aligned along Oy. We shall suppose that a magnetic field $\underline{B}_0$ is applied along Oz. As the wave propagates into the plasma, the E_y field induces electron oscillations along Oy and the resultant $\underline{v} \times \underline{B}$ force effectively produces particle motion in the direction of propagation. Thus by charge separation along the density gradient, an electrostatic field component E_x is produced. This is of course just the extraordinary mode in the plasma. The interest in this mode stems from the fact that N_R, the density at which the wave resonates at the local upper hybrid frequency, and N_C, the cut-off density, are related by $N_C \simeq N_R(1 - \Omega_e/\omega_0)$, where Ω_e is the electron cyclotron frequency and, ω_0, the frequency of the incident wave. Consequently, if $\Omega_e \ll \omega_0$, as is certainly the case in Nd laser produced plasmas, then $N_C \simeq N_R$. We then have a situation analogous to that of obliquely incident radiation in unmagnetized plasmas. The difference between the two cases is that, in the latter, the separation between the cut-off and resonant densities is governed by the angle of incidence of the wave, whereas in the magnetized plasma considered here, this separation is governed effectively by the strength of the magnetic field. Thus resonant absorption of a normally incident wave is made possible by the magnetic field and has been examined both theoretically and by computer simulations.

This resonance takes the form of a plasma disturbance which produces a large localized, oscillating, electrostatic field. The rapid spatial variation of this field produces anharmonic oscillations of the electrons, due to their being subjected to varying electric field strengths over their excursion lengths. This electron behaviour may be represented as a series of Fourier modes at ω_0, $2\omega_0$, $3\omega_0$ ... and these modes then provide a current density source with components at $2\omega_0$, $3\omega_0$ ... . The particular modes responsible for the generation of the $2\omega_0$ current density are the ω_0 and $2\omega_0$ electron oscillations. The former beats with the oscillating electron number density N^{ω_0} to produce a component $-eN^{\omega_0}V_e^{\omega_0}$ while the latter combines with the unperturbed number density to give a term $-eN_0V_e^{2\omega_0}$. Hence as a direct result of the resonant mechanism a current density $J^{2\omega_0}$ is produced which, in turn, provides the source of second harmonic emission.

To find the relation between the power in the incident wave and that reemitted as second harmonic, we have to determine the current density. This is then treated as "free" current and is used as a source term in the second harmonic wave equation. This relationship has been evaluated and figure 8.07 shows a comparison between the theoretical results and those obtained from computer simulations. The parameter on the abscissa is the ratio of the distance between cut-off and resonant layers and the scale of variation of the electromagnetic wave near cut-off; $k_0 = \omega_0/c$ and L is the plasma scale length i.e. the distance between the critical density and the boundary. While there is some discrepancy between the theoretical results and those from the computer experiment, the overall agreement is quite good.

We have also examined the influence of the magnetic field effects on the harmonic line profiles. Figure 8.08, taken from a run of the 1½-D electromagnetic code shows the line structure present on the second harmonic emission spectrum. The frequency shift of the first side band, relative to the line centre, can be seen. This is strongly dependent on magnetic field intensity.

Figure 8.09 shows a comparison of results from our computer experiments with intensities measured elsewhere (8.11). The figure shows the intensities of the second, third and fourth harmonics. The experimental results refer to light backscattered at an angle of 45° to the incident direction. Those from the simulations are for light directly backscattered, but have been adjusted theoretically to allow comparison with the experimental re-

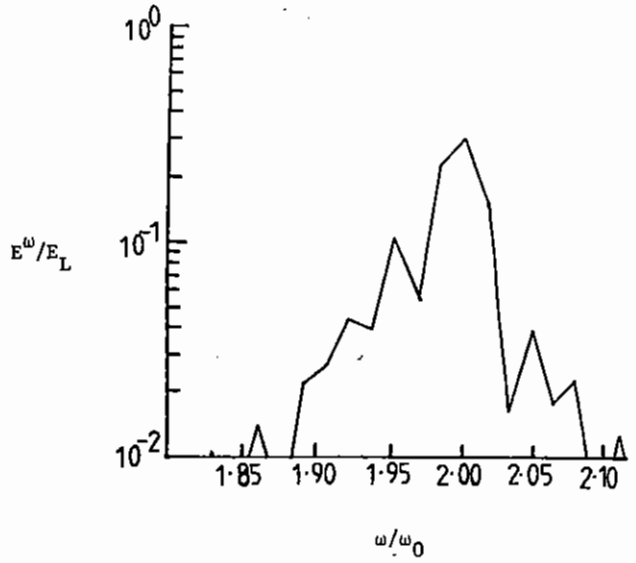

Fig.8.08

Magnetic field intensity-dependent structure on the second harmonic emission line.

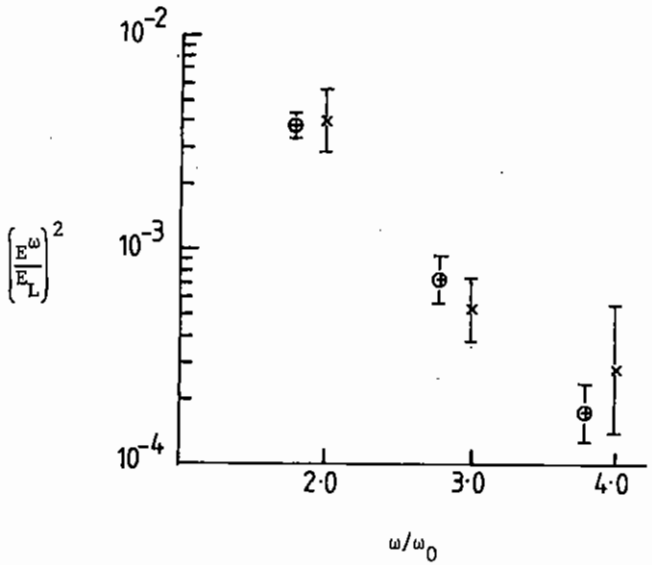

X - Experimental results (8.11); ⊕ - Computational results

Fig.8.09

Comparison between computational and experimental results for the relative intensities of the higher harmonic emission, backscattered at 45°.

sults. (The results from the simulations have been plotted slightly displaced from the harmonic number for sake of clarity.)

Further work on the line structure is in progress.

8.3.3 Emission at $3\omega_0/2$ through Two-Plasmon Decay

This work complements those experiments reported in section 3.3. The mechanism invoked to explain the emission observed at $3\omega_0/2$ is the two-plasmon decay instability i.e. where the incident radiation (ω_0, $k_0\hat{x}$) decays into two obliquely propagating electron plasma waves (8.12). It is an absolute instability strongly localized at $n_c/4$. The dispersion relation for the plasmons, based on a model of radiation normally incident on a linear density ramp, is

$$\omega = \frac{\omega_0}{2} + \frac{3k_0 K v_e^2}{2\omega_0} \qquad \left(K = k_x - \frac{k_0}{2}\right) .$$

It is independent of density and incident flux. The optimum growth rate is $\gamma \simeq k_0 v_0/4$ (i.e. for an Nd laser $\gamma \simeq 3.10^5\sqrt{q_{inc}}$, q_{inc} in watts/cm^2) but is limited primarily by the density gradient (scale length L) which implies a threshold condition

$$\frac{1}{44}\left(\frac{v_0}{v_e}\right)^2 \quad k_0 L > 1$$

(i.e. $q_{inc} > 2.5 \times 10^{16} T_e/L$, T_e in KeV, L in μm for Nd laser). Near threshold, growth is slow and only a narrow bandwidth of plasmons is excited absolutely unstable. Well above threshold a wide spectrum is excited, the fastest growing being those with shortest wavelength (since they sample or 'see' less of the density gradient).

The recombination of three plasmons or the recombination of a plasmon with an incident photon both give nominal $3\omega_0/2$ emission. Selection rules largely preclude the latter process; however, phase matching is possible in the former case for a wide spectrum of plasmons. The linear nature of the dispersion relation yields a simple expression, identical for both processes, for the frequency shift from the nominal value of $3\omega_0/2$. Note also that it is independent of the particular plasmons taking part in the interaction.

$$\Delta\omega = 3\frac{k_0^2 v_e^2}{\omega_0}\left[\frac{k_{3/2}}{k_0}\cos\theta - \frac{3}{2}\right]$$

(i.e. for Nd laser $\Delta\lambda \simeq -33.4\ T_e(\cos\theta - .92)$ Å)

where θ is the scattering angle. Thus directly backscattered radiation is always red shifted. A blue wing arises when forward scattered radiation encounters its critical surface at $9n_c/4$ and is reflected. The spectral width (red peak - blue peak) of the consequent doublet is

$$\Delta\omega = 6\,\frac{k_0^2 v_e^2}{\omega_0}\,|\cos\theta|\,\frac{k_{3/2}}{k_0}$$

(for Nd laser $\Delta\lambda \simeq 66.7\,|\cos\theta|\,T_e$ Å)
while the whole structure is shifted to the red by

$$\Delta\omega = -9\,\frac{k_0^2 v_e^2}{\omega_0}$$

(i.e. for Nd laser $\Delta\lambda \simeq 31\,T_e$ Å).
The experiments bear out the former prediction although yielding a rather high electron temperature. However, agreement is reasonable if a component of hot electrons is included. A net shift of the whole structure is not observed.

The line intensities may be computed as a function of the turbulence level of the plasmons in a straightforward if somewhat lengthy manner. For the recombination of three plasmons an estimate of the flux in the $3\omega_0/2$ emission is

$$q_{3/2} \sim 2.6 \times 10^{13} T_e L\, s \left(\frac{\delta n}{n_0}\right)^6 \quad \text{watts/cm}^2$$

where s is of order 1 ($s \simeq 1$ near threshold, $s \simeq 1/\sqrt{3}$ far above threshold). For example, if $T_e = 4.5$ KeV, $L = 15$ μm, $s = 1/\sqrt{3}$, $q_{inc} = 6.10^{16}$ watts/cm^2 and assuming a conversion factor of 10^{-7}, then $\delta n/n_0 \sim 13\%$. Thus one may sample and estimate the turbulence level of the plasmons generating the harmonic. More ambitiously, to estimate the emitted flux we need to compute $\delta n/n_0$ and hence need to decide on a saturation mechanism for the instability. There are various candidates. One such mechanism is profile modification which reduces scalelengths, increases thresholds and finally detunes the resonance. A form of this is soliton formation suggested by Chen and Liu (8.13) who estimate the saturation level at

$$\frac{\delta n}{n_e} = \left(\frac{3\pi^2}{4}\right)^{1/4} \frac{v_0}{c}\, k\lambda_D \,.$$

For a Nd laser and using the maximum k which is absolutely unstable this implies

$$\frac{\delta n}{n_e} \sim .48 \times 10^{-17}\, q_{inc}/\sqrt{T_e}$$

e.g. $q_{inc} = 6.10^{16}$, $T_e = 4.5 \rightarrow \frac{\delta n}{n_0} \sim 13\%$. Thus such a saturation mechanism could well be consistent with the observations.

8.3.4 Raman-generated Cascade of Half-Integral Harmonics

Some preliminary work on Raman generated half-integral harmonic emission was reported last year (8.05). Simulations using the 1½-D particle-in-cell code, EMPIRE, have continued and further theoretical work has been undertaken.

The Raman instability is excited just below the quarter-critical density, in which region it is an absolute instability. A large amplitude electron plasma wave is generated, the initial phase of this being well understood from linear theory. However, that nonlinear effects quickly dominate the dynamics is seen clearly from the results of the numerical experiments. Electron trapping in the large electrostatic field near quarter-critical is shown by the test-particle orbit in phase space in figure 8.10. Trapping gives rise to a nonlinear frequency shift (to $0.485\,\omega_0$) and leads to saturation of the instability.

It is possible through the presence of this large amplitude plasma wave to develop a cascade process leading to harmonic generation. The backscattered electromagnetic wave is blue-shifted to preserve frequency matching and combines with the plasma wave to produce a mode at the fundamental. Then by Raman up-conversion we may generate the sequence

	ω/ω_0	ω/ω_0 (observed)
$\omega_0 + \frac{\omega_0}{2} = \frac{3\omega_0}{2}$	1.485	1.485
$\frac{3\omega_0}{2} + \frac{\omega_0}{2} = 2\omega_0$	1.970	1.967
$2\omega_0 + \frac{\omega_0}{2} = \frac{5\omega_0}{2}$	2.455	2.452

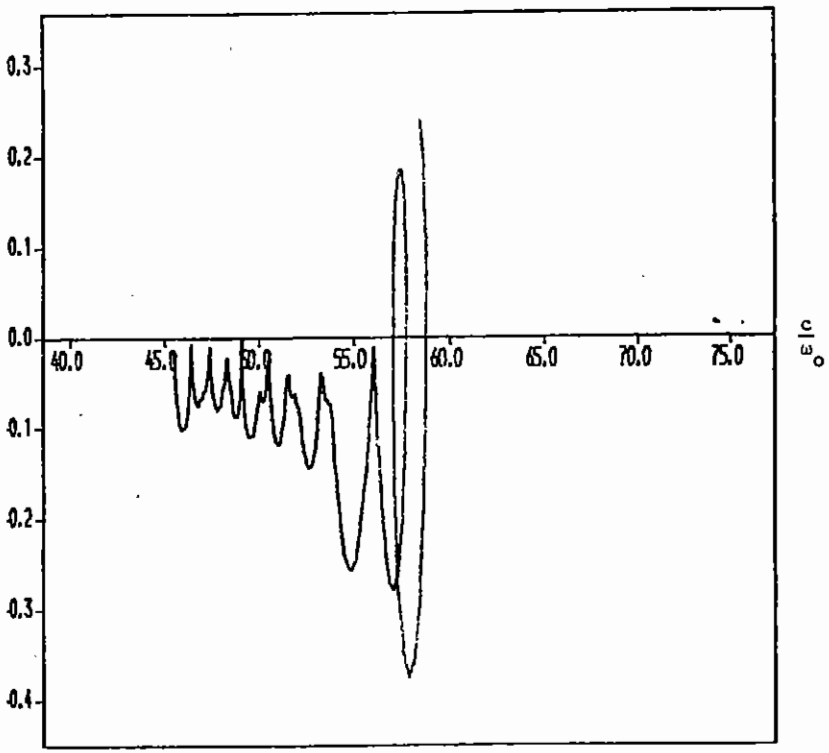

Fig.8.10
Test particle orbit in phase space.

	ω/ω_0	ω/ω_0 (observed)
$\frac{5\omega_0}{2} + \frac{\omega_0}{2} = 3\omega_0$	2.940	2.933

The values of ω/ω_0 in the last column are those found from the computer simulations, in satisfactory agreement with the predictions.

The evolution of the first three components of the cascade is shown in figure 8.11. The higher half-integral harmonics saturate at lower levels in agreement with a theoretical prediction and there is some indication that a further prediction that waves with higher mode numbers grow faster is not inconsistent with the results of the numerical experiment.

Figure 8.12 shows the relative harmonic amplitudes in a semilog plot taken towards the end of a simulation. From this the relative intensities satisfy the relation

$$I_{\frac{n}{2}} \sim \frac{1}{6} I_{\frac{n-1}{2}} .$$

The point at $\omega/\omega_0 = 1$ is anomalous on account of the contribution from the pump reflection at the boundary.

8.3.5 Magnetic Field Generation Due to Resonant Absorption

In section 8.3.2 harmonic emission from a magnetized plasma was discussed; the source of the emission was seen to be the resonantly induced current density. In this section we look at another effect of this current density. Consider the electromagnetic pump wave propagating along Ox and normally incident on the plasma density ramp. The electric field is aligned along Oy, and we shall suppose that the external magnetic field is applied along Oz.

Now the dominant component of the resonantly induced current density lies across the density gradient, i.e. along Oy. This component is responsible for inducing a magnetic field along Oz. This field is quasi-static and, in the cold plasma limit, is restricted spatially to the plasma resonant region. However warm plasma theory predicts that the magnetic field will extend into the over-dense region, and this is observed in the computer

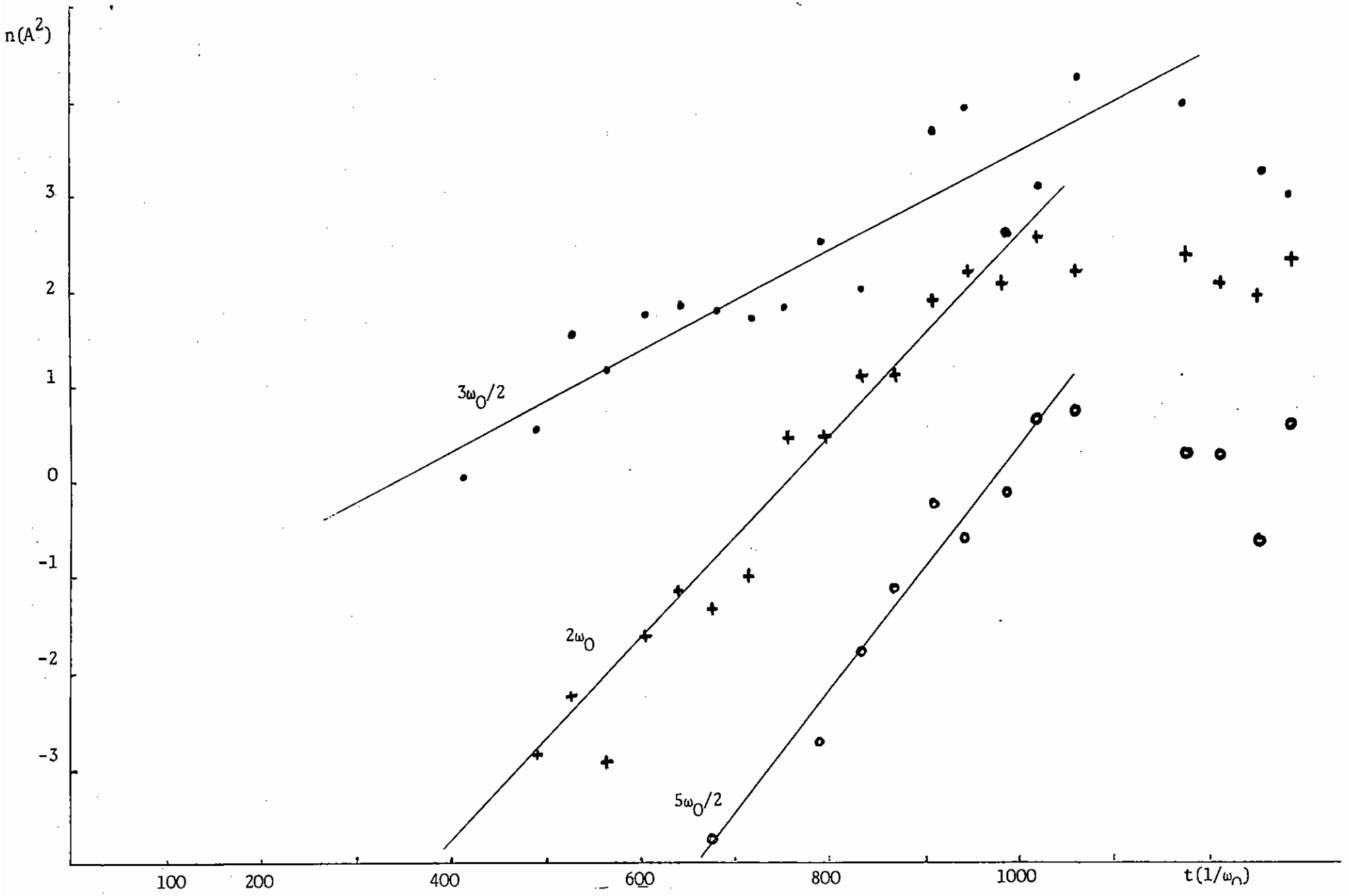

Fig.8.11

Time evolution of the square of the $3\omega_o/2$, $2\omega_o$ and $5\omega_o/2$ harmonic mode amplitudes. Saturation occurs for $t \sim 1000\ \omega_o^{-1}$.

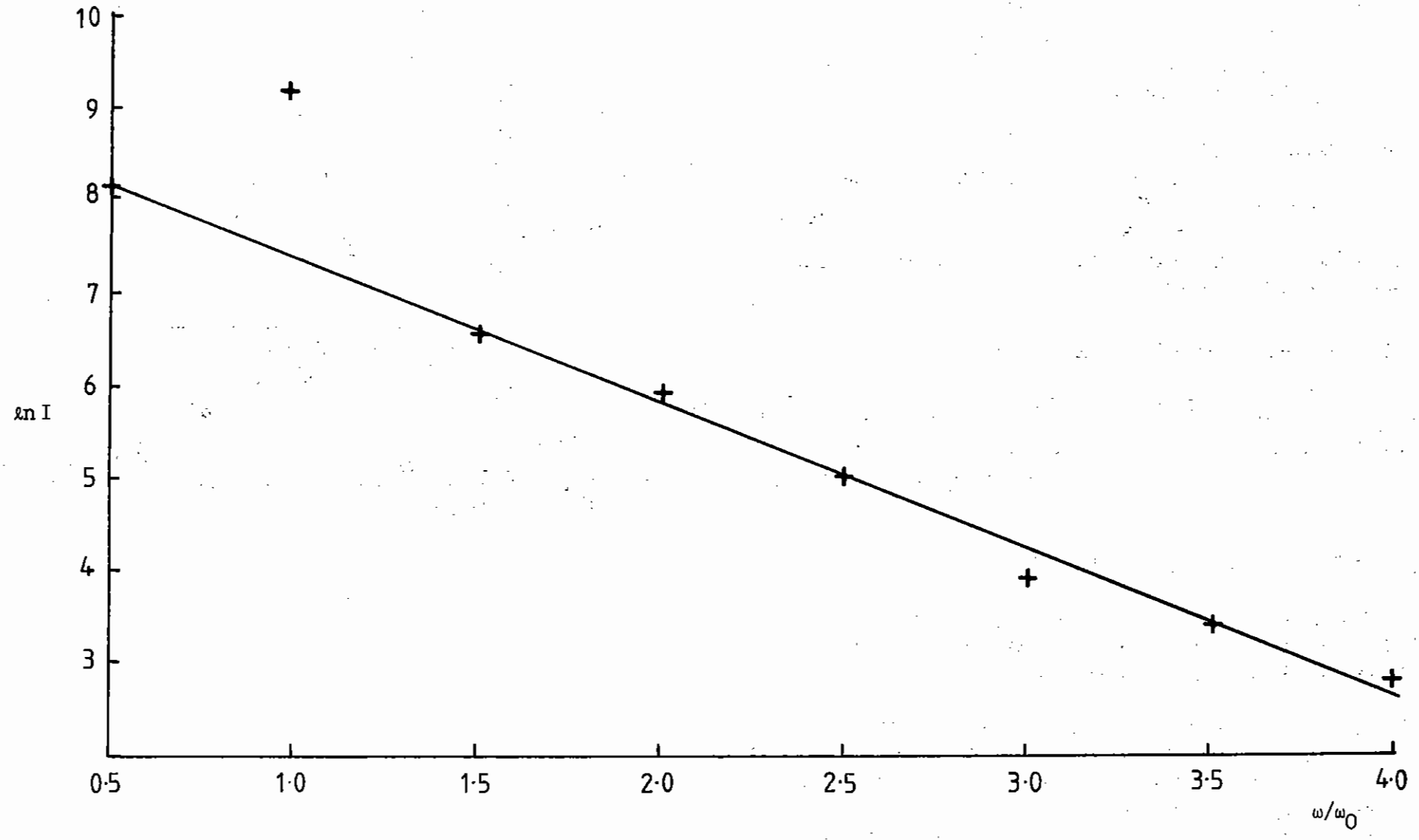

Fig.8.12

Relative half-harmonic intensities.

simulation.

Figure 8.13 shows a plot of the time averaged magnetic field, from a simulation executed with $k_0L = 20$ and $\Omega_e/\omega_0 = 0.1$; $k_0 = \omega_0/c$ and L is the plasma scale length, i.e. the distance between the critical region and the boundary. The pump wave frequency is ω_0 and, Ω_e, the electron cyclotron frequency. The ratio of the frequencies used in the simulations implies that the external magnetic field ≃ 10 MG, in the case of a Nd glass laser. The direction of the field reverses inside the resonant region, which extends over 2Δ , and the field is seen to extend into the over-dense plasma.

These results show similar structure to those from other computer simulations and analysis (8.14, 8.15) though these refer to radiation incident obliquely on unmagnetized plasmas.

Further theoretical work concerned with the structure and effects of this self-generated field, is in progress.

8.3.6 Resonant Absorption at a Rippled Critical Surface

An approximate analytic treatment of resonant absorption of light normally incident onto plasma with a rippled critical surface has previously been developed (8.16). In this work it was shown that the equation for the plasma waves driven in the neighbourhood of the critical surface is of the form

$$\underset{\sim}{\nabla}.\left[(x - \mu \cos(ky))\ \underset{\sim}{\nabla}\phi\right] = k\mu \sin(ky)E_0 ,$$

where ϕ is the potential in the waves, E_0 is the driving field due to the incident light and μ and k are the amplitude and wavenumber of the density ripple perpendicular to the main density gradient.

In (8.16) an approximate solution of this equation, correct to first order in μ, was given. The calculation has now been carried to second order in μ, in which approximation the absorption coefficient given in equation (15) (8.16) is multiplied by a factor $1 + \mu A$. The value of A is plotted, as a function of k, which is the only variable on which it depends, in figure 8.14 where k is in units of the wavenumber of the incident light. From

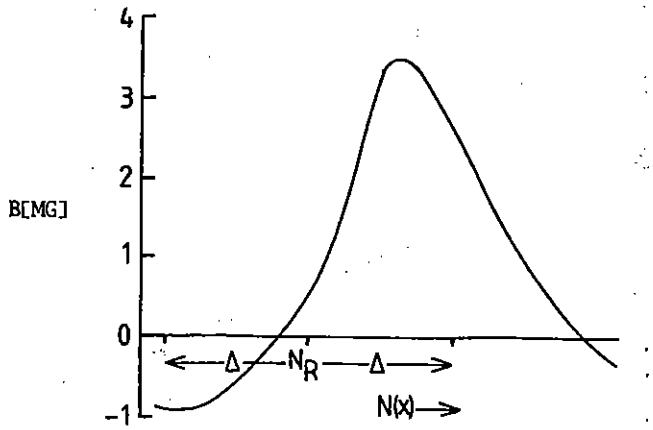

Fig.8.13

Time averaged plot, from a computer simulation, of the resonantly induced quasi-static magnetic field over the resonant region of spatial extent 2Δ.

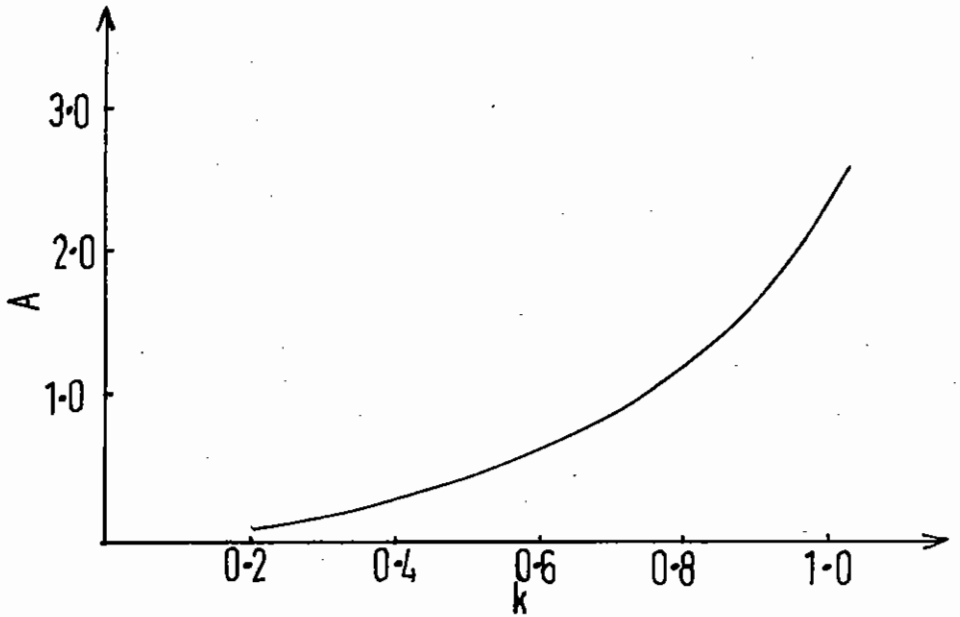

Fig.8.14

The value of the second order correction to the absorption coefficient as a function of k.

this it can be seen that this correction leads to an increase in the value of the absorption coefficient which is most pronounced for short wavelength perturbations.

8.3.7 Analytic Theory of Resonant Absorption in a Warm Plasma

Ponderomotive force steepening can cause the density gradients in the vicinity of the critical density surface to be very great. Furthermore the finite temperature of the plasma cannot be ignored. As a result we find that the inclusion of the ambipolar electric field ($\nabla p_e/ne$) leads to extra terms in the otherwise usual pair of coupled second order differential equations. These terms involve the electrons temperature, are comparable in magnitude with the other warm plasma terms, and become particularly important when the density scale length is comparable with the wavelength of laser radiation. Solutions of the equations show that inclusion of the extra terms has a marked effect on the maximum value of electric field in the resonance absorption region. This work is continuing.

8.3.8 1½-D PIC Simulation of Resonance Absorption

The main progress that has been made on this code since the paper presented at the Oxford meeting (8.17) has been in the refinement of the boundary conditions. The work was carried out during the CECAM workshop on fast electron transport in laser fusion held at Orsay in the Summer of 1978 in collaboration with Dr. Nishihora of Osaka University.

The principal defect in the code previously was the inconsistent boundary conditions on the electric field in the plasma. Originally the boundary condition was constructed to simulate a semi-infinite plasma allowing no reflection of waves, but unfortunately such a boundary condition is inconsistent with Maxwell's fourth relation in one dimension

$$0 = \underline{J} + \frac{1}{c}\frac{\partial \underline{E}}{\partial t}$$

Previously the particles reaching the edge of the simulation region were replaced by particles from a random velocity distribution, so that even though there was no total change of charge in the volume, locally near the boundary it was possible to have $\underline{J} \neq 0$ causing polarisation to occur.

This resulted in an electrostatically noisy boundary region, generating electrostatic waves. The solution to this problem was to reflect each particle specularly (thus giving $\underline{J} = 0$ exactly) and also to impose $\underline{E} = 0$ at the boundary for all time. Then the Maxwell fourth relation is trivially satisfied.

Particle in cell codes can only simulate a small region of the laser-plasma experiment, indeed only a few wavelengths. It is a pity that well-behaved boundary conditions cannot be found that allow the boundary of the problem to represent the start of a semi-infinite Maxwellian plasma representing the high density transport and core regions.

8.3.9 1½-D PIC Code

The particle code EMPIRE has continued to be used in various studies of harmonic generation in target plasmas, magnetic field generation and in a long pulse Brillouin scattering experiment. EMPIRE is a 1½-D code, in which quantities are permitted to vary in just one space direction, along Ox, but velocity and field components perpendicular to Ox are allowed.

With these assumptions it is possible to simulate the interaction of electromagnetic waves in a plasma inhomogeneous in the x direction. A consistent picture of the processes involved can be built up if each particle (ion or electron) is visualised as a sheet infinite in the directions perpendicular to x. Particle velocities may become very large so that relativistic effects are fully allowed for in the model. The problem domain is divided into cells and the particles, selected from a Maxwellian velocity distribution, are shared amongst them in such a way as to reproduce the number density profile required. The distributions of charge and currents so produced are used to calculate grid values appropriate to the numerical scheme used for the solution. A staggered finite difference mesh is used in which mesh values of charge density are associated with cell centres whereas mesh values of current density are associated with cell walls, both distributions being set up using the area weighting techniques of the particle-in-cell method.

When the code is run, at each time step Maxwell's equations are solved directly to produce a distribution of electric and magnetic field components. The finite difference scheme used is time centred, second order accurate

and time reversible. Steps are taken to ensure that self fields are eliminated and that the charge and field distributions are mutually consistent. In the second stage the particles are pushed and their new velocities and coordinates are computed. Multistepping is sometimes employed. By following the motion of the particles and the evolution of the state variables the various processes that characterize one dimensional interactions between an incident electromagnetic wave and an inhomogeneous plasma may be simulated.

The experiments on Raman scattering reported previously (8.05) have been completed and are discussed in section 8.3.4. Attempts to follow the evolution of the instability from the linear to the nonlinear regime were unsuccessful. In spite of the incorporation of a quiet start the enhanced noise in the code made this impossible.

A series of experiments on radiation induced magnetic fields and on magnetically generated harmonics has been completed (see 8.3.2 and 8.3.4). Experiments on Brillouin scattering from a long pulse beam are in progress.

8.3.10 2½-D PIC Code

On the 23rd of October 1978, agreement was reached between members of the department of applied mathematics, The University College of North Wales (Bangor) and the laser division, Rutherford Laboratory to begin work on a particle-in-cell (PIC) code. The programme was to simulate 2½ dimensions (i.e. two spacial and three velocity) following the general lines used by ZOHAR (8.18). An upper limit on the mesh size was set at 128 by 128, with some 20 particles per cell (some 3×10^5 particles in all). The fields were to be electromagnetic and defined by $\underline{E}$ and $\underline{B}$ rather than the potentials $\underline{A}$ and ϕ. The particles were to obey relativistic mechanics.

To provide a common programming standard, the Olympus system (8.19) was adopted, which is available on the Rutherford Laboratory IBM 360/195 computing system.

A simplified version of the programme has been written and is undergoing tests.

The two main computing problems to be faced with any code of this type are the large amount of CPU time that the programme will use, and the large amount of data that it has to process. The programme specification called for the storage of some 1.3 M bytes of field information ($\underline{E}$, $\underline{B}$, current density and charge density) and 15 M bytes of particle coordinates. It was clearly necessary to hold this data on disk and to 'page' it into core in pieces (pages). The size of a page is limited to the track size of the disk, namely 13030 bytes. The fields can be contained in 11 pages and the particles require some 1200 pages.

To reduce the amount of disk I/O, a page must contain all the field quantities for a part of the mesh (a slice). All the particles in a given page must refer to the same slice and so there must be some partial ordering of the particles by one spatial coordinate. The final system, the 'full paging' version, therefore requires very complex data management. To enable the programme to be developed and tested as fast as possible, a three stage approach was taken.

i) A simple programme working on a 32 by 32 (maximum) mesh with some 300 particles in all. This is the 'no paging' version, so called because it does not page its particles or fields.

ii) An intermediate programme using the same mesh but with many more particles. This 'simple paging' version would require the particles only to be paged. No partial ordering of the particles would be required.

iii) The final 'full paging' system.

Currently the no paging version has been written and is undergoing tests.

The electromagnetic fields are advanced by one time step in two stages.

Firstly, the electric and magnetic fields are evaluated over the computational region, at the new time level, from an explicit difference form of the Maxwell's equations:

$$1/c\ \partial\underline{B}/\partial t = -\ \underline{\nabla} \times \underline{E}$$

$$1/c\ \partial\underline{E}/\partial t = \underline{\nabla} \times \underline{B} - \underline{I}$$

where $\underline{I} = \underline{J}/c$.

Secondly, a correction to the electric field is calculated, which corrects for the numerical error in the assignment of the source terms to the grid points.

The fields are formed on a mesh displaced from the particle mesh and arranged so as to make the difference form of the derivatives second order accurate.

The CFL stability condition limits the size of the time step by which the fields may be advanced much more than it restricts the particle time step. Since the majority of the computer time is spent advancing the particles, it is advantageous to take several field time steps per particle time step. The current version of the field solver can select either two or four field steps per particle step.

The boundary conditions employed in the x direction are the simple 1-D wave conditions or those of Lindman (8.20), which involve the numerical approximation to operators which are extensions to $2\frac{1}{2}$-D of the simple 1-D conditions. In effect a correction is performed on the 1-D wave conditions using past data at the boundary to minimise reflection of obliquely incident waves. Storage requirements are minimal for theoretical reflection coefficients less than 10^{-2} over a range of incident angles of 0 - 89, but so far these boundaries are untested.

The system is periodic in y whatever boundary conditions in x are selected. This has the minor disadvantage that any waves being launched into the computational region must satisfy a relation of the form

$$n\lambda = (\text{no. of mesh points in y}) * \Delta y * \sin\theta$$

to prevent interference of the imput beam, where n is an integer and θ is the angle of incidence.

The correction $-\nabla\delta\psi$ to be applied to the electric field is found by ensuring Gauss' equation is satisfied

$$-\nabla^2\delta\psi = \rho - \underline{\nabla} \cdot \underline{E}$$

which has the form of Poissons equation once the right hand side has been found from the uncorrected data. It is solved by Fourier analysis in the y direction using the periodicity there to employ a fast transform then reduction of the resulting matrix equations by the Thomas algorithm. The correction is applied and finally the fields are averaged back onto the particle mesh to facilitate the particle pusher.

The particles are advanced in time by the leapfrog method (8.18). The position of the particles are known at time $n\Delta t$, where n is an integer and Δt is the particle timestep, while the velocities are known at time $(n - \frac{1}{2})\ \Delta t$.

The velocity of each particle is advanced to time $(n + \frac{1}{2})\ \Delta t$ using a four step algorithm

i) add half the electric impulse
ii) perform a half rotation due to magnetic field
iii) perform the second half rotation due to magnetic field
iv) add half the electric impulse

which is time centred and second order accurate.

The position of each particle is advanced using the new (time centred)velocity.

Some computational effort has been saved by replacing the variables $\underline{v}$ and $\underline{J}$ by $\underline{w}$ and $\underline{I}$ where

$$\underline{w} = \gamma\underline{v}/c$$

$$\underline{I} = \underline{J}/c$$

and

$$\gamma = (1 - \underline{v} \cdot \underline{v}/c^2)^{-\frac{1}{2}}.$$

Some simple diagnostics are being developed for testing purposes. The final programme, however, will produce a diagnostic tape rather than graphical output. The programme for analysing this tape (ATHENA) is currently under development.

8.4 Transport Processes

8.4.1 Multi Group Transport

In order to handle the transport of fast electrons and also of photons in our 1-D Lagrangian code a multi-group diffusion package has been written along the lines of Corman et al (8.21) for α- particle transport.

Starting from the Fokker Planck equation for the particle distribution and taking only the first term in an angular expansion in Legendre Polynomials the usual diffusion equation is obtained.

$$\frac{\partial N_{(E)}}{\partial t} + \frac{\partial J_{(E)}}{\partial x} = \frac{1}{t_E}\ \frac{\partial}{\partial E}\ (E\ N_{(E)}) + S$$

where $N_{(E)}$ is the number density of electrons in the energy range $E \to E + dE$ t_E is the energy relaxation time and S is the source function.. For flux limited diffusion we may write

$$J_E = -D_E \frac{\partial N_{(E)}}{\partial x}\ ;\ D_E = \frac{v_E}{3/\lambda + 1/L}$$

where v_E is the particle velocity, λ is the 90^o deflection mean free path and

$$1/L = 1/N_{(E)} \frac{\partial N_{(E)}}{\partial x}\ .$$

This is a modified form of Fick's Law which gives the correct free streaming limit.

If these equations are now integrated over a set of discrete energy intervals we obtain the multi-group equations with

$$N_g = \int_{E_n}^{E_{n+1}} N_E\ d_E \quad :$$

$$\frac{\partial N_g}{\partial t} = \nabla(D_g(\nabla N_g)) - \frac{N_g}{\tau_g} + \frac{N_{g+1}}{\tau_{g+1}} + S_g$$

Here N_g/τ_g represents the loss of particles to the next lowest energy group and N_{g+1}/τ_{g+1} is the gain of particles from the next highest group.

This set of equations is solved with fully implicit differencing so that there is no restriction on the length of the time step of the hydro-code compared with the relaxation times τ_g. For the case of electron transport the equations must be solved in descending order of energy so that N_{g+1} is always a known quantity. For photon transport with no frequency redistribution the term N_{g+1}/τ_{g+1} is not present and the equations may be solved in any arbitrary order.

In order to perform useful calculations of fast electron transport it is also necessary to include the effects of electric fields and thermal electron resistivity. Work on including these effects in a consistent manner is in progress.

8.4.2 Ion Acoustic Turbulence and Heat Flux Limitation

Suprathermal electrons produced by absorption processes primarily at the critical density of laser-plasmas are a dominant feature in the energetics of solid target compression studies. At the same time the heat flux is estimated at a fraction of the free streaming value (e.g. $f \simeq 1/20$). It has been suggested that this heat flux is anomalously limited by ion acoustic wave turbulence which may be generated by the return current of cool electrons arising to maintain charge neutrality with the current of suprathermal electrons. Growth is limited by ion trapping. Simple trapping arguments are widely used to predict saturation levels which we believe are considerable overestimates.

We have attempted to predict the saturation level for ion acoustic waves as a function of the flux of hot electrons using various models to simulate the electron distribution function. Our approach is now a familiar one, namely to derive a nonlinear dispersion relation which incorporates resonances turbulently broadened due to particle (ions in this case - it can be shown that electrons may be treated linearly) orbits being modified ("scattered") by the unstable waves. (A theory originally due to Dupree (8.22) and Weinstock (8.23)). When $ZT_e/T_i \gg 1$ then the phase velocity is well clear of the body of the ion distribution; however, if the ion resonance is broadened such that a significant number of ions resonate with the wave then acceleration of such ions forms an efficient sink for the wave energy. This broadening and hence the turbulence level necessary to saturate the instability depends on the linear growth rate and thus on the exact shape of the electron distribution function. Expressing the result in a way suggested by trapping arguments, we may write approximately

$$\frac{e\phi}{T_c} \simeq \frac{1}{4}\left[1 - \sqrt{\frac{\chi T_i}{ZT_c}}\right]^2$$

where

$$\chi = \ell n \left[\frac{.057\ ZT_c/T_i}{\frac{e\phi}{T_c}\left[\frac{\gamma}{\omega}\right]^2}\right].$$

This is an equation to be solved for $e\phi/T_c$. γ is the electron contribution to the linear growth rate. Trapping arguments set $\chi \simeq 3$ but in practice it may be much higher.

To model the electrons we adopt a two temperature model (T_c, T_h) with the cold component carrying a heat flux (f x the cold free streaming value) and a return current (v_c) due to the hot electron current. The hot electrons are modelled by a drifting (v_h) low density (ϵ x total electron density) Maxwellian. Given T_c, f, ϵ, zero net current, a hot "temperature" ($t^2 T_c = T_h + mv_h^2$) leaves one free parameter with which to adjust the net flux of hot electrons to the target core. If the heat flux is measured with respect to the total electron distribution, we require

$$\frac{f}{2} > \sqrt{\frac{Zm}{M}}$$

for instability. For typical figures, e.g. $\epsilon = 3\%$, $f = .05$, $T_h/T_c = 8$, $T_c/T_i \sim 2$, $Z = 10$, $Z/M = .5$, this is only marginally satisfied and $\gamma/\omega \simeq 5.6 \times 10^{-3}$ whence $e\phi/T_c \simeq .13\%$ which is very small. However, is f is the flux associated with the cold skewed electron distribution only, we require

$$\frac{f}{2} + \epsilon\sqrt{t^2 - \frac{T_h}{T_c}} > \sqrt{\frac{Zm}{M}}.$$

Optimum conditions for instability are $T_h/T_c \ll t^2$ (i.e. the fast electrons are monoenergetic with a speed t; this is obviously unrealistic but it gives an upper bound for $e\phi/T_c$) then the instability condition is easily satisfied and $\gamma/\omega \simeq .06$. In this case $e\phi/T_c \simeq 2.5\%$. Whichever way we look at the problem, the saturation level of ion acoustic waves is small and hence its efficiency as a flux limitation mechanism low.

8.4.3 J x B Production of Fast Ions

Whilst it is well known that fast (non-thermal) ions can be produced from the expanding sheath in a two temperature electron distribution, another mechanism exists which can produce fast ions in the 100 KeV range. This is described in detail in a recent paper by R.S. Craxton and M.G. Haines (8.24). The mechanism can be described as follows.

When magnetic fields (∿ megagauss) are generated through the existence of the $\nabla T \times \nabla n$ term, the currents associated with the azimuthal magnetic field are in the poloidal plane. In the region where the plasma density is low the current is radial and interacts with B_θ to give an accelerating force in the direction of ablation (i.e. towards the laser). Because the density is low the specific acceleration is large and it results in very fast ions travelling in a narrow cone in velocity space. Comparison computer runs were conducted for two different initial density ramps and for two power levels. Fast ions from the $\underline{J} \times \underline{B}$ force dominated over fast ion production from the hot ring region when short laser pulses were employed. Indeed hot rings resulting from laser absorption in highly magnetized regions only occurred in runs with longer laser pulses.

8.4.4 Incorporation of Radiative Transport into MEDUSA

Introduction: We summarize the work done at Glasgow during the past year on radiative transport problems encountered in laser-compression simulations. We have made use of MEDUSA (8.25) which is a 1-D Lagrangian computer code. In this code thermal electrons and ions are considered to be the only means of energy transport. It is, however, well known that this picture is not completely satisfactory. In fact, the mean free path of suprathermal electrons and photons created at the critical density is much longer than the mean free path of thermal electrons. The suprathermal electrons and the photons can therefore penetrate the target at a much faster rate, preheating the core. As a result the shock front will be weakened and the quality of implosion will be degraded. It is therefore very important to include the latter two transport mechanisms into the computer program.

In the present work, we are interested in the radiative transport problem only. We have incorporated into MEDUSA the transport of continuum radiation, namely, free-free and free-bound radiation using a diffusion approximation. In the following we describe this work in detail. Some typical simulation results are given in the Appendix.

Physical model: This model assumes that the photons achieve a Planckian equilibrium characterized by a radiation temperature T_r, at a rate much faster than their equilibrium rate with matter. This equilibrium radiation field is characterized by:

Specific internal energy: $$U_r = \frac{4\sigma T_r^4}{\rho c} \quad (1)$$

Specific heat: $$(Cv)_r = \frac{\partial U_r}{\partial T_r} \quad (2)$$

Pressure: $$P_r = \frac{1}{3} U_r \quad (3)$$

where σ is Stefan's constant, ρ is the plasma density and c is the speed of light.

The radiation energy equation may be written as

$$(Cv)_r \frac{\partial T_r}{\partial t} + B_r \frac{\partial \rho}{\partial t} + P_r \frac{\partial V}{\partial t} = H_r + K_{re} \quad (4)$$

where V is the specific volume

and $$B_r = \left(\frac{\partial U_r}{\partial \rho}\right) = -3 P_r \left(\frac{1}{\rho^2}\right) \quad (5)$$

The two source terms on the R.H.S. of equation (4), i.e. H_r and K_{re}, are the radiation thermal conduction rate and the electron-radiation energy exchange rate respectively. We deal with these two terms as follows.

(i) Radiation heat conduction term H_r:

$$H_r = \frac{1}{\rho} \nabla \cdot (D_r \nabla T_r) \quad (6)$$

where the radiation thermal conductivity

$$D_r = \frac{16\sigma \ell_R T_r^3}{3} \quad (7)$$

ℓ_R is known as the Rosseland mean free path for the radiation, given by

$$\ell_R = \frac{\int_0^\infty \ell_\nu' \left(\frac{dU_{\nu p}}{dT}\right) \nu}{\int_0^\infty \frac{dU_{\nu p}}{dT} d\nu} \tag{8}$$

where ℓ_ν' is the absorption mean free path corrected for induced emission and $U_{\nu p}$ is the equilibrium energy density for the radiation of frequency ν

(ii) Electron-radiation Energy Exchange:

$$K_{re} = (Cv)_e \, \omega_{re} \, (T_e - T_r) \tag{9}$$

where $(Cv)_e$ is the electron specific heat and ω_{re} is the electron-radiation collision frequency given by

$$\omega_{re} = \frac{4K_p(T_e^2 + T_r^2)(T_e + T_r)}{(Cv)_e \rho} \tag{10}$$

Here

$$K_p = \frac{\int_0^\infty K_\nu' U_{\nu p} d\nu}{\int_0^\infty U_{\nu p} d\nu} \tag{11}$$

and is known as the Planck mean capacity. In equation (11) K_ν' is the absorption coefficient corrected for induced emission for radiation of frequency ν. It should be noted that equation (10) is valid under the condition of near equilibrium only i.e. $T_e \simeq T_r$. This condition is fulfilled in the core of the laser-plasma whereas in the corona region $T_r << T_e$. In such a case equation (10) becomes (8.26):

$$\omega_{re} = 8.5 \times 10^{-14} \left[\frac{\bar{Z}^2 \, \bar{Z} \, Ni}{M \, T_e^{\frac{1}{2}} \, (Cv)_e}\right] I_g \tag{12}$$

where

$$I_g = \int_0^\infty \frac{\xi(e^{\xi u} - e^u)}{(\xi-1)(e^{\xi u}-1)(e^u-1)} du \tag{13}$$

In the above two equations, $\bar{Z}$, $\bar{Z}^2$, N_i, M and T_e denote mean ionization, mean squared ionization, ion number density, molecular weight of the plasma ions and electron temperature respectively. Also $\xi = T_e/T_r$ and $u = \frac{h\nu}{KT_e}$ where the symbols have their usual meaning.

The radiation energy equation is solved for the radiation temperature, T_r, implicitly using Gauss' elimination scheme (8.27). Typically 5-10 iterations are required for convergence of T_r.

Validity of the diffusion approximation: The applicability of the diffusion approximation requires that the radiation energy density should not change appreciably over a distance of the order of the radiation mean free path ℓ_ν': the gradients of the radiation energy density in the medium should be small, which is true for an optically thick medium. If x denotes the characteristic scale length for the radiation energy density then the diffusion flux can be written as (8.28)

$$S_\nu \simeq \frac{\ell_\nu'}{x}(cU_\nu) \tag{14}$$

The quantity cU_ν is the maximum possible radiation flux which corresponds to the case when all the photons are travelling in the same direction. For an optically thick medium $\ell_\nu'/x < 1$ and correspondingly $S_\nu < cU_\nu$. The smaller the flux S_ν, the more applicable is the diffusion approximation. On the other hand, in an optically thin medium like the corona region, $\ell_\nu'/x > 1$ and the diffusion flux S_ν exceeds the upper limit cU_ν, which emphasizes the inapplicability of the diffusion approximation here. In such a case the photon flux must therefore be restricted by this upper limit.

Appendix

We present some results of the compression of solid micro -spheres and gas filled microballoons which show the effect of radiative preheat on compression.

(a) Solid micro-spheres

We consider a 10 μg solid carbon micro-sphere with initial conditions:

radius: $R_o = 106$ μm

density: $\rho_o = 2 \times 10^3 \text{Kg/m}^3$

temperature: $T_o = 6 \times 10^4$ K .

An ideal laser-fusion pulse

$$P(t) = P_o \left(1 - \frac{t}{\tau}\right)^{-p}$$

with total energy 600 J/steradian is used to compress this target. For comparison we optimize the results not including the radiative transport and obtain a 10^4-fold compression. In this case, maximum density $\sim 3 \times 10^7$ Kg/m^3 is achieved corresponding to initial laser power $P_o = 10$ GW/steradian and pulse length $\tau = 4$ ns. We find however that the maximum density falls to 5×10^6 Kg/m^3 when radiative transport is included.

(b) Gas Filled Micro-Balloons:

In this section we deal with a solid carbon micro-shell filled with carbon at gas density. The initial conditions are as follows.

Inner radius:	$R = 35$ μm
Wall thickness:	$\Delta R = 1$ μm
Gas density:	$\rho_g = 10$ Kg/m^3
Shell density:	$\rho_s = 2 \times 10^3$ Kg/m^3
Initial temperature:	$T_o = 6 \times 10^4$ K .

This target is compressed by a Gaussian pulse with total energy 1.7 J/steradian, peak power 1.62×10^{10} W/steradian and 1/e width of the Gaussian, $\tau = 60$ ps. It is found that without the radiative transport, a maximum shell density $\sim 10^5$ Kg/m^3 is achieved whereas the gas on the average is compressed to a density $\sim 2.5 \times 10^4$ Kg/m^3. When the radiative transport was included, the maximum shell density dropped down to 8×10^3 Kg/m^3 whereas the average gas density becomes 10^4 Kg/m^3.

8.4.5 Theory

8.4.5(a) Line Broadening

In the recent past improvements have been made in the calculation of the plasma broadening of ion spectral lines. The main objective of these improvements was to present a range of line profiles which could be most useful as a diagnostic for the laser generated plasmas. This approach not only provides the experimenter with an improved diagnostic capability but may also allow the validation of the theoretical models. The improvements are in two areas, the calculation of helium-like ion transitions and the inclusion of fine structure in the calculation of the Lymanα hydrogenic-ion transition.

8.4.5(b) Helium-like Transitions

The calculation of the helium-like transitions $1\ ^1S(^1S^2) - n^1P$ (1s np) and the neighbouring dipole forbidden line profiles is complicated by the need for energy levels and matrix elements for the calculation. The helium-like ions require therefore a suitable self-consistent field calculation for the energy levels and radial matrix elements. This was provided by using the Cowan Zealot suite of codes implemented at Appleton Laboratory (8.29, 8.30). The calculational method involves a semi-empirical procedure, starting from a Hartree-X self-consistent field and using the best available input data (including any well supported experimental energy levels).

The energy levels determined were used then as the unperturbed levels in the line shape calculation. The "intralevel" radial matrix elements were calculated (i.e. those without change in principal quantum number) but are in fact well approximated by the appropriately scaled hydrogenic radial matrix elements. On the other hand, the radial transition matrix elements which largely determine the oscillator strengths of the transitions are not hydrogenic.

The results of a theoretical comparison of these calculations is presented below. In addition, these calculations have been used in the interactive diagnostic procedure to determine plasma electron density and optical depth. Thus, one should also consult the appropriate section of the Atomic and Radiation Physics report (section 6.4).

The calculations presented in this section are for two elements at two separate plasma conditions. The Si XIII series is calculated for a plasma with electron density, n_e, of 5.7×10^{22} cm^{-3} and temperature of 5.6×10^6 °K.

The ions and electrons are assumed to have the same temperature. The ions perturbing the emitter are taken to have a charge 9.3, for use in the calculation of the static microfield. The assumption that the many ions charges are represented by one average ion has been checked with high charge numbers and found to be valid, in the sense that there is an error of less than 1% in the final line profiles. For the full calculation, where ion dynamics is included the required ion mass is taken as the mass of an ion of atomic number 9.3. This specific set of plasma conditions was chosen because they have been observed in recent experiments on laser compression of glass micro-balloons. In Figures 8.15a,b and c, we illustrate the spectral series $1s^2\ ^1S - 1s\ np\ ^1P$ where n is 2, 3 and 4 respectively. The associated forbidden components ($1s^2\ ^1S - 1s\ ns\ ^1S$ ans $1s\ nd\ ^1D$, $1s\ nf\ ^1F$ where applicable) are also shown and labelled in each figure. The wavelength scale is in Ångstroms relative to the allowed line centre while the intensity is in relative units. The profiles are normalized to equal areas for ease of comparison. In all figures the solid line represents the standard calculations while the dashed line represents the full calculations.

Note that the full calculations have been shifted to the blue so that the differences between the two calculations can be discussed more clearly. In Table 8.01, we present the red shifts of the various full profiles. Thus the column representing the shift is a measure of the total red shift necessary to bring the central allowed components of the transition into agreement. This shift is therefore a measure of the red shift introduced by the combined effects of the first order shift, the frequency dependence of the shift operators and the asymmetries in the width part of the broadening operators. This graphical representation allows the asymmetry, which leads to enhancement of the red wing, to be seen as a distinct feature of the full calculations.

The asymmetry in the present cases will only reflect those effects included in the full calculations since the trivial asymmetries will be too small to be observable. Further the asymmetry is a function of wavelength defined by

$$A(\Delta\lambda) = \frac{I_B - I_R}{(I_B + I_R)/2} \qquad (1)$$

where I_B, I_R are the blue and red wing intensities at a wavelength separation $|\Delta\lambda|$, and tends to increase away from line center.

The effects of the inclusion in the full theory can be discussed in terms of the three effects, shift, asymmetry and width. In Figure 8.15a, the resonance transition is shown which has a shift of .8 mÅ. This is smaller than the shift of the comparable hydrogenic transition n = 1 to n = 2 in Al XIII. Further the same is true for the asymmetry and the width. That is, the comparable hydrogenic transition does not show the same behaviour as the helium like transition. The reason for the differences are two fold. First, the transition is not hydrogenic since the splitting of the $2\ ^1S$ level is extremely large relative to the width of the allowed line. This will cause the asymmetry to lessen since the optimum condition is for all components of the transition to have the point of zero asymmetry at the same line centre - see equation (1). This, of course, occurs in full degenerate hydrogenic transitions. Thus we see in Figure 8.15a that the asymmetry does not start until the far wing of the forbidden component. Second, the very narrow width of the $1s^2\ ^1S - 1s\ 2p\ ^1P$ transition makes it extremely sensitive to Doppler broadening. The percentage change in the fifth maximum defined by

$$\% = (\text{FULL}-\text{STANDARD})/\text{STANDARD} * 100 \qquad (2)$$

is 8% as shown in Table 8.01. However, without the Doppler broadening the change is 75%.

Figure 8.15b illustrates the $1s^2\ ^1S - 1s\ 3p\ ^1P$ Si XIII transition for the same conditions as Figure 8.15a. The shift is 2mA with very little effect in the width as indicated in Table 8.01. This is caused by the absence of the central component which is most seriously affected by the dynamic broadening. In the present case the full calculations smooth out the central region and lead to a balancing of the peak intensities. The blue (allowed) peak is still larger than the red(forbidden) peak, which is distinct from the hydrogenic Lyβ (n = 1 to n = 3) transition of AL XIII where the full theory produces a red peak enhancement over the blue peak. Further the asymmetry is not developed to the same extent as the comparable hydrogenic transition. Thus although the full theory does cause red asymmetries to arise in both hydrogenic and helium-liked transitions, the final profiles are distinct. The $1s^2\ ^1S - 1s\ 4p\ 4^1P$ transition of Si XIII is shown in Figure 8.15c for the same plasma conditions as shown in Figure 8.15a. The same basic effects are seen for this transition but here the "hydrogenic"

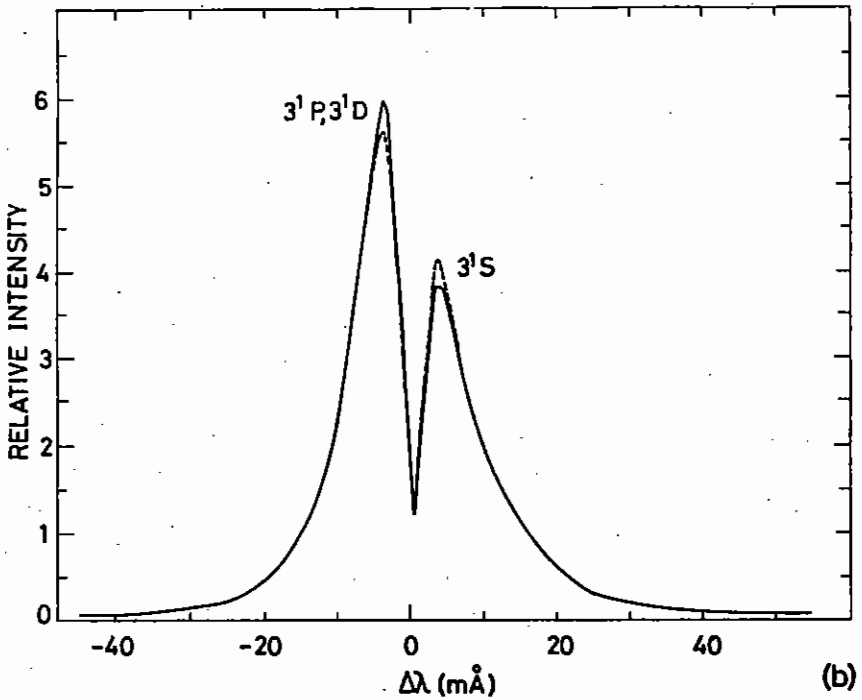

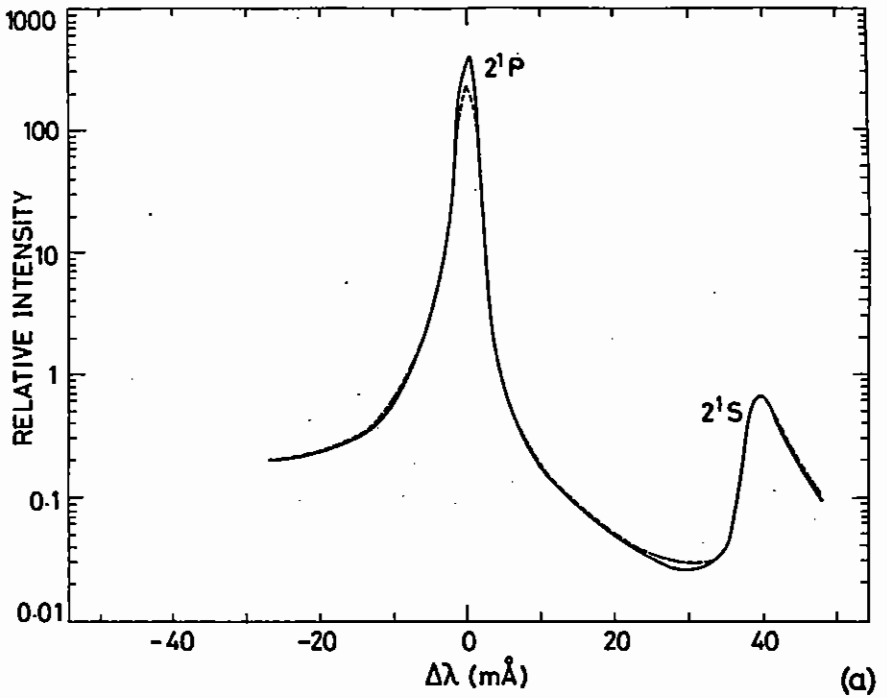

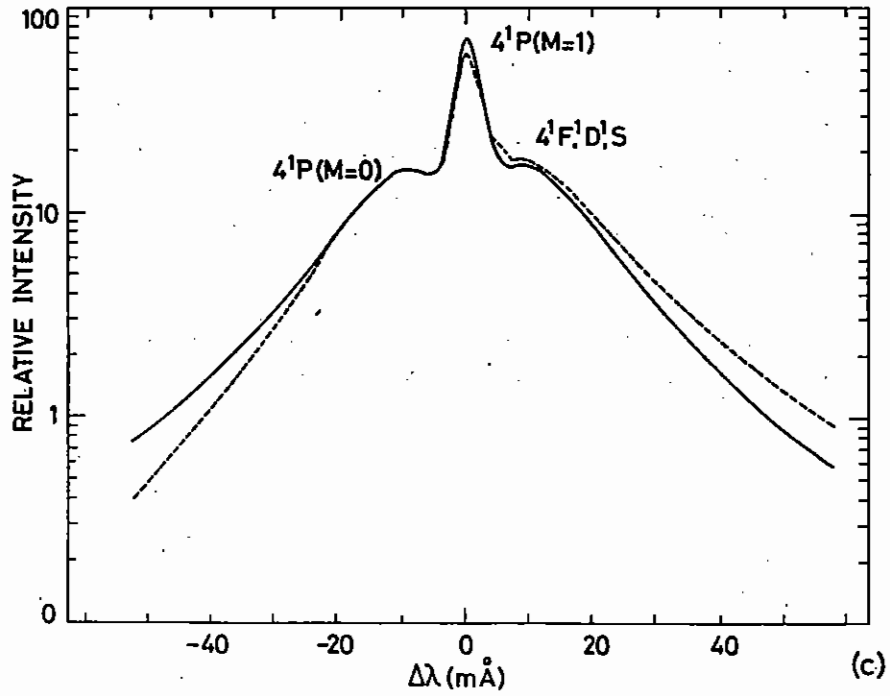

FIG. 8.15
LINE PROFILES OF THE $1s^2\,{}^1S - 1s\,np\,{}^1P$ SPECTRAL SERIES OF HELIUM-LIKE SI XIII FOR A PLASMA WITH $n_e = 5\times10^{22}\,cm^{-3}$ AND $T = 5\times10^6$°K. ABSCISSA IS WAVELENGTH IN ANGSTROMS MEASURED FROM LINE CENTRE AND THE ORDINATE IS RELATIVE INTENSITY.

(————) STANDARD CALCULATIONS.
(– – – –) FULL CALCULATIONS, AS DEFINED IN THE TEXT, SECTION 8.4.5(b).
( ) $1^1S-2^1P, 1^1S-2^1S$, (———) SHIFTED BY .8m Å
( ) $1^1S-3^1P, 1^1S-3^1S, 3^1D$. (– – –) SHIFTED BY 1.9m Å
( ) $1^1S-4^1P, 1^1S-4^1S, 4^1D, 4^1F$. (– – –) SHIFTED BY 2.4m Å

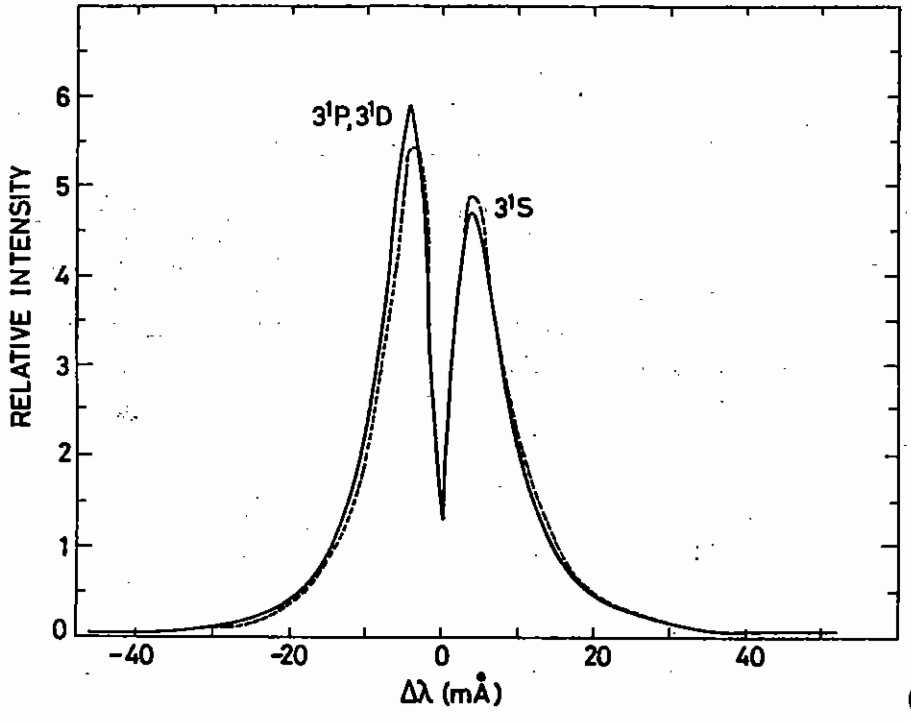

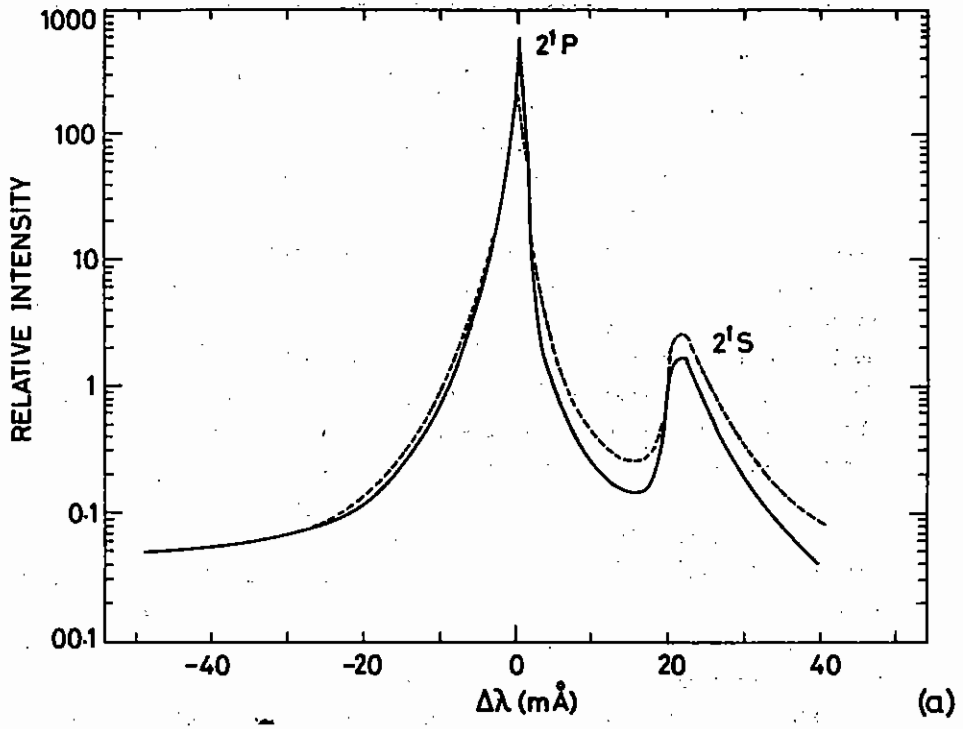

FIG.8.16

LINE PROFILES FOR THE $1s^2\ ^1S$-$1s\ np\ ^1P$ SPECTRAL SERIES OF HELIUM-LIKE AR XVII FOR A PLASMA WITH $n_e = 5 \times 10^{23} cm^{-3}$ AND $T = 8 \times 10^6$ °K. ABSCISSA IS WAVELENGTH IN ANGSTROMS MEASURED FROM LINE CENTRE AND THE ORDINATE IS RELATIVE INTENSITY.

(————) STANDARD CALCULATIONS
(– – – – –) FULL CALCULATIONS, AS DEFINED IN THE TEXT, SECTION 8,4,5(b).

( ) 1^1S-2^1P, 1^1S-2^1S. (– – – –) SHIFTED BY 1.2 m Å.
( ) 1^1S-3^1P, 1^1S-3^1S, 3^1D. (– – – –) SHIFTED BY 2.7 m Å.
( ) 1^1S-4^1P, 1^1S-4^1S, 4^1D, 4^1F. (– – – –) SHIFTED BY 3.5 m Å.

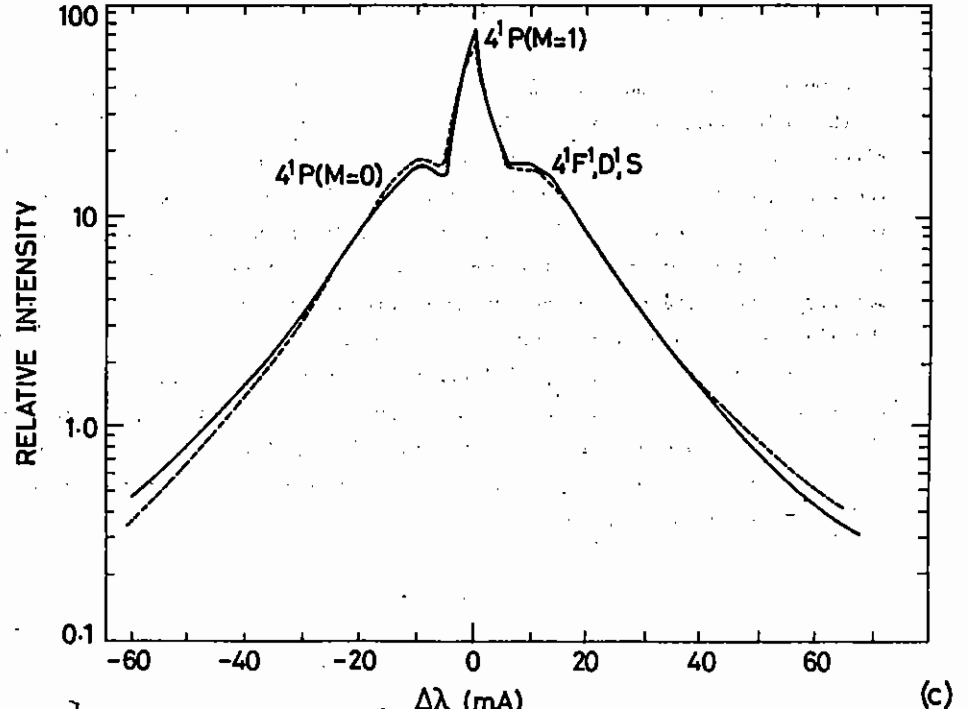

nature of the profile is more fully developed. The shift is 2.4 mÅ which is larger than the lower transitions. The asymmetry, as expected for higher-n transitions, is large since it is associated with the increased broadening and the overlapping of the levels. The slight asymmetry of the standard calculation in the core regions is due to the unperturbed energy level scheme. The slight bump on the shoulder of the full calculation is due to the first order shift of the 4^1F level away from the central region thus yielding a distinct feature. Although this transition is close to hydrogenic, the red shoulder is more intense than the blue (the opposite is true for the hydrogenic transition Al XIII Lyman γ (n = 1 to n = 4). Finally, the increase in the broadening is still small due to the Doppler effect and the decreased importance of the central peak.

The argon XVII transitions are shown in Figures 8.16a, b and c for a plasma with $n_e = 5 \times 10^{23}$ cm^{-3} and $T_e = 8 \times 10^6$ ^oK, which are chosen as typical conditions when argon will be used as a seed gas in the micro-balloons. The same general effects are evident. However, since the shifts and asymmetries introduced into the full calculations scale with the emitter charge and with the plasma density, we expect that the relative differences between the full and standard line profiles to be larger. This is indeed found to be the case.

In comparison with the lower z case in Figure 8.15, we find that the effects of the additional terms in the full calculations are becoming apparent. First, note that for the argon helium-like transitions the red shifts of the full theory are larger by about 50% as indicated in Table 8.01. This increase is due to the 30% increase in the emitter charge and the additional increase in the importance of the extra broadening terms due to the higher density. The increases in the asymmetry are obvious from a comparison of the Figures 8.15 and 8.16. However, it should be exphasized that the comparable hydrogenic transition still exhibits larger asymmetries. Note that the increase in the broadening operators definitely outstrips the effect of the Doppler broadening for the argon transitions. This is due in large part to the order of magnitude increase of the density as compared to about 60% increase in the temperature.

TABLE 8.01

Comparison of "Standard" and "Full" Calculations

Figure	Case	Red shift* of full w.r.t. standard (A)	% change in full width at fifth maximum (full-standard)/standard x 100%
1a	Silicon 1s-2p	0.8×10^{-3}	+ 8 (75)+
1b	" 1s-3p	1.9	+ 3
1c	" 1s-4p	2.4	+ 11
2a	Argon 1s-2p	1.2	+ 44
2b	" 1s-3p	2.7	+ 6
2c	" 1s-4p	3.5	+ 18

* In the figures, the curves for full calculations (dotted lines) have been blue-shifted by these amounts to bring the peaks of full and standard calculations into alignment (to demonstrate asymmetries).

\+ The figure in brackets is the % change in the width when Doppler broadening is ignored.

8.4.6 Fine Structure Effects

The effect of fine structure splitting on the shape of the Lyman α line profile is indeed important since the use of the Ly α transition essentially determines the opacity of the plasma (see section 4.7.1). The opacity in turn is related to the number density of ions and hence to the mass density (8.31). Thus, we obtain the experimentally important compression ratio. The results reported here are limited to a theoretical study; for a view of the effects of including the fine structure splitting appropriately one should reference the section where the diagnostic fitting is discussed.

The procedure using the optically thick line to determine compression ratio makes the Lyman α transition particularly interesting. Recently large discrepancies for this transition have been reported between theory and experiment (8.32), these discrepancies were resolved by the inclusion of ion dynamical addition to the profile (8.33), however, this will be of much reduced importance in the high z cases treated here where it is assumed no low z material is present. Moreover, corrections due to a combination of plasma screening, the high z of the plasma ions and the high emitter charge may cause noticeable effects on the Lyman α line (8.34). Beyond these latter corrections one particular effect which has not received appropriate attention in calculations of these high z Lyman α Stark broadened profiles is the fine structure splitting and the coupling scheme used in the calculations. Further, the fine structure splitting will be important in the high z Lyman α profiles of the emitters whether or not ion dynamics and plasma screening effects make contributions to these profiles.

In the present work a discussion of the calculation of the Lyman α fine structure splitting is given with emphasis on the modifications it makes in the line shape. The calculation of the n = 2 level of hydrogenic ions indicates that the spin orbit correction and the first relativistic corrections leads to an energy shift of the angular momentum sublevel, j, below the unperturbed energy of level n equal to (8.35)

$$\Delta E_j = \frac{z^4}{n^3}\left(\frac{1}{j + 1/2} - \frac{3}{4n}\right) \times 1.750 \times 10^{11} \text{ Hertz}$$

This indicates that for all hydrogenic species the splitting between

$2P_{3/2}$ and $2P_{1/2}$, $S_{1/2}$ is 5.39×10^{-3} Angstroms. This is indeed on the order of the width of, e.g. the Si XIIII Ly α line at an electron density of 10^{22} cm^{-3} and this will become even more important for high z emitters.

Two possible methods can be used to calculate the Ly α transition with this splitting included. First, as suggested by Bailey et al (8.36), the two components can be treated additively as two Lyman α lines with an appropriate shift and statistical weighting given by the factor (2j + 1). This method is simple but ignores the "non-hydrogenic" nature of the displacement of the two sublevels. Second, the full L-S coupling scheme can be employed to account for the fact that the transition now represents an interacting combination of degenerate "hydrogenic" levels, i.e. $P_{1/2}$, $S_{1/2}$ and a helium-like non-degenerate level, $P_{3/2}$, with a forbidden component $S_{1/2}$.

Calculations were performed using a standard plasma line broadening formulation to investigate the two methods mentioned above and show their deviation from each other and from a calculation ignoring the fine structure splitting completely. The calculations were carried out using the quasi-static microfields of Hooper and Tighe (8.37). The electron broadening was calculated using the random phase approximation for the plasma (8.38) and no ion dynamics were included. These calculations thus reduce to a standard form of the line shape theory (8.39), which is estimated to be accurate to within 20% for the cases studied here (8.40).

In Figure 8.17, the results of the computations are shown for Ne X at a plasma temperature of 5.10^6 °K and a plasma density of 5.10^{22} cm^{-3}. The abscissa is in Hertz measured form line centre which is taken as the $P_{3/2}$ component in the cases where the fine structure splitting is included. The ordinate is relative intensity with the profiles compared by wing fitting to best show the central region differences. The solid line is the case with no fine structure splitting, while the dashed and dotted lines represent the additive and L-S coupling scheme respectively. Here we see that the various calculations show signs of deviation. However, for this emitter the L-S coupling and no fine structure calculations are still suitable, so that no fine structure splitting is actually required. In Figure 8.18, the case for Ar XVIII for a temperature of 5.10^6 °K and a density of 5.10^{23} cm^{-3} is shown. In this case the different methods differ signicantly.

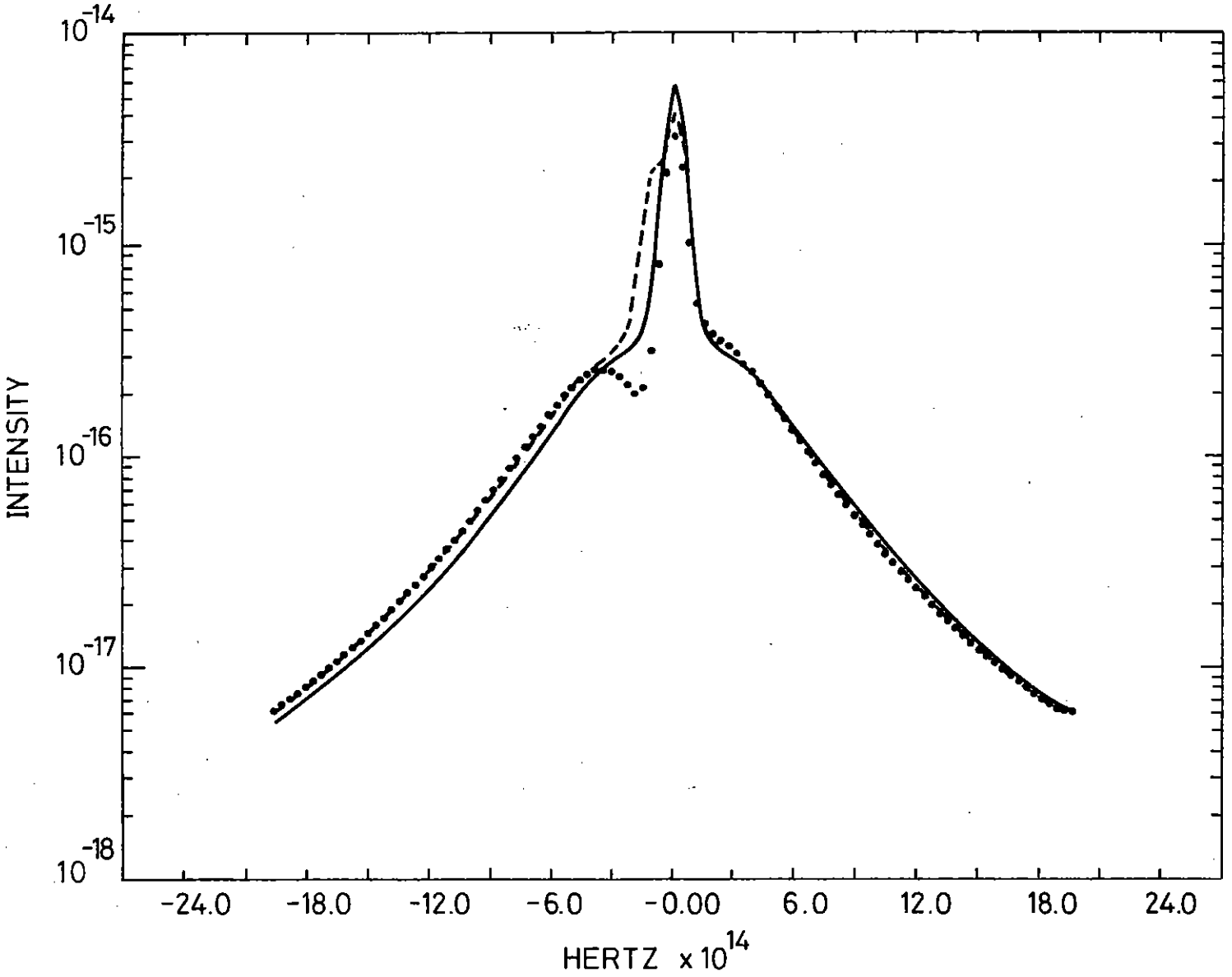

Fig.8.17

Neon Lyman α transition at plasma electron density and temperature of 5.10^{22} cm^{-3} and 5.10^{6} ^{o}K respectively.

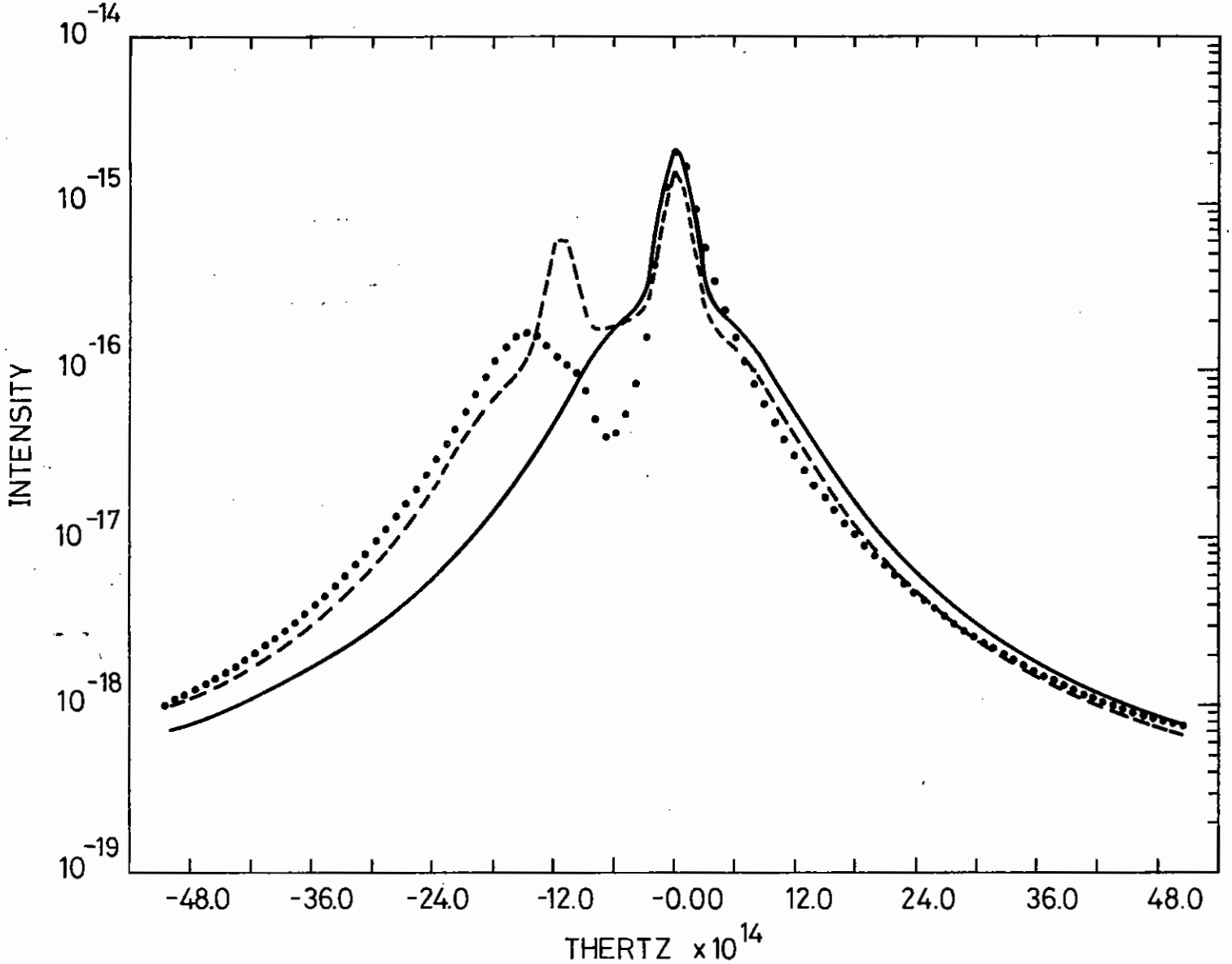

Fig.8.18

Argon Lyman α transition at plasma electron density and temperature of 5.10^{23} cm^{-3} and 5.10^{6} ^{o}K respectively.

Thus one is compelled to use the fuller L-S coupling treatment when fine structure splitting plays a significant role in the structure of the line shape. This result is even more crucial since one intends to use this particular transition to determine the integral of n_g, implying that the peaks of the profiles will be obliterated leaving only the region of the profile where the various treatments differ most drastically.

In conclusion, the effects of the fine structure of the n = 2 to n = 1 Lyman α transition from high z emitters in dense plasmas will be important in the interpretation of X-ray emission spectra. This report indicates both the limits of the effect at low z and the need to use the complete L-S coupling scheme when the effect is observable. As a final comment it should be noted that the measured $P_{1/2} - S_{1/2}$ levels shift for Ar XVIII of 38.10^{12} Hertz (8.41) is negligible compared to the plasma broadening.

8.4.7 Radiation Transport

Motivation: In the study of processes important in the evolution of the compressed core and ablating shell of the irradiated microballoons one major variable, the radiation field, has been grossly ignored. The reason for this is simply that a truly time dependent radiation-hydrodynamic model is not available. The difficulty is increased if we wish to study the spectral line information since the detailed knowledge of these lines requires a large number of frequency points, coupled to one another through the scattering integral in each line if partial or complete redistribution is appropriate. However, to improve our understanding of the processes involved in the time development of the hydrodynamics of the plasma, the effects of radiation transfer as an energy transfer mechanism should be studied in detail. Moreover, the effects of a detailed analysis of the Radiation Transport in the emergent lines is of particular interest for two further reasons. First, the possibility of finding additional diagnostic material is increased when the interaction of the radiation with the level population is studied. Second, the present use of line profiles emitted from the plasma as a diagnostic requires further corroboration. The latter arises from the fact that only simple transport models can be used for diagnostics since a computer interactive technique is employed.

Basic Required Data:

The basic approach employed is to use the best available radiative transport calculations with data generated by the line shape codes and by the hydrodynamic codes available.

The information required in a radiation transport calculation are the line profiles for the transitions of interest and the hydrodynamical variables. The line profiles of interest to us are those of the hydrogenic and helium-like ion species which tend to be present in the emission spectra, i.e. Neon, silicon, aluminium, etc. The theory of the line shapes which has been worked out and discussed in previous documents and papers, is used. Thus we are using the best available profiles for input into the calculation.

The hydrodynamical variables required are the temperature, mass density, velocity and elemental composition at the range of radial depths in the plasma. These variables are, of course, provided by numerical simulation, but use can also be made of idealized plasma conditions to ascertain limiting cases. Note that spherical symmetry is assumed throughout the calculational procedures.

Methods for Solving Radiation Transport Equation: The methods that are employed to perform the integration of the radial transfer equation to obtain a self-consistent radiation field (recall that the equation is integro-differential in nature if the scattering integral assumes partial or complete redistribution) are standard methods in astrophysics devised for problems similar to the one that confronts us. In particular two methods are employed for the solution of the transfer equation.

First, if the velocity fields are small, i.e. the maximum Doppler shift is only a fraction of the line width then the velocity is ignored. When this occurs the Feautrier method with the variable Eddington factor approach is employed. This method has the advantages of small storage requirements and great speed together with numerical stability. These qualities are essential if one is to use the approach on numerous line profiles for any one plasma condition without a great deal of effort in recalculating for each transition. The technique, which is described in detail in Kunasz and Hummer, 1972, and Mihalas 1978, depends on using a set of impact parameters traversing the sphere at various distances away from the sphere origin. These impact parameters take the place of the angular variable and

provide a radius-impact mesh to define the radiation field. Since the source function is assumed known in the variable Eddington factor technique, the solution is quite economical. The Eddington factors are calculated and the moment equation is solved for a new estimate of the scattering integral and hence the source function. The procedure is repeated until convergence. We have found, as documented previously, the convergence is found on the third iteration, except when the total optical depths exceed 10^3. The reason for this failure to converge in three iterations is due to the economizing which has been done to the radial grid, indeed if more grid points are used three iterations are all that is required. (Note, however, that in the plasmas of interest here there is rarely a case when the maximum total opacity exceeds 100.)

When the velocity fields cannot be ignored the variable Eddington factor ceases to be applicable since the moment equation becomes intractable. Thus we must make recourse to the Rybicki method (1971) of solution of the radiative transfer equation as set out by Hummer Kunasz (1974). This method employs the same mesh but regroups the variables so that the computation time is greatly reduced. The one additional difficulty that arises is the asymmetry of the line shapes with which we deal. This has the effect of making the number of frequencies required in the solution extremely large and the computation time increases accordingly. The fact that we never have very large Doppler shifts relative to the line width, which is usually Stark broadening dominated allows us to use this method with confidence without the recourse to a co-moving frame approach (see Mihalas 1978, Chapters 14 and 15). Further, this method allows non-monotonic velocity field and indeed these are present in the plasmas under investigation.

Calculational Procedures: In this section we define the calculational procedures which are now available. The simplest grouping is according to the computer codes that now exist and what their uses are intended to be.

ZERO: The calculational procedure called ZERO, affects the LTE radiation transport of numerous transitions. The level populations which are all assumed to be in LTE are calculated and the opacity and source functions defined based on the hydrodynamical information. Velocity fields are not permitted in this calculation.

The major use of this calculation is the simple analysis of the emergent profiles for quick analysis. This is quite helpful in analyzing the gross effects of temperature and density changes on the emergent radiation field.

ONE: The ground state level populations are calculated for all the ions of one species in either a simple rate equation model (extended coronal type model) or under LTE, whichever condition is valid for each radial position in the plasma. The line profiles are then defined and the opacity is specified.

For each transition a two level atom is then solved using the variable Eddington factor method. This does not treat velocity fields. The results indicate the effect of non-LTE transport in the various transitions studied. It is a further step in the analysis of the effects of the variations in the plasma structure.

THREE: This is the most complete version of the analysis of line profiles. Since it is somewhat more complicated both numerically and in its physical content it is also more difficult to use and interpret, thus the need for procedures ZERO and ONE become more obvious after attempting to analyze the results of THREE.

First, a summary of the program. It uses a complete set of non-LTE rate equations which accounts for numerous levels (specified by user). This includes the continuum processes such as bound-free, free-free but does not include electron scattering, which in the temperature density range encountered, is negligible. The number of implicit levels included in the rate equations is defined by a lower bound specified by the user and an upper bound dictated by the ionization potential depression. The code can treat both a pure species, such as neon in the core, as well as treat one element in a compound as silicon in the glass shell. Both core and shell type plasmas are permitted with inner boundary values dictated by the combination of the inner boundary plasma conditions, i.e. temperature, density, opacity. In addition, multiple level radiation transfer is performed using the equivalent two-level atom approach (ETLA) with bound-free and free-free processes included. In the case where velocity fields are present and must be accounted for, the Rybicki form of the solution of the transport equation is used for any individual transition that requires it. However, when

the velocity fields are too small to cause reasonably observable effects the Eddington factor method is applied. This leads to a substantial savings in time since the Rybicki is costly.

The procedure itself starts with the input of the hydrodynamical variables. The element of interest and the particular transitions are then specified together with the number of explicit levels to be treated.

The next step is an initialization sequence which determines which "cells" contain the element under investigation, solves the coronal equations to get a crude estimate of the electron density and refines it with a ground state ion stage calculation using either coronal or LTE. This is iterated after the potential depression is defined. The last stage of the initialization sequence is to set the scattering integrals, $\bar{J}$, equal to zero.

With the initialization complete the first estimates of the electron density are used in conjunction with the full non-LTE rate equation. (Of course, on this first sequence the radiation field is not present.) This yields a new set of level populations and electron density. Then the rate equations are iterated with the new potential depression, and electron density until convergence is found.

Given the temperature and electron density structure of the plasma the line profiles can be defined on the radial grid. This in turn allows us to define the total opacity, source function and components of the ETLA source function. Note the components of the source function are stored separately so that the velocity dependent cases require only modification of the logic of the transport calculations itself.

Next the grid required for the radiation transport calculation is defined. The constraints on the grid are twofold. First, the radiation field will change rapidly at the outer boundary for a small change in optical depth, $\Delta\tau \sim 1$. Thus the grid must not have larger steps than $\Delta\tau = 1$ in the region. Second, the step sizes in geometrical units cannot change too abruptly thus the grid is constrained to have smooth geometric type variations. The gridding is always performed for the optically thickest transition and no difficulty has been encountered when this grid is used for the less opaque transitions.

The transfer calculation is now performed and the scattering integrals are computed. Also, since convergence of the entire process relies on the level populations, all radiation quantities are stored for eventual output. The program returns for a new calculation of the level populations, this time with the radiation field.

Then iterations are continued between level populations and radiation field until the level populations converge.

Results: In using THREE we have found that the number of iterations needed to obtain level populations that converge to .5 percent is usually 5 or less. The difficulties with the ETLA 'converging' to wrong level population has been discounted by perturbing the levels from the obtained equilibrium. There results show a rapid return to the original converged level populations. The convergence tends to be rapid since the Ly α like transitions which we have studied are optically thick, but only moderately so, i.e. $\tau_{MAX} \leq 30$ (moderate that is on astrophysical scales). This moderate opacity coupled to the optical thinness of the higher transition leads to the rapid convergence properties.

8.4.8 Ion Emission from Laser Produced Plasmas with Two Electron Temperatures

A study of ion acceleration and emission processes in laser produced plasmas is being undertaken. Here we consider the effect of high velocity electrons produced at the plasmas critical density surface on ion acceleration.

The initial conditions assumed at time $t = 0$ (see figure 8.19) are a quasi-neutral collision-free plasma slab composed of ions with charge Ze, mass M and density n_o for $x < 0$ and vacuum for $x > 0$, where x is measured from the target surface. The electron velocity distribution in the plasma is represented as the superposition of hot and cold Maxwellians with temperatures T_h and T_c respectively, each following the appropriate density distribution $n_h = n_{ho} \exp(e\phi/KT_h)$ or $n_c = n_{co} \exp(e\phi/KT_c)$. Here n_h and n_c are the hot and cold electron number densities, ϕ is the electrostatic potential and quasineutrality requires that $Zn = n_c + n_h$, where n is the ion number density.

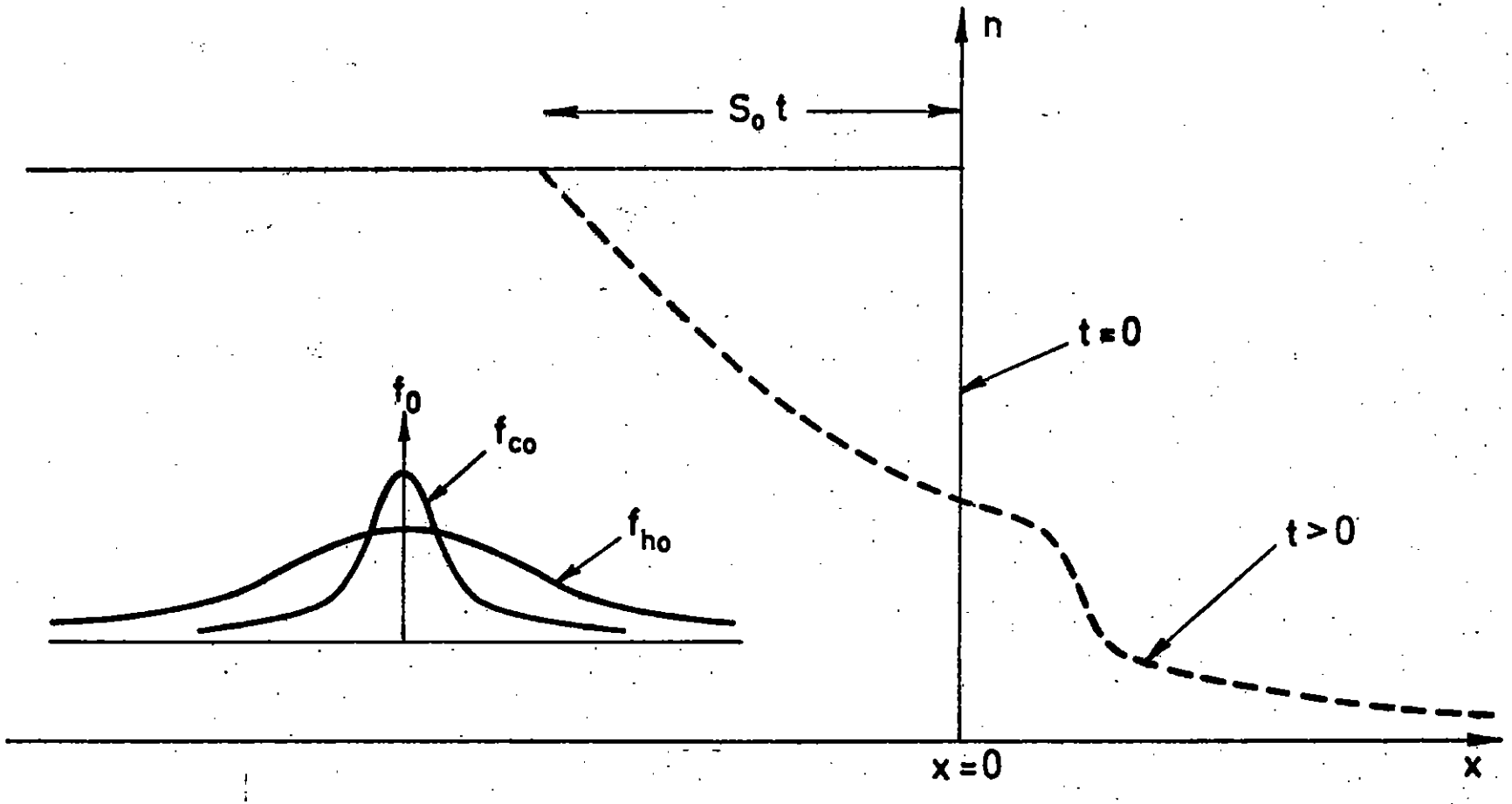

Fig.8.19

Schematic diagram of the ion density (n) initially and after time t. The inset shows a typical source plasma electron velocity distribution function (f_o) resolved into its hot (f_{ho}) and cold (f_{co}) components.

The expansion is assumed to be planar, so the ion continuity and momentum equations become

$$\frac{\partial n}{\partial t} + \frac{\partial}{\partial x}(nv) = 0$$

and

$$\frac{\partial v}{\partial t} + v\frac{\partial v}{\partial x} = -\frac{Ze}{M}\frac{\partial \phi}{\partial x} \qquad (1)$$

wher v is the ion velocity. Looking for self-similar solutions we transform the equations so that $\xi = \frac{x}{t}$ becomes the independent variable, giving

$$(v - \xi)\frac{dn}{d\xi} + n\frac{dv}{d\xi} = 0 \qquad (2)$$

and

$$(v - \xi)\frac{dv}{d\xi} + \frac{S^2}{n}\cdot\frac{dn}{d\xi} = 0 \qquad (3)$$

where

$$S^2 = \frac{(n_c + n_h)Z}{\left(\frac{n_c}{KT_c} + \frac{n_h}{KT_h}\right)M}$$

is the local ion acoustic speed in a plasma with a two electron temperature velocity distribution function. For non-zero solutions to (2) and (3) we have

$$(v - \xi) = S \qquad (4)$$

and from (1), (3) and (4)

$$\frac{dv}{d\xi} = -\frac{Ze}{SM}\cdot\frac{d\phi}{d\xi} \qquad (5)$$

Integrating (5) from the undisturbed source plasma out into the rarefaction expansion gives the ion velocity as a function of potential as

$$v = \left[\frac{1}{T_c} - \frac{1}{T_h}\right]^{-1}\left[\frac{C_c}{T_c}\log_e\left\{\frac{S-C_c}{S+C_c}\cdot\frac{S_o+C_c}{S_o-C_c}\right\} + \frac{C_h}{T_h}\log_e\left\{\left(\frac{C_h+S}{C_h-S}\cdot\frac{C_h-S_o}{C_h+S_o}\right)\right\}\right] \qquad (6)$$

where $C_h = (ZkT_h/M)^{\frac{1}{2}}$, $C_c = (ZkT_c/M)^{\frac{1}{2}}$ and S_o is the source plasma ion acoustic speed.

In the limit of $T_h \to T_c$ (6) becomes the well known isothermal rarefaction wave solution (8.42). Figures 8.20 and 8.21 show plots of ion density and velocity in the rarefaction expansion as obtained from equations 1, 4 and 6. The most important feature to note is the abrupt jump in ion density and velocity that occurs where the magnitude of the electrostatic potential is sufficiently large to exclude most of the cold electrons from the upstream region. The jump is most noticeable for larger values of hot electron temperature (cf. T_{hc}, the hot to cold electron temperature ratio) and occurs closer to the source plasma for larger hot electron number densities (cf. n_{hco}, the source plasma hot to cold electron number density ratio).

For $T_{hc} > 5 + \sqrt{24}$ the self-similar solution breaks down in the vicinity of the density jump, the solution becoming triple valued in this region (cf. figure 8.22). In reference (8.43) we analyse the flow in the vicinity of ξ_s by noting that since the electrostatic fields become large there the ions can be assumed to be in approximate equilibrium with the field and ion energy conservation applied. This is not valid elsewhere in the flow. The existence of oscillations around the singular points is indicated. In reference (8.44) a shock is fitted across the triple valued part of the solution. However, the analysis does use conservation of ion energy at a point in the quasineutral solution where it is not strictly valid. A more complete analysis, retaining the time dependent terms, should lead to an oscillatory solution with the shock as an average value.

To compare the above theory more directly with experiments on laser-produced micro-balloon plasmas it is assumed that the self-similar solution holds until a time t_o, after which no further ion acceleration occurs. The ions then freely drift to the walls with the velocity they have acquired from the self-similar potential. The ion velocity spectrum observed by a probe remote from the target is then the same as the ion velocity spectrum at time t_o. Since no source plasma is produced after the laser pulse ends it seems reasonable to identify t_o with the laser pulse duration and, since the ions move a distance of the order of the micro-balloon diameter during the laser pulse, we can approximate the self-similar phase of the expansion as planar. The plasma surface area A is then approximately that of the micro-balloon.

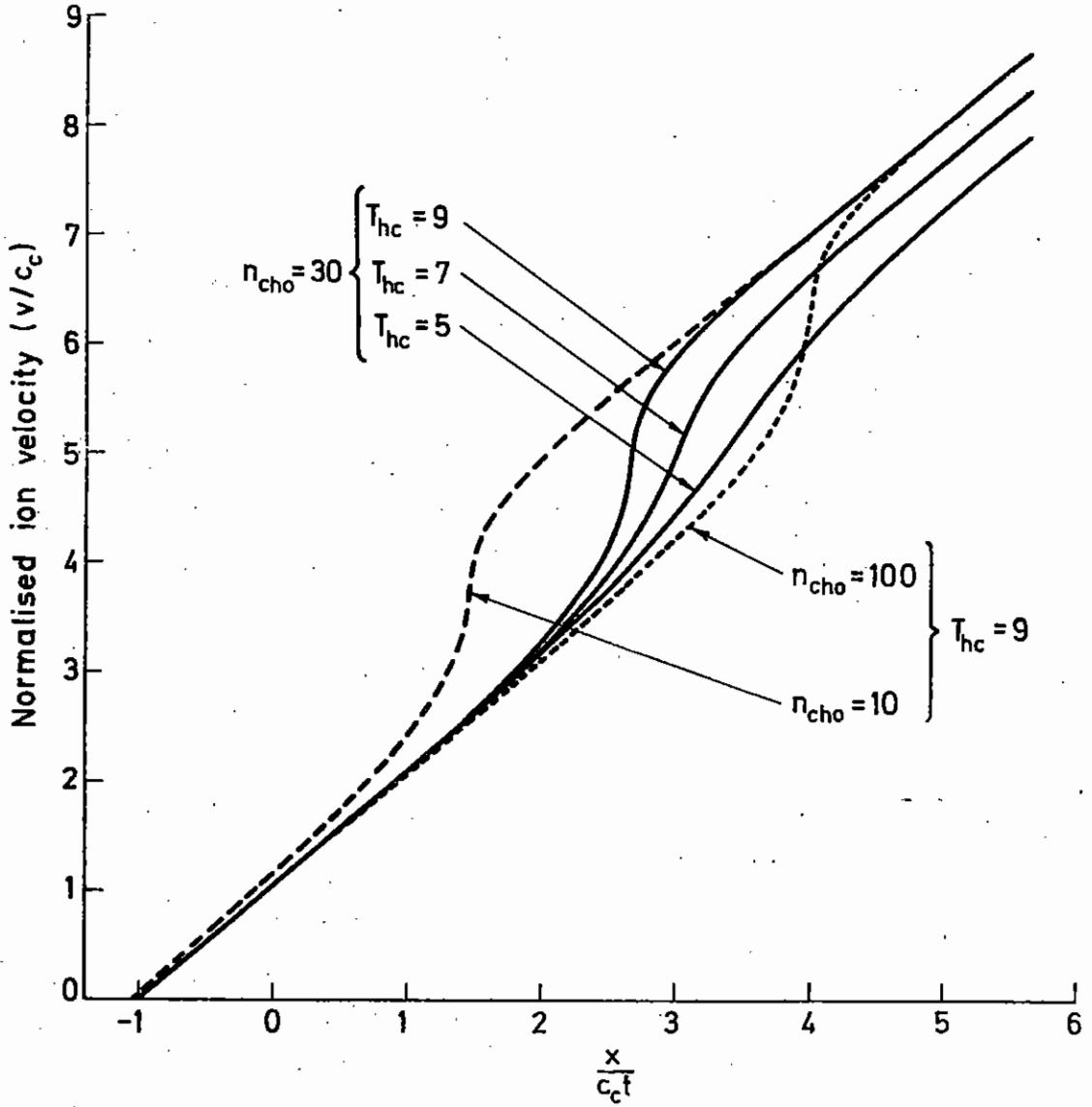

Fig.8.20

Variation of the normalised ion velocity (v/C_c) with $x/C_c t$ for a range of source plasma electron temperature (T_{hc}) and density (n_{cho}) ratios.

Let $(\partial N/\partial v)_{t = t_o} dv$ be the number of ions in the velocity range dv at a time t_o; then

$$\left(\frac{\partial N}{\partial v}\right)_{t = t_o} = \left(\frac{\partial N}{\partial x}\right)\left(\frac{\partial x}{\partial \xi}\right)_{t = t_o}\left(\frac{d\xi}{dv}\right) = At_o n \left(\frac{d\xi}{dv}\right)$$

and using the relation $v - \xi = S$ gives the ion velocity spectrum as

$$\frac{1}{At_o n_o}\left(\frac{\partial N}{\partial v}\right)_{t = t_o} = \frac{n}{n_o}\left[1 - \frac{n_c n_h}{2}\left[\frac{1/T_c - 1/T_h}{n_c/T_c + n_h/T_h}\right]^2\right] \qquad (7)$$

The ion velocity at a large distance R, from the source plasma is given by $v \simeq R/t_f$, where t_f is the ion time of flight. Now let $(dN/dt_f)dt_f$ be the number of ions arriving at the sphere of radius R in a time dt_f. Then, as the ion velocity spectrum $(\partial N/\partial v)$ is unchanged after time t_o,

$$\frac{dN}{dt_f} = -\frac{R}{t_f^2}\left(\frac{\partial N}{\partial v}\right)_{t = t_o}$$

and using (7) we find that the ion flux over 4π steradians at a distance R and time $t_f = R/v$ is given by

$$\frac{dN}{dt_f} = nv^2\left\{1 - \frac{n_c n_h}{2}\left[\frac{1/T_c - 1/T_h}{n_c/T_c + n_h/T_h}\right]^2\right\}\frac{At_o}{R} \qquad (8)$$

Figure 8.23 shows plots of normalised ion flux against normalised time as obtained from equations (6) and (8) for a range of source plasma conditions (the inset shows a theoretical current trace for longer times). Note the separation of the ions into a "fast" and a "slow" component. This agrees well with the findings of many laser produced plasma ion emission experiments. Figure 8.24 shows corresponding ion velocity spectra, as obtained from eqns (6) and (7). Theoretical ion distributions have been fitted to two experimental curves in Figure 8.25, giving reasonable agreement at low ion velocities. The poorer agreement at higher ion velocities may be caused by errors in the average ion charge to mass ratio, due to the presence of fast protons.

Comparison of the theoretical curves with these and many other experimental results allows the following statements to be made about the properties of the glass-shell plasma near critical density. The hot- to cold- electron temperature ratio (T_h/T_c) varies between 5 and 8 both from shot

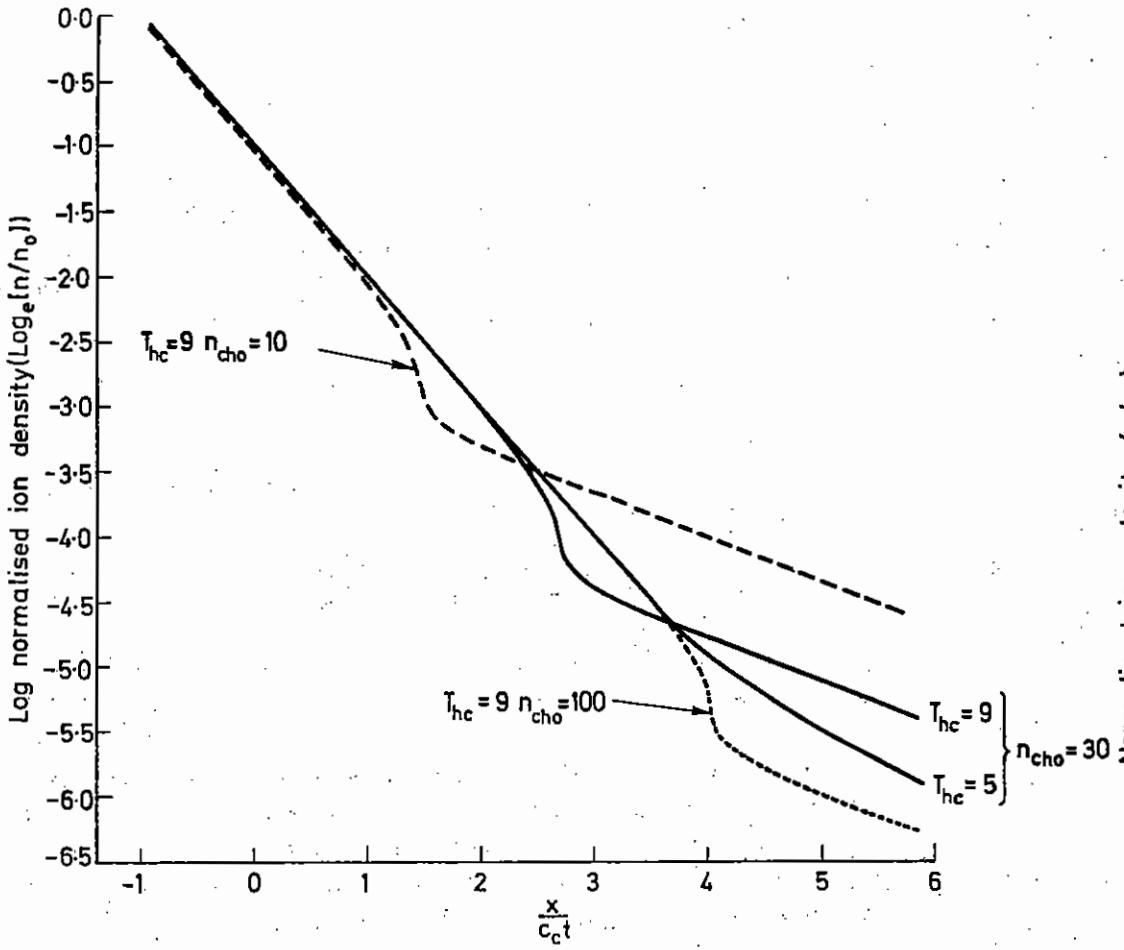

Fig.8.21

Variation of normalised ion density (n/n_o) with $x/C_c t$ for a range of source plasma electron temperature (T_{hc}) and density (n_{cho}) ratios.

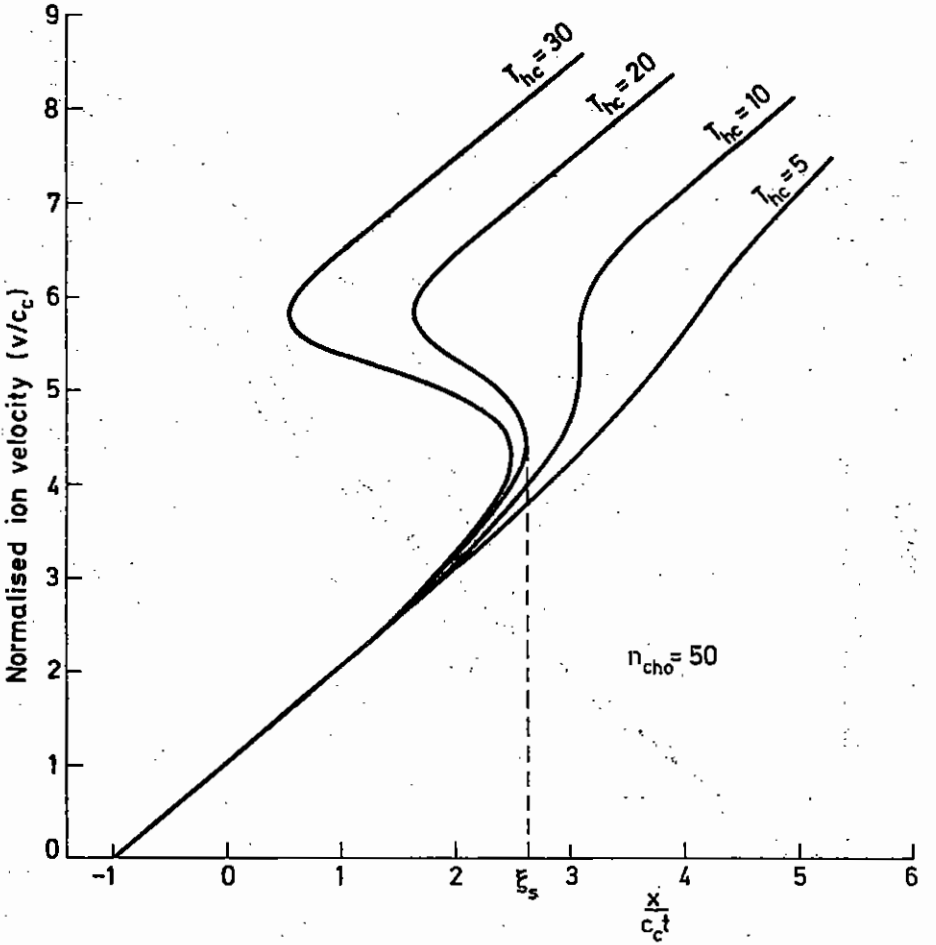

Fig.8.22

Normalised ion velocity (v/C_c) against $x/C_c t$ for n_{cho} = 50 and values of the electron temperature ratio (T_{hc}) such that the self-similar solution becomes singular at the point ξ_s.

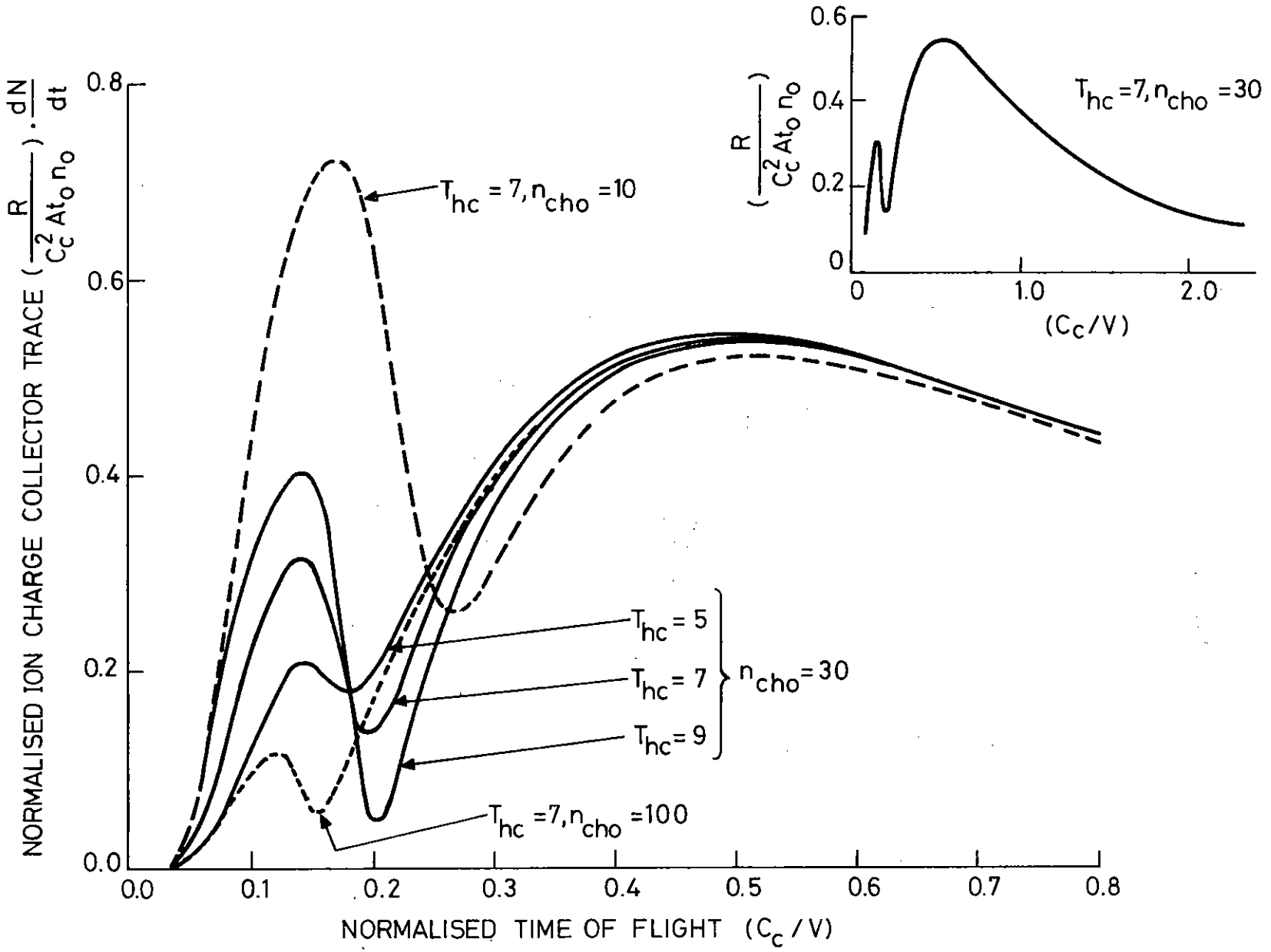

Fig.8.23

Normalised theoretical Faraday Cup Current $\{R/(C_c^2 A\ t_o)\}(dN/dt)$ as a function of normalised ion time of flight (C_o/v) for a range of source plasma electron temperature (T_{hc}) and density (n_{cho}) ratios. The inset shows a theoretical trace for longer times.

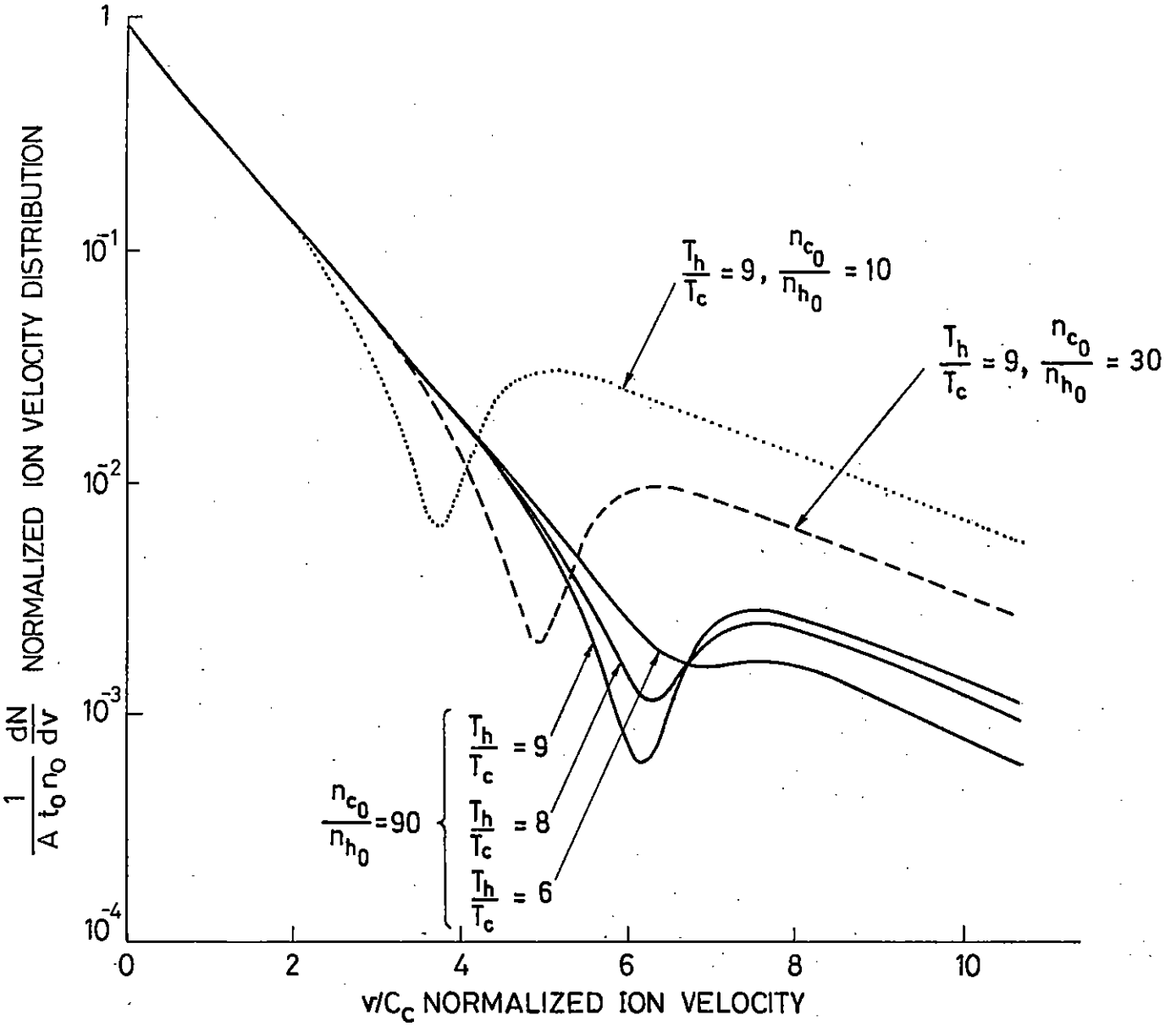

Fig.8.24

Theoretical normalized ion-velocity distributions obtained from Eqs.(2) and (3) for various values of the hot- to cold-electron temperature ratio (T_h/T_c) and target-plasma cold- to hot-electron density ratio (n_{co}/n_{ho})

(L.M Wickens, J E.Allen and P T Rumsby)

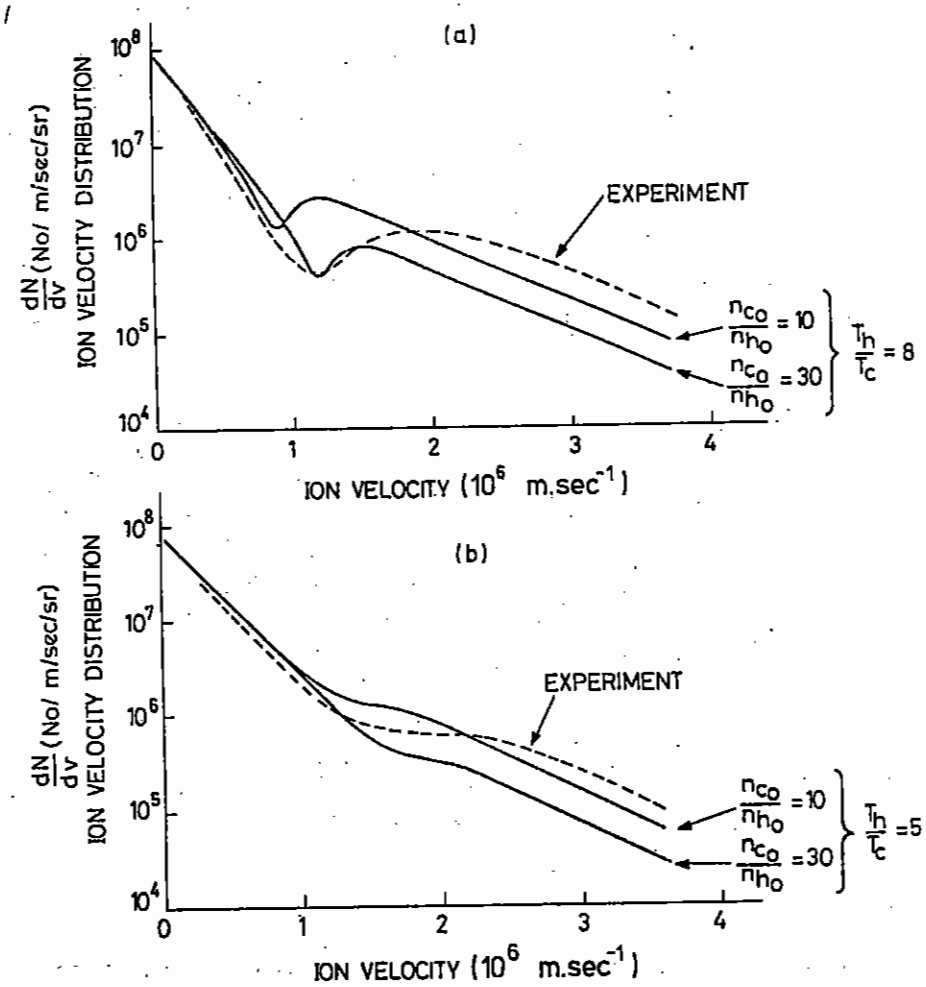

Fig.8.25

(a),(b) Comparison of experimental ion-velocity spectra with theoretical distributions. The two experimental curves were derived from the currents to a detector situated in the target equatorial plane for two consecutive shots on microballoon targets at intensities of 5×10^{19} W m^{-2}.

(L M Wickens, J E Allen and P T Rumsby)

to shot and also between different observation directions on the same shot. The cold - to hot-electron density ratio (n_{c_o}/n_{h_o}) remains reasonably constant with a value of about 30. Values of T_c and T_h observed cover the ranges 0.6-1.4 and 9.0-11.0 keV, respectively.

These temperatures and temperature ratios deduced from the ion velocity distributions can be compared with temperature measurements made by observation of the x-ray-emission spectrum using filtered diode arrays. Such measurements indicate values of T_h/T_c varying between 6 and 10 with values of T_c and T_h in the ranges 0.7-1.0 and 5-8 keV, respectively. These values are in remarkably good agreement with the ion results if we bear in mind that the x-ray data give information about a region of plasma of density considerably higher than critical and that averaging over the whole target takes place.

8.5 Gas Laser Development

8.5.1 Relativistic E-Beam Deposition Code

The electron-beam deposition code described here was developed in support of the gas-laser research programme. In particular it describes in detail the physical processes in the deposition of energy by the electron machine ELF (section 2.2).

Several aspects of the design of the e-beam machine contribute to making the problem a three dimensional one: (a) the aspect ratio of the e-beam diode and gas cell (5 cm x 75 cm), (b) the provision for the inclusion of a longitudinal magnetic field and (c) the positioning of the final laser cell (section 2.3.3). Considerable thought was given to the method of approach in order to conserve the intrinsically three dimensional nature of the problem and the inherent complexity of the solution of Boltzman's equation in the geometry. Previous approaches to this problem are acknowledged here. The 1-D homogeneous approach of the NRL code TEP (8.45) and the 3D Monte-Carlo simulation of the Sandia Laboratory code SANDYL. The approach adopted is somewhat in-between these two where the solution of the Boltzman equation is followed in the transport of the particles and the Monte-Carlo approach used in the scattering formulism (in order to model the small and large angle scattering) and straggling.

For a gas species k the Boltzman equation for the distribution f_k in the

presence of an electric and magnetic field can be written as

$$\underline{v}\cdot\nabla_r f_k + \frac{e_k}{m_k}\left\{\underline{E} + \frac{1}{c}(\underline{v}\wedge\underline{B})\right\}\cdot\nabla_v f_k = \left.\frac{\partial f_k}{\partial t}\right|_{coll} \qquad (1)$$

where $\underline{v}$ is the local velocity and e_k and m_k are the charge and mass of the k species. For a system in which binary collisions dominate, the right hand side of this equation can be written as the collision integral.

where $\underline{v}$, $\underline{v}'$ are the initial and $\overline{v}$, $\overline{v}'$ are the final velocities, σ the differential cross section for scattering, θ the scattering angle and $d\Omega = \mathrm{Sin}\,\theta\, d\theta\, d\phi$.

For small angle scattering this can be expanded to obtain

$$-\frac{\partial}{\partial\underline{v}}(f_k\langle\nabla\underline{v}\rangle) - \frac{1}{2}\frac{\partial^2}{\partial\underline{v}\partial\underline{v}}(f\langle\Delta\underline{v}\Delta\underline{v}\ldots$$

8.5.1(a) Motion in a Steady and Uniform Magnetic Field

In the absence of an electric field the acceleration imparted by the Lorentz force

$$F_L = \frac{e}{m}(\underline{B}\wedge\underline{v}) = \underline{w}\wedge\underline{v}$$

since the charge e on the electron is negative the vector $\underline{w} = -e/m\,\underline{B}$ is parallel to $\underline{B}$ and Eqn 1 becomes after some algebra

$$\underline{v}\cdot\nabla_r nf_k + \frac{e_k}{m_k}\frac{1}{c}\frac{\partial}{\partial r}(\underline{w}\wedge n\underline{f}_1) + \nu nf_1 = 0$$

where n is the number density of particles and ν is the effective cross section for momentum transfer.

The first task is to write down an expression for the function $\underline{f}_1(v)$. The loss of momentum through inelastic encounters (when $v < v_{in}$) is given by

$$(\tfrac{4}{3}\pi n v^3 dv)\, mf_1(v)\, Nvq_{in}\cdot I(v - v_{in})$$

where q_{in} is the inelastic scattering cross section, hence the total collision cross section is $q_{in}(v).I(v - v_{in})$ where I is a unit step function. When several forms j of inelastic encounters are active the net loss of momentum is

$$\nu(v)n = \nu_{el}(v) + \sum_j \{\nu'_{oj_{in}}(v).I(v - v_{in}) - Nc_{ij}q_{ij}(v_{ij})\frac{v_{ij}}{v}\frac{f_1(v_{ij})}{f_1(v)}\}$$

and

$$\nu'_{oj_{in}}(v) = Nc\, q_{oj_{in}}(v)$$

$\nu(v)$ thus appears as an apparent collision frequency. This summation is in fact a double summation where the index should range over j and k, the number of gas species being considered.

The complete vector equation for the electron motion can thus be written as

$$v\nabla_r(nf_k) + \frac{e_k}{m_k}\frac{\partial}{c\partial v}(\underline{w}\wedge n\underline{f}_1) =$$

$$-Nv\{q_{in\ el}(v) + \sum_j q_{oj_{in}}(v).\ I(v - v_{jin}) + q_{o_{in}}(v)\}uf_1(v)$$

$$+ N\{\sum_k\left[\frac{c_{1k}^2}{v}q_{1k_{in}}(v_{1k})n\underline{f}_1(v_{1k})\right.$$

$$\left. + (\frac{c_{2k}}{v})^2 q_{1k_s}(v_{2k})\ n\underline{f}_1(v_{2k}).I(v - v_{in})\right]\}$$

This equation is solved by transferring it to a finite difference equation and solving by a progressive iterative procedure.

8.5.1(b) Energy Loss Mechanism

The treatment of energy loss follows the basic theory of Bethe where collisional energy loss due to excitation (not completely treated) and ionization are considered. The basic assumptions made in the Continuous slowing down approximation (C.S.D.A.) are embraced such that $(\partial v/\partial r) = (\partial r/\partial v)^{-1}$ together with the further refinements for the relativistic treatment introduced by Rohrlich and Carlson (8.46). The energy loss Δv is then written as

$$\frac{\Delta E}{\Delta\underline{v}} = 7.88 + 10^4\psi(E).\ P\sum_k\{C_k\frac{Z_k}{A_k}(0.154 + \ln\frac{E}{E_k})\}$$

where C_k is the species weighting factor and I_k the mean ionization energy. The approximations introduced by the C.S.D.A. approach are allowed for using the Spencer-Fano (8.47) correction.

$$\simeq k\{1 + \ln(4\ E(\frac{E_o - E}{I_k^2}) + \ln(\frac{E_o}{E})\}^{-1}$$

In this code correction for the electron range straggling are carried out by a Monte-Carlo (8.48) technique as will be outlined in the next section.

8.5.1(c) The Treatment of Electron Scattering

The standard treatment of multiple scattering makes use of the linear scattering probability,

$$\lambda(S)^{-1} = \pi N \int_o^{\pi} \sigma(\alpha_1 S)(1 - \cos\alpha)\sin\alpha d\alpha.$$

which can lead to large errors for large scattering angles. In the scaler approach to the Boltzman equation the scattering term takes the form $\lambda(S)^{-1}.\nabla v^2(f_k)$ which tends to make the angular distribution isotropic at large distances thus over-emphasising the small angle scatter contribution. This treatment also provides a poor representation of large angle scattering particularly very early on in the calculation where single encounters play a significant role. In the Bethe approximation

$$\lambda(S)^{-1} = 9.84 \times 10^3 \frac{Z^2}{A\ E^2} \int_o^{\pi} (1 - F)(1 - \cos\alpha)d\alpha$$

where $F(\alpha) = (f/Z)$ is the scattering parameter. Using the Thomas Fermi model F is a function of the form $\{\text{Sin } \alpha/2/\lambda\}Z^{-1/3}$.

In the present work a Monte-Carlo approach (8.47) is adopted both for the scattering treatment and for the range straggling discussed above. The approach adopted in both areas is deterministic, in the latter case the random number generator operates within a generalized Gaussian distribution whilst in the latter case the Bethe multiple scattering angular distribution correlation (which is a function of the range energy) provides the folding envelope. An outline of this technique only will be given.

It $P(\vec{x})$ is the function that we wish to calculate in the Monte Carlo simulation we consider the variance of the function $f(\vec{x})$ defined by

$$\mu = \int P(\vec{x})\ f(\vec{x})\ d^n = \int f(\vec{x})dp$$

In this formulism $P(\vec{x})$ is known as the weight function with the properties

$$\left.\begin{aligned} P(\vec{x}) &\geq 0 \\ \int P(\vec{x})\ d^n x &= 1 \end{aligned}\right\}$$

$dp = P(\vec{x})\ d^n x$ represents the probability that a point is to be found within the range $d^n x$ at a, e.g. sometimes $P(\vec{x}) = 1/v = \text{const} = \text{volume of integration}$. We require a random point generator which generates a set $\{x_1\ x_2\ x_3 - - - - x_n\}$ such that the probability dp of finding a point within the range $d^n x$ at $\vec{x}$ is $P(\vec{x})d^n x$.

Consider the two statistics S_1 and S_2 formed from N points drawn from the random point generator. This we can write explicitly

$$S_1 = \frac{1}{N}\sum_{i=1}^{N} f(\vec{x}_i)$$

$$S_2 = \frac{1}{N-1}\{\frac{1}{N}\sum_{i=1}^{N} f^2(\vec{x}_i) - (\frac{1}{N}\sum_{i=1}^{N} f(\vec{x}))^2\}$$

$$= \frac{1}{N-1}\{\frac{1}{N}\sum_{i=1}^{N} f^2(\vec{x}_j) - S_1^2\}$$

We also define the variance of $f(\vec{x})$ by:

$$\sigma^2 = \int (f(\vec{x}) - \mu)^2\ P(\vec{x})\, d^n x = \int f^2(\vec{x}).\ P(\vec{x})\ d^n x - \mu^2$$

The expectation values are then

$$\langle S_1\rangle = \frac{1}{N}\sum_{i=1}^{N}\langle f(x)\rangle = \langle f(x)\rangle = \int f(\vec{x}).\ P(\vec{x})d^2x$$

$$\langle (S_1 - \mu)^2\rangle = \langle S_1^2\rangle - \mu^2 = \frac{1}{N^2}\sum_{i,\ j=1}^{N}\langle f(\vec{x}_i)\rangle - \mu^2$$

$$= \frac{1}{N^2}\{N\langle f^2(x)\rangle + N(N-1)\langle f(x)\rangle^2\} - \mu^2 = \sigma^2/N$$

$$\langle S_2\rangle = \frac{1}{N-1}\{\frac{1}{N}\sum_{i=1}^{N}\langle f^2(x_i)\rangle - \langle S_1^2\rangle\} = \frac{1}{N-1}\{\mu^2 + \sigma^2 - \langle S_1^2\rangle\} = \sigma^2/N$$

The distribution S_1 has a mean μ and a standard deviation $\sigma/\sqrt{N}$. Thus we can describe the function f(x) in terms of the statistical properties of a set of N random point numbers. It is not intended to deal with the truncation errors associated with such a set of numbers here.

As an illustration of this technique the function F discussed previously is calculated over a range of angles and compared with other approximations (Figure 8.26).

8.5.1(d) Comparison of Results

Some preliminary comparisons of the results obtained with the code with other published work, for example, the NRL code, TEP, have been very encouraging and show close agreement. For these comparisons the magnetic field terms in this code were 'switched off' and also the code was limited to one dimension. With these restrictions several comparative runs were carried out on a range of gases which have been selected and displayed in such a way that immediate comparisons can be made. Figures 8.27 and 8.29 show the energy deposition at beam energies of 200 keV and 300 keV, with similar results taken from the TEP code Figures 8.28 and 8.30.

8.6 Laser Optics

8.6.1 Diffraction Propagation Code

The code described here is designed to follow the passage of a laser pulse through a system of components which make up a laser chain. Basically, the time-independent Helmholtz equation is solved for a system of active and passive components, the equation being modified to take into account the non-linear behaviour of the laser material. Both non-linear refraction effects, large scale phase distortion and small scale filamentation are accounted for. The model is made more physical by taking into account non-uniform pumping and saturation within the rod or disc amplifiers. The program architecture is based on the OLYMPIAN format to facilitate future modifications and extensions.

Pulse propagation studies can be undertaken with the code, the positioning of laser components can be optimized and the beam quality on target assessed. Spacial filtering and image relaying techniques can also be carried out.

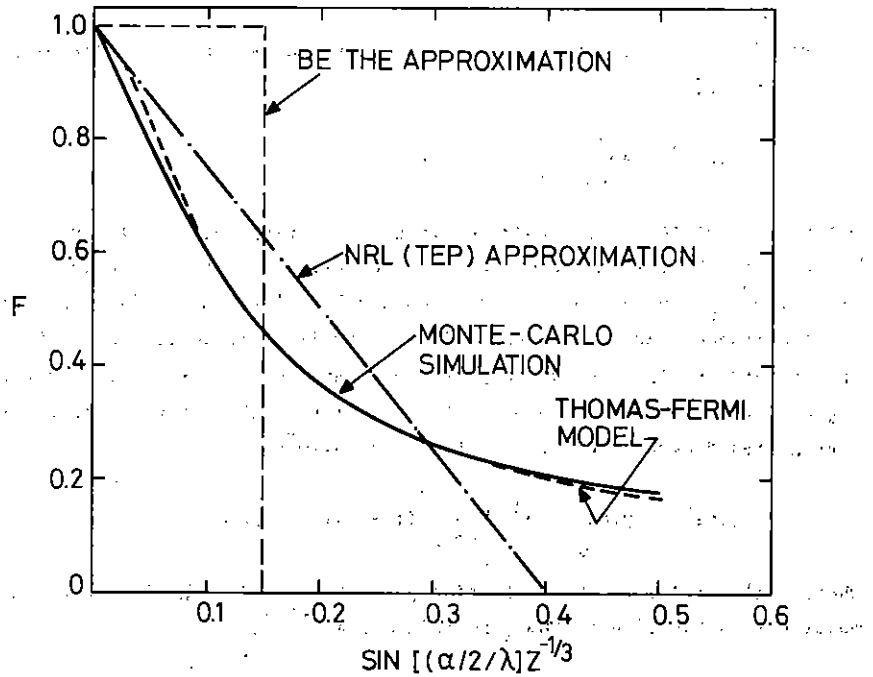

Fig.8.26

Function F calculated over a range of angles and compared with other approximations.

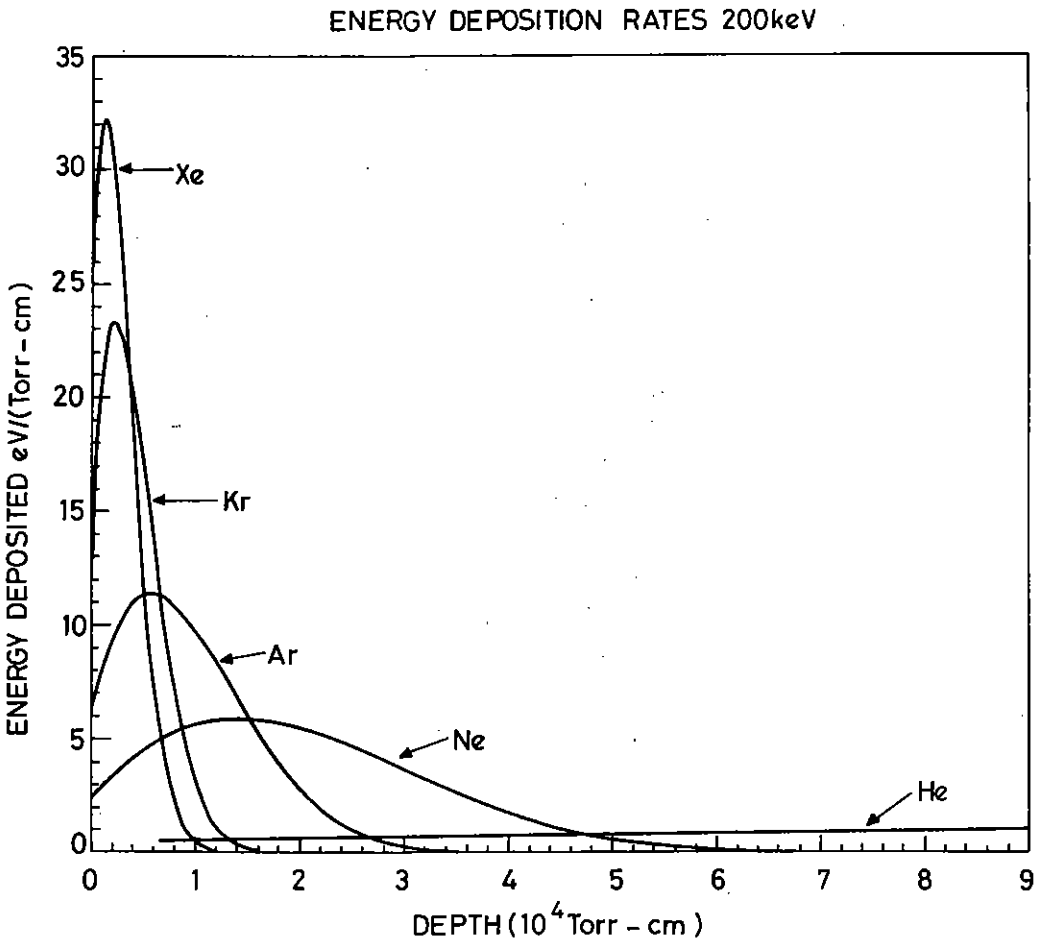

Fig.8.27

Calculated energy deposition as a function of gas target depth for 200 keV electron beam (Rutherford Laboratory code).

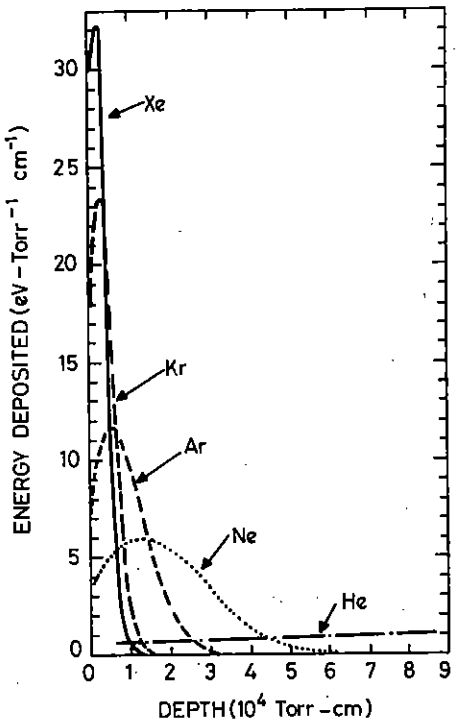

Fig.8.28

Calculated deposited energy as a function of depth for a 200 keV incident electron.

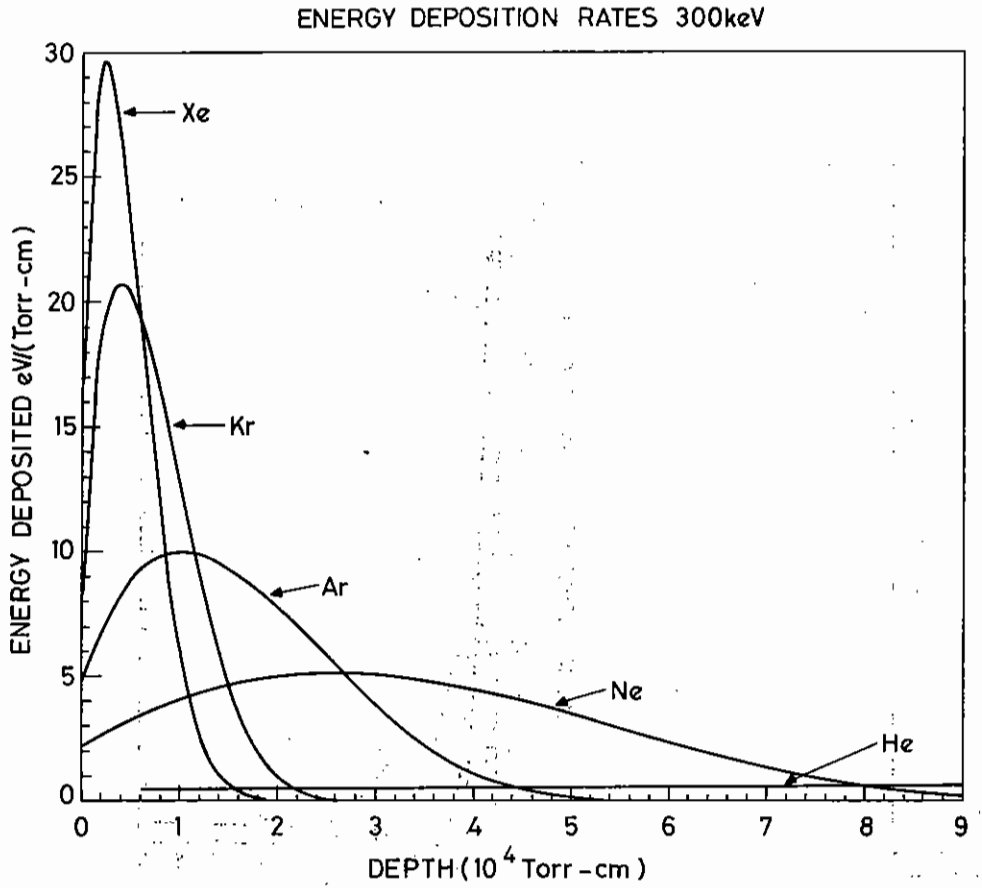

Fig.8.29

Calculated energy deposition as a function of gas target depth for 300 keV electron beam (Rutherford Laboratory code).

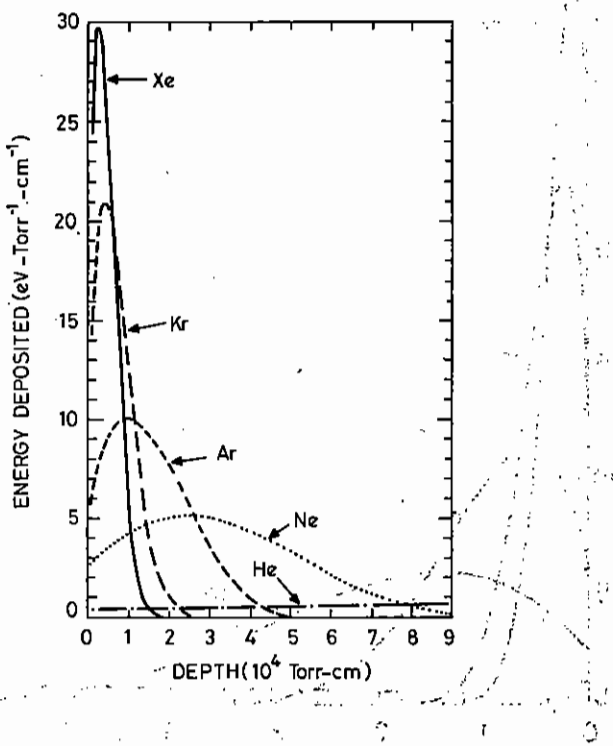

Fig.8.30

Calculated deposited energy as a function of depth for a 300 keV incident electron.

If we take the time dependent form of a propagating EM wave as $\underline{E}(r_1 t) = \text{Re}\ \tilde{\underline{E}}\ e^{-iwt}$ and substitute it into the wave equation

$$\nabla^2 \underline{E} - \frac{1}{v^2} \frac{\partial^2 \underline{E}}{\partial t^2} = 0$$

we can quickly derive the time-independent wave equation or the Helmholtz equation

$$\nabla^2 \tilde{\underline{E}} + k^2 \tilde{\underline{E}} = 0 \qquad (1)$$

with $k = {}^{2\pi}/_{\lambda} = {}^{2\pi n}/_{\lambda_o}$. It can be shown that $E = Ae^{i\phi} e^{-i\ \underline{k}.\underline{r}} = \tilde{A} e^{i\ \underline{k}.\underline{r}}$ is a proper solution of equation (1) that represents the spatial part of a plane wave propagating in the direction of the $\underline{k}$ vector and $\tilde{A}$ being a complex amplitude. Considering in particular a wave in cylindrical geometry propagation in the z direction equation (1) becomes

$$\frac{1}{r} \frac{\partial}{\partial r} \left(r \frac{\partial \tilde{E}}{\partial r}\right) + \frac{1}{r^2} \frac{\partial^2 \tilde{E}}{\partial \theta^2} + \frac{\partial^2 E}{\partial Z^2} + k^2 \tilde{E} = 0 \qquad (2)$$

with

$$\tilde{E} = Ae^{i\phi} e^{-ikz} = \tilde{A} e^{ikz}$$

Equation (2) then becomes (for a cylindrically symmetric system and neglecting $\partial^2 E/\partial Z^2$)

$$\frac{1}{r} \frac{\partial}{\partial r} \left(r \frac{\partial \tilde{A}}{\partial r}\right) + 2ik \frac{\partial \tilde{A}}{\partial Z} = 0$$

This equation if solved numerically with A specified on a radial mesh and advanced in Z: it forms the basic equation for the transport of the EM wave through the various components in the Laser chain.

Other components are treated as follows: All lenses are treated as thin lenses introducing a phase change of $(\pi r^2/f\lambda)$ into the wavefront aberation. For stops A = 0 for $r > r_o$ and apodizers are treated as modifying A to A $F(r/r_o)$ where $F(r/r_o)$ is specified across the radial mesh. Spatial filters are dealt with by a Fourier transform of the entrance pupil radial profile (OTF). Unpumped rods, Faraday rotators, beam-splitters etc. are treated as passive components but their non-linear contribution to the B

integral is taken into account as is the small scale self focussing. Eqn (3) therefore becomes modified to

$$2ik \frac{\partial \tilde{A}}{\partial Z} + \frac{1}{r} \left(r \frac{\partial \tilde{A}}{\partial r}\right) + r|\tilde{A}|^2 . \tilde{A} = 0 \qquad (4)$$

A pumped amplifier is treated as an active element. The basic equations relating P the power/unit area and α the amplifier gain/unit length are

$$\frac{\partial P}{\partial Z} = \alpha \underline{P}\ , \quad \frac{\partial \alpha}{\partial \tau} = -\beta \alpha \underline{P} \qquad (5)$$

where τ is the time coordinate of the beam pulse. We can therefore define a general pumping function $F(r,\tau)$ so that we can take into account such effects as non uniform pumping of the amplifiers and modify equation (4) as follows

$$\frac{1}{r} \frac{\partial}{\partial r} \left(r \frac{\partial \tilde{A}}{\partial Z}\right) + 2ik \frac{\partial \tilde{A}}{\partial Z} + r|\tilde{A}|^2 . \tilde{A} = 2ik . F(r,\tau) . \tilde{A} \qquad (6)$$

For the Nd/glass laser we can take a fairly simple model for the function $F(r,t)$ since we can write for β in equation (5) when dealing with a well resolved four level laser whose cover level decays slowly $\beta = ({}^{2\sigma}/_{h\nu})$ where σ is the $^4I_{11/2}$ which has a relaxation time $\tilde{}$ 65 nsec. The available stored energy in the system is then (α/β). The laser pulse is sliced up into a number of time steps and equations (5) are integrated over the pulse length at each mesh of equation (6). To take account of the possible complete depletion of the amplifier element, the increment in P is used to calculate the energy required by each time element. If the stored energy is insufficient to provide this then only the amount available is allowed to increment P, thus allowing for saturation.

8.6.2 Optical Design

The optical design codes developed at the Rutherford Laboratory have been used extensively in the design of specialized components for the Laser facility. Two such components will be described here: the first, a diffraction limited F/5 doublet designed primarily for operation at 1.06μm but which again has the capability of being ajusted for operation over a wide wavelength range, and the second a fast F/1.5 spherical doublet. This latter lens, which is simple and cheap to build was originally designed

as a 'back-up' for the F/1.0 aspheric in the laser focussing system.

8.6.2(a) Diffraction Limited F/5 Objective

The primary criterion placed on the design of this lens is that it should be as near diffraction limit as possible at F/5 and full aperture at 1.06 μm. Figure 8.31 shows the lens in its mount; Figure 8.32 gives details of its design. The lens is primarily corrected for spherical aberation and has a spot size (circle of least confusion) diameter of 1.8 μm. Tests on the lens carried out on a Zigo interferometer substantiate these calculations. The field angle for this lens is 0.35°.

8.6.2(b) Back-up Optics for the Rutherford Six-Beam System

The final aspheric focussing lenses are near the critical path for the six beam target irradiation system now under construction. It would therefore seem reasonable to consider the merits an alternative system (this might be used during an interim period or during some fault situation) which would involve the use of spherical lens components only. These would be manufactured using standard techniques and therefore capable of being produced by a number of firms which might not consider manufacturing our f/1 aspheric lenses.

We have looked at the designs of four spherical lenses ranging from f/5 to about f/2 based on the doublet design discussed previously. As we have seen the f/5 lens can be made diffraction limited with a fairly close tolerance placed on the first of the concave surfaces. The f/4 lens designed also operates just above its diffraction limit and is very similar in manufacturing difficulty, etc. to the f/5. The f/3 and f/2 lenses considered cannot be made on this design principle to be diffraction limited but focal spot sizes small enough to provide useful irradiance of the target can be produced.

The important feature to bear in mind in designing such focussing systems is however, shown in Figure 8.33. Here we have considered the natural divergence of the laser beam and folded this with the minimum spot size of the various lenses. Assuming a 100 μrad, uncorrectable divergence for the laser beam, a diffraction limited f/1 lens will produce a spot size of

around 10 μm. The spot size due to this uncorrectable divergence for the various spherical lenses that we have considered are plotted against the f number and increase monotonically. The minimum focal spot obtainable from the doublet lenses is also shown on the second curve. An optimum can be seen to occur somewhere around f/2.1 - f/2.2 beyond which there is little point in trying to decrease the focal spot obtainable from such a lens based purely on these considerations. The last statement above should be qualified somewhat since alignment problems are eased considerably if one can resolve the 1.5 μm - 2 μm stalk supporting the microsphere targets. The lens design finally chosen is the f/2.5 lens shown in Figure 8.34 with a second meniscus component. Although an f/2.5 lens (similar in design to the f/5 doublet) has almost the same focussing properties, the lens shown in Figure 8.34 has a larger field angle and smaller coma content making it easier to align in practice.

Taking this f/2.5 lens as an example, the lens would fit into the present mounting and adjustment cone which has been designed for the six-beam chamber. The lens could be back spaced on a series of adjusting stalks and would be controlled by the same pointing and moving mechanisms.

Obviously using larger f number lenses, the angle of incidence for the marginal rays is increased at the target surface and the distribution of illumination around the target would also be somewhat affected. We have therefore calculated distribution of illumination for the f/2.5, f/4 and f/5 lens and we show them in Figure 8.35 and 8.36.

Assuming we would not want the marginal ray angle to exceed about 50° because of the decreasing absorption the loss in uniformity is from about 0.75 with the f/1 aspherics to about 0.45 with the f/2.3 spherical lenses. Crudely speaking the performance is half as good as the f/1 system and would be adequate for many types of target which are intermediate between the exploding pusher and true ablative compression. It could be arranged that the f/2.5 system could be used to examine the sensitivity of various targets to illumination symmetry since it is difficult to set up the six aspheric lenses for a controlled non-uniformity of less than about 0.5 because the focal spots no longer overlap.

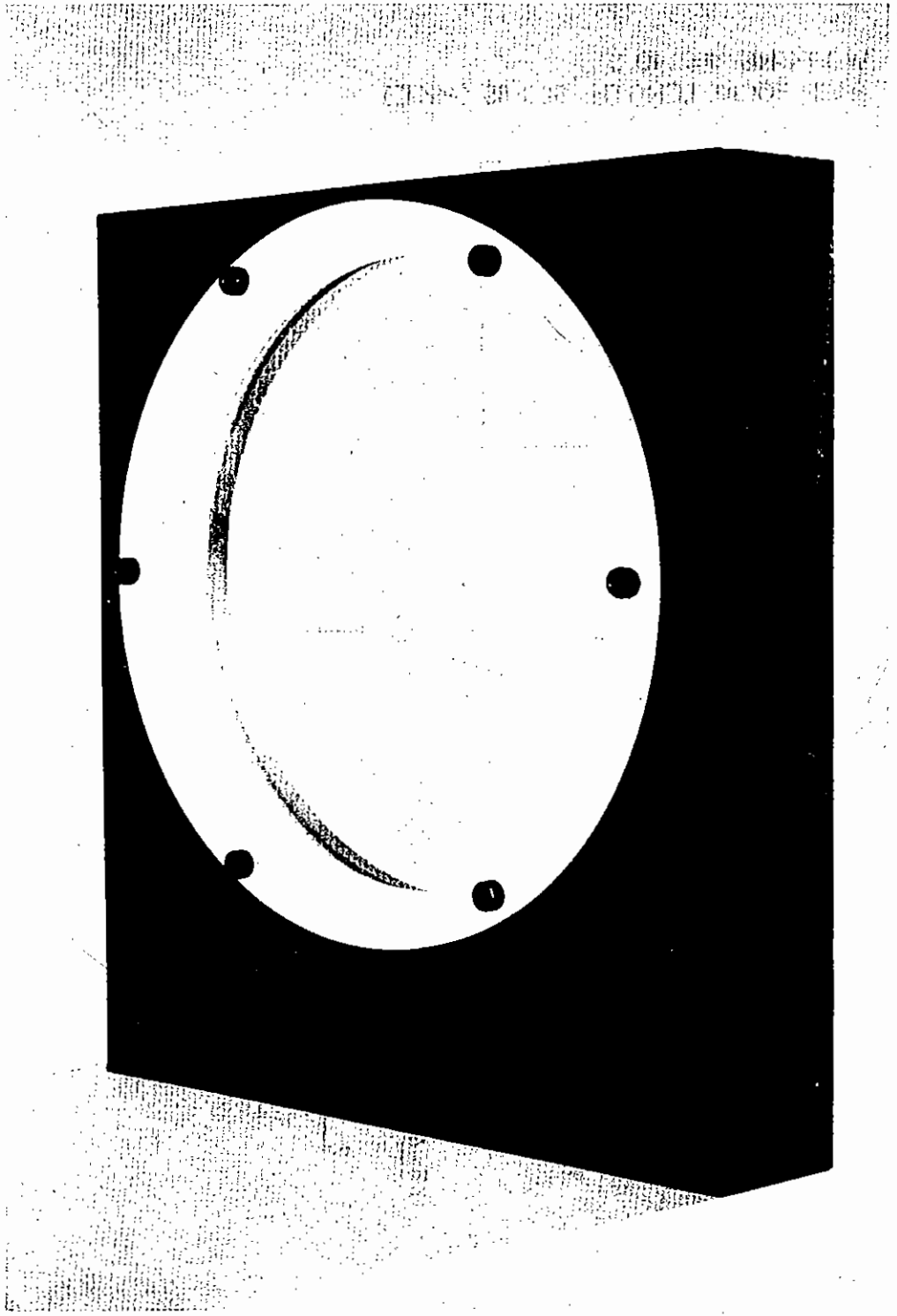

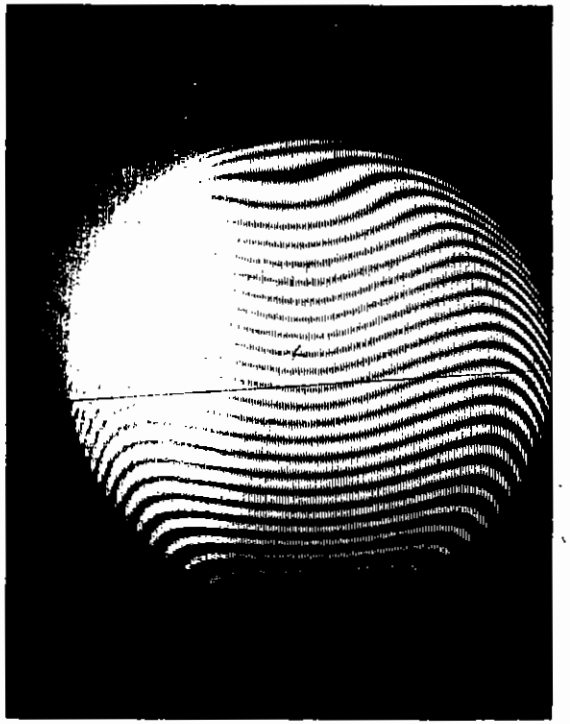

Fig.8.31

Photograph of lens and fringe pattern on Zigo.

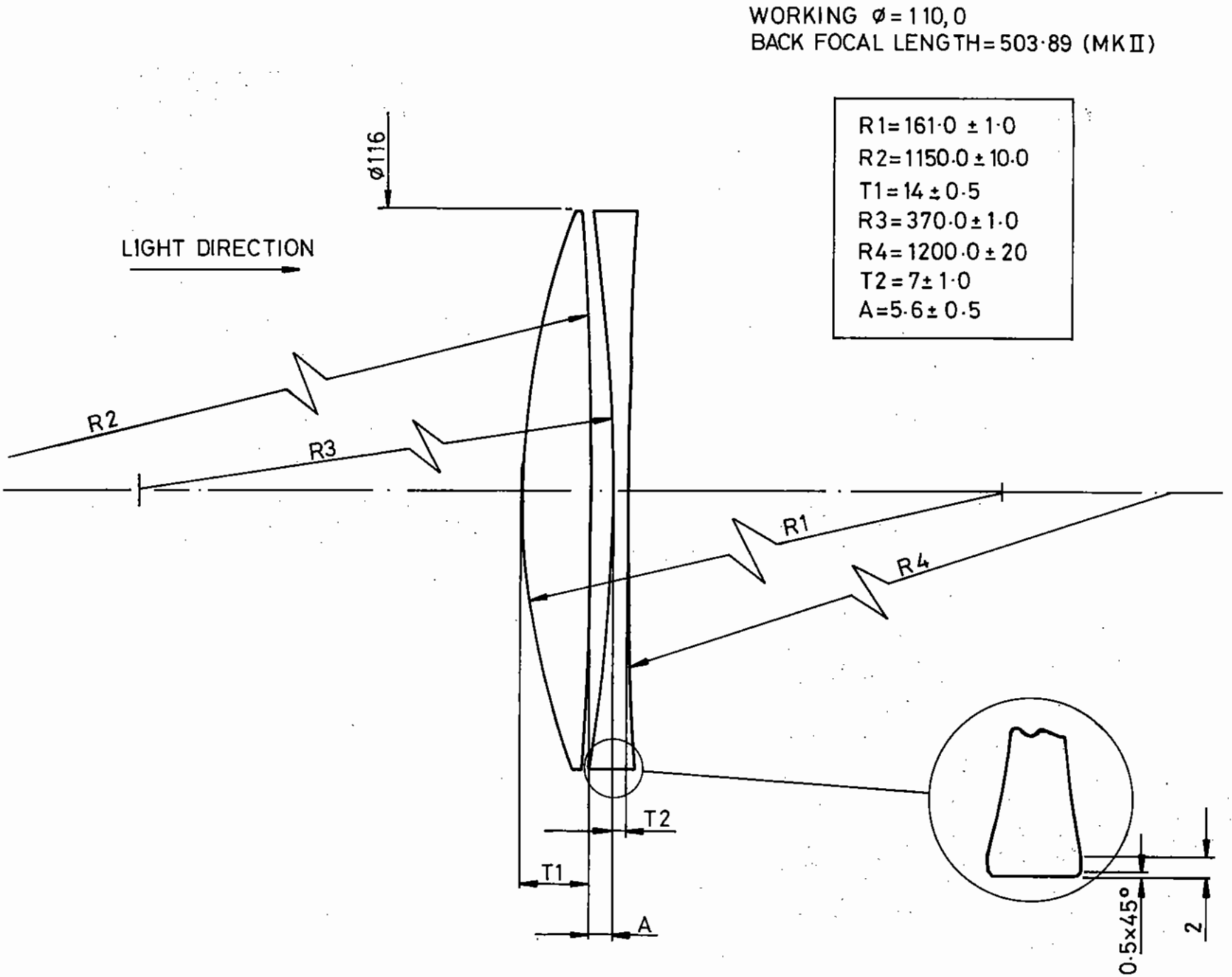

Fig.8.32

Design details of F/5 spherical doublet.

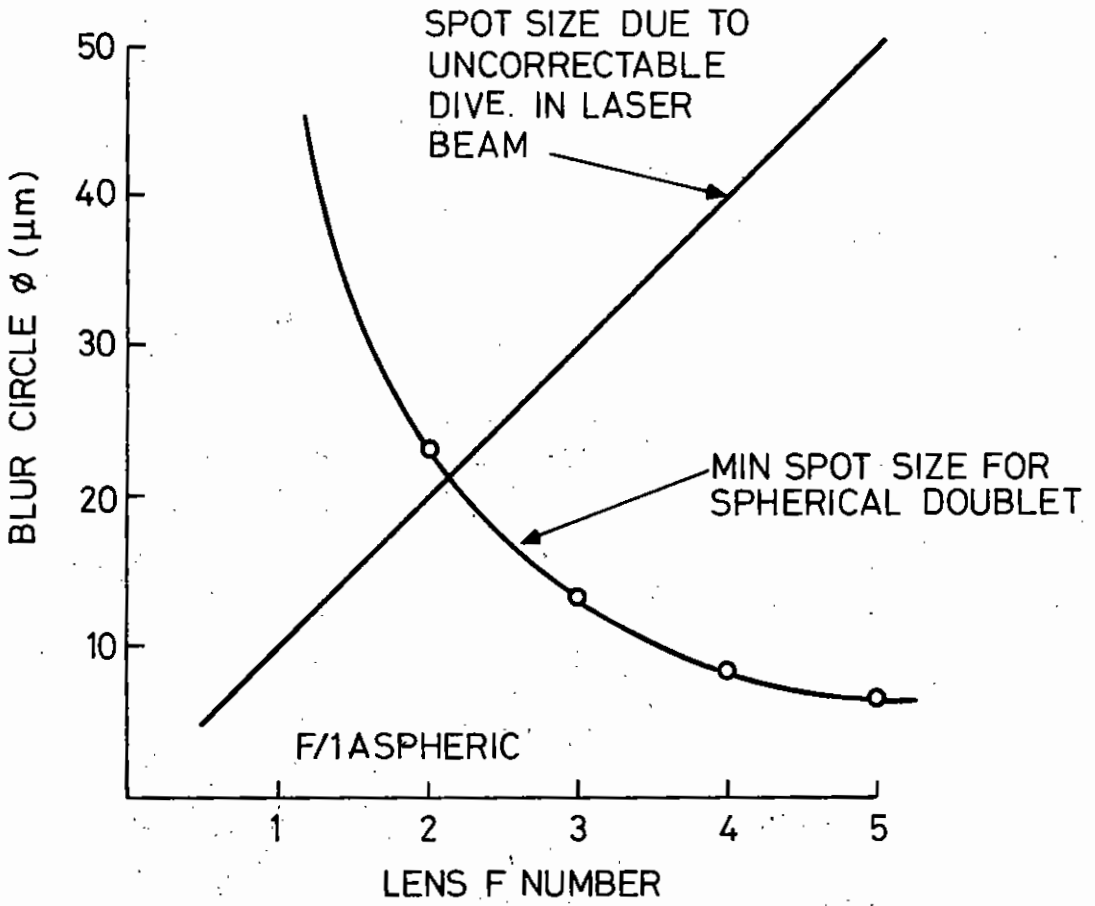

Fig.8.33

A criterion for minimum lens performance.

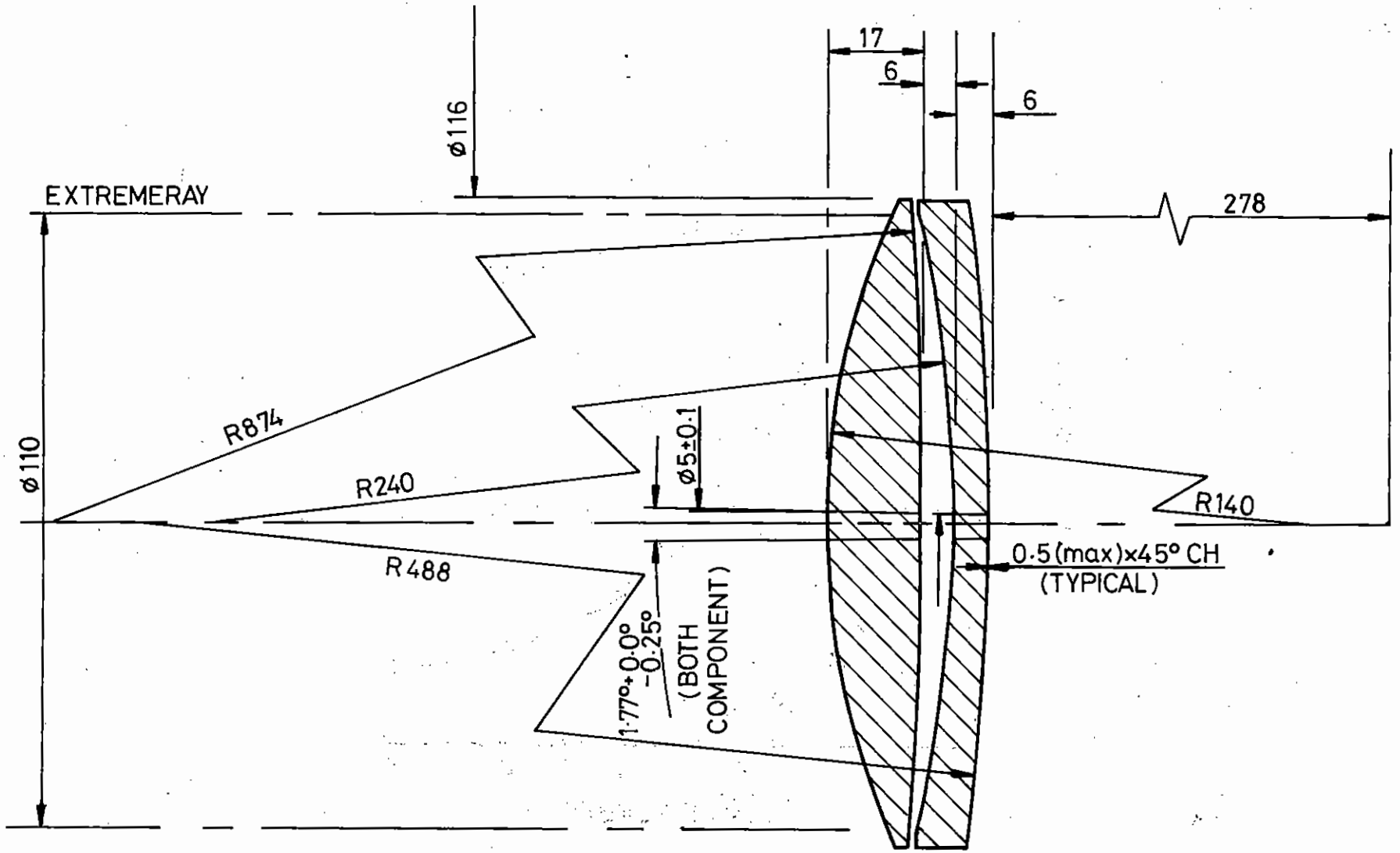

F/2·5 SPHERICAL LENS DOUBLET.

Fig.8.34

Design details of F/2.5 spherical doublet

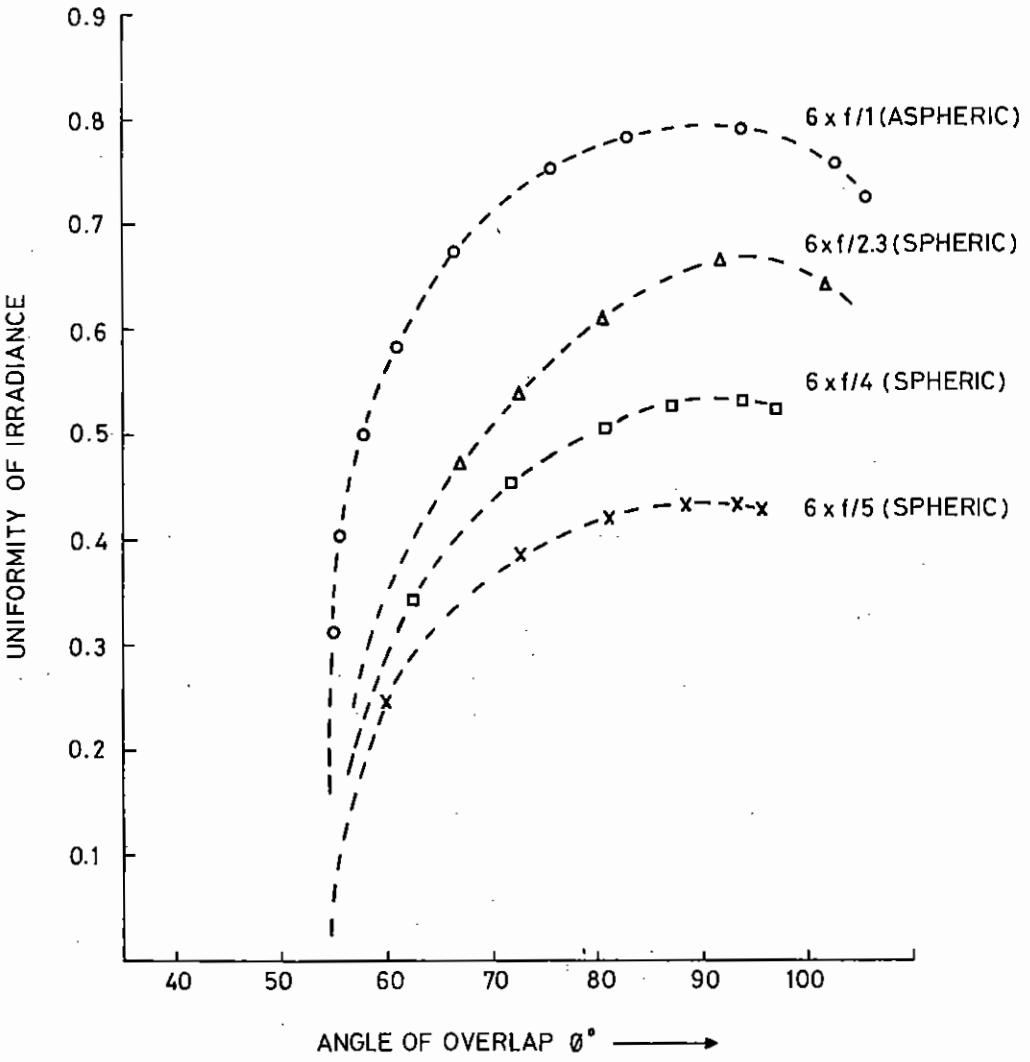

Fig.8.35

Uniformity of target irradiance.

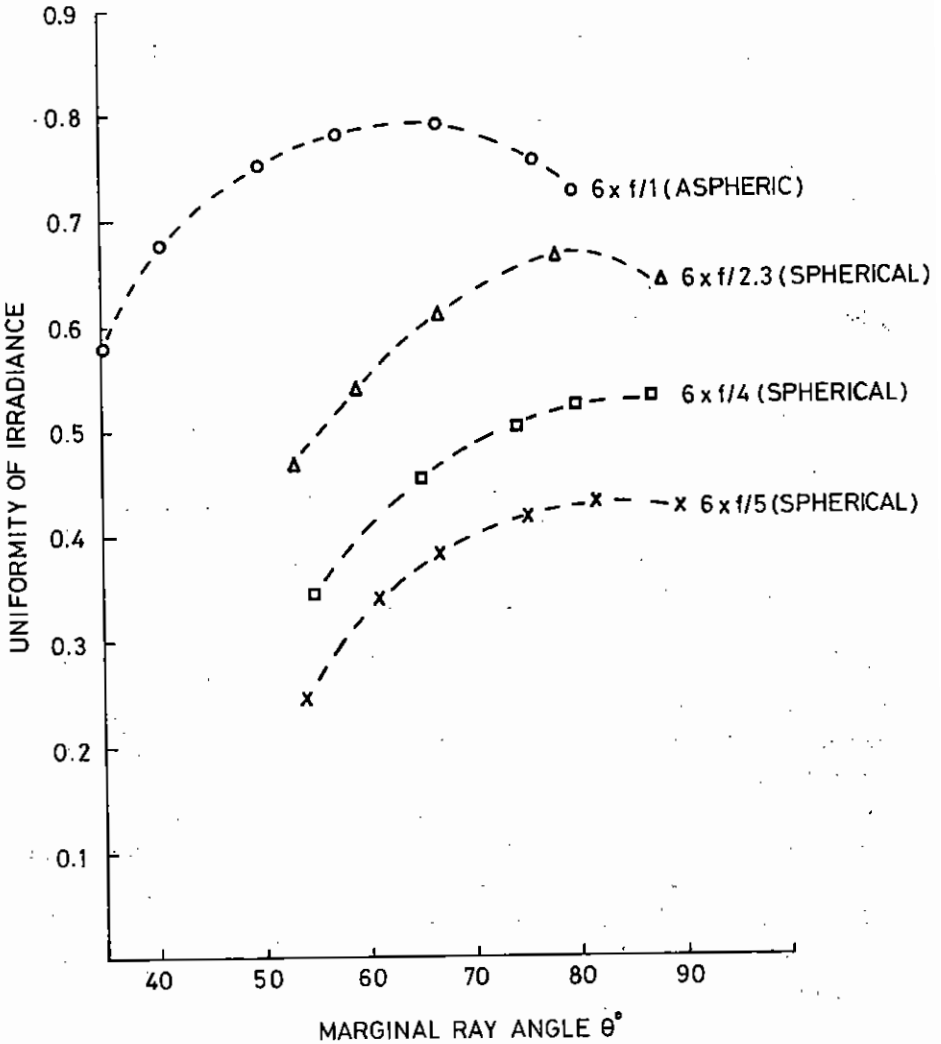

Fig.8.36

Uniformity of target irradiance V5 marginal ray angle.

8.7 Heavy Ion Fusion

8.7.1 Target Design for Heavy Ion Fusion

Following the Coseners' House meeting on Heavy Ion Fusion on 16 June 1978 a small working party on target design studies was set up, having its inaugral meeting in November 1978. The membership of this group is drawn from the Universitis of Birmingham, Glasgow, Strathclyde, Queen Mary College, London, and the Rutherford Laboratory. The initial strategy has been to adopt the 1-D hydrodynamic code MEDUSA to heavy ion work and to identify those areas of physics which require a detailed understanding for target design. The following topics have been given particular attention.

8.7.1(a) The Energy Deposition Process

This occurs predominantly through binary Coulomb interactions between the incident ion ($120 \leq A \leq 238$, 1 GeV $\leq E \leq$ 20 GeV) and the electrons in the outer shell of the spherical target. At present, classical descriptions of this process are deemed sufficient. Nuclear fragmentation effects can be shown to contribute insignificantly to the total energy deposited. More important is the effect on the radial distribution of the energy deposition that a multiple-beam geometry imposes. We illustrate this in Figure 8.37. If the ion beam is uniformly radially convergent on the target, the energy deposition profile is that shown in Figure 8.37a. The Bragg peak in the dE/dx curve contains the bulk of the deposited energy and it is at this point that the thermal shock originates. A more realistic illumination geometry is that shown in Figure 8.37b where a target is symmetrically bombarded by six beams even wider than the target. If we examine the energy deposition distribution in a diametrical plane containing any 4 of the 6 beam vectors, we obtain a multiple-Bragg effect, as seen in Figure 8.37b. This effect is spatially-averaged in the MEDUSA treatment to provide a wide effective Bragg peak.

8.7.1(b) Bremsstrahlung Effects

Prior to a plasma in-depth study of bremsstrahlumg emission and absorption in large H.I. fusion targets, a crude model for re-absorption has been developed. A spectrum-averaged effective photon absorption cross section is defined which gives a low temperature energy balance consistent with black body radiation. The effects of energy transport via re-absorption

can now be estimated.

8.7.1(c) Neutron Heating

About an MeV of the 14 MeV thermonuclear neutron energy can be transferred to the D^+ and T^+ ions during the highly compressed ($\rho R \sim 1$-$3\ gcm^{-2}$) burn stage, providing additional bootstrap heating in the cold plasma. Unlike the α-heating the neutron heating is relatively uniform. Effects on the hydrodynamics and neutron yield of the slowing down times of the 6-7 MeV recoil D^+ and T^+ ions have been shown to be negligible.

8.7.1(d) Alpha-Particle Heating

In the original version of MEDUSA all α's were considered to lose their energy locally. Modifications to the code now allow the α's to deposit their energy according to the appropriate dE/dx values for the density and temperature of the plasma.

8.7.1(e) Spectra of Recoil Electrons by Heavy Ion Interaction

A series of calculations of the energy (angle) distribution of recoil electrons have been under the following assumptions.

1) The Coulomb interactions are binary (no collective modes)
2) The heavy ions are fully stripped.

If $\Sigma(q)$ represents the differential Coulomb ion-electron scattering cross section for momentum exchange q, then $N(e_e)dE_e$, the density of electrons with energies between E_e, $E_e + dE_e$, produced per unit time per unit ion energy $E_I = \frac{1}{2}Mv_I^2$, is given by

$$N(E_e) = \frac{v_I}{hv_e}\ \Sigma(q).$$

$\Sigma(q)$ is evaluated via the Born approximation for a plasma at a finite temperature. The electrons are assumed at rest in order to compute the energy-angle (i.e. q, w) correlations. For our plasma at a temperature kT, this is valid approximation provided $\alpha >> 1$ where $\alpha^2 = M_e E_I / M_I E_e$. For example a 10 GeV ^{238}U ion will have lost 99.55% of its energy when

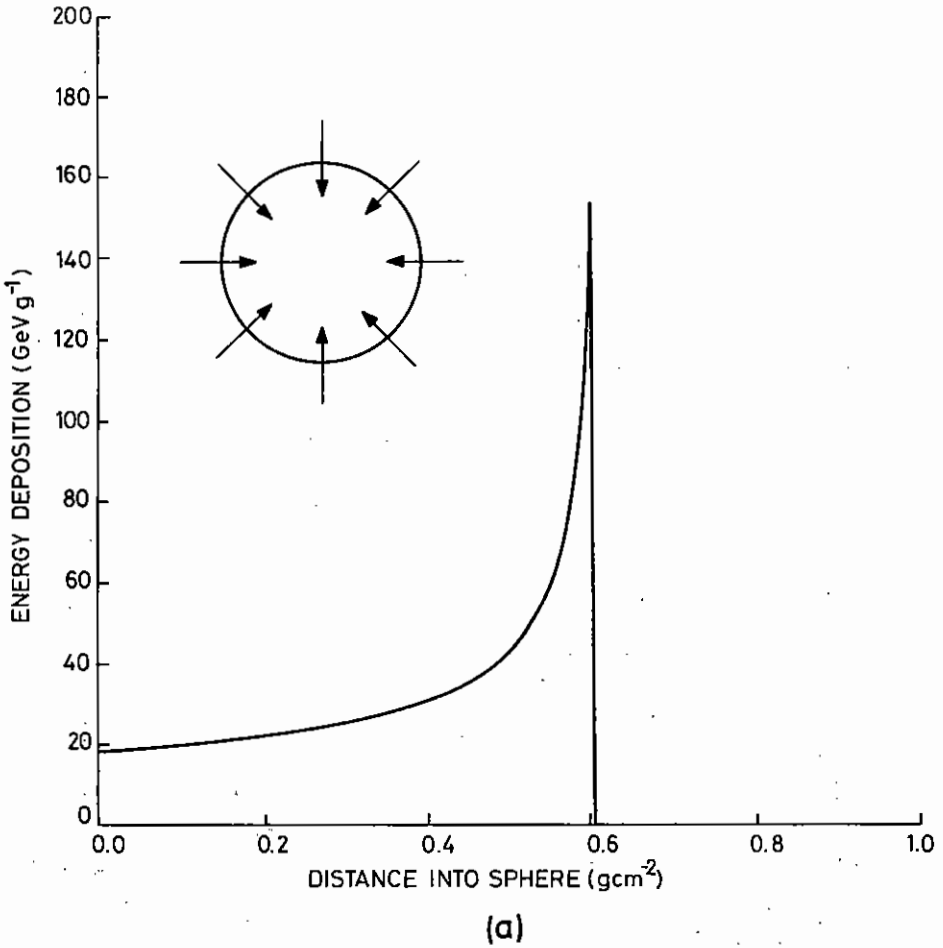

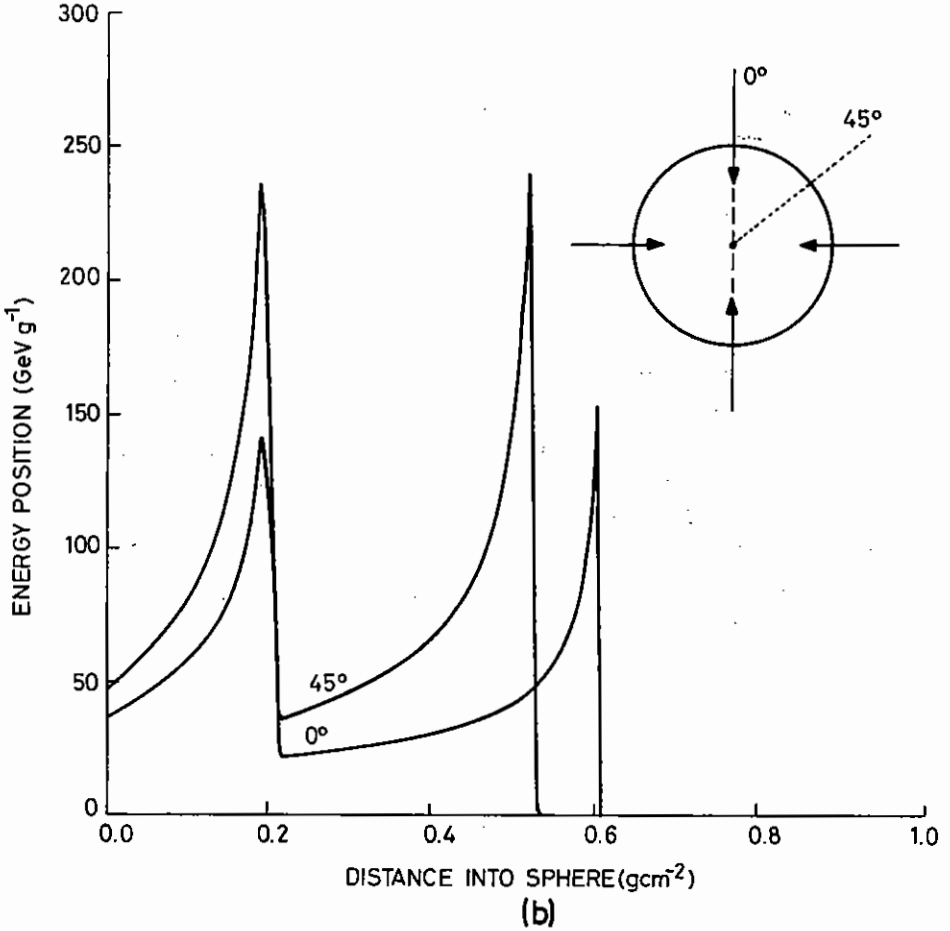

Fig.8.37

Energy deposition profiles for 20 GeV ^{238}V ions in the glass shell of a target; (a) profile for a uniformly radially convergent beam (b) profiles at the 0° and 45° directions for a symmetric 6-beam illumination.

$\alpha = 1$.

The Coulomb shielding has been evaluated in terms of the C-system minimum scattering angle as defined by Longmire which is then transformed to the L-system, again assuming zero electron motion.

A consistency check on the calculation is made via the relationship

$$\frac{1}{v_I} \int E_e N(E_e) dE_e = -\frac{dE}{dx}$$

where dE/dx is calculated separately.

Figure 8.38 shows a typical result for a 10 GeV ^{238}U ion. Note that the ratio ϕ/N will give $\overline{v}_e$.

Items (a) through (e) have now been encoded in MEDUSA and a series of studies have been made for single shell targets; outer radius of glass shell 2.5 mm, inner radius 1.5 mm, filled with solid deuterium and irradiated with 1-10 MJ of fully stripped 10 GeV ^{238}U ions. These studies indicate that the target gains (fusion energy/incident beam energy) are very sensitive to the modelling of bremsstrahlung processes and the alpha-particle energy deposition. Depending on the model assumptions, gains can vary by an order of magnitude.

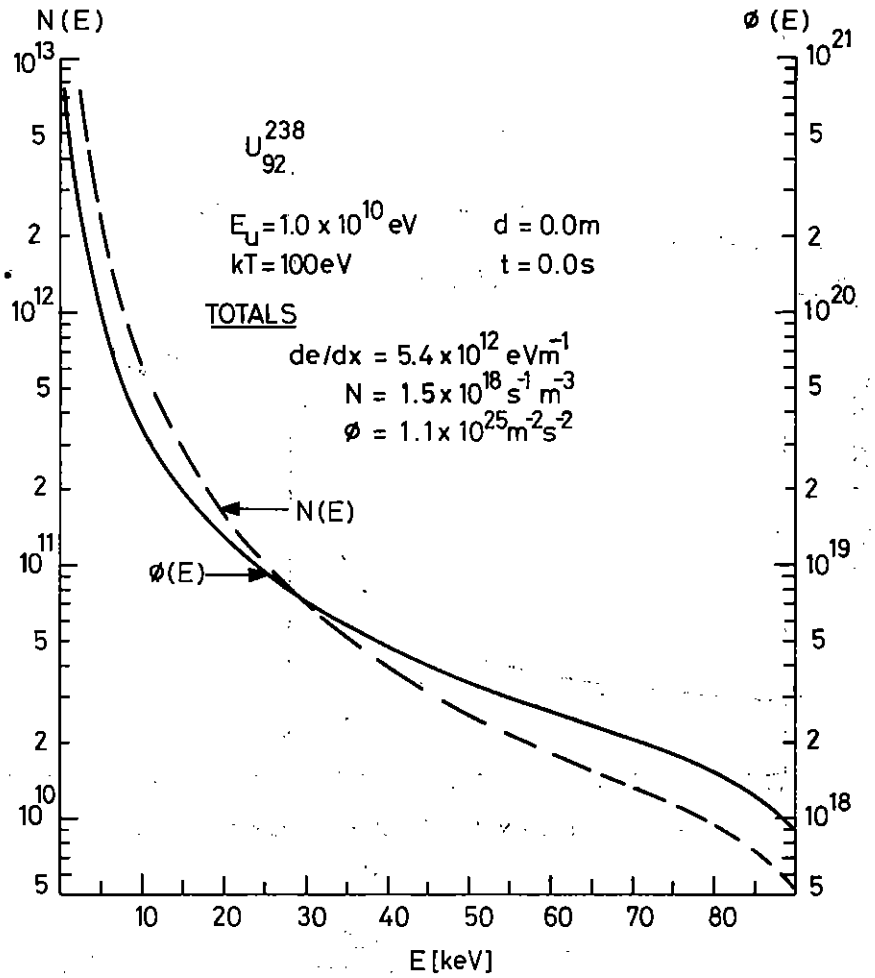

Fig.8.38

Spectra of electron density (N(E)), and flux ($v_e N(E)$) due to Coulomb scattering of heavy ions of density 1 m^{-3} and energy E in an electron plasma at temperature kT.

(Note, $N = \int_0^\infty N(E)dE, \phi = \int_0^\infty \phi(E)dE$)

CHAPTER 8 REFERENCES

8.01 J.P. Christiansen and N.K. Windsor, to be published in Comp. Phys. Comm.

8.02 S.I. Braginskii, Reviews of Plasma Physics, Editor M.A. Leontovich, Consultants Bureau, New York (1965).

8.03 A. Raven, O. Willi, and P.T. Rumsby, Phys. Rev. Lett. 41, 554 (1978).

8.04 J.P. Christiansen and N.K. Windsor, to be published in J. Comp. Phys.

8.05 Rutherford Laboratory Laser Division Report LD/78/04 - Annual Report to the Laser Facility Committee 1978.

8.06 R.A. Cairns, J. PLasma Phys., to be published.

8.07 R. Cano, I. Fidone and M.J. Schwartz, Phys. Rev. Lett. 27, 783 (1971)

8.08 T.J.M. Boyd and I. Fidone, Phys. Fluids 16, 427 (1973).

8.09 W.L. Kruer and K. Estabrook, Phys. Fluids 20, 1688 (1977).

8.10 W. Woo, K. Estabrook and J.S. De Groot, Phys. Rev. Lett. 40, 1094 (1978)

8.11 E.A. McLean et al., Appl. Phys. Lett. 31, 825 (1977).

8.12 C.S. Liu, M.N. Rosenbluth, Phys. Fluids, 19, 967 (1976)

8.13 H.H. Chen, C.S. Liu, Phys. Rev. Lett. 39, 881 (1977).

8.14 W. Woo and J.S. De Groot, Phys. Fluids 21, 2072 (1978).

8.15 T. Speziale and P.J. Catto, Phys. Fluids 21, 2063 (1978).

8.16 R.A. Cairns, Plasma Phys. 20, 991 (1978).

8.17 European Conf. on Laser-plasma interactions, (1977)

8.18 A.B. Langdon, B.F. Lasinski, Methods in Comp. Phys. 16, 327 (1976).

8.19 J.P. Christiansen, K.V. Roberts, Comp. Phys. Comm. 7, 245 (1974).

8.20 Lindman, J. Comp. Phys. 18, 66 (1975).

8.21 E.G. Corman, W.E. Loewe, G.E. Cooper, A.M. Winslow, Nuclear Fusion, 15, p377 (1975).

8.22 T.H. Dupree, Phys. Fluids 9, 1773 (1966).

8.23 J. Weinstock, Phys. Fluids 12, 1045 (1969).

8.24 R.S. Craxton, M.G. Haines, Plasma Phys. 20, 487 (1978).

8.25 J.P. Christiansen, D.E.T.F. Ashby and K.V. Roberts, Comp. Phys. Comm. 7, 271 (1974).

8.26 N.A. Tahir Ph.D. Thesis (1978) (Glasgow University).

8.27 Richtmyer and Morton, Difference Methods for Initial Value Problems, Wiley (1967).

8.28 Zel'dovich and Raizer, Physics of Shock Waves and High Temperature Hydrodynamic Phenomena, Academic Press (1967).

8.29 G.E. Bromage, 1978. SRC Appleton Laboratory Report AL-R3.

8.30 R.D. Cowan, J.O.S.A. 58, 808 (1968).

8.31 B. Yaakobi, D. Steel, E. Thorsos, A. Hauer, B. Perry, Phys. Rev. Lett. 39, 1526 (1977).

8.32 K. Grutzmacher and B. Wende, Phys. Rev. A. 16, 243 (1977).

8.33 D. Voslamber, Phys. Lett. 611, 27 (1977).
J. Seidel, Z. Naturforsch, 32a, 1207 (1977).
R. Lee, J. Phys. B. 11, L167 (1978).

8.34 R. Lee, J. Phys. B. (1978), in print.

8.35 B.W. Shore and D.H. Menzel, Principles of Atomic Spectra, (Wiley, New York, 1968).

8.36 Laser Program Annual Report - 1976, Lawrence Livermore Laboratory Report UCRL - 50021 - 76.

8.37 R.S. Tighe and C.F. Hooper, Phys. Rev. A. 14, 1514 (1976).

8.38 R. Lee, J. Phys. B. 6, 1044 (1973).

8.39 H.R. Griem, Spectral Line Broadening by Plasmas, (Academic, New York, 1974).

8.40 P.C. Kepple and H.R. Griem, NRL Memorandum Report 3634 (1978).
H.R. Griem, M. Blaha, and P.C. Kepple, Phys. Rev. A (1979) (To be published).

8.41 H. Gould and R. Marrus, Phys. Rev. Lett. 41, 1457 (1978).

8.42 A.V. Gurevich, L.V. Pariishaya and L.P. Pitaevskii, Zh. Eksp. Teor. Fez. 49, 647 (1965) (Sov. Phys. J ETP 22, 449 (1966)).
J.E. Allen and J.G. Andrews, J. Plasma Phys., 4, 187 (1970).
J.E. Crow, P.L. Auer and J.E. Allen, J. Plasma Phys. 14, 65 (1975).

8.43 L.M. Wickens, J.E. Allen and P.T. Rumsby, Phys. Rev. Lett., 41, 243 (1978).
L.M. Wickens and J.E. Allen - J. Plasma Phys. - in press.

8.44 B. Bezzerides, D.W. Forsland and E.L. Lindman, Phys. Fluids 21,

2179 (1978).

8.45 NRL Report No. 3084, July 1975.

8.46 F. Rohrlich and B.C. Carlson, Phys. Rev., 93, 38 (1954).

8.47 L.V. Spencer and V. Fano, Phys. Rev., 93, 1172 (1954).

8.48 J.M. Hammersley and D.C. Handscomb, Monte Carlo Methods, Methuen Monographs.

APPENDIX

CENTRAL LASER FACILITY PUBLICATIONS

RESEARCH PAPERS

T.J.M. Boyd, J.G. Turner
Three and Four Wave Interactions in Hot Plasma
J. Math. Phys. 19, 1403 (1978)

T.J.M. Boyd
Shock Waves in Collisionless Plasmas
Proc. XIth International Symposium on Shock Waves,
University of Washington Press, Seattle, 156 (1978)

T.J.M. Boyd, J.G. Turner
Soliton Formation in Magnetized Vlasov Plasmas
J. Plasma Phys. (in press)

G.E. Bromage, R.D. Cowan, B.C. Fawcett, A. Ridgeley
Classification of Be I-like and B I-like Iron and Vanadium Spectra from Laser-produced Plasmas
J. Opt. Soc. Am. 68, No. 1 pp 48 (1978)

G.E. Bromage et al
The Laser-produced Spectrum of Fe XVII to Fe XXI Below 18°A
Culham Laboratory Report CLM-R170 (1978)

D.D. Burgess
Spectroscopy of High Density Plasmas
Invited papers of Symposium on Physics of Ionized Gases
published by Institute of Physics, Beograd 1978 (in press)

D.D. Burgess
Recent Advances in Experimental Plasma Spectroscopy
Invited papers of Symposium on Physics of Ionized Gases
published by Institute of Physics, Beograd 1978 (in press)

R.A. Cairns
Resonant Absorption at a Rippled Critical Surface
Plasma Physics 20, 991 (1978)

P.D. Carter, S.M.L. Sim, H.C. Barr and R.G. Evans
Time Resolved Observations of the Three Halves Harmonic Spectra from Laser Produced Plasmas
Submitted to Phys. Rev. Letts.

P.D. Carter, S.M.L. Sim, T.P. Hughes
Time Resolved Spectroscopy of Second Harmonic Emission from Laser Irradiated Microballoons
Optics Communications 27, 423 (1978)

R.S. Craxton, M.G. Haines
J x B Acceleration of Fast Ions in Laser-Target Interactions
Plasma Physics 20, 487 (1978)

A.F. Gibson
High Power Pulsed Lasers
Phys. Technol 9, 72 (1978)

A.F. Gibson, M.H. Key
Target Experiments at Rutherford
Laser Focus 14, 36 (1978)

J.D. Hares, J.D. Kilkenny, M.H. Key and J.G. Lunney
Measurement of Fast Electron Energy Spectra and Preheating in Laser Irradiated Targets
Phys. Rev. Letts. (in press)

R.J. Hutcheon, L. Cooke, M.H. Key, C.L.S. Lewis, G.E. Bromage
Neon-like and Fluorine-like X-ray Emission Spectra for Elements from Cu to Sr
Phys. Scripta 19, 276 (1979)

M.H. Key, C.L.S. Lewis, J.G. Lunney, A. Moore, T.A. Hall, R.G. Evans
Production and Diagnosis by Pulsed X-ray Shadowgraphy of Dense Cool Laser Imploded Plasmas
Phys. Rev. Letts. 41, 1467 (1978)

M.H. Key
Megagauss Magnetic Fields in Laser Produced Plasmas
Nature 276, 210 (1978)

M.H. Key, C.L.S. Lewis, M.J. Lamb
Transient Population Inversion at 18.2 nm in a Laser Produced CVI Plasma
Optics Communications 28, 331 (1979)

M.H. Key, M.J. Lamb, C.L.S. Lewic, A. Moore, R.G. Evans
X-ray Streak Camera Study of the Dynamics of Laser Imploded Microballoons
Appl. Phys. Letts. (in press)

M.H. Key, J.G. Lunney, J.M. Ward, R.G. Evans and P.T. Rumsby
Plasma Parameters in Laser Imploded Targets fron Space Resolved X-ray Spectroscopy
J. Phys. B. 12, L213 (1979)

R.W. Lee
Plasma Line Broadening of the Lyman α Transition Including Ion Dynamics
J. Phys. B. 11, L167 (1978)

R.W. Lee
Study of the Plasma Broadening of Spectral Lines of Hydrogenic Ions
J. Phys. B.(1979)(in press)

R.W. Lee
Study of Ion Dynamic Effects on Lyman and Balmer Hydrogenic Lines
J. Phys. B. (1979)(in press)

R.W. Lee
A Model Study of Non-Thermal Effects in the Plasma Broadening of Spectral Lines J. Phys. B. (1979) (in press)

M.W. McGeoch
An Electrostatic Analyser for Laser-Produced Plasmas: Ion Spectra for Polythene at 10.6 μm
Culham Laboratory Report CLM-R-186 (1978)

M.W. McGeoch
Scaling Laws for Plasma Production and Pellet Acceleration by Laser
Nuclear Fusion 19, 633 (1979)

D.J. Nicholas, C. Pataky and W.T. Welford
High Aperture Lens for Laser Compression Experiments: A New Type
Applied Optics 17, 3368 (1978)

N.J. Peacock
XUV Emission as a Diagnostic of Laser Heated Plasmas
Proceedings of 1978 Varenna Summer School in Plasma Diagnostics
(in press, Pergammon)

A. Raven and O. Willi
Electron Density Structures in Laser Produced Plasmas at High Irradiances
Submitted to Phys. Rev. Letts.

A. Raven, O. Willi, P.T. Rumsby
Megagauss Magnetic Field Profiles in Laser Produced Plasmas
Phys. Rev. Letts. 41, 554 (1978)

M.J. Shaw
Excimer Lasers
Progress in Quantum Electronics 13, 1 (1979)

W.P.S. Tan, E.W. Laing
Anomalous Magnetic Field Reversal in Laser-Plasma Interaction
Phys. Lett. 67A, 272 (1978)

L.M. Wickens, J.E. Allen, P.T. Rumsby
Ion Emission from Laser Produced Plasmas with Two Electron Temperatures
Phys. Rev. Lett. 41, 243 (1978)

O. Willi, A. Raven and P.T. Rumsby
Self-Generated Magnetic Fields in Laser Produced Plasmas
submitted to Phys. Lett.

CONFERENCE CONTRIBUTIONS

Papers presented at the Fifth Annual Conference on Plasma Physics, St. Andrews, June 1978:

T.J.M. Boyd
Theory and Numerical Experiment in Plasma Physics - a Symbiosis?
(Invited Lecture)

H.C. Barr
Generation of $3\omega_0/2$ Harmonic by the Two-Plasmon Decay Instability

W.T. Hewitt, G.A. Gardner
Harmonic Generation by Stimulated Raman Scattering in Laser Produced Plasmas

A. Raven, P.T. Rumsby, O. Willi
Megagauss Magnetic Field Profiles in Laser Produced Plasmas

Paper presented at the Topical meeting on Inertial Confinement Fusion, San Diego, February 1978:

M.H. Key et al
Laser Driven Implosion of Gas Filled Microballoons (paper WA2, available as report RL-78-020)

Paper presented at Seventh International Conference on Plasma Physics and Controlled Nuclear Fusion Research, Innsbruck, August 1978:

R.G. Evans et al
Dynamics of Laser Produced Implosion of Gass Filled Microballoon Targets
(Paper IAEA-CN-37-D-5, available as report RL-78-095)

Papers presented at the Twelth European Conference on Laser Interaction with Matter, Moscow, December 1978:

M.H. Key
Review of Recent Progress in Laser Plasma Interaction and Laser Compression Work at the SRC Rutherford Laboratory Central Laser Facility
(available as report RL-79-014)

L. Cooke, T.A. Hall, M.H. Key, M.J. Lamb, C.L.S. Lewis, J.C. Lunney, L.M. Newell, A. Moore
Ablative Compression Experiments at Rutherford Laboratory

J. Lunney, J. Kilkenny, J.D. Hares, P. Salter, M.H. Key
Energy Transport by Fast Electrons

W. Toner
Experiment with Thin Plastic Foils

Paper presented at the Am. Institute of Physics 31st Gaseous Electronics Conference, Buffalo, October 1978:

M.W. McGeoch
Energy Transfer in the Mercury Cadmium System
(paper AA4, Abstract to appear in Bull. Am. Phys. Soc.